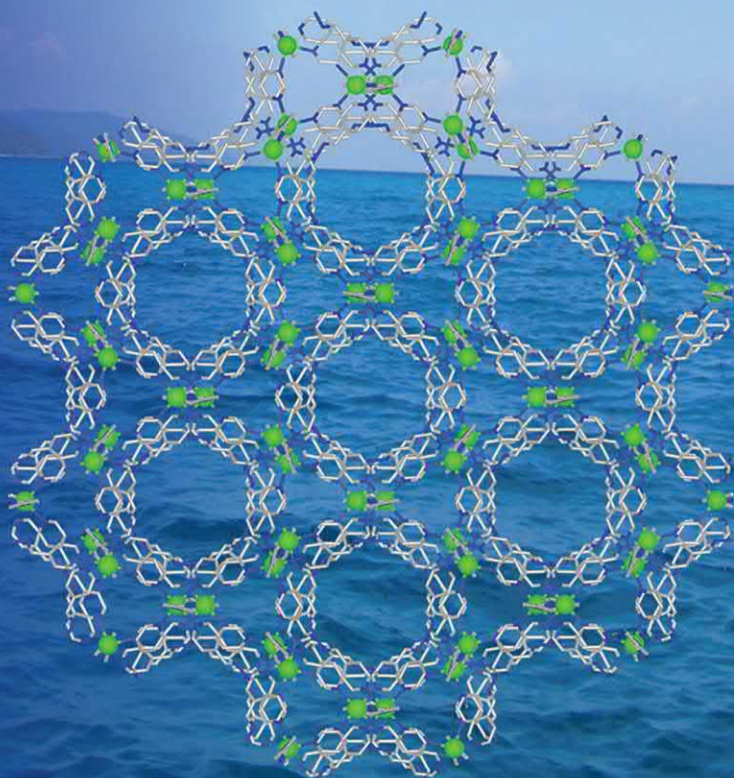


METAL-ORGANIC FRAMEWORKS (MOFs) FOR ENVIRONMENTAL APPLICATIONS



Edited by
SUJIT K. GHOSH

Metal-Organic Frameworks (MOFs) for Environmental Applications

Metal-Organic Frameworks (MOFs) for Environmental Applications

Edited by

Sujit K. Ghosh

Department of Chemistry, Indian Institute of Science Education and Research (IISER), Pune, India

Centre for Energy Science, Indian Institute of Science Education and Research (IISER), Pune, India



ELSEVIER

Elsevier

Radarweg 29, PO Box 211, 1000 AE Amsterdam, Netherlands
The Boulevard, Langford Lane, Kidlington, Oxford OX5 1GB, United Kingdom
50 Hampshire Street, 5th Floor, Cambridge, MA 02139, United States

Copyright © 2019 Elsevier Inc. All rights reserved.

No part of this publication may be reproduced or transmitted in any form or by any means, electronic or mechanical, including photocopying, recording, or any information storage and retrieval system, without permission in writing from the publisher. Details on how to seek permission, further information about the Publisher's permissions policies and our arrangements with organizations such as the Copyright Clearance Center and the Copyright Licensing Agency, can be found at our website: www.elsevier.com/permissions.

This book and the individual contributions contained in it are protected under copyright by the Publisher (other than as may be noted herein).

Notices

Knowledge and best practice in this field are constantly changing. As new research and experience broaden our understanding, changes in research methods, professional practices, or medical treatment may become necessary.

Practitioners and researchers must always rely on their own experience and knowledge in evaluating and using any information, methods, compounds, or experiments described herein. In using such information or methods they should be mindful of their own safety and the safety of others, including parties for whom they have a professional responsibility.

To the fullest extent of the law, neither the Publisher nor the authors, contributors, or editors, assume any liability for any injury and/or damage to persons or property as a matter of products liability, negligence or otherwise, or from any use or operation of any methods, products, instructions, or ideas contained in the material herein.

British Library Cataloguing-in-Publication Data

A catalogue record for this book is available from the British Library

Library of Congress Cataloging-in-Publication Data

A catalog record for this book is available from the Library of Congress

ISBN: 978-0-12-814633-0

For Information on all Elsevier publications
visit our website at <https://www.elsevier.com/books-and-journals>

Publisher: Susan Dennis

Acquisition Editor: Emily McCloskey

Editorial Project Manager: Michael Lutz

Production Project Manager: Prem Kumar Kaliamoorthi

Cover Designer: Greg Harris

Typeset by MPS Limited, Chennai, India



List of Contributors

Melih Baci Department of Chemistry, Texas A&M University, College Station, TX, United States

Moises A. Carreon Department of Chemical and Biological Engineering, Colorado School of Mines, Golden, CO, United States

Wenmiao Chen Department of Chemistry, Texas A&M University, College Station, TX, United States

Kevin Dedecker Institut Lavoisier de Versailles, UMR CNRS 8180, Université de Versailles St-Quentin-en-Yvelines, Université Paris-Saclay, 78035 Versailles Cedex, France; Centre de Recherche sur la Conservation (CRC), Muséum National d'Histoire Naturelle, CNRS, Ministère de la Culture, USR3224, 36 rue Geoffroy Saint Hilaire, 75005, Paris, France

Aamod V. Desai Department of Chemistry, Indian Institute of Science Education and Research (IISER), Pune, India

Eddy Dumas Institut Lavoisier de Versailles, UMR CNRS 8180, Université de Versailles St-Quentin-en-Yvelines, Université Paris-Saclay, 78035 Versailles Cedex, France

Subhajit Dutta Department of Chemistry, Indian Institute of Science Education and Research (IISER), Pune, India

Paolo Falcaro Institute of Physical and Theoretical Chemistry, Graz University of Technology, Graz, Austria

Yu Fang Department of Chemistry, Texas A&M University, College Station, TX, United States

Omar K. Farha Department of Chemistry, International Institute of Nanotechnology, Northwestern University, Evanston, IL, United States; Department of Chemistry, Faculty of Science King Abdulaziz, University Jeddah, Jeddah, Saudi Arabia

Mingbao Feng Department of Environmental and Occupational Health, School of Public Health, Texas A&M University, College Station, TX, United States

Sujit K. Ghosh Department of Chemistry, Indian Institute of Science Education and Research (IISER), Pune, India; Centre for Energy Science, Indian Institute of Science Education and Research (IISER), Pune, India

Ashlee J. Howarth Department of Chemistry and Biochemistry, Concordia University, Montréal, QC, Canada

Angelo A. Kirchon Department of Chemistry, Texas A&M University, College Station, TX, United States

Susumu Kitagawa Institute for Integrated Cell-Material Science (iCeMS), Kyoto, Japan

Amrit Kumar Department of Chemical Sciences, Bernal Institute, University of Limerick, Limerick, Republic of Ireland

Subhajit Laha Molecular Materials Laboratory, Chemistry and Physics of Materials Unit, School of Advanced Materials, Jawaharlal Nehru Centre for Advanced Scientific Research, Bangalore, India

Bertrand Lavédrine Centre de Recherche sur la Conservation (CRC), Muséum National d'Histoire Naturelle, CNRS, Ministère de la Culture, USR3224, 36 rue Geoffroy Saint Hilaire, 75005, Paris, France

Shengqian Ma Department of Chemistry, University of South Florida, Tampa, FL, United States

Zachary Lawrence Magnuson Department of Chemistry, University of South Florida, Tampa, FL, United States

Marek B. Majewski Department of Chemistry and Biochemistry, Concordia University, Montréal, QC, Canada

Tapas Kumar Maji Molecular Materials Laboratory, Chemistry and Physics of Materials Unit, School of Advanced Materials, Jawaharlal Nehru Centre for Advanced Scientific Research, Bangalore, India

Soumya Mukherjee Department of Chemical Sciences, Bernal Institute, University of Limerick, Limerick, Republic of Ireland

Raffaele Ricco Institute of Physical and Theoretical Chemistry, Graz University of Technology, Graz, Austria

Syamantak Roy Molecular Materials Laboratory, Chemistry and Physics of Materials Unit, School of Advanced Materials, Jawaharlal Nehru Centre for Advanced Scientific Research, Bangalore, India

Partha Samanta Department of Chemistry, Indian Institute of Science Education and Research (IISER), Pune, India

Christian Serre Institut des Matériaux poreux de Paris (IMAP), UMR CNRS 8004, Ecole Normale Supérieure de Paris, Ecole Supérieure de Physique et de Chimie Industrielles de Paris, PSL University, 75005, Paris, France

Shivani Sharma Department of Chemistry, Indian Institute of Science Education and Research (IISER), Pune, India

Virender K. Sharma Department of Environmental and Occupational Health, School of Public Health, Texas A&M University, College Station, TX, United States

Nathalie Steunou Institut Lavoisier de Versailles, UMR CNRS 8180, Université de Versailles St-Quentin-en-Yvelines, Université Paris-Saclay, 78035 Versailles Cedex, France

Mark J. Styles CSIRO Manufacturing, Clayton South, VIC, Australia

Qi Wang Department of Chemistry, Texas A&M University, College Station, TX, United States

Shuao Wang State Key Laboratory of Radiation Medicine and Protection, School for Radiological and Interdisciplinary Sciences (RAD-X), Collaborative Innovation Center of Radiation Medicine of Jiangsu Higher Education Institutions, Soochow University, Suzhou, P.R. China

Chengliang Xiao State Key Laboratory of Radiation Medicine and Protection, School for Radiological and Interdisciplinary Sciences (RAD-X), Collaborative Innovation Center of Radiation Medicine of Jiangsu Higher Education Institutions, Soochow University, Suzhou, P.R. China

Liqiu Yang Department of Chemical and Biological Engineering, Colorado School of Mines, Golden, CO, United States

Michael J. Zaworotko Department of Chemical Sciences, Bernal Institute, University of Limerick, Limerick, Republic of Ireland

Peng Zhang Department of Chemistry, Texas A&M University, College Station, TX, United States

Hong-Cai Zhou Department of Chemistry, Texas A&M University, College Station, TX, United States

Introduction

1

Sujit K. Ghosh^{1,2,*} and Susumu Kitagawa^{3,*}

¹Centre for Energy Science, Indian Institute of Science Education and Research (IISER), Pune, India, ²Department of Chemistry, Indian Institute of Science Education and Research (IISER), Pune, India, ³Institute for Integrated Cell-Material Science (iCeMS), Kyoto, Japan

*Corresponding authors: e-mail address: sghosh@iiserpune.ac.in and kitagawa-g@icems.kyoto-u.ac.jp

Metal-organic frameworks (MOFs) or porous coordination polymers (PCPs) form a distinguished subset in the domain of coordination chemistry: they are broadly regarded as coordination networks bearing potential voids [1]. Constructed from organic struts which extend infinitely in a periodic manner through metal nodes, MOFs represent an advanced class of porous materials that have been subject to a remarkable upsurge over the last few decades. The myriad choice of building blocks along with access to combinatorial chemistry affords the synthesis on demand of architectures whose properties can be directly linked to the structural characteristics. These features have made MOFs highly sought-after over congener porous solid materials, for example, zeolites and activated carbon. Further, the ability to modulate nanospace properties, control pore size and nature, access mesoporosity, utilize reticular chemistry, and incorporate active sites in porous compounds as per demand has resulted in MOFs commanding research interest across disciplines. The spectrum of potential applications using MOFs has broadened with the evolution of this field, which prominently include gas storage/separation, adsorptive separation of industrially challenging liquid mixtures, ion-conduction, sensing and photonics, heterogeneous catalysis, drug delivery, etc. [2,3].

The rise of MOF chemistry can be primarily ascribed to the following broad reasons: growing knowledge of structural characteristics retrieved from a library of reported compounds, and the greater precision to obtain read-out and control host–guest chemistry in different media. In particular the rise of third generation of MOFs (soft porous crystals) has actuated the development of MOFs toward applications based on such host–guest chemistry [4]. The ability to have guest-responsive structural dynamics has further propelled their ability to operate as functional solids with a high precision and selectivity of guest accommodation and recognition response. Apart from softness, MOFs bear the inherent ability to incorporate specific active sites which have promoted the applicability of these compounds toward a wide array of gas or liquid adsorption, which are either environmentally noxious or industrially relevant. In addition to the liberty of designing a specific

probe/sorbent, MOFs offer the choice to pick transduction mechanisms based on the specific field of application, such as electromagnetic responses, photonic responses, and naked-eye colorimetry. Other than conventional applications, recently MOFs have started demonstrating affirmative potential toward their utility in the recognition, capture, and detoxification of environmental toxins that are present in different media including air, water, and soil.

Addressing environmental pollution has become one of the greatest challenges for human civilization in the 21st century. This is clearly reflected in the list of sustainable development goals benchmarked by the United Nations [5]. The direct correlation in the higher emission or release of toxic species with the change in ecological balance has prompted the pressing need to curb the presence of pollutants. For instance, in 2018, a report by World Health Organization (WHO) raised the alarm, by suggesting that more than 90% of the human population on Earth is breathing polluted air [6].

Porous materials have emerged as suitable receptors to entrap environmental pollutants or detoxify them into safe substances on account of very high surface areas, high porosity, and ease in design of molecular scale functional voids. Due to several advantages MOFs score over conventional porous adsorbents, but the major bottleneck in pursuit of MOFs realizing applicability in this domain has been the stability under operating conditions or susceptibility of MOF compounds to decompose upon exposure to moisture. Recently, there has been a conscious effort in the field to address this issue and encouraging progress and long-term promise has been witnessed [7]. Apart from stability, another issue which has retarded the investigation of MOFs under real-time conditions has been the lack of strategies to form devices from microcrystalline MOF powders. Hence, composites based on MOFs have received greater attention, and more intensive research in this regard can propel the realization of MOF-based devices [8]. In addition to these major roadblocks, issues such as toxicity, durability, life-cycle assessment studies (LCA), bulk-scale synthesis, and cost-effectiveness are unavoidable and require careful consideration while proposing the utility of a newly developed material in real-time scenarios [9,10].

The book attempts to focus on the progress of MOFs and understand the long-term trends which have been studied and proposed by the leading names across the globe. Chapter 8, Metal-organic frameworks for detection and desensitization of environmentally hazardous nitro-explosives and related high energy materials, by Ghosh and coworkers emphasizes the utility of MOFs toward sensing and desensitization of nitroaromatic compounds (NACs) and related explosive compounds. Chapter 2, Metal-organic framework-based carbon capture and purification technologies for clean environment, by Zawrotko and coworkers revisits the major milestones in the domain of MOFs for the storage and separation of greenhouse gas carbon dioxide (CO₂) and explains the roadmap going ahead. Carreon and coworkers have described the role of MOFs as heterogeneous catalysts for the greener ways of generating fuels in Chapter 9, Green deoxygenation of fatty acids to transport fuels over metal-organic frameworks as catalysts and catalytic supports. The subsequent two chapters, Chapter 3, Sensing and sequestration of inorganic cationic pollutants by metal-organic frameworks (Ma and coworkers) and Chapter 4,

Metal-organic frameworks for recognition and sequestration of toxic anionic pollutants (Ghosh and coworkers), deal with the various approaches wherein MOFs have been able to sense or trap ionic pollutants. Chapter 5, Metal-organic frameworks for the capture of volatile organic compounds and toxic chemicals, by Serre and coworkers discusses the state-of-art for utilizing MOFs for air-pollution control. Chapter 6, Metal-organic frameworks for capture and detoxification of nerve agents, by Farha and coworkers extends the discussion in previous chapter and highlights the progress of MOFs toward the capture and detoxification of chemical warfare agents. Zhou and coworkers (Chapter 7: Metal-organic frameworks for capture and degradation of organic pollutants) and Maji and coworkers (Chapter 10: Potential of hydrophobic metal-organic framework-based materials for environmental applications) provide a flavor of the research carried out toward remediation of water pollution with the focuses on degradation of organic pollutants and separation of oil–water mixtures, respectively. The growing dependence on nuclear power has resulted in the emission of high quantum of nuclear waste in aqueous streams. Wang and coworkers (Chapter 11: Radionuclide sequestration by metal-organic frameworks) describe the progress of MOFs toward the capture of such radioactive species. Finally the chapter by Ricco and coworkers (Chapter 12: Metal-organic framework-based devices for detection and removal of environmental pollutants) gives the reader a flavor of the research in the community devoted toward the development of MOFs in workable forms or as components of portable devices.

All the contributing authors are thanked for their insightful contributions, and the Elsevier team are thanked for all the backroom support. The book endeavors to provide the reader, either in academia or industry, with an essence of the research in the domain of MOFs devoted toward pressing practical concerns, and the editor hopes that the wide array of topics covered in this book can accomplish that objective.

References

- [1] S.R. Batten, N.R. Champness, X.-M. Chen, J. Garcia-Martinez, S. Kitagawa, L. Ohrstrom, et al., Terminology of metal–organic frameworks and coordination polymers (IUPAC Recommendations 2013), *Pure Appl. Chem.* 85 (2013) 1715–1724.
- [2] H. Furukawa, K.E. Cordova, M. O’Keeffe, O.M. Yaghi, The chemistry and applications of metal-organic frameworks, *Science* 341 (2013) 1230444.
- [3] S. Yuan, L. Feng, K. Wang, J. Pang, M. Bosch, C. Lollar, et al., Stable metal–organic frameworks: design, synthesis, and applications, *Adv. Mater.* (2018). Available from: <https://doi.org/10.1002/adma.201704303>.
- [4] S. Horike, S. Shimomura, S. Kitagawa, Soft porous crystals, *Nat. Chem.* 1 (2009) 695–704.
- [5] www.un.org/sustainabledevelopment/sustainable-development-goals/.
- [6] <http://www.who.int/airpollution/data/cities>.
- [7] A.J. Howarth, Y. Liu, P. Li, Z. Li, T.C. Wang, J.T. Hupp, et al., Chemical, thermal and mechanical stabilities of metal–organic frameworks, *Nat. Rev. Mater.* 1 (2016) 15018.

- [8] P. Falcaro, R. Ricco, C.M. Doherty, K. Liang, A.J. Hill, M.J. Styles, MOF positioning technology and device fabrication, *Chem. Soc. Rev.* 43 (2014) 5513–5560.
- [9] P.A. Julien, C. Mottillo, T. Friscic, Metal–organic frameworks meet scalable and sustainable synthesis, *Green Chem.* 19 (2017) 2729–2747.
- [10] C.A. Grande, R. Blom, A. Spjelkavik, V. Moreau, J. Payet, Life-cycle assessment as a tool for eco-design of metal-organic frameworks (MOFs), *Sust. Mater. Technol.* 14 (2017) 11–18.

Metal-organic framework based carbon capture and purification technologies for clean environment

2

*Soumya Mukherjee, Amrit Kumar and Michael J. Zaworotko**

Department of Chemical Sciences, Bernal Institute, University of Limerick, Limerick, Republic of Ireland

*Corresponding author. email address: xtal@ul.ie

2.1 Introduction—the societal relevance of carbon capture and sequestration

The human race is now in the “age of gas,” which means that gases and vapors have largely replaced liquids with respect to fuels for society and feedstocks for the chemical industry [1]. The energy footprint associated with gas and vapor purification is enormous; currently 40% of the energy consumed in the chemical industry is used just for commodity separations and purification. This equates to roughly 15% of global energy production and it has been estimated that the demand for commodities could triple by 2050 [2]. Whereas EU member states are committed to a 40% reduction in greenhouse gas emissions as part of the 2030 climate and energy framework [3], which also calls for 27% improvement in energy efficiency, these ambitious societal goals will likely become moot if the high energy footprint associated with commodity purification remains unaddressed.

The foremost anthropogenic gas carbon dioxide, CO₂, lies at the heart of achieving energy sustainability for several reasons. Sustained burning of fossil fuels since the beginning of the industrial revolution has increased atmospheric CO₂ concentration to >400 ppm from 280 ppm [4]. Today’s power plants will emit a further 300 billion tons of CO₂ in the future, enough to contribute an additional 20 ppm of CO₂ to the atmosphere. Atmospheric CO₂ is not just relevant to climate change, it becomes a major health issue as concentrations of as little as 600 ppm can lead to respiratory illnesses [5]. Occupational health and safety regulations dictate that CO₂ concentrations in confined spaces should be limited to <0.5% CO₂ [6]. In this context, air purification devices are employed in spacecraft and submarines to control CO₂ concentrations [7]. Industrially, trace removal of CO₂ is important in purification of flue gas and natural gas (NG) processing. Specifications require CO₂ concentrations in NG liquefaction (LNG) of <50 ppm to avoid corrosion and CO₂

freezing [8]. These applications encompass a diverse range of CO₂ concentrations, conditions, and gas mixtures, thereby making it unlikely that there is a single solution for C-capture. Rather, bespoke approaches and materials with optimal properties are needed to address the specific requirements of a given carbon capture application.

Since fossil fuels will remain the primary energy source for generations and gases with CO₂ impurities are important feedstocks for the chemical industry, new approaches to cost-effective and energy-efficient carbon capture and sequestration (CCS) are urgently needed. The broad roll-out of CCS has thus far been hampered by high costs (50–100 US\$ per ton of CO₂ captured at best), the techno-economic uncertainties of CCS technologies, and to date, the lack of suitable material alternatives to liquid amine-based CCS technologies [9]. Liquid amine CCS technologies are the current state-of-the-art for carbon capture and they have been utilized in this context for over half a century. This is despite the fact that liquid amines rely upon chemical reactions that are energy-intensive, they are not economically viable for broad deployment, and they offer little room for innovation. The ambitious targets for CO₂ emissions reductions by 2030 therefore require innovative approaches to CCS technologies that improve both the energy footprint and cost-effectiveness of CCS. In this chapter, we focus upon the potential offered by new classes of advanced physisorbents for carbon capture, C-capture, which in principle are capable of reducing the energy footprint of C-capture processes by up to 90% [2]. Table 2.1 lists the various approaches to C-capture and presents their advantages/disadvantages along with an assessment of their upside potentials. The state-of-the-art with respect to bulk-scale C-capture can be subdivided into two main classes as defined by the mode of capture.¹

1. *Chemisorption* functions through chemical reaction between the capture material (sorber) and CO₂ (Fig. 2.1, left). The primary advantage of chemisorbents is that they are typically highly selective but, because recycling of the sorber requires the breakage of chemical bonds, they tend to exhibit a high energy footprint. In addition, the kinetics of chemisorption processes is likely to be relatively slow if CO₂ concentrations are low. Examples of chemisorbents include the following:
 - a. The state-of-the-art for bulk-scale C-capture at industrial scale involves *liquid amines* as chemisorbents. These processes, initially developed in the 1930s, are built around liquid amine solutions that chemically react with CO₂. *Drawbacks*: Whereas liquid amine-based “wet scrubbers” are effective at C-capture they suffer from high regeneration energy (> 140°C), large equipment size, amine degradation, and equipment corrosion [10]. These factors collectively amount to a 30%–40% reduction in the overall efficiency of a power plant when liquid amine CCS is employed for postcombustion C-capture and the associated costs are in the range of €70–100 per ton. Further, there is very limited potential to significantly improve performance.
 - b. Solid chemisorbents such as *soda lime* have also been used for C-capture, especially in closed circuit breathing environments. *Drawback*: reactions are too slow for large-scale C-capture applications.
 - c. Liquid chemisorbents developed for wet air C-capture have also used the *soda-lime* process. *Drawback*: CO₂ abatement costs are prohibitively high, the *American Physical Society* estimating costs of US\$600 per ton of CO₂ [11].

Table 2.1 Comparison of the strengths and weaknesses of selected C-capture methods.

	Amine grafted inorganics	Liquid amines	Amine grafted MOFs	Ionic liquids	Soda lime	Zeolites	MOFs	HUMs	Molecular sieves
Selectivity	High	High	High	High	High	Low	Low	Very high	Infinite
Stability	High	Low	Medium	High	High	High	Low	Medium	Low
Humidity effect	Low	Low	Medium	Low	Low	High	High	Medium	Low
Material cost	Medium	Low	High	Low	Low	Low	Medium/high	Low	High
Process cost	Medium	Low	High	Medium	Low	Low	Medium	Low	High
Recycling cost	Medium	High	Medium	Medium/high	Very high	High	High	Low	N/A
Working capacity	Medium	Medium	Medium	Low	Medium	Medium	High	Medium	N/A
Kinetics	Medium	Fast	Medium	Fast	Fast	Medium	Medium	Fast	N/A
Upside potential	Medium	Low	Medium	Medium	Low	Low	High	High	High

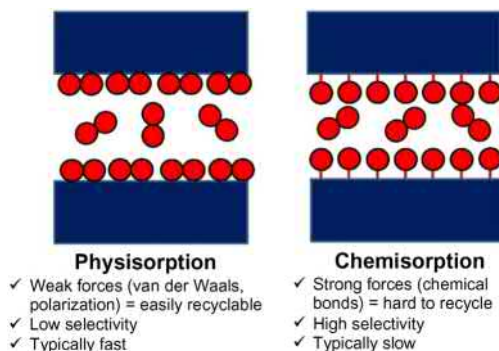


Figure 2.1 Types of sorption based separation/purification: chemisorption versus physisorption.

- d. *Amine-modified porous materials*: the introduction or “grafting” of amine functional groups onto porous materials (typically MOFs, mesoporous silicas, and zeolites) can significantly increase the affinity of a porous material towards CO₂. *Drawbacks*: high regeneration energy (>90°C), the materials can be typically expensive and/or difficult to produce, and they can suffer from chemical and thermal instability [12,13].
 - e. *Ionic liquids (ILs)* which contain amine groups have been touted as a potential long-term replacement for liquid amines in CCS technologies as ILs have been found to exhibit significantly better chemical and thermal stability than aqueous amines. *Drawbacks*: ILs exhibit relatively low uptake and working capacity and IL–CO₂ interactions are based upon the same chemisorption process as liquid amines so they also require elevated temperatures during the IL regeneration cycle [14].
2. *Physisorption* represents a fundamentally different approach to C-capture since it relies upon the physical properties of CO₂ such as its ability to engage in noncovalent interactions and its size (Fig. 2.1, right). In principle, as indicated by Table 2.1, advanced physisorbents that selectively capture CO₂ from gas mixtures offer the greatest upside potential for a revolution in C-capture technology since they would require much less energy for recycling, can exhibit high working capacity, and, if designed properly, will be unaffected by moisture. However, there are still obstacles that must be overcome before deployment becomes feasible.
- a. Porous physisorbents offer potential to improve the energy efficiency of C-capture because of their relatively low energy footprint for recycling. The current benchmark physisorbents are *zeolites* and *metal-organic frameworks, MOFs*, specifically, zeolite 13X and Mg-MOF-74, respectively. *Drawbacks*: these top-performing physisorbents are handicapped by relatively poor selectivity for CO₂ over the other components of industrial gas mixtures (principally CH₄, N₂, O₂, and, especially, H₂O), which limits their use for trace C-capture. The relatively high cost and/or poor stability of MOFs are also of concern [15].
 - b. *Size exclusion* could be used by *molecular sieves* to separate CO₂ from larger gas molecules [16]. *Drawbacks*: requires a material with a very specific pore size, fabrication into a membrane is difficult, and would not restrict water vapor, which exhibits a smaller kinetic diameter (2.65 Å) than that of CO₂.
 - c. *Hybrid ultramicroporous materials (HUMs)*. HUMs [17,18] are a recently introduced class of physisorbents that exhibit new benchmarks for CO₂ selectivity versus important gases such as N₂ and CH₄. HUMs therefore have the potential to address the full

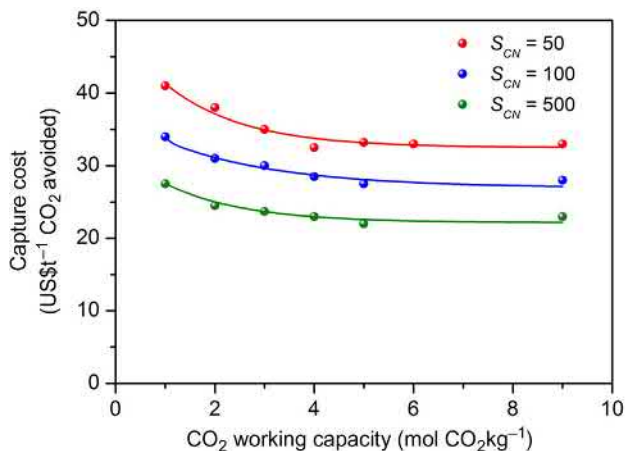


Figure 2.2 Relationship between the costs of C-capture, CO₂ selectivity, and working capacity for solid physisorbents [23].

range of C-capture applications, including trace capture. HUMs combine <0.7 nm pores with strong electrostatics that enhance the energetics of sorbent–sorbate interactions [19–22]. HUMs are therefore highly selective and can target even the most challenging separations/purifications, such as removal of trace impurities of CO₂ from gas mixtures and C-capture from complex wet gas mixtures. The selectivity performance of HUMs ($S_{CN} > 1000$) is such that they can be projected to significantly improve the process cost of carbon capture (Fig. 2.2) [23].

In this chapter we focus on the potential for advanced physisorbents based upon porous coordination networks such as MOFs [24], porous coordination polymers, PCPs [25], and HUMs [17,18] to enable innovation with respect to their deployment in CCS technologies. We emphasize how the molecular level control of pore size and pore chemistry that can be achieved in such physisorbents and their compositional diversity can be used to tailor performance with respect to separation of gas mixtures in a manner that is not so readily achieved in other classes of sorbents. However, we also address the hurdles that remain to be overcome before implementation can occur.

2.2 Spectrum of performance parameters and criteria for evaluation of sorbents

Before we discuss specific classes of sorbents, it would be appropriate to address relevant performance parameters and criteria. A spectrum of performance parameters must be addressed and evaluated before a sorbent is selected as a lead candidate. Some are more relevant to early stage discovery whereas others matter at later stages of development. These criteria are presented in Fig. 2.3 and are discussed individually in this section.

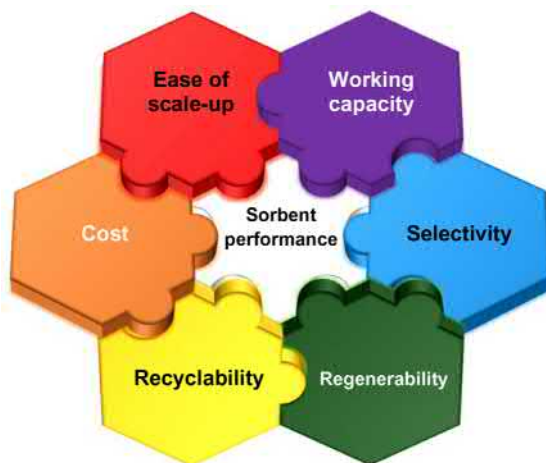


Figure 2.3 The spectrum of performance parameters that must be met by a sorbent being considered for development with respect to storage and/or purification technologies.

2.2.1 Working capacity

Working capacity is a key criterion for evaluating sorbent performance since it influences how much sorbent is required for a particular process. The saturation uptake of a sorbent provides information on the maximum amount of CO_2 that can be adsorbed by a given sorbent and can be readily determined using pure gas adsorption experiments that provide gravimetric or volumetric measures of uptake. Gravimetric saturation uptake capacity is the amount of CO_2 adsorbed per unit mass sorbent ($\text{gram CO}_2 \text{ g}^{-1}$ sorbent, or $\text{cm}^3 \text{ CO}_2 \text{ g}^{-1}$ sorbent) at 195K. Volumetric saturation uptake capacity is the CO_2 uptake per volume of sorbent ($\text{g CO}_2 \text{ cm}^{-3}$ sorbent, or $\text{cm}^3 \text{ CO}_2 \text{ cm}^{-3}$ sorbent) at 195K. These saturation uptake values are useful as a first assessment of the potential utility of a sorbent. However, the uptake of CO_2 adsorbed at the loading conditions that are relevant to the process in question is a more relevant parameter. Working capacity (ΔN_{CO_2}), the difference between the uptake of CO_2 at the adsorption (loading) and desorption (release) conditions of temperature and pressure of the process in question, is the most relevant measure of uptake performance.

$$\Delta N_{\text{CO}_2} = N_{\text{ads}} - N_{\text{des}}$$

Whereas CO_2 uptake values at 1 bar are relatively easy to measure and frequently reported, they are unlikely to be reliable indicators of sorbent performance at the partial pressures of CO_2 typically present in a complex gas mixture [26]. CO_2 uptake at the process relevant partial pressure(s) serves as a more appropriate parameter and can also be determined from pure gas isotherms (Fig. 2.4). Fig. 2.4 also highlights how important the type of isotherm can be with respect to working capacity. Most rigid sorbents exhibit type-I or Langmuir isotherms (Fig. 2.4, left)

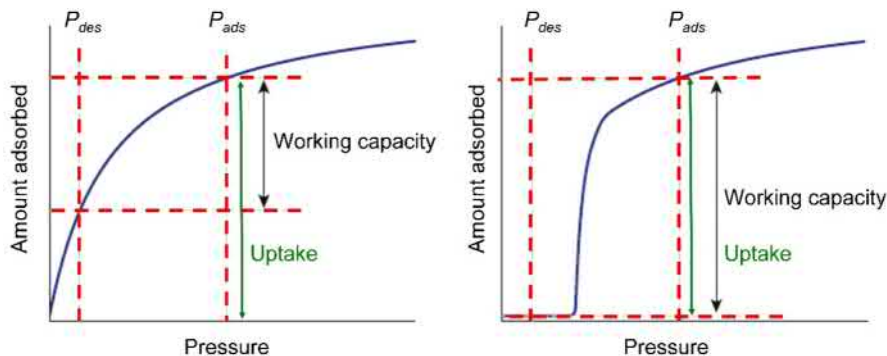


Figure 2.4 Schematic illustrating how the working capacity can differ between adsorbents with the same uptake but with two distinct isotherm types. Left: a type-I isotherm as exhibited by most rigid microporous sorbents; right: a type F-IV isotherm as found in flexible sorbents that can switch between closed (nonporous) and open (porous) phases [27].

whereas flexible sorbents can exhibit stepped or type F-IV [27] isotherms (Fig. 2.4, right). The latter is much less common but can be highly advantageous since working capacity can be 100% of uptake capacity in flexible materials.

2.2.2 CO_2 selectivity, $S_{\text{ads}}(\text{CO}_2)$

CO_2 selectivity for a sorbent defines the sorption uptake ratio of CO_2 over another gas under a given set of conditions. Selectivity versus nitrogen (S_{CN}) is relevant with respect to postcombustion C-capture whereas selectivity versus methane (S_{CM}) is particularly relevant for NG purification. As revealed by Fig. 2.2, a fivefold increase in S_{CN} , for example, from 100 to 500, would be expected to significantly reduce C-capture expense per tonne (> 45 to $\sim 30\text{€ t}^{-1} \text{CO}_2$) [23]. Selectivity also impacts the purity of adsorbed gas and levels in the outlet (effluent) gas stream. For a binary mixture, the *adsorption selectivity* (S_{ads} or α_{ij}) is defined as follows

$$S_{\text{ads}} = \frac{q_i/q_j}{p_i/p_j}$$

where $q_{i,j}$ and $p_{i,j}$ denote the working capacities and partial pressures for components i and j , respectively. This is also referred to as *Ideal selectivity (IS)* or *molar selectivity*.

An alternative method is to calculate *Henry's law selectivity*, wherein the CO_2 selectivity over N_2 is calculated based on the Henry's constants (K_H) of the gases:

$$S_{\text{CN}} = \frac{K_{\text{H}(\text{CO}_2)}}{K_{\text{H}(\text{N}_2)}}$$

The ratio of the Henry's law constants, that is, Henry's law selectivity reflects the real mixture selectivity only at very low pressure and low loadings [28].

IAST. A commonly used method to estimate selectivity is based upon Ideal Adsorbed Solution Theory (IAST), which uses the single-component adsorption isotherms of CO₂ and competing gas(es) [29]. IAST calculations, which can be performed using a modified version of the program IAST [29], pyIAST [30], are limited by three assumptions:

1. The pure components form an ideal mixture (no change in area or enthalpy upon mixing of pure components), a reasonable approximation for most systems.
2. The area accessible to both adsorbates is equal (i.e., the sorbent is not a molecular sieve).
3. The thermodynamic properties of the sorbent do not change relative to the thermodynamic properties of the sorbate (i.e., there is no sorbate-induced phase transition).

IAST uses the data points of the experimental single-component isotherms under a particular temperature for different gases interpolated via numerical quadrature:

$$\frac{A}{RT}\pi_i(P_i^\circ) = \int_0^{P_1} \frac{n_i^\circ(P)}{P} dP + \sum_{j=1}^{k-1} \int_{P_j}^{P_{j+1}} \frac{n_i^\circ(P)}{P} dP + \int_{P_k}^{P_i^\circ} \frac{n_i^\circ(P)}{P} dP \quad (2.1)$$

A model of each isotherm is formulated where the spreading pressure, $A/RT\pi_i(P_i^\circ)$, from absolute vacuum to the first data point is assumed to follow Henry's law:

$$n_i^\circ(P) = K_H P \quad (2.2)$$

where n_i° is uptake, and P is pressure, and therefore:

$$\int_0^{P_1} \frac{n_i^\circ(P)}{P} dP \approx \int_0^{P_1} K_H dP = n_i^\circ(P_1) \quad (2.3)$$

Between the first to the last experimental isotherm data points, the function $n_i^\circ(P)$ is approximated via linear interpolation:

$$\int_{P_j}^{P_{j+1}} \frac{n_i^\circ(P)}{P} dP \approx m_j(P_{j+1} - P_j) + b_j \log\left(\frac{P_{j+1}}{P_j}\right) \quad (2.4)$$

where m_j is the slope and b_j is the intercept of the line that passes through the points $(P_j, n_i^\circ(P_j))$ and $(P_{j+1}, n_i^\circ(P_{j+1}))$. The index k defines the range $P_k \leq P_i^\circ \leq P_{k+1}$. Therefore the integral $\int_{P_k}^{P_i^\circ} \frac{n_i^\circ(P)}{P} dP$ acts in the same way as Eq. (2.4) but accounts for the line that passes through interpolated points. This means that the spreading pressure is most sensitive to the low-coverage regime of the single-component adsorption isotherm [30]. It is important to note that Langmuir, BET, Langmuir–Freundlich, dual-site Langmuir–Freundlich and quadratic equations can be employed instead of Henry's law to fit/model the pure component isotherms, as applicable [31].

The practical advantage of selectivity values derived from IAST and Henry's Law is that they enable estimation of the separation performance solely from single-component sorption isotherms without the need for complicated and costly mixed-gas equipment. However, breakthrough measurements in a fixed-bed reactor with model i.e., simulated gas mixtures are much closer to the actual practice of gas capture/separation, and sorption selectivity predicted from IAST calculations can drastically differ from real mixed-gas separations because the latter is conducted under kinetic flow conditions, often under nonequilibrium conditions [32]. Moreover, regenerability and recyclability (particularly, moisture-mediated) cannot be accurately evaluated using adsorption instruments, whereas these parameters can be addressed by mixed gas breakthrough measurements. Further, a few process engineering aspects, such as particle size influence on backpressure of the column or heat management issues, can be modeled that are beyond the reach of pure gas adsorption measurements [33]. Therefore, dynamic breakthrough experiments using dry and wet gas mixtures are in general a much better indicator of real-world performance.

Breakthrough experiments are typically conducted at room temperature with ~ 0.5 g of pre-activated sample placed in a quartz tubing of predetermined uniform diameter to form a "fixed bed." The sorbent bed is purged under a steady flow of He before the breakthrough experiment is conducted. Upon cooling to 25°C , a multicomponent gas mixture of desired composition, typically with He as the carrier gas, is introduced. For C-capture/commodity purification testing, this feed is generally binary in nature, that is, CO_2/N_2 , CO_2/CH_4 , $\text{CO}_2/\text{C}_2\text{H}_2$, H_2/CO_2 (each, either dry or moisture-mediated). Whereas the inlet gas composition is precisely controlled and kept unaltered during experiment(s), the outlet gas composition is continuously monitored by mass spectrometry (MS) or gas chromatography (GC) until complete breakthrough is achieved. Experiments in the presence of controlled relative humidity (% RH) are performed by passing the gas stream through a water vapor saturator at 25°C . After each dry and wet breakthrough experiment, the packed column bed is regenerated using temperature or pressure swing or a combination of both, under constant He flow for extended time to ensure complete sample regeneration. The amount of adsorbed gas i (q_i) is calculated from the breakthrough curve as follows:

$$q_i = \frac{V_T \Delta T P_i}{m}$$

Here, V_T is the total flow rate of gas ($\text{cm}^3 \text{min}^{-1}$), P_i is the partial pressure of gas i (atm), ΔT is the time for initial breakthrough of gas i to occur (minutes), and m is the mass of the sorbent (g). The separation factor (α) for the breakthrough experiment, that is, breakthrough derived selectivity, is determined as follows:

$$\alpha = \frac{q_1 y_2}{q_2 y_1}$$

where y_i is the partial pressure of gas i in the gas mixture. In the case where one gas component has negligible adsorption, the amount of gas adsorbed is treated as $\leq 1 \text{ cm}^3$ for calculation purposes. To compare the relative C-capture/purification efficiency of different adsorbents, it is important to consider three parameters: separation factor (α), working capacity (as calculated from the breakthrough profiles), and breakthrough time. Strong CO_2 -sorbent interactions and fast kinetics will improve these performance parameters.

2.2.3 Regenerability

Minimizing the energy input for regeneration via fine-tuning of the thermodynamics of interaction between the sorbent and CO_2 is one of the most critical considerations to improve the energy efficiency of C-capture [26]. This is dependent upon two factors: enthalpy of adsorption and adsorption/desorption kinetics. Pressure swing (PSA), vacuum swing (VSA), and temperature swing (TSA) are the methods most commonly used to regenerate sorbents. For PSA (Fig. 2.5, middle) or VSA (Fig. 2.5, right) recycling, the column pressure is reduced after adsorption in order to desorb the captured gas, that is, $P_{des} < P_{ads}$. For PSA, the inlet gas is pressurized via compression and flowed through the column until it reaches saturation. On closing the inlet valve, the column pressure declines toward ambient pressure. During this process, significant amounts of sorbate desorb and elute from the column. VSA reduces column pressure to subatmospheric pressure after adsorption at a higher pressure to remove the sorbate. For gas release near ambient pressure (e.g., post-combustion), compressing or evacuating such a large volume of gas is difficult, and TSA ($T_{des} > T_{ads}$) is likely to be more viable (Fig. 2.5, left) [34]. That precombustion involves an inherently pressurized gas stream (after the conversion reactions)

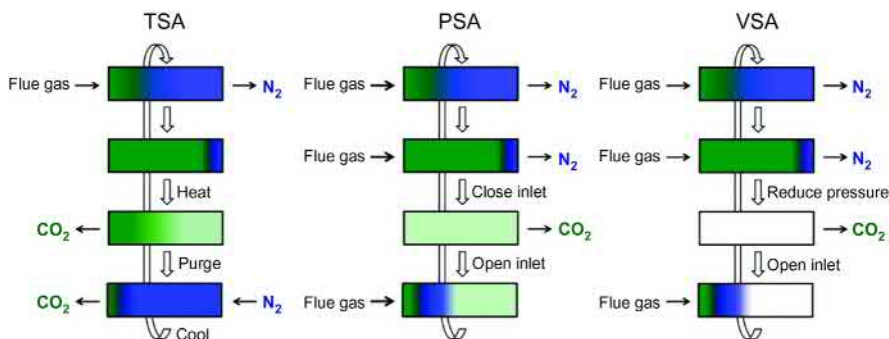


Figure 2.5 Schematic diagrams of temperature swing adsorption (TSA), pressure swing adsorption (PSA), and vacuum swing adsorption (VSA) employed for sorbent regeneration in a fixed-bed column.

Source: Reprinted with permission from K. Sumida, D.L. Rogow, J.A. Mason, T.M. McDonald, E.D. Bloch, Z.R. Herm, et al., Carbon dioxide capture in metal-organic frameworks, *Chem. Rev.* 112 (2012) 724–781. Copyright (2016) American Chemical Society.

means that a PSA cycle is most likely to be preferred [35]. The efficiency of sorbent regeneration is affected by two primary factors, the enthalpy associated with adsorption and the kinetics of adsorption/desorption.

2.2.3.1 Enthalpy of adsorption (Q_{st})

Isosteric enthalpy of adsorption, Q_{st} , is a measure of the heat released during adsorption and therefore provides a guide to the energy required to regenerate the sorbent. The amount of heat needed to regenerate a sorbent is a parameter that significantly influences regeneration cost. $Q_{st}(\text{CO}_2)$ for a sorbent can be calculated from its low-pressure CO_2 adsorption isotherms collected at different temperatures (often the temperatures studied are 273K, 283K, and 298K). In general, virial-type equations are used to fit at least ten low-pressure points in the adsorption data at multiple temperatures (Eq. 2.5) [36].

$$\ln P = \ln n + \left(\frac{1}{T^2}\right) \sum_{i=0}^j a_i n^i + \sum_{i=0}^k b_i n^i \quad (2.5)$$

Q_{st} is then calculated from the virial model using Eq. (2.6).

$$-Q_{st} = -R \sum_{i=0}^j a_i n^i \quad (2.6)$$

Q_{st} is the coverage-dependent enthalpy of adsorption, and R is the universal gas constant. Generally, higher relative enthalpies of adsorption result in higher selectivity and would render a sorbent more suited for removal of trace amounts of adsorbate from industrial gas streams. However, a high enthalpy of adsorption would also be expected to result in a high energy footprint for recycling the sorbent. This is an area where physisorbents would be expected to offer significant advantages over chemisorbents because even a high Q_{st} value for a physisorbent is likely to be less than that of a chemisorbent. For example, some physisorbents that have been subjected to temperature swing regeneration require a regeneration temperature of $<55^\circ\text{C}$ (e.g., HUMs like SIFSIX-2-Cu-i [19], TIFSIX-2-Cu-i [37], SIFSIX-14-Cu-i [20]), whereas $\sim 75^\circ\text{C}$ – 150°C treatment is required for chemisorbents studied for C-capture such as PEI (Polyethyleneimine) modified MCM-41 [38] and TEPA (tetraethylenepentamine) modified SBA-15 [39].

2.2.3.2 Sorption kinetics

Adsorption–desorption cycle time is greatly dependent upon the CO_2 adsorption–desorption kinetics of a given material. Kinetics can be measured via dynamic breakthrough and temperature-programmed desorption experiments. This aspect of sorption performance remains thus far understudied in MOFs and PCPs. Sorbents that adsorb and desorb CO_2 in a shorter time are preferred as these reduce cycle

time as well as the amount of sorbent required, and ultimately curtail cost. This is another performance parameter where physisorbents might be expected to offer significant advantages over chemisorbents, especially for trace capture of CO₂.

2.2.4 Recyclability (hydrolytic, mechanical, and thermal stability)

A sorbent must demonstrate stability under the conditions of a process and during many cycles of adsorption–desorption. Strong thermal, mechanical, and hydrolytic stability under the conditions of a process are essential for recycling of sorbents. Unfortunately, poor mechanical stability to pressure changes and/or poor hydrolytic stability that result in poor recyclability plague most MOFs. Sorbents which need heating during regeneration, either TSA or PTSA (pressure-temperature swing) must be thermally robust since repeated heating cycles will otherwise cause sorbent degradation.

The thermal stability of sorbents can be evaluated using two complementary methods. High-resolution thermogravimetric analysis coupled with either MS or FT-IR can be used to determine the identity and quantity of component weight loss versus temperature. Variable-temperature PXRD can probe if elevated temperatures result in reversible or irreversible structural changes. These tests can be used to determine the optimal activation procedures for a sorbent during gas sorption experiments and temperature swing recycling. Hydrolytic stability can be addressed by using standard stability tests that were designed to measure shelf-life of drug substances and drug products. In particular, accelerated stability tests conducted at 40°C and 75% RH over 1, 7, and 14 days [40] can determine the likely shelf-life of a sorbent. Unlike most MOFs, a number of HUMs were found to exhibit hydrolytic stability comparable to inorganic materials such as silicas and zeolites [15,41].

2.2.5 Sorbent cost based upon substrates

Sorbents that exhibit excellent sorption performance must also be judged based upon the cost of substrates used to prepare the sorbent. The practicality of using a MOF sorbent in a C-capture process will not just rely on its physicochemical properties but also upon the cost of its ingredients. That metal salts are generally inexpensive means that linker ligand cost is typically the main factor that will affect the cost of a sorbent. Many MOF sorbents are based upon polycarboxylate ligands, some of which are prepared using cross-coupling reactions. Nevertheless, there are a number of commercially available, inexpensive ligands. For example, 4,4'-bipyridine, bipy, is the most common ligand in the recently published MOF subset of the Cambridge Structural Database, CSD with over 4000 entries [42]. Among carboxylates, 1,4-benzenedicarboxylate (BDC) based structures are the most commonly studied with ~3100 entries. These ligands would be highly appropriate starting points for sorbent design, synthesis, and manufacture given the scale of sorbent production that would be needed for most C-capture applications.

2.2.6 Feasibility of scale-up

Scale-up can represent an obstacle to the development of a sorbent [43]. Upon identifying a sorbent candidate with desirable properties and performance, it must be determined if it can be manufactured in sufficient quantity to enable later stage development including formulation and pilot-scale testing. Synthetic methods that are amenable to scale-up are generally understudied in the context of MOFs, yet such studies are needed in order to move a sorbent to higher technological readiness levels (TRLs). Pilot-scale MOF production through direct mixing or solvent-free solid-state grinding, that is, mechanochemical methods (e.g., ball milling, high pressure compression, single or twin-screw extrusion (TSE), solvent-free grinding with heating), is desirable but not always viable. Nevertheless, TSE has been implemented for kg per hour-scale MOF production and offers the advantages of continuous synthesis with reduced or no solvent requirements [44]. Given that mechanochemical synthesis is a subject of growing academic interest [45], the amenability of a sorbent to mechanochemical synthesis is likely to become a part of sorbent selection protocols.

2.3 Overall evaluation of sorbent performance: sorbent selection parameters

The ideal sorbent would be expected to optimally address all of the parameters discussed in Section 2.2. In the early stages of sorbent development, selectivity, working capacity, and adsorption enthalpy are of particular relevance to identify potential lead candidates for further development. However, it is likely that there will be a trade-off between these factors since, for example, high surface area materials are less likely to offer high selectivity. Evaluating a series of candidate sorbents is a nontrivial task because of trade-offs. A few selection metrics have recently emerged to simplify the process of identifying lead candidate sorbents.

- The *adsorbent performance indicator (API)* was recently proposed by Llewellyn et al. [46]. API considers the volumetric working capacity (WC), adsorption enthalpies ($\Delta_{ads}h$) and selectivity values ($\alpha_{1/2}$), as indicated below:

$$API = \frac{(\alpha_{1/2} - 1)^A WC_1^B}{\Delta_{ads}h^C}$$

A, B, and C are multiples used to weigh the relative importance of each term that is used to calculate the API for a sorbent for gas 1 over 2. Selectivity of component 1 over component 2 ($\alpha_{1/2}$) can be calculated from IAST selectivity or molar selectivity [29]. The API affords a parameter that can be used to compare sorbents in order to facilitate selection of a lead candidate for a given process. However, it does not address some of the later stage parameters discussed above.

- The *separation potential* (ΔQ) has been put forward by Krishna as a key sorbent selection criteria, which combines $S_{ads}(\text{CO}_2)$ and working capacity (ΔN_{CO_2}) in a manner which mimics aspects of a fixed bed adsorption process [47].

$\Delta Q = N_{ads,\text{CO}_2} \times (p_i/p_{\text{CO}_2}) - N_{ads,i}$; p_i and p_{CO_2} denote the partial pressures for component i (N_2 or CH_4 , in general) and CO_2 , respectively.

- Keskin et al. proposed a new approach of considering *percent regenerability* ($R\%$) to comparatively assess MOFs because high CO_2 selectivities in sorbents often suffer from very low $R\%$ ($<75\%$) [48].

$$R\% = \frac{\Delta N_{\text{CO}_2}}{N_{ads,\text{CO}_2}} \times 100\%$$

- The *adsorbent performance score* (APS) was introduced in 2018 [49] and is the product of selectivity and working capacity. Efficient adsorbents that exhibit high selectivity and high working capacity would offer high APS values.

$\text{APS} = S_{ads(\text{CO}_2)/i} \times \Delta N_{\text{CO}_2}$; in general, i : N_2 or CH_4 in the binary mixture.

2.4 Current CO_2 capture technologies

2.4.1 Point-source CO_2 capture

Reduction of CO_2 emissions from point sources such as power plants can be addressed using three main approaches: (1) postcombustion; (2) precombustion; and (3) oxy-fuel combustion (Fig. 2.6). All three approaches suffer an energy penalty of c. 10%–14% on account of the energy footprint associated with gas feed separation, capture, conditioning, and compression/liquefaction of the captured CO_2 [50].

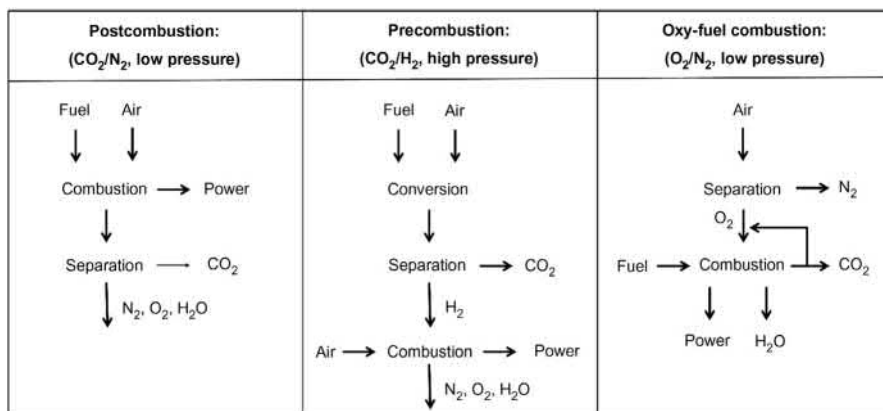


Figure 2.6 The three types of point-source CO_2 capture.

Source: Adapted from K. Sumida, D.L. Rogow, J.A. Mason, T.M. McDonald, E.D. Bloch, Z. R. Herm, et al., Carbon dioxide capture in metal-organic frameworks, Chem. Rev. 112 (2012) 724–781.

This reduces power plant efficiency and somewhat overshadows the upside potentials of all these technologies [51].

2.4.1.1 Postcombustion

Processes that involve C-capture after combustion must take into account flue gas cleaning processes such as removal of dust, nitrogen, and sulfur compounds and are collectively termed “Postcombustion” processes [52]. In postcombustion capture, CO₂ is removed from the flue gas that results after combustion of the fuel in air (composition as described in Table 2.2). This is predominantly a CO₂/N₂ gas separation owing to high N₂ content in the ambient air used for combustion and has been the most explored strategy thus far since a postcombustion C-capture system could be retrofitted to existing power plants. *Liquid amine absorption* or *amine scrubbing* currently represent the state-of-the-art for bulk CCS and CCU but liquid amines suffer from cost and corrosion challenges.

Liquid amine processes have been tested and applied for industrial CO₂ removal from process gas streams largely because they are based upon chemisorption and they can exhibit high separation/purification performance [38,53]. The most commonly used amines are alkanolamines, such as monoethanolamine (MEA), diethanolamine (DEA), and methyldiethanolamine (MDEA), dissolved in water. A schematic illustration of a liquid amine absorption plant for CO₂ postcombustion capture is presented in Fig. 2.7A. Liquid amine absorption is an energy-intensive technology and its most extensive use is in the context of NG sweetening.

Table 2.2 Typical conditions for the three major C-capture processes: postcombustion, precombustion, and natural gas sweetening processes.

	Precombustion	Postcombustion ^a	Natural gas upgrading
Gas composition (by mole)			
CO ₂	10%–15%	37.7%	0.1%–8%
H ₂ O	5%–10%	0.14%	
O ₂	3%–4%	55.5%	0%–0.2%
H ₂			
CO	20 ppm	3.9%	70%–95%
NO _x	< 800 ppm		
N ₂	70%–75%	0.4%	0%–15%
SO _x	< 500 ppm		
CH ₄			0%–15%
H ₂ S			0%–15%
C ²⁺			
Conditions			
Temperature (°C)	40–75	40	30–40
Pressure (bar)	1	30	5–120

^aAfter water-gas shift reaction is over.

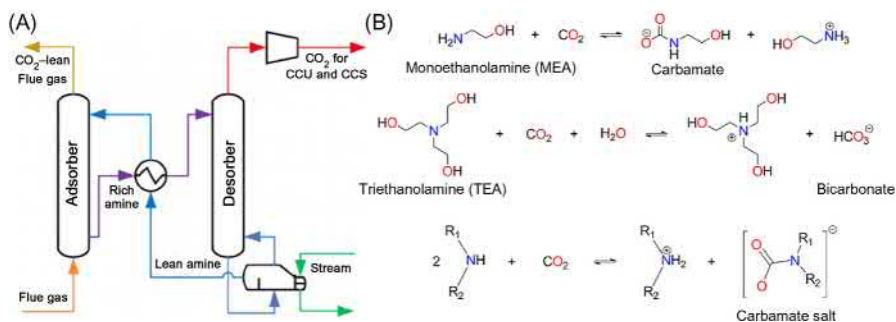


Figure 2.7 (A) Schematic of a typical liquid amine scrubber system. (B) CO₂ capture with monoethanolamine (MEA) (reacts in 1:2 stoichiometry) to yield carbamate, and the analogous reaction with triethanolamine (TEA) (reacts in 1:1 stoichiometry) leading to bicarbonate species.

Source: (A) Adapted from B. Dutcher, M. Fan, A.G. Russell, Amine-based CO₂ capture technology development from the beginning of 2013—a review, *ACS Appl. Mater. Interfaces* 7 (2015) 2137–2148 [54]. (B) Adapted from K. Sumida, D.L. Rogow, J.A. Mason, T.M. McDonald, E.D. Bloch, Z.R. Herm, et al., Carbon dioxide capture in metal-organic frameworks, *Chem. Rev.* 112 (2012) 724–781.

The utility of liquid amines with respect to power plants is handicapped by their high energy footprint, c. 30% of the power plant's output and the inherent corrosive nature of amine absorbents. The high energy cost for amine regeneration results from the relative stability of the carbamate or bicarbonate species generated after reaction between CO₂ and amines (Fig. 2.7B) [55]. A bicarbonate requires less energy to recycle than a carbamate, so the energy required to reverse amine–CO₂ interactions usually follows the trend primary > secondary > tertiary amines. The overall regeneration energy in a C-capture system would also depend on other factors such as amine concentration [26]. Amine scrubbing technologies typically suffer from decomposition of liquid amines in the presence of oxygen, other foreign substances (e.g., dust) and SO_x or NO_x mediated amine degradation [50].

2.4.1.2 Precombustion

Precombustion methods combine converting the fuel in question (composition as presented in Table 2.2) to hydrogen-rich synthesis gas and capturing the resulting CO₂ prior to combustion. Decarbonized fuel gas is then channeled to a combined gas and steam turbine cycle for electricity production. The C-capture process occurs next to fuel gas production and CO conversion to CO₂ and H₂. Precombustion can therefore be regarded as C-capture from the reformed synthesis gas of an upstream gasification unit (Fig. 2.6) [50]. Plant designs enable conversion of the gas produced from gasification (commonly known as “syngas”) to H₂ and CO₂ and removal of CO₂ from the syngas stream prior to the combustion of the H₂ rich gas in the gas turbine [56]. The state-of-the-art with regards to precombustion is deployed in NG processing and NG reforming, whereby CO₂ acid gas removal

(AGR) is accomplished using liquid amine absorption [57]. The AGR stripping and regeneration processes are consequently energy-intensive and reduce the overall efficiency of the NG production process.

2.4.1.3 Oxy-fuel combustion

The terms “oxy-fuel combustion” or “oxy-fuel process” denote the combustion of carbon containing fuels with pure oxygen (Fig. 2.6). Instead of air, use of nearly pure O₂ for fuel combustion results in CO₂ enrichment of the flue gas. Unlike conventional power plants, for which CO₂ content in flue gas is typically 12%–15% by volume, CO₂ content for combustion products from oxy-fuel plants lies around c. 90% by volume [10]. On condensing the steam produced in such plants, pure CO₂ flue gas can be obtained which, after demineralization, drying, and compression, can be transported to a storage site [58]. An advantage to this technology is that combustion products can be pumped directly to the storage site without any further purification due to the high CO₂ content present in the outgas feed. However, recycling a considerable fraction of flue gas stream back into the combustion chamber along with a changed volume of excess air present a number of technical/scientific challenges. For example, the lowered fraction of excess O₂ can lead to burning out issues and corrosion of the combustion chamber walls. In addition, thermodynamic integration of the CO₂ processing units into multistaged CO₂ condensers is a challenge.

2.4.2 Direct air capture of CO₂

Direct air capture (DAC) is the process of capturing CO₂ directly from air and generating a concentrated stream of CO₂ for sequestration or industrial use as a commodity [59]. DAC belongs to a group of technologies referred to as negative emissions, or carbon dioxide removal technologies [10], as it is capable of scavenging CO₂ that has already been released from point sources [60]. First introduced by Lackner in 1999 [61], there has been much discussion of the benefits and need of DAC, which is a subject of growing scientific and technological interest. An increasing number of academics have been shifting their attention to developing materials and processes for DAC and several start-up companies (e.g., Climeworks, based in Zurich) are pushing this technology from lab scale to pilot-scale demonstration. DAC technology can also be relevant to control of CO₂ levels in confined spaces such as submarines and spacecraft [62]. For indoor environmental quality, DAC materials could facilitate onsite trace (1000–10,000 ppm) capture of CO₂ [63].

DAC requires the presence of strong yet reversible CO₂ binding sites in the sorbent and, in the case of physisorbents, optimal pore size and shape. That the kinetic diameters of CO₂ (3.3 Å), O₂ (3.46 Å), and N₂ (3.64 Å) are similar and the atmospheric concentration of CO₂ is relatively low, makes DAC a technical and scientific challenge of the highest order. DAC is also economically challenged since costs have been estimated of c. \$600 per ton of CO₂ [64] and can only be partly compensated by reusing CO₂ in greenhouses. The emergence of high-performance

sorbents means, however, that this “artificial trees technology” could cost \$100 per ton of CO₂ by 2025 or 2030 and capture 1% of global CO₂ emissions by 2025 [64].

2.4.3 Industrial trace CO₂ removal

A number of industrially relevant gas mixtures contain trace-level impurities of CO₂ that must be removed. Some of the more important gas mixtures are discussed below.

2.4.3.1 Acetylene purification

Acetylene (C₂H₂) is an important chemical commodity that, amongst other uses, serves as a source of acrylic acid to manufacture acrylic fibers, glasses, paints, resins, and polymers [65]. The closely related physicochemical properties of C₂H₂ and CO₂ (Fig. 2.8; boiling points: −84.7°C and −78.5°C, respectively; molecular dimensions 3.3 × 3.3 × 5.7 and 3.2 × 3.3 × 5.4 Å, respectively) mean that separating these gases is challenging [37]. Current C₂H₂ production methods involve the partial combustion of methane (CH₄) or separation from the distillates produced during steam cracking in the petroleum-refining process. Both methods introduce CO₂ as contaminant which must be removed later. C₂H₂ purification currently deploys organic solvents (DMF or acetone) to extract CO₂ and generates a large amount of solvent waste. Physisorbents that offer highly selective C₂H₂/CO₂ sorption performances would be much more energy-efficient than solvent extraction [66] but the strict upper pressure limits for processes involving pure C₂H₂ (2 bar) and the aforementioned closeness in physicochemical properties means that physisorbents are yet to be deployed.

2.4.3.2 Natural gas sweetening

NG, which is comprised of methane (80%–95%), ethane, propane, butane, and nitrogen, has a lower carbon-content than petroleum fuels such as diesel and gasoline (Table 2.2) [67]. Global NG production has grown an average of 2.3% per year over the past decade in OECD (Organization for Economic Cooperation and Development) countries [68]. Emerging economies such as Iran (+6.2%) and China (+4.7%) recorded even higher consumption increases in 2015 [68]. NG is the

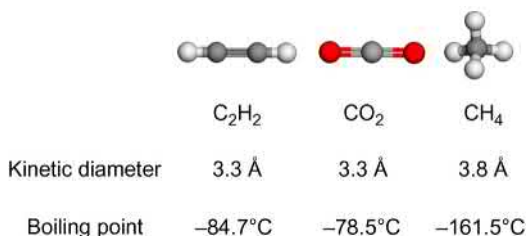


Figure 2.8 The similar physical parameters of C₂H₂, CH₄, and CO₂.

second largest energy source in power generation, now representing 22% of generated power globally, and it is the only fossil fuel whose share of primary energy consumption is projected to grow [69]. A large proportion of NG is transported globally in liquefied form (LNG). However, before liquefaction of NG is conducted, CO₂ levels must be reduced to below 50 ppm to avoid corrosion [70]. The similar kinetic diameters (3.8 vs 3.3 Å) and close boiling points of CH₄ and CO₂ once again represent a separation challenge (Fig. 2.8).

Three approaches can be used to purify NG: absorption, adsorption, and membranes. Chemisorption by liquid amines is the state-of-the-art despite the aforementioned toxic, volatile, and corrosive properties of amines. Further, liquid amines are prone to decomposition and loss of performance over time [54]. They also suffer a high energy penalty during regeneration [71]. Membrane technology is a promising alternative for removing CO₂ from NG, however its utilization is limited as it is difficult to fabricate large-area, defect-free membranes. Although physisorbents have been studied for upgrading NG, landfill gas, or biogas (15%–50% CO₂ impurity), reducing trace levels of CO₂ from NG to below 50 ppm is a challenging task as traditional porous solids such as activated carbons (ACs) and zeolites do not exhibit high enough selectivity (> 200) to accomplish this task.

2.4.3.3 Hydrogen purification

H₂ is an important feedstock for multiple industries such as the metallurgical and steel industries, petrochemical and refining industries, glass manufacturing, and H₂O₂ production. The purification or separation of hydrogen has traditionally utilized solid-state diffusion technology, that is, noble metal (Pd) and metal alloy (Ag-Pd) membranes [72]. For hydrogen recovery/purification where the feed stream is at low to intermediate pressure (<1000 pounds per square inch) and where downstream process requirements demand minimum pressure reduction/high purity hydrogen product, PSA technology can meet process demands [73]. Isothermal PSA process with only depressurization needed to regenerate the sorbent bed results in a higher lifetime of the adsorbent material. However, slow kinetics and limited performance parameters, including a trade-off between diffusivity and working capacity for this membrane-based state-of-the-art necessitates the search for advanced physisorbents.

2.5 Types of sorbents currently being studied for CO₂ capture

2.5.1 Ionic liquids

ILs are often regarded as a potential long-term substitute for liquid amines in CCS technologies as ILs can exhibit significantly better physicochemical stability than aqueous amines [74–76]. Thus, the use of ILs as alternative solvents would result in a number of advantages over traditional amine-based CO₂ extraction methods.

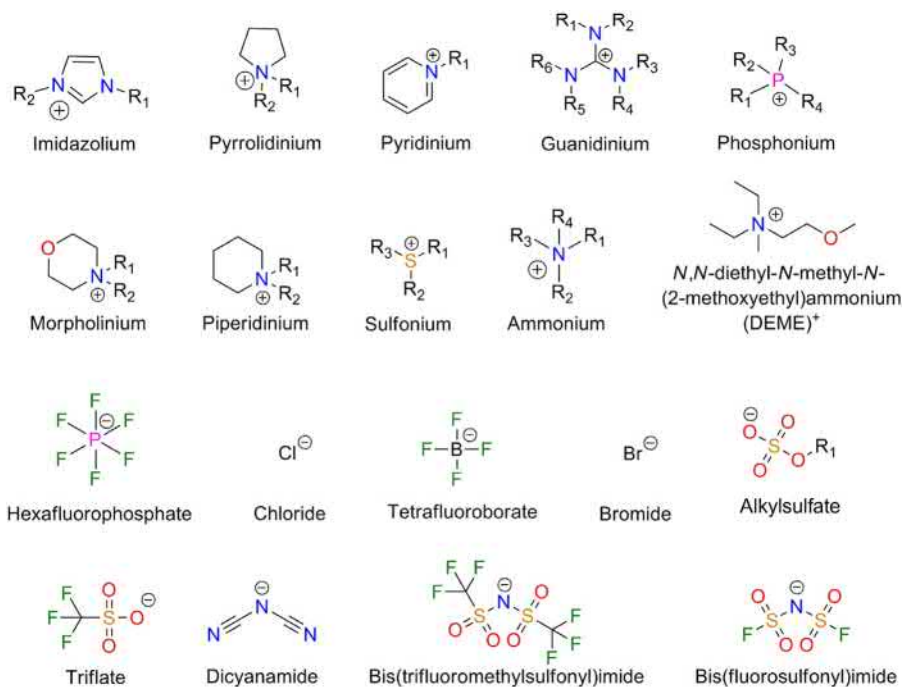


Figure 2.9 Common cations and anions used in ionic liquids studied for C-capture.

ILs are salts that are liquid at or near ambient conditions and common examples of the ions used in ILs are presented in Fig. 2.9. Negligible vapor pressure is perhaps the main advantage of ILs since this means zero contamination of the gas stream and negligible loss of IL during a separation process. In addition to offering a lower energy footprint in the solvent regeneration step because of low volatility, key properties of ILs include high CO₂ solubility, good thermal stability, and the possibility of systematically tuning composition toward improved properties [77]. Amine-modified ILs, also known as task-specific ILs (TSILs), are widely discussed in literature in terms of their physical and chemical interactions with CO₂ [78]. Shear viscosity, η plays a role in process design of ILs because high viscosity after CO₂ adsorption can lead to mass transfer limitations [79]. Other drawbacks of ILs are that they exhibit relatively low capacity and the origin of IL–CO₂ interactions is chemisorption. Relatively high temperatures are therefore needed for IL regeneration [14]. Recent reports have introduced amine-IL mixtures with low viscosity/cost [80] but much work will be needed to overcome the other limitations of ILs/TSILs.

2.5.2 Solid adsorbents

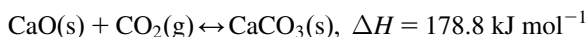
A large number of solid sorbents, including MOFs, have been recently investigated as potential candidates for low temperature C-capture [26,55,81,82]. As discussed

in Section 2.2, selection of candidates cannot be based just upon their adsorption properties (working capacity, enthalpy of adsorption, kinetics) because other factors must play a role in the selection of lead candidates. A lead candidate should therefore exhibit high CO₂ uptake at low-pressure, high CO₂ selectivity, fast adsorption/desorption kinetics, good mechanical properties, high hydrothermal and chemical stability, and low cost of ingredients and manufacture.

2.5.2.1 Chemical adsorbents/chemisorbents

IUPAC defines chemisorption as adsorption that results from chemical bond formation (strong interaction) between the chemisorbent and the adsorbate in a monolayer on the surface [83]. A number of chemisorption processes are being investigated.

Calcium looping/soda lime process: Calcium looping (CaL) technology, which is based on multicycle carbonation/calcination of CaO in gas–solid fluidized bed reactors at high temperature, has emerged in the last few years as a potential C-capture technology [84]. CaL is in essence a family of C-capture technologies that use CaO as a regenerable sorbent for CO₂:



Both carbonation and calcination reactions are conducted at elevated temperatures (650°C–700°C and 900°C, respectively) to allow efficient heat recovery in the process or during the steam cycle of power generation [85]. Use of this chemical loop was first attempted in the 19th century as it was noted that gasification gases would afford higher heating power when coal was gasified in the presence of CaO.

The alkali carbonate-based process offers potential due to the relatively small energy penalty imposed upon a power station (estimated at 6%–8%), its potential use in large-scale circulating fluidized beds (a mature technology), and the low cost of CaO (crushed limestone) [86]. The major downside to this process lies with the significant decline in limestone reactivity over repeated cycles [87]. Ongoing research concerning this process therefore revolves around investigating different methods to either reduce the rate of decay in reactivity, to boost the long-term reactivity of sorbent, or to improve sorbent reactivation.

Amine-modified inorganic materials (AMIMs): An advantage of some porous inorganic solids is their amenability to grafting of active groups such as amines onto their internal pore surface. Inorganic porous materials such as mesoporous silicas (i.e., MCM-41, SBA-15 etc.) are generally characterized by low CO₂ uptake due to weak surface interactions with CO₂. However, their highly ordered pore systems and tuneable pore sizes offer large surface areas/pore volumes and a high density of surface silanols provides excellent opportunities for grafting and modification of sorption properties.

In 1995, Leal and Bolivar introduced C-capture in amine-modified silica when they functionalized a silica aerogel with propylamine [88]. Since then, CO₂ adsorption by AMIM sorbents has been a subject of great interest. In 2002, Xu et al.

developed PEI modified MCM-41 to serve as a nanoporous “molecular basket” for CO_2 in waste gas streams (Fig. 2.10). CO_2 adsorption capacity of as high as $133 \text{ mg CO}_2 \text{ g}^{-1}$ adsorbent was achieved [38]. Yue et al. subsequently studied the CO_2 sorption performance of TEPA modified SBA-15 (mesoporous silica). By leaving the organic template in situ, micelles were used for dispersing guest species and the TEPA dispersed within the channels of SBA-15 were found to be highly accessible to CO_2 . A high adsorption capacity of $173 \text{ mg CO}_2 \text{ g}^{-1}$ adsorbent was reported [89].

Belmabkhout et al. induced a series of modifications on MCM-41: they synthesized a pore-expanded form (PE-MCM-41) and successively introduced amine groups in its expanded form (TRI-PE-MCM-41) [91,92]. TRI-PE-MCM-41, which combines the advantages of a large pore structure due to the presence of amine groups, showed a dramatic improvement in adsorption capacity, especially in the low-pressure region. CO_2 uptake at 0.1 bar and 25°C was comparable with that of zeolite 13X (2.2 mmol g^{-1}). Despite its capacity being comparable with zeolite 13X, the amine-modified sample exhibited a significant increase of CO_2 uptake in the presence of water, which is critical for most C-capture applications. The use of a secondary amine was found to improve the recyclability of this adsorbent thanks to reduced amine degradation and deactivation [13,93,94].

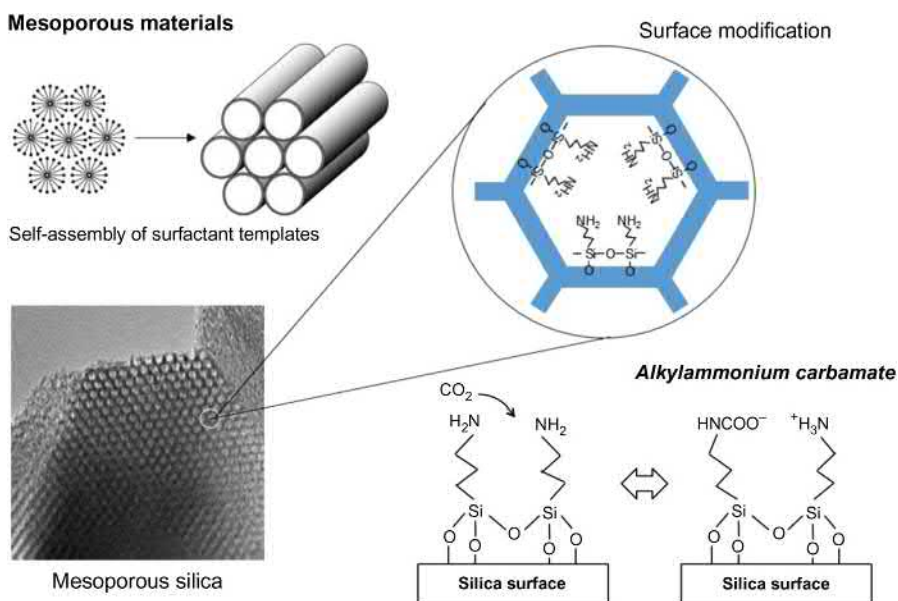


Figure 2.10 CO_2 adsorption mechanism on aminosilane modified mesoporous silica.

Source: Adapted with permission from <http://www.rite.or.jp/chemical/en/theme/2014/04/solid2.html>, Research Institute of Innovative Technology for the Earth (accessed 20.10.18) [90]. Copyright (2018), Chemical Research Group, CO_2 Capture and Green Processes (Kyoto, Japan).

Despite exhibiting strong performance, these materials suffer from a number of limitations. As chemisorbents, AMIMs can suffer from issues such as sorbent degradation over repeated cycling and amine deactivation in the presence of NO_x , SO_x , O_2 , and CO_2 [13,95]. Similarly, amine-modified adsorbents exhibit $Q_{st}(\text{CO}_2)$ values of 70–100 kJ mol^{-1} . Whereas these high $Q_{st}(\text{CO}_2)$ values lead to high CO_2/N_2 selectivity, this strong affinity demands temperatures $>70^\circ\text{C}$ to reverse the process [96].

2.5.2.2 Physical adsorbents/phisorbents

IUPAC defines physisorbents as sorbents in which the adsorptive forces are intermolecular forces (van der Waals forces) of the same kind as those responsible for the imperfection of real gases and the condensation vapors, and which do not involve a significant change in the electronic orbital patterns of the species involved [97]. There are several classes of physisorbents as discussed below.

Zeolites: Zeolites are crystalline, microporous aluminosilicates based upon tetrahedral building units. These frameworks are anionic in nature and so they allow for ion exchange and their robust nature enables reversible dehydration [98]. Type X and A zeolites are the most well-studied adsorbents in terms of their C-capture applications [99–103]. Zeolite NaX (or 13X) is considered to be a benchmark CO_2 physisorbent suitable for PSA regeneration, especially at conditions relevant to postcombustion capture (0.15 bar and 40°C–50°C). The moderately high $Q_{st}(\text{CO}_2)$ exhibited by 13X (c. 44 kJ mol^{-1}) is driven by sodium open metal sites and narrow pore channels. This leads to high values of $S_{CN} \sim 420$ and CO_2 uptake at low CO_2 partial pressures (c. 3 mmol g^{-1} at 0.1 bar) [19]. 13X is therefore a benchmark CO_2 sorbent under low temperature and low partial pressure conditions.

Despite these promising adsorption properties, zeolites suffer from being strongly hydrophilic. Introduction of moisture into the gas stream significantly reduces their C-capture performance [15]. The presence of water alters the electric field and reduces interaction strength between the quadrupole of CO_2 and cations, therefore resulting in lower uptake [104]. The presence of even very small amounts of moisture therefore greatly reduces the separation performance of zeolites. Moisture can also alter the morphological structure of zeolites, which can in turn influence adsorption kinetics [105]. The high affinity to moisture also significantly affects the regeneration energy requirements during adsorption–desorption cycles. Regeneration temperatures as high as 300°C are required to remove water molecules which are strongly bound to the open metal sites in zeolites [15]. The hydrophilic nature of most zeolites therefore results in high energy for regeneration and has limited their utility in C-capture.

ACs: Carbon-based adsorbents have also been studied for CO_2 separations including materials such as ACs, carbon nanotubes, and graphene. ACs are amorphous in nature and can exhibit relatively high surface area. While the surface properties of ACs can vary widely, these materials are advantageous because of their inertness to moisture [106] and, thanks to the lack of strong polar groups, they tend to exhibit low moisture affinity. However, the lack of active sites also reduces the

strength of interactions with CO₂, results in lower enthalpy of adsorption, and lowers CO₂ uptake at low partial pressures and ambient conditions [107]. $Q_{st}(\text{CO}_2)$ values are generally lower for ACs than for other classes of sorbent with values in the range 15–30 kJ mol⁻¹ [102,106,108]. Adsorption studies on ACs have therefore tended to focus upon high pressure C-capture applications as uptake is much better at high pressure. Very few studies on ACs have investigated their feasibility for low-pressure flue gas applications using vacuum or temperature swing regeneration approaches. However, when compared to zeolites, ACs' ability to maintain their sorption performance and structural integrity, even under harsh operating conditions, make them an option for eventual use in industrial CO₂ separation and adsorption processes.

2.6 Metal-organic frameworks

MOFs, which can be regarded as a subclass of metal-organic materials (MOMs) [109], have been widely touted as C-capture alternatives to traditional amine-based sorbents [24,110,111]. Their primary advantage lies with their enormous structural and compositional diversity, a consequence of their amenability to design from first principles [112–114]. Initial approaches to design exploited the “node-and-linker” concept [115–117] whereby metal cations or clusters serve as nodes and organic bifunctional linker ligands sustain the connectivity of the resulting network. The first, and still the most studied linker ligands, [118,119] were 4,4'-bipyridine, which was used to design *sql* [120,121] and *dia* [122,123] topology networks, and 1,4-benzenedicarboxylate [124], which was exploited as a linker in *sql* [124] and *pcu* [125] topology networks. The use of crystal engineering approaches enabled materials chemists to tailor pore size and chemistry by rational selection of the organic linker ligand, its functional groups and the metal-based node. Certain topologies [126] are particularly amenable to design because of the large number of available nodes, especially square lattice (*sql*) [121], primitive cubic (*pcu*) [17], diamond (*dia*) [123], and twisted boracite (*tbo*) [127]. The modular nature of such coordination networks means that systematic structure–function studies can be readily conducted in a way that is not feasible for inorganic porous materials such as zeolites. Such studies of “platforms” of related porous materials can provide insight into how subtle changes in pore size and chemistry address important sorption properties such as working capacity and selectivity [19,128].

MOF platforms can be evaluated with respect to their uptake capacity and selectivity for adsorption of CO₂ from mixed-gas streams. As discussed earlier, postcombustion C-capture requires sorbents which exhibit high CO₂ uptake and selectivity at ambient or just above ambient temperatures and CO₂ partial pressures of around 0.15 bar. In the cases of biogas production and NG sweetening, sorbents must perform at CO₂ partial pressure of up to 0.5 bar. Applications such as DAC and CH₄ purification for LNG production must be effective when CO₂ is present as a trace gas in gas mixtures (<0.01 bar CO₂). Table 2.3 presents a summary of the

Table 2.3 CO₂ sorption data of selected MOFs relative to traditional benchmark sorbents.

Adsorbent	Functionality	$Q_{st}(\text{CO}_2)$ (kJ mol ⁻¹)	Surface area (m ² g ⁻¹)	Uptake (mmol g ⁻¹)			Selectivity (S_{CN})	Temperature (K)	Reference(s)
				Low pressure (mbar)	0.15 bar	1 bar			
Zeolite 13X		49	780		3.3	6.9	440 (IS)	298	[19,129]
Zeolite NaX		40	570		3.0		68 (IS)	298	[82,130]
MIL-100(Cr)	UMC	63	1716	NA	NA	1.6	NA	298	[131]
Mg-MOF-74	UMC	47	1495	NA	5.35	8.1	182 (IS)(15:85)	296	[132]
Mg ₂ (dobpdc)	UMC	44	3270	NA	4.85	6.42	NA	298	[133]
MIL-101(Cr)	UMC	44	4230	NA	0.3	4	12.64 (IS)	303	[134,135]
Cu-TDPAT	UMC	42.2	1938	NA	1.38	5.89	34 (IS)(15:75)	298	[136]
Ni-MOF-74	UMC	41	1070	NA	4.28	7.09	307 (IAST)(15:85)	296	[132]
UiO-66-(CH ₃) ₂	UMC	38	868	NA	1.3	4.01	58 (IS)(15:75)	293	[137]
Co-MOF-74	UMC	37	1080	NA	2.76	6.69	NA	296	[132]
HKUST-1	UMC	35	2257	NA	1.33	5.35	28 (IS)	298	[127,138]
Cu-TPBTM	UMC	26.3	3160	NA	NA	~ 3.1	22 (IS)(15:85)	298	[128]
Zn ₄ (pydc) ₄	UMC	27.7	319	NA	0.8	2.05	42 (Henry)	296	[139]
UiO-66	UMC	26	1105	NA	NA	1.8	23 (IAST)(15:75)	298	[140]
PCN-61	UMC	22	3000	NA	NA	2.8	15 (IS)	298	[141]
CPO-27-Mg-c	AFS	132	400	2(5)	3.6	5.42	NA	298	[142]
MIL-101-DETA	AFS	98	1644	NA	1.95	3.56	346 (IS) (15:85)	296	[143]
mnen-CuBTTri	AFS	96	870	NA	2.38	4.2	327 (IAST) (15:75)	298	[144]
[Mg ₂ (dobdc) (N ₂ H ₄) _{1.8}]	AFS	90	1012	3.89(0.4)	5.18	5.51	NA	298	[145]
en-CuBTTri	AFS	90	345	NA	~ 0.6	1.27	25 (IS) (1:1)	298	[146]
en-MIL-100(Cr)	AFS	80	484	NA	NA	2.4	NA	308	[131]
dmen- Mg ₂ (dobpdc)	AFS	75	675	NA	3.77	~ 5	554 (IS) (15:75)	298	[147]
mnen- Mg ₂ (dobpdc)	AFS	71	70	2.05(0.4)	3.13	3.86	200 (IS) (15:75)	298	[133]

(Continued)

Table 2.3 (Continued)

Adsorbent	Functionality	$Q_{st}(\text{CO}_2)$ (kJ mol ⁻¹)	Surface area (m ² g ⁻¹)	Uptake (mmol g ⁻¹)			Selectivity (S_{CN})	Temperature (K)	Reference(s)
				Low pressure (mbar)	0.15 bar	1 bar			
en-Mg ₂ (dobpdc)	AFS	51	1253	3.3(5)	3.62	4.57	230 (IS)(15:75)	298	[148]
MIL-101(Cr)-NH ₂	AFS	50	1675	NA	0.4	2	16 (IS)	298	[149]
CAU-1	AFS	48	1268	NA	2.5	7.2	101 (IS)	273	[150]
bio-MOF-11	AFS	45	1040	NA	1.8	4.1	75 (IS)	298	[151]
[Co ₃ (OH) ₂ (btca) ₂]	AFS	42.9	125	NA	1.45	5.089	46.3 (IS)	273	[152]
[Zn ₂ (tept)OH]	AFS	40.9	905	NA	0.8	3.125	33.6 (IS)	298	[153]
Zn ₂ (Atz) ₂ (ox)	AFS	40.8	782 (CO ₂ 273K)	NA	~2	3.78	NA	293	[154,155]
NH ₂ -MIL-53(Al)	AFS	38.4	400	NA	1.1	1.9	18 (IS)(273K)	296	[156]
<i>rht</i> -MOF-9	AFS	32	2420	NA	1.75	5.75	NA	298	[157]
UiO-66-NH ₂	AFS	28	1123	NA	1.15	2.6	32 (IS)	298	[140]
MAF-66	AFS	26	1014	NA	1.2	4.4	225 (IS)(15:85)	298	[158]
men-Mg ₂ (dobpdc)	AFS		1036	NA	3.7	4.5	131 (IS)(15:75)	298	[159]
PEI-MIL-100(Cr)	AFS		608	NA	4.2	5	609 (IS)	298	[160]
MOFOUR-1-Ni	SMC/HUM	56	456 (CO ₂ 195K)	NA	1.8	2.45	86 (IAST)(10:90)	298	[161]
NbOFFIVE-1-Ni	SMC/HUM	55.4	280 (CO ₂ 273K)	1.3(0.4)	2.15	2.2	601 (IAST) (15:85)	298	[162]
TIFSIX-3-Ni	SMC/HUM	55.3	209 (CO ₂ 298K)	1.1(0.4)	2.36	2.46	492 (IAST) (15:85)	298	[163]
TIFSIX-3-Co	SMC/HUM	54.6	211 (CO ₂ 298K)	0.8 (0.4)	2.45	2.4	480 (IAST)	298	Our work
SIFSIX-3-Cu	SMC/HUM	54	215 (CO ₂ 298K)	1.24 (0.4)	2.4	2.5	10500 (BT) 0.1:99.99	298	[164]
NbOFFIVE-1-Zn	SMC/HUM	53.1	205 (CO ₂ 298K)	0.55	2.29	2.4	383 (IAST)(15:85)	298	Our work
LIFM-11	SMC	53	1176	NA	0.9	3.5	69 (IAST)(15:85)	298	[165]
NbOFFIVE-1-Co	SMC/HUM	52.9	215 (CO ₂ 298K)	0.625	2.47	2.56	395 (IAST)(15:85)	298	Our work
TIFSIX-3-Zn	SMC/HUM	51.6	206 (CO ₂ 298K)	0.53 (0.4)	2.41	2.44	381 (IAST)(15:85)	298	Our work
SIFSIX-3-Ni	SMC/HUM	50.8	215 (CO ₂ 298K)	0.35(0.4)	2.32	2.57	380 (IAST)(15:85)	298	[15]

CROFOUR-1-Ni	SMC/HUM	50	505 (CO ₂ 195K)	NA	1.05	1.9	195 (IAST)(10:90)	298	[161]
UiO-66-AD ₆	SMC	49.85	1020	NA	0.6	2.6	NA	298	[166]
SIFSIX-3-Co	SMC/HUM	49	223	0.17	2.5	2.6	307 (IAST)(15:85)	298	[167]
SIFSIX-3-Zn	SMC/HUM	45	250 (CO ₂ 298K)	0.089(0.4)	2.45	2.67	99 (BT)(10:90)	298	[19]
TMU-5	SMC	44	400	NA	0.44	1.78	32 (IAST)(1:1)	298	[168]
SIFSIX-3-Fe	SMC/HUM	42.4	358	0.089	2.5	2.56	180 (IAST)(15:85)	298	[169]
(Na,Cd)-MOF	SMC	42	526	NA	1.5	2.71	50 (IS)(15:75)	298	[170]
NJU-Bai7	SMC	40.5	1155	NA	1.8	2.95	97 (IS)(273)	298	[171]
NJU-Bai8	SMC	37.7	1103	NA	1.23	2.61	97 (IS)(273)	298	[171]
DICRO-3-Ni-i	SMC/HUM	37	388	NA	1.11	2.45	79.3 (IAST)(15:85)	293	[172]
NJU-Bai3	SMC	36.5	2690	NA	NA	~3	60 (IS)(1:1)	273	[173]
SNU-100-Co	SMC	36	1000	NA	1.11	3.79	31 (IS)(15:85)	298	[174]
UTSA-16	SMC	35	628	NA	4.4	7.14	314.7 (IAST) (15:85)	296	[175]
Ni-4PyC	SMC	35	945	NA	0.7	5.5	NA	298	[176]
TIFSIX-2-Cu-i	SMC/HUM	35	685	NA	1.9	4.1	NA	298	[37]
SNU-100-Ni	SMC	34.5	982	NA	1.1	3.79	37.4 (IS)(15:85)	298	[174]
MOF-5	SMC	34	3800	NA	NA	2.1	10.1 (IS)	298	[160]
SIFSIX-2-Cu-i	SMC/HUM	32	735	NA	1.71	5.36	70 (BT)(10:90)	298	[19]
JUC-132	SMC	30.3	253	NA	0.6	1.7	32 (IAST)(15:85)	298	[177]
ZIF-78	SMC	29	620	NA	0.9	2.6	50 (IS)	298	[178]
SNU-151	SMC	27.1	1563	NA	0.66	3.34	30 (IAST)(15:85)	298	[179]
PCN-88	SMC	27	3308	NA	1.16	4.01	25 (IAST)(15:85)	298	[180]
SIFSIX-1-Cu	SMC/HUM	27	1468	NA	1.36	6.25	NA	298	[21]
UTSA-49	SMC	27	710	NA	0.66	3.125	94 (IAST)(15:85)	298	[158]
NJU-Bai21, PCN-124	SMC	26.3	1979	NA	0.9	5.35	93 (IS)(15:85)	298	[181]
NOTT-125	SMC	25.4	2471	NA	NA	4.04	16 (IS)	298	[182]
NOTT-122	SMC	24.5	3286	NA	NA	4.6	NA	298	[182]
MOF-505	SMC	23.5	2304	NA	0.4	1.5	NA	304	[183]
DMOF-1	SMC	22	1870	NA	NA	2	4 (IS)	303	[184]
SIFSIX-2-Cu	SMC/HUM	22	3140	NA	0.27	1.83	8.4 (BT)(10:90)	298	[19]

Abbreviations: BT, breakthrough selectivity; IAST, ideal adsorbed solution theory derived selectivity; IS, ideal selectivity; NA, not applicable.

C-capture performance parameters of the best-performing MOFs including their uptake capacities at 0.15 and 1.0 bar, CO₂/N₂ selectivity (S_{CN}), and $Q_{st}(\text{CO}_2)$. Table 2.3 is organized into three sections based upon the key functionality of the sorbent that drives the C-capture process: the presence of unsaturated metal centers (UMCs); pores that contain amine-functionalized sites (AFSs); structures that are based upon saturated metal centers (SMCs) for which a different sorption mechanism must occur. The latter section also includes high-performing HUMs in which there are both organic and inorganic linker ligands. The ensuing discussion addresses these three classes of MOFs individually.

In the context of the performance parameters presented in Table 2.3, the desired C-capture sorbent should ideally balance low $Q_{st}(\text{CO}_2)$, high selectivity (S_{CN}), and high working capacity. Unfortunately, these three performance parameters are usually mutually exclusive. For example, despite excellent working capacity, the top-performing UMC-rich MOFs suffer from moderate S_{CN} . With respect to AFS-rich MOFs, whereas the selectivity and working capacity can be strong, there is typically a high energy penalty for regeneration if the $Q_{st}(\text{CO}_2)$ is $>60 \text{ kJ mol}^{-1}$. Most MOFs based upon SMCs exhibit $Q_{st}(\text{CO}_2)$ that is $<40 \text{ kJ mol}^{-1}$, a value that is too low to offer strong selectivity. However, certain classes of SMC-based sorbents are amenable to the introduction of combinations of organic and inorganic linkers, allowing custom-design of sorbents with optimal pore size and strong electrostatics that strike the right balance of selectivity (new benchmarks), $Q_{st}(\text{CO}_2)$ ($45\text{--}60 \text{ kJ mol}^{-1}$), and working capacity ($>2 \text{ mmol g}^{-1}$). In particular, several HUMs exhibit optimal thermodynamics and kinetics of the type that is well-suited for both trace and bulk C-capture.

2.6.1 Unsaturated metal centers

UMCs, also referred to as “open metal sites”, are one of the most commonly employed strategies for promoting selective gas sorption in solid physisorbents. UMCs in MOFs are typically created by activation of the as-synthesized materials. Activation typically means removing guest solvent molecule(s) that are coordinated to the metal nodes. Once the solvent molecules are removed, the UMCs serve as the primary binding sites for CO₂ molecules through weak coordination or interactions between UMCs and CO₂ driven by the high quadrupole moment $43.0 \times 10^{-27} \text{ esu}^{-1} \text{ cm}^{-1}$, that is, $1.34 \times 10^{-39} \text{ Cm}^2$ of CO₂. The presence of UMCs enhances CO₂ uptake even under reduced CO₂ concentrations. In situ neutron diffraction studies have established that UMCs can function as CO₂ binding sites through the strong dipole–quadrupole interactions [32,185].

UMC-rich MOFs studied as potential C-capture sorbents include the benchmark MOF Mg-MOF-74. Mg-MOF-74 (Fig. 2.11B) has been made by several groups [186–188] and is a member of the platform of materials known as M-MOF-74, CPO-27-M or M/M₂(dobdc) (M = Mg, dobdc⁴⁻: 2,5-dioxido-1,4-benzenedicarboxylate). Mg-MOF-74 exhibits the highest CO₂ uptake of any porous physisorbent, 8.1 mmol g^{-1} or 162 cc cc^{-1} at 298K and 1 bar, and is one of the most selective C-sorbent MOFs [132,189]. The structure of Mg-MOF-74 is comprised of

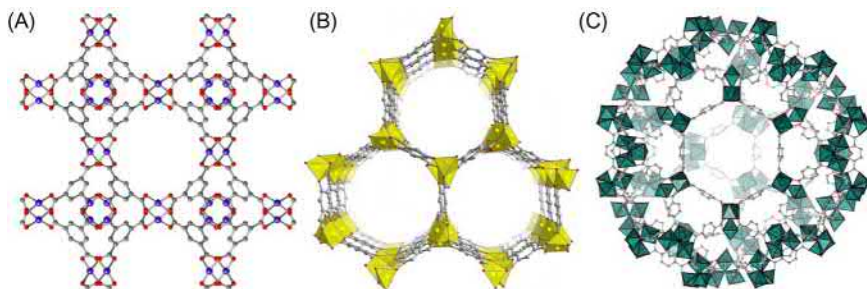


Figure 2.11 The porous structures of (A) HKUST-1; (B) Mg-MOF-74; and (C) MIL-101 (Cr). C, O, Cu are represented by gray, red, purple spheres, respectively while yellow and green polyhedra denote Mg and Cr, respectively.

Source: Reproduced from http://www.metal-organic-frameworks.eu/adsorbentien_engl.shtml#mofs (accessed 26.07.18) [191] with permission. Copyright (2018) Materials Center at TU Dresden.

[Mg₂O₂(O₂CR)₂] infinite rod-shaped secondary building units and linear 2,5-dioxido-1,4-benzenedicarboxylate (dobdc) linkers that generate cylindrical channels with a diameter of c. 11 Å. After activation, the walls of the channels are lined with UMCs. Mg-MOF-74 is a platform because its structure is maintained with different metal cations. The Lewis acidity of the UMCs dramatically impacts C-capture performance as reflected in the respective $Q_{st}(\text{CO}_2)$ values under conditions relevant to C-capture. The high uptake at 0.15 bar (5.35 mmol of CO₂ per gram) is a consequence of the high $Q_{st}(\text{CO}_2)$ value (47 kJ mol⁻¹ at low coverage). Under flue gas postcombustion conditions (15:85 CO₂/N₂), the $S_{CN} \sim 182$ of Mg-MOF-74 is higher than its Zn, Co, Ni, Fe and Mn variants and, thanks to its lower density, it exhibits the highest BET surface area, 1495 m² g⁻¹, among M-MOF-74 variants [19,175]. Breakthrough experiments suggest that the CO₂/CH₄ separation performance of Mg-MOF-74 exceeds that of NaX, MIL-53-NH₂ and ZIF-78, producing a high purity CH₄ stream from a 20% CO₂/80% CH₄ gas mixture (Fig. 2.12) [190].

The superior uptake at 0.15 bar and high zero-loading $Q_{st}(\text{CO}_2)$ of Mg-MOF-74 have been attributed to the ionic character of the Mg-O bonds formed between the UMCs and CO₂, though its CO₂ binding affinity falls to c. 30 kJ mol⁻¹ at higher loadings after the UMC sites are occupied. Though Mg-MOF-74 exhibits exceptional CO₂ sorption capacity and selectivity, its performance and those of its isostructural M-MOF-74 variants suffer in the presence of moisture. Exposure to 20:80 CO₂/N₂ at 70% RH [192] reduced the initial CO₂ uptake capacity of Mg-MOF-74 by ~84% after a single regeneration cycle (150°C under Ar), whereas Ni- and Co-MOF-74 retained 60% and 85% of their initial capacity, respectively. The negative impact of humidity on CO₂ uptake has also been observed in other UMC-rich MOFs and require much harsher sorbent bed regeneration conditions [138]. Replacing dobdc by dobpdc (dobpdc⁴⁻: 4,4'-dioxidobiphenyl-3,3'-dicarboxylate), an expanded analog of Mg-MOF-74, Mg₂(dobpdc), with 18.4 Å wide channels, resulted in lower $Q_{st}(\text{CO}_2)$ and higher BET surface area (3270 m² g⁻¹) [133].

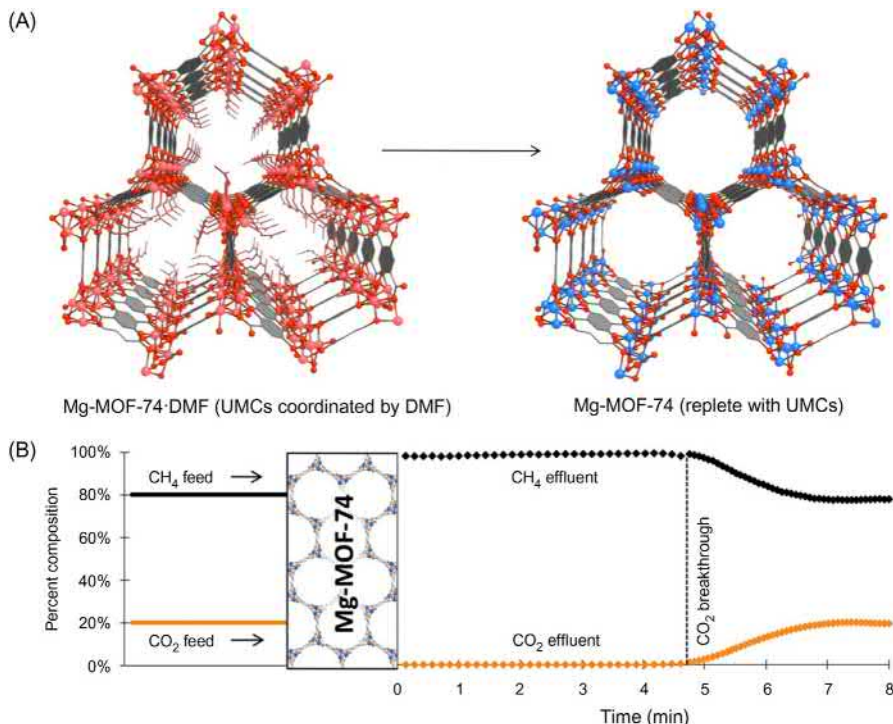


Figure 2.12 (A) The channel structure of activated Mg-MOF-74 is replete with UMCs; (B) dynamic gas breakthrough experiments for a 20% mixture of CO₂ in CH₄ for Mg-MOF-74. *Source:* Adapted from D. Britt, H. Furukawa, B. Wang, T.G. Glover, O.M. Yaghi, Highly efficient separation of carbon dioxide by a metal-organic framework replete with open metal sites, *Proc. Natl. Acad. Sci. U.S.A.* 106 (2009) 20637–20640 with permission.

Nevertheless, Mg₂(dobpdc) ranks second among UMC MOFs in terms of gravimetric uptake of CO₂ at 0.15 bar.

A high density of UMCs, dipole–quadrupole CO₂ interactions through NH...OCO hydrogen bonds and/or pore surface-appended Lewis basic sites (LBSs) in (3,24)-*c rht*-type MOFs (e.g., Cu-TPBTM, PCN-61 and Cu-TDPAT) afforded good uptake and selectivity at 0.15 and 1 bar. The $Q_{st}(\text{CO}_2)$ of Cu-TDPAT (42.2 kJ mol⁻¹ at zero loading) makes it the top-performing *rht*-type MOF. However, the CO₂ selectivities are only moderate in the broader context with Cu-TDPAT (34) > Cu-TPBTM (22) > PCN-61 (15). This order is likely linked to decreasing LBS-density in concert with more confined UMC-rich pores [128,136,193]. Some other UMC-functionalized MOFs with relatively high $Q_{st}(\text{CO}_2)$ values include mesoporous MILs such as MIL-100(Cr) and MIL-101(Cr), which exhibit large pore windows of 2.5 × 2.9 nm (MIL-100) and 2.9 × 3.4 nm (MIL-101) (Fig. 2.11C). MIL-100(Cr) was found to exhibit the highest $Q_{st}(\text{CO}_2)$ (63 kJ mol⁻¹) of all UMC-rich MOFs that have been studied in this context [134].

Among microporous MOFs with UMCs as the primary functionality of relevance to C-capture, UiO-66-(CH₃)₂ i.e., Zr₆O₄(OH)₄(2,5-Me-bdc)₆ [137], and HKUST-1 [127,194] (Fig. 2.11A) exhibit S_{CN} values of ~ 58 and 28, respectively. These values are consistent with low coverage $Q_{st}(\text{CO}_2)$ values of 38 and 35 kJ mol⁻¹, respectively.

While decorating mesopores with UMCs has afforded examples of MOFs with exceptional sorption and separation performance, this approach is handicapped by the tendency of UMCs to bind strongly with water molecules and/or the possibility that UMCs will be hydrolytically unstable [195]. Under industrially relevant conditions, MOFs replete with UMCs have tended to exhibit dramatically reduced performance when exposed to CO₂ containing gas streams that also contain water vapor [196]. When UMCs exhibit strong water affinity then there will be competition between H₂O and CO₂, thus reducing the density of available CO₂ binding sites. Further, coordinated water molecules often require elevated temperatures ($> 200^\circ\text{C}$) for sorbent regeneration [15,41]. In some cases, sorbent degradation has been shown to afford a significant drop in C-capture performance [15,197,198]. For these reasons it seems unlikely that MOFs based upon UMCs will be viable candidates for industrial scale C-capture from flue gases.

2.6.2 Amine-functionalized sites

The grafting of nitrogen-containing functional groups, particularly amines, onto the Connolly surfaces of sorbents has evolved as a paradigm to enhance CO₂ adsorption capacity and selectivity. Grafting is typically accomplished by postsynthetic modification (PSM) of classes of porous materials such as silicas and zeolites. The crystalline and modular nature of MOFs offers a more diverse approach to molecular level tuning in order to study amine-driven C-capture performance [26,81]. There are two approaches that have been used to introduce amine functionality into MOFs.

The first approach involves covalent modification of linker ligands with amine groups (1-, or 2-, or 3-degree amine) prior to synthesis of the MOF, that is, pre-synthetic functionalization. Incorporation of pendant amine groups into the guest-accessible void space of MOFs can greatly enhance the C-capture properties versus the corresponding parent structures. Further, the ready commercial availability of aromatic amine containing linkers, especially 2-aminoterephthalic acid, NH₂-BDC, has resulted in the generation of a number of amine-functionalized MOFs. IRMOF-3, Zn₄O(NH₂-BDC)₃, (Fig. 2.13A) [199], a variant of MOF-5, has been studied in this context [125]. At 298K and 1.1 bar, IRMOF-3 exhibits CO₂ uptake of 5.0 wt.%, higher than that of its parent IRMOF-1 [Zn₄O(BDC)₃], 4.6 wt.%, despite reduced BET surface area of 2160 versus 2833 m² g⁻¹.

Other examples of amine-functionalized linker ligands in MOFs include MIL-101(Cr)-NH₂ (50) [149,200], CAU-1 [Al₄(OH)₂(OCH₃)₄(H₂N-BDC)₃] (48) [150], bio-MOF-11 [Co₂(ad)₂(CO₂CH₃)₂] (45) (Fig. 2.13B) [151], [Co₃(OH)₂(btca)₂] (btca: benzotriazole-5-carboxylic acid) (42.9) [152], [Zn₂(tcpt)OH] (tcpt: 2,4,6-tris-(4-carboxyphenoxy)-1,3,5-triazine) (40.9) [153], [Zn₂(Atz)₂(ox)] (Atz: 3-amino-1,

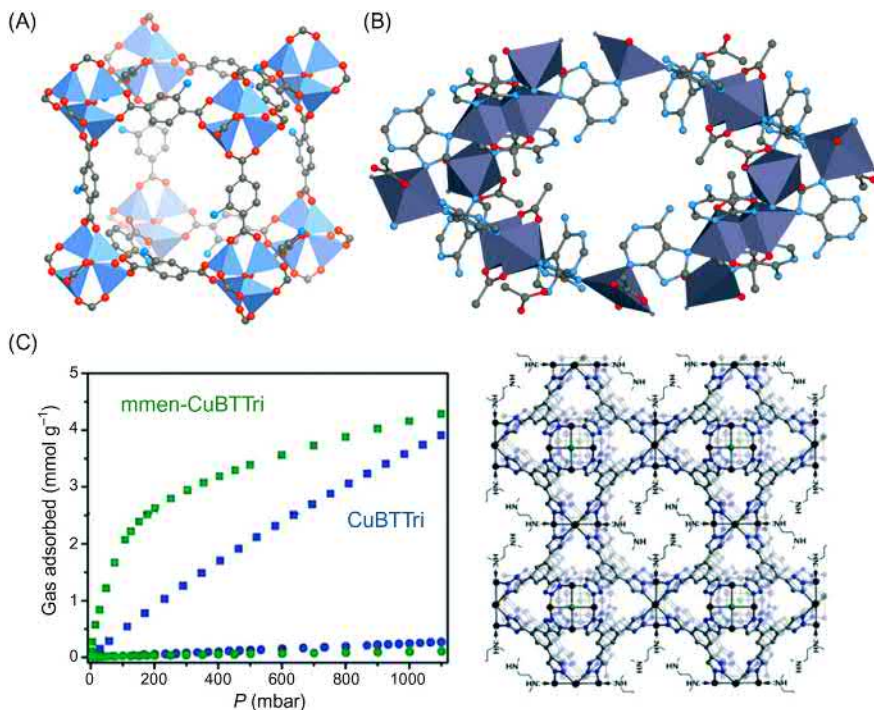


Figure 2.13 Structures of (A) IRMOF-3 and (B) bio-MOF-11. (C) Pure component isotherms for CO₂ (squares) and N₂ (circles) adsorption at 298K for mmen-CuBTtri (green) (packing view on right) and CuBTtri (blue).

Source: Adapted from T.M. McDonald, D.M. D'Alessandro, R. Krishna, J.R. Long, Enhanced carbon dioxide capture upon incorporation of N,N'-dimethylethylenediamine in the metal-organic framework CuBTtri, *Chem. Sci.* 2 (2011) 2022–2028; <http://matrixsensorsinc.com/wp-content/themes/matrixsensors/assets/images/mofs/IRMOF-3.jpg> (accessed 27.08.18) [204] with permission.

2,4-triazole; ox: oxalate) (40.8) [154,155], NH₂-MIL-53(Al), that is, [Al(OH)(NH₂-BDC)] (38.4) [156], *rht*-MOF-9 (32) [157], Uio-66-NH₂ (28) [140], MAF-66 [Zn(atz)₂] (26) [158] (numbers in parentheses denote the $Q_{st}(\text{CO}_2)$ values in kJ mol⁻¹ at low coverage, for the respective MOF). Interestingly, although the strategy of using 2-aminoterephthalate (NH₂-BDC) as a linker instead of BDC is effective from a design perspective, improvements in selectivity and ensuing separation performance were only modest for Uio-66-NH₂, NH₂-MIL-53(Al), CAU-1, MIL-101(Cr)-NH₂, Zn₂(NH₂-BDC)₂(TED) [201], Ni₂(NH₂-BDC)₂(TED) [202], and In(OH)(NH₂-BDC) [203] (TED: triethylenediamine).

An alternative approach to incorporating amines into MOFs revolves around PSM of MOFs. PSM has afforded MOFs with high $Q_{st}(\text{CO}_2)$, 70–130 kJ mol⁻¹ at low coverage, and high $S_{ads}(\text{CO}_2)$. Typically, interactions between the localized amine dipoles and the quadrupole moment of CO₂ would be alone enough to

enhance C-capture performance, but there is also the possibility of chemisorption. NH_2 -functionalized MOFs might also be expected to be less impacted by the presence of moisture than UMC-rich MOFs, especially if the amines bond to UMCs. However, if the presence of amines in pore voids results in chemisorption there will be elevated energy requirements for sorbent bed regeneration. 60% UMC functionalization of CPO-27-Mg, i.e., Mg-MOF-74, with ethylenediamine by Bernini et al. afforded CPO-27-Mg-c, a chemisorbent with $Q_{st}(\text{CO}_2) \sim 132 \text{ kJ mol}^{-1}$ [142]. Although saturation uptake at 298K, 5.42 mmol g^{-1} is less than the parent, Mg-MOF-74, the amine-on-UMC strategy enhanced sorbent– CO_2 interactions with a ~ 2.8 -fold increase in $Q_{st}(\text{CO}_2)$. Chen and colleagues reacted hydrazine with $\text{Mg}_2(\text{dobdc})$ to form $[\text{Mg}_2(\text{dobdc})(\text{N}_2\text{H}_4)_{1.8}]$ [145], a MOF that set a new record for C-capture performance at atmospheric CO_2 (0.4 mbar, 3.89 mmol g^{-1}) and postcombustion-relevant (150 mbar, 5.18 mmol g^{-1}) conditions. The high concentration of hydrazine-derived free $-\text{NH}_2$ groups (6.01 mmol g^{-1} or $7.08 \text{ mmol cm}^{-3}$) enabled reversible carbamic acid formation with CO_2 and a high $Q_{st}(\text{CO}_2)$ value of $\sim 90 \text{ kJ mol}^{-1}$. This amine-tethered MOF was studied by temperature-vacuum swing adsorption and was found to exhibit a lower regeneration temperature than that of other alkylamine-functionalized MOFs. An expanded analog of dobdc (dobpdc: 4,4'-dihydroxy-(1,10-biphenyl)-3,3'-dicarboxylic acid) was used to prepare $\text{Mg}_2(\text{dobpdc})$, a MOF with $\sim 18.4 \text{ \AA}$ pore diameter. $\text{Mg}_2(\text{dobpdc})$ was modified with *N,N'*-dimethylethylenediamine (mmen) to afford mmen- $\text{Mg}_2(\text{dobpdc})$ [133], which has a small BET surface area of $70 \text{ m}^2 \text{ g}^{-1}$ but strong 298K C-capture: 2.05 mmol g^{-1} at 0.0004 bar; 3.13 mmol g^{-1} at 0.15 bar; 3.86 mmol g^{-1} at 1 bar. This performance is consistent with chemisorption with a low loading $Q_{st}(\text{CO}_2)$ of $\sim 71 \text{ kJ mol}^{-1}$. However, after CO_2 loading of $\sim 2.5 \text{ mmol g}^{-1}$, accessible $-\text{NH}_2$ sites saturate and $Q_{st}(\text{CO}_2)$ is reduced to $\sim 23 \text{ kJ mol}^{-1}$. Other PSM approaches using $\text{Mg}_2(\text{dobpdc})$ afforded dmen- $\text{Mg}_2(\text{dobpdc})$ [147] and en- $\text{Mg}_2(\text{dobpdc})$ [148] (dmen: *N,N'*-dimethylethylenediamine; en: ethylenediamine). Both MOFs were found to exhibit strong C-capture properties, but there is a regeneration energy penalty because of the high $Q_{st}(\text{CO}_2)$ values 75 and 51 kJ mol^{-1} , respectively. Ethylenediamine (en) was used by Long and coworkers to modify CuBTTri, $\text{H}_3[(\text{Cu}_4\text{Cl})_3(\text{BTTri})_8]$ (H_3BTTri : 1,3,5-tris(1H-1,2,3-triazol-5-yl)benzene) and form en-CuBTTri, a MOF that features Cu^{II} UMCs [146] and a high $Q_{st}(\text{CO}_2)$ of $\sim 90 \text{ kJ mol}^{-1}$. CuBTTri serves as a proof-of-principle for AFS sorbents prepared by PSM from UMC-rich parent MOFs. A high zero-coverage $Q_{st}(\text{CO}_2)$ of $\sim 96 \text{ kJ mol}^{-1}$ for its analog mmen-CuBTTri [144] (mmen replacing en during PSM) is a handicap even though its C-capture performance is excellent: 4.2 and 2.38 mmol g^{-1} , at 1 and 0.15 bar, respectively (Fig. 2.13C); $S_{CN} \sim 327$ (IAST; CO_2/N_2 : 15:75) [144].

The UMC-lined mesopores of MIL-101(Cr) were modified with diethylenetriamine (DETA) to yield MIL-101-DETA [143], a MOF with BET surface area $\sim 1644 \text{ m}^2 \text{ g}^{-1}$, c. 48% less than MIL-101(Cr). This MOF was found to exhibit $Q_{st}(\text{CO}_2)$ of $\sim 98 \text{ kJ mol}^{-1}$. Using a simple “impregnation” process, Liang Chen and coworkers developed a series of MIL-101(Cr) variants with different polyethyleneimine (PEI) loadings [160]. Other mesoporous MOFs, for example, MIL-100

(Cr), have also been tethered with alkyl amines and en-MIL-100(Cr) exhibits a low loading $Q_{st}(\text{CO}_2)$ of $\sim 80 \text{ kJ mol}^{-1}$. Different types of LBSs, for example, aliphatic, aromatic, and heterocyclic amines may show diverse effects on improving material properties versus the corresponding parent MOFs. While amine-functionalized MOFs can be readily prepared and in many cases exhibit improved C-capture performances over their parent MOFs, there are still challenges to overcome. Given that chemisorption is the mechanism of C-capture, relatively high regeneration energies are typically needed ($> 90^\circ\text{C}$) [205]. Further, their production can be energy-intensive [12] and they may still be prone to chemical/thermal/hydrolytic instability [13,94,206]. Finally, even if low loading $Q_{st}(\text{CO}_2)$ is enhanced, once the amine sites are saturated, high loading $Q_{st}(\text{CO}_2)$ will likely be greatly reduced. Overall, AFS MOFs tend to offer C-capture performances for dry and wet gas mixtures that is superior to their parent MOFs and some traditional physisorbents [196], but it is unclear if they can compete on cost and performance with cheaper amine-modified materials such as silicas and zeolites.

2.6.3 Saturated metal centers

Whereas UMCs and amine functionalization are validated to enhance C-capture under ideal conditions, they tend to be negatively affected by industrially relevant conditions, especially the presence of moisture [144,207]. MOFs and related materials with SMCs offer the possibility of a different approach whereby C-capture performance is driven by optimal pore size and pore chemistry for C-capture versus other relevant gases and vapors. Such an approach is gaining relevance thanks to the amenability of certain MOF platforms to crystal engineering and the strong performance of some of the resulting SMC materials. The use of crystal engineering approaches means that sorbents which are modular in nature, as is the case for several MOF platforms, can be systematically fine-tuned through careful selection of metal nodes and/or organic linkers, and, in some cases, by control of interpenetration [109]. This type of sorbent can be subdivided into two classes of materials: (1) MOFs in which organic ligands are used to control pore size and pore chemistry; (2) ultramicroporous materials that are based upon combinations of organic and inorganic linker ligands (HUMs).

2.6.3.1 Metal-organic frameworks in which organic ligands are used to control pore size and pore chemistry

Among MOFs containing SMCs, zeolitic imidazolate frameworks (ZIFs) are perhaps the most widely studied sorbents. ZIFs are based upon polyhedral cages formed from tetrahedral nodes and angular imidazolate linkers. These neutral coordination networks can exhibit zeolitic topologies and feature pores that are larger in scale than those of zeolites. Structures of ZIFs can be fine-tuned by variation of the linker ligand functionality. However, whereas ZIFs are structurally diverse and tend to exhibit thermal and hydrolytic stability, they generally exhibit low CO_2 uptake at 0.15 and 1 bar and poor selectivity versus CH_4 and N_2 . ZIF-78 (BET surface area:

$620 \text{ m}^2 \text{ g}^{-1}$), the top-performing ZIF with respect to C-capture, is decorated with nitro groups and exhibits CO_2 uptake of c. 2.6 mmol g^{-1} at 298K and 1 bar, but its selectivity (~ 50) is average. Such selectivity values are indicative of the weak CO_2 -sorbent interactions that tend to occur in MOFs with SMCs and exclusively organic linkers with no AFS functionality.

Control over pore size, in particular in the ultramicroporous regime (pore diameter $< 7 \text{ \AA}$), has resulted in significant developments with respect to selectivity and uptake values. $[\text{K}(\text{H}_2\text{O})_2\text{Co}_3(\text{cit})(\text{Hcit})]$ (H_4cit = citric acid), a diamondoid, *dia*, network known as UTSA-16 [175], (BET surface area = $628 \text{ m}^2 \text{ g}^{-1}$) was found to exhibit volumetric CO_2 uptake of 160 cc cc^{-1} , a value second only to that of Mg-MOF-74 at 296K and 1 bar. Further, UTSA-16 outperforms Mg-MOF-74, and therefore all other UMC-rich sorbents, in terms of CO_2/N_2 selectivity (314.7 vs 182). UTSA has pore dimensions of $3.3 \times 5.4 \text{ \AA}^2$ which facilitate multiple sorbent-sorbate interactions and are assumed to be behind its outstanding performance. Neutron powder diffraction measurements conducted upon CO_2 -loaded UTSA-16 revealed a CO_2 binding site in which coordinated water molecules and uncoordinated carboxylic OH groups interact with a CO_2 molecule. UTSA-16 loses its coordinated aqua ligand at elevated temperatures to afford a nonporous compound. The C-capture performance of UTSA-16 and its low cost ingredients make it a potential lead candidate for later stage development.

In 2015, Vaidhyanathan and coworkers reported a new ultramicroporous MOF, Ni-4PyC (4PyC: 4-pyridinecarboxylate) (Fig. 2.14A) with ultramicroporous pore windows ($3.5 \times 4.8 \text{ \AA}$). Ni-4PyC set a new benchmark for CO_2/H_2 selectivity (285) and working capacity (3.95 mmol g^{-1}) (Fig. 2.14B) [176]. The sorption performance of Ni-4PyC makes it a candidate for H_2 purification and precombustion trace C-capture processes. The performance of Ni-4PyC is likely a result of the high density of CO_2 binding sites and cooperative CO_2 - CO_2 interactions. An *agw* topology network, NJU-Bai3 [173], synthesized from an amide-functionalized tricarboxylate ligand 5-(4-carboxybenzoylamino)-isophthalate, was found to exhibit moderately high $Q_{st}(\text{CO}_2)$ of $\sim 36.5 \text{ kJ mol}^{-1}$. This high surface area ($2690 \text{ m}^2 \text{ g}^{-1}$) MOF also exhibits moderate S_{CN} (60) and CO_2 uptake capacity (3 mmol g^{-1} at 273K). The isorecticular (3,6)-connected networks NJU-Bai7 and NJU-Bai8, synthesized from 5-(pyridin-3-yl)isophthalate and 5-(pyrimidin-5-yl) isophthalate, respectively, contain uncoordinated N-atoms and exhibit good selectivity S_{CN} of 97 for NJU-Bai7, 111.3 for NJU-Bai8 and $Q_{st}(\text{CO}_2)$ (40.5 kJ mol^{-1} : NJU-Bai7 vs 37.7 kJ mol^{-1} : NJU-Bai8). $S_{CM} \sim 40.8$ makes NJU-Bai8 a potential candidate for further study in the context of NG purification.

Postsynthetic ligand exchange of the terephthalate moiety in UiO-66 with a series of alkanedioic acids ($\text{HO}_2\text{C}(\text{CH}_2)_n\text{CO}_2\text{H}$; n : 4, 6, 8, 10) resulted in free carboxyl moieties lining the pores. The CO_2 uptakes of UiO-66-AD $_n$ (n = 4, 8) were observed to be similar to that of UiO-66. However, UiO-66-AD $_6$ [166] was found to exhibit 1 bar uptake that is 34% higher at 298K and 58% higher at 323K versus that of UiO-66. $Q_{st}(\text{CO}_2)$ of $\sim 49.85 \text{ kJ mol}^{-1}$ is the highest yet reported for the UiO-66 platform of MOFs. The strong performance of UiO-66-AD $_6$ was attributed to carboxyl group- CO_2 interactions.

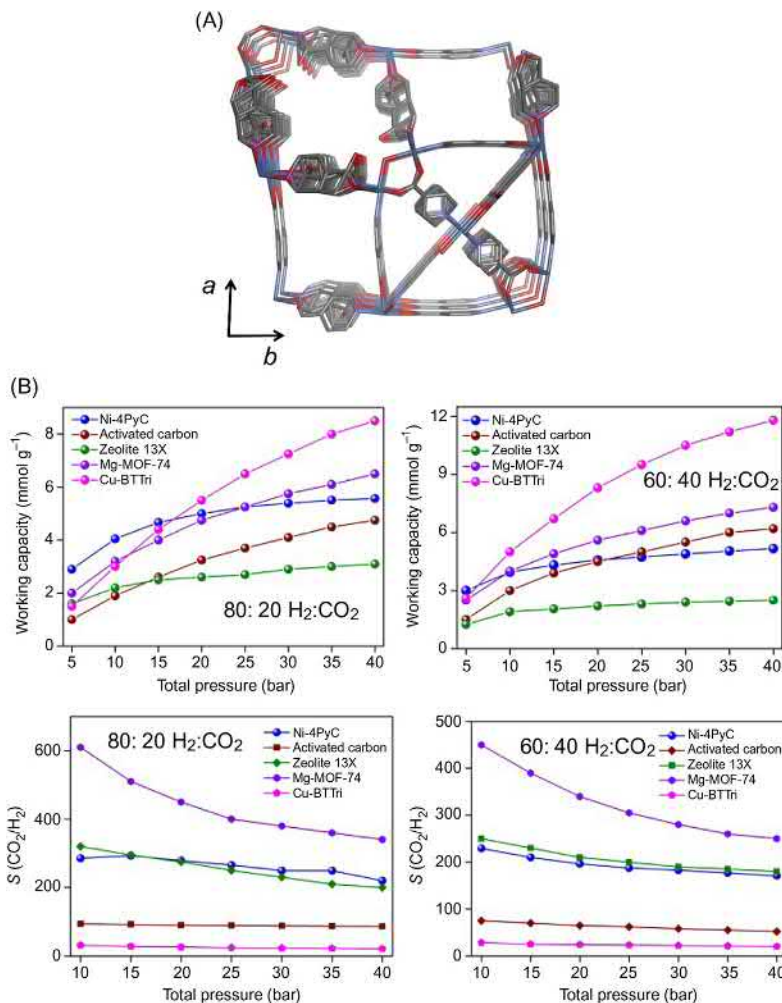


Figure 2.14 (A) Ultramicropores viewed along crystallographic *c*-axis of Ni-4PyC; (B) simulated comparison of working capacity and sorption selectivity characteristics of Ni-4PyC, relative to a few industrial sorbents and MOFs (determined from (i) H₂:CO₂ (80:20), and (ii) H₂:CO₂ (60:40) gas mixtures at 313K) [176].

Despite relatively low BET surface area of $\sim 400 \text{ m}^2 \text{ g}^{-1}$ and low saturation uptake, the azine-functionalized pore surface of the Zn(II) MOF TMU-5 was found to exhibit $Q_{st}(\text{CO}_2)$ of $\sim 44 \text{ kJ mol}^{-1}$. The strength of interaction was attributed to narrow pores (dimension: $5.6 \times 3.8 \text{ \AA}^2$) that facilitate CO₂-specific dipole–quadrupole interactions [168]. Microwave-assisted synthesis was recently used to prepare a heterobimetallic (Na,Cd)-MOF, $[\text{Cd}_3\text{Na}_6(\text{BTC})_4(\text{H}_2\text{O})_{12}]$, with high volumetric CO₂ adsorption capacity (5.2 mmol cm^{-3} at 298K and 1 bar) and a BET surface area of $\sim 526 \text{ m}^2 \text{ g}^{-1}$. Other sorption parameters are moderate with $Q_{st}(\text{CO}_2)$

of $\sim 42 \text{ kJ mol}^{-1}$ and $S_{CN} \sim 50$ [208]. $[\text{Cd}_3\text{Na}_6(\text{BTC})_4(\text{H}_2\text{O})_{12}]$ is facile to regenerate and can be prepared in 1 hour, thereby making it another example of an ultramicroporous sorbent that could be further studied for C-capture applications. Successive functionalization of a T-shaped ligand with amide and N-oxide groups led Xiong et al. to “open-donor” N-oxide sites in LIFM-11. The N-oxide sites impact its CO_2 sorption enthalpy (53 kJ mol^{-1} , the highest value among SMC-MOFs unless inorganic linkers are present) and the S_{CN} is ~ 69 at room temperature [165]. Mechanistic insights into its CO_2 adsorption and preferred binding sites suggest that N-oxidation of N-donor ligands is potentially a new approach to generate MOFs that offer good C-capture performance along with facile regeneration/recyclability.

SMC-based MOFs with $Q_{st}(\text{CO}_2)$ in the range $20\text{--}40 \text{ kJ mol}^{-1}$ offer an opportunity for energy-efficient C-capture as they require relatively low regeneration energy. However, sorbents based upon SMCs and exclusively organic linkers often suffer from weak C-capture performance because, ultimately, strong sorbent–sorbate interactions are required for selectivity driven separations such as trace C-capture under ambient conditions.

2.6.3.2 Ultramicroporous materials that are based upon combinations of organic and inorganic linker ligands (hybrid ultramicroporous materials)

The paradigm of fine-tuning pore size and pore chemistry mentioned earlier is exemplified by HUMs, which are based upon combinations of organic linkers and inorganic pillars. It should be noted that under the 2015 provisional recommendations of a IUPAC task group, HUMs should not be classified as MOFs. This is because HUMs exploit inorganic linkers and a MOF was defined as *a coordination network with organic ligands containing potential voids*. MOFs, therefore, would not include any inorganic species as linker ligand [209]. Further, the IUPAC panel explicitly discouraged use of the term “hybrid organic–inorganic materials,” an umbrella under which HUMs clearly belong.

The systematic study of pore size and pore chemistry in HUMs has afforded a number of HUM sorbents that offer new benchmarks, in some cases by more than an order of magnitude, for CO_2 selectivity over N_2 [19,162], H_2 [176], CH_4 [19], and C_2H_2 [37]. The first generation of HUMs was based upon crystal engineering of pillared *sql* networks that exist as *pcu* nets if an inorganic linker anion is used to pillar the *sql* networks. These HUMs are highly modular as there are at least three variables: the metal moiety; the linker used to generate the *sql* network (which typically controls pore size); the linker used to pillar the *sql* network (which typically controls pore chemistry) (Fig. 2.15). The prototypal pillared *sql* network, SIFSIX-1-Zn, $[\text{Zn}(4,4'\text{-bipyridine})_2(\text{SiF}_6)]_n$, was reported in 1995 (Fig. 2.16A) [17]. Its Cu analog, SIFSIX-1-Cu, was subsequently studied in the context of NG storage [210]. Another platform of pillared *sql* networks that would be classified as a MOF is exemplified by the *pcu* net DMOF-1 [211], which was reported in 2004. DMOF-1 is not a HUM because it is comprised of MOF-2, $[\text{Cu}(1,4\text{-BDC})_2]$ *sql* networks [124] pillared by the organic linker DABCO, 1-4-diazabicyclo[2.2.2]octane.

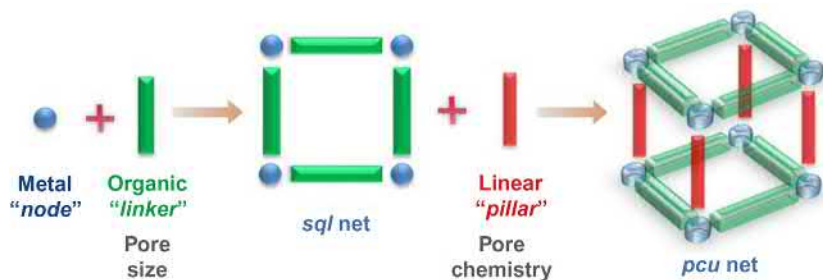


Figure 2.15 Schematic illustration of the modularity of pillared square grids that form *pcu* nets.

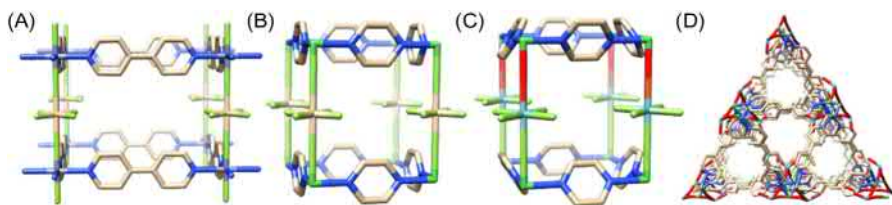


Figure 2.16 Prototypical HUMs as exemplified by: (A) SIFSIX-1-Zn; (B) SIFSIX-3-Zn; (C) NbOFFIVE-1-Ni; (D) MOOFOR-1-Ni.

DMOF-1 serves as the parent of a particularly large platform of sorbents because of the large number of readily accessible dicarboxylate linkers and di-aza linkers.

Several groups have studied these materials extensively [212–214]. Most recently, the use of extended ligands (X-ligands) has resulted in the generation of variants of DMOF-1 with high levels of interpenetration and the observation of stimulus-responsive phase changes [215].

It is perhaps surprising that the C-Capture performance of MFSIX (MF_6^{2-} , where $M = \text{Si}, \text{Ti}$, etc.) sorbents was not studied until 2012 [21], when SIFSIX-1-Cu and SIFSIX-4-Cu ($2 = 1,2\text{-bis}(4\text{-pyridyl})\text{ethane}$) were investigated. SIFSIX-1-Cu, the narrower pore, denser sorbent was found to exhibit higher gravimetric uptake thanks to its higher $Q_{st}(\text{CO}_2)$. The previously reported ultramicroporous variant SIFSIX-3-Zn ($3 = \text{pyrazine}$) (Fig. 2.16B), was concurrently studied and found to exhibit promising CO_2 uptake at low partial pressures and 298K [216]. In 2013, a crystal engineering approach from Zaworotko and coworkers enabled precise control over pore size in three members of the “SIFSIX” platform: SIFSIX-2-Cu, its interpenetrated polymorph, SIFSIX-2-Cu-i, and SIFSIX-3-Zn [19]. The smaller pore diameter (5.15 Å) of SIFSIX-2-Cu-i versus SIFSIX-2-Cu (13.05 Å) resulted in much stronger CO_2 –sorbent interactions as evidenced by higher $Q_{st}(\text{CO}_2)$ (31.9 vs 22 kJ mol $^{-1}$ for SIFSIX-2-Cu-i and SIFSIX-2-Cu, respectively) and higher CO_2 uptake (1.9 vs 0.22 mmol g $^{-1}$ for SIFSIX-2-Cu-i and SIFSIX-2-Cu, respectively) at low-pressure (0.1 bar) CO_2 and 298K. SIFSIX-3-Zn, the narrowest pore material

performed even better and unexpectedly set a benchmark for S_{CN} of ~ 1800 , almost an order of magnitude better than any existing physisorbent and two orders of magnitude better than most MOFs. Modeling studies indicated that a combination of ultramicropores with an aperture just above the kinetic diameter of CO_2 and strong electrostatics from the SiF_6^{2-} pillar afforded the very high $Q_{st}(\text{CO}_2)$ value of $\sim 45 \text{ kJ mol}^{-1}$. Subsequent work revealed that enhanced S_{CN} and S_{CM} could be manifested through systematic substitution of the pillar from SIFSIX-1-Cu (SiF_6^{2-}) to TIFSIX-1-Cu (TiF_6^{2-}) and SNIFSIX-1-Cu (SnF_6^{2-}) [217].

In 2014, Eddaoudi and coworkers reported that another HUM variant, SIFSIX-3-Cu [164], exhibits CO_2 uptake capacity of 1.24 mmol g^{-1} at 400 ppm and 298K, a new benchmark for CO_2 uptake under conditions relevant to DAC. Substitution of Zn for Cu reduced the pore diameter from 3.84 \AA in SIFSIX-3-Zn to 3.5 \AA in SIFSIX-3-Cu, resulting in an even higher $Q_{st}(\text{CO}_2)$ of $\sim 54 \text{ kJ mol}^{-1}$. Zaworotko and coworkers addressed the potential use of HUMs for DAC by comparing several sorbents including SIFSIX-3-Ni, two MOFs (HKUST-1 and Mg-MOF-74), zeolite 13X, and TEPA-SBA-15 (an amine-modified mesoporous silica). SIFSIX-3-Ni was found to be by far the best-performing physisorbent with equilibrium compositions of 8% CO_2 and 92% water upon exposure to humid laboratory air [15]. In a follow-up study [41], SIFSIX-3-Cu was evaluated for CO_2 DAC and found to have even higher CO_2 uptake under DAC conditions. These studies collectively reveal that even subtle pore size and pore chemistry changes can profoundly impact C-capture performance.

While the modular nature of the MFSIX platform enables systematic expansion of the MF_6^{2-} derived HUM platforms, there are other inorganic anions that can be used as pillars. Fluorinated oxy or “FOXY” anions such as NbOF_5^{2-} can also serve as pillars, the prototype being NbOFFIVE-1-Cu (1 = pyrazine), a compound first reported by Poeppelmeier in 1996 [218]. The DAC properties of NbOFFIVE-1-Ni (Fig. 2.16C) were investigated [162,219] and revealed new benchmarks for gravimetric and volumetric CO_2 uptake (c. 1.3 mmol g^{-1} and $51.4 \text{ cm}^3(\text{STP}) \text{ cm}^{-3}$) for any physisorbent at 400 ppm and 298K (Table 2.4 and Fig. 2.17).

HUMs are not limited to *pcu* nets. The first examples of uninodal 6-c *mmo* topology HUMs are members of the isostructural family MOFOUR-1-Ni (Fig. 2.16D), CROFOUR-1-Ni and WOFOUR-1-Ni [161]. Sharp type-I 298K CO_2 isotherms for all three sorbents revealed uptakes of 2.45, 2.27, and 1.91 mmol g^{-1} and low loading $Q_{st}(\text{CO}_2)$ values of 65.5, 56, and 50 kJ mol^{-1} , respectively. At flue gas composition and full loading (10:90 CO_2/N_2 binary mixture), S_{CN} values of 86, 195, and 179 exceed the values exhibited by almost all UMC-rich or amine-modified MOFs.

Another inorganic anion that can function as a pillar for HUMs is the dichromate ($\text{Cr}_2\text{O}_7^{2-}$) anion. The use of dichromate pillars and 4,4'-azobipyridine linkers coordinated to Zn^{2+} , Co^{2+} , Ni^{2+} , and Cu^{2+} resulted in the interpenetrated HUMs DICRO-3-*M-i* [$\text{M}'(\text{apy})_2(\text{Cr}_2\text{O}_7)$] $_n$ (apy: 4,4'-azopyridine, $\text{M}' = \text{Zn}^{2+}$, Co^{2+} , Ni^{2+} , Cu^{2+}). The interpenetrated variants were all found to exhibit better C-capture properties than the corresponding noninterpenetrated variants [172]. The benchmark performance of HUMs when combined with good stability, easy fine-tuning, and facile

Table 2.4 CO₂ DAC performances for representative sorbents.

Adsorbent	DAC (1 atm; 49% RH)				Moist CO ₂ (0.15 atm; 75% RH)				Dry CO ₂ (0.15 atm)	
	CO ₂	H ₂ O	CO ₂ L kg ⁻¹ (L L ⁻¹)	S _{CW}	CO ₂	H ₂ O	CO ₂ L kg ⁻¹ (L L ⁻¹)	S _{CW}	CO ₂	CO ₂ L kg ⁻¹ (L L ⁻¹)
TIFSIX-3-Ni	17.1% (17.9)		9.09 (14.97)	12.80	83% (92)		46.84 (77.15)	0.87	100% (105)	53.45 (88.03)
NbOFFIVE-1-Ni	16.5% (18.5)		9.42 (16.57)	12.35	85% (88)		44.80 (77.84)	0.91	100% (95)	49.28 (86.73)
SIFSIX-3-Ni	< 8% (8.0)	> 92% (93)	4.07 (6.55)	5.43	62% (76)	38% (46)	38.69 (62.29)	0.27	100% (109)	55.49 (89.34)
HKUST-1	1% (2.1)	99% (178)	1.07 (0.95)	0.63	8.5% (12.8)	> 91% (137)	6.52 (5.78)	0.02	100% (70)	35.64 (31.61)
Mg-MOF-74	< 4% (6.3)	> 96% (171)	3.21 (2.94)	2.60	51% (68)	49% (65)	34.62 (31.71)	0.17	100% (235)	119.64 (109.59)
Zeolite 13X	1% (1.5)	99% (146)	0.76 (0.99)	0.63	22% (26.3)	78% (93)	13.39 (17.54)	0.05	100% (140)	71.27 (93.36)
TEPA-SBA-15	93% (158)	7% (12)	80.44 n.a.	830	92% (130.3)	8% (11)	66.33 n.a.	1.92	100% (152)	77.38 n.a.
SIFSIX-3-Cu	13.8% (14.1)	> 86% (88)	7.18 (11.55)	10.03	65% (101)	35% (54)	51.42 (82.68)	0.31	100% (119)	60.58 (97.41)
DICRO-3-Ni-i	> 2% (1.9)	< 97% (80)	0.97 (1.40)	1.47	< 53% (19.2)	> 47% (17.2)	9.77 (14.08)	0.19	100% (23.9)	12.17 (17.54)
SIFSIX-2-Cu-i	1% (1.6)	99% (155)	< 1.00 (1.247)	0.63	59.5% (18.1)	40.5% (12.3)	9.21 (11.48)	0.24	100% (31)	15.78 (19.68)
MOFOUR-1-Ni	> 5% (2.5)	< 95% (49)	1.27 (1.60)	3.29	60% (39)	40% (26)	19.85 (25.01)	0.25	100% (58)	29.53 (37.21)
Ni-4PyC	2% (3.3)	98% (154)	1.68 (1.74)	1.28	61% (15.6)	39% (20.1)	7.94 (8.20)	0.26	100% (26)	13.24 (13.68)
DMOF-1	> 2% (1.3)	< 98% (56)	100 (0.83)	1.28	56% (9.7)	44% (7.7)	4.94 (4.08)	0.21	100% (17.3)	8.81 (7.28)
ZIF-8	23% (2.3)	77% (7.6)	1.20 (1.10)	18.67	75% (2.5)	25% (> 1)	1.27 (1.16)	0.50	100% (1.8)	0.92 (0.84)
MIL-101	< 1% (<1.0)	> 99% (95)	< 1.00 (0.62)	< 0.63	40% (11.2)	60% (16.8)	5.70 (3.53)	0.11	100% (33.1)	16.85 (10.45)
UiO-66	< 1% (0.7)	> 99% (195)	0.36 (1.45)	< 0.63	29.6% (8.4)	70.4% (19.6)	4.28 (5.30)	0.07	100% (31.8)	16.19 (20.04)
UiO-66-NH ₂	< 2% (11.2)	> 98% (237)	5.70 (7.38)	1.28	46.7% (51.3)	53.3% (58.5)	26.12 (33.83)	0.15	100% (59)	30.04 (38.90)

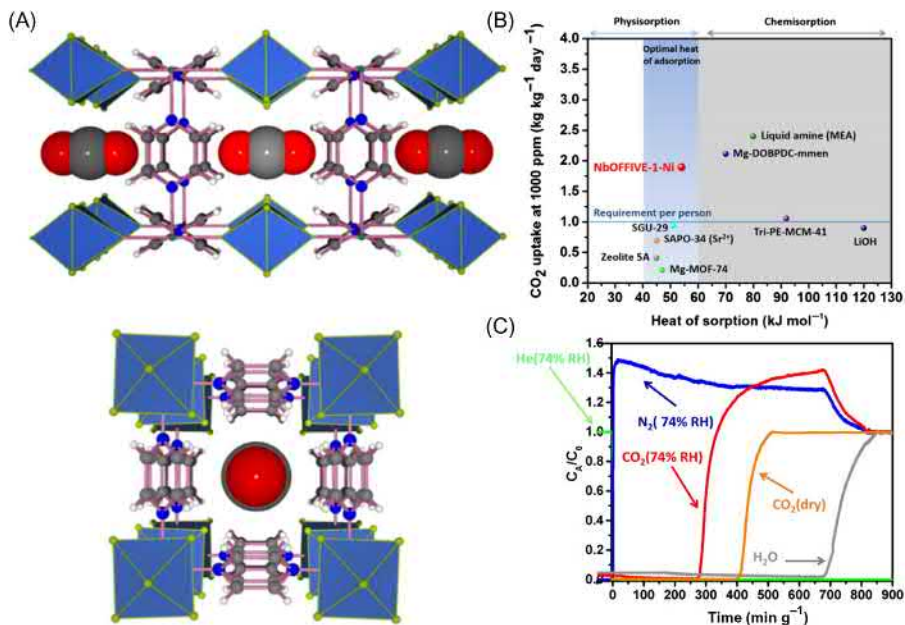


Figure 2.17 (A) Crystallographic direct visualization of CO₂ molecules trapped inside the NbOFFIVE-1-Ni ultramicroporous channels along [001] (top) and [010] (bottom) directions; (B) $Q_{st}(\text{CO}_2)$ versus CO₂ uptake (at 1000 ppm for 1 day) trade-off for NbOFFIVE-1-Ni when compared to CO₂ sorbent benchmarks; (C) binary breakthrough experiments for NbOFFIVE-1-Ni with dry and wet mixed-gas CO₂/N₂ (1%/99%) feeds at 1 bar and 298K (10 cm³ min⁻¹ flow rate).

Source: Reprinted (adapted) with permission from P.M. Bhatt, Y. Belmabkhout, A. Cadiau, K. Adil, O. Shekhah, A. Shkurenko, et al., A fine-tuned fluorinated MOF addresses the needs for trace CO₂ removal and air capture using physisorption, *J. Am. Chem. Soc.* 138 (2016) 9301–9307. Copyright (2016) American Chemical Society with permission.

recycling makes them attractive options for many C-capture applications and perhaps the top option of any sorbent class for trace C-capture applications. The possibility that HUMs might enable a new generation of carbon negative technologies such as DAC now exists and HUMs appear to be primed for study at higher TRL levels.

2.7 Summary and future outlook

Herein, we have described how MOFs and related materials such as HUMs have evolved as potential sorbents for use across a range of C-capture applications. The basic sorption properties of MOFs and HUMs, such as selectivity and working capacity, mean that the upside potential for their utility as energy-efficient C-capture sorbents is higher, perhaps much higher, than existing C-capture sorbents (Table 2.1).

This is largely because of two reasons: their inherent modularity can afford “platforms” of related sorbents with similar structure but different chemical composition to facilitate investigation of structure–function relationships; some of these platforms enable exquisite control over pore size and pore chemistry in a manner that is infeasible for other classes of sorbents. What we have learned to date is that pore chemistry and pore size are both critical with respect to their influence upon selectivity and working capacity. Selectivity is particularly important for trace separations, such as DAC, whereas working capacity is particularly relevant for high concentration C-capture separations, such as NG sweetening and flue gas remediation. However, in order for the full promise of MOFs and HUMs to be realized, they must address the spectrum of challenges that need to be overcome before they can be developed to higher TRL levels for industrial scale applications. As detailed in Fig. 2.3, there are several practical considerations that must also be taken into account such as sorbent cost (raw materials and manufacturing process), recyclability (stability to hydrolytic, thermal, and mechanical stress), and regeneration energy (the sweet spot seems to be in the 40–60 kJ mol⁻¹ range exhibited by strong physisorbents and weak chemisorbents).

2.7.1 Immediate challenges

It is highly unlikely that there will be a “one size fits all” C-capture sorbent since there are multiple C-capture applications and the process conditions of pressure, temperature, gas mixture composition (including wet and dry), and CO₂ levels (from trace to bulk) can vary so widely. This raises another challenge that arises from the fact that there are now on the order of 20–30,000 MOFs and HUMs in the public domain; the number of potential sorbents is presently growing faster than they can be systematically evaluated. In essence, we have managed to create an “embarrass des richesses” because there are so many potential sorbents thanks to the wide range of chemically different but functionally similar platforms of sorbents that now exist. The problem could be described as not so much having to find a needle in a haystack, but having to first find the right haystack (platform) so that the right sorbent can be developed for the right application. One way to partially address this challenge might be to use practical considerations such as cost, hydrolytic stability and thermal stability as early filters so that researchers do not invest much time and money on sorbents that will inevitably fail later in development. However, this approach would lessen the growth in fundamental knowledge concerning structure–property relationships and there are still gaps that must be filled in this fundamental knowledge. Another approach could be to develop predictive models of C-capture performance that are reliable enough to guide synthetic materials chemists. With respect to modeling, considerable progress has been made in recent years with respect to “virtual screening” of a large numbers of sorbents [220,221] and developing new force fields to better understand the energetics around why some sorbents such as HUMs perform better than others with similar features [222]. However, models that can reliably address how sorption

performance changes under different conditions and with different gas mixture compositions are not yet within reach.

2.7.2 The next big challenge

The development of membranes from top-performing sorbents is not yet generally viable but is a highly desirable goal. This is because there are engineering and economic advantages over competing separation technologies. For example, gas treating membrane systems represent a safe and efficient option for water vapor and CO₂ removal from NG, especially in remote locations. Membrane systems are also largely compliant with various gas volumes, CO₂ concentrations, and/or product-gas specifications. Commercialization of membrane technology for gas purification/separation commenced about three decades ago using polymer materials such as polysulfones, cellulose acetate, and polyimides, with emphasis upon NG upgrading and nitrogen blanketing [223]. The guest-accessible ultramicro-/micro-/mesoporosity (inferring high fluxes) and the tunable pore apertures and chemically tailorable surface chemistry of MOFs and HUMs should in principle enable them to serve as C-capture membranes. However, inconsistent intergrowth at the membrane–support interface, poor moisture stability, and little control over “nonporous pathways” typically result in poor separation performances for MOF membranes [224]. Moreover, successful fabrication of pure high quality MOF membranes is challenging even when compared to zeolite membranes because of the following reasons: low heterogeneous nucleation density; less propensity for direct chemical bond formation between the organic linkers of MOFs and the support surfaces; the reduced bond strength of coordination bonds versus metal oxides and intergrowth of MOF crystals [225]. Also, the differential thermal expansion coefficients between the MOF layer and the support have led to crack formation during membrane activation and/or solvent removal. These are perhaps the main reasons behind the current scarcity of MOF membranes in the literature, in general, and C-capture membranes, in particular.

Nevertheless, there are some indications that MOF membranes could become viable. A bottom-up approach led MOF-5 to be introduced as the first pure MOF thin film, whereby nucleation of the crystallites occurred on self-assembled organic monolayers terminated by carboxylic acid functional groups attached to an Au(111) substrate [226]. However, Knudsen diffusion behavior (i.e., pore size is comparable to kinetic diameter of the gas adsorptives) driven separation of gases (CO₂, H₂, CH₄, N₂, and SF₆) could be only harnessed by a fabricated MOF-based membrane (MOF-5 on porous α -alumina) [227]. ZIF-8, [Zn(2-mIm)₂] was prepared as a porous alumina composite membrane and recorded high S_{CM} because of a molecular sieving mechanism [228]. The separation of CO₂ from H₂ was demonstrated using the exfoliated material with up to 1 nm thickness. Size exclusion governed H₂/CO₂ selectivity (> 200) at 393K and 1 bar was reported for an exfoliated membrane comprised from the 2D framework [Zn₂(bIm)₄] (bIm = benzimidazolate) [229]. In general, CO₂ size selective MOFs that combine a small pore aperture (within the range of the kinetic diameter of the target gas) and strong sorbent–CO₂

interactions are the best current candidates for membrane-based C-capture applications. Small apertures and high CO_2 affinity promote the diffusion and solubility parameters, positively influencing the membrane separation process. Nevertheless, implementation of MOFs in membrane technology must still overcome intercrystalline growth [185].

Cu BPDC-TED/PAET (TED: triethylenediamine, PAET: poly(3-acetoxyethylthiophene)) was used to introduce MOFs into the domain of mixed-matrix membranes (MMMs) in which single gas permeation measurements led to S_{CM} of 3.2 [230]. Polymer combination-aided MMMs have been reported from only c. 15 different MOFs [185]. For example, 10 wt.% Mg-MOF-74/PI MMMs made of glassy polyimide (PI) and Mg-MOF-74, were found to exhibit enhanced CO_2 permeability (from 650 to 850 barrers) and S_{CN} (from 14 to 23) when compared to the pure PI membrane performance [231]. Post-treatment of the membrane, enhancing interfacial adhesion between polymer and MOF fillers, PSM, and tweaking the membrane morphology to alter the effects of permselectivity, solubility, and diffusivity could end up affording MMMs that meet industrial specifications (Fig. 2.18) [232]. However, limitations such as lower permeation from MMMs, solidification, and higher MOF loading-derived defect formation remain to be addressed before these MMMs can be studied at higher TRLs.

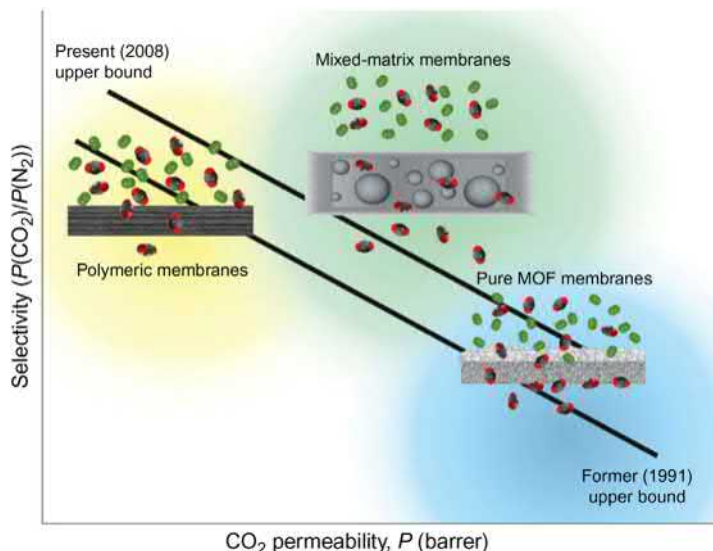


Figure 2.18 CO_2 selectivity (S_{CN}) versus CO_2 permeability (in barrer) plots for pure polymeric, mixed-matrix, and pure MOF membranes, relative to the Robeson upper bound profiles.

Source: Reprinted by permission from C.A. Trickett, A. Helal, B.A. Al-Maythalyon, Z.H. Yamani, K.E. Cordova, O.M. Yaghi, The chemistry of metal-organic frameworks for CO_2 capture, regeneration and conversion, *Nat. Rev. Mater.* 2 (2017) 17045, [copyright] (2017).

Acknowledgment

M.J.Z. gratefully acknowledges the Science Foundation Ireland (13/RP/B2549 and 16/IA/4624).

References

- [1] S. Kitagawa, Porous materials and the age of gas, *Angew. Chem. Int. Ed.* 54 (2015) 10686–10687.
- [2] D.S. Sholl, R.P. Lively, Seven chemical separations to change the world, *Nature* 532 (2016) 432–437.
- [3] A 2030 framework for climate and energy policies European Commission. Brussels. <http://eur-lex.europa.eu/legal-content/EN/TXT/PDF/?uri=CELEX:52013DC0169&from=EN>, 2013.
- [4] R. Monastersky, Global carbon dioxide levels near worrisome milestone, *Nature* 497 (2013) 13–14.
- [5] J.G. Demain, Climate change and the impact on respiratory and allergic disease: 2018, *Curr. Allergy Asthma Rep.* 18 (2018) 22.
- [6] United States Department of Labor, Carbon Dioxide in Workplace Atmospheres, 2018.
- [7] J.C. Knox, Development of Carbon Dioxide Removal Systems for NASA's Deep Space Human Exploration Missions 2016-2017, 2017.
- [8] T.E. Rufford, S. Smart, G.C.Y. Watson, B.F. Graham, J. Boxall, J.C. Diniz da Costa, et al., The removal of CO₂ and N₂ from natural gas: a review of conventional and emerging process technologies, *J. Pet. Sci. Eng.* 94–95 (2012) 123–154.
- [9] R.B.S. Wong, The Inter-American Association of Sanitary and Environmental Engineering (AIDIS) Report: Carbon dioxide separation technologies, 2002.
- [10] M.E. Boot-Handford, J.C. Abanades, E.J. Anthony, M.J. Blunt, S. Brandani, N. Mac Dowell, et al., Carbon capture and storage update, *Energy Environ. Sci.* 7 (2014) 130–189.
- [11] R. Socolow, et al., Direct Air Capture of CO₂ with Chemicals: A Technology Assessment for the APS Panel on Public Affairs, American Physics Society, 2011.
- [12] T.M. McDonald, J.A. Mason, X. Kong, E.D. Bloch, D. Gygi, A. Dani, et al., Cooperative insertion of CO₂ in diamine-appended metal-organic frameworks, *Nature* 519 (2015) 303.
- [13] A. Sayari, A. Heydari-Gorji, Y. Yang, CO₂-induced degradation of amine-containing adsorbents: reaction products and pathways, *J. Am. Chem. Soc.* 134 (2012) 13834–13842.
- [14] D.R. MacFarlane, N. Tachikawa, M. Forsyth, J.M. Pringle, P.C. Howlett, G.D. Elliott, et al., Energy applications of ionic liquids, *Energy Environ. Sci.* 7 (2014) 232–250.
- [15] A. Kumar, D.G. Madden, M. Lusi, K.-J. Chen, E.A. Daniels, T. Curtin, et al., Direct air capture of CO₂ by physisorbent materials, *Angew. Chem. Int. Ed.* 54 (2015) 14372–14377.
- [16] J.Y.S. Lin, Molecular sieves for gas separation, *Science* 353 (2016) 121–122.
- [17] S. Subramanian, M.J. Zaworotko, Porous solids by design: [Zn(4,4'-bpy)₂(SiF₆)_n · xDMF]_n, a single framework octahedral coordination polymer with large square channels, *Angew. Chem. Int. Ed.* 34 (1995) 2127–2129.
- [18] H.S. Scott, A. Bajpai, K.-J. Chen, T. Pham, B. Space, J.J. Perry, et al., Novel mode of 2-fold interpenetration observed in a primitive cubic network of formula [Ni(1,2-bis(4-pyridyl)acetylene)₂(Cr₂O₇)_n]_n, *Chem. Commun.* 51 (2015) 14832–14835.

- [19] P. Nugent, Y. Belmabkhout, S.D. Burd, A.J. Cairns, R. Luebke, K. Forrest, et al., Porous materials with optimal adsorption thermodynamics and kinetics for CO₂ separation, *Nature* 495 (2013) 80.
- [20] X. Cui, K. Chen, H. Xing, Q. Yang, R. Krishna, Z. Bao, et al., Pore chemistry and size control in hybrid porous materials for acetylene capture from ethylene, *Science* 353 (2016) 141–144.
- [21] S.D. Burd, S. Ma, J.A. Perman, B.J. Sikora, R.Q. Snurr, P.K. Thallapally, et al., Highly selective carbon dioxide uptake by [Cu(bpy-n)₂(SiF₆)] (bpy-1 = 4,4'-Bipyridine; bpy-2 = 1,2-Bis(4-pyridyl)ethene), *J. Am. Chem. Soc.* 134 (2012) 3663–3666.
- [22] M.H. Mohamed, S.K. Elsaidi, T. Pham, K.A. Forrest, B. Tudor, L. Wojtas, et al., Pillar substitution modulates CO₂ affinity in “mmo” topology networks, *Chem. Commun.* 49 (2013) 9809–9811.
- [23] M.T. Ho, G.W. Allinson, D.E. Wiley, Reducing the cost of CO₂ capture from flue gases using pressure swing adsorption, *Ind. Eng. Chem. Res.* 47 (2008) 4883–4890.
- [24] L.R. MacGillivray, *Metal-Organic Frameworks: Design and Application*, John Wiley & Sons, 2010.
- [25] S. Kitagawa, R. Kitaura, S.-i. Noro, Functional porous coordination polymers, *Angew. Chem. Int. Ed.* 43 (2004) 2334–2375.
- [26] K. Sumida, D.L. Rogow, J.A. Mason, T.M. McDonald, E.D. Bloch, Z.R. Herm, et al., Carbon dioxide capture in metal–organic frameworks, *Chem. Rev.* 112 (2012) 724–781.
- [27] Q.-Y. Yang, P. Lama, S. Sen, M. Lusi, K.-J. Chen, W.-Y. Gao, et al., Reversible switching between highly porous and nonporous phases of an interpenetrated diamondoid coordination network that exhibits gate-opening at methane storage pressures, *Angew. Chem. Int. Ed.* 57 (2018) 5684–5689.
- [28] Y.-S. Bae, R.Q. Snurr, Development and evaluation of porous materials for carbon dioxide separation and capture, *Angew. Chem. Int. Ed.* 50 (2011) 11586–11596.
- [29] A.L. Myers, J.M. Prausnitz, Thermodynamics of mixed-gas adsorption, *AIChE J.* 11 (1965) 121–127.
- [30] C.M. Simon, B. Smit, M. Haranczyk, pyIAST: ideal adsorbed solution theory (IAST) Python package, *Comput. Phys. Commun.* 200 (2016) 364–380.
- [31] R.T. Yang, *Adsorbents: Fundamentals and Applications*, Wiley, 2007.
- [32] M. Oschatz, M. Antonietti, A search for selectivity to enable CO₂ capture with porous adsorbents, *Energy Environ. Sci.* 11 (2018) 57–70.
- [33] Y. Zhao, K.X. Yao, B. Teng, T. Zhang, Y. Han, A perfluorinated covalent triazine-based framework for highly selective and water-tolerant CO₂ capture, *Energy Environ. Sci.* 6 (2013) 3684–3692.
- [34] J.A. Mason, K. Sumida, Z.R. Herm, R. Krishna, J.R. Long, Evaluating metal–organic frameworks for post-combustion carbon dioxide capture via temperature swing adsorption, *Energy Environ. Sci.* 4 (2011) 3030–3040.
- [35] Z.R. Herm, J.A. Swisher, B. Smit, R. Krishna, J.R. Long, Metal – organic frameworks as adsorbents for hydrogen purification and precombustion carbon dioxide capture, *J. Am. Chem. Soc.* 133 (2011) 5664–5667.
- [36] M. Dincă, A. Dailly, Y. Liu, C.M. Brown, D.A. Neumann, J.R. Long, Hydrogen storage in a microporous metal – organic framework with exposed Mn²⁺ coordination sites, *J. Am. Chem. Soc.* 128 (2006) 16876–16883.
- [37] K.-J. Chen, H.S. Scott, D.G. Madden, T. Pham, A. Kumar, A. Bajpai, et al., Benchmark C₂H₂/CO₂ and CO₂/C₂H₂ separation by two closely related hybrid ultramicroporous materials, *Chem* 1 (2016) 753–765.

- [38] X. Xu, C. Song, J.M. Andresen, B.G. Miller, A.W. Scaroni, Novel polyethylenimine-modified mesoporous molecular sieve of MCM-41 type as high-capacity adsorbent for CO₂ capture, *Energy Fuels* 16 (2002) 1463–1469.
- [39] A. Zhao, A. Samanta, P. Sarkar, R. Gupta, Carbon dioxide adsorption on amine-impregnated mesoporous SBA-15 Sorbents: experimental and kinetics study, *Ind. Eng. Chem. Res.* 52 (2013) 6480–6491.
- [40] K.C. Waterman, in: K. Huynh-Ba (Ed.), *Handbook of Stability Testing in Pharmaceutical Development*, Springer, New York, 2009, pp. 116–135.
- [41] D.G. Madden, H.S. Scott, A. Kumar, K.-J. Chen, R. Sani, A. Bajpai, et al., Flue-gas and direct-air capture of CO₂ by porous metal–organic materials, *Philos. Trans. R. Soc. A* 375 (2017).
- [42] C.R. Groom, I.J. Bruno, M.P. Lightfoot, S.C. Ward, The Cambridge structural database, *Acta Crystallogr. B* 72 (2016) 171–179.
- [43] M. Rubio-Martinez, C. Avci-Camur, A.W. Thornton, I. Imaz, D. Maspocho, M.R. Hill, New synthetic routes towards MOF production at scale, *Chem. Soc. Rev.* 46 (2017) 3453–3480.
- [44] D. Crawford, J. Casaban, R. Haydon, N. Giri, T. McNally, S.L. James, Synthesis by extrusion: continuous, large-scale preparation of MOFs using little or no solvent, *Chem. Sci.* 6 (2015) 1645–1649.
- [45] J. Ren, X. Dyosiba, N.M. Musyoka, H.W. Langmi, M. Mathe, S. Liao, Review on the current practices and efforts towards pilot-scale production of metal-organic frameworks (MOFs), *Coord. Chem. Rev.* 352 (2017) 187–219.
- [46] A.D. Wiersum, J.-S. Chang, C. Serre, P.L. Llewellyn, An adsorbent performance indicator as a first step evaluation of novel sorbents for gas separations: application to metal–organic frameworks, *Langmuir* 29 (2013) 3301–3309.
- [47] R. Krishna, Screening metal–organic frameworks for mixture separations in fixed-bed adsorbers using a combined selectivity/capacity metric, *RSC Adv.* 7 (2017) 35724–35737.
- [48] D. Dokur, S. Keskin, Effects of force field selection on the computational ranking of MOFs for CO₂ separations, *Ind. Eng. Chem. Res.* 57 (2018) 2298–2309.
- [49] C. Altintas, G. Avci, H. Daglar, A. Nemati Vesali Azar, S. Velioglu, I. Erucar, et al., Database for CO₂ separation performances of MOFs based on computational materials screening, *ACS Appl. Mater. Interfaces* 10 (2018) 17257–17268.
- [50] P. Markewitz, W. Kuckshinrichs, W. Leitner, J. Linssen, P. Zapp, R. Bongartz, et al., Worldwide innovations in the development of carbon capture technologies and the utilization of CO₂, *Energy Environ. Sci.* 5 (2012) 7281–7305.
- [51] IPCC, Carbon Dioxide Capture and Storage—Special Report of the Intergovernmental Panel on Climate Change, Cambridge University Press, Cambridge, 2005.
- [52] M. Wang, A. Lawal, P. Stephenson, J. Sidders, C. Ramshaw, Post-combustion CO₂ capture with chemical absorption: a state-of-the-art review, *Chem. Eng. Res. Des.* 89 (2011) 1609–1624.
- [53] U. Desideri, A. Paolucci, Performance modelling of a carbon dioxide removal system for power plants, *Energy Convers. Manag.* 40 (1999) 1899–1915.
- [54] B. Dutcher, M. Fan, A.G. Russell, Amine-based CO₂ capture technology development from the beginning of 2013—a review, *ACS Appl. Mater. Interfaces* 7 (2015) 2137–2148.
- [55] Z. Zhang, Z.-Z. Yao, S. Xiang, B. Chen, Perspective of microporous metal-organic frameworks for CO₂ capture and separation, *Energy Environ. Sci.* 7 (2014) 2868–2899.

- [56] G.C. Institute, Pre-Combustion Capture, Global Carbon Capture and Storage Institute, Canberra, 2011.
- [57] IEA, Energy Technology Perspectives – Scenarios & Strategies to 2050, Paris, 2006.
- [58] G.C. Institute, Oxy Combustion with CO₂ Capture, Global Carbon Capture and Storage Institute, Canberra, 2011.
- [59] <https://www.carbonbrief.org/explainer-10-ways-negative-emissions-could-slow-climate-change> (accessed 18.07.18).
- [60] H. Li, K. Wang, Y. Sun, C.T. Lollar, J. Li, H.-C. Zhou, Recent advances in gas storage and separation using metal–organic frameworks, *Mater. Today* 21 (2018) 108–121.
- [61] K.S. Lackner, H.-J. Ziock, P. Grimes, The 24th International Conference on Coal Utilization & Fuel Systems, Clearwater, FL, 1999.
- [62] E.S. Sanz-Pérez, C.R. Murdock, S.A. Didas, C.W. Jones, Direct capture of CO₂ from ambient air, *Chem. Rev.* 116 (2016) 11840–11876.
- [63] M.J.M. Usha Satish, K. Shekhar, T. Hotchi, D. Sullivan, S. Streufert, W.J. Fisk, Is CO₂ an indoor pollutant? Direct effects of low-to-moderate CO₂ concentrations on human decision-making performance, *Environ. Health Perspect.* (2012). Available from: <https://doi.org/10.1289/ehp.1104789>.
- [64] <https://www.carbonbrief.org/swiss-company-hoping-capture-1-global-co2-emissions-2025> (accessed 18.07.18).
- [65] P. Pässler, W. Hefner, K. Buckl, H. Meinass, A. Meiswinkel, H.-J. Wernicke, et al., Acetylene, *Ullmann's Encyclopedia of Industrial Chemistry*, Wiley-VCH Verlag GmbH & Co. KGaA, 2000.
- [66] H.S. Scott, M. Shivanna, A. Bajpai, D.G. Madden, K.-J. Chen, T. Pham, et al., Highly selective separation of C₂H₂ from CO₂ by a new dichromate-based hybrid ultramicro-porous material, *ACS Appl. Mater. Interfaces* 9 (2017) 33395–33400.
- [67] D.L.V. Katz, *Handbook of Natural Gas Engineering*, McGraw-Hill, 1959.
- [68] BP, BP Statistical Review of World Energy 2016, London, 2016.
- [69] World Energy Resources 2016, published by the World Energy Council 2016, ISBN: 978 0 946121 62 5.
- [70] I.G.K. Wood, B. Ho, S. Kerr, S. Cavanagh, D. Wood, A. Haywood, Guidebook to Gas Interchangeability and Gas Quality, 2011.
- [71] R. Sabouni, H. Kazemian, S. Rohani, Carbon dioxide capturing technologies: a review focusing on metal organic framework materials (MOFs), *Environ. Sci. Pollut. Res. Int.* 21 (2014) 5427–5449.
- [72] <http://www.technology.matthey.com/article/27/4/157-169/> (accessed 19.01.18).
- [73] <https://www.uop.com/equipment/hydrogen-separation/> (accessed 19.01.18).
- [74] L.A. Blanchard, D. Hancu, E.J. Beckman, J.F. Brennecke, Green processing using ionic liquids and CO₂, *Nature* 399 (1999) 28.
- [75] X. Zhang, X. Zhang, H. Dong, Z. Zhao, S. Zhang, Y. Huang, Carbon capture with ionic liquids: overview and progress, *Energy Environ. Sci.* 5 (2012) 6668–6681.
- [76] X. Zhu, C.-L. Do-Thanh, S. Dai, Ionic liquid-derived carbonaceous adsorbents for CO₂ capture, in: A.-H. Lu, S. Dai (Eds.), *Porous Materials for Carbon Dioxide Capture*, Springer Berlin Heidelberg, Berlin, Heidelberg, 2014, pp. 1–14.
- [77] S. Zeng, X. Zhang, L. Bai, X. Zhang, H. Wang, J. Wang, et al., Ionic-liquid-based CO₂ capture systems: Structure, interaction and process, *Chem. Rev.* 117 (2017) 9625–9673.
- [78] J. Zhang, C. Jia, H. Dong, J. Wang, X. Zhang, S. Zhang, A novel dual amino-functionalized cation-tethered ionic liquid for CO₂ capture, *Ind. Eng. Chem. Res.* 52 (2013) 5835–5841.

- [79] M. Ramdin, T.W. de Loos, T.J.H. Vlught, State-of-the-art of CO₂ capture with ionic liquids, *Ind. Eng. Chem. Res.* 51 (2012) 8149–8177.
- [80] L.-L. Zhang, J.-X. Wang, Y. Xiang, X.-F. Zeng, J.-F. Chen, Absorption of carbon dioxide with ionic liquid in a rotating packed bed contactor: mass transfer study, *Ind. Eng. Chem. Res.* 50 (2011) 6957–6964.
- [81] J.-R. Li, Y. Ma, M.C. McCarthy, J. Sculley, J. Yu, H.-K. Jeong, et al., Carbon dioxide capture-related gas adsorption and separation in metal-organic frameworks, *Coord. Chem. Rev.* 255 (2011) 1791–1823.
- [82] J.A. Mason, K. Sumida, Z.R. Herm, R. Krishna, J.R. Long, Evaluating metal-organic frameworks for post-combustion carbon dioxide capture via temperature swing adsorption, *Energy Environ. Sci.* 4 (2011) 3030–3040.
- [83] J.G. Calvert, Glossary of atmospheric chemistry terms (Recommendations 1990), *Pure Appl. Chem.* 62 (1990) 2167–2179.
- [84] A. Perejón, L.M. Romeo, Y. Lara, P. Lisbona, A. Martínez, J.M. Valverde, The calcium-looping technology for CO₂ capture: on the important roles of energy integration and sorbent behavior, *Appl. Energy* 162 (2016) 787–807.
- [85] J.M. Valverde, The Ca-looping process for CO₂ capture and energy storage: role of nanoparticle technology, *J. Nanoparticle Res.* 20 (2018) 39.
- [86] M. Broda, R. Pacciani, C.R. Müller, CO₂ capture via cyclic calcination and carbonation reactions, in: A.-H. Lu, S. Dai (Eds.), *Porous Materials for Carbon Dioxide Capture*, Springer Berlin Heidelberg, Berlin, Heidelberg, 2014, pp. 181–222.
- [87] J. Blamey, E.J. Anthony, J. Wang, P.S. Fennell, The calcium looping cycle for large-scale CO₂ capture, *Prog. Energy Combust. Sci.* 36 (2010) 260–279.
- [88] O. Leal, C. Bolívar, C. Ovalles, J.J. García, Y. Espidel, Reversible adsorption of carbon dioxide on amine surface-bonded silica gel, *Inorg. Chim. Acta* 240 (1995) 183–189.
- [89] M.B. Yue, Y. Chun, Y. Cao, X. Dong, J.H. Zhu, CO₂ capture by as-prepared SBA-15 with an occluded organic template, *Adv. Funct. Mater.* 16 (2006) 1717–1722.
- [90] <http://www.rite.or.jp/chemical/en/theme/2014/04/solid2.html>, Research Institute of Innovative Technology for the Earth (accessed 20.10.18).
- [91] Y. Belmabkhout, A. Sayari, Isothermal versus non-isothermal adsorption – desorption cycling of triamine-grafted pore-expanded MCM-41 mesoporous silica for CO₂ capture from flue gas, *Energy Fuels* 24 (2010) 5273–5280.
- [92] Y. Belmabkhout, R. Serna-Guerrero, A. Sayari, Adsorption of CO₂-containing gas mixtures over amine-bearing pore-expanded MCM-41 silica: application for gas purification, *Ind. Eng. Chem. Res.* 49 (2010) 359–365.
- [93] A. Sayari, Y. Belmabkhout, E. Da'na, CO₂ deactivation of supported amines: does the nature of amine matter?, *Langmuir* 28 (2012) 4241–4247.
- [94] A. Heydari-Gorji, A. Sayari, Thermal, oxidative, and CO₂-induced degradation of supported polyethylenimine adsorbents, *Ind. Eng. Chem. Res.* 51 (2012) 6887–6894.
- [95] A.P. Hallenbeck, J.R. Kitchin, Effects of O₂ and SO₂ on the capture capacity of a primary-amine based polymeric CO₂ sorbent, *Ind. Eng. Chem. Res.* 52 (2013) 10788–10794.
- [96] C.W. Jones, CO₂ capture from dilute gases as a component of modern global carbon management, *Annu. Rev. Chem. Biomol. Eng.* 2 (2011) 31–52.
- [97] IUPAC, 46, 71, *Manual of Symbols and Terminology for Physicochemical Quantities and Units - Appendix II. Definitions, Terminology and Symbols in Colloid and Surface Chemistry. Part II: Heterogeneous Catalysis*, 1976, p. 75.
- [98] J.V. Smith, Definition of a zeolite, *Zeolites* 4 (1984) 309–310.

- [99] J. Merel, M. Clause, F. Meunier, Experimental investigation on CO₂ post – combustion capture by indirect thermal swing adsorption using 13X and 5A zeolites, *Ind. Eng. Chem. Res.* 47 (2008) 209–215.
- [100] X. Hu, E. Mangano, D. Friedrich, H. Ahn, S. Brandani, Diffusion mechanism of CO₂ in 13X zeolite beads, *Adsorption* 20 (2014) 121–135.
- [101] S.V. Sivakumar, D.P. Rao, Modified duplex PSA. 1. Sharp separation and process intensification for CO₂ – N₂ – 13X zeolite system, *Ind. Eng. Chem. Res.* 50 (2011) 3426–3436.
- [102] D.P. Bezerra, R.S. Oliveira, R.S. Vieira, C.L. Cavalcante, D.C.S. Azevedo, Adsorption of CO₂ on nitrogen-enriched activated carbon and zeolite 13X, *Adsorption* 17 (2011) 235–246.
- [103] J. Mérel, M. Clause, F. Meunier, Carbon dioxide capture by indirect thermal swing adsorption using 13X zeolite, *Environ. Prog.* 25 (2006) 327–333.
- [104] F. Brandani, D.M. Ruthven, The effect of water on the adsorption of CO₂ and C₃H₈ on Type X zeolites, *Ind. Eng. Chem. Res.* 43 (2004) 8339–8344.
- [105] G. Li, P. Xiao, P. Webley, J. Zhang, R. Singh, M. Marshall, Capture of CO₂ from high humidity flue gas by vacuum swing adsorption with zeolite 13X, *Adsorption* 14 (2008) 415–422.
- [106] R.V. Siriwardane, M.-S. Shen, E.P. Fisher, J.A. Poston, Adsorption of CO₂ on molecular sieves and activated carbon, *Energy Fuels* 15 (2001) 279–284.
- [107] D.M. D'Alessandro, B. Smit, J.R. Long, Carbon dioxide capture: prospects for new materials, *Angew. Chem. Int. Ed.* 49 (2010) 6058–6082.
- [108] C. Lu, H. Bai, B. Wu, F. Su, J.F. Hwang, Comparative study of CO₂ capture by carbon nanotubes, activated carbons, and zeolites, *Energy Fuels* 22 (2008) 3050–3056.
- [109] J.J. Perry Iv, J.A. Perman, M.J. Zaworotko, Design and synthesis of metal-organic frameworks using metal-organic polyhedra as supermolecular building blocks, *Chem. Soc. Rev.* 38 (2009) 1400–1417.
- [110] D. Farrusseng, *Metal–Organic Frameworks: Applications from Catalysis to Gas Storage*, Wiley-VCH Verlag GmbH, Weinheim, 2011.
- [111] S. Kaskel, *The Chemistry of Metal–Organic Frameworks: Synthesis, Characterization, and Applications*, Wiley, 2016. Available from: <http://dx.doi.org/10.1002/9783527693078>.
- [112] B. Moulton, M.J. Zaworotko, From molecules to crystal engineering: supramolecular isomerism and polymorphism in network solids, *Chem. Rev.* 101 (2001) 1629–1658.
- [113] M.J. Zaworotko, Molecules to crystals, crystals to molecules ... and back again? *Cryst. Growth Des.* 7 (2007) 4–9.
- [114] S.R. Batten, Coordination polymers, *Curr. Opin. Solid State Mater. Sci.* 5 (2001) 107–114.
- [115] B.F. Hoskins, R. Robson, Infinite polymeric frameworks consisting of three dimensionally linked rod-like segments, *J. Am. Chem. Soc.* 111 (1989) 5962–5964.
- [116] A.F. Wells, *Three Dimensional Nets and Polyhedra*, Wiley, New York, 1977.
- [117] J.J. Perry Iv, J.A. Perman, M.J. Zaworotko, Design and synthesis of metal–organic frameworks using metal–organic polyhedra as supermolecular building blocks, *Chem. Soc. Rev.* 38 (2009) 1400–1417.
- [118] F. Allen, The Cambridge Structural Database: a quarter of a million crystal structures and rising, *Acta Crystallogr. B* 58 (2002) 380–388.
- [119] O.K.F.H. Allen, 3D search and research using the Cambridge Structural Database, *Chem. Des. Automat. News* 8 (1993) 31–37.

- [120] R.W. Gable, B.F. Hoskins, R. Robson, A new type of interpenetration involving enmeshed independent square grid sheets. The structure of diaquabis-(4,4'-bipyridine) zinc hexafluorosilicate, *J. Chem. Soc. Chem. Commun.* (1990) 1677–1678. Available from: <https://doi.org/10.1039/C39900001677>.
- [121] M. Fujita, Y.J. Kwon, S. Washizu, K. Ogura, Preparation, clathration ability, and catalysis of a two-dimensional square network material composed of cadmium(II) and 4,4'-bipyridine, *J. Am. Chem. Soc.* 116 (1994) 1151–1152.
- [122] L.R. MacGillivray, S. Subramanian, M.J. Zaworotko, Interwoven two- and three-dimensional coordination polymers through self-assembly of Cu cations with linear bidentate ligands, *J. Chem. Soc. Chem. Commun.* (1994) 1325–1326. Available from: <https://doi.org/10.1039/C39940001325>.
- [123] M.J. Zaworotko, Crystal engineering of diamondoid networks, *Chem. Soc. Rev.* 23 (1994) 283–288.
- [124] H. Li, M. Eddaoudi, T.L. Groy, O.M. Yaghi, Establishing microporosity in open metal-organic frameworks: gas sorption isotherms for Zn(BDC) (BDC = 1,4-Benzenedicarboxylate), *J. Am. Chem. Soc.* 120 (1998) 8571–8572.
- [125] H. Li, M. Eddaoudi, M. O’Keeffe, O.M. Yaghi, Design and synthesis of an exceptionally stable and highly porous metal-organic framework, *Nature* 402 (1999) 276.
- [126] M. O’Keeffe, M.A. Peskov, S.J. Ramsden, O.M. Yaghi, The Reticular Chemistry Structure Resource (RCSR) database of, and symbols for, crystal nets, *Acc. Chem. Res.* 41 (2008) 1782–1789.
- [127] S.S.-Y. Chui, S.M.-F. Lo, J.P.H. Charmant, A.G. Orpen, I.D. Williams, A chemically functionalizable nanoporous material $[\text{Cu}_3(\text{TMA})_2(\text{H}_2\text{O})_3]_n$, *Science* 283 (1999) 1148–1150.
- [128] B. Zheng, J. Bai, J. Duan, L. Wojtas, M.J. Zaworotko, Enhanced CO_2 binding affinity of a high-uptake rht-type metal-organic framework decorated with acylamide groups, *J. Am. Chem. Soc.* 133 (2011) 748–751.
- [129] T. Remy, S.A. Peter, S. Van der Perre, P. Valvekens, D.E. De Vos, G.V. Baron, et al., Selective dynamic CO_2 separations on Mg-MOF-74 at low pressures: a detailed comparison with 13X, *J. Phys. Chem. C* 117 (2013) 9301–9310.
- [130] M. Ansari, A. Aroujalian, A. Raisi, B. Dabir, M. Fathizadeh, Preparation and characterization of nano-NaX zeolite by microwave assisted hydrothermal method, *Adv. Powder Technol.* 25 (2014) 722–727.
- [131] C.P. Cabello, G. Berlier, G. Magnacca, P. Rumori, G.T. Palomino, Enhanced CO_2 adsorption capacity of amine-functionalized MIL-100(Cr) metal-organic frameworks, *CrystEngComm* 17 (2015) 430–437.
- [132] S.R. Caskey, A.G. Wong-Foy, A.J. Matzger, Dramatic tuning of carbon dioxide uptake via metal substitution in a coordination polymer with cylindrical pores, *J. Am. Chem. Soc.* 130 (2008) 10870–10871.
- [133] T.M. McDonald, W.R. Lee, J.A. Mason, B.M. Wiers, C.S. Hong, J.R. Long, Capture of carbon dioxide from air and flue gas in the alkylamine-appended metal-organic framework mmen- $\text{Mg}_2(\text{dobpdc})$, *J. Am. Chem. Soc.* 134 (2012) 7056–7065.
- [134] P.L. Llewellyn, S. Bourrelly, C. Serre, A. Vimont, M. Daturi, L. Hamon, et al., High uptakes of CO_2 and CH_4 in mesoporous metal-organic frameworks MIL-100 and MIL-101, *Langmuir* 24 (2008) 7245–7250.
- [135] K. Munusamy, G. Sethia, D.V. Patil, P.B. Somayajulu Rallapalli, R.S. Somani, H.C. Bajaj, Sorption of carbon dioxide, methane, nitrogen and carbon monoxide on MIL-101(Cr): volumetric measurements and dynamic adsorption studies, *Chem. Eng. J.* 195-196 (2012) 359–368.

- [136] B. Li, Z. Zhang, Y. Li, K. Yao, Y. Zhu, Z. Deng, et al., Enhanced binding affinity, remarkable selectivity, and high capacity of CO₂ by dual functionalization of a rht-type metal-organic framework, *Angew. Chem. Int. Ed.* 51 (2012) 1412–1415.
- [137] Y. Huang, W. Qin, Z. Li, Y. Li, Enhanced stability and CO₂ affinity of a UiO-66 type metal-organic framework decorated with dimethyl groups, *Dalton Trans.* 41 (2012) 9283–9285.
- [138] J. Liu, Y. Wang, A.I. Benin, P. Jakubczak, R.R. Willis, M.D. LeVan, CO₂/H₂O adsorption equilibrium and rates on metal-organic frameworks: HKUST-1 and Ni/DOBDC, *Langmuir* 26 (2010) 14301–14307.
- [139] S.R. Ahrenholtz, C. Landaverde-Alvarado, M. Whiting, S. Lin, C. Slebodnick, E. Marand, et al., Thermodynamic study of CO₂ sorption by polymorphic microporous MOFs with open Zn(II) coordination sites, *Inorg. Chem.* 54 (2015) 4328–4336.
- [140] G.E. Cmarik, M. Kim, S.M. Cohen, K.S. Walton, Tuning the adsorption properties of UiO-66 via ligand functionalization, *Langmuir* 28 (2012) 15606–15613.
- [141] D. Yuan, D. Zhao, D. Sun, H.C. Zhou, An isoreticular series of metal-organic frameworks with dendritic hexacarboxylate ligands and exceptionally high gas-uptake capacity, *Angew. Chem. Int. Ed.* 49 (2010) 5357–5361.
- [142] M.C. Bernini, A.A. Garcia Blanco, J. Villarroel-Rocha, D. Fairen-Jimenez, K. Sapag, A.J. Ramirez-Pastor, et al., Tuning the target composition of amine-grafted CPO-27-Mg for capture of CO₂ under post-combustion and air filtering conditions: a combined experimental and computational study, *Dalton Trans.* 44 (2015) 18970–18982.
- [143] Y. Hu, W.M. Verdegaal, S.H. Yu, H.L. Jiang, Alkylamine-tethered stable metal-organic framework for CO₂ capture from flue gas, *ChemSusChem* 7 (2014) 734–737.
- [144] T.M. McDonald, D.M. D'Alessandro, R. Krishna, J.R. Long, Enhanced carbon dioxide capture upon incorporation of N,N'-dimethylethylenediamine in the metal-organic framework CuBTTri, *Chem. Sci.* 2 (2011) 2022–2028.
- [145] P.-Q. Liao, X.-W. Chen, S.-Y. Liu, X.-Y. Li, Y.-T. Xu, M. Tang, et al., Putting an ultrahigh concentration of amine groups into a metal-organic framework for CO₂ capture at low pressures, *Chem. Sci.* 7 (2016) 6528–6533.
- [146] A. Demessence, D.M. D'Alessandro, M.L. Foo, J.R. Long, Strong CO₂ binding in a water-stable, triazolate-bridged metal-organic framework functionalized with ethylenediamine, *J. Am. Chem. Soc.* 131 (2009) 8784–8786.
- [147] W.R. Lee, H. Jo, L.-M. Yang, H. Lee, D.W. Ryu, K.S. Lim, et al., Exceptional CO₂ working capacity in a heterodiamine-grafted metal-organic framework, *Chem. Sci.* 6 (2015) 3697–3705.
- [148] W.R. Lee, S.Y. Hwang, D.W. Ryu, K.S. Lim, S.S. Han, D. Moon, et al., Diamine-functionalized metal-organic framework: exceptionally high CO₂ capacities from ambient air and flue gas, ultrafast CO₂ uptake rate, and adsorption mechanism, *Energy Environ. Sci.* 7 (2014) 744–751.
- [149] Y. Lin, C. Kong, L. Chen, Direct synthesis of amine-functionalized MIL-101(Cr) nanoparticles and application for CO₂ capture, *RSC Adv.* 2 (2012) 6417–6419.
- [150] X. Si, C. Jiao, F. Li, J. Zhang, S. Wang, S. Liu, et al., High and selective CO₂ uptake, H₂ storage and methanol sensing on the amine-decorated 12-connected MOF CAU-1, *Energy Environ. Sci.* 4 (2011) 4522–4527.
- [151] J. An, S.J. Geib, N.L. Rosi, High and selective CO₂ uptake in a cobalt adeninate metal-organic framework exhibiting pyrimidine- and amino-decorated pores, *J. Am. Chem. Soc.* 132 (2010) 38–39.

- [152] H.-Y. Ren, X.-M. Zhang, Enhanced selective CO₂ capture upon incorporation of dimethylformamide in the cobalt metal–organic framework [Co₃(OH)₂(btca)₂], *Energy Fuels* 30 (2016) 526–530.
- [153] X. Zhang, Y.-Z. Zhang, D.-S. Zhang, B. Zhu, J.-R. Li, A hydrothermally stable Zn(ii)-based metal-organic framework: structural modulation and gas adsorption, *Dalton Trans.* 44 (2015) 15697–15702.
- [154] R. Vaidhyanathan, S.S. Iremonger, K.W. Dawson, G.K.H. Shimizu, An amine-functionalized metal organic framework for preferential CO₂ adsorption at low pressures, *Chem. Commun.* (2009) 5230–5232. Available from: <https://doi.org/10.1039/B911481E>.
- [155] R. Vaidhyanathan, S.S. Iremonger, G.K.H. Shimizu, P.G. Boyd, S. Alavi, T.K. Woo, Direct observation and quantification of CO₂ binding within an amine-functionalized nanoporous solid, *Science* 330 (2010) 650–653.
- [156] H.R. Abid, Z.H. Rada, X. Duan, H. Sun, S. Wang, Enhanced CO₂ adsorption and selectivity of CO₂/N₂ on amino-MIL-53(Al) synthesized by polar co-solvents, *Energy Fuels* (2017). Available from: <https://doi.org/10.1021/acs.energyfuels.7b03240>.
- [157] R. Luebke, Ł.J. Weseliński, Y. Belmabkhout, Z. Chen, Ł. Wojtas, M. Eddaoudi, Microporous heptazine functionalized (3,24)-connected rht-metal–organic framework: synthesis, structure, and gas sorption analysis, *Cryst. Growth Des.* 14 (2014) 414–418.
- [158] S. Xiong, Y. Gong, H. Wang, H. Wang, Q. Liu, M. Gu, et al., A new tetrazolate zeolite-like framework for highly selective CO₂/CH₄ and CO₂/N₂ separation, *Chem. Commun.* 50 (2014) 12101–12104.
- [159] H. Jo, W.R. Lee, N.W. Kim, H. Jung, K.S. Lim, J.E. Kim, et al., Fine-tuning of the carbon dioxide capture capability of diamine-grafted metal–organic framework adsorbents through amine functionalization, *ChemSusChem* 10 (2017) 541–550.
- [160] D. Saha, Z. Bao, F. Jia, S. Deng, Adsorption of CO₂, CH₄, N₂O, and N₂ on MOF-5, MOF-177, and Zeolite 5A, *Environ. Sci. Technol.* 44 (2010) 1820–1826.
- [161] M.H. Mohamed, S.K. Elsaidi, L. Wojtas, T. Pham, K.A. Forrest, B. Tudor, et al., Highly selective CO₂ uptake in uninodal 6-connected “mmo” nets based upon MO₄²⁻ (M = Cr, Mo) pillars, *J. Am. Chem. Soc.* 134 (2012) 19556–19559.
- [162] P.M. Bhatt, Y. Belmabkhout, A. Cadiou, K. Adil, O. Shekhah, A. Shkurenko, et al., A fine-tuned fluorinated MOF addresses the needs for trace CO₂ removal and air capture using physisorption, *J. Am. Chem. Soc.* 138 (2016) 9301–9307.
- [163] A. Kumar, C. Hua, D.G. Madden, D. O’Nolan, K.-J. Chen, L.-A.J. Keane, et al., Hybrid ultramicroporous materials (HUMs) with enhanced stability and trace carbon capture performance, *Chem. Commun.* 53 (2017) 5946–5949.
- [164] O. Shekhah, Y. Belmabkhout, Z. Chen, V. Guillermin, A. Cairns, K. Adil, et al., Made-to-order metal-organic frameworks for trace carbon dioxide removal and air capture, *Nat. Commun.* 5 (2014) 4228.
- [165] Y. Xiong, Y.-Z. Fan, R. Yang, S. Chen, M. Pan, J.-J. Jiang, et al., Amide and N-oxide functionalization of T-shaped ligands for isorecticular MOFs with giant enhancements in CO₂ separation, *Chem. Commun.* 50 (2014) 14631–14634.
- [166] D.H. Hong, M.P. Suh, Enhancing CO₂ separation ability of a metal–organic framework by post-synthetic ligand exchange with flexible aliphatic carboxylates, *Chem. Eur. J.* 20 (2014) 426–434.
- [167] S.K. Elsaidi, M.H. Mohamed, H.T. Schaefer, A. Kumar, M. Lusi, T. Pham, et al., Hydrophobic pillared square grids for selective removal of CO₂ from simulated flue gas, *Chem. Commun.* 51 (2015) 15530–15533.

- [168] M.Y. Masoomi, K.C. Stylianou, A. Morsali, P. Retailleau, D. Maspoch, Selective CO₂ capture in metal–organic frameworks with azine-functionalized pores generated by mechanosynthesis, *Cryst. Growth Des.* 14 (2014) 2092–2096.
- [169] S.K. Elsaïdi, M.H. Mohamed, C.M. Simon, E. Braun, T. Pham, K.A. Forrest, et al., Effect of ring rotation upon gas adsorption in SIFSIX-3-M (M = Fe, Ni) pillared square grid networks, *Chem. Sci.* 8 (2017) 2373–2380.
- [170] C. Palomino Cabello, C.O. Arean, J.B. Parra, C.O. Ania, P. Rumori, G. Turnes Palomino, A rapid microwave-assisted synthesis of a sodium-cadmium metal-organic framework having improved performance as a CO₂ adsorbent for CCS, *Dalton Trans.* 44 (2015) 9955–9963.
- [171] L. Du, Z. Lu, K. Zheng, J. Wang, X. Zheng, Y. Pan, et al., Fine-tuning pore size by shifting coordination sites of ligands and surface polarization of metal–organic frameworks to sharply enhance the selectivity for CO₂, *J. Am. Chem. Soc.* 135 (2013) 562–565.
- [172] H.S. Scott, N. Ogiwara, K.-J. Chen, D.G. Madden, T. Pham, K. Forrest, et al., Crystal engineering of a family of hybrid ultramicroporous materials based upon interpenetration and dichromate linkers, *Chem. Sci.* 7 (2016) 5470–5476.
- [173] J. Duan, Z. Yang, J. Bai, B. Zheng, Y. Li, S. Li, Highly selective CO₂ capture of an agw-type metal-organic framework with inserted amides: experimental and theoretical studies, *Chem. Commun.* 48 (2012) 3058–3060.
- [174] H.J. Park, M.P. Suh, Enhanced isosteric heat, selectivity, and uptake capacity of CO₂ adsorption in a metal-organic framework by impregnated metal ions, *Chem. Sci.* 4 (2013) 685–690.
- [175] S. Xiang, Y. He, Z. Zhang, H. Wu, W. Zhou, R. Krishna, et al., Microporous metal-organic framework with potential for carbon dioxide capture at ambient conditions, *Nat. Commun.* 3 (2012) 954.
- [176] S. Nandi, P. De Luna, T.D. Daff, J. Rother, M. Liu, W. Buchanan, et al., A single-ligand ultra-microporous MOF for precombustion CO₂ capture and hydrogen purification, *Sci. Adv.* 1 (2015).
- [177] H. He, Y. Song, C. Zhang, F. Sun, R. Yuan, Z. Bian, et al., A highly robust metal-organic framework based on an aromatic 12-carboxyl ligand with highly selective adsorption of CO₂ over CH₄, *Chem. Commun.* 51 (2015) 9463–9466.
- [178] R. Banerjee, H. Furukawa, D. Britt, C. Knobler, M. O’Keeffe, O.M. Yaghi, Control of pore size and functionality in isoreticular zeolitic imidazolate frameworks and their carbon dioxide selective capture properties, *J. Am. Chem. Soc.* 131 (2009) 3875–3877.
- [179] M.H. Choi, H.J. Park, D.H. Hong, M.P. Suh, Comparison of gas sorption properties of neutral and anionic metal–organic frameworks prepared from the same building blocks but in different solvent systems, *Chem. Eur. J.* 19 (2013) 17432–17438.
- [180] J.-R. Li, J. Yu, W. Lu, L.-B. Sun, J. Sculley, P.B. Balbuena, et al., Porous materials with pre-designed single-molecule traps for CO₂ selective adsorption, *Nat. Commun.* 4 (2013) 1538.
- [181] Z. Lu, J. Bai, C. Hang, F. Meng, W. Liu, Y. Pan, et al., The utilization of amide groups to expand and functionalize metal–organic frameworks simultaneously, *Chem. Eur. J.* 22 (2016) 6277–6285.
- [182] N.H. Alsmail, M. Suyetin, Y. Yan, R. Cabot, C.P. Krap, J. Lü, et al., Analysis of high and selective uptake of CO₂ in an oxamide-containing {Cu₂(OOCR)₄}-based metal–organic framework, *Chem. Eur. J.* 20 (2014) 7317–7324.
- [183] Z. Zhao, Z. Li, Y.S. Lin, Adsorption and diffusion of carbon dioxide on metal–organic framework (MOF-5), *Ind. Eng. Chem. Res.* 48 (2009) 10015–10020.

- [184] L. Bastin, P.S. Barcia, E.J. Hurtado, J.A.C. Silva, A.E. Rodrigues, B. Chen, A microporous metal – organic framework for separation of CO₂/N₂ and CO₂/CH₄ by fixed-bed adsorption, *J. Phys. Chem. C* 112 (2008) 1575–1581.
- [185] C.A. Trickett, A. Helal, B.A. Al-Maythaly, Z.H. Yamani, K.E. Cordova, O.M. Yaghi, The chemistry of metal–organic frameworks for CO₂ capture, regeneration and conversion, *Nat. Rev. Mater.* 2 (2017) 17045.
- [186] N.L. Rosi, J. Kim, M. Eddaoudi, B. Chen, M. O’Keeffe, O.M. Yaghi, Rod packings and metal – organic frameworks constructed from rod-shaped secondary building units, *J. Am. Chem. Soc.* 127 (2005) 1504–1518.
- [187] P.D.C. Dietzel, Y. Morita, R. Blom, H. Fjellvag, An in situ high-temperature single-crystal investigation of a dehydrated metal–organic framework compound and field-induced magnetization of one-dimensional metal–oxygen chains, *Angew. Chem. Int. Ed.* 44 (2005) 6354–6358.
- [188] W.L. Queen, M.R. Hudson, E.D. Bloch, J.A. Mason, M.I. Gonzalez, J.S. Lee, et al., Comprehensive study of carbon dioxide adsorption in the metal–organic frameworks M₂(dobdc) (M = Mg, Mn, Fe, Co, Ni, Cu, Zn), *Chem. Sci.* 5 (2014) 4569–4581.
- [189] P.D.C. Dietzel, B. Panella, M. Hirscher, R. Blom, H. Fjellvag, Hydrogen adsorption in a nickel based coordination polymer with open metal sites in the cylindrical cavities of the desolvated framework, *Chem. Commun.* (2006) 959–961. Available from: <https://doi.org/10.1039/B515434K>.
- [190] D. Britt, H. Furukawa, B. Wang, T.G. Glover, O.M. Yaghi, Highly efficient separation of carbon dioxide by a metal-organic framework replete with open metal sites, *Proc. Natl. Acad. Sci. U.S.A.* 106 (2009) 20637–20640.
- [191] http://www.metal-organic-frameworks.eu/adsorbentien_engl.shtml#mofs (accessed 26.07.18).
- [192] A.C. Kizzie, A.G. Wong-Foy, A.J. Matzger, Effect of humidity on the performance of microporous coordination polymers as adsorbents for CO₂ capture, *Langmuir* 27 (2011) 6368–6373.
- [193] R. Luebke, J.F. Eubank, A.J. Cairns, Y. Belmabkhout, L. Wojtas, M. Eddaoudi, The unique rht-MOF platform, ideal for pinpointing the functionalization and CO₂ adsorption relationship, *Chem. Commun.* 48 (2012) 1455–1457.
- [194] A.Ö. Yazaydin, A.I. Benin, S.A. Faheem, P. Jakubczak, J.J. Low, R.R. Willis, et al., Enhanced CO₂ adsorption in metal-organic frameworks via occupation of open-metal sites by coordinated water molecules, *Chem. Mater.* 21 (2009) 1425–1430.
- [195] N.C. Burtch, H. Jasuja, K.S. Walton, Water stability and adsorption in metal–organic frameworks, *Chem. Rev.* 114 (2014) 10575–10612.
- [196] J.A. Mason, T.M. McDonald, T.-H. Bae, J.E. Bachman, K. Sumida, J.J. Dutton, et al., Application of a high-throughput analyzer in evaluating solid adsorbents for post-combustion carbon capture via multicomponent adsorption of CO₂, N₂, and H₂O, *J. Am. Chem. Soc.* 137 (2015) 4787–4803.
- [197] P.M. Schoenecker, C.G. Carson, H. Jasuja, C.J.J. Flemming, K.S. Walton, Effect of water adsorption on retention of structure and surface area of metal–organic frameworks, *Ind. Eng. Chem. Res.* 51 (2012) 6513–6519.
- [198] H. Jasuja, N.C. Burtch, Y.-g. Huang, Y. Cai, K.S. Walton, Kinetic water stability of an isostructural family of zinc-based pillared metal–organic frameworks, *Langmuir* 29 (2013) 633–642.
- [199] M. Eddaoudi, J. Kim, N. Rosi, D. Vodak, J. Wachter, M. O’Keeffe, et al., Systematic design of pore size and functionality in isorecticular MOFs and their application in methane storage, *Science* 295 (2002) 469–472.

- [200] S. Bernt, V. Guillermin, C. Serre, N. Stock, Direct covalent post-synthetic chemical modification of Cr-MIL-101 using nitrating acid, *Chem. Commun.* 47 (2011) 2838–2840.
- [201] Y. Zhao, H. Wu, T.J. Emge, Q. Gong, N. Nijem, Y.J. Chabal, et al., Enhancing gas adsorption and separation capacity through ligand functionalization of microporous metal–organic framework structures, *Chem. Eur. J.* 17 (2011) 5101–5109.
- [202] B. Arstad, H. Fjellvåg, K.O. Kongshaug, O. Swang, R. Blom, Amine functionalised metal organic frameworks (MOFs) as adsorbents for carbon dioxide, *Adsorption* 14 (2008) 755–762.
- [203] L. Wu, M. Xue, S.-L. Qiu, G. Chaplais, A. Simon-Masseron, J. Patarin, Amino-modified MIL-68(In) with enhanced hydrogen and carbon dioxide sorption enthalpy, *Microporous Mesoporous Mater.* 157 (2012) 75–81.
- [204] <http://matrixsensorsinc.com/wp-content/themes/matrixsensors/assets/images/mofs/IRMOF-3.jpg> (accessed 27.08.18).
- [205] D. Madden, T. Curtin, Carbon dioxide capture with amino-functionalised zeolite- β : a temperature programmed desorption study under dry and humid conditions, *Microporous Mesoporous Mater.* 228 (2016) 310–317.
- [206] A. Heydari-Gorji, Y. Belmabkhout, A. Sayari, Degradation of amine-supported CO₂ adsorbents in the presence of oxygen-containing gases, *Microporous Mesoporous Mater.* 145 (2011) 146–149.
- [207] J. Canivet, A. Fateeva, Y. Guo, B. Coasne, D. Farrusseng, Water adsorption in MOFs: fundamentals and applications, *Chem. Soc. Rev.* 43 (2014) 5594–5617.
- [208] Y. Fu, J. Su, Z. Zou, S. Yang, G. Li, F. Liao, et al., Syntheses, structures, and gas adsorption properties of two novel cadmium–sodium organic frameworks with 1,3,5-benzenetricarboxylate ligands, *Cryst. Growth Des.* 11 (2011) 3529–3535.
- [209] S.R. Batten, N.R. Champness, X.-M. Chen, J. Garcia-Martinez, S. Kitagawa, L. Ohrstrom, M. O’Keeffe, et al., Terminology of metal-organic frameworks and coordination polymers (IUPAC recommendations 2013), *Pure Appl. Chem.* 85 (2013) 1715–1724.
- [210] S.-i. Noro, S. Kitagawa, M. Kondo, K. Seki, A. New, Methane adsorbent, porous coordination polymer $[\{\text{CuSiF}_6(4,4'\text{-bipyridine})_2\}_n]$, *Angew. Chem. Int. Ed.* 39 (2000) 2081–2084.
- [211] D.N. Dybtsev, H. Chun, K. Kim, Rigid and flexible: a highly porous metal–organic framework with unusual guest-dependent dynamic behavior, *Angew. Chem. Int. Ed.* 43 (2004) 5033–5036.
- [212] B. Chen, S. Ma, E.J. Hurtado, E.B. Lobkovsky, H.-C. Zhou, A. Triply, Interpenetrated microporous metal–organic framework for selective sorption of gas molecules, *Inorg. Chem.* 46 (2007) 8490–8492.
- [213] K. Seki, S. Takamizawa, W. Mori, Design and gas adsorption property of a three-dimensional coordination polymer with a stable and highly porous framework, *Chem. Lett.* 30 (2001) 332–333.
- [214] B. Chen, C. Liang, J. Yang, D.S. Contreras, Y.L. Clancy, E.B. Lobkovsky, et al., A microporous metal–organic framework for gas-chromatographic separation of alkanes, *Angew. Chem. Int. Ed.* 45 (2006) 1390–1393.
- [215] M. Shivanna, Q.-Y. Yang, A. Bajpai, E. Patyk-Kazmierczak, M.J. Zaworotko, A dynamic and multi-responsive porous flexible metal–organic material, *Nat. Commun.* 9 (2018) 3080.
- [216] P. Kanoo, S.K. Reddy, G. Kumari, R. Haldar, C. Narayana, S. Balasubramanian, et al., Unusual room temperature CO₂ uptake in a fluoro-functionalized MOF: insight

- from Raman spectroscopy and theoretical studies, *Chem. Commun.* 48 (2012) 8487–8489.
- [217] P. Nugent, V. Rhodus, T. Pham, B. Tudor, K. Forrest, L. Wojtas, et al., Enhancement of CO₂ selectivity in a pillared pcu MOM platform through pillar substitution, *Chem. Commun.* 49 (2013) 1606–1608.
- [218] P. Halasyamani, K.R. Heier, M.J. Willis, C.L. Stern, K.R. Poeppelmeier, Syntheses and structures of two new Cu/Nb/pyrazine complexes: three dimensional CuNb (pyz)₂OF₅·(pyz)(H₂O) and two dimensional [Cu(pyz)_{2.5}]⁺[NbF₆]⁻·(pyz), *Z. Anorg. Allg. Chem.* 622 (1996) 479–485.
- [219] K. Adil, P.M. Bhatt, Y. Belmabkhout, S.M.T. Abtab, H. Jiang, A.H. Assen, et al., Valuing metal–organic frameworks for postcombustion carbon capture: a benchmark study for evaluating physical adsorbents, *Adv. Mater.* 29 (2017) 1702953.
- [220] C.E. Wilmer, M. Leaf, C.Y. Lee, O.K. Farha, B.G. Hauser, J.T. Hupp, et al., Large-scale screening of hypothetical metal–organic frameworks, *Nat. Chem.* 4 (2011) 83.
- [221] C.E. Wilmer, O.K. Farha, Y.-S. Bae, J.T. Hupp, R.Q. Snurr, Structure–property relationships of porous materials for carbon dioxide separation and capture, *Energy Environ. Sci.* 5 (2012) 9849–9856.
- [222] A.L. Mullen, T. Pham, K.A. Forrest, C.R. Cioce, K. McLaughlin, B. Space, A polarizable and transferable PHAST CO₂ potential for materials simulation, *J. Chem. Theory Comput.* 9 (2013) 5421–5429.
- [223] S. Kim, Y.M. Lee, High performance polymer membranes for CO₂ separation, *Curr. Opin. Chem. Eng.* 2 (2013) 238–244.
- [224] S.R. Venna, M.A. Carreon, Metal organic framework membranes for carbon dioxide separation, *Chem. Eng. Sci.* 124 (2015) 3–19.
- [225] J. Gascon, F. Kapteijn, Metal-organic framework membranes—high potential, bright future? *Angew. Chem. Int. Ed.* 49 (2010) 1530–1532.
- [226] S. Hermes, F. Schröder, R. Chelmowski, C. Wöll, R.A. Fischer, Selective nucleation and growth of metal – organic open framework thin films on patterned COOH/CF₃-terminated self-assembled monolayers on Au(111), *J. Am. Chem. Soc.* 127 (2005) 13744–13745.
- [227] Y. Liu, Z. Ng, E.A. Khan, H.-K. Jeong, C.-b Ching, Z. Lai, Synthesis of continuous MOF-5 membranes on porous α -alumina substrates, *Microporous Mesoporous Mater* 118 (2009) 296–301.
- [228] Y. Liu, J.H. Pan, N. Wang, F. Steinbach, X. Liu, J. Caro, Remarkably enhanced gas separation by partial self-conversion of a laminated membrane to metal–organic frameworks, *Angew. Chem. Int. Ed.* 54 (2015) 3028–3032.
- [229] Y. Peng, Y. Li, Y. Ban, H. Jin, W. Jiao, X. Liu, et al., Metal-organic framework nanosheets as building blocks for molecular sieving membranes, *Science* 346 (2014) 1356–1359.
- [230] H. Yehia, T.J. Pisklak, J. Ferraris, K. Balkus, I.H. Musselman, Methane facilitated transport using copper(II) biphenyl dicarboxylatetriethylenediamine/poly(3-acetoxethylthiophene) mixed matrix membranes, *Polym. Preprints* 45 (2004) 35–36.
- [231] T.-H. Bae, J.R. Long, CO₂/N₂ separations with mixed-matrix membranes containing Mg₂(dobdc) nanocrystals, *Energy Environ. Sci.* 6 (2013) 3565–3569.
- [232] B. Seoane, J. Coronas, I. Gascon, M.E. Benavides, O. Karvan, J. Caro, et al., Metal-organic framework based mixed matrix membranes: a solution for highly efficient CO₂ capture?, *Chem. Soc. Rev.* 44 (2015) 2421–2454.

Sensing and sequestration of inorganic cationic pollutants by metal-organic frameworks

Zachary Lawrence Magnuson and Shengqian Ma*

Department of Chemistry, University of South Florida, Tampa, FL, United States

*Corresponding author: e-mail address: sqma@usf.edu

3.1 Cationic inorganic pollutants

Each section of this chapter includes a short synopsis of the cationic inorganic pollutant being addressed in the research discussed. Importantly, these introductions contain information on the speciation of the pollutant in relevant environmental compartments as well as the health effects and hazards they pose, particularly to humankind. Cationic inorganic pollutants consist of heavy metals and their oxidation products that are exotic and injurious to the environment and exhibit a tendency to exist in a cationic state. These compounds, which originate from the waste and/or end-product of industrial processes, can and should be remediated due to the negative effects they have. In most cases, alternative materials have been developed that are phasing out the need for products from these negligent industrial operations.

The materials discussed herein include cadmium, chromium, lead, mercury, and the nuclear waste products uranium, barium, cesium, and rubidium.

3.2 Design of metal clusters and organic linkers

The ability of metal-organic frameworks (MOFs) to selectively sense and sequester cationic inorganic pollutants depends on the careful selection of both of its components—the metal cluster and the organic linker. While the latter is most frequently functionalized, as we will see they each are capable of being controlled to serve some desirable purpose. The adsorption of cationic species to MOF structures is addressed by several key concepts. Firstly, the physical quality of the porous materials can be tailored with functional groups to draw the pollutant from the solution and localize it at the MOF in equilibrium with the rest of the solution [1]. The availability of these functional sites depends on their orientation in the crystal structure as well as the pore size and shape. Ideally, the functional part of linking ligands and metal clusters will point outward into the pore void, allowing for effective

interaction with the adsorbate, while the size of the pore can be tuned as a sieve, preventing atoms or molecules of certain size or shape (that may otherwise compete with the desired adsorbate) from entering the MOF. Secondly, the MOF can be designed to produce an electrostatic or Lewis acid–base interaction between its components and the cationic pollutant. A functional group amended to the MOF such as a thiol, sulfone, amine, or azine among others [2,3] can be utilized as a Lewis base to interact with the Lewis acidic cation, binding them together at the MOF's surface or within its porous interior directly. These binding sites can be occupied by guest ions that are less favorable than the pollutant, allowing for a controlled ion-exchange mechanism. Conditions for ion exchange can be optimized by consideration of hard–soft acid–base interactions, choice of nascent guest ion, ion concentration, and pH. Hydrogen bonding is also frequently considered and found to be the cause of effective adsorption.

3.3 Detection

High fidelity detection of cationic inorganic pollutants without employing destructive techniques can be designed in MOFs by considering the effects saturation with a desired analyte will have on how the clusters or ligands behave. This can manifest itself as changes in color, vibrational energies, electronic transitions, conductivity, luminescence quenching, and secondary or even tertiary interactions with concomitant compounds [4,5]. These methodologies will be highlighted in each section as they are employed in the work discussed. The changes that occur in the material can be analyzed using techniques such as Fourier-transform IR (FT-IR), X-ray photoelectron spectroscopy (XPS), UV-Vis diffuse reflectance, or even chronoamperometric measurements, among others; these data can then be correlated to the known concentration of analyte in a solution and used to determine unknown concentrations in real samples.

3.4 Selectivity

An effective sensor or remediator should also be able to target an analyte with high specificity and measure content accurately, ideally in the presence of multiple contaminants. Careful tuning using the concepts just mentioned enables this and testing is performed using detection analysis methods coupled with several types of studies, which likewise are highlighted in the research being reviewed. An example method would be parallel testing, where the MOF is exposed to individual competitive ion solutions to show results for each, followed by addition of the analyte to show a change in results. This technique and variations of these kinds of studies are common for characterization of MOFs, as are the ever-important real-world sample studies!

3.5 Cadmium

The element cadmium was discovered simultaneously as an impurity in zinc carbonate, also known as calamine, by Friedrich Stromeyer and Karl Leberecht Hermann in 1817. Its name is taken from the Latin word *cadmia*, for the mineral it was found in. Much like its periodic neighbors zinc and mercury, cadmium is most commonly found in a +2 oxidation state. The group 12 metal does not have partly filled *d* or *f* electron shells making it unlike most other transition metals in terms of reactivity and electronic behavior. Its most common uses in alloying, electroplating, and battery manufacture have fallen to the wayside as less toxic alternatives have been discovered.

3.5.1 Health and hazards

Cadmium is present in human diet as an oxide, having the highest known concentration in shellfish, seeds, and grains. These foodstuffs, among others, most effectively accumulate the metal from their environment [6]. Dietary intake is minor compared to routes involving gaseous or colloidal inhalation, which occur in occupational settings where the metal is processed and in cigarette smoke. These routes can result in lung cancer [7] among other kinds [8], as well as renal diseases and osteoporosis. Multiple regulatory agencies across the world have deemed cadmium a carcinogen.

3.5.2 Speciation

The IUPAC definition of speciation: “the distribution of an element amongst defined chemical species in a system” [9]. Speciation of the element being considered, in this section cadmium, is critical to understand how it will accumulate in various systems and determine the means of exposure. The natural occurrence of cadmium is scant, save for the zinc ores that are mined for it. Anthropogenic emissions present the main cause of cadmium pollution, resulting in particularly high concentrations around urban industrialized areas. Cadmium from industrial processes is often associated with chloride, resulting in highly soluble forms such as CdS, CdSO₄, CdCl₂, and Cd-aluminosilicates. In aqueous solution these compounds yield Cd(II) to some extent which is the form the MOFs reviewed here interact with.

3.5.3 Calcium-based metal-organic framework FJI-H9 [10]

Hui Xue, Maochun Hung, et al. had work published in Chemical Science in 2016 regarding the reversible uptake of Cd(II) in a regenerative MOF and characterized the materials' ability to both adsorb the metal and provide a means for in situ detection down to 10 ppm. Taking inspiration from work done for the adsorption of Hg(II) by strong Hg-S interactions [11], MOF FJI-H9 achieves up to 286 mg g⁻¹

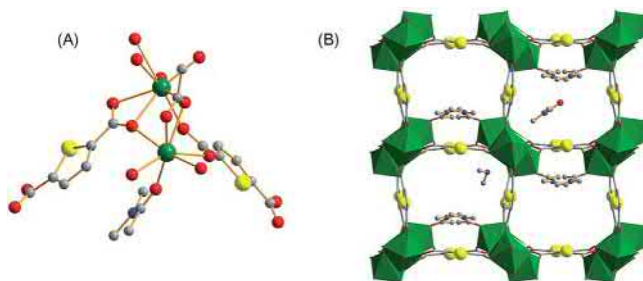


Figure 3.1 (A) Coordination environment of FJI-H9. Labeling follows C = gray, N = blue, O = red, S = yellow, Ca = green, and H is omitted. (B) Crystalline framework with Ca clusters as green polyhedra reveals pore shape and size, as well as functional group orientation.

Source: Adapted from H. Xue, Q. Chen, F. Jiang, D. Yuan, G. Lv, L. Liang, et al., A regenerative metal-organic framework for reversible uptake of Cd(II): from effective adsorption to in situ detection, *Chem. Sci.* 7 (9) (2016) 5983–5988 with permission from The Royal Society of Chemistry.

adsorption of Cd(II) ions. The MOF is generated by the reaction of 2,5-thiophenedicarboxylate with CaCl_2 , forming an orthorhombic crystal of structure $[\text{Me}_2\text{NH}_2^+][\text{Ca}_2(\text{C}_6\text{H}_2\text{O}_4\text{S}^{-2})_2(\text{CH}_3\text{COO}^-)(\text{DMA})]\cdot\text{DMA}$ (dimethylacetamide) (Fig. 3.1).

Crystals of FJI-H9 were soaked in 0.1 M cadmium nitrate/acetonitrile solution. The cadmium loaded MOF was washed with acetonitrile and characterized by several combustion analysis techniques—carbon/hydrogen/nitrogen analysis (CHN) and inductively coupled plasma (ICP), as well as elemental and thermogravimetry-mass spectrometry (TG-MS). The latter revealed a 2.5:1 cadmium to calcium ratio and TG-MS showed 15.5% composition of volatile solvents. These data led the group to report that 1 mol of the MOF was able to sequester 1.78 mol of Cd(II). The material moderately adsorbs mercury, but is otherwise selective.

Extended X-ray absorption fine structure (EXAFS) suggests unexpectedly that there is no CdS interaction, but rather three variants of Cd-O interactions and the presence of four waters for every cadmium. This belies the presence of $\text{Cd}(\text{H}_2\text{O})_4^{+2}$, possibly stabilized by closely held nitrate anions. Based on IR signal differences, the group posits that Cd(II) ions displace the methylammonium ions in the framework, providing more favorable counterion stability. FJI-H9 was shown to effectively indicate the presence of cadmium ions at low concentrations via a fluorescence quenching mechanism. Fig. 3.2 shows several concentrations of aqueous cadmium nitrate and the respective change in emission intensity.

The group believes this is a product of Cd(II)-DMA (dimethylacetamide) interaction. Under the same conditions, this quenching is not observed for other heavy metals such as Mg(II), Co(II), Ni(II), Mn(II), Zn(II), Fe(II), and Pb(II), and importantly, Hg(II), which is the only other heavy metal tested to have substantial adsorption. Importantly, the framework can be in situ deconstructed and subsequently regenerated with a 10% loss of material each cycle.

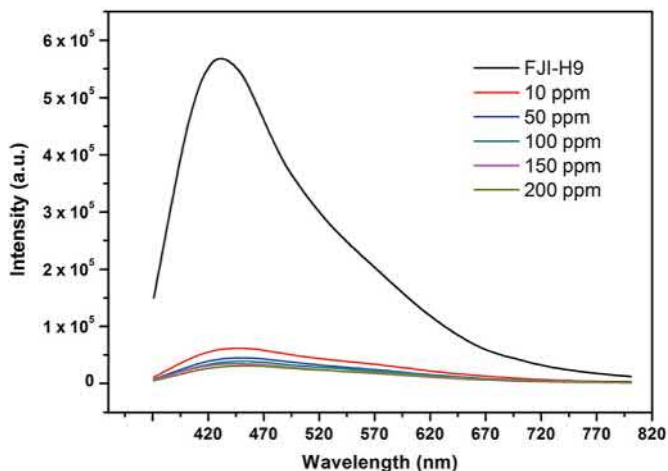


Figure 3.2 Fluorescence emission spectra for FJI-H9 in several Cd solution concentrations illustrating quenching effect.

Source: Adapted from H. Xue, Q. Chen, F. Jiang, D. Yuan, G. Lv, L. Liang, et al., A regenerative metal-organic framework for reversible uptake of Cd(II): from effective adsorption to in situ detection, *Chem. Sci.* 7 (9) (2016) 5983–5988 with permission from The Royal Society of Chemistry.

3.5.4 Copper-based metal-organic framework utilizing sulfonic acid moieties [12]

Yang Wang, Guiqin Ye, et al. had work published in the *Journal of Materials Chemistry A* by the Royal Society of Chemistry in 2015 regarding a copper-based MOF that was stepwise postsynthetically modified with sulfonic acid groups for the selective uptake of cadmium from aqueous solutions. The MOF $\text{Cu}_3(\text{BTC})_2\text{SO}_3\text{H}$ (BTC = 1,3,5-benzenetricarboxylate) or Cu-MOF for short was hydrothermally synthesized as $\text{Cu}_3(\text{BTC})_2$ and then postsynthetically amended with thiol pendants at the metal Cu metal clusters. These were then oxidized to sulfonic acids, and each compound in the series was characterized to illustrate the enhancement of cadmium uptake. Successful attachment of the sulfonic acid group was confirmed by FT-IR which revealed S-O stretch bands from 1000–1350 wavenumbers. Structural integrity was considered by PXRD: $\text{Cu}_3(\text{BTC})_2$ and Cu-MOF spectra were compared and found to be consistent. Spectra were also collected after the uptake of Cd(II) to further indicate structural steadfastness (Fig. 3.3). The BET surface area taken from N_2 adsorption isotherms at 77K of Cu-MOF was found to be $445 \text{ m}^2 \text{ g}^{-1}$, suggesting effective inclusion of the sulfonic acid groups as this is less than that of the unmodified $\text{Cu}_3(\text{BTC})_2$.

Adsorption of Cd(II) was optimized to a pH of 6 and an exposure time of 10 minutes. At pH below 2.1 the sulfonic acid groups bear positive charge and repel Cd(II), while above pH 6 Cd(II) tends to precipitate as a hydroxide salt. Kinetic studies relying on the Lagergren pseudo-second-order kinetic model [13] revealed a

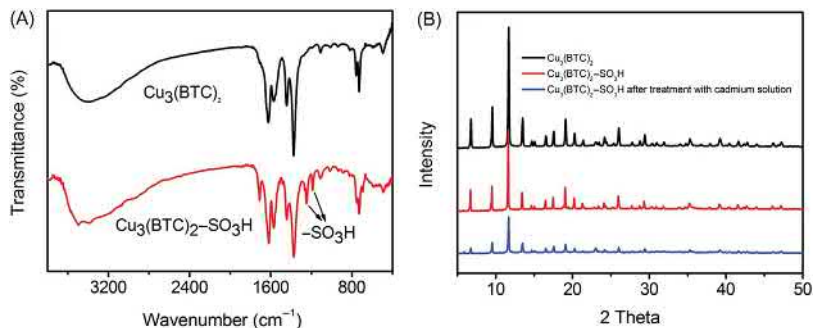


Figure 3.3 (A) FT-IR spectra showing introduction of sulfonic acid groups. (B) PXRD of $\text{Cu}_3(\text{BTC})_2$, $\text{Cu}_3(\text{BTC})_2\text{-SO}_3\text{H}$, and $\text{Cu}_3(\text{BTC})_2\text{-SO}_3\text{H}$ after treatment with Cd confirming structural integrity of Cu-MOF.

Source: Adapted from Y. Wang, G. Ye, H. Chen, X. Hu, Z. Niu, S. Ma, Functionalized metal-organic framework as a new platform for efficient and selective removal of cadmium (ii) from aqueous solution, *J. Mater. Chem. A*. 3 (29) (2015) 15292–15298 with permission from The Royal Society of Chemistry.

rate constant of $0.6818 \text{ g mg}^{-1} \text{ min}$ and the Langmuir model [14] (for monolayer adsorption) determined the maximum uptake capacity of 88.7 mg g^{-1} , conferring an ideal aging time. The adsorption was also characterized by the Freundlich model (for heterogeneous adsorption). The correlation coefficients (R^2) for each test point to the Langmuir model as a superior fit to the data collected, informing its use in determining the maximum uptake capacity. Further, adsorption isotherms were also taken for $\text{Cu}_3(\text{BTC})_2$ and $\text{Cu}_3(\text{BTC})_2\text{SH}$ to illustrate the enhanced uptake of Cu-MOF by the careful postsynthetic modifications, reporting an uptake capacity of 67.8 and 74.5 mg g^{-1} , respectively. The ability for the unmodified parent structure to show adsorption of cadmium is attributed to complexation with residual carboxylate groups.

Selectivity against competing ions was characterized by parallel metal ion solutions of Na(I), Mg(II), Ca(II), Pb(II), Cu(II), and Ni(II) at concentrations ranging from 0.5 to 100 mg L^{-1} (with 1 mg L^{-1} Cd(II)). Cu-MOF retained a removal efficiency of at least 95.1% with Pb(II) being the strongest competitor. Desorption of Cd(II) from Cu-MOF was easily achieved by rinsing the laden material with deionized water and after oven drying could be reused. The material experienced a 15% decrease in adsorption capacity after six cycles and preservation of the crystalline structure was confirmed by PXRD, making it practical for recycled use.

3.6 Chromium

The lustrous, corrosion-resistant transition metal chromium was discovered in in 1797 by a French pharmacist while working with the lead mineral crocoite. The bronze swords and arrowheads found on soldiers of the Qin dynasty Terracotta

Army from the late 300s BCE were found remarkably well preserved due to a coating of a chromium oxide [15], illustrating the element's resistance to corrosion through its passivation by a dense, impermeable oxidized layer. This quality constitutes 85% of its commercial use as an electroplating metal and in the production of stainless steel [16]. Other important uses are in dyeing and pigmentation as a vivid red or yellow color, like that often associated with American school buses, though use of the lead-containing chromate (and other antiquated metal-based pigments) has declined with the advent of organic pigments.

3.6.1 Health and hazards

The two important forms of chromium when considering both the environment and human health are of the trivalent and hexavalent oxidation states. Cr(III) is an essential trace nutrient for mammals while Cr(VI) is a genotoxic carcinogen. In the environment, these two species transmute between one another depending on various conditions such as pH or the presence of tightly binding ligands [17]. Most chromium-containing ore is processed through Cr(VI) to sodium dichromate dihydrate, from which virtually all materials and compounds are prepared. The prevalence of the hexavalent form in this way leads human exposure during processing and application. Individuals working with stainless steel welding, for example, can generate Cr(VI) particles that lead to lung carcinomas, asthma, and damage to nasal epithelia and skin.

3.6.2 Speciation and reactivity

Though Cr(III) is not considered toxic, it is nevertheless important to develop an understanding of how it exists in the environment due to its equilibrium relationship with Cr(VI). In the unlikely absence of molecules with which it can form complexes (when considering natural waters), trivalent chromium in neutral or alkaline water primarily exists as $\text{Cr}(\text{H}_2\text{O})_3$ and CrOH^{2+} . Cr(III) is a hard, acidic molecule that often forms hexacoordinate octahedral complexes with oxygen, nitrogen, and sulfur electron donors. Oxidation of Cr(III) to Cr(VI) in natural waters is generally low due to the high redox potential between the two species. It is reported [18] that the primary pathway involved mediation by manganese oxide. The presence and formation of Cr(VI) species hinges on both pH and concentration of Cr(VI). Within natural waters, CrO_4^{2-} , HCrO_4^- , and CrO_7^{2-} are prevailing species where the latter begins to condense to an orange-red dichromate ion above 10^{-2} M. Concentrations of chromium in freshwater range from 0.5 to 100 nM, while saltwater varies from 0.1 to 16 nM.

Speciation of chromium in terrestrial compartments likewise depends on pH—in acidic soils insoluble $\text{Cr}(\text{OH})_3$ aq. dominates, but above pH 5.5 mainly CrOH^{2+} is present. Regardless, both forms are strongly adsorbed by clay compounds or complexed by organic macromolecules such as humic acids which immobilize the metal. There are however complexing agents in soil, citric acid, for example, that enhance the solubility and mobility of chromium. Atmospheric chromium exists as

particles or droplets and serves as the main means of transport for the metal, with species following the same trends as those found in water, with a similar dependence of pH.

3.6.3 Cadmium metal-organic framework for Cr(VI) sensing and sorption [19]

Hung Fu, Ying Zhao, et al. had a manuscript accepted by Dalton Transactions in 2017 regarding the synthesis and characterization of a two-dimensional water stable MOF with high ethane and methane selectivity as well as efficient sensing and sorption of hexavalent chromium. The cadmium-based TIPA-MOF $[\text{Cd}(\text{TIPA})_2(\text{ClO}_4)_2] \cdot (\text{DMF})_3(\text{H}_2\text{O})_2$ is constructed of triisopropanolamine (TIPA) linkages and contains perchlorate ions that exchange with Cr(VI). Crystals were characterized by single-crystal X-ray, PXRD, elemental analysis, and IR. The sensing capabilities of this MOF were investigated via parallel aqueous phase fluorescence emission tests of several compounds (BF_4^- , VO_4^{3-} , MoO_4^{2-} , WO_4^{2-} , ClO_4^- , SO_4^{2-} , NO_3^- , Br^- , Cl^- , I^- , SCN^- , $\text{Cr}_2\text{O}_7^{2-}$, CH_3COO^- , OAc^- , $\text{C}_2\text{O}_4^{2-}$, OX^{2-}) at 0.0001 M concentration and 320 nm excitation wavelength. The dichromate ion was found to have the most significant quenching effect of the battery, the others being negligible (Fig. 3.4).

A solution containing potassium dichromate and concomitant ions at 10-fold greater concentration illustrated selectivity of the MOF for chromium as the quenching remained nearly the same as the equivalent solution of just dichromate. Titration experiments revealed an upper limit of 40 ppm and a lower limit of detection at 8 ppb. This is much lower than that of the contamination threshold of 100 ppb set by the US Environmental Protection Agency (EPA). Based on UV-Vis studies, the group proposes that the dichromate ions compete with the ligand for

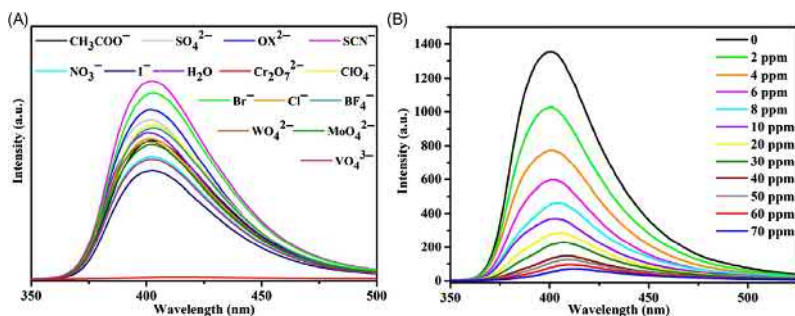


Figure 3.4 (A) Luminescence intensity spectra of TIPA-MOF in various anion solutions. (B) Emission spectra of TIPA-MOF in $\text{K}_2\text{Cr}_2\text{O}_7$ solutions at various concentrations.

Source: Adapted from H.-R. Fu, Y. Zhao, Z. Zhou, X.-G. Yang, L.-F. Ma, Neutral ligand TIPA-based two 2D metal-organic frameworks: ultrahigh selectivity of $\text{C}_2\text{H}_2/\text{CH}_4$ and efficient sensing and sorption of Cr(vi), Dalton Transact. 47 (11) (2018) 3725–3732 with permission from The Royal Society of Chemistry.

light absorbance, which would reduce ligand–metal charge-transfer ergo reducing luminescence. It is worth noting that PXRD revealed that quenching is not dependent on failure of the crystal structure, and in fact the material is reusable with 81% efficacy after five recycles. Adsorption of Cr(VI) was determined to be 116 mg g^{-1} at a 51% exchange with perchlorate ions after 24 hours.

3.6.4 Zirconium metal-organic framework MOR-2 high Cr(VI) adsorption [20]

Sofia Rapti, Debajit Sarma, et al. had a paper published by the Royal Society of Chemistry in the *Journal of Materials Chemistry A* in 2017 regarding a microporous MOF MOR-2 that can rapidly adsorb Cr(VI) with high capacity and be effectively adapted for use in ion-exchange chromatography.

The zirconium-based MOF ($\text{H}_{16}[\text{Zr}_6\text{O}_{16}(\text{H}_2\text{PATP})_4] \text{Cl}_8 \cdot x\text{H}_2\text{O}$, $x = 8-12$) contains ((pyridin-1-ium-2-ylmethyl)ammonio)terephthalate (H_2PATP) ligands which, notably, are the first example of presynthetic amending of the terephthalate moiety with the large ammonium-pyridinium structure illustrated (Fig. 3.5). Typically, large functional substituents such as this adversely affect the growth of MOF crystals [21]. The chloride ions present serve to interchange with Cr(VI). MOR-2 crystal structure was characterized by PXRD, elemental analyses, thermogravimetric analysis, and energy-dispersive X-ray spectroscopy (EDS). It was found to have a BET surface area of $354 \text{ m}^2 \text{ g}^{-1}$ and type-I adsorption–desorption isotherms (suggesting microporosity) and ion-exchange experiments fitted to the Langmuir model report a maximum sorption capacity of $193.7 \pm 6.7 \text{ mg g}^{-1}$, the highest reported when this work was published. Saturation of the compound with dichromate ion was reached within 1 minute with 99.1% removal capacity between pH of 2 and 9.

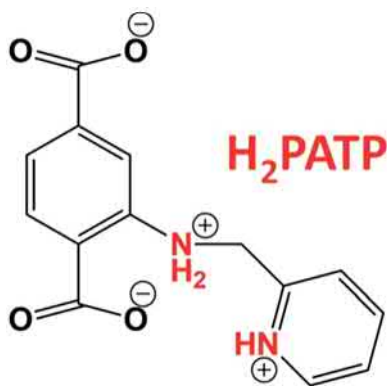


Figure 3.5 Illustration of the ligand H_2PATP highlighting functional sites.

Source: Adapted from S. Rapti, D. Sarma, S.A. Diamantis, E. Skliri, G.S. Armatas, A.C.

Tsipis, et al., All in one porous material: exceptional sorption and selective sensing of hexavalent chromium by using a Zr^{4+} MOF, *J. Mater. Chem. A* 5 (28) (2017) 14707–14719 with permission from The Royal Society of Chemistry.

The ion-exchange column edition exhibits excellent functionality when compared to similar materials. MOR-2-HA was designed for use as a stationary phase, formed by suspension of MOR-2 in sodium alginate with the addition of HCl. This composite with the polysaccharide was necessary to prevent elution of MOR-2 in aqueous media, under which conditions it forms a viscous gum. Some characterization of MOR-2-HA is tabulated and additional information including ion-exchange column tests are reported.

Photophysical properties were determined using UV-Vis diffuse reflectance and steady-state emission spectroscopy. The former of MOR-2 shows absorption around 266 nm and a lower energy band from 380 to 450 nm. These bands belong to $\pi-\pi^*$ and $n-\pi^*$ transitions (n being the lone pair of the methylammonium group). The higher energy band at 266 nm sees contribution from Zr cluster transitions [22].

In the presence of chromate and dichromate, additional and unique features are observed that reflect ligand to metal charge transfer (LMCT) as illustrated in Fig. 3.6. Fluorescence titration experiments were performed to collect calibration curve data. A limit of detection (LOD) and limit of quantification (LOQ) were found to be 4 and 13 ppb, respectively. Using real samples of chrome plating waste in distilled water an LOD of 6 and LOQ of 18 ppb were found. When potable water was used instead, these values increased dramatically to 35 and 110 ppb.

The selectivity of MOR-2 was characterized by parallel tests against competitive ions for Cr(VI) ion exchange. Chloride, nitrate, and bromide ions had negligible effect even at 1000-fold concentration, but sulfate ions were able to lower the adsorptive capacity of MOR-2 to 52% at two- to fourfold concentration. Potable and industrial water samples containing varying amounts of these ions were able to be effectively remediated of Cr(VI) by MOR-2 as well, showing similar

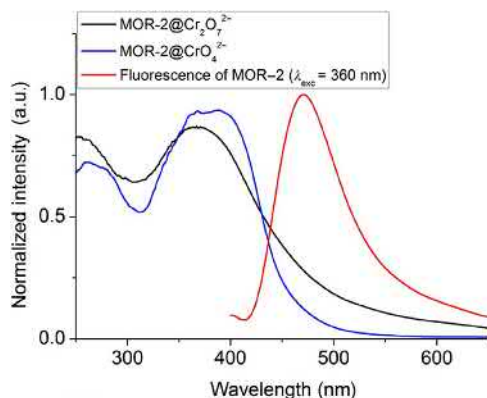


Figure 3.6 Diffuse reflectance spectra for MOR-2 adsorbed with chromate and dichromate against fluorescence spectra revealing some overlap.

Source: Adapted from S. Rapti, D. Sarma, S.A. Diamantis, E. Skliri, G.S. Armatas, A.C. Tsiapis, et al., All in one porous material: exceptional sorption and selective sensing of hexavalent chromium by using a Zr^{4+} MOF, *J. Mater. Chem. A* 5 (28) (2017) 14707–14719 with permission from The Royal Society of Chemistry.

fluorescence quenching resolution from 0 to 648 ppb. The mechanism proposed following density functional theory (DFT) calculations using $[\text{PhNH}_2\text{CH}_2\text{-PyH}]^{2+}$ as a model for H_2PATP suggested weak association of dichromate via three hydrogen bond interactions. Furthermore, chromate anions appear capable of deprotonating either the pyridinium or methylammonium ions, resulting in HCrO_4^- ions that likewise associate with the ligand via hydrogen bonding.

3.7 Lead

The soft, ductile carbon homolog lead has the highest atomic number of any stable element and three of its isotopes are the products of the naturally occurring radioactive decay chains. It is easily isolable, ancillary to silver ore processing, and was first known by prehistoric western Asian people. Its inertness, ductility, and other physical qualities led to its widespread use which peaked in ancient Rome as plumbing (derivative of its Latin name *plumbum*), currency, roofing, and munitions. It has been proposed that the advent of lead plumbing played a part in the fall of Rome, though arguments against this are asserted based on its passivation in moist air or aerated water [23]. Nevertheless, lead is highly poisonous and affects nearly every organ in the body. Its wide array of modern uses, particularly in paint and fuels, has been greatly diminished with the advent of less toxic alternatives.

3.7.1 Health and hazards

Unlike most other toxic compounds or metals, there is no minimum acceptable exposure. Lead is primarily distributed to the brain, liver, kidney, and bones. Most of it is eventually excreted but some amount remains stored in bones and teeth. Children are particularly susceptible to lead poisoning as they absorb and retain three to five times the amount adults do [24]. Common routes of exposure include mining and smelting of lead-containing ores as well as manufacturing and recycling of lead-based products. Most of the lead used now comes from recycling. The effects of lead exposure range in severity, but even at blood concentration levels of $5 \mu\text{g dL}^{-1}$ leads to changes in brain development that result in decreased intelligence quotients and anti-social behavior. It has also been linked to hypertension, anemia, immunotoxicity, and damage to reproductive organs. Organolead compounds are particularly dangerous as they are readily absorbed through the skin and lungs.

3.7.2 Speciation

Lead in nature commonly occurs in two oxidations states: Pb(IV) and Pb(II). The former is typical of lead's organic chemistry and common for the carbon group, while the latter is characteristic of its inorganic chemistry. The presence of organolead compounds in the environment is generally attributed to the use of alkylated species used as antiknocking agents in fuels. These tend to decompose to some extent but are highly bioavailable. Inorganic lead species are found as the free ion

and in other bound forms; the most common are PbBrCl and $\text{PbBrCl} \cdot (\text{NH}_4)_2\text{SO}_4$ as products of vehicle exhaust and $\text{Pb}(\text{SO}_4)$ which is associated with lead smelting processes. The species of lead present in terrestrial samples is directly related to concentration and pH [25,26].

3.7.3 Lanthanide-based metal-organic framework for selective detection of Pb(II) [27]

Guanfeng Ji, Jingjuan Liu, et al. had work published by the Royal Society of Chemistry in the *Journal of Materials Chemistry A* in 2017 regarding highly sensitive and selective detection of Pb(II) using a 2D terbium MOF. Produced under hydrothermal conditions, Tb-MOF ($[\text{Tb}(\text{3,5-dicarboxyphenolate anion})(\text{H}_2\text{O})_5]$) crystal structure was determined using single-crystal X-ray. Luminescence was characterized in solid state and aqueous conditions revealing excitation at 334 nm, common to lanthanides [28]. Emission peaks for the f-f transitions of Tb(III) were found at 492, 546, 587, and 623 nm and have been attributed to the LMCT from the antennae-like effect of the ligand. The group also reports negligible change in luminescence intensity after storage in deionized water or across pH values of 3–12, adjusted used HCl and NaOH.

Selectivity capabilities were analyzed using parallel metal ion aqueous solutions to determine the quenching effects of various metals, as shown in Fig. 3.7. These

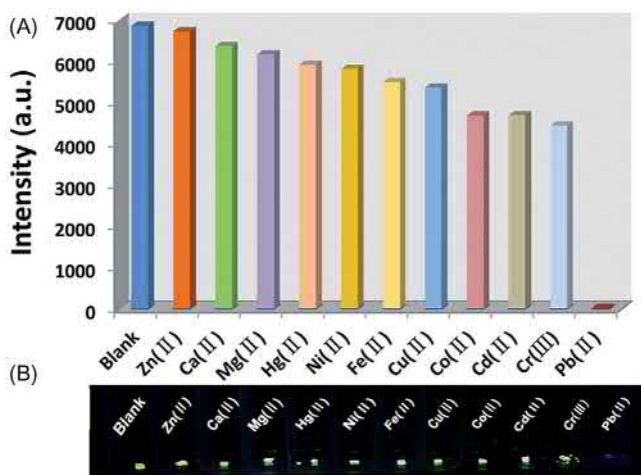


Figure 3.7 (A) Luminescence intensities of $^5\text{D}_4\text{-}^7\text{F}_5$ transitions [4] at 545 nm of Tb-MOF in 0.001 M metal ion solutions. (B) Images of Tb-MOF associated with each metal ion under UV light.

Source: Adapted from G. Ji, J. Liu, X. Gao, W. Sun, J. Wang, S. Zhao, et al., A luminescent lanthanide MOF for selectively and ultra-high sensitively detecting Pb^{2+} ions in aqueous solution, *J. Mater. Chem. A* 5 (21) (2017) 10200–10205 with permission from The Royal Society of Chemistry.

were prepared at 0.001 M and the results shown were determined after two hours. The quenching effect can be seen by the naked eye. Quantitative analysis of the quenching efficiency was characterized using a Stern–Volmer equation and suggest an excellent, nearly linear correlation coefficient at low concentrations (8×10^{-4} to 3.4×10^{-7} M, the lower concentration end being the LOD). At higher concentrations a meaningful deviation from linearity is reported; the group believes this to be due to self-absorption by the metal ions. Selectivity was characterized similarly, but the battery of solutions was replaced with a concomitant solution of previous metal ions, where their total concentration was 0.001 M. Luminescence intensity in this mixed solution remained above 88% and introduction of Pb(II) effectively quenched this.

Some applications work was performed. A thin film of Tb-MOF was fabricated by a hot-pressing process containing 0.5 wt.% of Tb-MOF. This material was applied to strips which were placed in a similar mixed-ion solution as that used for selectivity testing. These strips successfully made the qualitative determination of the presence of Pb(II) against other metal ions and show a simple and practical application of Tb-MOF for such analyses.

The mechanism of the quenching is believed to be due to electrostatic interactions between Pb(II) and the Lewis basic phenolic oxygen of the ligand. Characterization was done following luminescence lifetime studies which point toward a dynamic and a static mechanism. It was found that the UV-Vis absorption of the metal ions does not overlap with the absorption and emission spectra which could suggest that interaction between the ligand and Pb(II) significantly hinders the LMCT to the Tb(III). XPS and FT-IR confirmed a weak interaction between phenolic oxygen and Pb(II).

3.7.4 Electrochemical DNA-functionalized porphyrinic metal-organic framework for Pb(II) sensing [29]

Lin Cui, Jie Wu, et al. had work published in Analytical Chemistry in 2015 regarding an efficient electrochemical sensor for the detection of Pb(II) using an Fe(III) based MOF (FeP-MOF) containing porphyrinic ligands functionalized with DNA that amplifies electrochemical signals in the presence of Pb(II) against other metal ions, yielding a LOD of 0.034 nM. The complex functionality of this material relies on the catalytic cleavage of GR-5 DNA strand by Pb(II) from gold nanoparticles (AuNPs); the remaining strand attached to FeP-MOF via embedded AuNPs then hybridizes with a hairpin probe (HP) that is immobilized to a carbon electrode as illustrated in Fig. 3.8. The porphyrinic ligand then catalyzes the oxidation of chromogenic 3,3',5,5'-tetramethylbenzidine (TMB) by hydrogen peroxide which is followed by the electrochemical reduction of the oxidation product at the sensors surface. Measurements are then made using a chronoamperometric method that can be correlated to Pb(II) concentration as a significant increase in steady-state current.

The biomimetic oxidase-like catalytic properties of FeP-MOF were evaluated by reaction of TMB with H_2O_2 in aqueous solution. It was shown by current-voltage (CV) electrochemical measurement that modification of a carbon electrode with

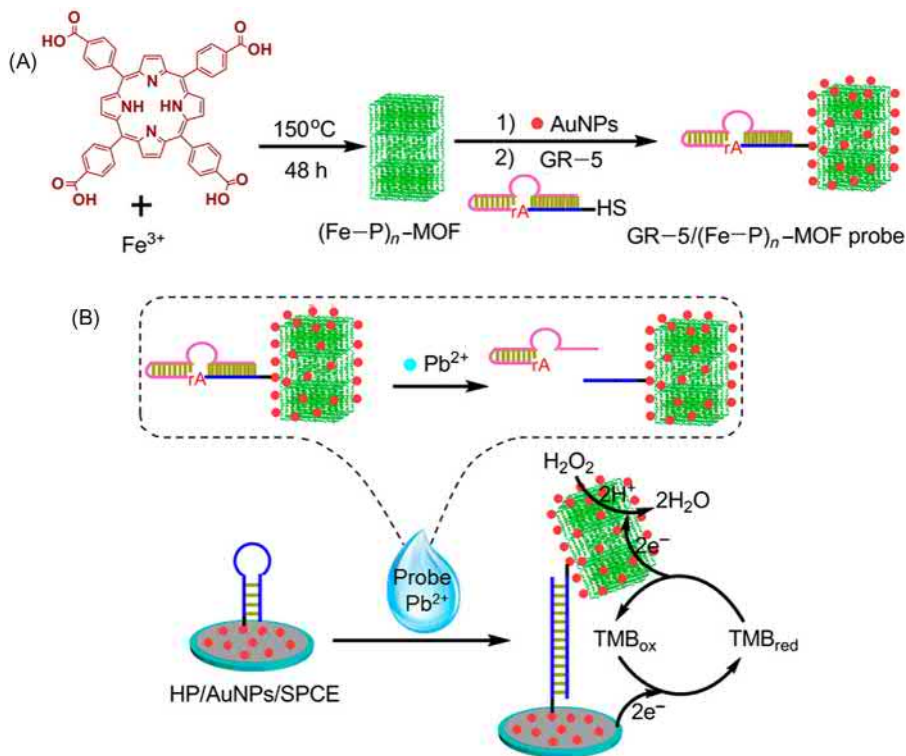


Figure 3.8 (A) FeP-MOF synthesis and functionalization with GR-5. (B) Ability of FeP-MOF to detect $\text{Pb}(\text{II})$ in solution and mimic peroxidase allowing it to interact with the cathode.

Source: Adapted from L. Cui, J. Wu, J. Li, H. Ju, Electrochemical sensor for lead cation sensitized with a DNA functionalized porphyrinic metal-organic framework, *Anal. Chem.* 87 (20) (2015) 10635–10641 with permission from the American Chemical Society.

FeP-MOF increased the reduction peak current, indicative of an electrocatalytic reaction. Stability of this component of the material's functionality was determined. FeP-MOF-modified carbon electrodes were exposed to pH ranging from 3 to 10 and temperatures from 4°C to 60°C for 2 hours. At pH of 3 and 10, catalytic activity was found to be 62.3% and 41.9%, respectively. At 60°C it maintained 87% activity. This is impressive compared to biological counterparts horseradish peroxidase and hemin, which maintain activities of 1.3% and 18.6% at pH 3, and 11.6% and 20.8% at pH 10, respectively.

The structure of the MOF that FeP-MOF is amended from was used to confirm the crystal structure of FeP-MOF by X-ray diffraction (XRD) [30]. The material has a BET surface area of $279\text{ m}^2\text{ g}^{-1}$ and FT-IR was used to show metalation with Fe (III) of the porphyrinic ligand. Embedding of AuNPs to FeP-MOF was shown by an absorption peak of 520 nm that did not occur prior to inclusion as well as SEM imaging revealing dispersion across the surface.

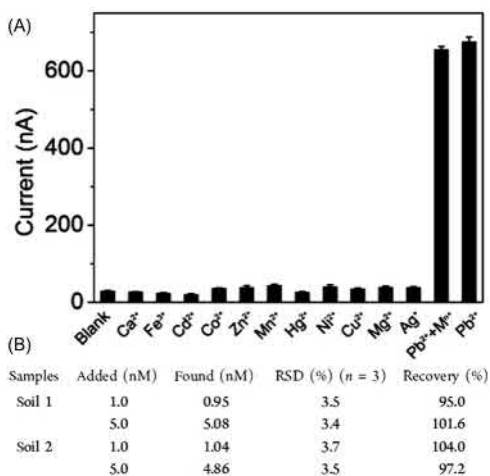


Figure 3.9 (A) Chronoamperometric response of FeP-MOF to 5 μM metal ion solutions at +100 mV. $\text{Pb}^{2+}\text{M}^{n+}$ data represents FeP-MOF in the presence of a mixed metal ion solution at same concentration. (B) Chart showing determination of Pb(II) in spiked soil samples. RSD is relative standard deviation.

Source: Adapted from L. Cui, J. Wu, J. Li, H. Ju, Electrochemical sensor for lead cation sensitized with a DNA functionalized porphyrinic metal-organic framework, *Anal. Chem.* 87 (20) (2015) 10635–10641 with permission from the American Chemical Society.

Sensitivity of the material to Pb(II) characterized under optimized conditions revealed an impressive correlation coefficient of 0.9994 ranging from 0.05 to 200 nm. The LOD of 0.034 nm is 350 times lower than that permitted in drinking water by WHO. Application of this material to real samples was done using spiked soil samples. Related data is tabulated in Fig. 3.9. Selectivity was investigated using a mixed metal ion solution. At 50-fold concentration of competing ions a negligible response was observed.

3.8 Mercury

The element mercury has been found in Egyptian tombs dating back past 1500 BCE. It has been known of and collected for various ritualistic and extravagant reasons for millennia. It was believed to be the *prima materia* (first material) of metal [31], from which all metals came, and possessed healing and life extending properties. Now, the heavy d-block element is known for its toxicity and modern usage in various measuring instrumentation such as thermometers and barometers. The application of mercury in these tools is being phased out as less harmful alternatives are found. Industrial uses of mercury, such as the production of sodium hydroxide and chlorine from salt, are also being replaced.

D	Dental problems and amalgam release of mercury
E	Endocrine toxicity and dysfunction
A	Affects adrenal function and hormone production (inhibiting of 21 α -hydroxylase)
D	Diabetes may be associated or caused
L	Likely inhibits myelin synthesis in developing feti and children
Y	Young's syndrome (Azoospermia sinopulmonary infections)
M	Methylation of inorganic mercury in body
E	Environmental accumulation (soil, water, air)
T	Toxic to GI, liver, and pancreas
H	Hypertension due to epinephrine excess (inhibits catecholamine metabolism)
Y	Young women should avoid some fish
L	Long biological half-life (may be >90 days)
M	Microorganisms (sulfate processors) synthesize from inorganic mercury
E	Enters food chain, bio accumulates, and biomagnifies
R	Red blood cell accumulation (competes with iron for hemoglobin binding)
C	Crosses blood-brain barrier and produces central nervous system toxicity
U	Uterine fetal toxicity
R	Renal toxicity, especially to renal tubules
I	Immune, enzyme, and genetic alterations
A	Association with many neurodegenerative diseases
L	Long-term toxicity on many organs and systems
S	Special senses affected

Figure 3.10 Mnemonic for various health effects induced by mercury exposure.

Source: Developed by K.M. Rice, E.M. Walker, M. Wu, C. Gillette, E.R. Blough, Environmental mercury and its toxic effects, *J. Prev. Med. Public Health* 47 (2) (2014) 74–83 [33].

3.8.1 Health and hazards

Mercury is the third most toxic substance on the planet, ranked by the Agency for Toxic Substances and Disease Registry, coming after arsenic and lead. Exposure to humans has three main routes: pigments used in paints and plastics predating 1990; mercury vapors present in fossil fuels, medical waste incineration, and industrial processes; and finally through bioaccumulation. The latter occurs through bacteria that consume inorganic mercury compounds that they fix into organic methylmercury. This tends to reach its highest biological concentration in fish, which are then consumed by humans [32]. The average body half-life for MeHg is 40 days—in the brain it can be up to 20 years.

The slew of negative health effects and issues caused by various forms of mercury has been contained in the mnemonic DEADLY METHYLMERCURIALS (Fig. 3.10). Mercury exposure can result in more than 250 unique symptoms which can complicate diagnosis.

3.8.2 Speciation

About half of the mercury introduced to the environment comes from volcanic activity, the other half primarily from coal-fired power plants and gold production. Elemental and mercuric forms, Hg(0) and Hg(II) respectively, exist in the atmosphere in equal parts but the latter is the most important when considering exposure and reactivity. Hg(II) is generally associated with halogens such as HgCl₂ and hydroxide. These species are highly water soluble and, as an example, can be

absorbed in cloudwater where it would later be introduced to the ground or bodies of water as rain. In general, these common species of mercury undergo several transformations, interchanging with one another: Hg(0) can be oxidized to Hg(II) by ozone, hydroxyl radicals, or hydrogen peroxide (all present in air moisture); Hg(II) can be reduced to Hg(0) by reaction with gaseous sulfates or aqueous sulfites [34]. While atmospheric mercury can interact directly, the deposition into terrestrial and aquatic systems that leads to bioaccumulation in the foods we eat accounts for the greatest amount of exposure.

3.8.3 Postsynthetically modified UiO-66 for selective detection [35]

Xin Zhang, Tifeng Kia, et al. had work published in the *Journal of Solid State Chemistry* in 2017 regarding a zirconium-based MOF for the selective sensing of Hg(II) in aqueous medium. The group utilizes copper catalyzed click chemistry to postsynthetically modify UiO-66-N₃ with phenylacetylene, generating a triazole with which Hg(II) is expected to bind. The intense luminescent properties of this moiety are strongly quenched in the presence of mercury- readily differentiated from concomitant metals due to their lesser binding affinities. Experimental characterization of this follows like solutions (1 mL, 10 – 2 M) of several cationic metals M(NO₃)_z (Mz + = Ca²⁺, Al³⁺, Cr³⁺, Fe²⁺, Fe³⁺, Co²⁺, Ni²⁺, Cu²⁺, Na⁺, K⁺, Mg²⁺, Ag⁺, Zn²⁺, Hg²⁺, and Pb²⁺) (Fig. 3.11). Results suggest a high specificity

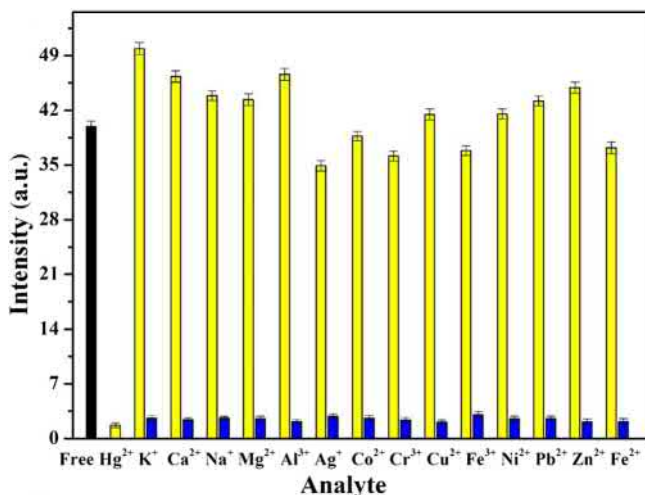


Figure 3.11 Black bar represents fluorescence of UiO-66-PSM at 544 nm. Yellow bars are 30 s after the addition of 10 mM of metal ion, while blue bars measure these solutions after the addition of Hg(II).

Source: Adapted from X. Zhang, T. Xia, K. Jiang, Y. Cui, Y. Yang, G. Qian, Highly sensitive and selective detection of mercury (II) based on a zirconium metal-organic framework in aqueous media, *J. Solid State Chem.* 253 (2017) 277–281 with permission from Elsevier.

for mercury which the group attributes to several factors: Hg(II)'s relatively larger radius, its diverse coordination, the rigidity and soft-acid character of the triazole moiety, and the strong Hg-N interaction.

The crystal structure of UiO-66-PSM was characterized with scanning electron microscopy, showing an octahedral geometry and nanoparticle size of 500–600 nm, and powder X-ray diffraction, which yielded a pattern in good accordance with that of simulated UiO-66 [36]. FT-IR spectra of UiO-66-N₃ displayed one peak at 2120 wavenumbers, indicative of an azide asymmetric stretch. Following postsynthetic modification this peak is reduced, which is ascribed to the change from azide to triazole. For the N₂ sorption studies at 77K gave a BET surface area of 412.45 m² g⁻¹ for UiO-66-PSM. The postsynthetic transformation is further elucidated by excitation and emission studies. UiO-66-N₃ had very weak fluorescence due to the electron withdrawing azide, while UiO-66-PSM, upon excitation at 484 nm, produced a strong broad band emission around 544 nm from the $\pi-\pi^*$ transition of the organic linkers. The bonding of Hg(II) into the PSM MOF at the triazole is characterized by XPS. The N 1s peak at 403.4 eV is shifted to 406 eV upon the addition of mercury, showing N–Hg interaction that explains the quenching effect.

A linear relationship between fluorescence quenching and mercury concentration was established from 0 to 78.1 μM and indicates UiO-66-PSM can be used for quantitative determination of Hg(II) (Fig. 3.12). A limit of detection value of 5.88 μM is comparable to previously reported fluorescence sensors. A final test against real water samples with added mercury describe the practical application of the MOF.

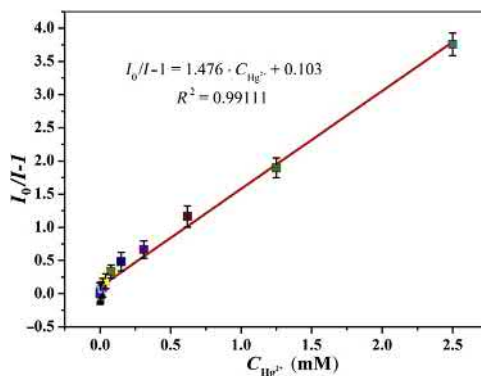


Figure 3.12 Stern–Volmer plot of $I_0/I-1$ versus the concentration of Hg(II), showing a good fit. Where I_0 and I are the luminescence intensities before and after Hg(II) inclusion. *Source:* Adapted from X. Zhang, T. Xia, K. Jiang, Y. Cui, Y. Yang, G. Qian, Highly sensitive and selective detection of mercury (II) based on a zirconium metal-organic framework in aqueous media, *J. Solid State Chem.* 253 (2017) 277–281 with permission from Elsevier.

3.8.4 UiO-66-NH₂ DNA [37]

Lan-Lan Wu, Zhuo Wang, et al. had work published in ChemPubSoc Europe in 2016 regarding the preparation of a MOF-DNA hybrid for the selective fluorescent-based sensing and sequestration of Hg(II), down to 17.6 nM concentration. The key to this material's functionality lies in the binding affinity of mercury ions to thymine–thymine (T-T) mismatched pairs in oligonucleotides. Mercury fits between the interacting faces of the base pairs, creating a thymine–Hg(II)–thymine sandwich complex (T-Hg²⁺-T) [38]. The group incorporates a thymine rich single-stranded DNA (ssDNA) labeled with a fluorophore (FAM) at the 3' end to serve as a probe (Fig. 3.13).

The probe strongly fluoresces at 480 nm under 510 nm light. When in the presence of UiO-66-NH₂, photoinduced energy transfer (PET) quenches the probe via hydrogen interactions and π – π stacking between the aromatic organic linker and the base-pair groups of the dye. When Hg(II) is introduced, the formation of hairpin-like T-Hg(II)-T structures affect the conformation of the dye and isolate it from UiO-66-NH₂, restoring fluorescence. This suggests that the MOF-DNA system's fluorescence intensity is a function of mercury concentration. To characterize their theory, fluorescence emission spectra under varying conditions in a 7.4 pH tris-HCl buffer were collected. The free probe has strong emission at 510 nm which declines with the introduction of the modified UiO-66; the fluorescence quenching efficiency (Q_c) is found to be close to 75% (Fig. 3.14). Further, the introduction of Hg(II) significantly enhances the otherwise quenched signal, noting that the probe is not affected by just mercury—the presence of UiO-66-NH₂ is necessary. Inversely, the UV/Vis diffuse reflectance spectrum of UiO-66-NH₂ shows there is no absorbance from the material at the dyes emission wavelength, indicating fluorescence resonance energy transfer does not occur between the two.

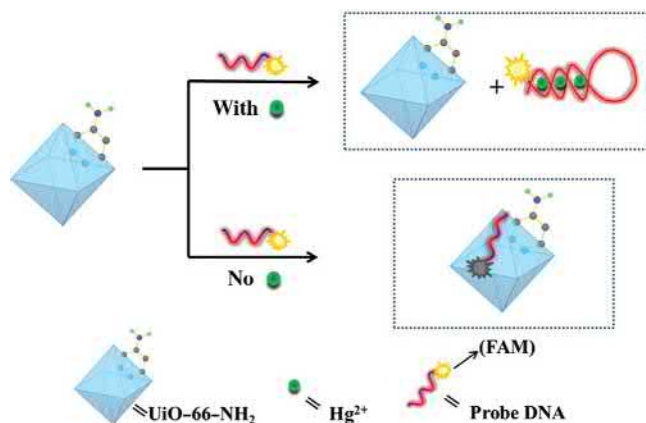


Figure 3.13 Conceptual illustration of the fluorescence mechanism.

Source: Adapted from V. Guillermin, S. Gross, C. Serre, T. Devic, M. Bauer, G. Férey, A zirconium methacrylate oxocluster as precursor for the low-temperature synthesis of porous zirconium(IV) dicarboxylates, *Chem. Commun.* 46 (5) (2010) 767–769 with permission from the American Chemical Society.

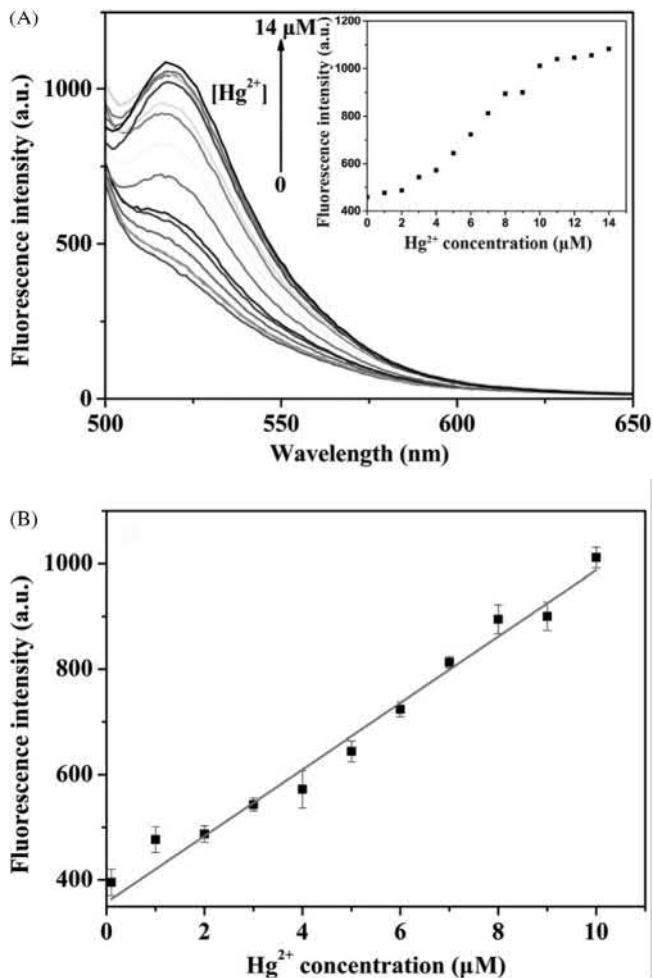


Figure 3.14 (A) illustrates the relationship between $\text{Hg}(\text{II})$ concentration and fluorescence intensity across 500–650 nm. Each fluorescence curve is representative of a point on the inset graph. (B) Expresses the linear relationship between fluorescence intensity and $\text{Hg}(\text{II})$ concentration.

Source: Adapted from X. Zhang, T. Xia, K. Jiang, Y. Cui, Y. Yang, G. Qian, Highly sensitive and selective detection of mercury (II) based on a zirconium metal-organic framework in aqueous media, *J. Solid State Chem.* 253 (2017) 277–281.

The selectivities for various metals were tested under identical conditions to that of the $\text{Hg}(\text{II})$ fluorescence tests. Fig. 3.15 illustrates the significant fluorescence enhancement relative to the other cationic metals tested. It is worth noting that the detection limit reported is lower than the toxicity level in drinking water (30 nM) for mercury as defined by the World Health Organization (WHO) (Fig. 3.16).

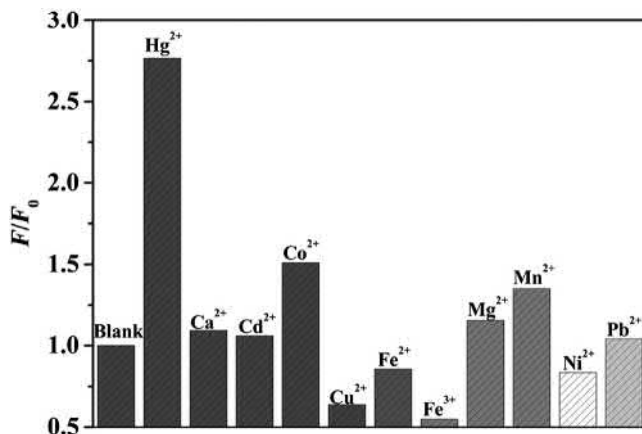


Figure 3.15 Selectivity of the MOF-DNA system against other metals. F_0 and F represent the fluorescence intensity before and after the addition of 10 μM metal ions, respectively. *Source:* Adapted from V. Guillermin, S. Gross, C. Serre, T. Devic, M. Bauer, G. Férey, A zirconium methacrylate oxocluster as precursor for the low-temperature synthesis of porous zirconium(IV) dicarboxylates, *Chem. Commun.* 46 (5) (2010) 767–769 with permission from the American Chemical Society.

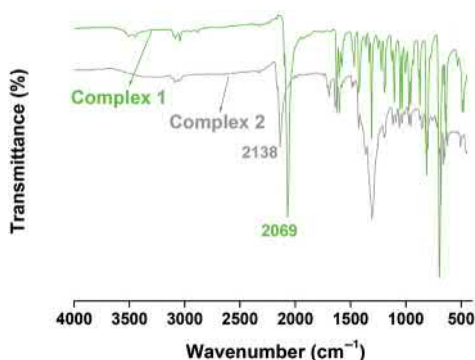


Figure 3.16 FT-IR spectra showing SCN-MOF (Complex 1) prior to inclusion of Hg(II) and after (Complex 2), illustrating the blueshift effect of the metal ion adsorption. *Source:* Adapted from H. Urata, E. Yamaguchi, T. Funai, Y. Matsumura, W. Si, Incorporation of thymine nucleotides by DNA polymerases through T–HgII–T base pairing, *Angew. Chem.* 122 (37) (2010) 6666–6669 with permission from The Royal Society of Chemistry.

3.8.5 Nickel-based metal-organic framework for visual detection and selective remediation [39]

Shibashis Halder, John Mondal, et al. published work in the journal *Dalton Transactions* in 2017 regarding a MOF capable of remediation of Hg(II) ions from water with high selectivity for the cation and a visual indication of its presence.

Relying on the affinity of Hg(II) to coordinate with large, soft atoms such as sulfur [40], the group proposes a nickel-based MOF $[\text{Ni}(\text{3-bpd})_2(\text{NCS})_2]_n$, where 3-bpd is 1,4-bis(3-pyridyl)-2,3-diaza-1,3-butadiene, referred to as SCN-MOF. Analyses show that two thiocyanato moieties bind the Ni center with uncoordinated S, offering conditions for the binding of Hg(II). This is confirmed by FT-IR spectra where the typical 2069 wavenumbers band of SCN^- blueshifts in the presence of Hg(II) as CN bond order increases and electron density is pulled away from the sulfur.

Mercury uptake studies were performed by measuring change in color (from green to gray) of a Hg(II) and SCN-MOF solution over time, and efficiency was characterized by the amount of Hg(II) remaining in the solution after the uptake studies completed. Selectivity was characterized by a battery of tests against other metals and metalloids (Al^{3+} , Zn^{2+} , Fe^{3+} , Na^+ , K^+ , Mg^{2+} , Ca^{2+} , Pb^{2+} , Cd^{2+} , As^{3+} , and Ag^+) that relied on the observation of color change, all performed in aqueous solution under ambient conditions. No other metal tested elicited a visually appreciable change in color, suggesting little to no interaction through a similar mode as Hg(II). The insolubility of the MOF in aqueous solution provides a simple means of separation—filtration of the solid complex after Hg(II) uptake effectively remediates the water of its mercury content. The group suggests a 2:1 ratio of nickel to mercury in the Hg(II)·MOF complex by theoretical calculations, where two Hg(II) bond through one sulfur via S-Hg and weak Hg-Hg interaction. The possibility of transmetalation was explored by analysis of mother liquor for free nickel ions with dimethylglyoxime in ammoniacal medium, which was not positively confirmed by a telling red precipitate. The binding and removal process was found to be irreversible. Treatment of the Hg(II)·MOF complex with thiourea and hydrochloric acid precipitated mercuric sulfide but also resulted in the decomposition of the MOF.

3.9 Radioactive wastes

The waste generated from the manufacture and use of nuclear fuel is separated into three phases: the front end, when radioactive ore is processed into fissionable material; the service period, during which the fuel is being spent; and the back end, when the spent fuel is reprocessed into forms suitable for safe storage. On the front end of the process, uranium ore is located and mined using open-pit or leaching methods. The ore is milled into U_3O_8 , also known as yellowcake, then converted either to UF_6 which is later enriched, or UO_2 , depending on the kind of reactor it is meant for. The service period includes safe and reliable transport of fissile material and management of the active fuel rods. The back end considers methods for separation of remaining fissile material (for reuse) from spent fuel which is solution-based and increases the overall amount of waste but generally reduces its radioactivity [40]. There are multiple methods for this, but the most commonly employed is PUREX (Plutonium and Uranium Recovery by Extraction).

3.9.1 Health and hazards

Ionizing radiation can cause damage and abnormalities in living tissue. This is particularly dangerous with respect to DNA as changes to genetic material can result in cancer among other negative effects. Acute exposure to radiation can result in sickness or death within hours to days, while chronic exposure leads to delayed health issues such as cataracts, cancer, and benign tumors [41]. Routes of exposure are categorized and internal and direct. Internal exposure includes ingestion or inclusion of radioactive material into the body, where alpha and beta particles pose a serious threat to health. Direct exposure regards radiation from outside of the body. Alpha particles are too large to pass through clothing and skin, but beta and gamma radiation can penetrate the body.

3.9.2 Speciation

The constituents of radioactive waste considered here come from spent fuel rods. Materials that interact directly with the fuel rod such as cladding or fuel rod pools contain some amount of radioactive material as well and are also considered a waste product of nuclear reactors. Waste is classified as low-level (LLW), intermediate-level (ILW), and high-level (HLW). Spent fuel rods contain fission products of ^{235}U , primarily of which are ^{90}Sr and ^{137}Cs , but can include various other transuranic species, some of which are described in Fig. 3.17. Strontium is divalent and behaves similarly to calcium while Cesium is monovalent. Uranium has several common oxidation states (III, IV, and II) while plutonium has states I through IV.

3.9.3 Cryptand inspired metal-organic framework for detection and adsorption [42]

Sergey A. Sapchenko, Pavel A. Demakov, et al. had work published in *Chemistry: A European Journal* by ChemPubSoc Europe in 2017 regarding a zinc-based cryptand ligand MOF with luminescence dependent on the adsorption of group I metal cations. The material shows selectivity toward heavier alkali metals, Rb(I) and Cs

4.5%-7%	0.04%-1.25%	<0.001%
90-Sr	155-Eu	113-Cd
137-Cs and 135-Cs	85-Kr	121-Sn
99-Tc	151-Sm	
93-Zr	126-Sn	
	79-Se	
	107-Pd	
	129-I	

Figure 3.17 List of elements and their isotopes by percent content of the fission products of ^{235}U .

(I) in particular. $(\text{H}_3\text{O})_2[\text{Zn}_4(\text{ur})(\text{Hfdc})_2(\text{fdc})_4]$ (ur = urotropine, H_2fdc = furan-2,5-dicarboxylic acid) or C1 for short, was produced under solvothermal conditions and characterized using single-crystal X-ray revealing a 3D framework with 61% accessible volume containing two distinct pore types; one is hydrophobic and hosts DMF and water molecules, while the other has void-facing oxygens from the fdc^{2-} ligands with hydroxonium counterions. The latter pore is similar to the container-like cryptand supramolecules which strongly complex cationic guests by oxygen and nitrogen lone-pair interactions.

Adsorption of metal cations by C-MOF was characterized by soaking in 0.01 M metal nitrate solutions in NMP for 1 day. Crystal stability was confirmed by PXRD and metal content was determined by dissolution in $\text{H}_2\text{O}_2/\text{DMF}$ followed by atomic emission spectroscopy (AES), revealing preferential binding for Rb(I) and Cs(I) over Li(I), Na(I), or K(I). Selectivity was characterized with a 0.001 M concomitant metal nitrate solution containing all five metals referred to previously. It was found that less than 10% of hydroxonium cations were replaced by Li(I) and Na(I) while about 40% were replaced by Cs(I) with an overall molar ratio of 1:15:34:47:69 = Li/Na/K/Rb/Cs.

Photoluminescence was found to occur under excitation at 340 nm showing a broad band around 470 nm in solid-state emission; the group attributes this to intraligand electron state transitions. Ion exchange with metal cations doesn't produce significant change in the emission band but rather the intensity and quantum yield are affected depending on the metal. Potassium and rubidium produced the most pronounced effect with around a 30% reduction, with cesium at a 19% reduction.

3.9.4 *Metal-organic framework-based ion traps for irreversible barium adsorption [43]*

Yagyuang Peng, Hongliang Huang, et al. had work published in *Applied Materials & Interfaces* by ACS in 2016 regarding a zirconium-based MOF (MOF-808- SO_4 , or Zr-MOF) postsynthetically functionalized with sulfate groups, as well as a chromium-based MOF (MIL-101- SO_3H , or Cr-MOF) with in situ sulfonic acid functionality for the highly efficient, irreversible uptake of Ba(II). The former exhibits excellent uptake capacity while the latter possesses rapid uptake kinetics.

Both Zr-MOF and Cr-MOF were characterized using PXRD, revealing by comparison to synthesis of unfunctionalized parent materials that both exhibit appropriate crystal structure. The decrease in N_2 adsorption corroborates a decreased BET surface area due to sulfate/sulfonic acid functionalization. The successful amendment of both MOFs with respective sulfur groups was shown by FT-IR and XPS. Sulfur-oxygen stretching bands at 1135 and 1080 wavenumbers, as well as sulfur 2p binding energies of 168.8 and 168.0 eV for Zr-MOF and Cr-MOF, respectively, are attributed to the attachment of the moieties to each framework. These values were found to shift for Zr-MOF with uptake of Ba(II). TGA and ICP reveal no excess Zr or Cr present in the MOF materials. This was done by comparing metal content of theoretical models of Zr-MOF and Cr-MOF with experimental metal content.

Barium uptake studies were performed at an optimized 5.8 pH in aqueous solutions. Both Zr-MOF and Cr-MOF were shown to include >90% of Ba(II) in 5 minutes, and >99% at equilibrium; Cr-MOF showed faster overall sorption. The group attributes this quality to superior pore structure. Cr-MOF induced a decrease in pH to 4.7 while Zr-MOF did not due to differing sorption mechanisms, where the sulfonic group chelates the metal by proton exchange. This mechanism was used to explain Cr-MOF's lower capacity in terms of ion competition. Sorption isotherms were used to show almost no uptake in parent materials, while Zr-MOF possesses a saturation capacity of 131.1 mg g^{-1} and Cr-MOF's is 70.5 mg g^{-1} . Cr-MOF vastly outperforms many sorbents used for this purpose. Adsorption across a temperature range was determined to be an endothermic process by calculation of the adsorption free energy.

Selectivity for Ba(II) was characterized against ions present in nuclear wastewater (Cs(I), Zn(II), Ni(II), Co(II), Sr(II), La(III), Eu(III)) as shown in Fig. 3.18.

Both MOFs maintain an efficiency over 93% in mixed metal ion solutions with concomitant ions having a magnitude higher concentration. Release of Ba(II) into clean water was found to be small. Each MOF was saturated with Ba(II) and rinsed with water, then allowed to soak with shaking for 7 days. Zr-MOF retained 98% while Cr-MOF retained 92% of adsorbed Ba(II)—this was determined by ICP of the MOFs.

The lower uptake capacity for Cr-MOF is believed to be due to its competitive ion mechanism as well as the nature of its functional group. The sulfonic acid is partly less active due to the terephthalate ligand it is attached to, making the lower uptake particularly evident when compared to Zr-MOF, where the sulfate group is connected to the metal cluster and does not experience the competitive ion effect or the deactivation as illustrated in Fig. 3.19. This interpretation is reinforced by DFT calculations [44].

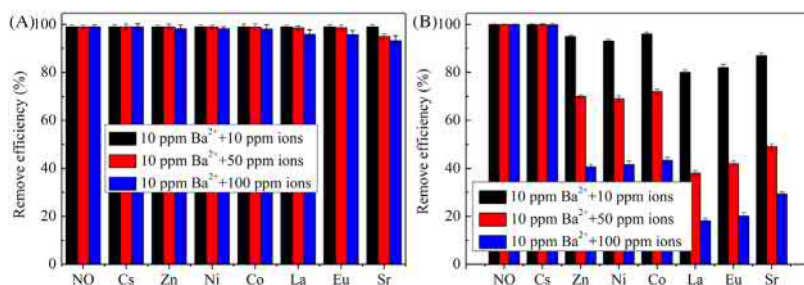


Figure 3.18 Effect of mixed metal ions on the adsorption of Ba(II) by Zr-MOF (A) and Cr-MOF (B).

Source: Adapted from Y. Peng, H. Huang, D. Liu, C. Zhong, Radioactive barium ion trap based on metal-organic framework for efficient and irreversible removal of barium from nuclear wastewater, *ACS Appl. Mater. Interfaces* 8 (13) (2016) 8527–8535 with permission from the American Chemical Society.

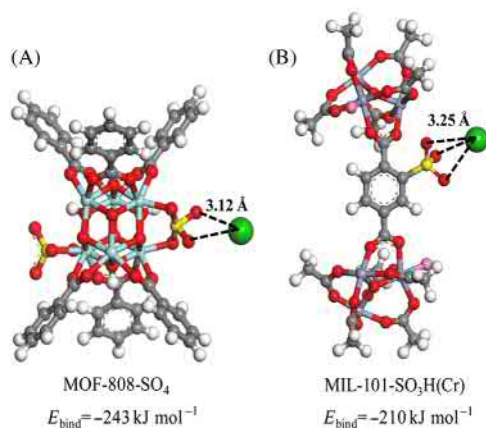


Figure 3.19 Optimized geometries illustrating the interactions of Ba(II) with Zr-MOF metal cluster (A) and Cr-MOF ligand (B) (Zr in cyan, Cr light blue, Ba green, C gray, S yellow, O red, H white).

Source: Adapted from Y. Peng, H. Huang, D. Liu, C. Zhong, Radioactive barium ion trap based on metal-organic framework for efficient and irreversible removal of barium from nuclear wastewater, *ACS Appl. Mater. Interfaces* 8 (13) (2016) 8527–8535 with permission from the American Chemical Society.

3.9.5 Terbium-based metal-organic framework for selective uranium detection [45]

Wei Liu, Xing Dai, et al. had work published in *Environmental Science & Technology* in 2017 regarding a terbium MOF (Tb-MOF) functionalized with highly Lewis basic ligands for the selective sensing of uranyl (UO_2^{2+}) in aqueous solutions. Tb-MOF was synthesized under solvothermal conditions and its structure determined by single-crystal X-ray revealing a mesoporous, noninterpenetrated 3D framework. It was found to have a surface area of $525 \text{ cm}^2 \text{ g}^{-1}$ based on the BET method. The H₃TATAB ligands in the material orient such that the extensive Lewis basic amine and triazine sites were coordinated inwards toward the pore voids with carboxylate groups connecting to the [Tb₂(CO₂)₄] metal clusters (Fig. 3.20). Hydrolytic stability was confirmed by aging in various metal salt solutions as well as real lake and seawater samples with pH ranging from 2 to 10. Solubility of Tb-MOF in these solutions was found to be low, ranging from 1.15% to 5.35% lost to solution at pH 4, which was decidedly the optimized pH for uptake. Gamma radiation resistance ensures application to HLW solutions.

Fluorescence detection experiments were carried out by establishing presence of characteristic Tb(III) transition bands at 488, 545, 581, and 620 nm—each representing a 4f-4f transition type [46] with a quantum yield up to 44.8%. Following, Tb-MOF was saturated with various concentrations of $\text{UO}_2(\text{NO}_3)_6(\text{H}_2\text{O})$ in deionized water at pH 4. Quenching was attributed to LMCT and supported by DFT calculations, EXAFS, and XANES—it could be observed by the naked eye. The Langmuir model was used to fit the quenching ratio as a function of uranium

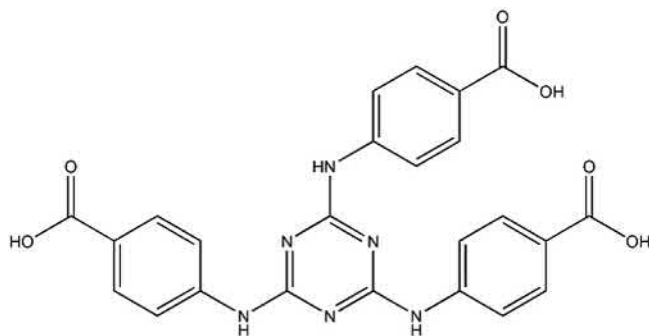


Figure 3.20 H₃TATAB (4,4',4''-((1,3,5-triazine-2,4,6-triyl)tris(azanediyl))tribenzoic acid).

Source: Adapted from J. Zhao, Y.-N. Wang, W.-W. Dong, Y.-P. Wu, D.-S. Li, Q.-C. Zhang, A robust luminescent Tb (III)-MOF with Lewis basic pyridyl sites for the highly sensitive detection of metal ions and small molecules, *Inorg. Chem.* 55 (7) (2016) 3265–3271 with permission from the American Chemical Society.

concentration with an R^2 value of 0.9911. Further, the quotient of uranyl concentration and the quenching ratio as a function of uranyl concentration revealed an impressive R^2 value of 0.9999, suggesting a highly accurate quantitative detection of uranyl over a concentration range of 0.2–350 mg L⁻¹. Adsorption kinetics study showed a reasonably fast uptake with 98% removal at pH 4 at 5 and 50 mg L⁻¹. The LOD was shown to be Tb-MOF concentration dependent and was optimized to 0.05 g L⁻¹ of Tb-MOF in uranyl solution. The LOD value under these ideal conditions was determined to be 0.9 μg L⁻¹.

Selectivity was characterized by a battery of highly concentrated (0.5 g L⁻¹) metal nitrate solutions (Th(IV), Eu(III), Al(III), Sr(II), Ca(II), Cs(I), Cs(I), and K(I)) and several mixed solutions of these metal nitrates. In the former, after confirmation of a negligible effect (except for Eu(III)), uranyl was added and found to effectively quench each solution's luminescence. In the latter case, it was found that these mixed metal ion solutions did not prevent selective uranyl uptake by Tb-MOF (Fig. 3.21).

Sorption was further characterized for NaCl, Na₂CO₃, and humic acid (a component of soil) mixtures. In all cases uranyl uptake remained above 93%. Calculations on tests run with fresh lake and seawaters reported LODs of 14.0 and 3.5 μg L⁻¹, respectively. An artificial seawater sample containing uranium was used to give perspective against ICP-MS determination of uranyl content. This technique reported a concentration of 114.6 μg L⁻¹ while the method described in this work reported 106.7 μg L⁻¹.

The pore environment and adsorption mechanism were elucidated by XANES, EXAFS, and DFT calculations. It was found that various degrees of hydrated uranyl are chelated via U-N bonding to the lone pairs of the Lewis basic sites primarily in a hexagonal bipyramid coordination geometry rather than interacting with oxygen of the carboxylate groups, which are saturated by Tb and sterically hindered by hydrophobic benzene. Uranyl complexation in this way has a negative free energy indicating thermodynamic favor.

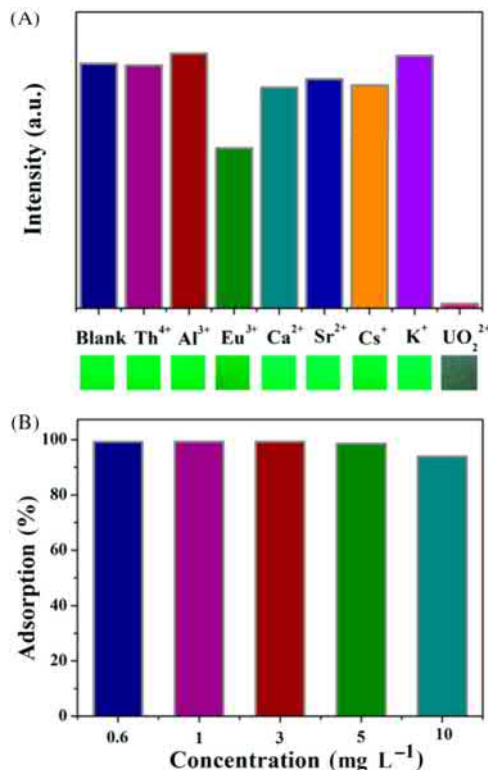


Figure 3.21 (A) Luminescence intensity of Tb-MOF in various metal ion solutions with respective image of luminescence under UV light. (B) Uranyl adsorption ratio in mixed metal ion solutions at various concentrations.

Source: Adapted from J. Zhao, Y.-N. Wang, W.-W. Dong, Y.-P. Wu, D.-S. Li, Q.-C. Zhang, A robust luminescent Tb (III)-MOF with Lewis basic pyridyl sites for the highly sensitive detection of metal ions and small molecules, *Inorg. Chem.* 55 (7) (2016) 3265–3271 with permission from the American Chemical Society.

References

- [1] Y. Georgiou, J.A. Perman, A.B. Bourlinos, Y. Deligiannakis, Highly efficient arsenite [As(III)] adsorption by an [MIL-100(Fe)] metal–organic framework: structural and mechanistic insights, *J. Phys. Chem. C* 122 (9) (2018) 4859–4869.
- [2] E. Tahmasebi, M.Y. Masoomi, Y. Yamini, A. Morsali, Application of mechano-synthesized azine-decorated zinc (II) metal–organic frameworks for highly efficient removal and extraction of some heavy-metal ions from aqueous samples: a comparative study, *Inorg. Chem.* 54 (2) (2014) 425–433.
- [3] F. Ke, L.-G. Qiu, Y.-P. Yuan, F.-M. Peng, X. Jiang, A.-J. Xie, et al., Thiol-functionalization of metal-organic framework by a facile coordination-based postsynthetic strategy and enhanced removal of Hg²⁺ from water, *J. Hazard. Mater.* 196 (2011) 36–43.

- [4] Z. Hu, B.J. Deibert, J. Li, Luminescent metal–organic frameworks for chemical sensing and explosive detection, *Chem. Soc. Rev.* 43 (16) (2014) 5815–5840.
- [5] W. Morris, W.E. Briley, E. Auyeung, M.D. Cabezas, C.A. Mirkin, Nucleic acid–metal organic framework (MOF) nanoparticle conjugates, *J. Am. Chem. Soc.* 136 (20) (2014) 7261–7264.
- [6] Wolfgang Maret, J-MM. Cadmium: From Toxicity to Essentiality 2013.
- [7] T. Nawrot, M. Plusquin, J. Hogervorst, H.A. Roels, H. Celis, L. Thijs, et al., Environmental exposure to cadmium and risk of cancer: a prospective population-based study, *Lancet Oncol.* 7 (2) (2006) 119–126.
- [8] T.S. Nawrot, J.A. Staessen, H.A. Roels, E. Munters, A. Cuypers, T. Richart, et al., Cadmium exposure in the population: from health risks to strategies of prevention, *Biometals* 23 (5) (2010) 769–782.
- [9] M. Nordberg, J. Duffus, D.M. Templeton, Glossary of terms used in toxicokinetics (IUPAC Recommendations 2003), *Pure Appl. Chem.* (2004) 1033.
- [10] H. Xue, Q. Chen, F. Jiang, D. Yuan, G. Lv, L. Liang, et al., A regenerative metal-organic framework for reversible uptake of Cd(II): from effective adsorption to in situ detection, *Chem. Sci.* 7 (9) (2016) 5983–5988.
- [11] K.K. Yee, N. Reimer, J. Liu, S.Y. Cheng, S.M. Yiu, J. Weber, et al., Effective mercury sorption by thiol-laced metal-organic frameworks: in strong acid and the vapor phase, *J. Am. Chem. Soc.* 135 (21) (2013) 7795–7798.
- [12] Y. Wang, G. Ye, H. Chen, X. Hu, Z. Niu, S. Ma, Functionalized metal-organic framework as a new platform for efficient and selective removal of cadmium(II) from aqueous solution, *J. Mater. Chem. A* 3 (29) (2015) 15292–15298.
- [13] Y.S. Ho, G. McKay, Pseudo-second order model for sorption processes, *Process Biochem.* 34 (5) (1999) 451–465.
- [14] I. Langmuir, The adsorption of gases on plane surfaces of glass, mica and platinum, *J. Am. Chem. Soc.* 40 (9) (1918) 1361–1403.
- [15] Z. Luo, *China's Imperial Tombs and Mausoleums*, 1993.
- [16] J. Kotaś, Z. Stasicka, Chromium occurrence in the environment and methods of its speciation, *Environ. Pollut.* 107 (3) (2000) 263–283.
- [17] D.C. Schroeder, G.F. Lee, Potential transformations of chromium in natural waters, *Water, Air, Soil Pollution* 4 (3) (1975) 355–365.
- [18] K.G. Stollenwerk, D.B. Grove, Adsorption and desorption of hexavalent chromium in an alluvial aquifer Near Telluride, Colorado I, *J. Environ. Qual.* 14 (1) (1985) 150–155.
- [19] H.-R. Fu, Y. Zhao, Z. Zhou, X.-G. Yang, L.-F. Ma, Neutral ligand TIPA-based two 2D metal-organic frameworks: ultrahigh selectivity of C₂H₂/CH₄ and efficient sensing and sorption of Cr(VI), *Dalton Transact.* 47 (11) (2018) 3725–3732.
- [20] S. Rapti, D. Sarma, S.A. Diamantis, E. Skliri, G.S. Armatas, A.C. Tsipis, et al., All in one porous material: exceptional sorption and selective sensing of hexavalent chromium by using a Zr⁴⁺ MOF, *J. Mater. Chem. A* 5 (28) (2017) 14707–14719.
- [21] T.-F. Liu, D. Feng, Y.-P. Chen, L. Zou, M. Bosch, S. Yuan, et al., Topology-guided design and syntheses of highly stable mesoporous porphyrinic zirconium metal-organic frameworks with high surface area, *J. Am. Chem. Soc.* 137 (1) (2015) 413–419.
- [22] D. Sun, Y. Fu, W. Liu, L. Ye, D. Wang, L. Yang, et al., Studies on photocatalytic CO₂ reduction over NH₂-Uio-66(Zr) and its derivatives: towards a better understanding of photocatalysis on metal–organic frameworks, *Chem. Europ. J.* 19 (42) (2013) 14279–14285.
- [23] J.O. Nriagu, Saturnine gout among roman aristocrats, *New Engl. J. Med.* 308 (11) (1983) 660–663.

- [24] A. Torrago, Case studies in environmental medicine (CSEM) lead toxicity, Agency Toxic Subst. Disease Registry (2012).
- [25] D.C. Baxter, W. Frech, Speciation of lead in environmental and biological samples (Technical Report), Pure Appl. Chem. (1995) 615.
- [26] S. Sauvé, M.B. McBride, W.H. Hendershot, Speciation of lead in contaminated soils, Environ. Pollut. 98 (2) (1997) 149–155.
- [27] G. Ji, J. Liu, X. Gao, W. Sun, J. Wang, S. Zhao, et al., A luminescent lanthanide MOF for selectively and ultra-high sensitively detecting Pb^{2+} ions in aqueous solution, J. Mater. Chem. A 5 (21) (2017) 10200–10205.
- [28] J.-N. Hao, B. Yan, A water-stable lanthanide-functionalized MOF as a highly selective and sensitive fluorescent probe for Cd_2^{+} , Chem. Commun. 51 (36) (2015) 7737–7740.
- [29] L. Cui, J. Wu, J. Li, H. Ju, Electrochemical sensor for lead cation sensitized with a DNA functionalized porphyrinic metal–organic framework, Anal. Chem. 87 (20) (2015) 10635–10641.
- [30] E.Y. Park, Z. Hasan, I. Ahmed, S.H. Jung, Preparation of a composite of sulfated zirconia/metal organic framework and its application in esterification reaction, Bullet. Korean Chem. Soc. 35 (6) (2014) 1659–1664.
- [31] M.A. Atwood, A Suggestive Inquiry Into the Hermetic Mystery: With a Dissertation on the More Celebrated of the Alchemical Philosophers Being an Attempt Towards the Recovery of the Ancient Experiment of Nature 19, Kessinger Publishing, 1999.
- [32] J.G. Omichinski, Toward methylmercury bioremediation, Science 317 (5835) (2007) 205.
- [33] K.M. Rice, E.M. Walker, M. Wu, C. Gillette, E.R. Blough, Environmental mercury and its toxic effects, J. Prev. Med. Public Health 47 (2) (2014) 74–83.
- [34] L. Sa, W. Stratton, Atmospheric mercury speciation: concentrations and behavior of reactive gaseous mercury in ambient air, Environ. Sci. Technol. 32 (1) (1998) 49–57.
- [35] X. Zhang, T. Xia, K. Jiang, Y. Cui, Y. Yang, G. Qian, Highly sensitive and selective detection of mercury (II) based on a zirconium metal-organic framework in aqueous media, J. Solid State Chem. 253 (2017) 277–281.
- [36] V. Guillermin, S. Gross, C. Serre, T. Devic, M. Bauer, G. Férey, A zirconium methacrylate oxocluster as precursor for the low-temperature synthesis of porous zirconium(IV) dicarboxylates, Chem. Commun. 46 (5) (2010) 767–769.
- [37] L.L. Wu, Z. Wang, S.N. Zhao, X. Meng, X.Z. Song, J. Feng, et al., A metal–organic framework/DNA hybrid system as a novel fluorescent biosensor for mercury(II) ion detection, Chem. Europ. J. 22 (2) (2016) 477–480.
- [38] H. Urata, E. Yamaguchi, T. Funai, Y. Matsumura, W. Si, Incorporation of thymine nucleotides by DNA polymerases through T–HgII–T base pairing, Angew. Chem. 122 (37) (2010) 6666–6669.
- [39] S. Halder, J. Mondal, J. Ortega-Castro, A. Frontera, P. Roy, A Ni-based MOF for selective detection and removal of Hg^{2+} in aqueous medium: a facile strategy, Dalton Transact. 46 (6) (2017) 1943–1950.
- [40] P.D. Wilson, The Nuclear Fuel Cycle from Ore to Wastes, Oxford University Press, 1996.
- [41] Radiation UNSCotEoA, Sources and Effects of Ionizing Radiation, United Nations Publications, 2000.
- [42] S.A. Sapchenko, P.A. Demakov, D.G. Samsonenko, D.N. Dybtsev, M. Schröder, V.P. Fedin, A cryptand metal–organic framework as a platform for the selective uptake and detection of group I metal cations, Chem. Europ. J. 23 (10) (2017) 2286–2289.

-
- [43] Y. Peng, H. Huang, D. Liu, C. Zhong, Radioactive barium ion trap based on metal–organic framework for efficient and irreversible removal of barium from nuclear wastewater, *ACS Appl. Mater. Interfaces* 8 (13) (2016) 8527–8535.
- [44] M. Frisch, G. Trucks, H. Schlegel, G. Scuseria, M. Robb, J. Cheeseman, et al., *Gaussian 03*, Revision c. 02, Gaussian Inc, Wallingford, CT, 2004, p. 4.
- [45] J. Zhao, Y.-N. Wang, W.-W. Dong, Y.-P. Wu, D.-S. Li, Q.-C. Zhang, A robust luminescent Tb (III)-MOF with Lewis basic pyridyl sites for the highly sensitive detection of metal ions and small molecules, *Inorg. Chem.* 55 (7) (2016) 3265–3271.
- [46] W. Liu, X. Dai, Z. Bai, Y. Wang, Z. Yang, L. Zhang, et al., Highly sensitive and selective uranium detection in natural water systems using a luminescent mesoporous metal–organic framework equipped with abundant lewis basic sites: a combined batch, X-ray absorption spectroscopy, and first principles simulation investigation, *Environ. Sci. Technol.* 51 (7) (2017) 3911–3921.

Metal-organic frameworks for recognition and sequestration of toxic anionic pollutants

Aamod V. Desai¹, Shivani Sharma¹ and Sujit K. Ghosh^{1,2,*}

¹Department of Chemistry, Indian Institute of Science Education and Research (IISER), Pune, India, ²Centre for Energy Science, Indian Institute of Science Education and Research (IISER), Pune, India

*Corresponding author: e-mail address: sghosh@iiserpune.ac.in

List of abbreviations






Å	angstrom
AG	acid red
ARS	alizarin red S
DMF	<i>N,N'</i> -dimethyl formamide
EPA	Environment Protection Agency
FT-IR	Fourier transform infrared
g	gram
HSAB	hard soft acid base
IC	indigo carmine
iMOF	ionic metal-organic framework
IUPAC	International Union of Pure and Applied Chemistry
J-T effect	Jahn–Teller effect
K	kelvin
kcal	kilocalorie
K_d	distribution coefficient
kJ	kilojoule
K_{sv}	Stern–Volmer constant
LDH	layered double hydroxide
LMCT	ligand-to-metal charge transfer
M	molar
MB	methylene blue
MeOH	methanol
mg	milligram
min	minutes
mL	milliliter
MO	methyl orange
MOF	metal-organic framework
mol	moles
MR	methyl red

NMR	nuclear magnetic resonance
ppb	parts per billion
ppm	parts per million
PSM	postsynthetic modification
PXRD	powder X-ray diffraction
SC-SC	single-crystal to single-crystal
SCXRD	single-crystal X-ray diffraction
UV–vis	ultraviolet visible
WHO	World Health Organization
ΔG	differential Gibbs energy

4.1 Introduction

Anions are ubiquitous in nature with the presence of anions in inorganic minerals, biological systems, etc., wherein they are known to play crucial roles in various life processes [1,2]. Many inorganic anions that play crucial roles like PO_4^{3-} pose a threat above a permissible concentration limit leading to significant environmental pollution. The advent of global development can be regarded as a major cause for the pollution of natural ecosystems. Among the major sources of contaminants, toxic/polluting anions are recognized as a significant contributor towards pollution. Widespread industrialization including mineral and coal mining, development of various pharmaceuticals/cosmetics/textiles industry has had a direct impact in increasing the concentration of such anions in various rivers and lakes, thus contaminating the potable drinking water [3,4]. Development of nuclear power plants has also contributed towards the rise of toxic anions. Nuclear power plants release radioactive anions with a longer half-life thus making it essential to sequester such anions [5]. The alarming levels of toxic anions, viz., pertechnetate (TcO_4^-), arsenate (AsO_4^{2-}), dichromate ($\text{Cr}_2\text{O}_7^{2-}$), selenate (SeO_4^{2-}), hypochlorite (OCl^-), etc., in potable drinking water pose a serious threat to living species as they disrupt the normal metabolic functions and may lead to gene mutations. One of the most lethal anions, that is, cyanide (CN^-) is a highly potent poison that is well-known for its killing properties. Anionic pollutants especially phosphate anions are well known for river eutrophication owing to the extensive usage in pesticides. The US Environmental Protection Agency (EPA) has categorized these anions as extremely toxic and has specified the exact permissible concentration range for drinking water [6] (Table 4.1). The rise in concentration of hazardous anions has been directly linked with several diseases including cancers, lung and kidney dysfunction, brain diseases including Alzheimer's, etc. [9–12]. Several of these pollutant anions also include bulky anions, that is, dye molecules utilized in food/textile industries for various purposes [13]. These industrial waste effluent streams consist of variable pH, extreme ratios of such toxic anions which are omnipresent that lead to selectivity issues, thus posing a challenge for the designing materials that exhibit selective capture and sequestration of such anions [14,15]. Anions having similar shape, size, and charge are known to exhibit similar physical and chemical properties thus

Table 4.1 Some of the elements in their anionic forms as recognized toxic by the regulatory bodies [7,8] along with the different forms in which they commonly exist

S. No.	Element	Anions	Geometry and Shape	Chemical Diagram	Guideline Concentration
1	Arsenic	AsO_4^{3-} , HAsO_4^{2-}	Tetrahedral		$10 \mu\text{g L}^{-1}$
2	Selenium	SeO_4^{2-} , SeO_3^{2-} , HSeO_3^-	Tetrahedral, Distorted pyramidal		0.04 mg L^{-1}
3	Chromium	CrO_4^{2-} , $\text{Cr}_2\text{O}_7^{2-}$, HCrO_4^-	Tetrahedral		0.05 mg L^{-1}
4	Technetium	TcO_4^-	Tetrahedral		900 pCi L^{-1}
5	Chloride	ClO_4^- , ClO^-	Tetrahedral, Linear		250 mg L^{-1}
6	Fluoride	F^-	Linear	—	1.5 mg L^{-1}
7	Cyanide	CN^-	Linear	—	0.2 mg L^{-1}

rendering it difficult to capture toxic/pollutant anions in the presence of its congeners that have high binding tendencies accompanied with unusually high concentration levels. As compared to the isoelectronic cation, anions have a larger size, thus a lower charge/size ratio, thereby decreasing the electrostatic interaction between the anion and the framework.

Anion capture and sequestration has gathered widespread attention within the scientific community as it poses extreme challenges to the design of materials that can selectively capture toxic anions in the presence of highly competing anions [16]. To target highly selective and specific capture response, materials that exhibit high distribution coefficient (k_d) $\sim 10^4$ towards specific anions are targeted for selective removal of trace levels of toxic anions in water, from a mixture of competing anions that have a similar response towards the material. To accompany the selectivity, facile regeneration plays a crucial role in deciding the cost-effectiveness of the capture process. An easier recyclability tendency of a material plays an extremely vital role in bringing down the cost of the operation leading to large-scale implementation.

Such low-cost materials are desired when industries directly release waste effluent directly to rivers thus contaminating major water bodies and making it extremely difficult to find drinking water that meets the demands of the World Health Organization (WHO) requiring major contaminating anions within ppb concentration levels. Extensive research and development is currently being pursued in order to develop novel materials with the aforementioned features accompanied with low-cost input for the global-scale implementation of toxic anion sorbent materials.

4.1.1 Classification of anionic pollutants

Anionic pollutants can be classified on the basis of charge, size, toxicity, mineral/organic-based anions, hydration energies, HSAB principle, and geometry. Such a classification is shown in Table 4.1.

Anions can be classified on the basis of charge, that is, monoanionic, dianionic, trianionic in nature. A few examples of monoanionic pollutant anions include CN^- , Cl^- , MnO_4^- ; diatomic anions include CrO_4^{2-} , HAsO_4^{2-} , SeO_4^{2-} ; trianionic anions include PO_4^{3-} , AsO_4^{3-} . Another convention based on the different geometry of the anions can be widely classified as linear, trigonal, tetrahedral, pentagonal, octahedral, pentagonal, bipyramidal, etc. [17]. The geometry of anions often seldom plays a vital role in the exchange, wherein the nontoxic surrogate anion with similar geometry leads to a facile exchange phenomenon, thus validating the importance of geometry. Owing to the varied size of the pollutant anions and their charge, these anions pose varied range of hydration energies. The hydration enthalpies of pollutant anions are a crucial factor in designing materials. Anions are also classified on the basis of the hard–soft acid–base principle [18]. An anion with a high charge/size ratio is considered as hard, while anions with a low charge/size ratio are considered as soft in nature. Anions that are hard in nature,

that is, having a high negative charge can attract a positive charge. Thus it becomes facile to capture harder anions selectively in the presence of the competing softer anion counterpart.

The Hofmeister effect is a crucial phenomenon linked with the observed anion exchange behavior [19]. The Hofmeister effect describes in general the order of anion exchange based on hydration energy, solvation energy, etc. In a liquid/liquid separation medium, depending on the solvent medium, it can be summarized that in solvents/sorbents having no potential hydrogen bond donor sites the feasibility of the anion exchange is directly dependent on the size/charge ratio. The hydrophobicity of the anion also determines the feasibility of any anion exchange process. Size/charge ratio is inversely proportional to the facile behavior of the anion exchange process. The equation that is involved in the overall process can be summarized as follows:

$$\Delta G_p^\circ = \Delta G_s^\circ - \Delta G_h^\circ$$

wherein ΔG_p is the Gibbs energy of partition; ΔG_s is Gibbs energy of solvation; and ΔG_h is Gibbs energy of hydration. These are very important parameters to consider the thermodynamic parameters like hydration energies of the targeted pollutant anions in order to design materials for the capture of the anions. Hydration energies of anions with a significant Z^2/r ratio pose a high enthalpy of hydration, thus sorbate materials having multiple potential hydrogen donor sites should overcome the expense of the dehydration of the sphere of hydration.

4.1.2 State-of-art for remediation of such pollutants

As already described, anionic pollutants are a major concern for living species due to their highly toxic nature. The advent of industrialization has had a large-scale impact on ecosystems in an adverse way. A very crucial source for the sustainability of life on Earth comprises of the fresh drinking water bodies, and the vast usage of such anions in various industries and households has led to the widespread contamination of such resources, which has led to several diseases and gene mutation in a few cases. Thus extreme concerns were raised globally for the capture of pollutant anions for environmental remediation to lessen the effect on the natural habitat. A significant extent of research associated with the capture of such anionic pollutants has already been carried out. Various materials including anion exchange resins, Layered double hydroxides (LDHs), porous polymers, Zeolites, etc., have been explored in detail for the capture of toxic anions via ion exchange mechanisms. Anion exchange resins are made of an insoluble polymer network to which exchangeable anions are electrostatically bound which can be exchanged with the targeted pollutant anions in solution. LDHs are constituted of the formula $[M_{1-x}^{2+}M_x^{3+}(\text{OH})_2]^{x+} [A_{x/n}]_m\text{H}_2\text{O}$ wherein A: anion [20]. In this material, anions are present within the interlamellar layers and the exchange process involves the exchange of these anions with

the toxic anions [21]. Due to the problems present in the existing materials researchers are investigating novel materials for tackling the present issues. A novel domain of anion exchange materials that have emerged in the last decade are the porous coordination polymers that have shown interesting anion exchange properties.

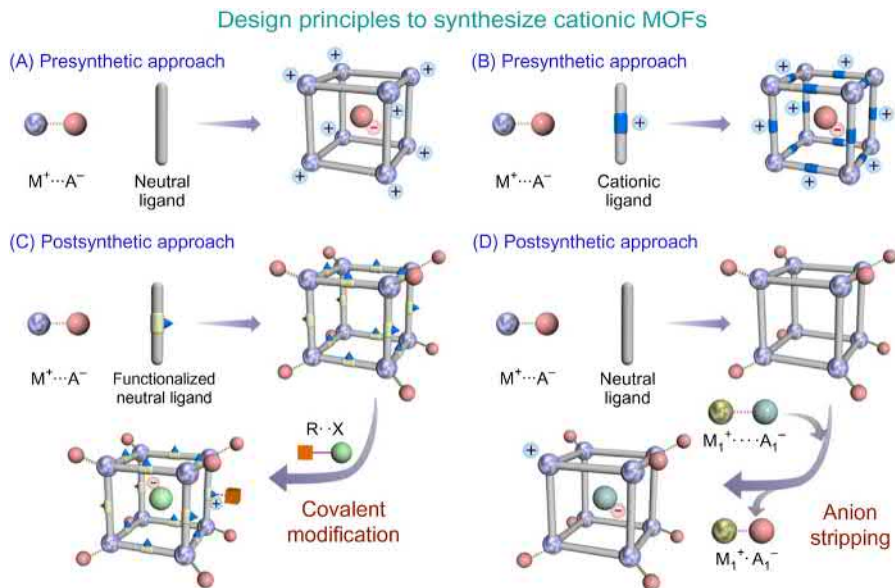
4.1.3 *Metal-organic frameworks and their classification*

Metal-organic frameworks (MOFs) have emerged as an attractive subset of porous materials, which simultaneously incorporate the features of a single crystalline nature along with advantages of conventional polymers [22]. As per IUPAC, a MOF is defined as a “coordination network with an open framework having potential voids” [23]. These coordination polymers are built from bi-/multidentate organic struts which are held periodically by coordination bonds with metal nodes (ions/clusters). On account of ample combinatorial liberty, MOFs offer remarkable synthetic advantages over congener porous solids such as zeolite and porous carbons. Further, the ability to perform isoreticular chemistry to modulate electronic, physical, or chemical features on demand makes MOFs a fascinating subclass of polymeric solids.

Owing to the facile ability to functionalize such materials, MOFs have found suitability for a range of applications [24]. Functionalization in MOFs can be pre-designed or achieved postsynthetically by tuning the building blocks of any MOF, viz., metal ion/cluster, ligand, or guest molecules. The unambiguous structure–property correlation makes development of such functional compounds for real-time applications an exciting area of exploration. Broadly, MOFs can be classified into two classes based on the charge of the coordination bonded polymer into (1) neutral MOFs and (2) ionic MOFs. Although neutral MOFs have been predominantly reported in the literature of MOFs, ionic MOFs provide inherent functionalization owing to the presence of the uncoordinated charged species [25]. The typical synthetic approaches to synthesize functional MOFs for the recognition/capture of anionic pollutants are described below.

4.1.3.1 *Neutral metal-organic frameworks*

Typically, neutral MOFs can be regarded as unsuitable scaffolds as receptors of anionic species, but there have been certain reports where neutral MOFs have been found to respond to anions. In such cases, either the metal-anion bond in the parent compound has been disrupted to permit the entry of the foreign anion (anion stripping) or the ligand backbone has been employed for screening anions based on affinity. In certain cases, postsynthetic modification (PSM) reactions to systems having modifiable sites can be executed to impart ionicity to compounds which are electronically neutral (Scheme 4.1).



Scheme 4.1 Schematic illustration of the different pathways to synthesize cationic MOFs. Reproduced with permission from A. Karmakar, A.V. Desai, S.K. Ghosh, Ionic metal-organic frameworks (iMOFs): Design principles and applications, *Coord. Chem. Rev.* 2016 (307) 313–341. Copyright (2016) Elsevier.

4.1.3.2 Ionic metal-organic frameworks

Ionic metal-organic frameworks (iMOFs) form an important subset of MOFs, which bear the presence of uncoordinated ions in the porous voids. Ionic MOFs are further classified into cationic MOFs and anionic MOFs based on the charge of the framework. Although cationic MOFs offer intrinsic characteristics for reception of anions, the synthetic approaches for target-specific applications are not trivial, as less research has been reported for such compounds. Generally, cationic MOFs are synthesized using neutral N-donor bi-/multidentate ligands, leaving the maintenance of the charge equilibrium to the anionic component of the metal salt used in the synthesis. Another presynthetic approach to synthesize cationic MOFs is based on the use of zwitterionic linkers, which may bear either carboxylate or neutral N-heterocyclic terminal moieties. The backbone of such polymers inherently affords the presence of substitutable anions making such compounds of interest for anion sensing or trapping. In principle, anionic MOFs are unsuitable receptors for interacting with incoming anions owing to the seemingly unfavorable repulsion within the coordination nanospace. Thus it is unusual to propose design strategies to prepare anionic MOFs for interaction with anions. Despite this background, in certain cases anionic MOFs have found suitability for recognition or capture of anions; opening up the possibility of remediation of anionic pollutants by all kinds of MOFs.

4.1.4 Mechanism for anion capture in metal-organic frameworks

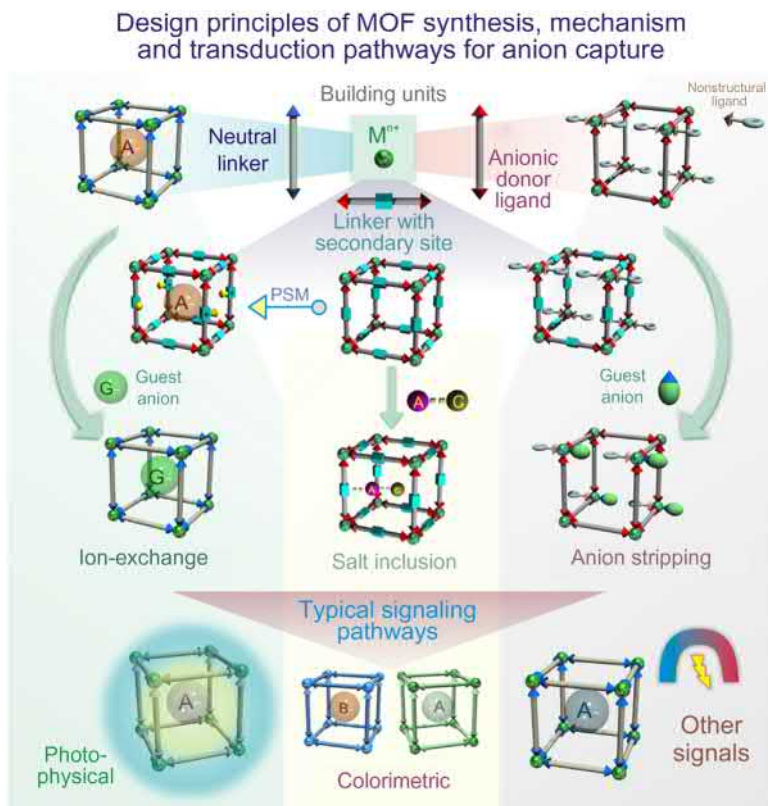
Interaction of guest anions with MOFs can happen via an ion exchange process in which the entrapment can happen through noncovalent interactions or a chemical reaction with the framework backbone, or coordination to the metal nodes. The brief modes of anion interactions have been discussed below.

4.1.4.1 Anion trapping

Ion exchange has been the preferred approach for the capture of anionic pollutants owing to the highly favorable interaction between the host and the sorbent thus leading to the highly specific capture of anionic pollutants. Usually the preferred route is the exploration of the inherent ionic nature of cationic MOFs. These frameworks are built from neutral nitrogen donors leading to the formation of cationic framework with extra-framework anions which are utilized for anion exchange with toxic anions. The other pathway towards the formation of cationic framework is the anion stripping method, wherein the oxidation of the metal center leads to charge imbalance and thus an anion needs to be incorporated rendering the framework cationic in nature [26]. These anions can be exchanged with toxic anions for environmental remediation. Yet another approach involves the replacement of nonstructural labile linkers which can be easily replaced via strongly coordinating toxic anions thus leading to capture [27]. This strategic replacement of nonframework linkers has been recently developed and is widely explored in Zr(IV)-based MOFs. A postsynthetic approach, that is, chemical modification of framework via synthetic approach, such as the reaction with alkyl halide, leads to the formation of a cationic network which can be used for anion exchange [28]. Salt inclusion is another technique wherein anion incorporation within the framework occurs in combination within the cations, thus a concomitant capture of anions happens for remediation [29].

4.1.4.2 Anion recognition

MOFs bear the feature of having multiple readout transduction modes, making them highly sought-after as recognition centers for various kinds of analytes. These typically include colorimetric, photoluminescence, electrical, changes to surface areas, magnetic responses, etc. [30–33]. The change in signals is brought by the difference of the interaction of foreign anions with the framework through direct coordination bonding or via noncovalent interactions, such as anion- π , H-bonding with the framework backbone, against the original compound (Scheme 4.2).



Scheme 4.2 Schematic representation of the broad pathways to prepare MOFs for the capture or recognition of anionic species along with the broad outline of mechanisms involved in capture and signaling processes.

4.2 Recognition and sequestration of anionic pollutants by metal-organic frameworks

MOFs have shown immense potential to sense, entrap, and detoxify several noxious anionic pollutants. The overview of such reports has been presented further using representative examples.

4.2.1 Sensing of anionic pollutants

The ability to tailor the framework building blocks, bestows the ability for MOFs to function as sensors for a variety of targeted species. In the case of anionic species, various noncovalent interactions of the guest with the framework backbone can

alter the transduction pathway of the readout signal. On account of tunable architectures and pore surface character, MOFs have been screened as sensory probes to recognize different anionic pollutants; some of the important findings in this regard have been summarized further.

4.2.1.1 Oxoanion pollutants

Among the different oxoanion pollutants released in water streams, oxoanions of Cr (VI) have commanded significant research attention. Some of the important reports of MOFs being employed for sensing of these pollutants are provided further.

In an early example by Wang and coworkers, a Ag(I)-based cationic MOF $\{[\text{Ag}_2(\text{btr})_2] \cdot 2\text{ClO}_4 \cdot 3\text{H}_2\text{O}\}_n$ [btr = 4,4'-bis(1,2,4-triazole)], was reported which functioned as a sorbent to capture dichromate anions (Fig. 4.1A) [34]. In addition, owing to the presence of Ag(I) metal centers, the luminescence response during the ion exchange process was checked. The emission peak in the parent MOF corresponding to the LMCT transition (ligand-to-metal-charge transfer) was significantly quenched upon ion-inclusion of $\text{Cr}_2\text{O}_7^{2-}$ in the framework (Fig. 4.1B). The change in intensity was ascribed to the decrement in the LMCT process owing to the stronger interactions of $\text{Cr}_2\text{O}_7^{2-}$ with the ligand.

Wang and coworkers further explored the scope of MOFs to function as luminescent probes for the detection of dichromate anions [35]. The authors explored the ability of a Zn(II)-based MOF, viz., $\{[\text{Zn}_{2.5}(\text{cpbda})(\text{OH})_2] \cdot \text{solvent}_2\}_n$, where H_3cpbda : 4,4'-((5-carboxy-1,3-phenylene)bis(oxy)dibenzoic acid, to detect different anions and cations. The parent compound exhibited a LMCT-based peak which underwent quenching upon incremental addition of Cr(VI) anions. The authors observed a notable change in luminescence intensity even at a low concentration of

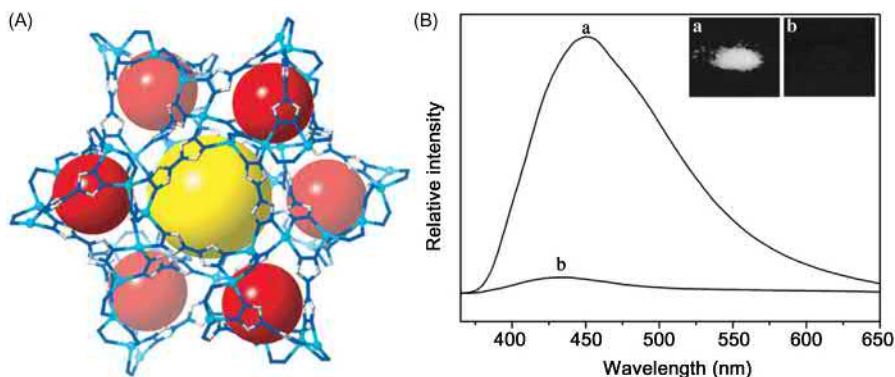


Figure 4.1 (A) Packing diagram of the Ag(I)-MOF $\{[\text{Ag}_2(\text{btr})_2] \cdot 2\text{ClO}_4 \cdot 3\text{H}_2\text{O}\}_n$. (B) Solid-state emission responses of the (a) parent compound, (b) $\text{Cr}_2\text{O}_7^{2-}$ exchange.

Source: Reproduced with permission from X. Li, H. Xu, F. Kong, R. Wang, A cationic metal-organic framework consisting of nanoscale cages: capture, separation, and luminescent probing of $\text{Cr}_2\text{O}_7^{2-}$ – through a single-crystal to single-crystal process, *Angew. Chem. Int. Ed.* 52 (2013) 13769–13773. Copyright (2013) John Wiley & Sons.

164 ppm for $\text{Cr}_2\text{O}_7^{2-}$ (6.4%) and CrO_4^{2-} (8.9%). The quenching process was ascribed to the photoinduced electron transfer happening on the surface of the framework and guest molecules.

Zhao and coworkers reported an investigation of sensing activity by two Zn(II)-based MOFs, viz., $[\text{Zn}(\text{btz})_n]$ and $[\text{Zn}_2(\text{ttz})\text{H}_2\text{O}]_n$ where H_2btz : 1,5-*bis*(5-tetrazolo)-3-oxapentane, H_3ttz : 1,2,3-*tris*-[2-(5-tetrazolo-ethoxy)]propane [36]. The two linkers were prepared in situ during the synthesis of MOFs from respective cyano-terminal linkers. The authors observed distinct emission profiles for the two compounds which was ascribed to the $\pi^*-\pi$ and π^*-n transitions in the ligands. Significant quenching was observed upon addition of Cr(VI) oxoanions, which was retained even in the concurrent presence of competing anions. The detection limits for $\text{Cr}_2\text{O}_7^{2-}$ anions for the two MOFs were calculated to be 2×10^{-6} and $2 \times 10^{-5} \text{ mol L}^{-1}$; while the K_{sv} values were found to be 4.23×10^3 and $2.19 \times 10^3 \text{ L mol}^{-1}$, respectively. Similar trends were observed for CrO_4^{2-} also. The sensor could be recovered and used to sense the Cr(VI) oxoanions over multiple cycles.

The groups of Gu and Liu reported an amino functionalized MOF, viz., $[\text{Zn}_2(\text{TPOM})(\text{NH}_2\text{-BDC})_2] \cdot 4\text{H}_2\text{O}$, where TPOM stands for tetrakis(4-pyridyloxy-methylene)methane and $\text{NH}_2\text{-BDC}$ for 2-aminoterephthalic acid, as a fluorescent probe for the detection of Cr(VI) anions [37]. The MOF exhibited a strong emission peak at 420 nm which underwent quenching upon addition of Cr(VI) anions ($\text{Cr}_2\text{O}_7^{2-}$ and CrO_4^{2-}), and the fluorescence response was selective even in concurrent addition of competing anions. The K_{sv} values for detection were calculated to be 7.59×10^3 and $4.45 \times 10^3 \text{ M}^{-1}$ for $\text{Cr}_2\text{O}_7^{2-}$ and CrO_4^{2-} , respectively. The detection limits were estimated to be 3.9 and 4.8 μM , respectively. The authors reported a control experiment of using a MOF with no secondary functional site and found that the limits of detection had a drastic variation. Thus the presence of the pendant amine groups for detection of Cr(VI) was ascribed as the primary reason for the observed fluorescence change.

As a step towards practical implementation of MOF-based adsorbents for the capture of heavy metal oxoanions, Manos and coworkers synthesized a MOR (metal-organic resin) which could be used to prepare ion exchange materials (detailed discussion in subsequent sections). Apart from adsorption, the compound was tested as a fluorescent sensory probe towards Cr(VI) oxoanions (Fig. 4.2) [38]. The MOR had a low detection limit of 4 ppb and the sensing ability was retained over a wide pH range. The quenching behavior was attributed to the energy transfer from the $n-\pi^*$ levels of the ligand to the $\text{Cr}_2\text{O}_7^{2-}$ LMCT transition. The sensing behavior was found to be retained even in the presence of excess SO_4^{2-} anions.

Wang and coworkers reported the synthesis of a Eu(III)-based MOF and studied its ability to sense Cr(VI) in aqueous medium [39]. The Eu(III)-nodal MOF, viz., $[\text{Eu}_7(\text{mtb})_5(\text{H}_2\text{O})_{16}] \cdot \text{NO}_3 \cdot 8\text{DMA} \cdot 18\text{H}_2\text{O}$, where H_4mtb stands for 4-*[tris*(4-carboxy-phenyl)methyl]benzoic acid, was found to be thermally stable and resistant over a wide pH range of 2–12. Owing to its cationic nature and stability, the authors reported the sensing performance of the MOF towards chromate ions, and it was found to be highly sensitive (limit of detection 0.56 ppb) and selective in the

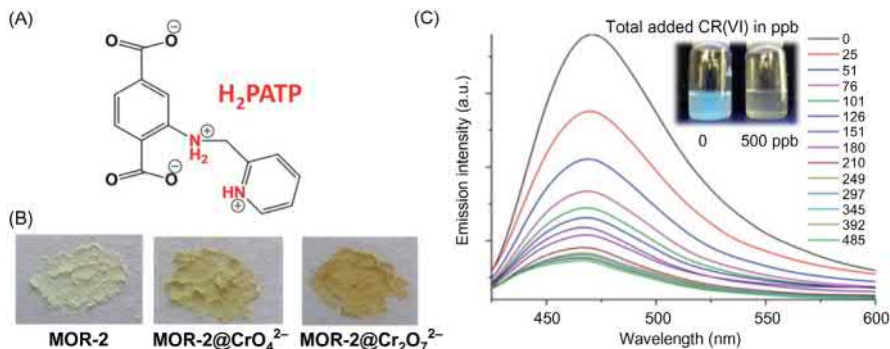


Figure 4.2 (A) Representation of the ligand used in the synthesis of the MOF. (B) Optical pictographs of MOR-2 (Metal-organic resin) and respective anion exchanged phases. (C) concentration-dependent titration of MOR-2 against aqueous solution of $K_2Cr_2O_7$. *Source:* Reproduced with permission from S. Rapti, D. Sarma, S.A. Diamantis, E. Skliri, G. S. Armatas, A.C. Tsipis, et al., All in one porous material: exceptional sorption and selective sensing of hexavalent chromium by using a Zr^{4+} MOF. *J. Mater. Chem. A* 5 (2017) 14707–14719. Copyright (2017) Royal Society of Chemistry.

presence of common anions. The sensing ability was also evaluated in Dushu lake water and seawater, wherein the detection limits were found to be within the EPA permissible limit. The change in luminescence was attributed to a combination of multiple factors including energy transfer and light absorption.

Further, Cheng and coworkers reported a series of $Cd(II)$ -based coordination polymers and explored their ability to sense chromate and dichromate anions [40]. The CPs, viz., $\{[Cd_2(bptc)(2,2'-bipy)_2(H_2O)_2]\}_n$, $\{[Cd_2(bptc)(phen)_2].4H_2O\}$ and $\{[Cd_2(bptc)(4,4'-bipy)(H_2O)_2].4H_2O\}_n$, featured structural diversity including 1D ladder chain, 2D layer, and 3D porous framework. The authors studied the compounds for their ability to sense both chromate and dichromate anions in an aqueous medium and they were found to be selective in nature. The presence of both light absorption and energy transfer from donor (coordination polymers) to acceptors was ascribed as the pathways for fluorescence quenching.

Cao and coworkers assessed a series of benchmark stable MOFs for the function of dichromate capture and recognition [41]. The authors narrowed their interest to HKUST-1, ZIF-8, MIL-100(Fe), UiO-66, UiO-67, and NU-1000. Among these MOFs, NU-1000 exhibited superior capture ability for dichromate with an uptake capacity of 76.8 mg g^{-1} , which stands among the highest for a neutral MOF (Fig. 4.3). The selective capture was observed over a pH range of 1–7. Apart from capture, NU-1000 was found to be an efficient sensor with a detection limit of $1.8 \mu\text{M}$, with a fluorescence quenching response. The authors ascribed this to the presence of active sites such as $Zr-OH$ groups.

Li and coworkers extended the work on novel MOF-based luminescent sensors by reporting a new $Zr(IV)$ -based luminescent MOF, viz., $Zr_6O_4(OH)_7(H_2O)_3(BTBA)_3$ (BUT-39) where H_3BTBA stands for 4,4',4''-(1*H*-benzo[d]imidazole-2,4,7-triyl)

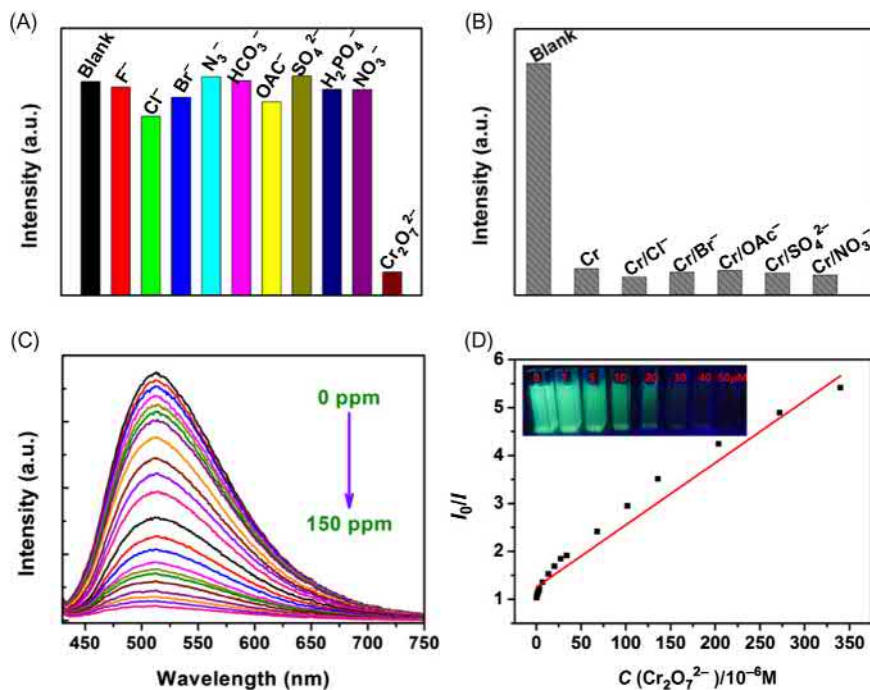


Figure 4.3 (A) Change in fluorescence emission intensity of NU-1000 upon addition of different anions. (B) Change in luminescence intensities in binary mixtures of $\text{Cr}_2\text{O}_7^{2-}$ and competing anions; (C) concentration-dependent fluorescence titration of NU-1000 against $\text{Cr}_2\text{O}_7^{2-}$; and (D) corresponding Stern–Volmer plot.

Source: Reproduced with permission from Z.-J. Lin, H.-Q. Zheng, H.-Y. Zheng, L.-P. Lin, Q. Xin, R. Cao, Efficient capture and effective sensing of $\text{Cr}_2\text{O}_7^{2-}$ from water using a zirconium metal-organic framework. *Inorg. Chem.* 56 (2017) 14178–14188. Copyright (2017) American Chemical Society.

tribenzoic acid [42]. The MOF was found to be stable in different conditions and exhibited a strong fluorescence signal. The compound was able to selectively and rapidly detect dichromate anions at low concentrations (Fig. 4.4). The Stern–Volmer constant for the quenching process was estimated to be $1.57 \times 10^4 \text{ M}^{-1}$, while the limit of detection was calculated to be $1.5 \mu\text{M}$. The MOF could also function as a reversible sorbent which could be regenerated using 2 M KNO_3 solution.

4.2.1.2 Cyanide

Apart from ionic MOFs, neutral compounds also have been found to be suitable receptors for the detection of anionic species. Ghosh and coworkers presented the utility of a neutral, stable MOF, viz., ZIF-90, modified with a secondary site for the recognition of toxic cyanide anions [43]. The authors utilized the post-synthesis modification (PSM) pathway to incorporate the dicyanovinyl group

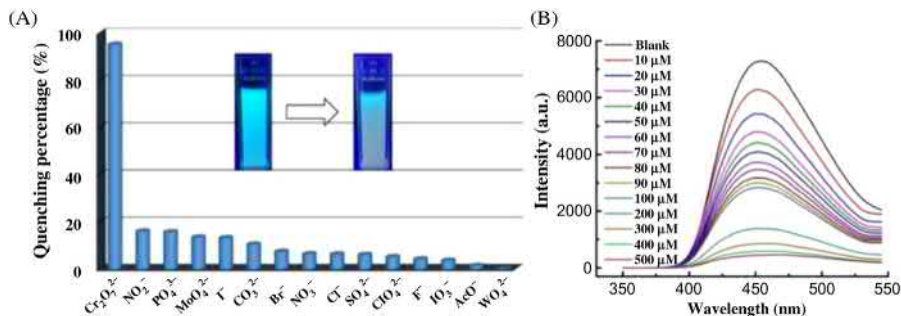


Figure 4.4 (A) Bar diagram showing differential response of fluorescence quenching upon addition of different anions to BUT-39; (B) concentration-dependent fluorescence quenching of BUT-39 towards $\text{Cr}_2\text{O}_7^{2-}$.

Source: Reproduced with permission from T. He, Y.-Z. Zhang, X.-J. Kong, J. Yu, X.-L. Lv, Y. Wu, et al., Zr(IV)-based metal-organic framework with T-shaped ligand: unique structure, high stability, selective detection, and rapid adsorption of $\text{Cr}_2\text{O}_7^{2-}$ in water, *ACS Appl. Mater. Interfaces* 10 (2018) 16650–16659. Copyright (2018) American Chemical Society.

(DCV) by Knoevenagel reaction. The DCV groups function as the specific active site as the cyanide anions form adducts with the DCV group (Fig. 4.5A). The addition of CN^- to the MOF dispersed in $\text{H}_2\text{O}/\text{DMSO}$ (1:1) resulted in a quenching response (Fig. 4.5B). The luminescence response was selective with no changes towards other competing anions such as F^- , Cl^- , Br^- , SCN^- , NO_3^- , NO_2^- , and N_3^- . Additionally, the response towards CN^- was retained in binary mixtures of anions as well. The limit of detection was estimated to be 0.54 ppm and the quenching constant value was reported to be $3.3 \times 10^5 \text{ M}^{-1}$.

Apart from detection, detoxification of toxic anions is equally important from an environmental perspective. In this regard, Ghosh and coworkers reported the investigation of a postsynthetically modified MOF which could function as a sensory probe and a substrate to detoxify toxic cyanide anions [44]. The well-established bio-MOF-1 was chosen as the basic compound; it bears the presence of uncoordinated cations. The free cations were substituted with 3,6-diaminoacridinium cations (DAAC) by an ion exchange protocol which yielded 70% loading (Fig. 4.5C). The cyanide anions could react with the DAAC dye molecules and led to the formation of a covalently linked product which could leach out from the system. The initially clear supernatant solution turned fluorescent upon release of the product dye and a turn-on response with an emission in the green region was achieved. The feasibility of reaction-based sensing was validated by no response with other common anions, and selective response upon addition of cyanide anions in binary mixtures (Fig. 4.5D). The detection limit was reported to be 5.2 ppb, which is well below the permissible limits of cyanide ions in sources of water. Apart from batch studies, the feasibility of detection was checked in cancer cells and the cell toxicity was also studied. The cell toxicity studies revealed that the by-product of the reaction did not affect the cells significantly, further endorsing the design strategy and choice of the compound.

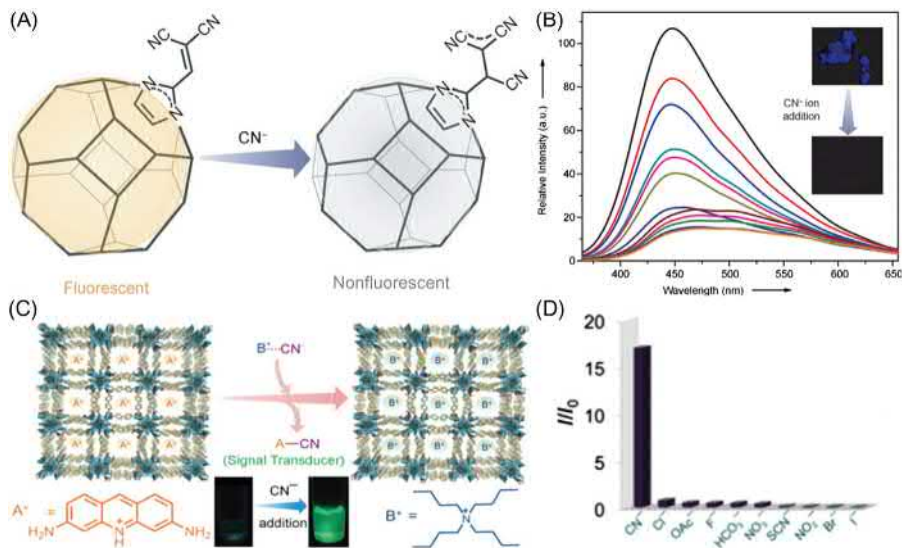


Figure 4.5 (A) Proposed mechanism of reaction-based response of postsynthetically modified ZIF-90 towards cyanide anions; (B) luminescence spectra showing concentration-dependent response of M-ZIF-90 for cyanide; (C) schematic illustration showing chemodosimetric approach for recognition of cyanide anions; (D) bar diagram representing the changes in the fluorescence intensities for different anions towards bio-MOF-1 \supset DAAC. *Source:* For (A) and (B), reproduced with permission from A. Karmakar, N. Kumar, P. Samanta, A.V. Desai, S.K. Ghosh, A post-synthetically modified MOF for selective and sensitive aqueous-phase detection of highly toxic cyanide ions, *Chem. Eur. J.* 22 (2016) 864–868. Copyright (2015) John Wiley & Sons. For (C) and (D), reproduced with permission from A. Karmakar, B. Joarder, A. Mallick, P. Samanta, A.V. Desai, S. Basu, et al., Aqueous phase sensing of cyanide ions using a hydrolytically stable metal-organic framework, *Chem. Commun.* 53 (2017) 1253–1256. Copyright (2017) Royal Society of Chemistry.

4.2.1.3 Other anions

Apart from a luminescence signal, detection by naked-eye response holds much importance. In this regard, Dong and coworkers reported a two-dimensional Cu(II)-MOF, viz., $\{[\text{CuL}_2(\text{H}_2\text{O})_{0.5}](\text{NO}_3)_2 \cdot 3.25(\text{CH}_2\text{Cl}_2) \cdot (\text{CH}_3\text{OH}) \cdot 0.5\text{H}_2\text{O}\}_n$, (L—4,4'-(9,9-dibutyl-9H-fluorene-2,7-diyl)dipyridine), which had the presence of both weakly coordinated and noncoordinated nitrate anions in the framework (Fig. 4.6A) [45]. The authors carried out ion exchange with several monodentate anions such as F⁻, Cl⁻, Br⁻, I⁻, SCN⁻, and N₃⁻, where a drastic color change from blue (in the case of parent MOF) to different shades of brown and green in a very short time was observed (Fig. 4.6B). The naked-eye change was ascribed to the presence of Jahn–Teller distortion commonly observed in Cu(II)-based coordination complexes. Apart from single ion capture, responses to binary mixtures were carried out which showed separation could be achieved.

Bu and coworkers further explored the ability of Cu(I)-based MOFs for the function of naked-eye recognition of different anions [46]. The fourfold interpenetrated

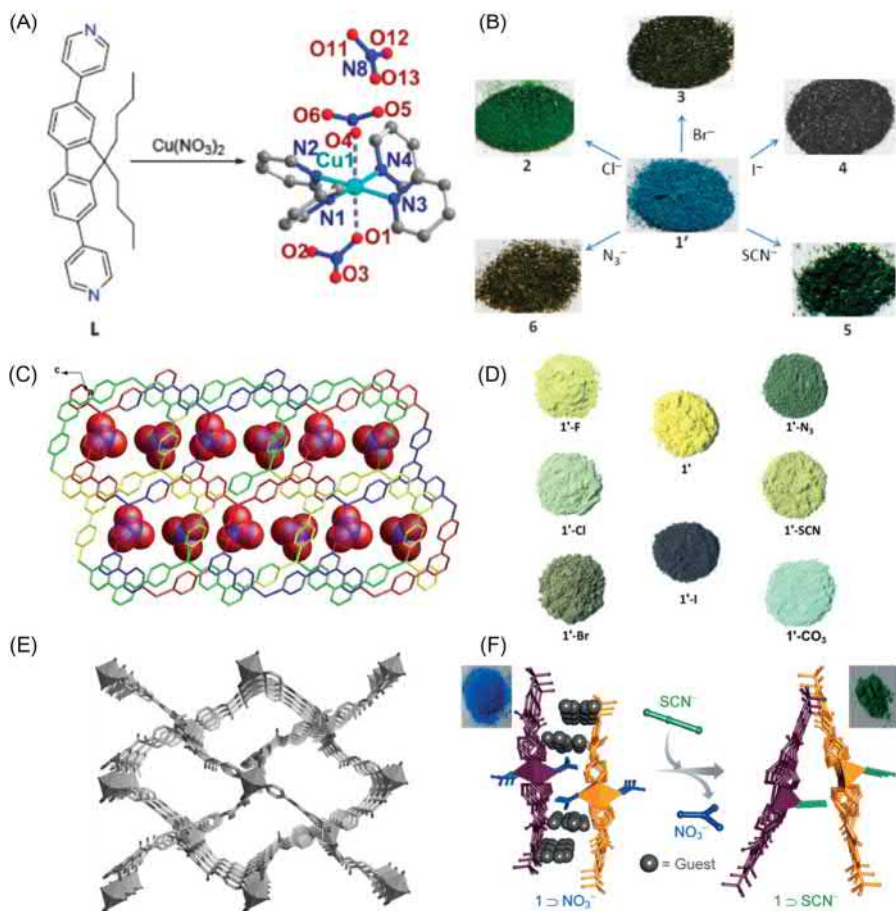


Figure 4.6 (A) Synthesis protocol employed for the preparation of Cu(II)-based cationic MOF; (B) naked-eye responses upon inclusion of different anions; (C) packing diagram showing presence of free nitrate anions in the cationic MOF; (D) colorimetric responses of the parent compound upon encapsulation of anions; (E) packing diagram of compound showing porous channel; (F) SC-SC response transformation upon inclusion of anion and corresponding optical pictographs of the respective phases.

Source: For (A) and (B), reproduced with permission from J.-P. Ma, Y. Yu, Y.-B. Dong, Fluorene-based Cu(II)-MOF: a visual colorimetric anion sensor and separator based on an anion-exchange approach. *Chem. Commun.* 48 (2012) 2946–2948. Copyright (2012) Royal Society of Chemistry. For (C) and (D), reproduced with permission from Y.-Q. Chen, G.-R. Li, Z. Chang, Y.-K. Qu, Y.-H. Zhang, X.-H. Bu, A Cu(I) metal-organic framework with 4-fold helical channels for sensing anions, *Chem. Sci.* 4 (2013) 3678–3682. Copyright (2013) Royal Society of Chemistry. For (E) and (F), reproduced with permission from A. Karmakar, A.V. Desai, B. Manna, B. Joarder, S.K. Ghosh, An amide-functionalized dynamic metal-organic framework exhibiting visual colorimetric anion exchange and selective uptake of benzene over cyclohexane, *Chem. Eur. J.* 21 (2015) 7071–7076. Copyright (2015) John Wiley & Sons.

MOF, viz., $\{[\text{Cu}(\text{pytpy})]. \text{NO}_3. \text{CH}_3\text{OH}\}_n$ where pytpy stands for 2,4,6-*tris*(4-pyridyl)pyridine, underwent structural transformation in a SC-SC process to have water molecules replace the methanol solvent molecules to obtain a new phase $\{[\text{Cu}(\text{pytpy})]. \text{NO}_3. \text{H}_2\text{O}\}_n$ (Fig. 4.6C). The authors sought to sense a range of anions (F^- , Cl^- , Br^- , I^- , N_3^- , SCN^- , CO_3^{2-}) by ion exchange. Upon anion exchange a drastic color change was observed which was linked to the choice of the incoming anion (Fig. 4.6D). In addition to naked-eye response, the ion exchange process could be monitored using fluorescence response owing to the presence of conjugated linker and Cu(I) metal node. Inclusion of different anions resulted in either a shift of peak maximum of the MOF emission or a change in intensity.

On similar lines, Ghosh and coworkers reported an investigation of a Cu(II)-centered MOF which exhibited a colorimetric response towards SCN^- anions (Fig. 4.6E and F) [47]. A one-dimensional coordination polymer, viz., $\{[\text{CuL}_2(\text{NO}_3)_2]. (\text{o-xylene}). \text{DMF}\}_n$ where L: 5-(*tert*-butyl)-*N*1, *N*3-di(pyridin-4-yl)isophthalamide, was treated with different anions such as SCN^- , N_3^- , Cl^- , Br^- , I^- , and F^- . In the case of SCN^- , a naked-eye colorimetric change was observed from blue (parent MOF) to green which could be studied using SC-SC transitions. The anion exchange was associated with drastic structural transformation, wherein the color change could directly be associated with the J-T effect prevalent for Cu(II) complexes.

The study on anion recognition by a luminescent MOF was reported by Ghosh and coworkers [48]. A dynamic MOF, viz., $\{[\text{Zn}(\text{L})(\text{MeOH})_2](\text{NO}_3)_2 \cdot x\text{G}\}_n$ where L stands for (1*E*,1'*E*)-*N,N'*-(ethane-1,2-diyl-*bis*(4,1-phenylene))*bis*(1-(pyridin-2-yl)methanimine), was reported which underwent structural transformation upon the loss of guest solvent molecules. The cationic MOF could encapsulate a range of anions such as ClO_4^- , SCN^- , N_3^- , $\text{N}(\text{CN})_2^-$. The parent compound had an emissive signature which showed drastic changes in the luminescence for the anion exchanged phases (Fig. 4.7A). The differential fluorescence responses were attributed to the varied interactions of the anions with the framework. On similar lines, the group reported similar anion-modulated luminescence behavior in a flexible luminescent MOF, viz., $\{[\text{Zn}(\text{L})_2](\text{NO}_3)_2 \cdot x\text{G}\}_n$ where L stands for [(*E*)-*N'*-[1-(pyridin-4-yl)ethyldene]hydrazine carbohydrazide [49]. The parent cationic MOF was exchanged with ClO_4^- and BF_4^- anions and the exchange was accompanied with distinct changes in the luminescence profiles (Fig. 4.7B). Wang and coworkers further reported exploration in this domain by synthesizing a Ag(I)-based luminescent porous coordination polymer [50]. A 3D compound, viz., $\{[\text{Ag}_2(\mu_3\text{-L})_2](\text{ClO}_4)_2\}_n$, where L stands for *N*-(4-(4*H*-1,2,4-triazol-4-yl) phenyl)formamide, was prepared which exhibited anion-dependent changes in the emission signature of the parent compound.

4.2.2 Capture of toxic anionic species

4.2.2.1 Capture of inorganic pollutants

4.2.2.1.1 Cr(VI)-based oxoanion pollutants

The interconvertible form of chromate ion is dichromate anion which is also found in several effluents. Unlike chromate, the size and geometry of dichromate anion is

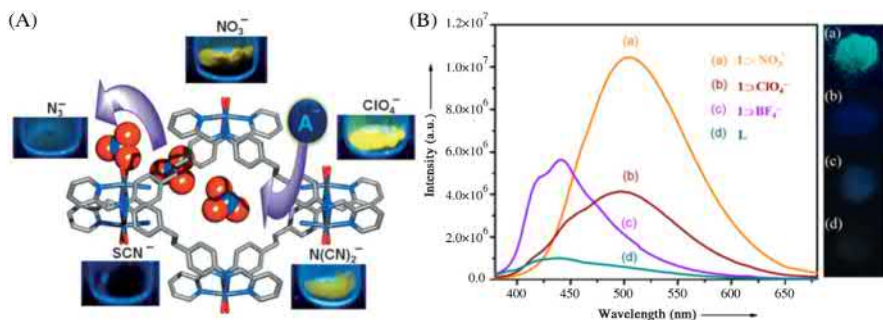


Figure 4.7 (A) Representation of the anion exchange process in the Zn(II)-based cationic MOF and the corresponding fluorescence responses under UV light; (B) solid-state fluorescence spectra of the ligand, parent MOF, and the anion exchanged phases. The corresponding images are shown alongside.

Source: For (A), reproduced with permission from B. Manna, A.K. Chaudhari, B. Joarder, A. Karmakar, S.K. Ghosh, Dynamic structural behavior and anion-responsive tunable luminescence of a flexible cationic metal-organic framework, *Angew. Chem. Int. Ed.* 52 (2013) 998–1002. Copyright (2012) John Wiley & Sons. For (B), reproduced with permission from A. Karmakar, B. Manna, A.V. Desai, B. Joarder, S.K. Ghosh, Dynamic metalorganic framework with anion-triggered luminescence modulation behavior, *Inorg. Chem.* 53 (2014) 12225–12227. Copyright (2014) American Chemical Society.

bigger and has two atoms of Cr(VI) per molecule of the anion. Much research has been devoted to the capture of Cr(VI) species using MOFs. Some of the key highlights have been described below.

In an early report of employing MOFs to capture chromate anions, Oliver and coworkers chose a cationic MOF previously reported by the same group, viz., $[\text{Ag}_2(4,4'\text{-bipyridine})_2(\text{O}_3\text{SCH}_2\text{CH}_2\text{SO}_3) \cdot 4\text{H}_2\text{O}]$, referred to as SLUG-21 [51]. The cationic compound bearing weakly interacting 1,2-ethanedisulfonate anions was found to be an efficient host for many oxoanions, including chromate anions (Fig. 4.8). The capacity of the compound was reported to be 60 mg g^{-1} for chromate.

The authors extended their investigation to related systems having binuclear complexes [52]. Two isostructural mononuclear compounds, viz., Zn-SLUG-35 $\{[\text{Zn}(\text{H}_2\text{O})_4(4,4'\text{-bipyridine})_2](\text{O}_3\text{S-C}_2\text{H}_4\text{-SO}_3) \cdot 4\text{H}_2\text{O}\}$ and Co-SLUG-35 $\{[\text{Co}(\text{H}_2\text{O})_4(4,4'\text{-bipyridine})_2](\text{O}_3\text{S-C}_2\text{H}_4\text{-SO}_3) \cdot 4\text{H}_2\text{O}\}$, were synthesized hydrothermally and further binuclear compounds having similar cationic structures were formed. The compound having Zn:Co ratio as 1:1 was found to have the highest capacity to trap chromate anions (68.5 mg g^{-1}) by exchanging EDS anions which are present in the interlamellar region. The superior performance of the solid solution was highlighted in the selective uptake even in the presence of excess anions such as nitrate and sulfate.

This idea of employing cationic materials for trapping of inorganic oxanion pollutants was extended by Zhao and coworkers [53]. The authors synthesized a mixed-metal MOF, viz., $\{[\text{Dy}_2\text{Zn}(\text{BPDC})_3(\text{H}_2\text{O})_4](\text{ClO}_4)_2 \cdot 10\text{H}_2\text{O}\}_n$ [BPDC—4,4'-dicarboxylate-2,2'-dipyridine anion], having perchlorate anions uncoordinated in

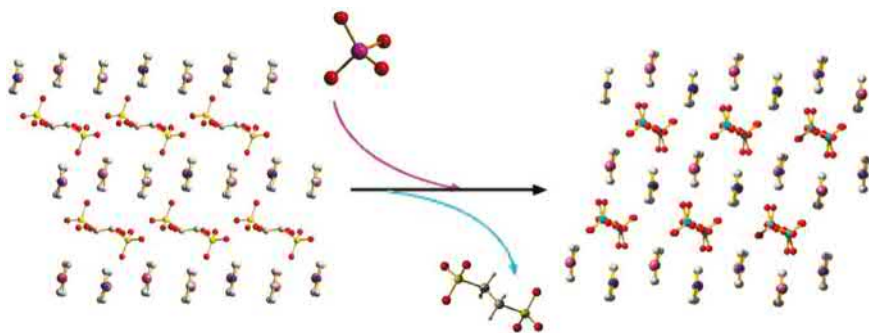


Figure 4.8 SC-SC transformation in SLUG-21 showing inclusion of perchlorate anions.

Source: Reproduced with permission from H. Fei, M.R. Bresler, S.R.J. Oliver, A New Paradigm for anion trapping in high capacity and selectivity: crystal-to-crystal transformation of cationic materials, *J. Am. Chem. Soc.* 133 (2011) 11110–11113. Copyright (2011) American Chemical Society.

the structure. The cationic MOF was able to capture CrO_4^{2-} anions rapidly with an uptake capacity of $0.85 \text{ mol mol}^{-1}$. As a step relevant for practical implementation, selectivity and recyclability of the sorbent were studied, wherein the MOF was found to have selective affinity over common anions and the release was achieved by adding an excess of CO_3^{2-} or SO_4^{2-} anions. As the MOF is composed of a luminescent core, it could also function as a luminescent probe for the sensing of chromate anions.

In an elegant early work of showcasing the utility of MOFs for trapping dichromate, Wang and coworkers synthesized a Ag(I)-based cationic MOF consisting of octahedral and tetrahedral cages, and bearing uncoordinated ClO_4^- anions, viz., $\{[\text{Ag}_2(\text{btr})_2] \cdot 2\text{ClO}_4 \cdot 3\text{H}_2\text{O}\}_n$ [btr = 4,4'-bis(1,2,4-triazole)] [34]. The compound was found to be stable in water and routine organic solvents. The MOF having 1D-porous channels bearing free anions could function as a heterogeneous ion exchanger and the process was monitored unambiguously using SC-SC studies. The uptake capacity of the MOF was reported to be $0.73\text{--}0.93 \text{ mol mol}^{-1}$. The MOF was able to operate even under low concentration and selectively over common ions such as NO_3^- , CF_3SO_3^- , and BF_4^- . Owing to the presence of ligand-to-metal-charge-transfer (LMCT), the parent MOF was highly emissive and the entrapment of dichromate could be sensed by a drastic change in the fluorescence intensity.

Soon thereafter, Ding and coworkers investigated Ag(I) and triazole-linker-based compounds for the capture of dichromate and permanganate [54]. Two compounds, viz., $\{[\text{Ag}_4(\text{L}_1)_6](\text{BF}_4)_4\}_n$ and $\{[\text{Ag}_2(\text{H}_2\text{O})(\text{L}_2)_2](\text{BF}_4)_2\}_n$ [L_1 —4-(4-methyl-2-pyridine)-1,2,4-triazole; L_2 —4-(5-methyl-3-pyridine)-1,2,4-triazole], having a cationic framework showed aqueous phase capture of the two anions. The uptake capacities were calculated to be $0.55 \text{ mol mol}^{-1}$ (KMnO_4) and $0.53 \text{ mol mol}^{-1}$ ($\text{K}_2\text{Cr}_2\text{O}_7$) for compound $\{[\text{Ag}_4(\text{L}_1)_6](\text{BF}_4)_4\}_n$; while the corresponding values for the other compound were 0.51 and $0.56 \text{ mol mol}^{-1}$, respectively. The capture of dichromate was found to be selective even in the concurrent presence of competing anions.

The utility of Ag(I) and triazole-based systems as stable, cationic sorbent materials was further emphasized in a report by the groups of Ding and Li [55]. The synthesis of a metal-organic nanotube, viz., $\{[\text{Ag}(\mu_3\text{-abt})] \cdot (\text{NO}_3) \cdot (0.125\text{H}_2\text{O})\}_n$ [abt = 1-(4-aminobenzyl)-1,2,4-triazole] was reported. The uncoordinated nitrate anions were found to be suitable for exchange with $\text{Cr}_2\text{O}_7^{2-}$ anions with absorption capacity of 211.8 mg g^{-1} . The compound could be recovered (although not completely) after the addition of excess (200-fold) nitrate ions and used for adsorption over multiple cycles.

Du and coworkers also explored the possibility of Cr(VI) trapping in a Ag(I)-based MOF obtained by tandem SC-SC processes [56]. The cationic compound after two steps, viz., $[\text{Ag}(\text{L})](\text{CF}_3\text{CO}_2)(\text{H}_2\text{O})$, could be used as an ion exchange sorbent for $\text{Cr}_2\text{O}_7^{2-}$ in a SC-SC manner resulting in the formation of the compound $[\text{Ag}(\text{L})](\text{Cr}_2\text{O}_7)_{0.5}(\text{solvent})$ (Fig. 4.9). The uptake performance was calculated to be

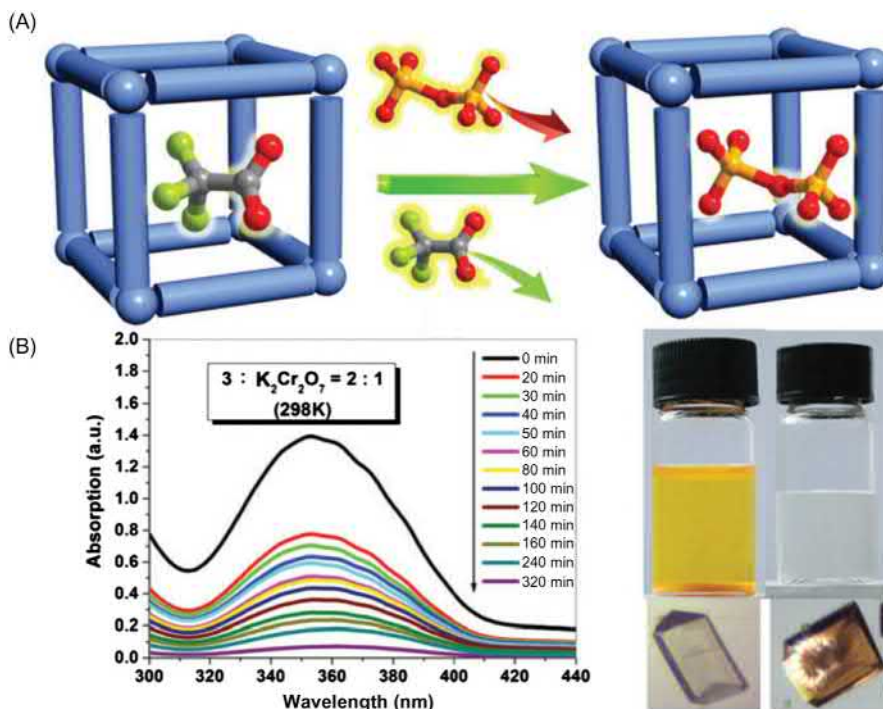


Figure 4.9 (A) Schematic illustration showing encapsulation of dichromate anions. (B) UV–vis absorption spectra of the supernatant for titration of Ag(I)-based MOF against aqueous dichromate solution and the corresponding photographs of the bulk solution and the single crystals.

Source: Reproduced with permission from C.-P. Li, H. Zhou, S. Wang, J. Chen, Z.-L. Wang, M. Du, Highly efficient $\text{Cr}_2\text{O}_7^{2-}$ removal of a 3D metal-organic framework fabricated by tandem single-crystal to single-crystal transformations from a 1D coordination array, *Chem. Commun.* 53 (2017) 9206–9209. Copyright (2017) Royal Society of Chemistry.

207 mg g^{-1} , with the distribution coefficient of $2.8 \times 10^3 \text{ mL g}^{-1}$. The water-stability of the MOF was harnessed in studying the trapping ability in a chromatographic column. The binary competing experiments revealed the compound to be a selective sorbent towards dichromate. The compound could be regenerated by dipping in 120-fold excess of KNO_3 , with about 86.8% release of trapped dichromate.

Similarly, Zhang and coworkers reported trapping of dichromate using two Zn (II)-based cationic MOFs $\{[\text{Zn}_2(\text{tipa})_2(\text{OH})] \cdot 3\text{NO}_3 \cdot 12\text{H}_2\text{O}\}_n$ (FIR-53) and $\{[\text{Zn}(\text{tipa})] \cdot 2\text{NO}_3 \cdot \text{DMF} \cdot 4\text{H}_2\text{O}\}_n$ (FIR-54), from a tripodal neutral N-donor linker [tipa—*tris*(4-(1*H*-imidazol-1-yl)phenyl)amine] [57]. Both the compounds were highly porous with FIR-53 having cross-section porous channels of $18 \times 13 \text{ \AA}^2$. The compound was found to exhibit dichromate uptake capacity of 74.2 mg g^{-1} and the authors could achieve SC-SC ion exchange (Fig. 4.10A), providing significant insight into the exchange process. Also, FIR-53 could function as a selective and a reversible sorbent with no remarkable effect on the uptake efficiency after regeneration (Fig. 4.10B). Likewise FIR-54 having pore windows of $10.5 \times 10.5 \text{ \AA}^2$, had a high capture amount of 103 mg g^{-1} for dichromate. Unlike FIR-53, the reversibility for FIR-54 was found to be poor, suggesting that the structural aspects had an important role in directing ion exchange of oxoanions.

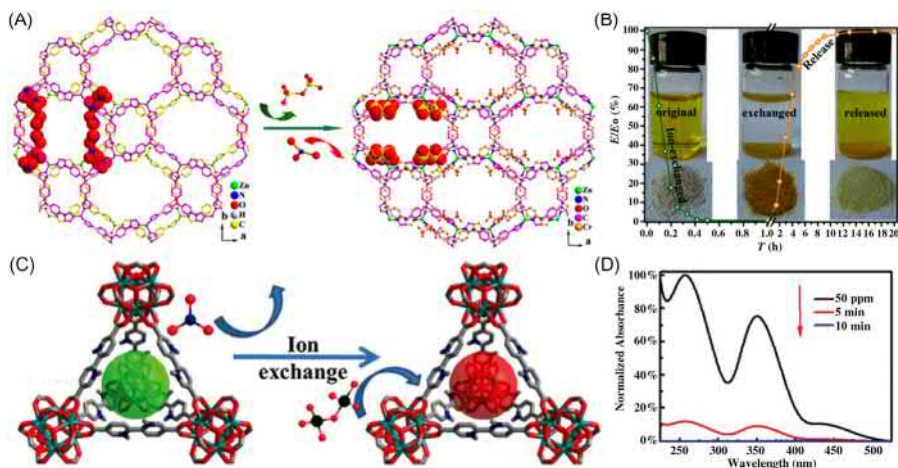


Figure 4.10 (A) SC-SC transformation for the anion exchange process; (B) cycling experiment for dichromate anion capture and release; (C) representation of the approach employed for the ion exchange-based capture of dichromate anions; (D) time-dependent UV-vis spectra of the supernatant solution for titration against dichromate anions.

Source: For (A) and (B), reproduced with permission from H.-R. Fu, Z.-X. Xu, J. Zhang, Water-stable metal-organic frameworks for fast and high dichromate trapping via single-crystal-to-single-crystal ion exchange, *Chem. Mater.* 27 (2015) 205–210. Copyright (2015) American Chemical Society. For (C) and (D), reproduced with permission from Q. Zhang, J. Yu, J. Cai, L. Zhang, Y. Cai, Y. Yang, et al., A porous Zr-cluster-based cationic metal-organic framework for highly efficient $\text{Cr}_2\text{O}_7^{2-}$ removal from water, *Chem. Commun.* 51 (2015) 14732–14734. Copyright (2015) Royal Society of Chemistry.

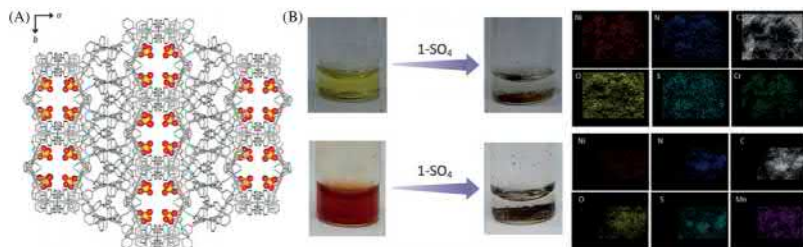


Figure 4.11 (A) Packing diagram showing presence of aligned sulfate anions. (B) Photographs of the anion exchange experiments and EDX mapping profiles showing homogeneous loading of the guest anions in the compound.

Source: Reproduced with permission from A.V. Desai, B. Manna, A. Karmakar, A. Sahu, S. K. Ghosh, A water-stable cationic metal-organic framework as a dual adsorbent of oxoanion pollutants, *Angew. Chem. Int. Ed.* 55 (2016) 7811–7815. Copyright (2016) John Wiley & Sons.

Along with mechanistic understanding, chemical and thermal stability is an important facet of material development. Among the well-studied MOFs, compounds based on Zr(IV) have commanded notable attention owing to robust structures and high chemical resistance. Typically, these MOFs are neutral and are unsuitable as ion exchange sorbents. Qian and coworkers employed the PSM reaction on a neutral bipyridyl-functional MOF-867 (ligand [BPYDC]—2,2′-bipyridine-5,5′-dicarboxylate), to impart ionicity leading to the subsequent isostructural framework ZJU-101 having extra-framework anions (Fig. 4.11A) [58]. The uncoordinated NO_3^- anions were substituted with incoming $\text{Cr}_2\text{O}_7^{2-}$ anions with a high uptake capacity of 245 mg g^{-1} (Fig. 4.11B). The performance was appreciably high even in the concurrent presence of competing ions such as Cl^- , Br^- , NO_3^- , SO_4^{2-} , I^- , and F^- . Control adsorption experiments with MOF-867 validated the ion exchange process.

The contribution of Zhou and coworkers towards the development of Zr(IV)-based MOFs, was extrapolated to examine the efficacy for such applications [60]. A mixed-linker MOF $\{\text{Zr}_6\text{O}_4[\text{OH}]_6[\text{H}_2\text{O}]_2[\text{BTB}]_2[\text{TCPP}]\}$ [PCN-134; TCPP—tetraakis(4-carboxyphenyl)porphyrin; BTB—benzene tribenzoate], exhibited removal of 95% of dichromate from an aqueous solution (50 ppm) within 10 minutes. The coordinated hydroxides and water molecules were ascribed for the dichromate binding to the framework. The authors examined the adsorption tendencies by varying the linker ratios, and optimized the best performing MOF as PCN-134-22%TCPP. The adsorption performance was found to be retained even in concurrent presence (twofold excess) of some common ions. The authors further evaluated the tendency of the compound to photocatalytically reduce the adsorbed Cr(VI) to Cr(III) and found the activity was better than some reported compounds, such as MIL-125- NH_2 .

The work on Zr(IV)-based compounds was later extended by Liu's group [61]. The authors synthesized a Zr(IV)-based MOF for the sorption of $\text{Cr}_2\text{O}_7^{2-}$. The

MOF, viz., $[\text{Zr}_6\text{O}_4(\text{OH})_4\text{L}_4(\text{H}_2\text{O})_2(\text{HCOO})_4] \cdot 9\text{DMF} \cdot 12\text{H}_2\text{O}$ [JLU-MOF50; L—5'-methyl-(1,1',3',1''-terphenyl)-4,4'-dicarboxylic acid] had the Zr_6 clusters with coordination from hydroxides. As such Zr-bonded hydroxides have been known to be useful for the sorption of oxoanions, the authors examined the utility of the MOF for capture of Cr(VI) oxoanions. Although the uptake capacity for $\text{Cr}_2\text{O}_7^{2-}$ was 92 mg g^{-1} , the porosity and suitably aligned hydroxide groups rendered a remarkably high capture rate of $32.5 \text{ mg g}^{-1} \text{ min}^{-1}$. The adsorption performance was retained even in a high concentration (10-fold molar) of competing anions such as Cl^- , Br^- , I^- , NO_3^- , and SO_4^{2-} .

To extend the systematic development of cationic MOFs for such applications, Ghosh and coworkers presented a rational design strategy to construct stable cationic MOFs targeting the capture of oxoanions [59]. The building blocks of the framework, viz., Ni(II), tridentate imidazole-based linker, and SO_4^{2-} anions, were combined for assimilating a hydrolytically stable framework $\{[\text{Ni}_2(\text{tipa})_3(\text{SO}_4)(\text{H}_2\text{O})_3] \cdot (\text{SO}_4) \cdot x\text{G}\}_n$ (1- SO_4 ; G—guest molecules) (Fig. 4.11A). The authors proposed that the geometry of the anion in the host-framework also plays a vital role in the exchange ability and efficiency. The exchange of two different oxoanions—permanganate (as a surrogate for TcO_4^-) and dichromate—was reported, validating the hypothesis (Fig. 4.11B). Although the uptake kinetics were comparatively slower, the MOF exhibited high loading capacity of dichromate of 166 mg g^{-1} . The affinity towards MnO_4^- and $\text{Cr}_2\text{O}_7^{2-}$ was retained even in the concurrent presence of common ions, and anions with tetrahedral geometries such as ClO_4^- , NO_3^- , BF_4^- , and CF_3SO_3^- .

Extending the work on cationic MOFs built from tridentate neutral N-donor ligands, Guo and coworkers reported the utility of a Cd(II)-based MOF $\{[\text{Cd}(\text{tipo})(\text{HCOO})(\text{H}_2\text{O})] \cdot \text{NO}_3 \cdot \text{DMF}\}_n$ [tipo—*tris*(4-(1*H*-imidazol-1-yl)phosphine oxide), as an effective sorbent for the trapping of $\text{Cr}_2\text{O}_7^{2-}$ [62]. The MOF exhibited a capture limit of 228 mg g^{-1} . On account of large pores, the MOF was able to undergo ion exchange rapidly with over 91% removal within 30 minutes. The capture was reported to be selective even in the presence of interfering anions such as Cl^- , Br^- , I^- , NO_3^- , and SO_4^{2-} .

The ability of a sorbent to provide a readout during the adsorption process is highly desirable. Likewise MOFs equipped with the feasibility of tuning the physical properties can be functionalized to provide a signal upon capture of the foreign guests. In this regard, Li and coworkers reported a Cu(II)-based cationic MOF $\{[\text{Cu}_4(\mu_3\text{-OH})_2(\text{mtrb})_2(1,4\text{-bda})_2] \cdot \text{Br}_2 \cdot 6\text{H}_2\text{O}\}_n$ [bda—1,4-benzenediacetate; mtrb—1,3-*bis*(1,2,4-triazol-4-ylmethyl)benzene] for the rapid and efficient capture of dichromate anions [63]. Unlike previously synthesized MOFs, this MOF was a rare example of a cationic MOF connected by tetra-copper clusters. The MOF is highly porous with a 1D channel of $12 \times 12 \text{ \AA}^2$ facilitating the anion exchange process. The authors could monitor the process via SC-SC, providing significant insight regarding the mechanism. The uptake limit for the MOF was calculated to be 128 mg g^{-1} and the cycling experiments yielded satisfactory regeneration of the parent phase. Also, the performance was found to be selective in binary mixtures of $\text{Cr}_2\text{O}_7^{2-}$ with ClO_4^- , NO_3^- , BF_4^- , Br^- , and SO_4^{2-} . Owing to the MOF based on Cu

(II) nodes, the ion exchange process was accompanied with naked-eye colorimetric change, providing an additional transduction pathway.

Li and coworkers reported another Cu(II)-based MOF $\{[\text{Cu}_2\text{L}(\text{H}_2\text{O})_2] \cdot (\text{NO}_3)_2 \cdot 5.5\text{H}_2\text{O}\}_n$ [H_4LCl_2 —1,1'-*bis*(3,5-dicarboxyphenyl)-4,4'-bipyridinium chloride] for the removal of dichromate anions [64]. The authors employed the relatively uncommon design strategy of using a zwitterionic ligand to synthesize a cationic framework. The compound was held by the $[\text{Cu}_2(\text{O}_2\text{C})_4]$ paddlewheel units and had two kinds of porous channels with dimensions of 5 Å and 15.54 Å. The MOF had a relatively high uptake capacity of 222.5 mg g⁻¹.

Among the targeted objectives in the development of MOFs, scalability is among the prominent facets. Yang and coworkers extended the research in this domain by reporting an easily scalable Ag(I)-centered cationic MOF $\{[\text{Ag}_8(\text{tz})_6] \cdot (\text{NO}_3)_2 \cdot 6\text{H}_2\text{O}\}_n$ [tz—3,5-diphenyl-1,2,4-triazolate] [65]. The hydrophobic nature of the pores was correlated with the ion exchange process. The exchange of HCrO_4^- was found to be rapid and reversible with a saturation capacity of Cr(VI) of 37 mg g⁻¹ at 303K.

While the vital aspects of material development are being examined at the batch-scale experiment level, it is important to investigate the viability for practical implementation. In this regard, Manos and coworkers demonstrated the utility of MOF-composite as feasible ion exchange sorbent towards real-time application [66]. Typically, MOFs are obtained as powders and form suspensions in water; hence they cannot be directly employed as sorbents for real-world remediation. The protonated form of UiO-66-NH₂, referred to as MOR-1 $[\text{Zr}_6\text{O}_4(\text{OH})_4(\text{NH}_3^+ \text{-BDC})_6] \text{Cl}_6$ [BDC—1,4-benzene dicarboxylate], was employed to form a composite with alginate acid (HA) to yield a composite of MOR-1-HA (Fig. 4.12A and B). The composite in mixture with sand was applied as the stationary phase in an ion exchange column for the trapping of $\text{Cr}_2\text{O}_7^{2-}$ in a cost-effective manner. From batch studies the sorption limit for $\text{Cr}_2\text{O}_7^{2-}$ was estimated to be 242 ± 17 mg g⁻¹ for MOR-1-HA, with 2.7 ± 0.2 moles per formula unit of MOR-1 (Fig. 4.12C). Also the removal performance was retained (91%–98%) over pH range of 3–8; and satisfactory capacities under high acidic conditions (81% and 90% at pH 1 and 2). The authors further extended their investigation for synthesis of these composites by developing a protocol for green and rapid synthesis of the composite MOR-1-HA [67].

The principal authors of the previous work, elaborated the scope of their idea by modifying the UiO-66 framework to make it cationic [38]. The MOF $[\text{H}_{16}(\text{Zr}_6\text{O}_{16}(\text{H}_2\text{PATP})_4)\text{Cl}_8 \cdot x\text{H}_2\text{O}]$ [referred to as MOR-2, where H_2PATP —2-((pyridine-1-ium-2-ylmethyl)ammonio)terephthalate], formed a composite with alginate acid (HA) to function as the stationary phase in an ion exchange column. The studies with MOR-2 yielded uptake capacity of 194 mg g⁻¹ with rapid capture (<1 minute). The column experiments with satisfactory reusability (<20% loss of performance) over multiple cycles validated the efficacy of the composite material.

Apart from a standalone ion exchange process, capture of Cr(VI) species has been observed in some neutral MOFs such as ZIF-67 or Cu(BTC) by different mechanisms [68–73]. Also, MOF-based composites have been found to offer

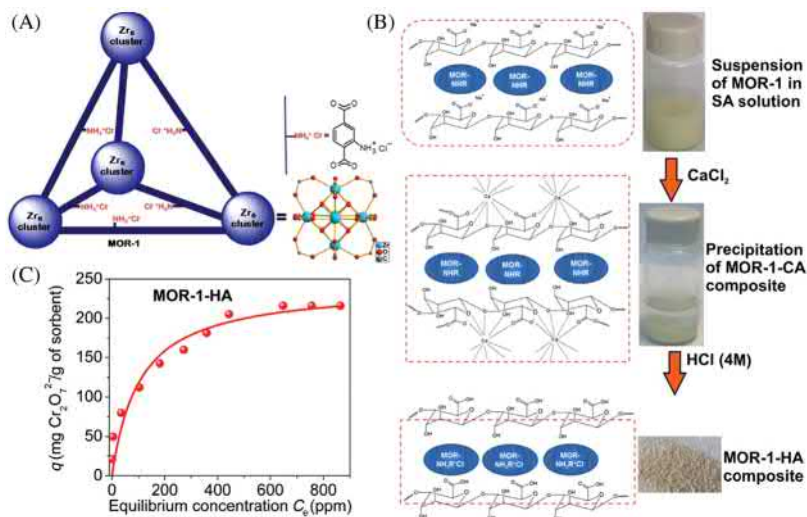


Figure 4.12 (A) Schematic illustration showing the approach employed by the authors for preparing MOR-1; (B) stepwise representation of the protocol employed for the preparation of the composite material MOR-1-HA; (C) adsorption profile for MOR-1-HA at pH = 3 for dichromate anion sorption.

Source: Reproduced with permission from S. Rapti, A. Pournara, D. Sarma, I.T. Papadas, G.S. Armatas, A.C. Tsipis, et al., Selective capture of hexavalent chromium from an anion-exchange column of metal organic resin–alginate composite *Chem. Sci.* 7 (2016) 2427–2436. Copyright (2016) Royal Society of Chemistry.

interesting features towards remediation of such pollutants [74]. Broadly, although the exploration is still in its nascent stages, MOFs are showing encouraging potential as sorbents for trapping Cr(VI) species, which is evidenced by their relative performance with competing materials. The ability to tune, modulate features of MOFs with existing knowledge will actuate the realization in real-time applications.

4.2.2.1.2 Radioactive oxoanion pollutants

Use of nuclear energy and employment of radionuclides for medical purposes has resulted in a large consumption and disposal of radioactive pollutants. In particular the long half-life and rapid mobility in aqueous media necessitates the development of robust materials to entrap such hazardous species. MOFs too have found suitability for such applications and some of the important reports are discussed below.

Ziegler and coworkers presented an early report to demonstrate the effectiveness of cationic MOFs for adsorbing ReO_4^- anions, which is a model for the radioactive TcO_4^- [75] The authors chose a previously reported crystalline solid, viz., $\text{Pb}[\text{B}(\text{Im})_4] \cdot (\text{NO}_3) \cdot (n\text{H}_2\text{O})$ [where Im—Imidazole] for carrying out the ion exchange studies (Fig. 4.13A). Detailed NMR studies with the exchanged phases were carried out and a single crystal was formed in the presence of fivefold excess of perchlorate

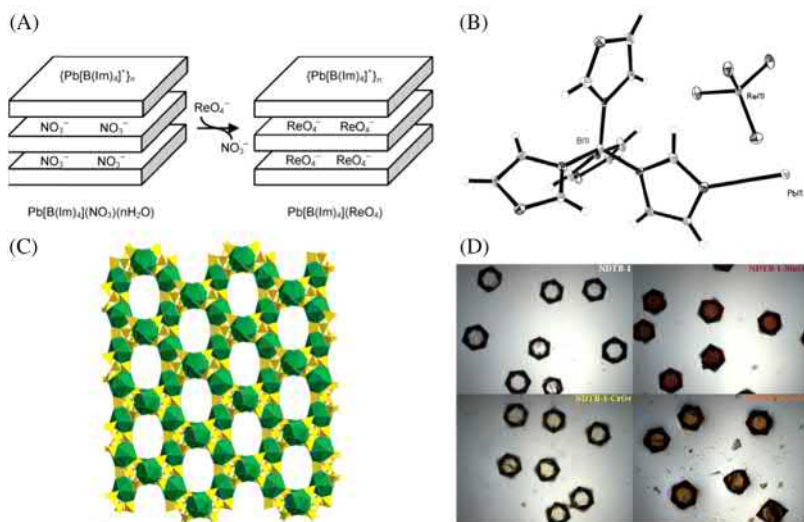


Figure 4.13 (A) Illustration showing anion exchange process employed for the trapping of perchlorate anions; (B) Ortep diagram for the perchlorate exchanged phase; (C) packing diagram for NDTB-1; and (D) photographs of the crystals for NDTB-1 and corresponding anion exchanged phases.

Source: For (A) and (B), reproduced with permission from B.H. Hamilton, T.A. Wagler, M. P. Espe, C.J. Ziegler, Sequestering perchlorate with a borate-based coordination polymer: a model for pertechnetate separation, *Inorg. Chem.* 44 (2005) 4891–4893. Copyright (2005) American Chemical Society. For (C) and (D), reproduced with permission from S. Wang, P. Yu, B.A. Purse, M.J. Orta, J. Diwu, W.H. Casey, et al., Selectivity, kinetics, and efficiency of reversible anion exchange with TcO_4^- in a supertetrahedral cationic framework, *Adv. Funct. Mater.* 22 (2012) 2241–2250. Copyright (2012) John Wiley & Sons.

ions. The crystal structure supported the claim of ion exchange as ReO_4^- anions were located in the interlayer spacing of the structure (Fig. 4.13B).

In an early work on utilizing cationic frameworks as ion exchanger for TcO_4^- , Albrecht-Schmitt, Alekseev, and coworkers reported a robust borate-based cationic solid $[\text{ThB}_5\text{O}_6(\text{OH})_6][\text{BO}(\text{OH})_2] \cdot 2.5\text{H}_2\text{O}$ (NDTB-1) for trapping oxoanions (Fig. 4.13C) [77]. The ion exchange ability towards several oxoanions was initially investigated, with particular focus on the removal of TcO_4^- from aqueous solutions. The authors reported removal of 72% anions within 36 hours. The same group later extended this work with extensive investigation of the ion exchange process with regard to capacity, kinetics, and distribution coefficient (Fig. 4.13D) [76]. The ion exchange for TcO_4^- was found to proceed with second-order kinetics with a rate constant of $0.059 \text{ s}^{-1}\text{M}^{-1}$. The uptake capacity was estimated to be 162.2 mg g^{-1} with K_d of $1.0534 \times 10^4 \text{ mL g}^{-1}$. The compound could be recovered by removing the entrapped anions by exchanging with excess solutions of PO_4^{3-} or SeO_4^{2-} . Although the compound was bearing radioactive metal nodes, it provided a proof-of-concept for further exploration and development of cationic materials for entrapping radioactive oxoanions.

Later Zhou, Wang, and coworkers presented another thorium-based MOF for the capture of ReO_4^- and $\text{Cr}_2\text{O}_7^{2-}$ [78]. The authors presented the first example of a mesoporous cationic MOF, viz., $[\text{Th}_3(\text{bptc})_3\text{O}(\text{H}_2\text{O})_{3.78}]\text{Cl} \cdot (\text{C}_5\text{H}_{14}\text{N}_3\text{Cl}) \cdot 8\text{H}_2\text{O}$ [SCU-8; H_3bptc —(1,1'-biphenyl)-3,4',5-tricarboxylic acid], which was synthesized by an ionothermal reaction. The MOF was found to be stable over a wide pH range (4–12), making it suitable for anion exchange. SCU-8 was found to be an efficient anion exchanger for $\text{Cr}_2\text{O}_7^{2-}$ and ReO_4^- . In the case of the latter, more than 80% removal was observed for a 0.04 mmol L^{-1} solution within 2 minutes and the equilibrium was reached in 10 minutes. The uptake capacity was reported to be $534.07 \text{ mmol mol}^{-1}$.

Oliver's group proposed the utility of their layered compound, viz., SLUG-21 and SLUG-22 $\{\text{Cu}_2(4,4'\text{-bipyridine})_2(\text{O}_3\text{SCH}_2\text{CH}_2\text{SO}_3) \cdot 3\text{H}_2\text{O}\}$ for capturing ReO_4^- and MnO_4^- , both of whom act as surrogates for the radioactive TcO_4^- [79]. The comparative findings suggested that SLUG-21 (Ag(I)-metal node) bearing higher redox stability could function as a more efficient sorbent for both ReO_4^- and MnO_4^- over SLUG-22 (Cu(I)-metal node).

Wang's group extended their work on Ag(I)-centered triazole-based MOFs to report a series of cationic frameworks [80]. Among the synthesized MOFs, the compound $[\text{Ag}(\text{btr}) \cdot \text{PF}_6 \cdot 0.5\text{CH}_3\text{CN}]$ [btr—4,4'-bis(1,2,4-triazole)] was found to be a selective ion exchanger towards MnO_4^- in aqueous solution. The uptake capacity was reported to $0.56 \text{ mol mol}^{-1}$, with noticeable change in the luminescence response during the ion exchange process. The selectivity was confirmed by the preferential uptake of MnO_4^- even from a mixture of common ions such as NO_3^- , BF_4^- , and ClO_4^- .

As discussed previously, Zr(IV)-based MOFs have been found to present high chemical resistance, making them highly sought-after for practical applications. Thallapally and coworkers reported the utility of modified UiO-66-NH₂ for the capture of ReO_4^- , which was employed as a model for TcO_4^- [81]. The modification of the compound included protonation of the primary amine by treatment with 2 M HCl solution. The capture limit for ReO_4^- was estimated to be 159 mg g^{-1} .

Wang's group synthesized the first cationic MOF based on uranyl clusters, viz., $[(\text{UO}_2)(\text{HTTTPC})(\text{OH})]\text{Br} \cdot 1.5\text{DMF} \cdot 4\text{H}_2\text{O}$ [SCU-7; $\text{H}_3\text{TTTPCBr}_3$ —1,1',1''-(2,4,6-trimethylbenzene-1,3,5-triyl)-trimethylene-tris(4-carboxypyridinium)tribromide], having a 2D structure [82]. The synthesis of the compound was optimized by varying the reaction conditions to obtain SCU-7 over the neutral framework SCU-6. The compound exhibited capture for ReO_4^- by ion exchange in an aqueous solution of 1 ppm with 90% trapping within 2.5 hours.

Wang and coworkers extended their work on the development of MOFs for the capture of TcO_4^- by reporting a Ag(I)-based eightfold cationic framework [83]. The synthesized framework $[\text{Ag}_2(\text{tipm})] \cdot 2\text{NO}_3 \cdot 1.5\text{H}_2\text{O}$ [SCU-100; tipm—tetrakis[4-(1-imidazolyl)phenyl]methane] was found to present high hydrolytic stability and resistance towards high doses of β and γ radiation (Fig. 4.14A).

Ion exchange studies for capture of TcO_4^- revealed that about 95.2% concentration was reduced within 30 minutes (Fig. 4.14B), suggesting rapid kinetics. Detailed experiments on the capture of ReO_4^- yielded that the exchange is feasible

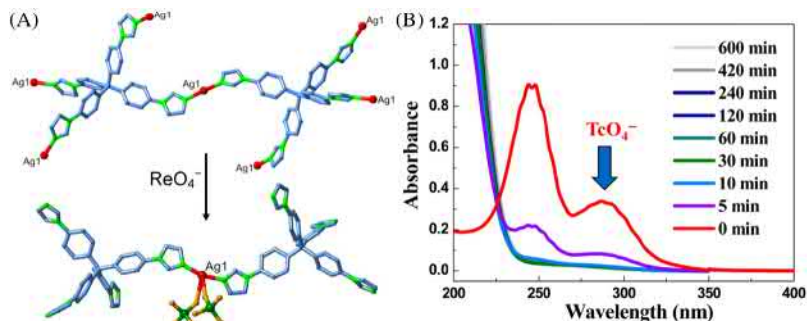


Figure 4.14 (A) Structural transformation for the Ag(I)-MOF towards inclusion of perchrenate anions; (B) time-dependent UV–vis spectra for TcO_4^- exchange experiment. *Source:* Reproduced with permission from D. Sheng, L. Zhu, C. Xu, C. Xiao, Y. Wang, Y. Wang, et al., Efficient and selective uptake of TcO_4^- by a cationic metal-organic framework material with open Ag^+ sites, *Environ. Sci. Technol.* 51 (2017) 3471–3479. Copyright (2017) American Chemical Society.

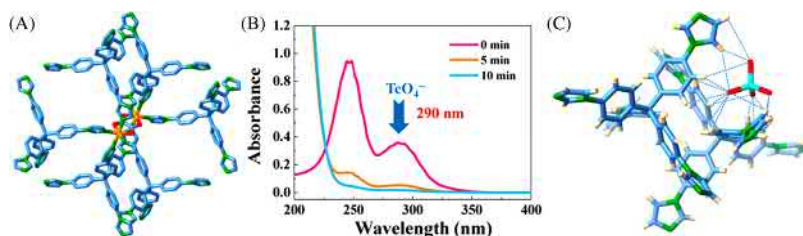


Figure 4.15 (A) Coordination environment for Ni(II)-MOF; (B) time-dependent UV–vis spectra for TcO_4^- inclusion studies; and (C) figure showing interaction of TcO_4^- anion with the framework.

Source: Reproduced with permission from L. Zhu, D. Sheng, C. Xu, X. Dai, M.A. Silver, J. Li, et al., Identifying the recognition site for selective trapping of $^{99}\text{TcO}_4^-$ in a hydrolytically stable and radiation resistant cationic metal-organic framework, *J. Am. Chem. Soc.* 139 (2017) 14873–14876. Copyright (2017) American Chemical Society.

even in the presence of high doses of SO_4^{2-} and NO_3^- , with gradual decrement in the uptake amounts with increasing concentration in the case of later. The open metal site of Ag(I) was found to be the driving force for the uptake of the oxoanion. Treating the ReO_4^- -exchanged phase in high concentration of NaNO_3 (1 M) led to the recovery of the parent phase with 86% removal. The capture limit of ReO_4^- was reported to be 541 mg g^{-1} and K_d value to be $1.9 \times 10^5 \text{ mL g}^{-1}$.

These studies were extended on a more stable Ni(II)-based framework built from the same ligand backbone, viz., $[\text{Ni}_2(\text{tipm})_2(\text{C}_2\text{O}_4)](\text{NO}_3)_2 \cdot 2\text{H}_2\text{O}$ (SCU-101) (Fig. 4.15A) [84]. Like the previous case, initial experiments were carried out with TcO_4^- but detailed investigations were reported with the surrogate

ReO_4^- . SCU-101 could remove >95% anions from an aqueous solution in 10 minutes (Fig. 4.15B), which is faster than commercially available resins such as A532E and A530E. The capacity for ReO_4^- was estimated to be 217 mg g^{-1} with K_d of $7.5 \times 10^5 \text{ mL g}^{-1}$. Treatment with excess NaNO_3 led to recovery of the parent phase and the recycling performance was found to be satisfactory over four cycles. Further, the ion exchange process was found to be feasible over a wide pH range of 3–12, showcasing the advantages of MOFs over conventional inorganic layered materials. Additionally, competing anion experiments exhibited preferential uptake for ReO_4^- , even when the competing anions were present in very high concentration. Owing to the high crystallinity of the framework, the authors could gain structural insights after the ion exchange process of TcO_4^- (Fig. 4.15C). The binding energy of interaction of TcO_4^- was calculated to be $-20.42 \text{ kcal mol}^{-1}$.

Further, the same group investigated trapping of radioactive oxoanions in a previously reported Ag(I)-based layered cationic coordination polymer, viz., $[\text{Ag}(4,4\text{-bipyridine})]\text{NO}_3$ (denoted as SBN) [85]. The authors obtained the single crystal of the exchanged phase which revealed strong binding of the ReO_4^- anions with the accessible coordination sites of Ag(I) nodes. Interestingly, the exchanged phase was found to be highly stable, which was also confirmed by theoretical calculations, and the removal of the adsorbed anion was not possible. The uptake capacity was reported to be 786 mg g^{-1} .

4.2.2.1.3 Selenium-based oxoanion pollutants

Selenium is observed to enter the environment via both organic and inorganic forms. On account of bioavailability and higher solubility, inorganic forms of selenite (SeO_3^{2-}) and selenate (SeO_4^{2-}) have become important oxoanions of interest in material development. In this regard, MOFs can offer potential alternatives for the capture of such anionic pollutants in water sources.

The features of Zr(IV)-centered MOFs, including robustness and higher physico-chemical stability, have made them highly sought-after for several applications. Farha and coworkers explored the possibility of trapping selenite and selenate by investigating a series of established Zr(IV)-based MOFs [86]. The authors chose the well-studied UiO-series MOFs with different pendant groups and the NU-1000 compound. Aqueous solutions of 100ppm concentration of selenate and selenite were initially taken to test the adsorption ability the different MOFs (Fig. 4.16A). While UiO-66 could adsorb 54% (selenite) and 34% (selenate), UiO-66- NH_2 and UiO-66- $(\text{NH}_2)_2$ showed higher uptakes. The authors ascribed the adsorption in only UiO-66 to the ion exchange with the bound hydroxides, while in the case of the other two MOFs the additional uptakes were on account of the hydrogen bonding interactions with amine groups. NU-1000 bears the presence of nonstructural ligands which facilitated the high capture of selenate (88%) and selenite (90%). Detailed mechanistic investigations were carried out to understand the kinetics, uptake preferences, and binding sites (Fig. 4.16B). Importantly, NU-1000 could function as an efficient sorbent even under low concentration of oxoanions of selenium.

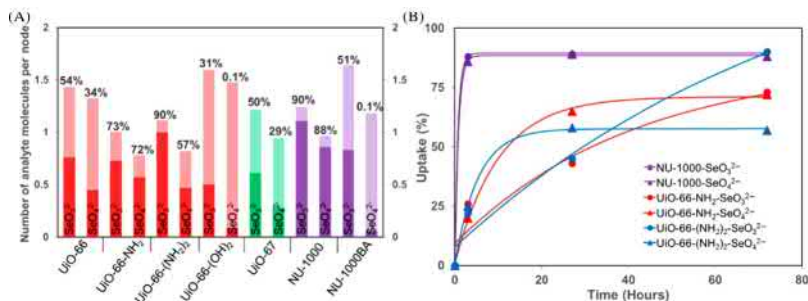


Figure 4.16 (A) Bar diagram showing the extend of adsorption of selenite or selenate anions in different Zr(IV)-based MOFs; (B) kinetic profile for the adsorption profile for selenate and selenite anions.

Source: Reproduced with permission from A.J. Howarth, M.J. Katz, T.C. Wang, A.E. Platero-Prats, K.W. Chapman, J.T. Hupp, et al., High efficiency adsorption and removal of selenate and selenite from water using metal-organic frameworks, *J. Am. Chem. Soc.* 137 (2015) 7488–7494. Copyright (2015) American Chemical Society.

4.2.2.1.4 Arsenic-based oxoanion pollutants

Arsenic which is a highly toxic element is prevalent in groundwater in the form of its oxyanions. Typically it exists in the form arsenite ($H_xAsO_3^{3-x}$) and arsenate ($H_xAsO_4^{3-x}$). MOFs offer promise as sorbents of such toxic anions and below are a few representative illustrations.

Capture of As(V) was investigated by Huang and coworkers by testing the ability of Fe-BTC (BTC—1,3,5-benzene tricarboxylate) porous coordination polymer [87]. The authors found that arsenic could be adsorbed in the interior of the MOF and exhibited significantly higher uptake over iron oxide nanoparticles. The kinetic studies revealed that the adsorption could be fitted in a pseudo-second-order kinetic model.

Some other benchmark MOFs, including MIL-53(Al) and MIL-53(Fe), were investigated for the capture of arsenate [88,89]. In the case of the former, the authors observed an uptake capacity of 105.6 mg g^{-1} , with the optimal condition of capture at pH 8. Competing anions did not alter the performance, except for the presence of PO_4^{3-} . Detailed characterization suggested that electrostatic attraction and hydrogen bonding were influencing the adsorption process. Vu et al. reported similar studies for the ability of MIL-53(Fe) to capture arsenate. The uptake capacity was reported to be 21.27 mg g^{-1} and the kinetics were found to follow pseudo-second-order behavior.

The ability of the highly porous and stable ZIF-8 compound to capture arsenate was evaluated by Li and coworkers [90]. The capacity of adsorption was estimated to be 76.5 mg g^{-1} and a very low equilibrium concentration ($9.8 \mu\text{g L}^{-1}$). The authors proposed the mechanism of adsorption to initial dissociative adsorption of water yielding a high distribution of surface hydrogens. These hydrogen bond groups hold the incoming As(V) species and lead to high capture.

Liu, Zhang, and coworkers reported the ability of ZIF-8 nanoparticles for the capture of As(III) and As(V) species [91]. The uptake limits were calculated to be

49.49 and 60.03 mg g⁻¹ for As(III) and As(V), respectively, at 298K and pH 7.0. Common ions such as SO₄²⁻ and NO₃⁻ were found to have almost no effect on the uptake of arsenic species, but PO₄³⁻ and CO₃²⁻ retarded the adsorption process. Detailed characterization suggested that electrostatic interactions in addition to the presence of polar sites strongly influence the observed adsorption process.

Among MOFs which offer unusually high stability, Zr(IV)-systems have been found to prominently feature. Chen, Li, and coworkers examined the well-studied UiO-66 MOF for its applicability to capture arsenic species [92]. The MOF was able to uptake over a wide pH range of 1–10 with the highest uptake capacity at pH 2 of 303 mg g⁻¹. Notably this value was higher than the capacities for commercially available adsorbents. The mechanism for capture was attributed to the formation of Zr-O-As coordination bonds and the high uptake was ascribed to the presence of multiple active sites of hydroxyl groups and carboxylate ligands.

Li and coworkers reported the study with another Zr(IV)-based MOF, viz., MOF-808 [Zr₆O₄(OH)₄(BTC)₂(HCOO)₆] [93]. The authors synthesized nanoparticles of the MOF using microwave irradiation in a very short time and utilized them as sorbents of As(V) oxyanions. The uptake capacity for arsenic was reported to be 24.83 mg g⁻¹ and more importantly for practical implementation, the MOF was found to be recyclable and retained its performance (82.10% of initial uptake) even after five cycles of adsorption–desorption.

4.2.2.1.5 Trapping of other inorganic anions (phosphate/fluoride, etc.)

Although phosphate is not as toxic as other heavy metal pollutants, it commands significant attention as it is produced on a large scale and is required for several applications. The discharge into water streams can lead to the imbalance of aquatic ecosystems and hence its remediation is an important objective for material chemists.

With regard to MOFs, the strength of the metal–ligand bond is crucial when choosing the appropriate system for the capture of phosphates. Lin and coworkers investigated the utility of two isostructural systems, viz., UiO-66 and UiO-66@NH₂, as sorbents of phosphate anions [94]. The authors observed rapid and high uptake of phosphate anions for both the compounds, with higher adsorption for the MOF bearing pendant amine groups. The interaction of Zr-metal nodes with phosphate was ascribed as the main driving force for the uptake and, in the case of UiO-66@NH₂, the interaction with amine groups led to higher uptakes. Importantly, the adsorption was found to be selective over common ions such as bromate, nitrate, nitrite etc. As a proof-of-concept, the authors investigated the ability of the MOFs to remove phosphate present at a dilute concentration from human urine.

Lin and coworkers utilized the high binding affinity of phosphate anions to prepare porous metal phosphates using MOFs as precursors [95]. The authors proposed the concept of ligand extraction for the preparation of porous inorganic materials by removing the organic ligands by using high concentrations of phosphate anions. The prepared metal phosphates were subsequently used for the removal of radionuclides from simulated wastewater streams.

Similarly to phosphate, the remediation of fluoride anions from water streams is another application seeking greater relevance as the presence of excess fluoride can

result in a range of health hazards. Liu and coworkers screened a series of well-established water-stable MOFs to understand their effect on the adsorption of fluoride anions [96]. The authors observed that among the chosen MOFs (MIL-53, MIL-68, CAU-1, CAU-6, UiO-66, and ZIFs), UiO-66 exhibited the highest adsorption capacity of 41.36 mg g^{-1} . From the observations, the authors concluded that the presence of -OH groups is the strong driving force for defluorination by MOFs. The competing anion experiments were performed and the authors found that in the presence of CO_3^{2-} , the adsorption of F^- was significantly affected. Lin and coworkers extended such work by thoroughly investigating the ability of UiO-66@ NH_2 for the removal of fluoride from water [97]. The authors observed that the adsorption capacity was reduced for $\text{pH} > 7$, but the presence of other halides did not affect the performance. Several characterizations were recorded, which suggested that $\text{NH}_2\text{-F}^-$ interactions drove the high selectivity of fluoride anions.

De and coworkers investigated an Al(III)-fumarate-based MOF, which is known to be stable for the capture of fluoride anions (Fig. 4.17A) [98]. Owing to the high porosity and high stability in water, the compound was sought as a suitable sorbent for the application of interest. The uptake capacity was reported to be 600 mg g^{-1} at 293K (Fig. 4.17B). The authors proposed that the hydroxyl ions in the parent compound were replaced with incoming fluoride anions. The adsorption kinetics was found to follow the pseudo-second-order pathway. The adsorption was found to be selective even in the concurrent presence of anions such as Cl^- , HCO_3^- , NO_3^- , and PO_4^{3-} .

The work on fumarate-based MOF was extended by Wan and coworkers [99]. The authors chose MIL-88A, which is built from FeCl_3 and fumaric acid. The adsorption of fluoride ions was rapid and the equilibrium was attained within 10 minutes. The capacity at room temperature was reported to be 40.42 mg g^{-1} . Like the previous case, the authors found that the adsorption of fluoride was selective over common ions such as Cl^- , NO_3^- , SO_4^{2-} , PO_4^{3-} , and HCO_3^- . Based on detailed experiments, the authors inferred that the process was endothermic and the adsorption could occur under different temperatures also.

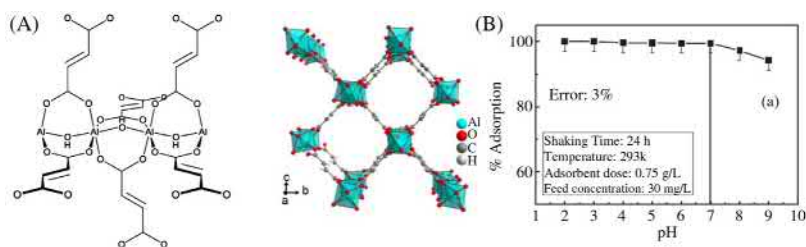


Figure 4.17 (A) Figure showing coordination environment in AlFu MOF and the packing diagram; (B) graph representing the pH-dependent adsorption of fluoride ions.

Source: Reproduced with permission from S. Karmakar, J. Dechnik, C. Janiak, S. De, Aluminium fumarate metal-organic framework: a super adsorbent for fluoride from water, *J. Hazard. Mater.* 303 (2016) 10–20. Copyright (2016) Elsevier.

The major reason for the growing interest in the development of MOFs is the ability to ascribe precise structure–property correlation. To demonstrate this feature, Dastidar and coworkers reported SC-SC-based capture of fluoride anions by a Cu(II)-based coordination polymer [100]. The second phase was characterized using ^{19}F -NMR in addition to SCXRD studies.

4.2.2.2 Capture of organic anionic pollutants

Bulkier anions, viz., anionic dye molecules, are categorized as very hazardous pollutants [101]. These anionic pollutants have very high absorption coefficients and they block sunlight in most of the lakes and rivers leading to eutrophication, and thus disturbing the food chain. With the widespread growth of textile industries, its direct impact has been towards the increase in the concentrations of such anionic dyes, thus contributing towards water pollution. Large chromophoric organic dyes have been diagnosed as potential causes for varied allergies and are potentially mutagenic and carcinogenic in nature. Thus, remediation of such organic dyes is very crucial for living species. For the removal of such anionic dyes, ion exchange materials have gained significant attention as they can selectively capture anionic pollutants. Cationic MOFs have exhibited immense potential in the capture of such anionic pollutants owing to the porous nature and exchangeable anions present within the voids of the frameworks. MOFs can be tailored to the needs, since frameworks with a vast range of pore size, aperture, and charge can be synthesized as per requirements which can be well suited to the capture of anions of different size and charge.

In 2013, PMOFs, that is, positive frameworks, were explored as an ion-exchange column for the separation of organic anions [102]. This report was an important example in the domain of MOFs which showed their tremendous potential in the selective capture of anionic dyes. The $\text{M}_3\text{O}(\text{COO})_6$ trimeric cluster was utilized for the building of highly stable positively charged frameworks along with the use of two types of linker, that is, monovalent anionic and divalent anionic linker, with NO_3^- anions for balancing the charge (Fig. 4.18A). This report categorized several anionic dyes according to the size of the organic dye, thus establishing a size criteria while the charge of the organic dyes were also varied by attaching different numbers of sulfonate groups. The effect of the charge and size was studied by performing exchange studies with PMOFs (Fig. 4.18B and D). Dyes with sizes greater than the pore aperture showed exclusion while dyes with sizes less than the pore aperture showed uptake depending on the shape of the dyes. Selective anionic dye capture was observed in presence of cationic dyes as well as neutral dyes. Also the authors observed rapid regeneration of the adsorbent with no loss in uptake capacity (Fig. 4.18C).

In another study by Kaskel and coworkers, cationic framework with molecular formula $[\text{Cu}(\text{Imid})(\text{H}_2\text{O})]^+$ was synthesized [103]. The inherent ionic nature of the linker led to the construction of a cationic framework which was utilized for ion exchange. The framework showed the adsorption of organic dyes, viz., fluorescein, methyl red (MR), Nile blue, with no uptake observed for Nile red. The ionic nature

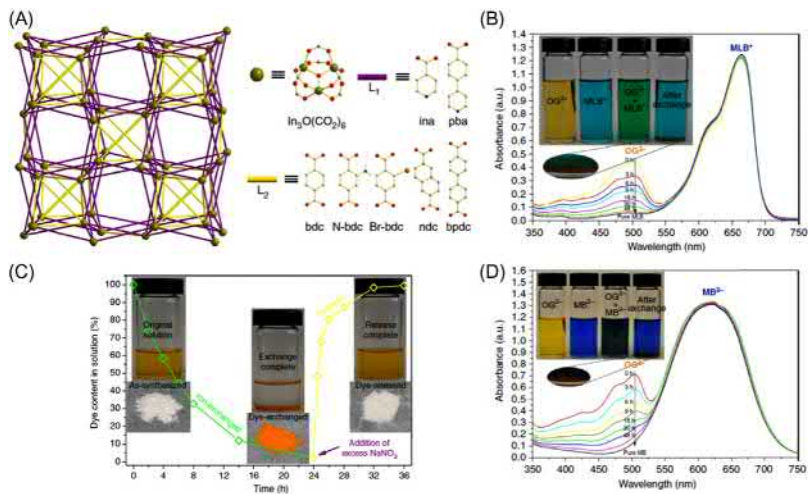


Figure 4.18 (A) Figure showing topology of the In(III)-MOFs along with the building blocks used. (B) UV-vis spectra of the supernatant showing selective anionic dye capture (inset: photograph of the vials during the exchange process). (C) Naked-eye change in color of MOF-powder and supernatant solution along with the time-dependent response in the UV-vis spectra for showing reversible uptake of methyl orange (MO) dye. (D) UV-vis spectra of the supernatant for two anionic dyes (OG^{2-} and MB^{2-}) and mixture phase showing size-selective capture of dye.

Source: Reproduced with permission from X. Zhao, X. Bu, T. Wu, S.-T. Zheng, L. Wang, P. Feng, Selective anion exchange with nanogated isorecticular positive metal-organic frameworks, *Nat. Commun.* 4 (2013) 2344. Copyright (2013) Springer Nature.

of the dye was very crucial, as observed from the uptake profiles. The corresponding anionic species of the dye can be adsorbed electrostatically to the pore walls and may also replace water molecules at the metal center thus making the MOF neutral in nature.

Cheng and coworkers synthesized a cationic cage-based framework solvothermally with the molecular formula $\{[(\text{Cu}_4\text{Cl})(\text{CPT})_4(\text{H}_2\text{O})_4] 3\text{NO}_3 \cdot 5\text{NMP} \cdot 3.5\text{H}_2\text{O}\}_n$ [NMP—*N*-methyl-2-pyrrolidone] [104]. The nitrate anions were exchanged with a MO in a methanolic solution, which was quantified using UV-Vis spectroscopy. The selectivity of the framework was examined towards anionic dyes by a comparative uptake experiment in which methylene blue showed no uptake at all. Rhodamine B and Congo Red were tested for their adsorption via exchange but they showed exclusion owing to the size effects. The reversibility was tested via short span thus establishing the reversibility criteria that is essential for real-time usage.

In another report, Du synthesized a cationic coordination polymer utilizing linker $L = 3$ -(2-pyridyl)-4-(3-pyridyl)-5-(4-pyridyl)-1,2,4-triazole with an overall molecular formula $[\text{Ag}_7(\text{L})_6](\text{ClO}_4)_7(\text{solvent})_n$ [105]. The porosity of the framework with an inherent ionic nature was utilized for the successful capture of Acid Red 26

which has been named as an important pollutant by the European Union (EU) (Fig. 4.19A and B). This dye is known for its subsequent release of aromatic amines and is classified as a carcinogen. The perchlorate anions present within the hexagonal channels of the framework were exchanged with varied dyes. The framework showed the highest sorption of anionic dye AG26²⁻ with an uptake of 96% (Fig. 4.19C). Competing sorption analysis was undertaken between AG26²⁻, Mordant Red 5, and Acid Red 4, of which AG26²⁻ showed the greatest uptake (Fig. 4.19D). The reversibility in the exchange process was further tested by exchanging with nitrate anions and this experiment revealed that the compound could successfully release the adsorbed dye, which is crucial.

Shosh and coworkers recently exhibited the capture of several anionic dyes in a wide pH range of 4–14. They synthesized a robust framework, viz. $[\{Ni(L)_2\} \cdot xG]_n$, utilizing multidentate linker L [$L = \text{Tris}(4-(1H\text{-imidazol-1-yl})\text{phenyl})\text{amine}$] and BPSA, that is, 4,4'-biphenyldisulfonic acid (Fig. 4.20A and B) [106]. The compound exhibited unusual stability among the cationic MOFs existing in the literature. This high stability and the inherent ionic character was harnessed for the capture of anionic dyes like MO, Alizarin Red S, Indigo Carmine, MR, while selectively excluding the cationic dyes like methylene blue.

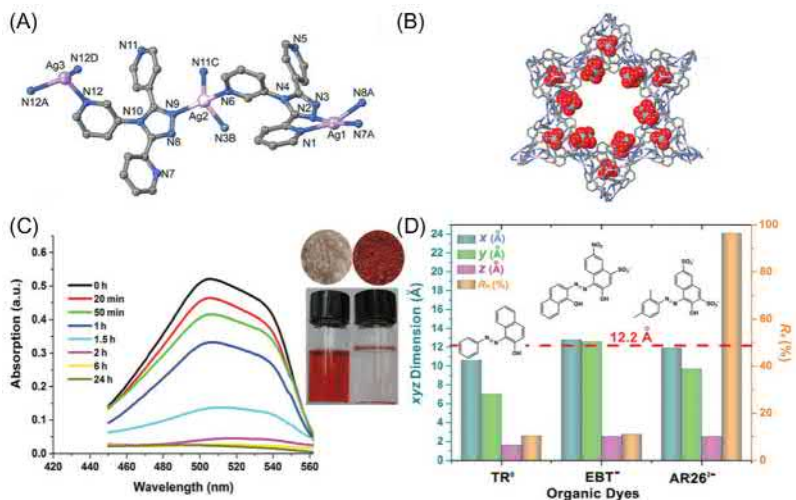


Figure 4.19 (A) Coordination environment in Ag(I)-MOF (anion and H-atoms have been omitted for clarity). (B) Packing diagram showing aligned arrangement of free ClO₄⁻ anions along the pore channel. (C) Time-dependent UV–vis spectra for ion exchange of Acid Red 26 dye. (D) Comparative description of the different dyes investigated for ion exchange and the relative uptake.

Source: Reproduced with permission from C.-P. Li, H. Zhou, S. Wang, H.-H. Yuan, S.-Z. Zhang, M. Du, A nanoporous Ag(I) coordination polymer for selective adsorption of carcinogenic dye Acid Red 26, *Chem. Commun.* 53 (2017) 4767–4770. Copyright (2017) Royal Society of Chemistry.

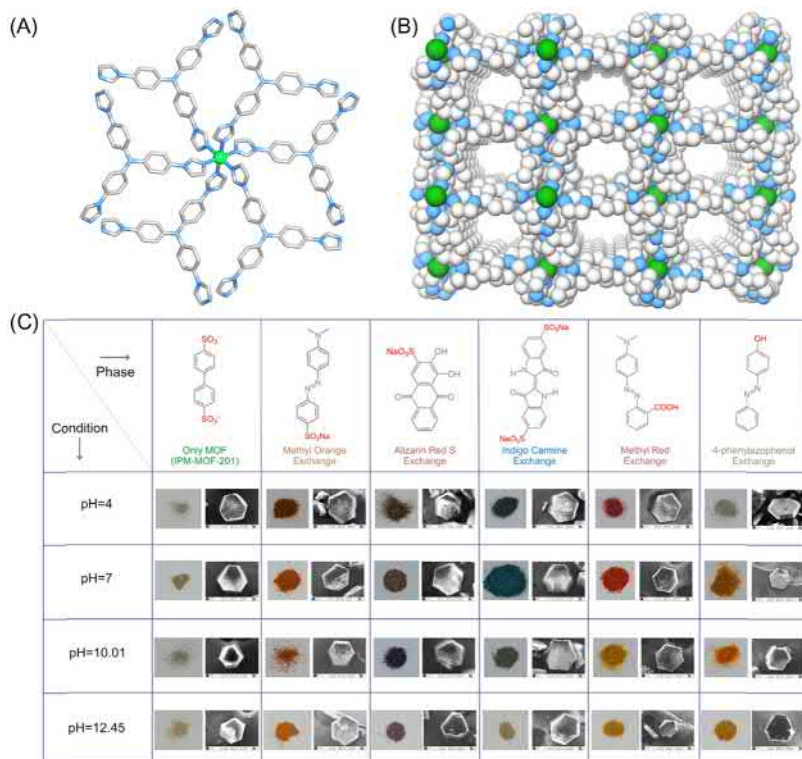


Figure 4.20 (A) Coordination environment and (B) packing diagram of Ni(II)-MOF used for the capture of different anionic dyes. (C) Table summarizing colorimetric response towards anionic dyes across a wide pH range and the corresponding FESEM images of the respective phases.

Source: Reproduced with permission from A.V. Desai, A. Roy, P. Samanta, B. Manna, S.K. Ghosh, Base-resistant ionic metal-organic framework as a porous ion-exchange sorbent, *iScience* 3 (2018) 21–30. Copyright (2018) Elsevier.

The framework showed a colorimetric response at different pH thus making this compound unique in terms of colorimetric response (Fig. 4.20C). The capture was successfully studied via UV–Vis studies and the crystals exhibited a transition to varied colors depending on the pH and dye thus substantiating the capture of various dyes.

4.2.3 Performance of metal-organic frameworks compared with known materials

MOFs have exhibited tremendous potential in the field of anion exchange via various batch investigation studies performed for studying such ion exchange. However, for the industrial usage MOFs need to be explored in comparison with the already existing materials, such as ion exchange resins, ion exchange columns,

etc. MOFs are isolated as powdered materials, thus until now batch investigation studies have been carried out extensively in literature. Most of the known materials, for example, ion exchange resins, etc., have shown a few disadvantages, as these materials swell up and thus result in slow kinetics of the exchange process.

The different materials for chromium capture include layered materials that have been explored. SLUG-21 [51] and Zn-Co-SLUG-35 [52] have shown selective uptake of chromium over other competing anions while no studies have been performed regarding the reuse, sorption kinetics, and capture over a varying pH range. LDHs also exhibited slower kinetics towards the oxoanion capture together with less selectivity in the presence of competing anions [107–110].

Further, in the case of selenate and selenite capture, other materials such as aluminum oxide, iron oxide, amino functionalized zeolites, amine-functionalized resins, and polymer resins have been analyzed for the capture of oxoanionic species of Se such as selenate and selenite. These materials exhibit lower exchange capacity and the kinetics of exchange experiments is quite slow [111]. For instance, the aluminum oxide materials show an uptake of $32.7/11.3 \text{ mg g}^{-1}$ for SeO_3^{2-} and SeO_4^{2-} , respectively [112]. Breakthrough sorption experiments have been performed in zirconium-loaded polymer resin which reported a capacity of 8.8 mg g^{-1} [113].

In the domain of sorption of toxic phosphate (PO_4^{3-}) oxoanions, metal-oxides and LDHs have been explored but these materials exhibit slow sorption kinetics and extremely low capacity. These materials also exhibit irreversibility in terms of phosphate exchange owing to the strongly coordinating nature of the anions, thus they cannot be reused [114–116].

Arsenic-based oxoanions sorption is also reported in the field of oxide-based materials, iron-chitosan flakes, treated laterite, activated alumina, etc. but the adsorption capacities are limited to a very low value. Thus, novel materials are required for the capture of such highly toxic arsenate anions. Other anions such as fluoride anion capture has been explored owing to the persistent problem of the presence of excessive fluoride anions in various water bodies [117,118].

Another important anion TcO_4^- , which is highly hazardous in nature, has been captured via various other materials such as polymeric resins exhibiting anion exchange. But owing to the slow kinetics, weak radiation resistance, poor selectivity, low sorption capacity, and poor chemical stability, there is a need for the exploration of novel materials [119–125].

Fluoride ion capture also has been extensively studied in various materials including ferric hydroxide, chitosan-based mesoporous materials, bone char, aluminum, carbon, calcium-based sorbent, etc. but the adsorption capacity of these sorbents are quite limited [126–131].

4.3 Conclusion and future outlook

Environmental remediation by novel ion exchangers has witnessed a rise recently owing to the widespread pollution worldwide. MOFs have recently emerged in the

field of ion exchange for the sequestration of toxic anions with the development of water-stable MOF-based systems. MOFs score over other porous materials in terms of the inherent tunability with regards to functionality which has been explored extensively. The molecular engineering facet of MOFs accompanied with the single crystalline nature gives a molecular level control of the interactions between the host sorbent and the pollutant—the derived knowledge from these is very important in the design principles. In addition, the mechanism of the exchange can be predicted via such SC-SC studies. Along with the direct visualization via SCXRD, features of MOF such as the pore size and pore apertures can be tuned with respect to the size and shape of the anion, resulting in enhanced selectivity towards the capture of toxic anions over other competing anions. MOFs have been utilized for the capture of varied kinds of hazardous anions including derivatives of Tc(VI), As (V), As (III), Se (IV), Se (VI), Cr(III), Cr(VI), Mo(VI), CN^- , and also radioactive anionic species such as ^{79}Se , ^{99}Tc , etc. In addition to the small toxic anions as mentioned above, MOFs have also been utilized for the capture of bulky anionic dyes such as MO, and Orange Red that have extensive utilization in the dye industry. Among others, recently the capture of toxic pharmaceuticals has been explored with MOFs. In general, the diverse applicability of MOFs towards reversible capture of very hazardous anionic pollutants has paved the way for these materials as potential anion exchange sorbent materials.

MOFs present a bright future as anion exchange—based materials. The tunable nature of the pore, selectivity, appended functionality, fast capture kinetics, and regeneration can yield MOFs that could be among the materials of the future. There are a few aspects in which more research on anion exchange in MOFs should be focused, including the regeneration and reversibility criteria. An important aspect that requires the attention of the scientific community is towards the development of composites for such anion exchange—based applications. MOFs as standalone powders may pose severe challenges before MOFs can be applied to real-time anion exchange—based systems. Thus, various polymeric forms should be explored in detail for actual scenarios. Another aspect that needs attention is the synthetic design principles of such ionic MOFs. The wastewater sludge usually varies dramatically in terms of the pH, thus ionic MOFs that have a wide range stability should be explored. The cost-effectiveness is another parameter that plays a crucial role in the long-term applicability. Hence, cost-effective materials that are cheap and widely available should be selected for the synthesis of ionic MOFs. Along with the cost, the anions that are eluted after such exchange processes should be environmental friendly in nature as they may provide a cleaner and greener way to go ahead. Thus, MOFs have extensive potential in toxic anions capture for environmental remediation.

Acknowledgments

The authors thank DST-SERB (EMR/2016/000410) for financial support. A.D. and S.S. thank IISER-Pune for their research fellowship.

References

- [1] C. Estarellas, A. Frontera, D. Quinonero, P.M. Deya, Relevant anion- π interactions in biological systems: the case of urate oxidase, *Angew. Chem. Int. Ed.* 50 (2011) 415–418.
- [2] P.A. Gale, R. Perez-Tomas, R. Quesada, Anion transporters and biological systems, *Acc. Chem. Res.* 46 (2013) 2801–2813.
- [3] L. Keith, W. Telliard, ES&T special report: priority pollutants: I-a perspective view, *Environ. Sci. Technol.* 13 (1979) 416–423.
- [4] World Health Organization. Water, Sanitation and Health Team. Guidelines for drinking water quality. Vol. 1, Recommendations, 3rd ed. Geneva: World Health Organization. <<http://www.who.int/iris/handle/10665/42852>>, 2004.
- [5] D. Banerjee, D. Kim, M.J. Schweiger, A.A. Kruger, P.K. Thallapally, Removal of TeO_4^- ions from solution: materials and future outlook, *Chem. Soc. Rev.* 45 (2016) 2724–2739.
- [6] <https://www.epa.gov/sites/production/files/2015-09/documents/priority-pollutant-list-epa.pdf>
- [7] Guidelines for drinking water quality, 4th ed. World Health Organization (WHO) Library, 2011. ISBN 9789241548151.
- [8] EPA Facts About Technetium-99, US Environment Protection Agency Booklet, 2002.
- [9] E.M. Brown, C.J. Pazoles, C.E. Creutz, G.D. Aurbach, H.B. Pollard, Role of anions in parathyroid hormone release from dispersed bovine parathyroid cells, *Proc. Natl. Acad. Sci. USA* 75 (1978) 876–880.
- [10] K. Jomova, Z. Jenisova, M. Feszterova, S. Baros, J. Liska, D. Hudecova, et al., Arsenic: toxicity, oxidative stress and human disease, *J. Appl. Toxic.* 31 (2011) 95–107.
- [11] P.F. Lito, J.P.S. Aniceto, C.M. Silva, Removal of anionic pollutants from waters and wastewaters and materials perspective for their selective sorption, *Water Air Soil Pollut* 233 (2012) 6133–6155.
- [12] P.A. Gale, E.N.W. Howe, X. Wu, Anion receptor chemistry, *Chem I* (2016) 351–422.
- [13] Pure Earth and Green Cross. The World's Worst Pollution Problems (2016): the Toxics Beneath Our Feet, 2016.
- [14] K.M.S. Sumathi, S. Mahimairaja, R. Naidu, Use of low-cost biological wastes and vermiculite for removal of chromium from tannery effluent, *Biores. Technol.* 96 (2005) 309–316.
- [15] D.C. Sharma, C.F. Forster, Column studies into the adsorption of chromium (VI) using sphagnum moss peat, *Biores. Technol.* 52 (1995) 261–267.
- [16] F. Lu, D. Astruc, Nanomaterials for removal of toxic elements from water, *Coord. Chem. Rev.* 356 (2018) 147–164.
- [17] P.D. Beer, P.A. Gale, Anion recognition and sensing: the state of the art and future perspectives, *Angew. Chem. Int. Ed.* 40 (2001) 486–516.
- [18] R.G. Pearson, Hard and soft acids and bases, HSAB, part 1: fundamental principles, *J. Chem. Edu.* 45 (1968) 581.
- [19] F. Hofmeister, Zur Lehre von der Wirkung der Salze, *Arch. Exp. Pathol. Pharmacol.* 24 (1888) 247.
- [20] Q. Wang, D. O'Hare, Recent advances in the synthesis and application of layered double hydroxide (LDH) nanosheets, *Chem. Rev.* 112 (2012) 4124–4155.
- [21] N. Chubar, R. Gilmour, V. Gerda, M. Micusik, M. Omastova, K. Heister, et al., Layered double hydroxides as the next generation inorganic anion exchangers: synthetic methods versus applicability, *Adv. Colloid Interface Sci.* 245 (2017) 62–80.

- [22] A.G. Slater, A.I. Cooper, Function-led design of new porous materials, *Science* 348 (2015) aaa8075.
- [23] S.R. Batten, N.R. Champness, X.-M. Chen, J. Garcia-Martinez, S. Kitagawa, L. Ohrstrom, et al., Terminology of metal–organic frameworks and coordination polymers, *Pure Appl. Chem.* 85 (2013) 1715–1724.
- [24] S. Kitagawa, R. Kitaura, S.-i. Noro, Functional porous coordination polymers, *Angew. Chem. Int. Ed.* 43 (2004) 2334–2375.
- [25] A. Karmakar, A.V. Desai, S.K. Ghosh, Ionic metal-organic frameworks (iMOFs): design principles and applications, *Coord. Chem. Rev.* 307 (2016) 313–341.
- [26] C. Mao, R.A. Kudla, F. Zuo, X. Zhao, L.J. Mueller, X. Bu, Anion stripping as a general method to create cationic porous framework with mobile anions, *J. Am. Chem. Soc.* 136 (2014) 7579–7582.
- [27] T. Islamoglu, S. Goswami, Z. Li, A.J. Howarth, O.K. Farha, J.T. Hupp, Postsynthetic tuning of metal–organic frameworks for targeted applications, *Acc. Chem. Res.* 50 (2017) 805–813.
- [28] J. Liang, R.-P. Chen, X.-Y. Wang, T.-T. Liu, X.-S. Wang, Y.-B. Huang, et al., Postsynthetic ionization of an imidazole containing metal–organic framework for the cycloaddition of carbon dioxide and epoxides, *Chem. Sci.* 8 (2017) 1570–1575.
- [29] Y. Noori, K. Akhbari, Post-synthetic ion-exchange process in nanoporous metal–organic frameworks; an effective way for modulating their structures and properties, *RSC Adv.* 7 (2017) 1782–1808.
- [30] G.M. Espallargas, E. Coronado, Magnetic functionalities in MOFs: from the framework to the pore, *Chem. Soc. Rev.* 47 (2018) 533–557.
- [31] W.P. Lustig, S. Mukherjee, N.D. Rudd, A.V. Desai, J. Li, S.K. Ghosh, Metal–organic frameworks: functional luminescent and photonic materials for sensing applications, *Chem. Soc. Rev.* 46 (2017) 3242–3285.
- [32] L. Sun, S.S. Park, D. Sheberla, M. Dinca, Measuring and reporting electrical conductivity in metal–organic frameworks: Cd₂(TTFTB) as a case study, *J. Am. Chem. Soc.* 138 (2016) 14772–14782.
- [33] Y. Wen, J. Zhang, Q. Xu, X.-T. Wu, Q.-L. Zhu, Pore surface engineering of metal-organic frameworks for heterogeneous catalysis, *Coord. Chem. Rev.* 376 (2018) 248–276.
- [34] X. Li, H. Xu, F. Kong, R. Wang, A cationic metal–organic framework consisting of nanoscale cages: capture, separation, and luminescent probing of Cr₂O₇²⁻ through a single-crystal to single-crystal process, *Angew. Chem. Int. Ed.* 52 (2013) 13769–13773.
- [35] W.-H. Huang, J.-Z. Li, T. Liu, L.-S. Gao, M. Jiang, Y.-N. Zhang, et al., A stable 3D porous coordination polymer as multi-chemosensor to Cr(IV) anion and Fe(III) cation and its selective adsorption of malachite green oxalate dye, *RSC Adv.* 5 (2015) 97127–97132.
- [36] C.-S. Cao, H.-C. Hu, H. Xu, W.-Z. Qiao, B. Zhao, Two solvent-stable MOFs as a recyclable luminescent probe for detecting dichromate or chromate anions, *CrystEngComm* 18 (2016) 4445–4451.
- [37] R. Lv, J. Wang, Y. Zhang, H. Li, L. Yang, S. Liao, et al., An amino-decorated dual-functional metal–organic framework for highly selective sensing of Cr(III) and Cr(VI) ions and detection of nitroaromatic explosives, *J. Mater. Chem. A* 4 (2016) 15494–15500.
- [38] S. Rapti, D. Sarma, S.A. Diamantis, E. Skliri, G.S. Armatas, A.C. Tsepis, et al., All in one porous material: exceptional sorption and selective sensing of hexavalent chromium by using a Zr⁴⁺, *MOF. J. Mater. Chem. A* 5 (2017) 14707–14719.

- [39] W. Liu, Y. Wang, Z. Bai, Y. Li, Y. Wang, L. Chen, et al., Hydrolytically stable luminescent cationic metal organic framework for highly sensitive and selective sensing of chromate anions in natural water systems, *ACS Appl. Mater. Interfaces* 9 (2017) 16448–16457.
- [40] Y. Lin, X. Zhang, W. Chen, W. Shi, P. Cheng, Three cadmium coordination polymers with carboxylate and pyridine mixed ligands: luminescent sensors for Fe(III) and Cr(VI) ions in an aqueous medium, *Inorg. Chem.* 56 (2017) 11768–11778.
- [41] Z.-J. Lin, H.-Q. Zheng, H.-Y. Zheng, L.-P. Lin, Q. Xin, R. Cao, Efficient capture and effective sensing of $\text{Cr}_2\text{O}_7^{2-}$ from water using a zirconium metal–organic framework, *Inorg. Chem.* 56 (2017) 14178–14188.
- [42] T. He, Y.-Z. Zhang, X.-J. Kong, J. Yu, X.-L. Lv, Y. Wu, et al., Zr(IV)-based metal-organic framework with T-shaped ligand: unique structure, high stability, selective detection, and rapid adsorption of $\text{Cr}_2\text{O}_7^{2-}$ in water, *ACS Appl. Mater. Interfaces* 10 (2018) 16650–16659.
- [43] A. Karmakar, N. Kumar, P. Samanta, A.V. Desai, S.K. Ghosh, A. Post-Synthetically, Modified MOF for selective and sensitive aqueous-phase detection of highly toxic cyanide ions, *Chem. Eur. J* 22 (2016) 864–868.
- [44] A. Karmakar, B. Joarder, A. Mallick, P. Samanta, A.V. Desai, S. Basu, et al., Aqueous phase sensing of cyanide ions using a hydrolytically stable metal–organic framework, *Chem. Commun.* 53 (2017) 1253–1256.
- [45] J.-P. Ma, Y. Yu, Y.-B. Dong, Fluorene-based Cu(II)-MOF: a visual colorimetric anion sensor and separator based on an anion-exchange approach, *Chem. Commun.* 48 (2012) 2946–2948.
- [46] Y.-Q. Chen, G.-R. Li, Z. Chang, Y.-K. Qu, Y.-H. Zhang, X.-H. Bu, A Cu(I) metal–organic framework with 4-fold helical channels for sensing anions, *Chem. Sci.* 4 (2013) 3678–3682.
- [47] A. Karmakar, A.V. Desai, B. Manna, B. Joarder, S.K. Ghosh, An Amide-functionalized dynamic metal–organic framework exhibiting visual colorimetric anion exchange and selective uptake of benzene over cyclohexane, *Chem. Eur. J* 21 (2015) 7071–7076.
- [48] B. Manna, A.K. Chaudhari, B. Joarder, A. Karmakar, S.K. Ghosh, Dynamic structural behavior and anion-responsive tunable luminescence of a flexible cationic metal–organic framework, *Angew. Chem. Int. Ed.* 52 (2013) 998–1002.
- [49] A. Karmakar, B. Manna, A.V. Desai, B. Joarder, S.K. Ghosh, Dynamic metal–organic framework with anion-triggered luminescence modulation behavior, *Inorg. Chem.* 53 (2014) 12225–12227.
- [50] Z. Fan, Y.Y. Wang, Y.Y. Xu, X.M. Su, X.X. Wu, J.Z. Huo, et al., Synthesis and characterization of a novel 3D porous luminescent Ag(I) framework with a multidentate triazole ligand, *Inorg. Chim. Acta* 410 (2014) 178–182.
- [51] H. Fei, M.R. Bresler, S.R.J. Oliver, A. New, Paradigm for anion trapping in high capacity and selectivity: crystal-to-crystal transformation of cationic materials, *J. Am. Chem. Soc.* 133 (2011) 11110–11113.
- [52] H. Fei, C.S. Han, J.C. Robins, S.R.J. Oliver, A cationic metal–organic solid solution based on Co(II) and Zn(II) for chromate trapping, *Chem. Mater.* 25 (2013) 647–652.
- [53] P.-F. Shi, B. Zhao, G. Xiaong, Y.-L. Hou, P. Cheng, Fast capture and separation of, and luminescent probe for, pollutant chromate using a multi-functional cationic heterometal-organic framework, *Chem. Commun.* 48 (2012) 8231–8233.
- [54] B. Ding, J.Z. Huo, Y.Y. Liu, X. Wang, X. Su, X.X. Wu, et al., Triazole based Ag coordination clusters: synthesis, structural diversity and anion exchange properties, *RSC Adv.* 5 (2015) 83415–83426.

- [55] B. Ding, C. Guo, S.X. Liu, Y. Cheng, X.X. Wu, X.M. Su, et al., A unique multi-functional cationic luminescent metal–organic nanotube for highly sensitive detection of dichromate and selective high capacity adsorption of Congo red, *RSC Adv.* 6 (2016) 33888–33900.
- [56] C.-P. Li, H. Zhou, S. Wang, J. Chen, Z.-L. Wang, M. Du, Highly efficient $\text{Cr}_2\text{O}_7^{2-}$ removal of a 3D metal-organic framework fabricated by tandem single-crystal to single-crystal transformations from a 1D coordination array, *Chem. Commun.* 53 (2017) 9206–9209.
- [57] H.-R. Fu, Z.-X. Xu, J. Zhang, Water-stable metal–organic frameworks for fast and high dichromate trapping via single-crystal-to-single-crystal ion exchange, *Chem. Mater.* 27 (2015) 205–210.
- [58] Q. Zhang, J. Yu, J. Cai, L. Zhang, Y. Cai, Y. Yang, et al., A porous Zr-cluster-based cationic metal–organic framework for highly efficient $\text{Cr}_2\text{O}_7^{2-}$ removal from water, *Chem. Commun.* 51 (2015) 14732–14734.
- [59] A.V. Desai, B. Manna, A. Karmakar, A. Sahu, S.K. Ghosh, A. Water-Stable, Cationic metal–organic framework as a dual adsorbent of oxoanion pollutants, *Angew. Chem. Int. Ed.* 55 (2016) 7811–7815.
- [60] S. Yuan, J.-S. Qin, L. Zou, Y.-P. Chen, X. Wang, Q. Zhang, et al., Thermodynamically guided synthesis of mixed-linker Zr-MOFs with enhanced tunability, *J. Am. Chem. Soc.* 138 (2016) 6636–6642.
- [61] X. Sun, S. Yao, C. Yu, G. Li, C. Liu, Q. Huo, et al., An ultrastable Zr-MOF for fast capture and highly luminescence detection of $\text{Cr}_2\text{O}_7^{2-}$ simultaneously in an aqueous phase, *J. Mater. Chem. A* 6 (2018) 6363–6369.
- [62] M. Gao, H. Guo, S. Liu, Y. Sun, X. Guo, A microporous cationic metal–organic framework for the efficient removal of dichromate and the selective adsorption of dyes from water, *RSC Adv.* 7 (2017) 51021–51026.
- [63] X.-X. Lv, L.-L. Shi, B.-L. Li, H.-Y. Li, An unusual porous cationic metal–organic framework based on a tetranuclear hydroxyl-copper(II) cluster for fast and highly efficient dichromate trapping through a single-crystal to single-crystal process, *Chem. Commun.* 53 (2017) 1860–1863.
- [64] C. Zhang, Y. Liu, L. Sun, H. Shi, C. Shi, Z. Liang, et al., Ligand-based cationic metal-organic framework for rapidly selective dye capture and highly efficient $\text{Cr}_2\text{O}_7^{2-}$ removal, *Chem. Eur. J.* 24 (2018) 2718–2724.
- [65] L.-L. Li, X.-Q. Feng, R.-P. Han, S.-Q. Zang, G. Yang, Cr(VI) removal via anion exchange on a silver-triazolate MOF, *J. Hazard. Mater.* 321 (2017) 622–628.
- [66] S. Rapti, A. Pournara, D. Sarma, I.T. Papadas, G.S. Armatas, A.C. Tsipis, et al., Selective capture of hexavalent chromium from an anion-exchange column of metal organic resin–alginate acid composite, *Chem. Sci.* 7 (2016) 2427–2436.
- [67] S. Rapti, A. Pournara, D. Sarma, I.T. Papadas, G.S. Armatas, Y.S. Hassan, et al., Rapid, green and inexpensive synthesis of high quality UiO-66 amino-functionalized materials with exceptional capability for removal of hexavalent chromium from industrial waste, *Inorg. Chem. Front.* 3 (2016) 635–644.
- [68] X. Li, X. Gao, L. Ai, J. Jiang, Mechanistic insight into the interaction and adsorption of Cr(VI) with zeolitic imidazolate framework-67 microcrystals from aqueous solution, *Chem. Engg. J.* 274 (2015) 238–246.
- [69] A. Maleki, B. Hayati, M. Naghizadeh, S.W. Joo, Adsorption of hexavalent chromium by metal organic frameworks from aqueous solution, *J. Ind. Engg. Chem.* 28 (2015) 211–216.

- [70] Y. Xiong, F. Ye, C. Zhang, S. Shen, L. Su, S. Zhao, Synthesis of magnetic porous $\gamma\text{-Fe}_2\text{O}_3/\text{C}@\text{HKUST-1}$ composites for efficient removal of dyes and heavy metal ions from aqueous solution, *RSC Adv.* 5 (2015) 5164–5172.
- [71] K. Zhu, C. Chen, H. Xu, Y. Gao, X. Tan, A. Alsaedi, et al., Cr(VI) reduction and immobilization by core-double-shell structured magnetic polydopamine@zeolitic idazolate frameworks-8 microspheres, *ACS Sustain. Chem. Eng.* 5 (2017) 6795–6802.
- [72] A. Nasrollahpour, S.E. Moradi, Hexavalent chromium removal from water by ionic liquid modified metal-organic frameworks adsorbent, *Microporous Mesoporous Mater.* 243 (2017) 47–55.
- [73] H. Niu, Y. Zheng, S. Wang, S. He, Y. Cai, Stable hierarchical microspheres of 1D Fe–gallic acid MOFs for fast and efficient Cr(VI) elimination by a combination of reduction, metal substitution and coprecipitation, *J. Mater. Chem. A* 5 (2017) 16600–16604.
- [74] P. Kumar, A. Pournara, K.-H. Kim, V. Bansal, S. Rapti, M.J. Manos, Metal-organic frameworks: challenges and opportunities for ion-exchange/sorption applications, *Prog. Mater. Sci.* 86 (2017) 25–74.
- [75] B.H. Hamilton, T.A. Wagler, M.P. Espe, C.J. Ziegler, Sequestering perchlorate with a borate-based coordination polymer: a model for pertechnetate separation, *Inorg. Chem.* 44 (2005) 4891–4893.
- [76] S. Wang, P. Yu, B.A. Purse, M.J. Orta, J. Diwu, W.H. Casey, et al., Selectivity, kinetics, and efficiency of reversible anion exchange with TcO_4^- in a supertetrahedral cationic framework, *Adv. Funct. Mater.* 22 (2012) 2241–2250.
- [77] S. Wang, E.V. Alekseev, J. Diwu, W.H. Casey, B.L. Phillips, W. Depmeier, et al., NDTB-1: a supertetrahedral cationic framework that removes TcO_4^- from solution, *Angew. Chem. Int. Ed.* 49 (2010) 1057–1060.
- [78] Y. Li, Z. Yang, Y. Wang, Z. Bai, T. Zheng, X. Dai, et al., A mesoporous cationic thorium-organic framework that rapidly traps anionic persistent organic pollutants, *Nat. Commun.* 8 (2017) 1354.
- [79] H. Fei, D.L. Rogow, S.R.J. Oliver, Reversible anion exchange and catalytic properties of two cationic metal–organic frameworks based on Cu(I) and Ag(I), *J. Am. Chem. Soc.* 132 (2010) 7202–7209.
- [80] X. Li, Y. Gong, H. Zhao, R. Wang, Anion-directed assemblies of cationic metal–organic frameworks based on 4,4'-bis(1,2,4-triazole): syntheses, structures, luminescent and anion exchange properties, *Inorg. Chem.* 53 (2014) 12127–12134.
- [81] D. Banerjee, W. Xu, Z. Nie, L.E.V. Johnson, C. Coghlan, M.L. Sushko, et al., Zirconium-based metal–organic framework for removal of perchlorate from water, *Inorg. Chem.* 55 (2016) 8241–8243.
- [82] Z. Bai, Y. Wang, Y. Li, W. Liu, L. Chen, D. Sheng, et al., First cationic uranyl–organic framework with anion-exchange capabilities, *Inorg. Chem.* 55 (2016) 6358–6360.
- [83] D. Sheng, L. Zhu, C. Xu, C. Xiao, Y. Wang, Y. Wang, et al., Efficient and selective uptake of TcO_4^- by a cationic metal–organic framework material with open Ag^+ sites, *Environ. Sci. Technol.* 51 (2017) 3471–3479.
- [84] L. Zhu, D. Sheng, C. Xu, X. Dai, M.A. Silver, J. Li, et al., Identifying the recognition site for selective trapping of $^{99}\text{TcO}_4^-$ in a hydrolytically stable and radiation resistant cationic metal–organic framework, *J. Am. Chem. Soc.* 139 (2017) 14873–14876.
- [85] L. Zhu, C. Xiao, X. Dai, J. Li, D. Gui, D. Sheng, et al., Exceptional perchlorate/pertechnetate uptake and subsequent immobilization by a low-dimensional cationic coordination polymer: overcoming the hofmeister bias selectivity, *Environ. Sci. Technol. Lett.* 4 (2017) 316–322.

- [86] A.J. Howarth, M.J. Katz, T.C. Wang, A.E. Platero-Prats, K.W. Chapman, J.T. Hupp, et al., High efficiency adsorption and removal of selenate and selenite from water using metal–organic frameworks, *J. Am. Chem. Soc.* 137 (2015) 7488–7494.
- [87] B.-J. Zhu, X.-Y. Yu, Y. Jia, F.-M. Peng, B. Sun, M.-Y. Zhang, et al., Iron and 1,3,5-benzenetricarboxylic metal–organic coordination polymers prepared by solvothermal method and their application in efficient As(V) removal from aqueous solutions, *J. Phys. Chem. C* 116 (2012) 8601–8607.
- [88] J. Li, Y.-n Wu, Z. Li, M. Zhu, F. Li, Characteristics of arsenate removal from water by metal-organic frameworks (MOFs), *Water Sci. Technol.* 70 (2014) 1391–1397.
- [89] T.A. Vu, G.H. Le, C.D. Dao, L.Q. Dang, K.T. Nguyen, Q.K. Nguyen, et al., Arsenic removal from aqueous solutions by adsorption using novel MIL-53(Fe) as a highly efficient adsorbent, *RSC Adv.* 5 (2015) 5261–5268.
- [90] J. Li, Y.-n Wu, Z. Li, B. Zhang, M. Zhu, X. Hu, et al., Zeolitic imidazolate framework-8 with high efficiency in trace arsenate adsorption and removal from water, *J. Phys. Chem. C* 118 (2014) 27382–27387.
- [91] M. Jian, B. Liu, G. Zhang, R. Liu, X. Zhang, Adsorptive removal of arsenic from aqueous solution by zeolitic imidazolate framework-8 (ZIF-8) nanoparticles, *Colloid Surf. A* 465 (2015) 67–76.
- [92] C. Wang, X. Liu, J.P. Chen, K. Li, Superior removal of arsenic from water with zirconium metal-organic framework UiO-66, *Sci. Rep.* 5 (2015) 16613.
- [93] Z.-Q. Li, J.-C. Yang, K.-W. Sui, N. Yin, Facile synthesis of metal-organic framework MOF-808 for arsenic removal, *Mater. Lett.* 160 (2015) 412–414.
- [94] K.-Y.A. Lin, S.-Y. Chen, A.P. Jochems, Zirconium-based metal organic frameworks: highly selective adsorbents for removal of phosphate from water and urine, *Mater. Chem. Phys.* 160 (2015) 168–176.
- [95] C.W. Abney, K.M.L. Taylor-Pashow, S.R. Russell, Y. Chen, R. Samantaray, J.V. Lockard, et al., Topotactic transformations of metal–organic frameworks to highly porous and stable inorganic sorbents for efficient radionuclide sequestration, *Chem. Mater.* 26 (2014) 5231–5243.
- [96] X. Zhao, D. Liu, H. Huang, W. Zhang, Q. Yang, C. Zhong, The stability and defluoridation performance of MOFs in fluoride solutions, *Microporous Mesoporous Mater.* 185 (2014) 72–78.
- [97] K.-Y.A. Lin, Y.-T. Liu, S.-Y. Chen, Adsorption of fluoride to UiO-66-NH₂ in water: stability, kinetic, isotherm and thermodynamic studies, *J. Colloid Inter. Sci.* 461 (2016) 79–87.
- [98] S. Karmakar, J. Dechnik, C. Janiak, S. De, Aluminium fumarate metal-organic framework: a super adsorbent for fluoride from water, *J. Hazard. Mater.* 303 (2016) 10–20.
- [99] F. Ke, G. Luo, P. Chen, J. Jiang, Q. Yuan, H. Cai, et al., Porous metal–organic frameworks adsorbents as a potential platform for defluoridation of water, *J. Porous Mater.* 23 (2016) 1065–1073.
- [100] N.N. Adarsh, A. Grelard, E.J. Dufourc, P. Dastidar, Sequestering hydrated fluoride in a three-dimensional non-interpenetrated octahedral coordination polymer via a single-crystal-to-single-crystal fashion, *Cryst. Growth Des.* 12 (2012) 3369–3373.
- [101] N.A. Khan, Z. Hasan, S.H. Jung, Adsorptive removal of hazardous materials using metal-organic frameworks (MOFs): a review, *J. Hazard. Mater.* 244 (2013) 444–456.
- [102] X. Zhao, X. Bu, T. Wu, S.-T. Zheng, L. Wang, P. Feng, Selective anion exchange with nanogated isoreticular positive metal-organic frameworks, *Nat. Commun.* 4 (2013) 2344.

- [103] G. Nickerl, A. Notzon, M. Heitbaum, I. Senkovska, F. Glorius, S. Kaskel, Selective adsorption properties of cationic metal–organic frameworks based on imidazolic linker, *Cryst. Growth Des.* 13 (2013) 198–203.
- [104] D.M. Chen, W. Shi, P. Cheng, A cage-based cationic body-centered tetragonal metal–organic framework: single-crystal to single-crystal transformation and selective uptake of organic dyes, *Chem. Commun.* 51 (2015) 370–372.
- [105] C.-P. Li, H. Zhou, S. Wang, H.-H. Yuan, S.-Z. Zhang, M. Du, A nanoporous Ag(I) coordination polymer for selective adsorption of carcinogenic dye Acid Red 26, *Chem. Commun.* 53 (2017) 4767–4770.
- [106] A.V. Desai, A. Roy, P. Samanta, B. Manna, S.K. Ghosh, Base-resistant ionic metal-organic framework as a porous ion-exchange sorbent, *iScience* 3 (2018) 21–30.
- [107] S. Kaneko, M. Ogawa, Effective concentration of dichromate anions using layered double hydroxides from acidic solutions, *Appl. Clay Sci.* 75 (2013) 109–113.
- [108] F. Zhang, N. Du, H. Li, X. Liang, W. Hou, Sorption of Cr(VI) on Mg–Al–Fe layered double hydroxides synthesized by a mechanochemical method, *RSC Adv.* 4 (2014) 46823–46830.
- [109] X. Yuan, Y. Wang, J. Wang, C. Zhou, Q. Tang, X. Rao, Calcined graphene/MgAl-layered double hydroxides for enhanced Cr(VI) removal, *Chem. Eng. J.* 221 (2013) 204–213.
- [110] M. McGuire, N. Blute, L. Fong, D. Forelich, P. Kavounas, G. Qin, Hexavalent Chromium Removal Using Anion Exchange and Reduction With Coagulation and Filtration. *Water Environment Research Foundation*, 2008.
- [111] T. Nishimura, H. Hashimoto, M. Nakayama, Removal of selenium(VI) from aqueous solution with polyamine-type weakly basic ion exchange resin, *Sep. Sci. Technol.* 42 (2007) 3155–3167.
- [112] Y.T. Chan, W.H. Kuan, T.Y. Chen, M.K. Wang, Adsorption mechanism of selenate and selenite on the binary oxide systems, *Water Res.* 43 (2009) 4412–4420.
- [113] T.M. Suzuki, D.A.P. Tanaka, M.A.L. Tanco, M. Kanetsato, T. Yokoyama, Adsorption and removal of oxo-anions of arsenic and selenium on the zirconium(IV) loaded polymer resin functionalized with diethylenetriamine-*N,N,N'*-polyacetic acid, *J. Environ. Monit.* 2 (2000) 550–555.
- [114] G. Zhang, H. Liu, R. Liu, J. Qu, Removal of phosphate from water by a Fe–Mn binary oxide adsorbent, *J. Colloid Interface Sci.* 335 (2009) 168–174.
- [115] R. Chitrakar, S. Tezuka, A. Sonoda, K. Sakane, K. Ooi, T. Hirotsu, Selective adsorption of phosphate from seawater and wastewater by amorphous zirconium hydroxide, *J. Colloid Interface Sci.* 297 (2006) 426–433.
- [116] X. Huang, X. Liao, B. Shi, Adsorption removal of phosphate in industrial wastewater by using metal-loaded skin split waste, *J. Hazard. Mater.* 166 (2009) 1261–1265.
- [117] S.M. Maliyekkal, L. Philip, T. Pradeep, As(III) removal from drinking water using manganese oxide-coated-alumina: performance evaluation and mechanistic details of surface binding, *Chem. Eng. J.* 153 (2009) 101–107.
- [118] A. Gupta, V.S. Chauhan, N. Sankaramakrishnan, Preparation and evaluation of iron–chitosan composites for removal of As(III) and As(V) from arsenic contaminated real life groundwater, *Water Res.* 43 (2009) 3862–3870.
- [119] W.R. Wilmarth, G.J. Lumetta, M.E. Johnson, M.R. Poirier, M.C. Thompson, P.C. Suggs, et al., Review: waste-pretreatment technologies for remediation of legacy defense nuclear wastes, *Solvent Extr. Ion Exch.* 29 (2011) 1–48.

- [120] P.V. Bonnesen, G.M. Brown, S.D. Alexandratos, L.B. Bavoux, D.J. Presley, V. Patel, et al., Development of bifunctional anion-exchange resins with improved selectivity and sorptive kinetics for pertechnetate: batch-equilibrium experiments, *Environ. Sci. Technol.* 34 (2000) 3761–3766.
- [121] K.M. Long, G.S. Goff, S.D. Ware, G.D. Jarvinen, W.H. Runde, Anion exchange resins for the selective separation of technetium from uranium in carbonate solutions, *Ind. Eng. Chem. Res.* 51 (2012) 10445–10450.
- [122] R.H. Wiley, G. Devenuto, Irradiation stability of sulfonated styrene resins crosslinked with various divinylbenzene isomers and mixtures thereof, *J. Appl. Poly. Sci.* 9 (1965) 2001–2007.
- [123] Y. Wang, H. Gao, Compositional and structural control on anion sorption capability of layered double hydroxides (LDHs), *J. Colloid Interface Sci.* 301 (2006) 19–26.
- [124] L.J. McIntyre, L.K. Jackson, A.M. Fogg, $\text{Ln}_2(\text{OH})_5\text{NO}_3 \cdot x\text{H}_2\text{O}$ ($\text{Ln} = \text{Y}, \text{Gd} - \text{Lu}$): a novel family of anion exchange intercalation hosts, *Chem. Mater.* 20 (2008) 335–340.
- [125] H.V. Goulding, S.E. Hulse, W. Clegg, R.W. Harrington, H.Y. Playford, R.I. Walton, et al., $\text{Yb}_3\text{O}(\text{OH})_6\text{Cl} \cdot 2\text{H}_2\text{O}$: an anion-exchangeable hydroxide with a cationic inorganic framework structure, *J. Am. Chem. Soc.* 132 (2010) 13618–13620.
- [126] E. Kumar, A. Bhatnagar, M. Ji, W. Jung, S.-H. Lee, S.-J. Kim, et al., Defluoridation from aqueous solutions by granular ferric hydroxide (GFH), *Water Res.* 43 (2009) 490–498.
- [127] S. Venkata Mohan, S.V. Ramanaiah, B. Rajkumar, P.N. Sarma, Removal of fluoride from aqueous phase by biosorption onto algal biosorbent *Spirogyra* sp.-IO2: sorption mechanism elucidation, *J. Hazard. Mater.* 141 (2007) 465–474.
- [128] S. Kagne, S. Jagtap, P. Dhawade, S.P. Kamble, S. Devotta, S.S. Rayalu, Hydrated cement: a promising adsorbent for the removal of fluoride from aqueous solution, *J. Hazard. Mater.* 154 (2008) 88–95.
- [129] S. Jagtap, M.K.N. Yenkie, N. Labhsetwar, S. Rayalu, Defluoridation of drinking water using chitosan based mesoporous alumina, *Microporous Mesoporous Mater.* 142 (2011) 454–463.
- [130] S. Ghorai, K.K. Pant, Investigations on the column performance of fluoride adsorption by activated alumina in a fixed-bed, *Chem. Eng. J.* 98 (2004) 165–173.
- [131] B.D. Turner, P. Binning, S.L.S. Stipp, Fluoride removal by calcite: evidence for fluoride precipitation and surface adsorption, *Environ. Sci. Technol.* 39 (2005) 9561–9568.

Metal-organic frameworks for the capture of volatile organic compounds and toxic chemicals

5

*Kevin Dedecker^{1,2}, Eddy Dumas¹, Bertrand Lavédrine²,
Nathalie Steunou¹ and Christian Serre^{3,*}*

¹Institut Lavoisier de Versailles, UMR CNRS 8180, Université de Versailles St-Quentin-en-Yvelines, Université Paris-Saclay, 78035 Versailles Cedex, France, ²Centre de Recherche sur la Conservation (CRC), Muséum National d'Histoire Naturelle, CNRS, Ministère de la Culture, USR3224, 36 rue Geoffroy Saint Hilaire, 75005, Paris, France, ³Institut des Matériaux poreux de Paris (IMAP), UMR CNRS 8004, Ecole Normale Supérieure de Paris, Ecole Supérieure de Physique et de Chimie Industrielles de Paris, PSL University, 75005, Paris, France

*Corresponding author: e-mail address: christian.serre@ens.fr

List of abbreviations

22DMB	2,2-dimethylbutane
23DMB	2,3-dimethylbutane
2MP	2-methylpentane
CO	carbon monoxide
CUS	coordinatively unsaturated site
DMA	dimethylacetamide
ED	ethylenediamine
H₂S	hydrogen sulfide
LPE	liquid-phase epitaxial
MOF	metal-organic framework
MX	meta-xylene
NH₃	ammonia
nm	nanometer
NO	nitric oxide
NO₂	nitrogen dioxide
O₃	ozone
OX	ortho-xylene
ppm	part per million
PX	para-xylene

RTO	regenerative thermal oxidizer
SO₂	sulfur dioxide
VCP	volatile chemical product
VOC	volatile organic compound

5.1 Context: volatile organic compounds, detrimental effects, emission sources, and removal

Nowadays, air quality is a major worldwide concern along with malnutrition, dietary risks, high blood pressure, and tobacco. In 2016, air pollution was responsible for 7.5% of all deaths and consequently ranked sixth in terms of disability-adjusted life years which represent the burden of disease that could be avoided by modifying the environment [1]. A lower air quality is often attributed to volatile organic compound (VOC) emissions which have notorious health effects, such as respiratory problems (asthma) [2], neurological symptoms (nausea, lethargy, headaches, and depressions) [3,4], and cancers (leukemia) [5]. More indirectly, these compounds may be oxidized in the presence of nitric oxides (e.g., NO and NO₂) to form tropospheric ozone (O₃) [6,7], a strong oxidizer able to induce respiratory diseases [8].

Amongst anthropogenic VOC sources, automotive vehicles, the petrochemical industry, and everyday household products are the most significant contributors in terms of emissions. Motor vehicles produce NO_x, carbon monoxide (CO), non-methane hydrocarbons, and carbon dioxide (CO₂) during combustion. This gas mixture has an impact on the O₃ level in urban regions. However, some studies show that pollution levels caused by car traffic have decreased by at least almost an order of magnitude over the last 20 years in Europe and in the United States thanks to the improvements made on the fuel composition, engine design, and use of better performing catalytic converters (oxidization of CO and hydrocarbons and reduction of NO_x) [9,10]. Consequently, the contribution of car emissions is less pronounced than decades ago and keeps decreasing with time. In the case of the petrochemical industry, the impact of VOCs on the local air pollution depends on the industrial activities and the strategies followed to reduce their ecological fingerprint. Several studies have been carried out in order to measure VOC, NO_x and O₃ concentrations produced by industrial plants. The largest US petrochemical estate in Houston has been shown to be responsible for a high level of ozone in the area because of its VOCs emissions. However, it has been revealed that amongst the emitted molecules, the capture of only two alkenes, ethene and propene, may reduce the majority of ozone produced [11]. In the case of the industrial complex near the urban region of La Plata in Argentina, VOCs concentrations in the area have decreased to an acceptable level after a program designed to reduce diffuse and fugitive emissions [12]. While VOCs emissions from industries and vehicles are decreasing with technological improvements, the use of volatile chemical products (VCPs) such as pesticides, coatings, printing inks, adhesives, personal care products, and cleaning agents represents a substantial part of VOCs emissions to the atmosphere, estimated

at half of what fossil fuel produces in industrialized cities. VCPs include several categories of organic molecules. Alcohols like ethanol and isopropanol can be found in cleaning agents, personal care products, and alcoholic beverages. In paint thinners, acetone is widely present and alkanes with long chains (nonane, decane, and undecane) are mainly found in solvents like mineral spirits [13]. For the other uncommon VOCs, they are produced during specific activities, such as cooking which releases aldehydes [14]. VCPs sources are less easy to locate than vehicle or industry emissions and therefore more difficult to regulate. However, these VOC concentrations may be high in spaces such as apartments, restaurants, and other indoor environments what raises serious public health problems.

In order to remove VOCs at a large scale, several industrial processes have been developed and are rather efficient. Amongst them, two main categories can be distinguished: (1) VOCs adsorption followed by their recovery and treatment for reuse or sale (including biological processes for chemical transformation into valuable products); and (2) complete degradation by incineration or thermal, catalytic, or biological oxidation. Typically, the removal of VOCs from automotive painting may be carried out by using an adsorbent such as activated carbons, zeolites, or both to increase their interactions with polar compounds. The VOC-laden air is introduced within a fixed-bed system composed of pelletized activated carbon. This material is replaced periodically once saturated (after years). The air from the adsorbent bed is then sent to an adsorption system containing an activated carbon and/or zeolite [15,16]. At this step, the adsorbents are continuously regenerated thermally on a cyclic basis. The adsorbed molecules are released and may be treated and stored. This process allows a removal efficiency between 90% and 99% [17]. However, the most common procedure adopted in the automotive industry, after the thermal desorption [18], consists of sending VOCs to regenerative thermal oxidizers (RTOs) for their complete degradation. RTOs are composed of a combustion chamber surrounded by two heat-storage sections with a heat-transfer medium for the storage of energy produced during the oxidation. The temperature within the combustion chamber is above 650°C [19] and is maintained constantly with the input of energy provided by the combustion of VOCs (15% of the energy demand) mostly using natural gas. The VOCs oxidation efficiency is very high, close to 98% [20].

Despite great technological progress in the field of the capture and treatment of VOCs, air pollution remains a critical issue due to the high energy penalty associated with their capture and abatement. This is why the design of more efficient materials or processes for their removal is still an important challenge.

In order to design efficient adsorbents for VOC removal, several criteria must be taken into account. Porous adsorbents may be of high interest due to the possible molecular sieving effect for the capture or separation of VOCs. A good matching between the pore diameter of the adsorbent and the kinetic diameter of gas molecules may favor both the selective capture of molecules and their confinement in the porosity of the adsorbents through attractive interactions. Zeolites present specific pore sizes generally between 0.3 and 3 nm according to the structure.

Besides, activated carbons have a broad range of pore sizes (micro-, meso-, and macroporosity) and, therefore, are less selective toward VOCs. However, activated carbons generally display higher adsorption capacities, pore volumes, and specific areas than zeolites. Consequently, a lower amount of adsorbent is required leading to a huge impact on the cost and design of the final adsorbent for the capture of VOCs. The affinity of VOCs for the adsorbent is also a key parameter for the selective and efficient capture of VOCs and requires strong host/guest interactions. Activated carbons are mainly hydrophobic but depending on the synthesis conditions, they can also exhibit functional surface polar groups (e.g., carboxyl group) [21], thereby allowing the adsorption of a broad range of molecules from apolar to polar. Zeolites are mainly known to be hydrophilic. However, it is possible to tune their hydrophobic/hydrophilic balance through dealumination which implies a decrease of the Al/Si ratio [22]. For both activated carbons and zeolites, water may interact with both the surface and the bulk, and potentially replace VOC already adsorbed. This phenomenon dramatically reduces the efficiency of these adsorbents and involves their use in specific environmental conditions. The selectivity for the adsorption of VOCs in humid conditions can be enhanced by tuning the physico-chemical properties of the adsorbents. The chemistry of zeolites is more versatile than activated carbons due to the presence of a wide range of negatively charged frameworks with different topologies and positively charged counterions. In this material, it is possible to tune the amount of Brønsted and Lewis acid sites, change the Al/Si ratio, and exchange the positively charged counterion with transition metals capable of interacting with adsorbates through π -complexation. However, the chemical composition of zeolites is mainly restricted to a small range of atoms (Si, Al, O) and the characteristics of their porosity in terms of diameter and geometry are not large enough to cover the adsorption of a wide range of VOCs. In the context of an industrial application, the cost and the adsorbent stability are other key parameters. Activated carbons are cheaper than natural or synthetic hydrophobic zeolites. Nevertheless, activated carbons must be replaced every 6 months to 5 years while zeolites are highly thermally stable and therefore do not need frequent replacement. Consequently, the investigation of new types of materials combining the advantages of both classes of adsorbents, activated carbons, and zeolites, is necessary for the selective and efficient adsorption of VOCs.

Recently, a new class of highly porous crystalline adsorbents, denoted metal-organic frameworks (MOFs), have emerged with a strong potential in the field of gas storage and/or separation, particularly for hydrogen [23], methane [24], and carbon dioxide [25] in the context of global warming. These highly versatile hybrid crystalline micro- or mesoporous solids, based on inorganic subunits and polycomplexing ligands, exhibit usually high surface area (up to $7000 \text{ m}^2 \text{ g}^{-1}$ for NU-109E and NU-110E) and pore volumes (3.75 and $4.40 \text{ cm}^3 \text{ g}^{-1}$ for NU-109E and NU-110E, respectively) as well as tunable sorption properties suitable for optimized sorbate–sorbent interactions [26]. Pore size may be modified for a given topology (same inorganic unit and crystal system) by choosing a suitable organic linker length as demonstrated previously [27]. Moreover, the functionalization of the organic linker by using chemical groups such as $-\text{CF}_3$, $-\text{alkyl chain}$, or $-\text{NH}_2$

may modulate the hydrophobicity/hydrophilicity balance of the MOF [28], while at the same time optimize the host/guest interactions. Beyond their level of versatility, the main critical issue concerns the lack of chemical stability, especially in aqueous solutions or humid conditions. However, recent studies provided a better comprehension of the parameters which govern this major limitation (thermodynamic and kinetic stability factors) [29,30]. Moreover, while activated carbons and zeolites are produced industrially at a large scale, reliable manufacturing procedures need to be developed for MOFs. For that purpose, various synthetic approaches have been investigated such as solvothermal, electrochemical, mechanochemical, and microwave-assisted synthesis [31]. The development and improvement of these approaches also allowed the shaping of MOFs in order to produce functional textile, pellets, paper sheets, membranes, foams, and granules [32,33].

This chapter is intended to give a useful survey of recent progress concerning the use of MOFs for the capture of VOCs and toxic gases for environmental applications. Our aim is to address the influence of a few selected physicochemical MOFs' features on the efficiency and selectivity of these key challenging separations. This chapter is divided into two main parts: capture of VOCs (hydrocarbons, alcohols, aldehydes, ketones, and carboxylic acids) and capture of toxic chemicals often in interactions with VOCs in the environment (SO_2 , H_2S , CO , and NO). The adsorption of NH_3 and the other species of the NO family are not included in this chapter but may be found in the recent review by Bobbitt et al. [34].

5.2 Design of metal-organic frameworks for the capture of volatile organic compounds

5.2.1 Hydrocarbons: from saturated to unsaturated molecules

Hydrocarbon emissions (including alkanes, alkenes, and aromatics) from petrochemical industries, vehicles, and the use of VCPs cause health problems. Amongst alkanes, it has been proven that *n*-hexane may be metabolized in the body to form different compounds, such as 2,5-hexanedione, which is highly neurotoxic for human beings [35]. Ethylene is an unsaturated molecule widely used in the industry of polymers but is also a plant hormone involved in many aspects of plant growth, development, and survival. However, even if ethylene is beneficial for plants, at concentrations as high as 1.0 ppm [36], it becomes harmful for vegetation inducing toxicity symptoms such as reduced growth, premature senescence, and reduced flowering and fruit production [37]. Mainly produced by petrochemical industries, benzene is responsible of aplastic anemia, leukemia, leukocytopenia, thrombocytopenia, granulocytopenia, and pancytopenia and has thus been classified as a human carcinogen, the limit of exposure of which decreases from year to year (100 ppm in 1927, 10 ppm in 1977, and 1 ppm in 2000) [38].

In order to compare MOFs to other materials, the adsorption properties of several zeolites, activated carbons, and a MOF (HKUST-1) have been studied by Zhu

et al. for the adsorption of ethane, propane, and butane [39]. The selective adsorption and catalytic properties of zeolites make them of great interest in the petrochemical industry [40,41]. The charge-compensating cations of zeolites may dramatically affect the adsorption properties of the material. The electric field generated by the cation may interact with the adsorbates through, for instance, the π -bond of ethylene (which has a strong quadrupole moment) leading to a better affinity. Three of the main critical parameters are the nature of this cation (atom and valence), the cation size, and the number of cations (Si/Al ratio) [42]. However, the uptake capacity of zeolites is generally quite limited as a result of their low pore volume and specific area in comparison to activated carbons and MOFs, as well as a possible partial blockage of the porosity due to the accommodation of solvated cations. Capture of hydrocarbons with activated carbons has been widely studied [43]. With their generally high surface area and pore volume and their hydrophobicity, activated carbons are prone to the adsorption of hydrocarbons in large amounts. However, the adsorption of hydrocarbons in these materials suffers from a lack of selectivity according to the high pore size distribution of activated carbons.

With their tunable pore size, hydrophobicity/hydrophilicity balance, and, therefore, adsorption properties, MOFs represent an excellent alternative for the efficient adsorption and separation of hydrocarbons.

Pirngruber et al. considered three types of MOFs that bear coordinatively unsaturated sites (CUS), or consist of apolar or anionic frameworks (Fig. 5.1). Their separation ability was studied through binary breakthrough experiments for different representative molecules: two aromatics (*o*- and *p*-xylene), one alkene (1-octene), and one alkane (*n*-octane) [44].

Authors first pointed out the unexpected selectivity of the apolar adsorbents (Table 5.1). Indeed, as the speed of elution in a gas chromatographic column is mainly driven by the adsorbate boiling point, the order of elution should be: 1-octene < *n*-octane < *p*-xylene. However, for the apolar adsorbents (ZIF-8, ZIF-76,

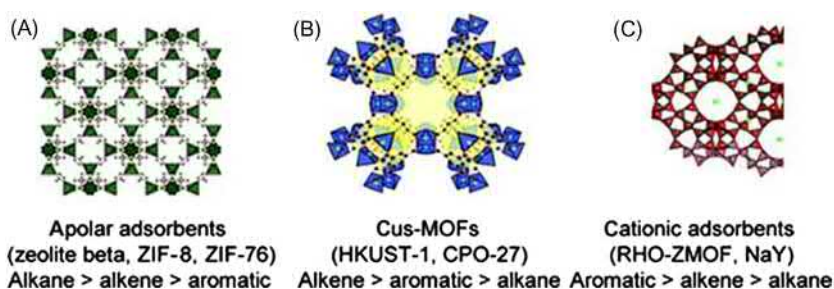


Figure 5.1 Series of materials composed of (A) apolar adsorbents, (B) CUS-MOFs, and (C) cationic adsorbents with their corresponding selectivity toward hydrocarbons.

Source: Reprinted (adapted) with permission from D. Peralta, G. Chaplais, A. Simon-Masseron, K. Barthelet, C. Chizallet, A.A. Quoineaud, G.D. Pirngruber, Comparison of the behavior of metal-organic frameworks and zeolites for hydrocarbon separations, *J. Am. Chem. Soc.* 134 (2012) 8115–8126. Copyright (2012) American Chemical Society.

Table 5.1 Selectivities for selected adsorbents^a at 298K

Pressure (Pa)	NaY	HKUST-1	CPO-27-Ni	RHO-ZMOF	ZIF-8	ZIF-76	Siliceous zeolite β
Selectivity	5.4	2.7	= C8/ <i>n</i> C8 3.8	1.0	0.9	0.9	0.7
Selectivity	27.2	1.5	PX/ <i>n</i> C8 1.6	1.5	0.7	0.8	0.2
Selectivity	9.6	0.7	PX/ = C8 0.7	1.6	0.7	0.9	0.3
Selectivity	1.4	1.3	OX/PX 3.3	1.3	0.3	1.1	0.5

In the binary mixtures, the molar fraction was between 0.005 and 0.007 (without xylenes) and between 0.003 and 0.004 (with xylenes).

^a*n*C8, *n*-octane; = C8, 1-octene; PX, *p*-xylene; OX, *o*-xylene.

and zeolite β), the elution order is instead *p*-xylene < 1-octene < *n*-octane. The rapid elution of *p*-xylene was shown to be due both to a diffusional limitation as well as weak interactions between the guest molecules and the structure. For ZIF-76 and zeolite β , only thermodynamic considerations were shown to rule the adsorption process. A similar observation has already been made previously for MIL-47 [45], a MOF without any polar adsorption site, whereas the better affinity for *n*-octane is attributed to weak hydrogen bonds between the oxygen atoms of the ligand and the CH groups of the alkane. Nevertheless, in the case of ZIFs, this assumption should be ruled out because of the absence of oxygen atoms within the structure. The high degree of flexibility of alkane chains may favor a high packing of these molecules and thus their preferred adsorption within the pores, whereas the confinement of unsaturated and rigid molecules cannot be optimized. This selectivity has been confirmed for a mixture of ethane/ethene and propane/propene; ZIF-8 adsorbs alkanes over alkenes through a sieving mechanism. Another example is given by Kapteijn et al. with ZIF-7 [46]. In that material, pores are too small (~ 0.3 nm) for a direct adsorption of ethane molecules. Ethane molecules interact with the organic linker (benzimidazolate) to induce their rotation (gate-opening effect) allowing their access to the main cavities. This observation has also been made for a mixture of propane/propene [47].

In the case of polar adsorbents, unsaturated molecules are prone to interact more strongly than alkanes with the framework (metal sites, acid sites) or the extra-framework cations. Double bonds have an electric multipolar moment which may interact with the electric field within the pores. Consequently, the expected order of elution is *n*-octane < 1-octene < *p*-xylene. This hypothesis is in fair agreement with the observed order of elution for RHO-ZMOF and zeolite NaY due to the counterions (DMA⁺ (DMA = dimethylacetamide) and Na⁺ for RHO-ZMOF and zeolite NaY, respectively) [48]. Nevertheless, 1-octene is preferentially adsorbed by MOFs with open metal sites (HKUST-1 and CPO-27-Ni) with respect to *p*-xylene.

Such a difference can be explained by the lower steric hindrance of alkenes that can additionally coordinate with the metal centers through the double bond. The adsorption selectivity based on the presence of CUSs has been firstly investigated with HKUST-1 by Semanscin et al. for the separation of ethane/ethene binary mixtures [49]. A computational study showed that ethylene interacts more strongly than ethane through hydrogen bonding interactions established between the oxygen atoms from the copper paddlewheel units and the $-\text{CH}_2$ protons of ethylene [50]. In the case of MIL-100(Fe), propene is retained within the structure by interactions with the iron trimers [51]. However, the partial reduction of Fe^{3+} into Fe^{2+} enhances the propylene/propane selectivity and increases the isosteric heat of propylene adsorption from -30 to -70 kJ mol^{-1} . The influence of the nature of the metal has also been studied for the $\text{M}_2(\text{dobdc})$ series by J.R. Long. This material exhibits high density of open metal sites and therefore may interact significantly with unsaturated molecules. The selectivity for ethylene/ethane and propylene/propane mixtures follows the trend $\text{Fe}^{2+} > \text{Mn}^{2+} > \text{Ni}^{2+} \approx \text{Co}^{2+} > \text{Mg}^{2+} > \text{Zn}^{2+}$ which is correlated to the softness of the metal center [52].

The adsorption selectivity for *o*-xylene (OX)/*p*-xylene (PX) mixture was also investigated by Pirngruber et al. for these categories of materials and emphasizes the potential of MOFs for the adsorption of specific molecules. Both molecules (OX and PX) may be distinguished on the basis of their dipole moment (0.64 and 0.00 D for OX and PX, respectively) and their critical diameter (7.4 and 6.7 Å for OX and PX). It appears that NaY, RHO-ZMOF, CPO-27-Ni, HKUST-1, and ZIF-76 are ortho-selective unlike ZIF-8 and siliceous zeolite β . The para-selectivity of ZIF-8 is due to a molecular sieving and, in the case of zeolite β , it can be explained by a favored arrangement of PX within the pores. This selectivity between xylene isomers may also be found in the mesoporous MIL-101(Cr) [53]. OX exhibits stronger retention caused by interactions between its two methyl groups and the terephthalate ligands of the MIL-101(Cr) framework. Moreover, the higher polarity of OX compared to PX leads to a more favorable adsorption within the pores [54].

The shape of the pores can also impact the adsorption properties and selectivity of MOFs for hydrocarbons. Serre et al. studied the effect of this parameter on the adsorption of benzene, linear and branched alkanes [55] into three different MOFs: UiO-66(Zr), MIL-125(Ti), and CuBTC (Fig. 5.2). UiO-66(Zr) is composed of $\text{Zr}_6\text{O}_4(\text{OH})_4$ hexanuclear oxoclusters interconnected through 12 terephthalate anions to give a cfc porous structure comprising large octahedral and small tetrahedral pores with a diameter of 10 and 7 Å respectively. MIL-125(Ti) is built up from $\text{Ti}_8\text{O}_8(\text{OH})_4$ oxoclusters 12-fold connected through 12 terephthalate anions to form a cubic-centered network comprising large octahedral and small tetrahedral pores with diameters of 12 and 6 Å, respectively. CuBTC (or HKUST-1) is formed from a combination of copper (II) dimers and benzene-1,3,5-tricarboxylate leading to the presence of large cages with diameters of 10 and 12 Å and smaller octahedral cages of 5.6 Å. In contrast to the other selected MOFs the adsorbate can pass through the large cages of HKUST-1 without passing through the small cages.

For these three materials, adsorption occurs first within the small cages (tetrahedral cages). Slight differences can nevertheless be pointed out in terms of selectivity

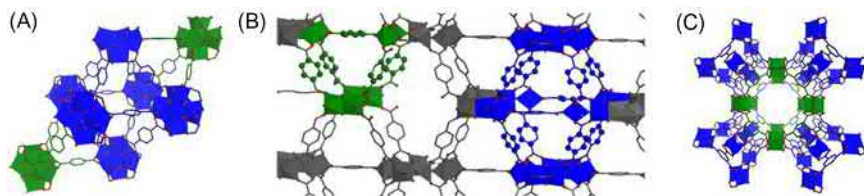


Figure 5.2 The pore structure of (A) UiO-66(Zr), (B) MIL-125(Ti), and (C) HKUST-1(Cu) where the large octahedral pore (*blue part*) is surrounded by tetrahedral pores (or channel) (*green part*).

Source: Reprinted (adapted) from N.A. Ramsahye, P. Trens, C. Shepherd, P. Gonzalez, T.K. Trung, F. Ragon, C. Serre, The effect of pore shape on hydrocarbon selectivity on UiO-66 (Zr), HKUST-1 and MIL-125(Ti) metal organic frameworks: insights from molecular simulations and chromatography, *Microporous Mesoporous Mater.* 189 (2014) 222–231. Copyright (2013) with permission from Elsevier.

Table 5.2 Selectivity for binary mixtures of hydrocarbons (50:50) in selected materials at 0.1 kPa evaluated from configurational bias grand canonical Monte Carlo simulations

	UiO-66(Zr)	MIL-125(Ti)	CuBTC
22DMB/ <i>n</i> C6	7.6	0.5	0.82
23DMB/ <i>n</i> C6	5.2	0.61	0.79
<i>n</i> C6/2MP	0.9	6.8	3.9
Benzene/ <i>n</i> C6	5.5	1.4	1.5

for the three types of hydrocarbons studied (Table 5.2). For UiO-66(Zr), the adsorption in small cages is governed by the degree of confinement. Therefore, bulkier branched alkanes 2,2-dimethylbutane (22DMB), 2,3-dimethylbutane (23DMB), and 2-methylpentane (2MP) are preferentially adsorbed from a binary mixture with *n*-hexane. The branched isomers have more numerous interactions with the pore wall. In the case of *n*-hexane, the different carbon groups of the molecule ($-\text{CH}_2$ and $-\text{CH}_3$ groups) may not interact with the structure due to a possible mismatch between the pore shape and the linear conformation of the alkane [56]. For MIL-125(Ti) and CuBTC a reverse selectivity is observed due to a better interconnection between the small and large cages delimiting almost small 1D channel. Indeed, *n*-hexane molecules remain linear and the $-\text{CH}_3$ and $-\text{CH}_2$ groups can interact more efficiently with the structure. It has to be noticed that for the three MOFs studied, benzene is always preferentially adsorbed compared to *n*-hexane. This is due to the formation of stacking configurations with the aromatic rings of the organic linker (a parallel alignment of benzene with the aromatic ring of the ligand). But this selectivity is less pronounced for MIL-125(Ti) and CuBTC as a result of the open tetrahedral pockets which diminish the confinement effect. In UiO-66(Zr), these pockets are closed and in order to make molecules enter into the pore, a rotation of the two phenyl rings of the organic linkers is required leading to a larger aperture.

The impact of the MOF topology has also been explored by De Vos et al. for the separation of xylene isomers [57]. Three MOFs (MIL-125(Ti), MIL-125(Ti)-NH₂, and CAU-1(Al)-NH₂) have been selected for a better understanding of their para-selectivity for a vapor mixture of *p*-, *o*-, and *m*-xylenes. On the basis of the computational analysis and experimental results, it appears that the combination of narrow tetrahedral and larger octahedral cages induces this para-selectivity. Accommodating xylene isomers within the small tetrahedral cages requires energy. However, because of their different kinetic diameter, the energy penalty for each isomer differs and follows the trend: PX < OX < MX. Moreover, several PX molecules may be adsorbed into the tetrahedral cages while OX and MX are too large and, therefore, present some difficulties to enter this cage. Consequently, it leads to enhancement of the selectivity for PX. In addition, microcalorimetric experiments showed that at low and high loadings, the adsorption enthalpy for PX is much more negative than those for MX and OX. This is due to a better host/guest interaction with the structure and a more efficient intermolecular packing arrangement between PX molecules.

For complementary information, we suggest to read the review of Long dealing with the separation of hydrocarbons by MOFs [58] and the one of Eddaoudi discussing the structure/separation relationship for hydrocarbon vapors [59].

5.2.2 Alcohols

Methanol is a precursor for the synthesis of more complex molecules of great importance such as ethylene and propylene and can also be considered as a bioderived fuel [60]. However, this alcohol possesses strong toxic side effects such as blindness (alcoholic beverage) [61]. Methanol vapors induce less significant damage to human beings but may cause nausea, fatigue, and irritation in the throat or airways [62]. Long-term ethanol vapor exposure produces psychological effects such as depression and anxiety [63]. Exposure to isopropanol for a long period of time may also provoke clinical symptoms of toxicity manifested by hypoactivity, ataxia, prostration, and kidney damages [64]. These chemicals may be found in body care and everyday products.

Due to their hydrophilic character, zeolites are usually preferred over activated carbons for the capture of alcohols. Zeolites are widely studied for the removal of water from bioethanol by tuning the pore size and the hydrophilic character [65] and are also used for the selective capture of biobutanol from the fermentation broth in the presence of water [66]. However, these acidic sorbents may catalytically convert alcohols into potentially more harmful chemicals [67]. MOFs therefore represent alternative candidates due to their high loading capacity and high adsorption selectivity for alcohols without playing any catalytic role and, therefore, avoiding the formation of undesirable by-products [68,69]. It is noteworthy that the separation of alcohols was mainly reported previously in liquid phase while this chapter only focuses on the adsorption of alcohol vapors [70,71].

Flexible MOFs are of great interest due to their unusual selective sorption behavior. This is mainly due to their ability to change their pore size in response to a stimulus (chemical, pressure, temperature). McGrail et al. designed a flexible MOF

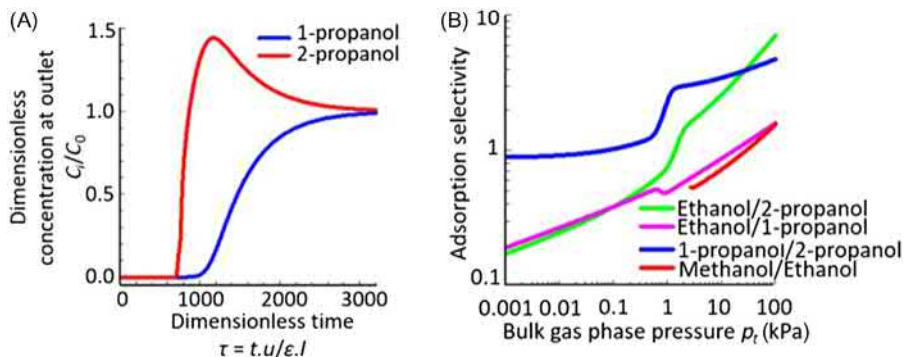


Figure 5.3 (A) Breakthrough simulation characteristics for the separation of 50/50 mixture of 1-propanol (*blue line*) and 2-propanol (*red line*) in an adsorber packed with TetZB at 20 kPa and 298K. (B) Adsorption selectivity obtained by IAST calculations for equimolar mixtures of ethanol/2-propanol (*green line*), ethanol/1-propanol (*pink line*), 1-propanol/2-propanol (*blue line*), and methanol/ethanol (*red line*) mixtures in TetZB at 298K.

Source: Reproduced (adapted) from R.K. Motkuri, P.K. Thallapally, H.V.R. Annapureddy, L. X. Dang, R. Krishna, S.K. Nune, C.A. Fernandez, J. Liu, B.P. McGrail, Separation of polar compounds using a flexible metal-organic framework, *Chem. Commun.* 51 (2015) 8421–8424 with permission of The Royal Society of Chemistry.

named TetZB from zinc nitrate, tetrakis[4-(carboxyphenyl)-oxamethyl]methane, and bipyridine for the adsorption of polar solvents such as propanol isomers, methanol, ethanol, water, acetone, and chloroform [72]. The flexible character of TetZB is due to the ability of the benzoate ring to twist around the central quaternary carbon allowing the organic linker to adopt different geometries such as tetrahedral, near-flattened, and irregular. The transient breakthrough simulation at 298K for a binary mixture (50/50) of 1-propanol and 2-propanol shows that both molecules can enter into the pores (Fig. 5.3). However, the first one exhibits a higher retention time even though these sorbates possess the same kinetic diameter (4.7 Å). This difference arises from the more linear shape of 1-propanol compared with 2-propanol which allows its easier adsorption into the pores. This indicates that this separation is mainly governed by molecular packing effects in favor of linear molecules compared to branched isomers. Ideal adsorbed solution theory (IAST) calculations for equimolar vapor mixtures of ethanol/2-propanol, ethanol/1-propanol, 1-propanol/2-propanol, and methanol/ethanol can give two main tendencies (Fig. 5.3). At low pressures below 1 kPa, adsorbates with long chains are preferentially retained within the structure. The same behavior is also observed for ZIF-8 and SAPO-34 [73,74]. However, at higher pressures above 1 kPa, the selectivity is reversed and the adsorption of smaller molecules is favored. This phenomenon is due to the higher saturation capacity of small alcohols.

The potentiality of flexible MOFs has also been explored by Férey et al. for MIL-53(Cr) [75]. This material was investigated by adsorption gravimetry, microcalorimetry, ex situ X-ray powder diffraction, thermal analysis, IR spectroscopy,

and molecular modeling. It appears that two structural transitions are induced by the adsorption of methanol and ethanol vapors (partial closing and reopening of the pores). In the narrow-pore form, four alcohol molecules are present per unit cell and in interaction with $-OH$ groups of the structure. Microcalorimetric measurements coupled to DFT calculations showed that the adsorption of ethanol is more energetically favored than methanol or water. This suggests a possible separation of ethanol vapors in humid conditions. It is interesting to note that two types of host/guest interactions have been identified: (1) hydrogen bonds between μ_2-OH groups from the surface of the MOF structure and the oxygen atom from the hydroxyl group of the alcohols; and (2) hydrogen bonds between the oxygen atoms from the carboxylate group of the organic linker and hydrogen from the alcohol. A dynamic pore-opening/pore-closing process occurs during the selective adsorption of C1–C3 alcohols by the flexible 1D MOF $[Cu(BF_4)_2(bpp)_2]$ ($bpp = 1,3$ -bis(4-pyridyl)propane) [76]. Without adsorbate within the structure, this material presents hexagonal cavities surrounded by six BF_4^- anions and does not show open porosity. The synchrotron powder analysis and single-crystal structural analysis explain the mechanism underlying the adsorption process. The adsorbate induces a dynamic structural transformation allowing the guest to enter into the hexagonal cavity followed by the pore-closing (Fig. 5.4). Methanol, ethanol, 1-propanol, and 2-propanol may be adsorbed according to this mechanism, unlike 1-butanol. The reason is that 1-butanol does not fit with the hexagonal cavity and therefore cannot induce the dynamic structural transformations required for the adsorption, resulting to its exclusion. This last example illustrates how MOF may separate alcohol molecules according to the molecular sieving effect.

Liquid-phase epitaxial (LPE) growth technique, also known as step-by-step deposition, was used to process thin films of MOFs with tunable properties such as the thickness, the size, and orientation of the MOF crystallites. Fischer et al. used this technique for the design of heterostructures containing more than one type of MOF (Fig. 5.5) [77]. The selected materials belong here to the $[Zn_4O(\text{carboxypyrazolate})_3]_n$ class of compounds and are combined to give a hierarchical structure. $[Zn_4O(3\text{-methyl-5-isopropyl-4-carboxypyrazolate})_3]_n$ (Zn-MI) and $[Zn_4O(3,5\text{-dimethyl-4-carboxypyrazolate})_3]_n$ (Zn-DM) may be associated to give a material denoted Zn-MI(x)-Zn-DM(y) (x and y refer to the number of deposition cycles of

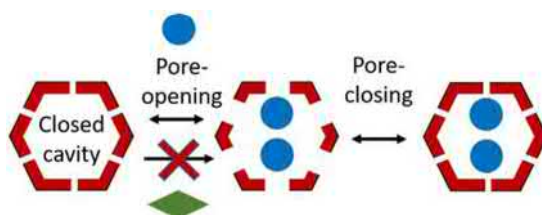


Figure 5.4 Illustration of the dynamical structural transformation of $[Cu(BF_4)_2(bpp)_2]$ leading to the adsorption of suitable species (blue disk) and the exclusion of nonsorbable species (green lozenge). BF_4^- anions are illustrated by red blocks.

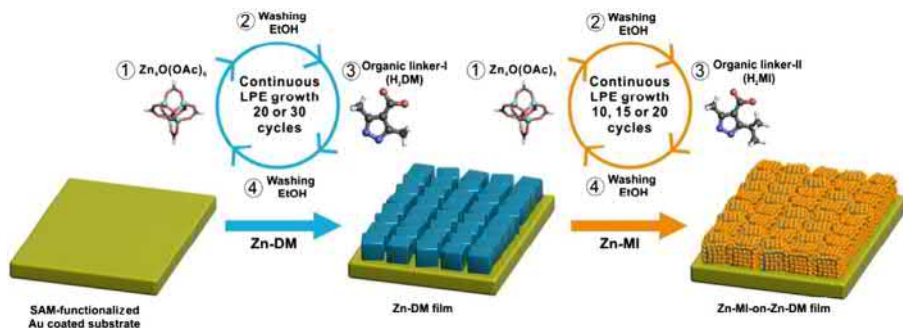


Figure 5.5 Illustration of the LPE process for the fabrication of heterostructured $[\text{Zn}_4\text{O}(\text{carboxypyrazolate})_3]_n$.

Source: Reproduced (adapted) from S. Wannapaiboon, M. Tu, K. Sumida, K. Khaletskaya, S. Furukawa, S. Kitagawa, et al., Hierarchical structuring of metal-organic framework thin-films on quartz crystal microbalance (QCM) substrates for selective adsorption applications, *J. Mater. Chem. A* 3 (2015) 23385–23394 with the permission of The Royal Society of Chemistry.

each MOF component), where Zn-DM is firstly formed on the substrate followed by the deposition of Zn-MI. Zn-DM presents a window aperture of $4 \times 4 \text{ \AA}$ with a pore diameter evaluated at 6 \AA [78]. Due to the bulkier chemical groups present in the ligand, Zn-MI exhibits smaller windows, the size of which is not given in the literature to the best of our knowledge. This assembly has been used for the selective adsorption of alcohols with various kinetic diameters (methanol (MeOH), 3.6 \AA ; isopropanol (iPrOH), 4.7 \AA) and in the presence of water (kinetic diameter of 2.6 \AA).

This technique allows tuning the adsorption properties of the final materials by varying the number of deposited MOF layers and thus, the composition of the shell surrounding the first deposited MOF. In the case of Zn-MI(x)-Zn-DM(y), the amount of methanol adsorbed increases from pure Zn-MI to pure Zn-DM with intermediate values for a mixture of them ($x = 10\text{--}20$ and $y = 20\text{--}30$). However, by using isopropanol as the adsorbate, the difference in adsorption capacity is less pronounced for heterostructures and remains similar to Zn-MI (Fig. 5.6). The accessibility of isopropanol being limited by the pore size of Zn-MI, and since Zn-MI constitutes the shell of Zn-DM with larger pores, isopropanol cannot penetrate the material. This complex structure is therefore capable of selectively adsorbing molecules according to a molecular sieving effect. Moreover, in the context of MeOH/water coadsorption, despite its smaller kinetic diameter, water is not adsorbed within the heterostructure while MeOH shows the same adsorption behavior as in pure phase. This specific selectivity is due to the intrinsic MOF hydrophobic character even in the presence of a binary mixture. This study demonstrates the ability of MOFs to selectively adsorb alcohol molecules according to their kinetic diameter, even in the presence of water, by varying the window aperture of the material.

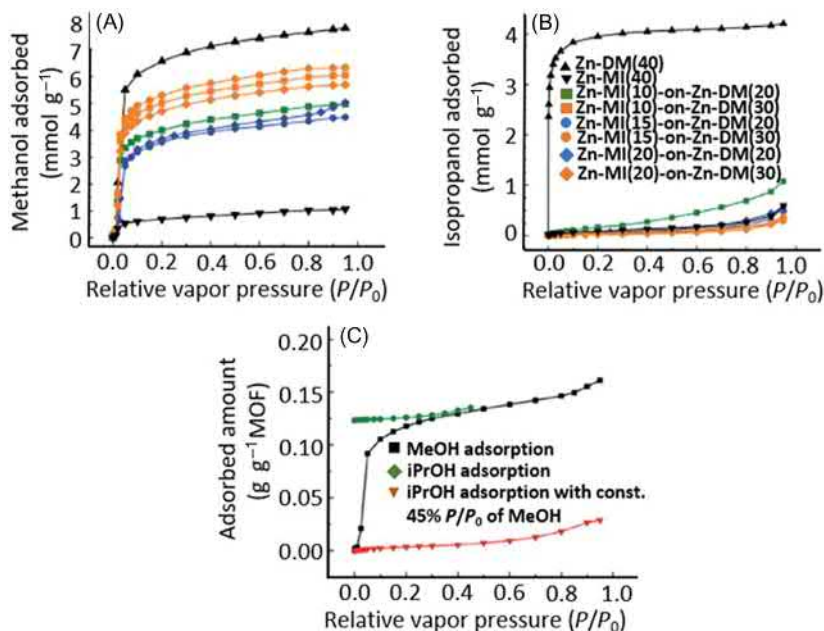


Figure 5.6 Adsorption isotherms of (A) methanol and (B) isopropanol at 25°C obtained with an environmental-controlled QCM for heterostructured materials Zn-MI(x)-on-Zn-DM(y). Adsorption isotherms of (C) isopropanol in the presence of 45% p/p_0 of methanol (*red triangle*) with the single component isotherms of methanol (*black square*) and isopropanol (*green square*) as references.

Source: Reproduced (adapted) from S. Wannapaiboon, M. Tu, K. Sumida, K. Khaletskaia, S. Furukawa, S. Kitagawa, et al., Hierarchical structuring of metal-organic framework thin-films on quartz crystal microbalance (QCM) substrates for selective adsorption applications, *J. Mater. Chem. A* 3 (2015) 23385–23394 with the permission of The Royal Society of Chemistry.

For more information about the selective adsorption and separation of alcohol vapor but also in liquid phase, we recommend reading the article of Li et al. [79].

5.2.3 Carbonyl compounds: aldehydes, ketones, and carboxylic acids

A few aldehydes and ketones such as formaldehyde, acetaldehyde, acetone and acrolein are classified as VOCs and present a strong negative environmental impact. Cooking is one of their major sources (e.g. barbecue) for aldehydes while ketones can be released from the use of paint thinners. Formaldehyde and acrolein are considered as highly carcinogenic and may provoke eye and respiratory irritations [80,81]. Acetone may be found in paint thinners and causes irritative and narcotic effects [82]. Due to their higher boiling point compared to other VOCs, carboxylic

acids are considered as semivolatile organic compounds (SVOCs). Oxidation of VOCs such as alkenes in the atmosphere can lead to the formation of carboxylic acids in the presence of ozone. As a result, formic and acetic acids are involved in the formation of acid rain [83]. Moreover, they can also be produced from cellulose-containing objects such as papers stored in libraries and archives [84]. An increase of carboxylic acid concentration may also lead to severe respiratory problems affecting, for example, the development of small airways in lung [85].

Amongst all carbonyls, formaldehyde is one of the most studied VOC adsorbates. Activated carbons are mainly used as adsorbents for its removal because of their high surface area and their high uptake capacity [86]. In the case of acetone, activated carbons are also typically used [87] while a combination of zeolites and an oxidant-generating device has been shown to be efficient for the removal of this VOC from air [88]. In the case of activated carbons, the adsorption of ketones may induce their transformation, such as for instance, the decomposition of methyl ethyl ketone (MEK) into 2,3-butanediol [89]. This type of side-reaction may also occur with zeolites but usually the use of hydrophobic zeolites with a controlled surface chemistry can circumvent that problem. This is why hydrophobic zeolites are generally preferred over activated carbons for the adsorption of ketones and aldehydes. The main disadvantages of zeolites are a loss of performance at high carbonyl concentrations and their limited uptake capacity. In the case of carboxylic acids, the choice of a suitable adsorbent is also dependent on the regeneration process. Because of their higher boiling point, the desorption process takes place at high temperatures, typically higher than 120°C. Consequently, activated carbons are not suitable for this separation. In contrast, zeolites may be used due to their high thermal stability [90]. However, the regeneration of zeolites requires a desorption step at high temperature due to the strong affinity of this adsorbent for carboxylic acids and this results in an energy penalty for the separation process. Concerning the adsorption of carbonyl compounds by MOFs, the available data are, to our knowledge, still very scarce.

According to Lamonier et al., an efficient adsorbent for formaldehyde must possess a combination of small pore sizes, high specific surface, and high micropore volume. The choice of the metal, such as Al, Ag, and Cu, is also crucial and may improve the adsorption efficiency [91]. Moreover, it has been shown that functional groups like hydroxyl, pyridonic, and pyridinic structures may improve the adsorption of aldehydes. From that statement, Zheng et al. compared the performance of MIL-101(Cr) and its ethylenediamine (ED) grafted-homolog (Fig. 5.7) [92]. It showed that the presence of ED significantly increased the amount of adsorbed formaldehyde within the structure, from 3.34 mmol g⁻¹ for bare MIL-101(Cr) to 5.49 mmol g⁻¹ for ED-MIL-101(Cr)-3 (MIL-101(Cr) modified with 18.5 mmol of ED). This last adsorption value is much higher than that reported for other adsorbents such as activated carbon and zeolites (~0.04 mmol g⁻¹), ferrihydrite/SiO₂ (0.27 mmol g⁻¹), and is in line with other amine-grafted porous solids such as amine-grafted silicas (4.3 mmol g⁻¹). According to Jones et al. the mechanism of formaldehyde adsorption in the presence of an amine (Fig. 5.7) can be explained by the attack of the lone pairs of nitrogen atoms (amines) by the carbonyl carbon followed by a proton exchange process leading to an unstable hemiaminal

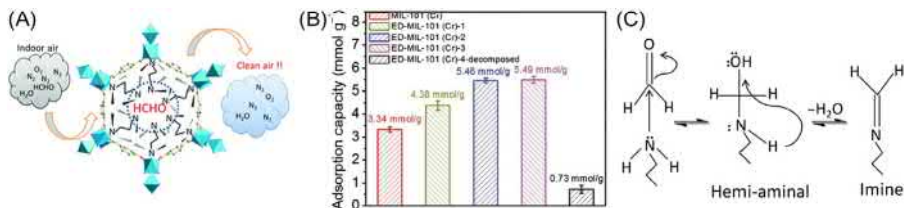


Figure 5.7 (A) Uptake of formaldehyde in ED-MIL-101(Cr). (B) Formaldehyde adsorption capacities of as-synthesized MIL-101(Cr) (red column) and of modified MIL-101 containing 1.32 mmol g⁻¹ (green column), 2.38 mmol g⁻¹ (blue column), 2.47 mmol g⁻¹ (pink column) of grafted ED and of the decomposed MIL-101(Cr). (C) Mechanism of imine formation from diamine and formaldehyde.

Source: Reproduced (adapted) from Z. Wang, W. Wang, D. Jiang, L. Zhang, Y. Zheng, Diamine-appended metal-organic frameworks: enhanced formaldehyde-vapor adsorption capacity, superior recyclability and water resistibility, *Dalton Trans.* 45 (2016) 11306–11311 with the permission of The Royal Society of Chemistry.

intermediate. Then, dehydration occurs to form an imine. All these reactions are reversible and consequently, ensure the recyclability of the adsorbate. Lamonier et al. have also confirmed this reversible adsorption–desorption process for MIL-53(Ga). However, this material exhibited lower uptake capacity compared to zeolites NaX, NaY, and CuX due to the presence of extra-framework cations. It was also noticed that formaldehyde polymerizes into paraformaldehyde within the pores of these zeolites and, consequently, between 2% and 8% of the adsorbed molecules could not be desorbed except at temperatures above 200°C. Moreover, these materials are strongly hydrophilic and interact with water molecules leading to a competition between formaldehyde and water, especially when one of them is very diluted.

Adsorption of acetone by CuBTC has been investigated by Trens et al., both experimentally and computationally [93]. It appears that acetone may be located at the center of the octahedral cages or coordinated to Cu(II) without any significant preference (similar adsorption energies comprised between -50 and -60 kJ mol⁻¹). Interestingly, desorption under vacuum leads to an almost complete regeneration of the adsorbent. However, the total recovery occurs when the material is exposed to humid atmosphere.

Until now, only a few studies have been reported for the capture of carboxylic acids by using MOFs, despite their notorious impact on the environment. In order to better understand the possible benefit of considering MOFs for acetic acid adsorption, Pinto et al. studied the impact of the organic linker functionalization, the pore size, and the hydrophobicity character of several MOFs in the context of the preservation of historical objects [94]. On the basis of the acetic acid isotherm results, the Henry's constant was evaluated for a series of MOFs: MIL-101(Cr), MIL-101(Cr)-en [en = ethylenediamine] (also named ED-MIL-101(Cr)), UiO-66, UiO-66-NH₂, UiO-66-2CF₃, UiO-NDC, ZIF-8, MIL-140A and B (Table 5.3). It appears that MIL-101(Cr), MIL-101(Cr)-en, and UiO-66-NH₂ show the best performances in pure phase. MIL-101(Cr) adsorbs a significant amount of acetic acid

Table 5.3 Evaluated Henry's constant of acetic acid adsorption at 25°C (K_H) and water adsorption at 30°C (K_w)

Material	Mean \pm SD		
	K_H (mmol g ⁻¹)	K_H (g _{vapor} g ⁻¹ _{sample})	K_w (mmol g ⁻¹)
MIL-101-Cr	212 \pm 7	12.7 \pm 0.4	46.8 \pm 2.5
MIL-101-Cr-en	89 \pm 5	5.4 \pm 0.3	18.3 \pm 0.1
UiO-66	21 \pm 1	1.2 \pm 0.1	20.4 \pm 2.9
UiO-66-NH ₂	193 \pm 21	11.6 \pm 1.3	27.2 \pm 1.2
UiO-66-2CF ₃	33 \pm 1	2.0 \pm 0.1	8.9 \pm 0.7
UiO-NDC	2.1 \pm 0.4	0.12 \pm 0.03	7.0 \pm 0.5
MIL-140A	2.1 \pm 0.1	0.13 \pm 0.01	2.1 \pm 0.2
MIL-140B	19 \pm 1	1.13 \pm 0.07	1.00 \pm 0.02
ZIF-8	0.5 \pm 0.1	0.03 \pm 0.01	0.67 \pm 0.002

These both constants were calculated from the initial slope of the isotherms.

thanks to its high pore volume and the presence of CUSs. However, it has to be noticed that the grafting of ethylenediamine on the metal center leads to a decrease of this adsorption efficiency due to a reduction of the pore volume. The case of UiO-66-NH₂ illustrates the impact of the functionalization of the organic linker on the adsorption of acetic acid since this compound exhibits the best performance compared to the other UiO-66 type MOFs. This study also demonstrated that the pore size effect has a strong impact on the affinity for the adsorbate. The comparison between isorecticular structures such as UiO-66/UiO-NDC and MIL-140A/MIL-140B indicates that a suitable pore size is a key parameter for an efficient adsorption. However, under realistic conditions of the preservation of cultural heritage in museums, acetic acid is released in a humid ambient atmosphere. It may be expected that the performance of adsorbents may dramatically change in humid conditions. Therefore, the coadsorption of acetic acid in the presence of water might be considered to evaluate the performance of adsorbents. In a homemade box composed of a sensor capable of evaluating the acetic acid concentration over time, the capture efficiency was compared between the selected adsorbents at 40% of relative humidity (RH) (Fig. 5.8). Here, a small amount of acetic acid is first injected in a closed chamber with humid atmosphere in the presence of the adsorbent. The concentration of acetic acid vapor in the chamber is measured with time. The lower the final acetic acid concentration is, the higher the adsorption capacity of the material is. Because of a potential competition between water and acetic acid molecules, hydrophobicity may increase the selectivity toward less polar molecules than water such as acetic acid for this study. Therefore, the performance of the less hydrophobic MOFs (e.g., UiO-NH₂, MIL-101, MIL-101-en) is significantly reduced compared to the results for the adsorption in pure phase. On the other hand, MIL-140B and UiO-66-2CF₃ surpass all other materials thanks to three main parameters: hydrophobicity, suitable pore size (MIL-140B), and strong interactions with the adsorbate ($-CF_3$ groups). Such results are confirmed by molecular simulations.

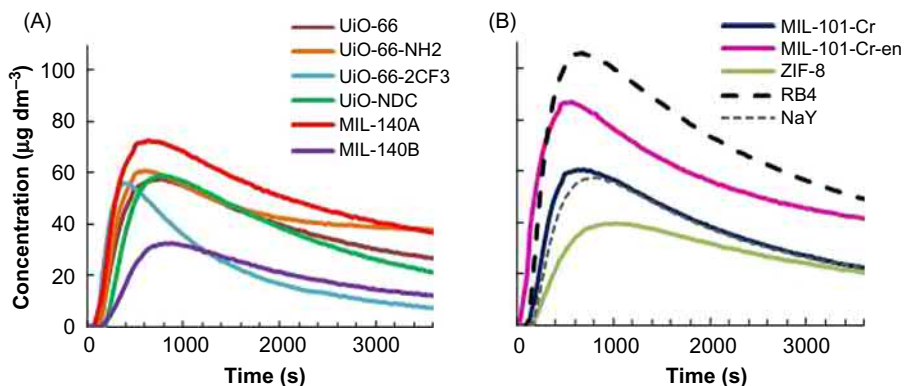


Figure 5.8 Acetic acid concentration over time inside a closed chamber at 23°C, 40% of humidity rate after the injection of 1 μL of acetic acid in the presence of 50 mg of (A) UiO-66 (brown), UiO-66-NH₂ (orange), UiO-66-2CF₃ (blue), UiO-NDC (green), MIL-140A (red) and MIL-140B (purple); and (B) MIL-101(Cr) (dark line), MIL-101(Cr)-en (pink line), ZIF-8 (green line), activated carbon RB4 (dashed black line), and zeolite NaY (dashed gray line).
 Source: Reprinted (adapted) with permission from K. Dedecker, R.S. Pillai, F. Nouar, J. Pires, N. Steunou, E. Dumas, G. Maurin, C. Serre, M.L. Pinto, Metal-organic frameworks for cultural heritage preservation: the case of acetic acid removal, ACS Appl. Mater. Interfaces 10 (2018) 13886–13894. Copyright (2018) American Chemical Society.

5.3 Design of metal-organic frameworks for the capture of toxic chemicals

5.3.1 Sulfur-containing compounds: sulfur dioxide

Sulfur dioxide is a gas inducing acid rains but is also harmful for human populations because of its irritating effects. SO₂ emissions are increasing due to human activity. These anthropogenic emissions come mainly from the combustion of coal and fuel containing some traces of sulfur compounds which are then oxidized into sulfur dioxide. Typically, in the case of coal, the gas produced after combustion can show a sulfur dioxide concentration between 500 and 3000 ppm [95]. Usually, a large part of that concentration (above 95%) is reduced by using different processes such as Wellman–Lord process and flue-gas desulfurization [96]. However, despite these precautions, traces of SO₂ are still released in the environment, although in urban regions its concentration should not exceed 8 ppb as recommended by the World Health Organization (WHO) [97]. Therefore, in order to reduce its impact on health and environment, it has been considered to use adsorbents for the SO₂ capture.

Usually, this adsorption process occurs in an atmosphere containing water and oxygen. In this case, activated carbons form strong interactions with SO₂ leading to the formation of sulfuric acid. Their uptake capacity is generally high because of their microporosity and specific area. However, it requires a treatment to remove

the by-products (H_2SO_4 or sulfate salts if hydroxides are impregnated into the material). Zeolites are also good candidates because of their microporosity and the strong influence of counter-cations on the adsorption capacity. However, the stability is a major concern for some of them (e.g., calcium-exchanged zeolite type Y) resulting in the formation of sulfate salts that are difficult to remove for the regeneration of the adsorbent. MOFs may be tuned for a suitable pore size inducing numerous interactions with SO_2 . Moreover, the stability of the material may be controlled to facilitate the regeneration of the material.

For a better comprehension of the parameters that drive the adsorption of SO_2 by MOFs, Qiu et al. recently published a molecular modeling study, dealing with the correlation between the structure of MOFs and their SO_2 uptake capacity. Ten typical MOFs were considered (IRMOF-1, -8, -9, -10, -15, MOF-177, MOF-505, CuBTC, MIL-47, and ZIF-8) [98]. At low pressure, the heat of adsorption is the most important parameter. In order to optimize this effect, a suitable pore size must be chosen to maximize the interactions between the structure and the gas molecules. Thus, ideally the pore size must be at least 0.4 nm what is close to the SO_2 dynamic diameter (4.11 Å). As a result, MOF-505 exhibits the highest uptake among the selected MOFs. At higher pressure, the main parameters are the free volume and accessible specific area which correlate well with the SO_2 uptake capacity. At 10^6 Pa (10 bar), IRMOF-10, MOF-177, and IRMOF-15 are the best materials. At intermediate pressures, heat adsorption, free volume, and accessible specific area must all be considered for an optimized SO_2 adsorption.

MFM-300(In) [$\text{In}_2(\text{OH})_2(\text{L})$] (H_4L = biphenyl-3,3',5,5'-tetracarboxylic acid) has been studied by Schröder et al. for its potential adsorption properties for SO_2 [99]. In situ synchrotron powder and single-crystal X-ray diffraction experiments have been carried out for the determination of the SO_2 molecule positions within the structure. Two sites of adsorption (SO_2^{I} and SO_2^{II}) have been established. The first site is located near the inorganic chain where hydroxyl groups interact with SO_2 ($\text{O}=\text{S}=\text{O}^{\text{I}}\cdots\text{H}-\text{O}$). The second site is located perpendicularly to SO_2^{I} ($\text{O}=\text{S}=\text{O}^{\text{II}}\cdots\text{S}=\text{O}^{\text{I}}$) leading to a high molecular compacity and a high SO_2 uptake evaluated at 8.28 mmol g^{-1} at 298K and 1 bar. Moreover, this material may be regenerated after adsorption by heating at 373K for 2 hours under reduced pressure and shows stability toward SO_2 uptake.

In order to obtain an adsorbent with better performances, Xing et al. studied four MOFs named SIFSIX-Cu-1, SIFSIX-Cu-2, SIFSIX-Cu-2-*i* (*i* = interpenetrated), and SIFSIX-Zn-3 presenting a pillared square-grid 3D structure where SiF_6^{2-} anions separate the metal centers [100]. Amongst them, SIFSIX-Cu-1 exhibits the highest SO_2 uptake with 11.01 mmol g^{-1} at 298K and 1 bar. This high value can be explained by the favorable $\text{S}^{\delta+}\cdots\text{F}^{\delta-}$ and $\text{O}^{\delta-}\cdots\text{H}^{\delta+}$ (hydrogen atoms from the organic linker) interactions which allow to keep four SO_2 molecules in an unit cell (Fig. 5.9). In addition, these adsorbed molecules may interact with two other SO_2 molecules to allow a secondary adsorption. SIFSIX-2-Cu possesses a lower adsorption efficiency because of its longer organic linker which induces an increase of the pore size and consequently diminishes the degree of confinement effect. This impact of the pore size is illustrated with SIFSIX-3-Zn for which the smaller pore

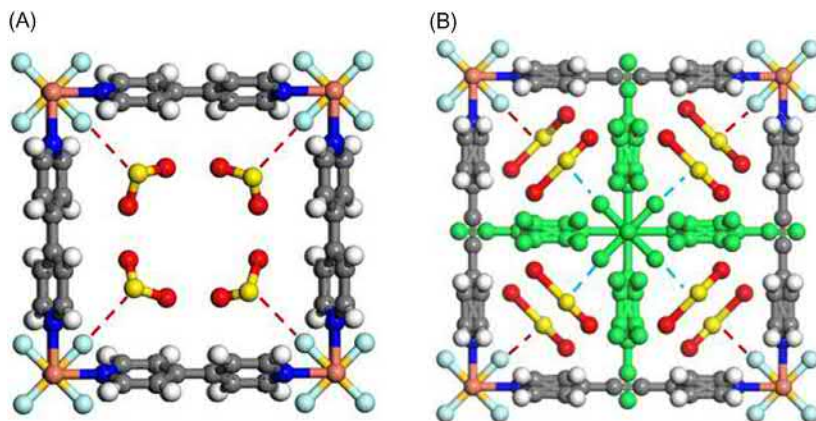


Figure 5.9 Crystal structure of (A) SO₂-loaded SIFSIX-1-Cu and (B) SIFSIX-2-Cu-i obtained from Rietveld refinement. Color code: (A) F, light blue; Si, light orange; C, gray; H, white; N, blue; Cu, light pink; O, red; S, yellow; S-F interaction, red dashed line; (B) the first interpenetrated net, normal colors; the second net, green; S-F interaction in the first net, red dashed line; S-F interaction in the second net, blue dashed line.

volume limits the SO₂ uptake despite its high adsorption enthalpy (54.1 kJ mol⁻¹). Interestingly, at low partial pressure, SIFSIX-2-Cu-i adsorbs more SO₂ than SIFSIX-Cu-1 (2.31 vs 1.80 mmol g⁻¹ at 0.002 p/p_0 at 298K). This is mainly due to the higher compacity of the structure leading to stronger intermolecular interactions.

In 2016, the stability of MOF was evaluated in conditions of the SO₂ capture. S. Nair et al. established that ZIF-8 (considered as a robust MOF in many conditions) was not chemically stable in the presence of SO₂ [101]. The structure remains intact with dry SO₂ gas or only with water vapor but in the presence of 10–20 ppm of SO₂ and 85% RH, the degradation of ZIF-8 occurs. It has been shown that H₂SO₃ and H₂SO₄ produced from SO₂ and water during the experiment induce the protonation of imidazolate (ZIF-8 organic linker) and lead to the formation of (bi) sulfite and (bi)sulfate groups and thus to the degradation of the MOF. The same year, another study has been published concerning the stability of MIL-125(Ti) and MIL-125-NH₂(Ti) toward SO₂ uptake [102]. Amongst both materials, MIL-125(Ti) is of lower stability than MIL-125-NH₂. As for ZIF-8, bisulfite by-products have been identified and therefore an identical degradation mechanism was proposed.

For complementary information, we recommend the review of Jones concerning the removal of SO₂ by various materials including activated carbons, zeolites, and MOFs [103].

5.3.2 Sulfur-containing compounds: hydrogen sulfide

At atmospheric pressure and room temperature, hydrogen sulfide is a gas characterized by a strong smell of rotten egg. It may induce irritation to nose, eyes, and

throat at 5 ppm and may cause a loss of consciousness at a concentration greater than 500 ppm [104]. This gas may be generated naturally by the hydrolysis of metal sulfides from volcanic rocks, the activity of sulfate-reducing bacteria, and rotten vegetation. Human activity is also a contributor to H₂S emissions. One of the main sources is in oil refineries where the sulfur content of crude petroleum is removed through, for instance, the hydrodesulfurization process involving a hydrogen gas stream and leading to H₂S production as a by-product.

In order to reduce their H₂S emissions, industries developed several processes which may be categorized as following: absorption processes (amine gas treating technologies), cryogenic distillation, and adsorption processes [105]. This latter offers the possibility to develop less energy-consuming and less expensive technologies for an efficient capture of H₂S. Amongst the adsorbents used for the capture of H₂S, activated carbons have been considered as an interesting candidate due to their low cost. Pure activated carbons may be used directly but the impregnation of amines or hydroxide salts leads to increased performance [106,107]. However, due to the presence of sulfur-containing products resulting from the reaction between H₂S and amines/hydroxides, the treatment and regeneration of these adsorbents may lead to more complex and energy-consuming processes. Zeolites have also been explored for the capture of H₂S [108] as they do not necessarily require activation with chemicals such as amines. Nevertheless, high temperatures are necessary for their regeneration and therefore, their use may make the process energy-consuming and expensive. MOFs were explored in the 2000s for their tunable adsorption properties for the capture of H₂S. Their high surface area, high adsorption selectivity, and their possible regeneration at moderate temperatures make them promising materials for H₂S removal.

For the adsorption of H₂S, different factors have been explored for the selection of an efficient MOF adsorbent. De Weireld et al. conducted a comparative study between several MOFs such as MIL-53s (Al, Fe and Cr), MIL-47(V), MIL-100(Cr), and MIL-101(Cr) characterized by differences in terms of flexibility/rigidity, nature of the metal center, presence of Lewis or Brønsted acid sites, and pore size/volume (Fig. 5.10) [109]. MIL-100(Cr) and MIL-101(Cr), rigid MOFs with the largest pore size and Lewis acid sites exhibit large H₂S uptake at 2 MPa of 16.7 and 38.4 mmol g⁻¹ respectively. The rigid MIL-47(V) presents a type I isotherm and a maximum uptake capacity of 14.6 mmol g⁻¹. For the flexible MIL-53 materials, as observed previously upon CO₂ or H₂O adsorption, a two-step isotherm is observed due likely to a contraction of the structure at low pressure as a result of interactions between H₂S molecules and the OH groups from the inorganic chains. At higher pressures a pore reopening occurs due to a breaking of H₂S...OH interactions and a total filling of the pores. It appears that H₂S adsorption for MIL-100(Cr) and MIL-101(Cr) is partially reversible because of strong interactions between H₂S with the metal sites and/or a possible partial structure degradation. However, the adsorption process of H₂S by MIL-47(V) and the MIL-53 series (except for the Fe analogue which is unstable) is fully reversible.

This reversibility has also been demonstrated for MIL-68(Al), a porous material forming a three-dimensional network constituted of straight chains of corner-sharing metal-centered octahedra of formula AlO₄(OH)₂ connected to each other by

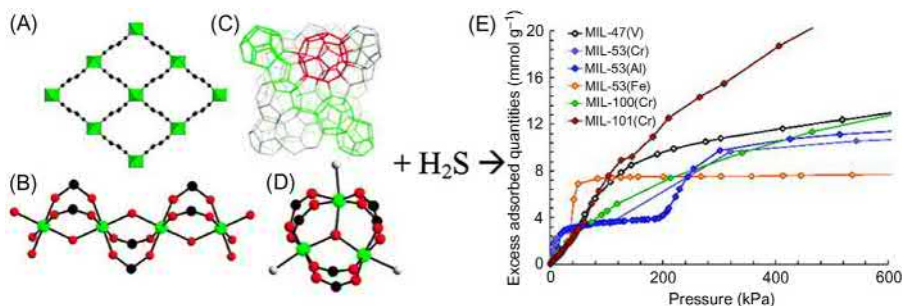


Figure 5.10 Crystalline structures of (A) the MIL-53's (Al, Cr, Fe) and MIL-47(V) composed of (B) corner-sharing chains as inorganic subunit and of (C) the MIL-100(Cr) and MIL-101(Cr) formed from (D) trimers chromium octahedra. (E) excess adsorbed quantities (mmol g⁻¹) evaluated at 303.1K for MIL-47(V) (black), MIL-53(Cr) (purple), MIL-53(Al) (blue), MIL-53(Fe) (orange), MIL-100(Cr) (green), and MIL-101(Cr) (red).

Source: Reprinted (adapted) with permission from L. Hamon, C. Serre, T. Devic, T. Loiseau, F. Millange, G. Férey, et al., Comparative study of hydrogen sulfide adsorption in the MIL-53(Al, Cr, Fe), MIL-47(V), MIL-100(Cr), and MIL-101(Cr) metal – organic frameworks at room temperature, *J. Am. Chem. Soc.* 131 (2009) 8775–8777. Copyright (2009) American Chemical Society.

terephthalate ligands and –OH groups. This assembly forms triangular and hexagonal pores with a diameter of 6.0–6.4 and 16–17 Å respectively (Fig. 5.11) [110]. Within this structure, H₂S molecules are preferentially located in the triangular pores due to the high degree of confinement leading to high adsorption energy (~21 kJ mol⁻¹) and uptake capacity (12 mmol g⁻¹ at 30°C and 12 bar). The effect of the functionalization of the organic linker was studied by Vaesen et al. for MIL-125(Ti) and MIL-125(Ti)-NH₂ structures [111]. The amount of H₂S adsorbed at 30°C and at 1 bar was evaluated at ~6 and ~8 mmol g⁻¹ for MIL-125(Ti) and MIL-125(Ti)-NH₂ respectively. The impact of the metal nature has been studied by Allan et al. with two isostructural CPO-27(M) [M = Ni, Zn] [112]. The exposure of H₂S induced the degradation of the CPO-27(Zn) structure while CPO-27(Ni) remained intact and exhibited a capacity uptake up to 12 mmol g⁻¹ at atmospheric pressure. However, the regeneration of this material, under vacuum at 150°C, was not complete and it was required to increase the desorption temperature (200°C) to allow the removal of a larger part of the adsorbate but inducing at the same time a partial degradation of the structure [113]. The MOF stability upon the H₂S sorption was evaluated for ZIF-8 and CuBTC [114]. It appears that the crystalline structure of ZIF-8 is altered under the exposure of H₂S while the degradation of CuBTC leads to the formation of CuS. Eddaoudi et al. have also explored the stability of isostructural soc-MOFs(In, Fe, Ga, and Al) for the capture of H₂S [115]. This structure results from the assembly of trinuclear metal carboxylate clusters [M₃O(O₂C-)₆] and 3,3',5,5'-azobenzenetetracarboxylate as organic linker, leading to the formation of an extended (4,6)-connected MOF (Fig. 5.11). The results showed that only soc-MOF(In) and soc-MOF(Ga) are chemically stable and may be

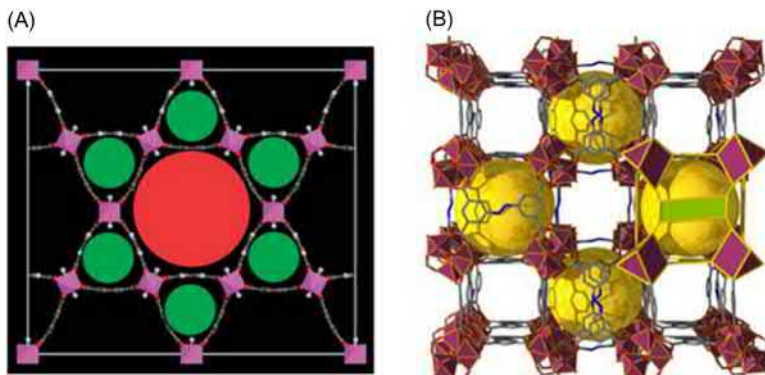


Figure 5.11 (A) Crystalline structure of MIL-68(Al) composed of triangular (green circle) and hexagonal (red circle) channels (*metal polyhedra, pink; carbon atoms, gray; oxygen atoms, red; hydrogen atoms, white*). (B) Crystalline structure of the soc-MOF (*M, plum; C, gray; N, blue; O, red; the cavity sphere, yellow sphere*). The structure is composed of trinuclear metal carboxylate clusters $[M_3O(O_2C)_6]$ (*purple polyhedral*) and 3,3',5,5'-azobenzenetetracarboxylate as organic linker (*green rectangle*).

Source: (A) Reproduced (adapted) from L. Hamon, C. Serre, T. Devic, T. Loiseau, F. Millange, G. Férey, et al., Comparative study of hydrogen sulfide adsorption in the MIL-53 (Al, Cr, Fe), MIL-47(V), MIL-100(Cr), and MIL-101(Cr) metal – organic frameworks at room temperature, *J. Am. Chem. Soc.* 131 (2009) 8775–8777 with the permission of The Royal Society of Chemistry. (B) Reproduced (adapted) from Y. Belmabkhout, R.S. Pillai, D. Alezi, O. Shekhah, P.M. Bhatt, Z. Chen, et al., Metal-organic frameworks to satisfy gas upgrading demands: fine-tuning the soc-MOF platform for the operative removal of H₂S, *J. Mater. Chem. A* 5 (2017) 3293–3303 with the permission of The Royal Society of Chemistry.

used for the efficient removal of H₂S. In another study, Peng confirmed the potentiality of soc-MOF(In) for the capture of H₂S, whose uptake capacity at 50 bar and 30°C was evaluated at 1.8 mmol g⁻¹ [116].

We suggest reading Siepmann's review concerning the main existing techniques for the capture of H₂S and the use of MOFs as adsorbent [105].

5.3.3 Carbon monoxide

Also called “the silent killer,” the emission of carbon monoxide has led to numerous deaths in the past and is still considered as the most common and dangerous in-house gas. According to a report from the center of disease control and prevention (CDC), CO is implied in more than 500 deaths per year in the United States [117]. On average, a concentration of 100 ppm or greater may affect health or even cause the death of the exposed person [118]. Its toxicity comes from its ability to bind strongly to blood to form carboxyhemoglobin which prevents oxygen to be set and carried in the body by hemoglobin [119]. CO can be produced from a partial combustion of carbon-containing compounds in the presence of an insufficient amount

of oxygen. This phenomenon can be encountered in houses because of a malfunction of the heating system or in chemical industries where carbon monoxide is either the desired product for other chemical processes or a by-product released out of the plant. In this latter case, the amount of CO emitted may accumulate in the atmosphere playing the role of a greenhouse gas and leading to the development of heart diseases [120].

In order to reduce the amount of CO released in the atmosphere, several technologies based on transition metals (Pt, Au, Ni, Ag, and Cu) are currently applied in industries (CO chemical conversion) and in vehicles (exhaust pipe). Metal salts/metal nanoparticles can be supported on porous materials in order to enhance their dispersion as well as the accessibility of the active metal sites to CO for its conversion (oxidation or reduction) or simply its adsorption. Activated carbons are often used for this purpose but the amount of metal salts required to induce a high affinity of the activated carbon toward CO may be very high. Typically, an activated carbon containing 8.6 wt.% of AgCl adsorbs 0.95 g kg^{-1} of CO at 323K and 101 kPa. Better results may be obtained at higher temperatures (423K) with 30.6 wt.% of PdCl₂ leading to the adsorption of 18 g kg^{-1} [121]. Zeolites show interesting CO adsorption properties thanks to their extra-framework cations which can interact with carbon monoxide [122]. This family of materials is promising for the capture of CO. However, it appears that it is difficult to increase the number of adsorption sites because of the limited number of structures and a lack of potential tunable characteristics (modification of the pore size, surface area, and the density of adsorption sites). The versatility of the MOF chemistry may potentially be a key for the design of adsorbents of CO due to the possibility of varying the metal center of the framework for better host/guest interactions and the porosity which may accommodate metal nanoparticles or metal complexes in order to increase the number of adsorption sites.

Walton et al. tried to gain insight about the design of a MOF with an optimal CO adsorption uptake [123]. They found that the amount of CO adsorbed in a series of MOFs (CuBTC, IRMOF-1, -3, and Zn₂[BDC]₂-[dabco]) is mainly ruled by the presence of CUS and to a much lesser extent by the pore size. This study demonstrated that CO has a better affinity for CuBTC, the only MOF composed of CUSs in the selected materials, than for the other candidates. The same authors studied the adsorption of CO onto CuBTC by atomistic grand canonical Monte Carlo simulation [124]. It appears that the adsorption is dominated by the interactions between CuBTC framework atoms and CO, while CO···CO interactions are negligible. Moreover, at low coverage, CO is located preferentially near the metal sites confirming the key role of the metal in the capture of CO (Fig. 5.12). Gumma et al. also compared CO adsorption efficiency of MIL-101(Cr) with CuBTC [125]. They noticed that CO exhibits stronger electrostatic interactions with MIL-101(Cr) leading to a higher adsorption enthalpy. According to the authors, the difference between both MOFs may be partially due to a lower number of available CUSs in CuBTC due to the presence of residual solvent molecules. Isostructural CPO-27(M) [M = Mg, Ni, Zn] series exhibit a high density of CUS and therefore have been investigated computationally by Valenzano et al. in order to evaluate the impact of the nature of the metal on the CO adsorption properties of these MOFs [126]. DFT calculations (B3LYP + D*) allowed

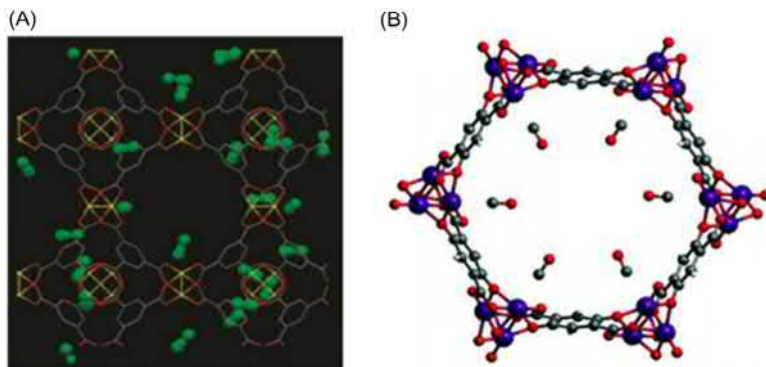


Figure 5.12 (A) Simulation of loading of 24 CO molecules (*green sphere*) in CuBTC unit cell at 320 kPa and 298K. (B) Arrangement of CO molecules in the CPO-27 (M) [M = Mg, Ni, Zn] channels (*metal, magenta; oxygen, red; carbon, gray; hydrogen, white*).

Source: (A) Reprinted (adapted) with permission from J.R. Karra, K.S. Walton, Effect of open metal sites on adsorption of polar and nonpolar molecules in metal – organic framework Cu-BTC, *Langmuir* 24 (2008) 8620–8626. Copyright (2008) American Chemical Society. (B) Reprinted (adapted) with permission from L. Valenzano, B. Civalleri, K. Sillar, J. Sauer, Heats of adsorption of CO and CO₂ in metal-organic frameworks: quantum mechanical study of CPO-27-M (M = Mg, Ni, Zn), *J. Phys. Chem. C* 115 (2011) 21777–21784. Copyright (2011) American Chemical Society.

predicting the sequence of binding energies for CO adsorption on open metal sites (Fig. 5.12) following the series: Ni (41.9 kJ mol⁻¹) > Mg (30.0 kJ mol⁻¹) > Zn (24.8 kJ mol⁻¹). This order of affinity for CO has been experimentally confirmed by Garcia et al. [127]. According to Bordiga et al., the favorable CO adsorption on CPO-27(Ni) is due to an electronic deficit of Ni atoms which may interact more strongly with CO through π -back-bonding [128].

However, since 2015, other strategies have been pursued in order to improve the amount of adsorbed CO in the MOF structure. Li et al. tried to enhance the adsorption capacity of MIL-100(Fe) by adding Cu⁺ ions within the structure by postsynthetic impregnation [129]. A strong increase of the performance has been reached with 2.78 mmol g⁻¹ for 0.8Cu(I)@MIL-100(Fe) compared to 0.38 mmol g⁻¹ for bare MIL-100(Fe). This is attributed to a strong π -complexation between the Cu(I) metal site and CO. Following this approach, improvement of CO adsorption capacity is expected for already tested MOFs and also for the design of new postmodified MOFs.

5.3.4 Nitric oxide

Two main sources of emissions of NO may be identified: natural emissions due to the nitrogen cycle, including bacterial and vegetation activities; and anthropogenic emissions caused by the combustion of fossil fuel [130]. The consequences of its presence in the atmosphere depend on its concentration. In the case of plants, nitric oxide as a biological agent may stimulate their growth or on the contrary reduce

dramatically the photosynthesis activity leading to a decrease of crop yield [131]. Nitric oxide also plays a role in human health such as DNA damage and tumor progression [132]. Nevertheless, a controlled release of NO may provide therapeutic tools to treat some diseases linked, for example, to the vascular system, skin integrity, and inflammatory reactions [133]. For this reason, the storage of NO within materials has been widely investigated.

Polymers functionalized with amine groups have been one of the first materials considered for the trapping of NO [134]. Amine groups react with NO to form diazeniumdiolates, which may be hydrolyzed to further release NO. For this type of polymer, the NO capture requires a dry atmosphere and this constitutes a serious limitation of such polymers for this application. Activated carbons are used for the industrial NO reduction process in the presence of ammonia (Selective Catalytic Reduction (SCR)) but are only used at low temperatures to avoid their early degradation [135]. Due to their higher thermal stability, zeolites were investigated for the capture of NO [136] but their uptake capacity is generally quite limited. Concerning the possible use of MOFs as adsorbents of nitric oxide, a certain number of studies were initiated, mostly by the team of prof. Russell Morris from St Andrews (UK). From these studies, it appears that the efficiency of the NO capture is strongly related to the density and the nature of CUS sites [137,138].

In order to study the impact of the CUS on NO adsorption uptake, Serre et al. selected three MOFs with large pores and high concentrations of CUSs: MIL-100 (Cr), MIL-100(Fe), and MIL-127(Fe) [139]. It appears that the maximum uptake of NO at room temperature for MIL-100(Cr^{III}, Fe^{III}) at 1 bar lies within the 2.7–3.2 mmol g⁻¹ range (Table 5.4) which is close to the theoretical amount of Lewis acid sites for the MIL-100 structure (~3.6 mmol g⁻¹). However, for MIL-127(Fe^{III}), the amount of adsorbed NO, in the same conditions, evaluated at 1.2 mmol g⁻¹ is smaller than the theoretical value (number of Lewis acid sites ~2.7 mmol g⁻¹). The lack of accessibility for NO in MIL-127(Fe) is presumably due to the smaller size of the pores (~5–7 Å). Moreover, under thermal activation conditions, Fe(III) ions may be partially reduced into Fe(II) ions, which have a clear favorable impact on the NO uptake and release, due to a stronger interaction between NO and Fe(II) sites. The reduction of the metal ions under activation conditions has also been observed for CuBTC used for NO storage and identified by infrared spectroscopy [140].

Table 5.4 Average adsorption capacity and residual capacity upon desorption (mmol g⁻¹) for selected MOFs at 1 bar

Material	Average adsorption capacity (mmol g ⁻¹) at 298K	Residual capacity upon desorption (mmol g ⁻¹) at 298K
MIL-100 (Cr)	3.2(2)	2.5(2)
MIL-100 (Fe ^{III})	2.7(2)	2.0(2)
MIL-100(Fe ^{II/III})	4.5(3)	3.2(2)
MIL-127 (Fe ^{III})	1.2(2)	0.75(10)
MIL-127 (Fe ^{II/III})	2.2(2)	1.4(2)

Morris et al. selected three members of the CPO-27(M) (M = Mg, Ni, Zn) family in order to evaluate the influence of the nature of the metal on the NO adsorption properties [141]. CPO-27(Ni) exhibits, to the best of our knowledge, the highest storage capacity reported in literature (6.1 mmol g^{-1} [142]) while the other selected isostructural MOFs show lower performances (Fig. 5.13). Since CO has a better affinity for Ni, the impact of the Ni content on the adsorption properties of MOF for NO was investigated by Morris et al. who succeeded in incorporating various amounts of Ni atoms into the inorganic part of CPO-27(Mg) and CPO-27(Zn) [143]. This study confirmed the key role of Ni^{2+} ions on the NO uptake of MOF and proposed this following trend: the higher the amount of Ni^{2+} , the higher the NO adsorption uptake (Fig. 5.13).

The functionalization of the organic linker may provide another way to enhance the NO adsorption properties of MOFs. Cohen et al. investigated the potential of amine groups to enhance the adsorption properties of IRMOF-3 (=MOF-5-NH₂) and UCMCM-1-NH₂ [144]. By a postsynthetic route, this amine group reacts with nitric oxide to form a diazeniumdiolate (NONOate) functional group (Fig. 5.14). By thermogravimetric analysis, the percentage of free amine converted in IRMOF-3 and UCMCM-1-NH₂ is 44% and 83%, respectively. The controlled release of NO may be possible by hydrolyzing this newly formed chemical group to recover the

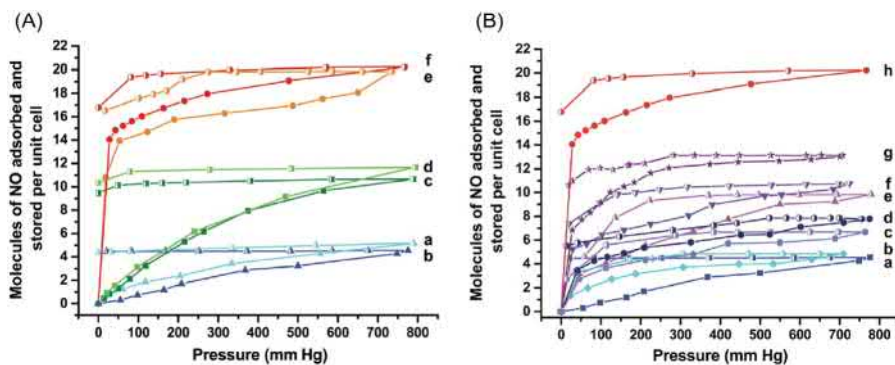


Figure 5.13 (A) Adsorption–desorption isotherms of NO at 298K for (a) CPO-27(Mg) after solvent exchange (solvothermal synthesis); (b) CPO-27(Mg) (synthesis under reflux conditions); (c) CPO-27(Zn) after solvent exchange (solvothermal synthesis); (d) CPO-27(Zn) (synthesis under reflux conditions); (e) CPO-27(Ni) without solvent exchange (solvothermal synthesis); and (f) CPO-27(Ni) (synthesis under reflux conditions). (B) Adsorption–desorption isotherms of NO at 298K for (a) CPO-27(Mg); (b) CPO-27(Mg) 1% Ni; (c) CPO-27(Mg) 2% Ni; (d) CPO-27(Mg) 5% Ni; (e) CPO-27(Mg) 10% Ni; (f) CPO-27(Mg) 20% Ni; (g) CPO-27(Mg) 40% Ni; and (h) CPO-27(Ni).

Source: (A) D. Cattaneo, S.J. Warrender, M.J. Duncan, R. Castledine, N. Parkinson, I. Haley, R. E. Morris, Water based scale-up of CPO-27 synthesis for nitric oxide delivery, Dalton Trans. 45 (2016) 618–629—Published by The Royal Society of Chemistry. (B) D. Cattaneo, S.J. Warrender, M.J. Duncan, C.J. Kelsall, M.K. Doherty, P.D. Whitfield, I.L. Megson, R.E. Morris, Tuning the nitric oxide release from CPO-27 MOFs, RSC Adv. 6 (2016) 14059–14067—Published by The Royal Society of Chemistry.

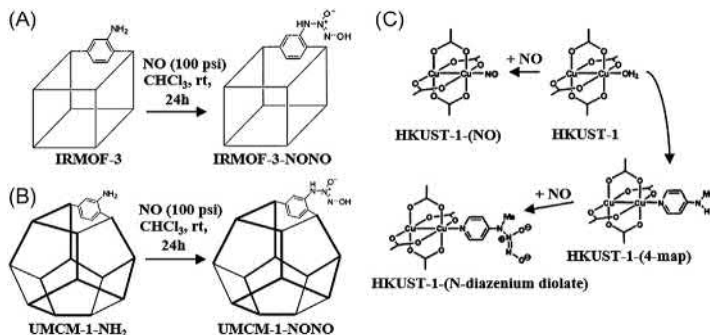


Figure 5.14 Synthesis by postfunctionalization of (A) IRMOF-3-NONO and (B) UMCM-1-NONO. (C) Synthesis route of postsynthetic HKUST-1-(*N*-diazenium diolate).

Source: (A and B) Reproduced (adapted) from J.G. Nguyen, K.K. Tanabe, S.M. Cohen, Postsynthetic diazeniumdiolate formation and NO release from MOFs, *CrystEngComm*. 12 (2010) 2335–2338 with the permission of The Royal Society of Chemistry. (C) Reprinted (adapted) with permission from M.J. Ingleson, R. Heck, J.A. Gould, M.J. Rosseinsky, Nitric oxide chemisorption in a postsynthetically modified metal – organic framework, *Inorg. Chem.* 48 (2009) 9986–9988. Copyright (2009) American Chemical Society.

amine and collect the nitric oxide. This strategy has also been followed by Rosseinsky et al. with HKUST-1 [145]. In this case, the postsynthetic modification consisted of the reaction of HKUST-1 with 4-(methylamino)pyridine. The 4-(methylamino)pyridine interacts with the copper ions of the framework through the nitrogen of the pyridine function, the free secondary amine group being accessible to react with NO to form diazeniumdiolate (Fig. 5.14). According to the preparation, it is possible to graft up to one amine per copper ion. This postsynthetic modification approach may therefore be followed in order to increase significantly the NO uptake capacity of efficient MOFs.

For more information about nitric oxide and its capture by MOFs, we recommend reading Morris and Serre's review [146] and DeCoste and Peterson's review concerning air purification of toxic chemicals [147].

5.4 Conclusion and perspectives

In the context of air pollution caused by anthropogenic VOC and toxic molecules emissions, MOFs have been considered as the next-generation adsorbents and catalytic materials. The competitive binding of several possible molecules has to be considered for the efficacy of adsorption-based separations, particularly for the capture of VOCs under humid conditions. In this context, MOFs could serve as an ideal platform owing to their large capacity for the adsorption of gases and their tremendous structural and chemical diversity. Actually, MOFs can be modified by varying the organic linkers, metal nodes, functional groups, as well as the shape and diameter of the pores, thereby modulating their hydrophilic/hydrophobic balance, the density and nature of

adsorption sites, or the molecular sieving effect. Such properties have been found to be crucial for the adsorption of numerous target molecules with high adsorption capacity and selectivity. Moreover, a high control over the amount or distribution of CUSs or the exposed redox-active metals (Fe^{2+} , Cu^+) as well as the fine-tuning of the electron density available at these adsorption sites through the modification of the organic linker were explored as valuable strategies to design MOF-based adsorbents for the selective adsorption of toxic gases such as NO_x and CO. More importantly, recent advances reported on the shaping of MOFs and the design of complex architectures can introduce novel functionalities and/or enhance the efficiency of adsorbents. As an example, the controllable modular growth of hierarchical MOF-on-MOF heterostructures paves the way for the design of modular and multifunctional devices combining catalytic and separation properties.

An efficient capture of VOCs and toxic chemicals is of high importance for the air purification process but their detection and quantification is also crucial for the human safety and the environment preservation (e.g., CO intoxication, effect of ethylene on plants, preservation of cultural heritage). Therefore, the design of a selective adsorbent for a specific range of molecules is an essential prerequisite for the development of sensitive sensors. However, the applicability of MOFs for VOCs sensing may suffer from a lack of information regarding the structure/properties relationships of MOFs for some specific molecules. While numerous studies may be found about the adsorption/separation of hydrocarbons, alcohols, and toxic chemicals by MOFs, only a limited number of publications have focused on the capture of carbonyls (aldehydes, ketones, and carboxylic acids) by MOFs, while studies that comprise real mixtures of VOCs (and toxic gases) have not been reported so far. These compounds have however a great impact on the environment and human health and must be taken into account for further investigation in the context of air purification. Moreover, this lack of studies concerns also a notorious class of ozone depleting compounds, namely chlorofluorocarbons today forbidden and replaced by hydrofluorocarbons following the Montreal protocol.

Acknowledgment

K. dedecker, E. Dumas, B. Lavédrine, N. Steunou, and C. Serre acknowledge the Investissement d'avenir Labex Patrima ANR-10-LABX-0094-01.

References

- [1] E. Gakidou, A. Afshin, A.A. Abajobir, K.H. Abate, C. Abbafati, K.M. Abbas, et al., Global, regional, and national comparative risk assessment of 84 behavioural, environmental and occupational, and metabolic risks or clusters of risks, 1990-2016: a systematic analysis for the Global Burden of Disease Study 2016, *Lancet* 390 (2017) 1345–1422.
- [2] K. Rumchev, J. Spickett, M. Bulsara, M. Phillips, S. Stick, Association of domestic exposure to volatile organic compounds with asthma in young children, *Thorax* 59 (2004) 746–751.

- [3] H. Guo, S. Lee, L. Chan, W. Li, Risk assessment of exposure to volatile organic compounds in different indoor environments, *Environ. Res.* 94 (2004) 57–66.
- [4] O. Herbarth, S. Matysik, Decreasing concentrations of volatile organic compounds (VOC) emitted following home renovations, *Indoor Air* 20 (2010) 141–146.
- [5] J. García-Pérez, G. López-Abente, D. Gómez-Barroso, A. Morales-Piga, E. Pardo Romaguera, I. Tamayo, et al., Childhood leukemia and residential proximity to industrial and urban sites, *Environ. Res.* 140 (2015) 542–553.
- [6] R. Atkinson, J. Arey, Atmospheric degradation of volatile organic compounds, *Chem. Rev.* 103 (2003) 4605–4638.
- [7] W.P.L. Carter, Development of ozone reactivity scales for volatile organic compounds, *Air Waste* 44 (1994) 881–899.
- [8] C.S. Malley, D.K. Henze, J.C.I. Kuylenstierna, H.W. Vallack, Y. Davila, S.C. Anenberg, et al., Updated global estimates of respiratory mortality in adults ≥ 30 years of age attributable to long-term ozone exposure, *Environ. Health Perspect.* 125 (2017) 1–9.
- [9] B.C. McDonald, D.R. Gentner, A.H. Goldstein, R.A. Harley, Long-term trends in motor vehicle emissions in U.S. Urban Areas, *Environ. Sci. Technol.* 47 (2013) 10022–10031.
- [10] G.J. Dollard, P. Dumitrean, S. Telling, J. Dixon, R.G. Derwent, Observed trends in ambient concentrations of C2–C8 hydrocarbons in the United Kingdom over the period from 1993 to 2004, *Atmos. Environ.* 41 (2007) 2559–2569.
- [11] T.B. Ryerson, M. Trainer, W.M. Angevine, C.A. Brock, R.W. Dissly, F.C. Fehsenfeld, et al., Effect of petrochemical industrial emissions of reactive alkenes and NO_x on tropospheric ozone formation in Houston, Texas, *J. Geophys. Res.* 108 (2003) 4249–4273.
- [12] J.E.C. Lerner, T. Kohajda, M.E. Aguilar, L.A. Massolo, E.Y. Sánchez, A.A. Porta, et al., Improvement of health risk factors after reduction of VOC concentrations in industrial and urban areas, *Environ. Sci. Pollution Res.* 21 (2014) 9676–9688.
- [13] R.A. Harley, M.P. Hannigan, G.R. Cass, Respeciation of organic gas emissions and the detection of excess unburned gasoline in the atmosphere, *Environ. Sci. Technol.* 26 (1992) 2395–2408.
- [14] F. Klein, S.M. Platt, N.J. Farren, A. Detournay, E.A. Bruns, C. Bozzetti, et al., Characterization of gas-phase organics using proton transfer reaction time-of-flight mass spectrometry: cooking emissions, *Environ. Sci. Technol.* 50 (2016) 1243–1250.
- [15] A. Golovoy, J. Braslaw, Adsorption of automotive paint solvents on activated carbon: I. Equilibrium adsorption of single vapors, *J. Air Pollut. Control Assoc.* 31 (1981) 861–865.
- [16] C.T. Chang, C.H. Lee, Y.P. Wu, F.T. Jeng, Assessment of the strategies for reducing volatile organic compound emissions in the automotive industry in Taiwan, *Resour. Conservat. Recycling* 34 (2002) 117–128.
- [17] L.P. Haack, R.S. Marano, T.L. Riley, S.P. Levine, Gas-chromatographic technique for the on-line evaluation of solvent emission abatement devices, *Environ. Sci. Technol.* 15 (1981) 1463–1467.
- [18] B.J. Cannon, Dual-chamber RTO oxidizers provide cost-effective VOC compliance for metal finishers and coaters, *Metal Finishing* 101 (2003) 53–56.
- [19] M.R. Wherrett, P.A. Ryan, VOC emissions from industrial painting processes as a source of fuel cell energy, *Metal Finishing* 102 (2004) 23–29.
- [20] Y.S. Matros, G.A. Bunimovich, V.O. Strots, C.R. Roach, C.M. Lorensen, M.R. Wherrett, Retrofitting a regenerative thermal oxidizer in an automotive assembly plant, *Metal Finishing* 97 (1999) 10–16.

- [21] S. Wang, Z.H. Zhu, A. Coomes, F. Haghseresht, G.Q. Lu, The physical and surface chemical characteristics of activated carbons and the adsorption of methylene blue from wastewater, *J. Colloid. Interface. Sci.* 284 (2005) 440–446.
- [22] M. Gehre, Z. Guo, G. Rothenberg, S. Tanase, Sustainable separations of C₄-hydrocarbons by using microporous materials, *ChemSusChem* 10 (2017) 3947–3963.
- [23] M.P. Suh, H.J. Park, T.K. Prasad, D.W. Lim, Hydrogen storage in metal–organic frameworks, *Chem. Rev.* 112 (2012) 782–835.
- [24] Y. He, W. Zhou, G. Qian, B. Chen, Methane storage in metal–organic frameworks, *Chem. Soc. Rev.* 43 (2014) 5657–5678.
- [25] K. Sumida, D.L. Rogow, J.A. Mason, T.M. McDonald, E.D. Bloch, Z.R. Herm, et al., Carbon dioxide capture in metal–organic frameworks, *Chem. Rev.* 112 (2012) 724–781.
- [26] O.K. Farha, I. Eryazici, N.C. Jeong, B.G. Hauser, C.E. Wilmer, A.A. Sarjeant, et al., Metal–organic framework materials with ultrahigh surface areas: is the sky the limit? *J. Am. Chem. Soc.* 134 (2012) 15016–15021.
- [27] M. Eddaoudi, J. Kim, N. Rosi, D. Vodak, J. Wachter, M. O’Keeffe, et al., Systematic design of pore size and functionality in isoreticular MOFs and their application in methane storage, *Science* 295 (2002) 469–472.
- [28] N.M. Padial, E. Quartapelle Procopio, C. Montoro, E. López, J.E. Oltra, V. Colombo, et al., Highly hydrophobic isoreticular porous metal-organic frameworks for the capture of harmful volatile organic compounds, *Angew. Chem.* 125 (2013) 8448–8452.
- [29] N.C. Burtch, H. Jasuja, K.S. Walton, Water stability and adsorption in metal–organic frameworks, *Chem. Rev.* 114 (2014) 10575–10612.
- [30] S. Yuan, L. Feng, K. Wang, J. Pang, M. Bosch, C. Lollar, et al., Stable metal-organic frameworks: design, synthesis, and applications, *Adv. Mater.* (2018) 1704303.
- [31] N. Stock, S. Biswas, Synthesis of metal-organic frameworks (MOFs): routes to various MOF topologies, morphologies, and composites, *Chem. Rev.* 112 (2012) 933–969.
- [32] M. Rubio-Martinez, C. Avci-Camur, A.W. Thornton, I. Imaz, D. Maspoch, M.R. Hill, New synthetic routes towards MOF production at scale, *Chem. Soc. Rev.* 46 (2017) 3453–3480.
- [33] M. Benzaqui, R.S. Pillai, A. Sabetghadam, V. Benoit, P. Normand, J. Marrot, et al., Revisiting the aluminum trimesate-based MOF (MIL-96): from structure determination to the processing of mixed matrix membranes for CO₂ capture, *Chem. Mater.* 29 (2017) 10326–10338.
- [34] N.S. Bobbitt, M.L. Mendonca, A.J. Howarth, T. Islamoglu, J.T. Hupp, O.K. Farha, et al., Metal–organic frameworks for the removal of toxic industrial chemicals and chemical warfare agents, *Chem. Soc. Rev.* 46 (2017) 3357–3385.
- [35] Y. Takeuchi, Y. Ono, N. Hisanaga, J. Kitoh, Y. Sugiura, A comparative study on the neurotoxicity of n-pentane, n-hexane, and n-heptane in the rat, *Occup. Environ. Med.* 37 (1980) 241–247.
- [36] C. Chang, Q&A: how do plants respond to ethylene and what is its importance? *BMC Biol.* 14 (2016) 1–7.
- [37] F.B. Abeles, H.E. Heggstad, Ethylene: an urban air pollutant, *J. Air Pollut. Control Assoc.* 23 (1973) 517–521.
- [38] J. Roma-Torres, J.P. Teixeira, S. Silva, B. Laffon, L.M. Cunha, J. Méndez, et al., Evaluation of genotoxicity in a group of workers from a petroleum refinery aromatics plant, *Mutat. Res. Genetic Toxicol. Environ. Mutagen.* 604 (2006) 19–27.
- [39] Y. Yang, N. Burke, S. Ali, S. Huang, S. Lim, Y. Zhu, Experimental studies of hydrocarbon separation on zeolites, activated carbons and MOFs for applications in natural gas processing, *RSC Adv.* 7 (2017) 12629–12638.

- [40] R. Krishna, Exploiting configurational entropy effects for separation of hexane isomers using silicalite-1, *Chem. Eng. Res. Design* 79 (2001) 182–194.
- [41] H.H. Funke, A.M. Argo, J.L. Falconer, R.D. Noble, Separations of cyclic, branched, and linear hydrocarbon mixtures through silicalite membranes, *Ind. Eng. Chem. Res.* 36 (1997) 137–143.
- [42] M. Ackley, S.U. Rege, H. Saxena, Application of natural zeolites in the purification and separation of gases, *Microporous Mesoporous Mater.* 61 (2003) 25–42.
- [43] S. Sircar, T.C. Golden, M.B. Rao, Activated carbon for gas separation and storage, *Carbon* 34 (1996) 1–12.
- [44] D. Peralta, G. Chaplais, A. Simon-Masseron, K. Barthelet, C. Chizallet, A.A. Quoineaud, et al., Comparison of the behavior of metal–organic frameworks and zeolites for hydrocarbon separations, *J. Am. Chem. Soc.* 134 (2012) 8115–8126.
- [45] V. Finsy, H. Verelst, L. Alaerts, D. De Vos, P.A. Jacobs, G.V. Baron, et al., Pore-filling-dependent selectivity effects in the vapor-phase separation of xylene isomers on the metal – organic framework MIL-47, *J. Am. Chem. Soc.* 130 (2008) 7110–7118.
- [46] C. Gücüyener, J. van den Bergh, J. Gascon, F. Kapteijn, Ethane/ethene separation turned on its head: selective ethane adsorption on the metal – organic framework ZIF-7 through a gate-opening mechanism, *J. Am. Chem. Soc.* 132 (2010) 17704–17706.
- [47] J. van den Bergh, C. Gücüyener, E.A. Pidko, E.J.M. Hensen, J. Gascon, F. Kapteijn, Understanding the anomalous alkane selectivity of ZIF-7 in the separation of light alkane/alkene mixtures, *Chem. A Eur. J.* 17 (2011) 8832–8840.
- [48] F. Nouar, J. Eckert, J.F. Eubank, P. Forster, M. Eddaoudi, Zeolite- like metal – organic frameworks (ZMOFs) as hydrogen storage platform: lithium and magnesium ion-exchange and H₂-(*rho*-ZMOF) interaction studies, *J. Am. Chem. Soc.* 131 (2009) 2864–2870.
- [49] Q. Min Wang, D. Shen, M. Bülow, M. Ling Lau, S. Deng, F.R. Fitch, et al., Metallo-organic molecular sieve for gas separation and purification, *Microporous Mesoporous Mater.* 55 (2002) 217–230.
- [50] S. Wang, Q. Yang, C. Zhong, Adsorption and separation of binary mixtures in a metal-organic framework Cu-BTC: a computational study, *Sep. Purif. Technol.* 60 (2008) 30–35.
- [51] J.W. Yoon, Y.-K. Seo, Y.K. Hwang, J.-S. Chang, H. Leclerc, S. Wuttke, et al., Controlled reducibility of a metal-organic framework with coordinatively unsaturated sites for preferential gas sorption, *Angew. Chem.* 122 (2010) 6085–6088.
- [52] S.J. Geier, J.A. Mason, E.D. Bloch, W.L. Queen, M.R. Hudson, C.M. Brown, et al., Selective adsorption of ethylene over ethane and propylene over propane in the metal–organic frameworks M₂(dobdc) (M = Mg, Mn, Fe, Co, Ni, Zn), *Chem. Sci.* 4 (2013) 2054–2061.
- [53] C.X. Yang, X.P. Yan, Metal–organic framework MIL-101(Cr) for high-performance liquid chromatographic separation of substituted aromatics, *Anal. Chem.* 83 (2011) 7144–7150.
- [54] Z. Hu, Y. Chen, J. Jiang, Liquid chromatographic separation in metal–organic framework MIL-101: a molecular simulation study, *Langmuir* 29 (2013) 1650–1656.
- [55] N.A. Ramsahye, P. Trens, C. Shepherd, P. Gonzalez, T.K. Trung, F. Ragon, et al., The effect of pore shape on hydrocarbon selectivity on UiO-66(Zr), HKUST-1 and MIL-125(Ti) metal organic frameworks: insights from molecular simulations and chromatography, *Microporous Mesoporous Mater.* 189 (2014) 222–231.
- [56] L. Pan, D.H. Olson, L.R. Ciemnomolonski, R. Heddy, J. Li, Separation of hydrocarbons with a microporous metal-organic framework, *Angew. Chem.* 118 (2006) 632–635.

- [57] F. Vermoortele, M. Maes, P.Z. Moghadam, M.J. Lennox, F. Ragon, M. Boulhout, et al., *p*-Xylene-selective metal-organic frameworks: a case of topology-directed selectivity, *J. Am. Chem. Soc.* 133 (2011) 18526–18529.
- [58] Z.R. Herm, E.D. Bloch, J.R. Long, Hydrocarbon separations in metal-organic frameworks, *Chem. Mater.* 26 (2014) 323–338.
- [59] K. Adil, Y. Belmabkhout, R.S. Pillai, A. Cadiou, P.M. Bhatt, A.H. Assen, et al., Gas/vapour separation using ultra-microporous metal-organic frameworks: insights into the structure/separation relationship, *Chem. Soc. Rev.* 46 (2017) 3402–3430.
- [60] G.A. Olah, Beyond oil and gas: the methanol economy, *Angew. Chem. Int. Ed.* 44 (2005) 2636–2639.
- [61] F. Önder, S. Ilker, T. Kansu, T. Tatar, G. Kural, Acute blindness and putaminal necrosis in methanol intoxication, *Int. Ophthalmol.* 22 (1999) 81–84.
- [62] L. Ernstgård, E. Shibata, G. Johanson, Uptake and disposition of inhaled methanol vapor in humans, *Toxicol. Sci.* 88 (2005) 30–38.
- [63] B.M. Walker, D.A. Drimmer, J.L. Walker, T. Liu, A.A. Mathé, C.L. Ehlers, Effects of prolonged ethanol vapor exposure on forced swim behavior, and neuropeptide Y and corticotropin-releasing factor levels in rat brains, *Alcohol* 44 (2010) 487–493.
- [64] H. Burleigh-Flayer, R. Garman, D. Neptun, C. Bevan, T. Gardiner, R. Kapp, et al., Isopropanol vapor inhalation oncogenicity study in Fischer 344 rats and CD-1 mice, *Fundam. Appl. Toxicol.* 36 (1997) 95–111.
- [65] T. Yamamoto, Y.H. Kim, B.C. Kim, A. Endo, N. Thongprachan, T. Ohmori, Adsorption characteristics of zeolites for dehydration of ethanol: evaluation of diffusivity of water in porous structure, *Chem. Eng. J.* 181–182 (2012) 443–448.
- [66] A. Farzaneh, R.F. DeJaco, L. Ohlin, A. Holmgren, J.I. Siepmann, M. Grahn, Comparative Study of the effect of defects on selective adsorption of butanol from butanol/water binary vapor mixtures in silicalite-1 films, *Langmuir* 33 (2017) 8420–8427.
- [67] D. Gunst, K. Alexopoulos, K. Van Der Borght, M. John, V. Galvita, M.F. Reyniers, et al., Study of butanol conversion to butenes over H-ZSM-5: effect of chemical structure on activity, selectivity and reaction pathways, *Appl. Catal. A: General* 539 (2017) 1–12.
- [68] K. Zhang, L. Zhang, J. Jiang, Adsorption of C₁–C₄ alcohols in zeolitic imidazolate framework-8: effects of force fields, atomic charges, and framework flexibility, *J. Phys. Chem. C* 117 (2013) 25628–25635.
- [69] G.F. de Lima, A. Mavrandonakis, H.A. de Abreu, H.A. Duarte, T. Heine, Mechanism of alcohol-water separation in metal-organic frameworks, *J. Phys. Chem. C* 117 (2013) 4124–4130.
- [70] J.K. Sun, M. Ji, C. Chen, W.G. Wang, P. Wang, R.P. Chen, et al., A charge-polarized porous metal-organic framework for gas chromatographic separation of alcohols from water, *Chem. Commun.* 49 (2013) 1624–1626.
- [71] R. Bueno-Perez, J.J. Gutiérrez-Sevillano, D. Dubbeldam, P.J. Merkling, S. Calero, Separation of amyl alcohol isomers in ZIF-77, *ChemPhysChem* 16 (2015) 2735–2738.
- [72] R.K. Motkuri, P.K. Thallapally, H.V.R. Annapureddy, L.X. Dang, R. Krishna, S.K. Nune, et al., Separation of polar compounds using a flexible metal-organic framework, *Chem. Commun.* 51 (2015) 8421–8424.
- [73] K. Zhang, R.P. Lively, M.E. Dose, A.J. Brown, C. Zhang, J. Chung, et al., Alcohol and water adsorption in zeolitic imidazolate frameworks, *Chem. Commun.* 49 (2013) 3245–3247.
- [74] T. Remy, J. Cousin Saint Remi, R. Singh, P.A. Webley, G.V. Baron, J.F.M. Denayer, Adsorption and separation of C₁ – C₈ alcohols on SAPO-34, *J. Phys. Chem. C* 115 (2011) 8117–8125.

- [75] S. Bourrelly, B. Moulin, A. Rivera, G. Maurin, S. Devautour-Vinot, C. Serre, et al., Explanation of the adsorption of polar vapors in the highly flexible metal organic framework MIL-53(Cr), *J. Am. Chem. Soc.* 132 (2010) 9488–9498.
- [76] T. Suzuki, R. Kotani, A. Kondo, K. Maeda, Structural investigation of a flexible MOF [Cu(BF₄)₂ (1,3-bis(4-pyridyl)propane)₂] showing selective gate adsorption with dynamic pore-opening/pore-closing processes, *J. Phys. Chem. C* 120 (2016) 21571–21579.
- [77] S. Wannapaiboon, M. Tu, K. Sumida, K. Khaletskaya, S. Furukawa, S. Kitagawa, et al., Hierarchical structuring of metal–organic framework thin-films on quartz crystal microbalance (QCM) substrates for selective adsorption applications, *J. Mater. Chem. A* 3 (2015) 23385–23394.
- [78] C. Montoro, F. Linares, E. Quartapelle Procopio, I. Senkovska, S. Kaskel, S. Galli, et al., Capture of nerve agents and mustard gas analogues by hydrophobic robust MOF-5 type metal–organic frameworks, *J. Am. Chem. Soc.* 133 (2011) 11888–11891.
- [79] D. Banerjee, B.J. Deibert, H. Wang, J. Li, Metal-organic frameworks: adsorption of hydrocarbons and alcohols, in: R.A. Scott (Ed.), *Encyclopedia of Inorganic and Bioinorganic Chemistry*, John Wiley & Sons, Ltd, Chichester, 2014, pp. 1–21.
- [80] H. Xu, Q. Zhang, N. Song, M. Guo, S. Zhang, G. Ji, et al., Personal exposure and health risk assessment of carbonyls in family cars and public transports—a comparative study in Nanjing, China, *Environ. Sci. Pollut. Res.* 24 (2017) 26111–26119.
- [81] J.F. Stevens, C.S. Maier, Acrolein: sources, metabolism, and biomolecular interactions relevant to human health and disease, *Mol. Nutr. Food Res.* 52 (2008) 7–25.
- [82] T. Satoh, K. Omae, H. Nakashima, T. Takebayashi, H. Matsumura, T. Kawai, et al., Relationship between acetone exposure concentration and health effects in acetate fiber plant workers, *Int. Arch. Occup. Environ. Health* 68 (1996) 147–153.
- [83] J.E. Lawrence, P. Koutrakis, Measurement of atmospheric formic and acetic acids: methods evaluation and results from field studies, *Environ. Sci. Technol.* 28 (1994) 957–964.
- [84] L.T. Gibson, A. Ewlad-Ahmed, B. Knight, V. Horie, G. Mitchell, C.J. Robertson, Measurement of volatile organic compounds emitted in libraries and archives: an inferential indicator of paper decay? *Chem. Cent. J.* 6 (2012) 1–22.
- [85] W.J. Gauderman, R. McConnell, G.F. Gilliland, S. London, D. Thomas, E. Avol, et al., Association between air pollution and lung function growth in Southern California children, *Am. J. Respir. Crit. Care. Med.* 166 (2002) 76–84.
- [86] K.J. Lee, J. Miyawaki, N. Shiratori, S.H. Yoon, J. Jang, Toward an effective adsorbent for polar pollutants: formaldehyde adsorption by activated carbon, *J. Hazard. Mater.* 260 (2013) 82–88.
- [87] J.H. Tsai, H.M. Chiang, G.Y. Huang, H.L. Chiang, Adsorption characteristics of acetone, chloroform and acetonitrile on sludge-derived adsorbent, commercial granular activated carbon and activated carbon fibers, *J. Hazard. Mater.* 154 (2008) 1183–1191.
- [88] T.S.C. Law, C.Y.H. Chao, G.Y.W. Chan, A.K.Y. Law, The use of zeolite and oxidant generating devices in air cleaning, *Indoor Built Environ.* 13 (2004) 45–51.
- [89] K.C. Nien, F.T. Chang, M.B. Chang, Adsorption–desorption characteristics of *methyl ethyl ketone* with modified activated carbon and inhibition of *2,3-butanediol* production, *J. Air Waste Manage. Assoc.* 65 (2015) 1317–1326.
- [90] S.W. Blocki, Hydrophobic zeolite adsorbent: a proven advancement in solvent separation technology, *Environ. Prog.* 12 (1993) 226–230.
- [91] J.P. Bellat, I. Bezverkhyy, G. Weber, S. Royer, R. Averlant, J.M. Giraudon, et al., Capture of formaldehyde by adsorption on nanoporous materials, *J. Hazard. Mater.* 300 (2015) 711–717.

- [92] Z. Wang, W. Wang, D. Jiang, L. Zhang, Y. Zheng, Diamine-appended metal–organic frameworks: enhanced formaldehyde-vapor adsorption capacity, superior recyclability and water resistibility, *Dalton Trans.* 45 (2016) 11306–11311.
- [93] T. Terencio, F. Di Renzo, D. Berthomieu, P. Trens, Adsorption of acetone vapor by Cu-BTC: an experimental and computational study, *J. Phys. Chem. C* 117 (2013) 26156–26165.
- [94] K. Dedecker, R.S. Pillai, F. Nouar, J. Pires, N. Steunou, E. Dumas, et al., Metal-organic frameworks for cultural heritage preservation: the case of acetic acid removal, *ACS Appl. Mater. Interfaces* 10 (2018) 13886–13894.
- [95] J.Y. Lee, T.C. Keener, Y.J. Yang, Potential flue gas impurities in carbon dioxide streams separated from coal-fired power plants, *J. Air Waste Manage. Assoc.* 59 (2009) 725–732.
- [96] S. Jafarinejad, Control and treatment of sulfur compounds specially sulfur oxides (SO_x) emissions from the petroleum industry: a review, *Chem. Int.* 2 (2016) 242–253.
- [97] World Health Organisation (WHO), WHO Air quality guidelines for particulate matter, ozone, nitrogen dioxide and sulfur dioxide. http://apps.who.int/iris/bitstream/handle/10665/69477/WHO_SDE_PHE_OEH_06.02_eng.pdf (accessed April 2018).
- [98] X.D. Song, S. Wang, C. Hao, J.S. Qiu, Investigation of SO₂ gas adsorption in metal–organic frameworks by molecular simulation, *Inorg. Chem. Commun.* 46 (2014) 277–281.
- [99] M. Savage, Y. Cheng, T.L. Easun, J.E. Eyley, S.P. Argent, M.R. Warren, et al., Selective adsorption of sulfur dioxide in a robust metal-organic framework material, *Adv. Mater.* 28 (2016) 8705–8711.
- [100] X. Cui, Q. Yang, L. Yang, R. Krishna, Z. Zhang, Z. Bao, et al., Ultrahigh and selective SO₂ uptake in inorganic anion-pillared hybrid porous materials, *Adv. Mater.* 29 (2017) 1606929.
- [101] S. Bhattacharyya, S.H. Pang, M.R. Dutzer, R.P. Lively, K.S. Walton, D.S. Sholl, et al., Interactions of SO₂-containing acid gases with ZIF-8: structural changes and mechanistic investigations, *J. Phys. Chem. C* 120 (2016) 27221–27229.
- [102] W.P. Mounfield, C. Han, S.H. Pang, U. Tumuluri, Y. Jiao, S. Bhattacharyya, et al., Synergistic effects of water and SO₂ on degradation of MIL-125 in the presence of acid gases, *J. Phys. Chem. C* 120 (2016) 27230–27240.
- [103] F. Rezaei, A.A. Rownaghi, S. Monjezi, R.P. Lively, C.W. Jones, SO_x/NO_x removal from flue gas streams by solid adsorbents: a review of current challenges and future directions, *Energy Fuels* 29 (2015) 5467–5486.
- [104] R.J. Reiffenstein, W.C. Hulbert, S.H. Roth, Toxicology of hydrogen sulfide, *Annu. Rev. Pharmacol. Toxicol.* 32 (1992) 109–134.
- [105] M.S. Shah, M. Tsapatsis, J.I. Siepmann, Hydrogen sulfide capture: from absorption in polar liquids to oxide, zeolite, and metal–organic framework adsorbents and membranes, *Chem. Rev.* 117 (2017) 9755–9803.
- [106] N.N. Zulkefli, M.S. Masdar, J. Jahim, E.H. Majlan, Overview of H₂S removal technologies from biogas production, *Int. J. Appl. Eng. Res.* 11 (2016) 10060–10066.
- [107] R. Sittikhankaeuw, S. Predapitakkun, R. (Wibulswas) Kiattikomol, S. Pumhiran, S. Assabumrungrat, N. Laosiripojana, Comparative study of hydrogen sulfide adsorption by using alkaline impregnated activated carbons for hot fuel gas purification, *Energy Procedia* 9 (2011) 15–24.
- [108] M. Ozekmekci, G. Salkic, M.F. Fellah, Use of zeolites for the removal of H₂S: a mini-review, *Fuel Process. Technol.* 139 (2015) 49–60.

- [109] L. Hamon, C. Serre, T. Devic, T. Loiseau, F. Millange, G. Férey, et al., Comparative study of hydrogen sulfide adsorption in the MIL-53(Al, Cr, Fe), MIL-47(V), MIL-100 (Cr), and MIL-101(Cr) metal – organic frameworks at room temperature, *J. Am. Chem. Soc.* 131 (2009) 8775–8777.
- [110] Q. Yang, S. Vaesen, M. Vishnuvarthan, F. Ragon, C. Serre, A. Vimont, et al., Probing the adsorption performance of the hybrid porous MIL-68(Al): a synergic combination of experimental and modelling tools, *J. Mater. Chem.* 22 (2012) 10210–10220.
- [111] S. Vaesen, V. Guillerm, Q. Yang, A. Wiersum, B. Marszalek, B. Gil, et al., A robust amino-functionalized Titanium (IV) based MOF for an improved separation of acid gases, *Chem. Commun.* 49 (2013) 10082–10084.
- [112] P.K. Allan, P.S. Wheatley, D. Aldous, M.I. Mohideen, C. Tang, J.A. Hriljac, et al., Metal–organic frameworks for the storage and delivery of biologically active hydrogen sulfide, *Dalton Trans.* 41 (2012) 4060–4066.
- [113] S. Chavan, F. Bonino, L. Valenzano, B. Civalleri, C. Lamberti, N. Acerbi, et al., Fundamental Aspects of H₂S Adsorption on CPO-27-Ni, *J. Phys. Chem. C* 117 (2013) 15615–15622.
- [114] J. Ethiraj, F. Bonino, C. Lamberti, S. Bordiga, H₂S interaction with HKUST-1 and ZIF-8 MOFs: a multitechnique study, *Microporous Mesoporous Mater.* 207 (2015) 90–94.
- [115] Y. Belmabkhout, R.S. Pillai, D. Alezi, O. Shekhah, P.M. Bhatt, Z. Chen, et al., Metal–organic frameworks to satisfy gas upgrading demands: fine-tuning the soc-MOF platform for the operative removal of H₂S, *J. Mater. Chem. A* 5 (2017) 3293–3303.
- [116] X. Peng, D. Cao, Computational screening of porous carbons, zeolites, and metal organic frameworks for desulfurization and decarburization of biogas, natural gas, and flue gas, *AIChE J.* 59 (2013) 2928–2942.
- [117] Centers for Disease Control and Prevention (CDC), Unintentional non-fire-related carbon monoxide exposures--United States, 2001-2003, *Morbidity Mortality Wkly. Rep.* 54 (2005) 36–39.
- [118] L.D. Prockop, R.I. Chichkova, Carbon monoxide intoxication: an updated review, *J. Neurol. Sci.* 262 (2007) 122–130.
- [119] M.F. Perutz, Mechanisms regulating the reactions of human hemoglobin with oxygen and carbon monoxide, *Annu. Rev. Physiol.* 52 (1990) 1–26.
- [120] G. Meyer, L. André, S. Tanguy, J. Boissiere, C. Farah, F. Lopez-Lauri, et al., Simulated urban carbon monoxide air pollution exacerbates rat heart ischemia-reperfusion injury, *Am. J. Physiol. Heart Circulatory Physiol.* 298 (2010) H1445–H1453.
- [121] H. Tamon, K. Kitamura, M. Okazaki, Adsorption of carbon monoxide on activated carbon impregnated with metal halide, *AIChE J.* 42 (1996) 422–430.
- [122] G. Sethia, R.S. Somani, H. Chand Bajaj, Adsorption of carbon monoxide, methane and nitrogen on alkaline earth metal ion exchanged zeolite-X: structure, cation position and adsorption relationship, *RSC Adv.* 5 (2015) 12773–12781.
- [123] J.R. Karra, K.S. Walton, Molecular simulations and experimental studies of CO₂, CO, and N₂ adsorption in metal – organic frameworks, *J. Phys. Chem. C* 114 (2010) 15735–15740.
- [124] J.R. Karra, K.S. Walton, Effect of open metal sites on adsorption of polar and nonpolar molecules in metal – organic framework Cu-BTC, *Langmuir* 24 (2008) 8620–8626.
- [125] P. Chowdhury, S. Mekala, F. Dreisbach, S. Gumma, Adsorption of CO, CO₂ and CH₄ on Cu-BTC and MIL-101 metal organic frameworks: effect of open metal sites and adsorbate polarity, *Microporous Mesoporous Mater.* 152 (2012) 246–252.

- [126] L. Valenzano, B. Civalieri, K. Sillar, J. Sauer, Heats of adsorption of CO and CO₂ in metal–organic frameworks: quantum mechanical study of CPO-27-M (M = Mg, Ni, Zn), *J. Phys. Chem. C* 115 (2011) 21777–21784.
- [127] E.J. García, J.P.S. Mowat, P.A. Wright, J. Pérez-Pellitero, C. Jallut, G.D. Pirngruber, Role of structure and chemistry in controlling separations of CO₂/CH₄ and CO₂/CH₄/CO mixtures over honeycomb MOFs with coordinatively unsaturated metal sites, *J. Phys. Chem. C* 116 (2012) 26636–26648.
- [128] S. Chavan, J.G. Vitillo, E. Groppo, F. Bonino, C. Lamberti, P.D.C. Dietzel, et al., CO adsorption on CPO-27-Ni coordination polymer: spectroscopic features and interaction energy, *J. Phys. Chem. C* 113 (2009) 3292–3299.
- [129] J. Peng, S. Xian, J. Xiao, Y. Huang, Q. Xia, H. Wang, et al., A supported Cu(I) @MIL-100(Fe) adsorbent with high CO adsorption capacity and CO/N₂ selectivity, *Chem. Eng. J.* 270 (2015) 282–289.
- [130] E. Robinson, R.C. Robbins, Gaseous nitrogen compound pollutants from urban and natural sources, *J. Air Pollut. Control Assoc.* 20 (1970) 303–306.
- [131] L.S. Anderson, T.A. Mansfield, The effects of nitric oxide pollution on the growth of tomato, *Environ. Pollut.* (1970) 20 (1979) 113–121.
- [132] P.K. Lala, C. Chakraborty, Role of nitric oxide in carcinogenesis and tumour progression, *Lancet. Oncol.* 2 (2001) 149–156.
- [133] M.T. Gewaltig, G. Kojda, Vasoprotection by nitric oxide: mechanisms and therapeutic potential, *Cardiovasc. Res.* 55 (2002) 250–260.
- [134] D.J. Smith, D. Chakravarthy, S. Pulfer, M.L. Simmons, J.A. Hrabie, M.L. Citro, et al., Nitric oxide-releasing polymers containing the [N(O)NO]-group, *J. Med. Chem.* 39 (1996) 1148–1156.
- [135] I. Mochida, Y. Korai, M. Shirahama, S. Kawano, T. Hada, Y. Seo, et al., Removal of SO_x and NO_x over activated carbon fibers, *Carbon* 38 (2000) 227–239.
- [136] P.S. Wheatley, A.R. Butler, M.S. Crane, S. Fox, B. Xiao, A.G. Rossi, et al., NO-releasing zeolites and their antithrombotic properties, *J. Am. Chem. Soc.* 128 (2006) 502–509.
- [137] B. Xiao, P.S. Wheatley, X. Zhao, A.J. Fletcher, S. Fox, A.G. Rossi, et al., High-capacity hydrogen and nitric oxide adsorption and storage in a metal – organic framework, *J. Am. Chem. Soc.* 129 (2007) 1203–1209.
- [138] S.R. Miller, E. Alvarez, L. Fradcourt, T. Devic, S. Wuttke, P.S. Wheatley, et al., A rare example of a porous Ca-MOF for the controlled release of biologically active NO, *Chem. Commun.* 49 (2013) 7773–7775.
- [139] J.F. Eubank, P.S. Wheatley, G. Lebars, A.C. McKinlay, H. Leclerc, P. Horcajada, et al., Porous, rigid metal(III)-carboxylate metal-organic frameworks for the delivery of nitric oxide, *APL Mater.* 2 (2014) 124112.
- [140] J. Szanyi, M. Daturi, G. Clet, D.R. Baer, C.H.F. Peden, Well-studied Cu–BTC still serves surprises: evidence for facile Cu²⁺/Cu⁺ interchange, *Phys. Chem. Chem. Phys.* 14 (2012) 4383–4390.
- [141] D. Cattaneo, S.J. Warrender, M.J. Duncan, R. Castledine, N. Parkinson, I. Haley, et al., Water based scale-up of CPO-27 synthesis for nitric oxide delivery, *Dalton Trans.* 45 (2016) 618–629.
- [142] F. Bonino, S. Chavan, J.G. Vitillo, E. Groppo, G. Agostini, C. Lamberti, et al., Local structure of CPO-27-Ni metallorganic framework upon dehydration and coordination of NO, *Chem. Mater.* 20 (2008) 4957–4968.

- [143] D. Cattaneo, S.J. Warrender, M.J. Duncan, C.J. Kelsall, M.K. Doherty, P.D. Whitfield, et al., Tuning the nitric oxide release from CPO-27 MOFs, *RSC Adv.* 6 (2016) 14059–14067.
- [144] J.G. Nguyen, K.K. Tanabe, S.M. Cohen, Postsynthetic diazeniumdiolate formation and NO release from MOFs, *CrystEngComm* 12 (2010) 2335–2338.
- [145] M.J. Ingleson, R. Heck, J.A. Gould, M.J. Rosseinsky, Nitric oxide chemisorption in a postsynthetically modified metal–organic framework, *Inorg. Chem.* 48 (2009) 9986–9988.
- [146] P. Horcajada, R. Gref, T. Baati, P.K. Allan, G. Maurin, P. Couvreur, et al., Metal–organic frameworks in biomedicine, *Chem. Rev.* 112 (2012) 1232–1268.
- [147] J.B. DeCoste, G.W. Peterson, Metal–organic frameworks for air purification of toxic chemicals, *Chem. Rev.* 114 (2014) 5695–5727.

Metal-organic frameworks for capture and detoxification of nerve agents

Ashlee J. Howarth¹, Marek B. Majewski¹ and Omar K. Farha^{2,3,*}

¹Department of Chemistry and Biochemistry, Concordia University, Montréal, QC, Canada, ²Department of Chemistry, International Institute of Nanotechnology, Northwestern University, Evanston, IL, United States, ³Department of Chemistry, Faculty of Science King Abdulaziz, University Jeddah, Jeddah, Saudi Arabia

*Corresponding author: e-mail address: o-farha@northwestern.edu

6.1 Introduction

Hazardous biological and chemical warfare agents (CWAs) have, historically, been leveraged by warring parties to gain the upper hand while engaged in conflict. Events where the use of toxins or microorganisms (from corpses and cadavers) coupled with strategically poisoned weapons or fire and smoke to handicap the adversary have been observed since antiquity. Early accounts of chemical and biological warfare agents use include such objectionable examples as the army of Hannibal launching clay jars filled with venomous snakes onto the ships of Pergamus at Eurymedon (and subsequently winning the Battle of the Eurymedon River) in 190 BCE; Frederick Barbarossa (the Holy Roman Emperor) employing cadavers to contaminate the water supplies of his enemies at the battle of Tortona in CE 1155; the Spanish tainting wine sold to their French enemies with the blood of leprosy patients in an effort to poison them in CE 1496; and the use of saliva from rabid dogs in hollow artillery rounds fired at the enemies by Polish artillery general Siemienowicz in CE 1650 [1–3].

Although no chemical weapons were deployed during the American Civil War (1861–65), soldiers on both sides proposed their use including unrealized proposals to fire chlorine-containing projectiles and drop canisters of poisonous gas from balloons [4]. The possibility of extended chemical warfare initiated the early development of protective equipment, including early gas mask/respirator models such as those patented by Lane (1850) [5] and Hoffman in 1866 (Fig. 6.1) [6], signifying the advent of chemical detoxification, degradation, and protection strategies.

During WWI in an attempt to cause mass injuries and casualties and prior to the egregious use of chlorine, a variety of chemical agents were tested in the field. These included the use of irritant ethylbromoacetate by French military forces (August 1914), the one-off use of sneezing agent *o*-dianisidine chlorosulfonate by

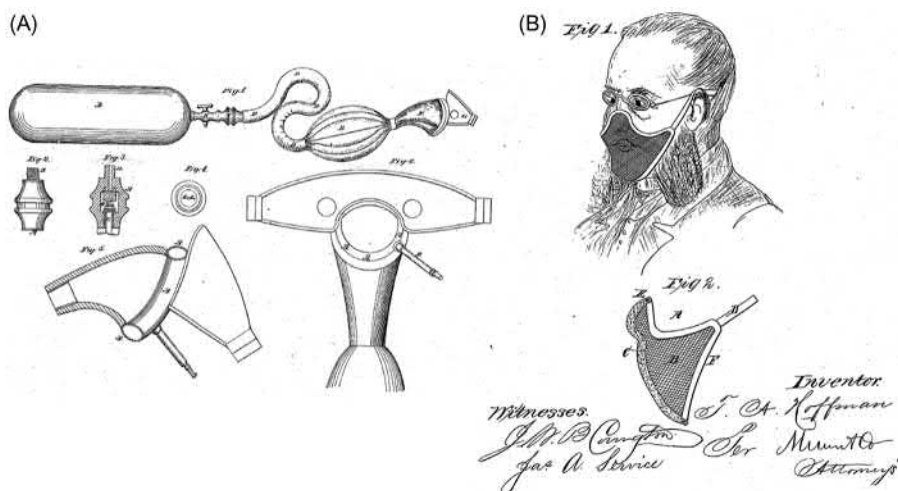


Figure 6.1 (A) Benjamin I. Lane's respirator patent including an air tank, goggles, and a rubber nose piece and (B) Theodore A. Hoffman's patented respirator/protective mask design. *Source:* Reprinted from US Patent No. 7,476 (July 2, 1850) and US Patent No. 58,255 (September 25, 1866).

German forces (October 1914), and the first use of irritant chloroacetone by the French military (November 1914) [2,7]. These events culminated in the German use of chlorine (a lung-damaging agent) in the attack at Ypres (April 22, 1915; at a site later to become known as Flanders Fields) marking the first large-scale chemical weapons attack—an event spearheaded by German scientist Fritz Haber—which killed an estimated 1100 soldiers while incapacitating many more [4,8]. The dramatic results of this attack demonstrated to all parties involved in the conflict that the use of chemical weapons was highly destructive and the next 3 years of the Great War saw the deployment and weaponization of numerous other incapacitants, choking agents, and blood agents including xylyl bromide, chloropicrin, phosgene, hydrogen cyanide, and sulfur mustard [2].

Sadly, despite the drafting and signing of the Geneva Protocol (or the Protocol for the Prohibition of the Use in War of Asphyxiating, Poisonous or other Gases, and of Bacteriological Methods of Warfare) in 1925 [9], and the genesis of the significantly more comprehensive Chemical Weapons Convention which entered into force in 1997 [10] (marking the formation of the Organisation for the Prohibition of Chemical Weapons; OPCW), chemical and biological warfare agent use continues to be of great concern today both with regards to stockpiling (or the destruction of stockpiles) and active use. Small amounts of modern chemical agents are capable of causing high numbers of casualties compared to conventional weapons (prompting the classification of CWAs as weapons of mass destruction) and the development of modern long-range missile systems enables the possibility of deploying chemical weapons at great distance necessitating an increased focus on the development of rapid and effective detoxification strategies.

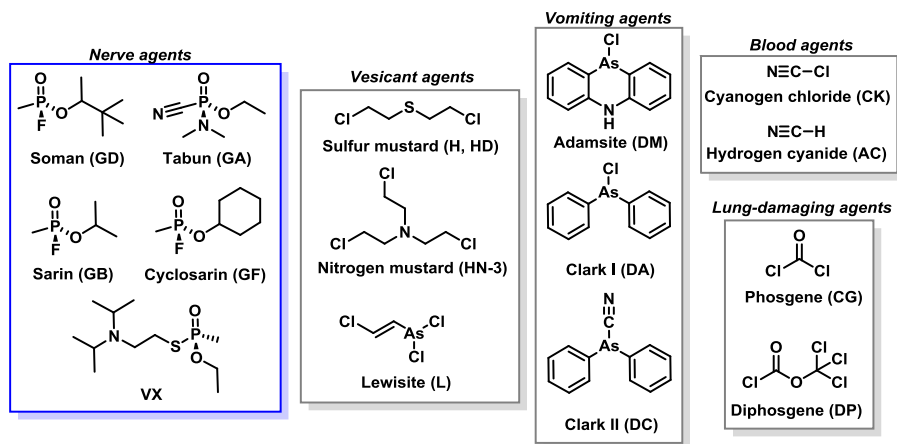


Chart 6.1 Chemical structures, common names, and US Army symbols of significant chemical warfare agents classified according to their target organs and tissues.

All chemical warfare agents are designed to produce acute effects with varying degrees of lethality and can be categorized according to their reactivity, physico-chemical features, and target organs/tissues (Chart 6.1) [2,11]. Influencing factors that regulate the lethality of chemical warfare agents are often linked to exposure and dose, where agents can be delivered as gas, liquid, aerosol (both solid and liquid), “sticky” substance, or as part of ammunition [11]. Perhaps the most insidious and destructive CWAs are those belonging to the nerve agent category. Often these agents cause death within a few minutes and owing to their inherent chemistry are particularly challenging to detoxify (Section 6.2).

Nerve agents are organophosphorus compounds and are typically structural variations of phosphoric acid esters (Chart 6.1). As their classification implies, they are lethal agents affecting the central nervous system, and were developed largely prior to and over the course of WWII. A project on synthetic insecticides in Germany (1936–37) led to the synthesis of many organophosphorus compounds, among which was the highly toxic ethyl-*N,N*-dimethylphosphoramidocyanidate (Tabun, GA) and isopropyl methylphosphonofluoridate (Sarin, GB) [2,7,12]. Pinacolyl methylphosphonofluoridate (Soman, GD) was synthesized in 1944 by Nobel laureate Richard Kuhn, while V-class nerve agents were identified by US and British laboratories with *o*-ethyl-*S*-(2-diisopropylamino-ethyl)-methyl-phosphonothiolate (VX) becoming arguably the most lethal CWA ever disclosed (estimated lethal dose of 0.3 mg per person after inhalation and 5 mg per person after dermal exposure) [2,7,12].

Nerve agents function by targeting the cholinergic synapses [11]. Briefly, organophosphorus compounds in this class bind irreversibly to the active site (Fig. 6.2) of acetylcholinesterase (AChE) which has the physiological function of inactivating the neurotransmitter acetylcholine (ACh) via hydrolytic metabolism. Inhibition of AChE activity leads to the accumulation of ACh in the synaptic space leading to

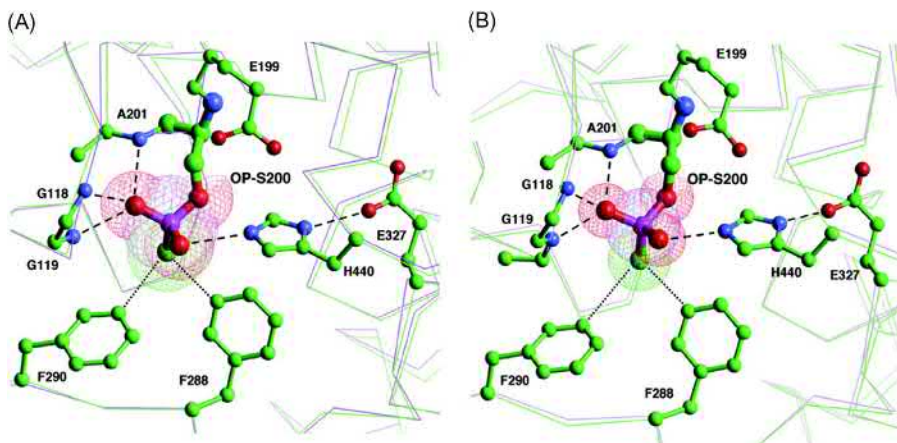


Figure 6.2 Active site of “aged” phosphylated *Torpedo californica* AChE (TcAChE) as determined by X-ray crystallography. The structures depicted were obtained by reaction of TcAChE with (A) Soman and (B) Sarin and illustrate the binding of organophosphorous compounds at the active site along with H-bonding interactions between the phosphonyl O atoms with proximal glycine, alanine, and histidine residues.

Source: Reprinted with permission from C.B. Millard, G. Kryger, A. Ordentlich, H.M. Greenblatt, M. Harel, M.L. Raves, et al., Crystal structures of aged phosphonylated acetylcholinesterase: nerve agent reaction products at the atomic level, *Biochemistry* 38 (22) (1999) 7032–7039 [13].

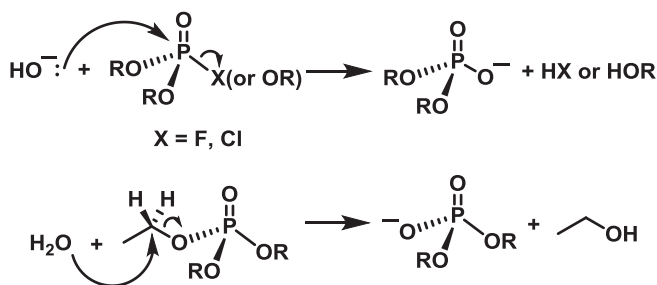
unremitting neuron stimulation. In motor neurons, the accumulation of ACh results in continuous muscle contraction leading to extreme exhaustion while in the gastrointestinal tract, the accumulated ACh acts at muscarinic receptors causing the increased secretion of fluids (and electrolytes) into the lumen of the intestine which results in severe watery diarrhea and death [14]. Because of the severity of these physiological responses to nerve agents, the US Army mandates a permissible exposure limit in air of $50 \mu\text{g m}^{-3}$ of Soman [15].

6.2 Nerve agent detoxification pathways and simulants

Early approaches to mass-detoxification of chemical warfare agents included the use of solutions of bleach or basic salts (e.g., NaOH or KOH) [16,17]. However, the logistical considerations (these solutions are corrosive and decrease in activity with prolonged storage) involved in using copious quantities of bleach solution are particularly difficult to reconcile [18]. These considerations prompted the development of new adsorbent and detoxification materials such as the M280 individual equipment decontamination kit or the M291 skin decontamination kit initially deployed in 1989 which featured fiber pads filled with high surface area carbonaceous materials for agent adsorption [16]. Additionally, this kit included strongly

acidic (cation) and basic (anion) exchange resins (Ambergard XE-555) to catalyze the hydrolysis of the adsorbed nerve agents; however, only Soman is detoxified by these materials (half-life of 30 hours) to any great effect [16,19,20].

Perhaps somewhat intuitively, the degradation of organophosphorous nerve agents proceeds via nucleophilic attack by water or OH^- and subsequent hydrolysis, converting the phosphate triester to the corresponding diester derivative [16,21–23]. Substitution can occur at either the central phosphorus atom or alternatively at sp^3 carbons present in attached alkyl groups (Scheme 6.1). In general, base catalyzed hydrolysis leads to P–O cleavage, while neutral or acid catalyzed hydrolysis favors C–O or C–S cleavage. The product distribution for organophosphorus ester hydrolysis is pH dependent with both the P–O cleavage and the C–O cleavage reaction involving $\text{S}_{\text{N}}2$ -like direct displacement (in the latter, the phosphate ester anion acts as the leaving group). In some cases, the catalytic pathway has crucial implications with regards to the nature of the products formed (vide infra). Hydrolysis can be accelerated through the coordination of the phosphoryl oxygen to a Lewis acidic atom increasing the susceptibility of the phosphorous center to nucleophilic attack [24,25]. Lewis acid participation greatly enhances the selectivity of the catalysis and we note that of importance is matching the association rate of the starting material and the dissociation rate of the products; rates which when properly balanced can afford *catalytic* (rather than stoichiometric) hydrolysis [26].



Scheme 6.1 Hydrolysis pathways of organophosphorus esters.

Owing to the high toxicity of CWAs, many lab-scale experiments are carried out on compounds acting as nerve agent simulants [27]. These compounds are structurally analogous organophosphorus molecules that feature reduced toxicity (Chart 6.2) and due to their anticipated similar chemical reactivity, these simulants act as sufficient surrogates for the nerve agents themselves. Caution, however, should be exercised when assuming that results obtained from the simulants automatically translate to the agent as many of these simulants mimic only certain aspects of the reactivity of any given agent [16]. It may be quite challenging to simulate all the properties of a target agent with just one chemical simulant. Nevertheless, many simulants have been shown to be effective surrogates as discussed in Sections 6.4 and 6.5. As an example, hydrolysis of a standard simulant dimethyl *p*-nitrophenyl

phosphate (DMNP) in the presence of a Lewis acidic catalyst yields dimethyl hydrogen phosphate and 4-nitrophenol (Scheme 6.2B) demonstrating similar reactivity to many G series agents with the 4-nitrophenyl acting as the de facto leaving group.

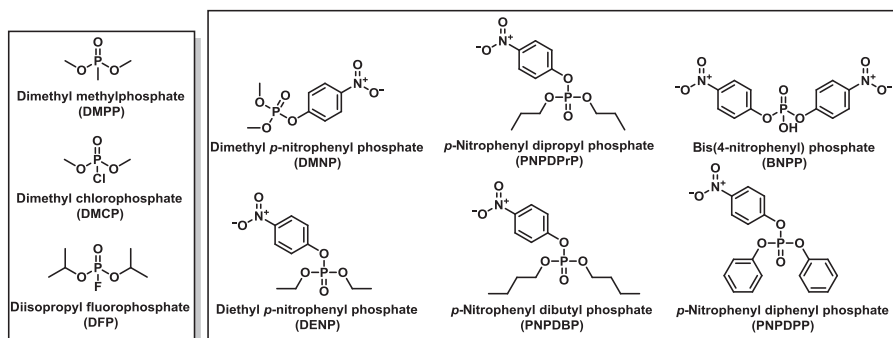
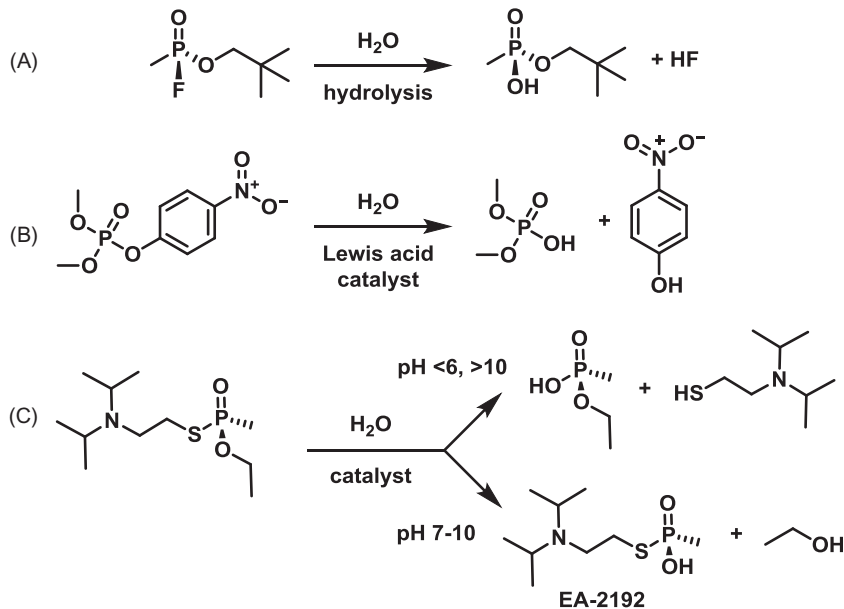


Chart 6.2 Chemical structures, names, and abbreviations for common nerve agent simulants.



Scheme 6.2 (A) Hydrolysis of Soman via nucleophilic attack by water; (B) catalytic hydrolysis of nerve agent simulant dimethyl *p*-nitrophenyl phosphate (DMNP) in the presence of a Lewis acid catalyst; and (C) two potential outcomes of the catalytic hydrolysis of nerve agent VX.

Organophosphorus nerve agents react slowly in aqueous solutions at midrange pH (6.5–7.5). The half-life of Soman in water is reported to be c. 60 hours (pH 6, 25°C); the half-life of Sarin ranges from 237 (pH 6.5) to 24 hours (pH 7.5); while the half-life of VX in water (pH 7, 25°C) ranges from 17 to 42 days [28]. Detoxification or catalytic hydrolysis of nerve agents such as Soman proceeds with the removal of the fluorine atom from the phosphorous center to give pinacolyl methylphosphonate and hydrofluoric acid (Scheme 6.2A). Hydrolysis of VX under mild conditions is particularly problematic because hydrolysis can proceed either via the P–O bond or via the P–S bond (Scheme 6.2C) [21,29]. In the former case, ethanol and highly toxic *S*-(2-(diisopropylamino)ethyl) *O*-hydrogen (*S*)-methylphosphonothioate EA-2192 are formed while in the latter case the agent is neutralized to two nontoxic products (Scheme 6.2C). The hydrolysis of VX emphasizes one challenging aspect with regards to the design of detoxification methods for nerve agents. While on the surface it appears that the use of water as the nucleophile is satisfactory (although little has been done to explore other nucleophiles), the choice of catalyst is particularly crucial with regards to the selectivity of the hydrolysis reaction to avoid the formation of toxic byproducts (Section 6.4).

One source of inspiration for the design of selective catalysts can be found in the oxyanion-linked pairs of Zn(II) ions in the active center of enzymes such as phosphotriesterase, methyl parathion hydrolase (MPH), and paraoxonase 1 (PON1). Belonging to a class of enzymes that can detoxify organophosphates these enzymes rely on metal-oxy/hydroxy species for catalytic activity [30,31]. The metal centers behave as Lewis acids, however the specifics of the activity of these enzymes ranges from binding and activation of the phosphoryl oxygen of the substrate organophosphorous compound to facilitating the delivery of a nucleophile [32]. Moreover, the dimeric metal sites are surrounded by residues (i.e., His) that enable catalysis through noncovalent interactions such as hydrogen bonding. The net result is spectacularly enhanced rates of hydrolysis (in some cases reaching nine orders of magnitude). In the end, these natural systems can serve as a design roadmap for the synthetic catalysts that obviate the target specificity often observed in enzymes while preserving a high degree of functionality.

6.3 Early generation supramolecular catalysts

Prior to the development of metal-organic framework (MOF) catalysts for nerve agent detoxification, a handful of supramolecular materials were explored for this potential application. Perhaps foreshadowing the use of MOFs, these supramolecular catalytic materials were designed and studied owing, in part, to the well-defined cavities, and site-isolated active sites that supramolecular assemblies impose. An early example by Van Hooijdonk et al. in 1970 examined the breakdown of Sarin catalyzed by α -cyclodextrin (Fig. 6.3) in aqueous alkaline solution [33]. It was concluded that a 1:1 α -CD:GB inclusion complex is an important intermediate in this reaction as it promotes nucleophilic attack on the phosphorus in Sarin by –OH

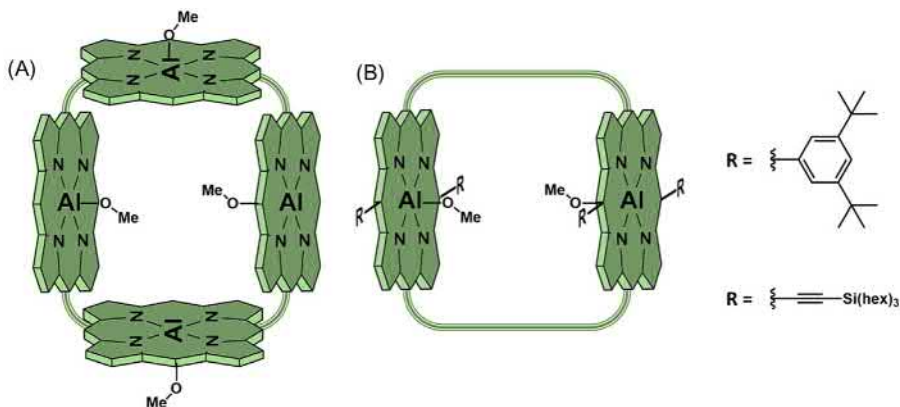


Figure 6.4 (A) Representation of the aluminum porphyrin box highlighting the nucleophilic Al-OMe moieties. (B) Aluminum porphyrin dyads with varying substituents on the porphyrin core.

In a related study, tuning the electronic properties of Al-porphyrin dyads (Fig. 6.4B) by the addition of $-\text{Si}(\text{hex})_3$ electron withdrawing groups on the porphyrin core, was found to increase the nucleophilicity of Al-OMe and the Lewis acidity of Al(III), resulting in a sevenfold increase in initial catalytic rate ($1.2 \times 10^{-6} \text{ M s}^{-1}$, 3 mol%) for the methanolysis of PNPDP compared to reactions performed with Al-porphyrin dyads with 3,5-di-*t*-butyl aryl substituents ($1.7 \times 10^{-7} \text{ M s}^{-1}$, 3 mol%) [42].

Expanding on the notion that substrate encapsulation and accessible Lewis acid sites are important parameters for catalytic nerve agent simulant detoxification, Farha, Hupp, Nguyen et al. reported catechol-containing porous organic polymers (POPs) functionalized with La(III) (Fig. 6.5) for the hydrolysis and methanolysis of DMNP [25]. Increasing the pore volume of the POP by replacing a carbon node in LaA_2B_1 with an adamantane cage node in LaA_2C_1 (Fig. 6.6) was found to increase the initial rate of DMNP methanolysis by a factor of c. 2.5 (7.0×10^{-7} vs $1.7 \times 10^{-6} \text{ M s}^{-1}$, 6 mol%). In addition, both POPs are capable of catalyzing the hydrolysis of DMNP with a similar initial rate ($1.1 \times 10^{-6} \text{ M s}^{-1}$, 6 mol%)—12 times faster than that of the uncatalyzed reaction. Due to the utility of these Al-porphyrin systems, as well as POPs, in the catalytic methanolysis of organophosphorus-based nerve agent simulants, and in a seemingly logical progression, Al-porphyrin POPs (Al-PPOPs) were designed and studied for the methanolysis of DMNP [43]. In this example, the importance of supercritical processing of the POPs was emphasized since proper activation (i.e., not collapsing the POP pores) was found to give a five- to sevenfold increase in the initial rate of methanolysis versus the thermally activated materials ($2.8\text{--}4.8 \times 10^{-7}$ vs $1.5\text{--}3.5 \times 10^{-6} \text{ M s}^{-1}$; 4 mol%). This is consistent with the previous study on La-POPs where higher pore volumes were found to lead to faster catalytic rates [25]. Although easier to synthesize than Al-porphyrin boxes and dyads, these

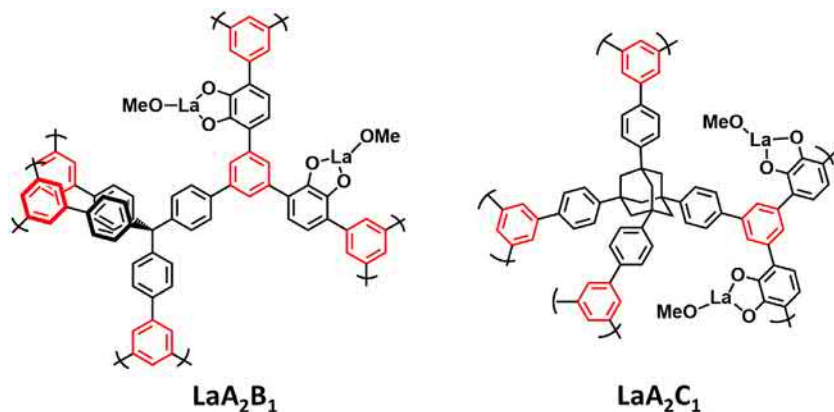


Figure 6.5 Idealized representation of La-based porous organic polymers with carbon versus adamantane core.

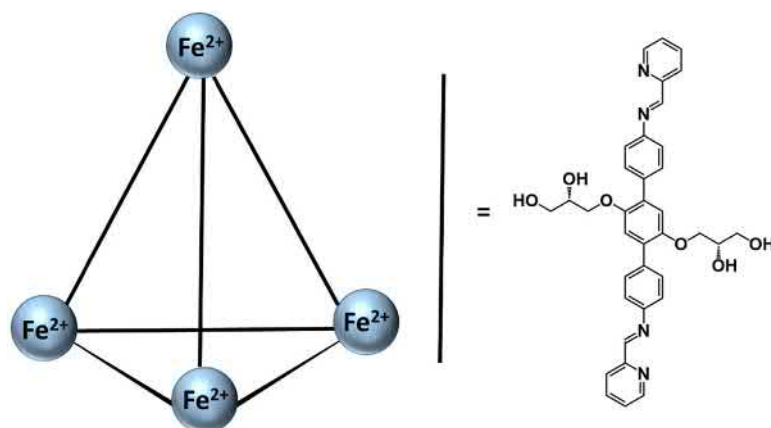


Figure 6.6 Fe_4L_6 cage and the terphenylene-based linker used to construct the cage.

POPs are still limited to performing nerve agent and simulant detoxification by methanolysis (rather than the more broadly applicable hydrolysis).

Concurrent to the development and exploration of porphyrin boxes and POPs as catalysts for nerve agent simulant detoxification, Nitschke et al. reported a water soluble $\text{Fe}(\text{II})$ cage [Fe_4L_6] (Fig. 6.6) capable of catalytically hydrolyzing 2,2-dichlorovinyl dimethyl phosphate (dichlorovos, a synthetic insecticide capable of AChE inhibition) [44]. This hydrophobic cage was demonstrated to encapsulate numerous guest molecules, yielding a half-life for detoxification of dichlorovos of less than 24 hours (1 mol% of the $\text{Fe}(\text{II})$ cage). The mechanism of the hydrolysis reaction in this example is thought to occur in a similar fashion to the cyclodextrin-based catalysts where hydroxy groups on the constituent ligands facilitate nucleophilic attack of the organophosphorus compound.

Although the half-lives for nerve agent simulant degradation in the examples discussed above are on the order of hours/days as opposed to seconds/minutes, these studies have played an important role in the subsequent development of porous catalysts for this application. In effect, these examples have set the stage for the design of MOF catalysts since key design rules such as the significance of cage/pore size, pore volume, Lewis acidity, and accessibility of Lewis acid sites were all discovered. All these features are vital parameters in designing the champion MOF catalysts discussed in the following Section 6.4. We note that supramolecular assemblies continue to be investigated and developed for catalytic nerve agent degradation, including such recent examples as the functionalization of sulfonatocalix [4]arenes which were shown to catalytically detoxify VX and related V-agents with half-lives as low as 2–3 minutes [45].

6.4 Metal-organic framework catalysts

The study of metal-organic frameworks as catalysts for nerve agent simulant degradation earnestly began in 2010–11 with the development of polyoxometalate-based Ho(III) [46] and Cu(II) [47] MOFs (PMOFs, Fig. 6.7) capable of hydrolytically detoxifying the organophosphorus-based compounds bis(4-nitrophenyl) phosphate (BNPP) and dimethyl methylphosphate (DMMP), respectively. While the catalytic activity of the Ho(III) PMOF was attributed to the accessible Lewis acidic Ho(III) sites of the MOF nodes, the activity of the Cu(II) PMOF (NENU-11) was suggested to come from the W(VI) polyoxometalate. A few years later, however, Halve et al. showed the catalytic hydrolysis of Sarin and its simulants using Cu(II)-based MOF, HKUST-1 (Fig. 6.7) [48] (the MOF component of the PMOF NENU-11), demonstrating that accessible Cu(II) sites can perform the hydrolysis reaction, and that the Cu(II) nodes in NENU-11 likely contribute to the overall catalytic activity of the PMOF. It is important to note that while the half-life for detoxification of Sarin using HKUST-1 was found to be 1 hour, Wagner et al. found that the half-lives for VX and Soman using the same MOF catalyst

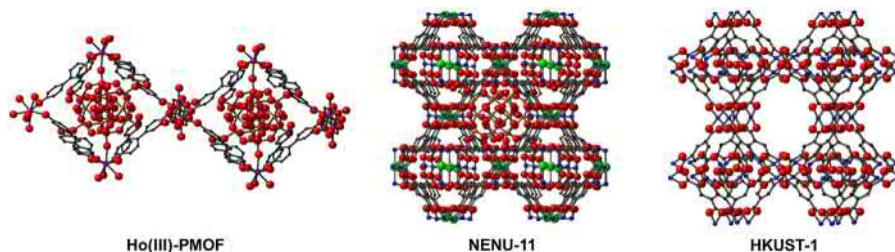


Figure 6.7 The first metal-organic frameworks studied for nerve agent simulant detoxification, Ho(III)-PMOF, NENU-11, and HKUST-1. Carbon, black; oxygen, red; nitrogen, light blue; holmium, purple; tungsten, orange; boron, blue; phosphorus, gray; chlorine, green.

under similar conditions were longer than 24 hours [49], potentially due to the increasing size of the nerve agents (Sarin < Soman < VX) leading to slower reactant diffusion or to electronic differences in the agents causing changes in reactivity. We note that while researchers began exploring MOF catalysts for nerve agent and simulant detoxification, simultaneously there were also several studies reporting the use of MOFs exclusively for the capture (i.e., adsorption) of these agents [50,51], however, the use of MOFs for both capture and degradation/detoxification is more prevalent (“all-in-one” functional materials) and is thus the focus here.

In 2013, Hatton et al. reported the catalytic hydrolysis of diethyl *p*-nitrophenyl phosphate (DENP) using the Cr(III)-based MOF, MIL-101, postsynthetically modified with dialkylaminopyridine ligands (DAAP) (Fig. 6.8) [52]. In this work, increasing the pH of the reaction solution from pH 7 to 10 while using the most successful catalyst of the series (MIL-101A), decreased the half-life for DENP hydrolysis from 18.9 to 5.0 hours. The enhanced catalytic activity of the MIL-101-DAAP series, compared to the parent MOF or DAAP ligands alone was attributed to a Lewis acid–Lewis base activation mechanism where the Lewis acid is the Cr(III) site and the Lewis base is the DAAP ligand installed postsynthetically in the MOF.

Concurrent to development and testing of Cu(II), Ho(III) and Cr(III) MOFs for nerve agent and simulant detoxification, Wagner, Peterson et al. reported the use of $Zr(OH)_4$ for the hydrolysis of Soman and VX [53]. The half-lives observed using an excess (i.e., neither catalytic nor stoichiometric amounts) of $Zr(OH)_4$ were 8.7 and 1 minutes respectively. $Zr(OH)_4$ was found to selectively hydrolyze VX at the P–S bond leading to the less toxic products ethyl methylphosphonic acid (EMPA) and 2-(diisopropylamino)ethanethiol (DESH). This is important since cleaving VX at the P–O bond leads to the formation of the highly toxic product *S*-2-(diisopropylaminoethyl) methyl phosphonothioic acid (EA-2192) [54]. Although not catalytic, the hydrolysis results observed using $Zr(OH)_4$ were certainly intriguing, warranting the exploration of Zr(IV)-based MOFs for catalytic hydrolysis applications. In 2014, Farha, Hupp et al. reported the first study of a Zr-based MOF for the catalytic

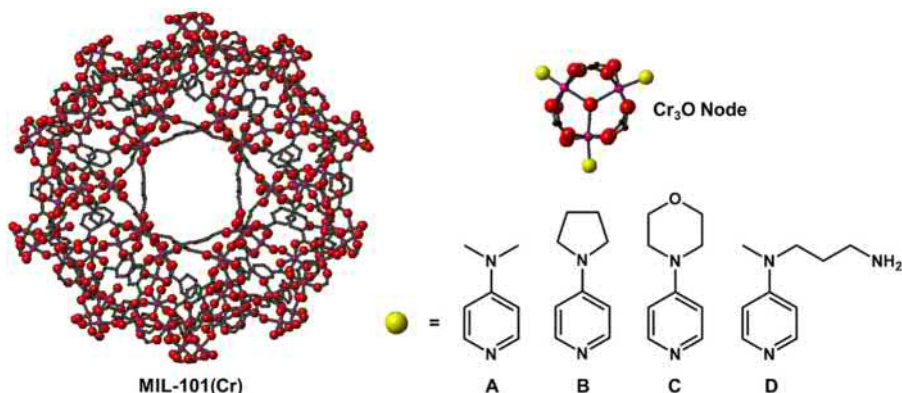


Figure 6.8 Structure of MIL-101(Cr) highlighting the Cr_3O node and the postsynthetically installed dialkylaminopyridine (DAAP) ligands. Carbon, black; oxygen, red; chromium, pink.

hydrolysis of a nerve agent simulant, DMNP [24]. In this example the prototypical Zr_6 -MOF, UiO-66 (Fig. 6.9) [55], was utilized as a catalyst and the half-life for the hydrolysis of DMNP was found to be 45 minutes. In a follow-up study this half-life decreased to 35 minutes [56], possibly due to the introduction of more defects in the structure of UiO-66 [57] or a decrease in the crystallite sizes of the sample tested [58]. Adjusting the pH of the buffer solution reaction medium from 10.2 to 8.6 was found to further increase the hydrolysis reaction rate when using UiO-66 as a catalyst [59]. Hupp, Farha et al. also demonstrated that increasing the pore and aperture size of the Zr_6 -MOF catalyst by using UiO-67 (Fig. 6.9) compared to UiO-66 leads to a significant decrease in the half-life for DMNP hydrolysis (4.5 minutes) [56], and Abrantes et al. reported similar success using UiO-67 [60]. Interestingly, the addition of amino groups on the MOF linkers led to a further decrease in the DMNP reaction half-life to 2 minutes for UiO-67-NH₂ and UiO-67-NMe₂ and 1 minute for UiO-66-NH₂ [56]. Mechanochemically synthesized samples of UiO-66-NH₂ were also demonstrated to hydrolyze DMNP with a half-life of 2.5 and 2 minutes for samples prepared by liquid-assisted grinding and accelerated aging, respectively [61]. It has also recently been shown by Farha et al. that not only the presence but also the proximity of amino groups to the Zr_6 -node has a significant effect on the hydrolysis half-life observed, owing to the fine tuning of the solvent

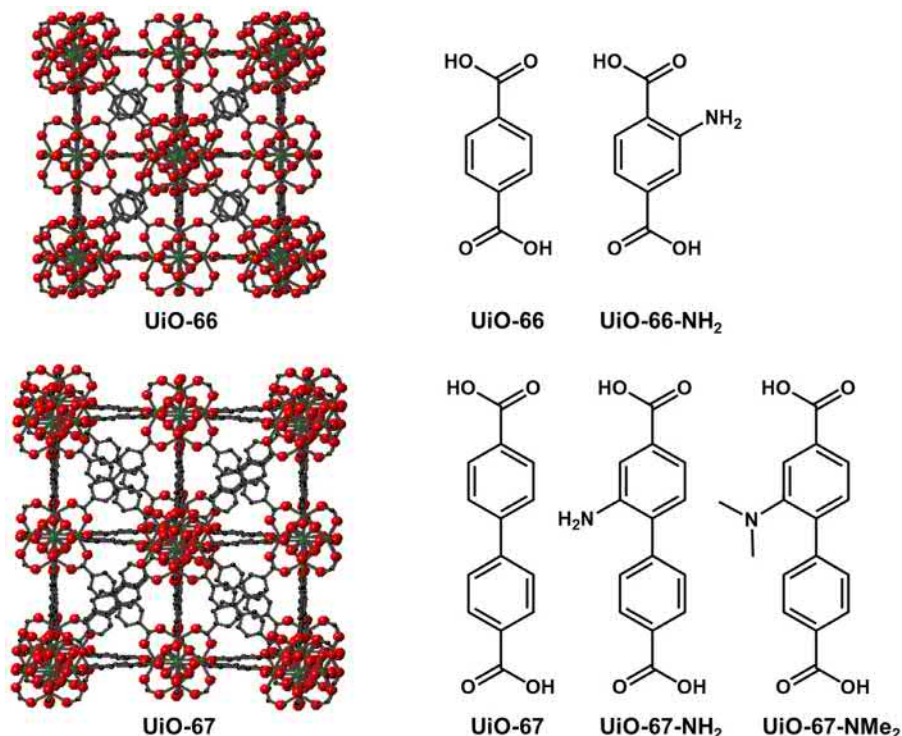


Figure 6.9 Structure of UiO-66 and UiO-67 showing the parent and amino-functionalized linkers used to construct the framework. Carbon, black; oxygen, red; zirconium, green.

coordination shell which is driven by the amino groups around defect sites (i.e., active Zr sites) on the node [62]. In addition to proving competent for the hydrolysis of nerve agent simulants, when tested as catalysts for the selective hydrolysis of VX, UiO-67-NH₂ and UiO-67-NMe₂ demonstrated half-lives of 6 and 1.8 minutes respectively, making UiO-67-NMe₂ among the best abiotic materials reported for VX detoxification [63]. The amino-derivatives of UiO-66 and UiO-67 were also shown to catalytically detoxify Soman with half-lives of less than 3 minutes [64].

To further enhance the catalytic reaction rates and decrease the half-lives for DMNP (and nerve agent) hydrolysis, Hupp, Farha et al. turned to Zr(IV)-MOFs with lower node connectivity and thus more accessible Lewis acidic Zr(IV) active sites, while also targeting structures with larger pore apertures to help promote reactant and product diffusion. NU-1000 (Fig. 6.10) is comprised of eight-connected Zr₆-nodes (as opposed to the 12-connected Zr₆-nodes of the UiO-MOFs, Fig. 6.11)

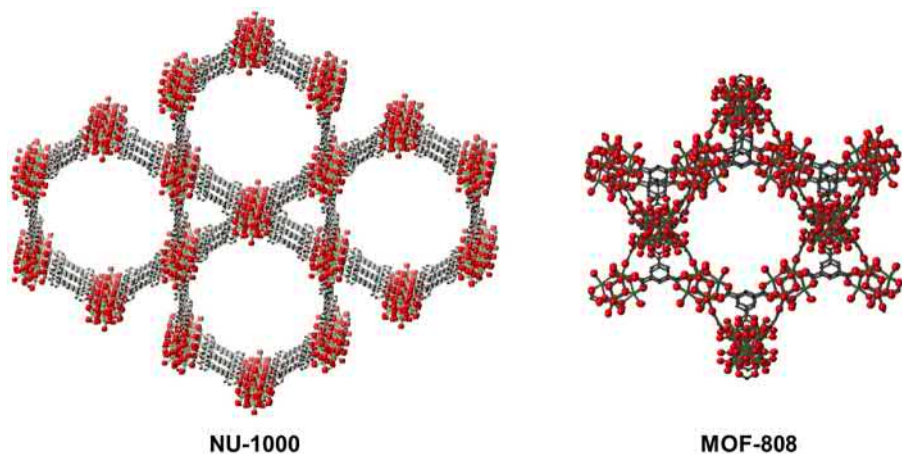


Figure 6.10 Structure of NU-1000 and MOF-808. Carbon, black; oxygen, red; zirconium, green.

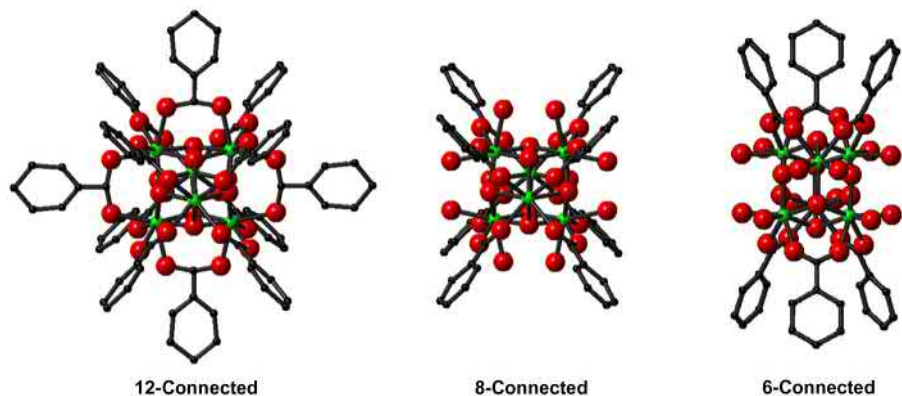


Figure 6.11 The varying connectivity of the Zr₆O₄(OH)₄-based node. Carbon, black; oxygen, red; zirconium, green.

with large 30 Å hexagonal channels as well as smaller 12 Å triangular channels [65]. While NU-1000 was found to catalytically hydrolyze DMNP with a half-life of 15 minutes, the dehydrated version of NU-1000 gave a half-life of only 1.5 minutes under the same conditions [66]. Given that removal of the terminal $-OH$ and $-OH_2$ ligands by dehydration leads to an enhancement in the reaction rate, these findings give experimental insight into the mechanism of nerve agent hydrolysis on Zr_6 -based MOF catalysts confirming that displacement of these ligands is required for nerve agent binding and for initiating the reaction. Nerve agent and simulant binding has been shown computationally [66,67] and experimentally [68] to be an important part of the reaction mechanism. By further lowering the Zr_6 -node connectivity of the MOF catalyst using the six-connected (Fig. 6.11) MOF-808 (Fig. 6.10), the half-life for DMNP hydrolysis was observed to be less than 30 seconds, making MOF-808 the fastest MOF catalyst studied for this reaction to date [69].

Apart from a few of the early examples of MOF catalysts for nerve agent and simulant degradation (i.e., HKUST-1, NENU-11, and Ho-PMOF), the hydrolysis reactions are typically performed at pH 10 in a buffer or pH adjusted solution. The most commonly employed aqueous buffer is *N*-ethylmorpholine, however *N*-cyclohexyl-2-aminoethanesulfonic acid buffer has also been used as well as the organic bases (not buffer solutions) *N*-methylmorpholine or trimethylamine (Chart 6.3) and Hupp, Farha et al. showed that the aqueous pH 10 buffer solution could be replaced with a heterogeneous buffer, polyethyleneimine (PEI). Using dehydrated NU-1000 as a catalyst and PEI with molecular weight 2500 $g\ mol^{-1}$ as a heterogeneous buffer, DMNP, Soman, and VX were hydrolyzed with half-lives of 1.8, 3.8, and 12.7 minutes, respectively [70]. The PEI heterogeneous buffer was also used with Ce-UiO-66 as a catalyst and the half-life for DMNP hydrolysis was found to be faster using the heterogeneous buffer (4.5 minutes) compared to using the homogeneous *N*-ethylmorpholine buffer (8 minutes) [71].

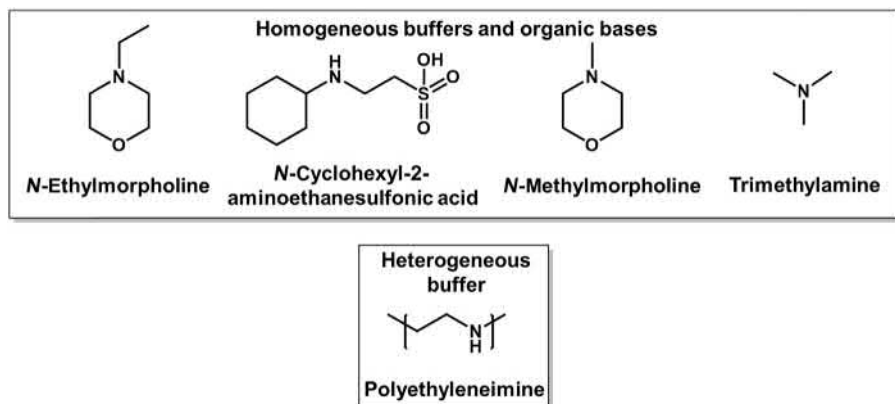


Chart 6.3 Structures of the homogenous buffers and organic bases as well as the heterogeneous buffer used as a reaction medium. Note: *N*-ethylmorpholine is mixed with acetic acid to generate a buffer solution.

The examples highlighted in this section demonstrate the considerable progress that has been made since 2010 in developing MOF catalysts for the hydrolysis of nerve agents and simulants. From catalysts with half-lives on the order of days to catalysts capable of hydrolyzing both simulants and nerve agents with half-lives <5 minutes, in addition to a shift from homogeneous to heterogeneous buffers for the reaction. In the next section the development of MOF-based textiles and antidotes will be highlighted as these represent continued progress toward the application of these materials.

6.5 Catalytic metal-organic framework composites: textiles and antidotes

One potential approach to applying the MOF catalysts discussed in Section 6.4 is to incorporate these materials in textiles, specialty fabrics, or coatings. An early example of this from Hatton et al. took advantage of $-\text{NH}_2$ groups on the surface of NH_2 -MIL-101(Al)-4-MAP (where 4-MAP is 4-methylaminopyridine) for covalent attachment to a polyisobutylene (PIB)-toluene diisocyanate (TDI) adhesive layer through reaction with isocyanate groups [72]. This PIB-TDI adhesive layer was chosen as it is too large to fit in the MOF pores, but reacts with the surface of the $-\text{NH}_2$ functionalized MOF as well as with hydroxyl groups present in natural fibers such as cotton and wool. The adhesive layer was used to attach the MOF catalysts to a butyl rubber glove and the MOF-glove composite was demonstrated to hydrolyze diisopropyl fluorophosphate (DFP) with a half-life of approximately 5 hours. A few years later, Navarro et al. coated electrospun silk fibroin with UiO-66 and lithium alkoxide doped UiO-66 and found half-lives using the composite material of 20 and 50 minutes for DFP and DMMP hydrolysis, respectively [73]. In this case the MOF catalyst was deposited onto the silk fibroin by spraying a methanolic suspension containing 200 nm MOF crystals directly onto the fiber.

NU-1000 has also been incorporated into textile composites, including a derivative of NU-1000 functionalized with the halochromic ligand, 5(6)-carboxynaphthofluorescein (CNF) [74]. Farha et al. showed that NU-1000-CNF embedded in a cellulose fiber membrane could colorimetrically detect the acidic byproduct produced (i.e., HF) during nerve agent hydrolysis (Fig. 6.12A). The NU-1000/PEI heterogeneous catalyst/buffer system discussed in Section 6.4 was also incorporated in cellulose (a cotton ball) and DMNP was hydrolyzed (97%) by the composite after 30 minutes (Fig. 6.12B) [70]. In each case the cellulose was soaked in a suspension of NU-1000 to create the composite material.

Using a different approach for the synthesis of MOF-textile composite materials, Peterson, Parsons et al. grew thin films of UiO-66, UiO-66- NH_2 , and UiO-67 on TiO_2 -coated electrospun nylon 6 nanofibers [75]. Nylon 6 nanofibers were coated with a 5-nm-thick layer of TiO_2 using atomic layer deposition and this coating was used as a nucleation site for the growth of Zr-based MOF thin films. The UiO-67/ TiO_2 /Nylon 6 composite gave a half-life for Soman hydrolysis of only 2.3 minutes.

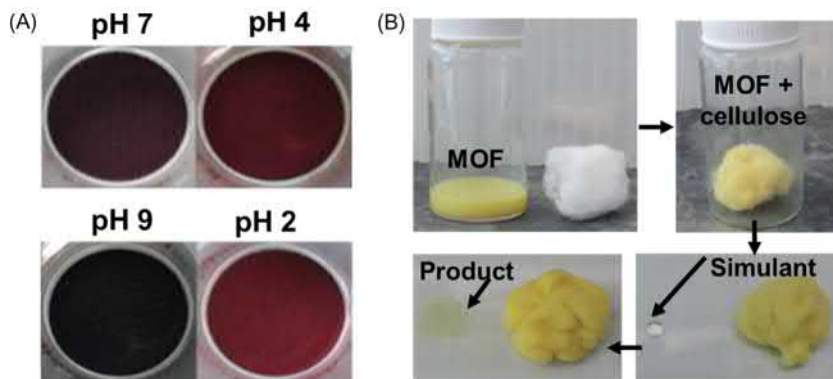


Figure 6.12 (A) NU-1000-5(6)-carboxynaphthofluorescein embedded in a cellulose fiber membrane after exposure to solutions of varying pH [74]. (B) NU-1000 and heterogeneous buffer, polyethyleneimine, incorporated in cellulose and tested for hydrolysis of DMNP (simulant) [70].

Follow-up studies looked at using β -cyclodextrin and cetyltrimethylammonium bromide as self-assembly agents (on top of the ALD coatings) [76], in addition to growth rates of MOF thin films on ZnO, Al₂O₃, and TiO₂-coated polypropylene fibers [77]. In the latter example the TiO₂-coated fibers were found to perform the best in terms of MOF uniformity and loading as well as stability during the nerve agent simulant hydrolysis reaction [77].

Some other MOF-textile composites include UiO-66 electrospun in a poly (methyl methacrylate)/Ti(OH)₄ matrix [78]. This material yields a half-life for DMNP hydrolysis of 29 minutes. Composites of HKUST-1 with cotton and graphitic carbon nitride nanospheres were also studied and found to be capable of adsorbing, degrading, and colorimetrically sensing the nerve agent simulant dimethyl chlorophosphate (DMCP), however no information about degradation half-lives were reported [79,80].

MOFs have also been used to encapsulate and protect nerve agent detoxifying enzymes [81,82]. Organophosphorus acid anhydrolase (OPAA) is a natural enzyme that is highly effective for the catalytic hydrolysis of the P–F, P–S, P–O, and P–CN bonds found in nerve agents. Although this enzyme is highly effective for nerve agent detoxification, like most enzymes, it is sensitive to its present environment and suffers from instability in organic solvent at elevated temperature and with changes in relative humidity. With this in mind, Farha et al. showed that OPAA can be encapsulated in the large hexagonal pores of the Zr-based MOF, PCN-128y, while keeping the smaller triangular pores empty and available for reactant and product diffusion (Fig. 6.13) [81]. Although the initial rate of DFP hydrolysis using the PCN-128y-OPAA composite was not as fast as that of the free enzyme, the composite retained catalytic activity after incubation at 55°C, while the free enzyme only reached 50% conversion of DFP under the same incubation conditions. Similarly, the composite reached 75% DFP conversion after incubation at

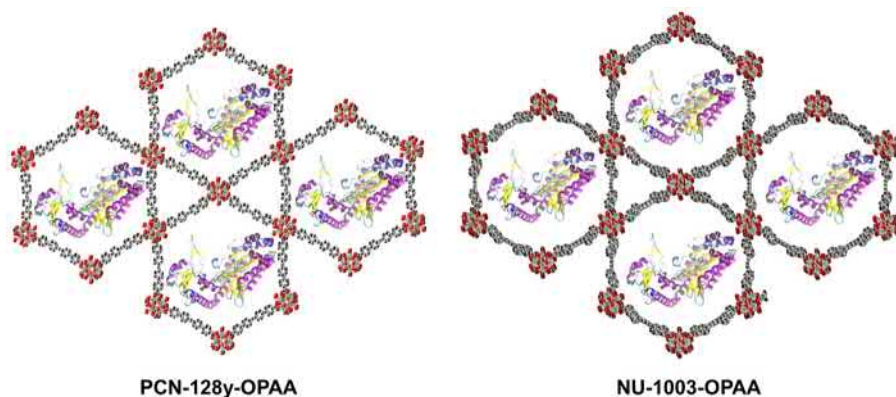


Figure 6.13 Structure of PCN-128y and NU-1003 with organophosphorus acid anhydrolase (OPAA) encapsulated in the larger hexagonal pores.

70°C while only 20% conversion was achieved using the free enzyme after 70°C incubation. Building on this work, Farha et al. showed that by extending the diameter of the MOF pores by 2 Å, using NU-1003 (Fig. 6.13), and by decreasing the particle size to 300 nm Soman could be catalytically hydrolyzed using the NU-1003-OPAA composite with an initial reaction rate three times faster than that of free OPAA [82]. Thus not only is the enzyme protected by the MOF, but its activity for nerve agent hydrolysis is also enhanced, possibly due to disruption of enzyme aggregation and/or preconcentration of the substrate and/or the stabilization of a highly active conformation of the enzyme in the MOF pores.

The materials outlined in this section demonstrate the significant potential for MOF catalysts to be incorporated as catalytically active constituents of speciality fabrics and textiles toward use in protective clothing. In addition, combining MOFs with well-studied enzymes capable of transforming organophosphorous compounds yields biocomposites that have the potential to act as MOF-based nerve agent “antidotes” where in one example the framework is used to encapsulate and protect the highly efficient OPAA enzyme.

6.6 Conclusion and outlook

There has been significant progress in the design and synthesis of catalytic materials for nerve agent and simulant detoxification—from the development of early generation supramolecular catalysts, to metal-organic frameworks, and MOF-composite materials. This is readily illustrated by considering the observed decreases in detoxification reaction half-lives for nerve agents and simulants. At the advent of molecular and macromolecular strategies for the detoxification of these insidious weapons, half-lives were first reported to be on the order of days while in modern catalyst designs they are now measured on the order of minutes.

As outlined in this overview, progress in this area has been rapid, but there remain important milestones to be reached. In the most effective catalytic systems the use of the liquid buffer solution reaction medium must be eliminated or heterogenized for practical application. Furthermore, catalytic reactions need to be optimized for efficacy in the gas phase for the elimination of agents delivered as a gas or aerosol, ostensibly for the deployment of these catalysts in modern versions of gas masks, respirators, protective equipment, and ventilation systems. Independent of these limitations, other aspects for improving the competency of MOFs as catalysts or as scaffolds for catalysts include recent efforts to develop consistent synthetic methodologies to prepare MOF crystallites with sizes in the nano-regime [82–85]. As expected, smaller MOF crystallites boast increased catalytic rates along with substrate access to catalytic sites further within the MOF particle. We anticipate that the continued development of these types of methodologies will impact the catalytic degradation of nerve agents regardless of the application (be it for destroying stockpiles or in protective equipment). In this respect, MOFs engender unique opportunities compared to other supramolecular catalysts. This is in addition to the consistent development of MOFs that are stable across wider ranges of pH and improved synthetic techniques making MOFs more accessible on a large scale.

To date, MOFs have successfully been used to capture and detoxify what is arguably the most repugnant of chemical warfare agents: nerve agents. There is still much to be learned about MOF catalysts for this application and how best to apply them in real-world applications be it in masks and clothing, or for the decontamination of military equipment and bulk stockpiles of nerve agents around the world.

References

- [1] J.K. Smart, History of chemical and biological warfare: an american perspective, in: F.R. Sidell, E.T. Takafuji, D.R. Franz (Eds.), *Medical Aspects of Chemical and Biological Warfare*, Office of The Surgeon General at TMM Publications: Borden Institute, Walter Reed Army Medical Center, Washington, DC, 1997, pp. 9–87.
- [2] L. Szinicz, History of chemical and biological warfare agents, *Toxicology* 214 (3) (2005) 167–181.
- [3] V. Barras, G. Greub, History of biological warfare and bioterrorism, *Clin. Microbiol. Infect.* 20 (6) (2014) 497–502.
- [4] S. Everts, A brief history of chemical war. <https://www.sciencehistory.org/distillations/magazine/a-brief-history-of-chemical-war> (accessed 23.04.18).
- [5] B.I. Lane, Respirator. 7476, 1850.
- [6] T.A. Hoffman, Respirator. 58255, 1866.
- [7] J.P. Robinson, M. Leitenberg, The rise of CB weapons, *The Problem of Chemical and Biological Warfare*, Vol. 1, Almqvist & Wiksell, Stockholm, 1971, p. 395.
- [8] S. Everts, When chemicals became weapons of war. <http://chemicalweapons.cenmag.org/> (accessed 23.04.18).
- [9] R.J. McElroy, The Geneva Protocol of 1925, in: M. Krepon, D. Caldwell (Eds.), *The Politics of Arms Control Treaty Ratification*, Palgrave Macmillan US, New York, 1991, pp. 125–166.

- [10] United Nations Office for Disarmament Affairs. <https://www.un.org/disarmament/wmd/chemical/> (accessed 23.04.18).
- [11] M. Schwenk, Chemical warfare agents. Classes and targets, *Toxicol. Lett.* (2017).
- [12] B. Holmstedt, Structure-activity relationships of the organophosphorus anticholinesterase agents, in: G.B. Koelle (Ed.), *Cholinesterases and Anticholinesterase Agents*, Springer Berlin Heidelberg, Berlin, Heidelberg, 1963, pp. 428–485.
- [13] C.B. Millard, G. Kryger, A. Ordentlich, H.M. Greenblatt, M. Harel, M.L. Raves, et al., Crystal structures of aged phosphonylated acetylcholinesterase: nerve agent reaction products at the atomic level, *Biochemistry* 38 (22) (1999) 7032–7039.
- [14] T.A. Bertram, J.W. Ludlow, J. Basu, S. Muthupalani, Chapter 56 - digestive tract A2 - Haschek, Wanda M., in: C.G. Rousseaux, M.A. Wallig (Eds.), *Haschek and Rousseaux's Handbook of Toxicologic Pathology*, third ed., Academic Press, Boston, 2013, pp. 2277–2359.
- [15] R.P.S. Pohanish, *Sittig's Handbook of Toxic and Hazardous Chemicals and Carcinogens*, sixth ed., William Andrew Publishing, Oxford, 2012, pp. 2328–2482.
- [16] Y.C. Yang, J.A. Baker, J.R. Ward, Decontamination of chemical warfare agents, *Chem. Rev.* 92 (8) (1992) 1729–1743.
- [17] J. Epstein, V.E. Bauer, M. Saxe, M.M. Demek, The chlorine-catalyzed hydrolysis of isopropyl methylphosphonofluoridate (Sarin) in aqueous solution, *J. Am. Chem. Soc.* 78 (16) (1956) 4068–4071.
- [18] Y.J. Jang, K. Kim, O.G. Tsay, D.A. Atwood, D.G. Churchill, Update 1 of: destruction and detection of chemical warfare agents, *Chem. Rev.* 115 (24) (2015) PR1–PR76.
- [19] B.J. Lukey, H.F. Slife, E.D. Clarkson, C.G. Hurst, E.H. Braue, Chemical warfare agent decontamination from skin, in: J.A. Romano, B.J. Lukey, H. Salem (Eds.), *Chemical Warfare Agents: Chemistry, Pharmacology, Toxicology, and Therapeutics*, CRC Press, Taylor & Francis Group, LLC, Boca Raton, FL, 2008, pp. 611–627.
- [20] G.W. Wagner, Q. Chen, Y. Wu, Reactions of VX, GD, and HD with nanotubular titania, *J. Phys. Chem. C* 112 (31) (2008) 11901–11906.
- [21] Y.-C. Yang, Chemical detoxification of nerve agent VX, *Acc. Chem. Res.* 32 (2) (1999) 109–115.
- [22] E.Bs Vladimir, Kinetics of the hydrolysis of phosphate esters, *Russ. Chem. Rev.* 46 (9) (1977) 828.
- [23] J. Florián, A. Warshel, Phosphate ester hydrolysis in aqueous solution: associative versus dissociative mechanisms, *J. Phys. Chem. B* 102 (4) (1998) 719–734.
- [24] M.J. Katz, J.E. Mondloch, R.K. Totten, J.K. Park, S.T. Nguyen, O.K. Farha, et al., Simple and compelling biomimetic metal–organic framework catalyst for the degradation of nerve agent simulants, *Angew. Chem.* 126 (2) (2014) 507–511.
- [25] R.K. Totten, M.H. Weston, J.K. Park, O.K. Farha, J.T. Hupp, S.T. Nguyen, Catalytic solvolytic and hydrolytic degradation of toxic methyl paraoxon with La(catecholate)-functionalized porous organic polymers, *ACS Catal.* 3 (7) (2013) 1454–1459.
- [26] Y. Liu, A.J. Howarth, N.A. Vermeulen, S.-Y. Moon, J.T. Hupp, O.K. Farha, Catalytic degradation of chemical warfare agents and their simulants by metal-organic frameworks, *Coord. Chem. Rev.* 346 (2017) 101–111.
- [27] S.L. Bartelt-Hunt, D.R.U. Knappe, M.A. Barlaz, A review of chemical warfare agent simulants for the study of environmental behavior, *Crit. Rev. Environ. Sci. Technol.* 38 (2) (2008) 112–136.
- [28] N.B. Munro, S.S. Talmage, G.D. Griffin, L.C. Waters, A.P. Watson, J.F. King, et al., The sources, fate, and toxicity of chemical warfare agent degradation products, *Environ. Health Perspect.* 107 (12) (1999) 933–974.

- [29] S.S. Talmage, N.B. Munro, A.P. Watson, J.F. King, V.D. Hauschild, The fate of chemical warfare agents in the environment, in: T.C. Marrs, R.L. Maynard, F.R. Sidell (Eds.), *Chemical Warfare Agents: Toxicology and Treatment*, John Wiley & Sons Ltd, West Sussex, 2007, pp. 89–127.
- [30] Z. Prokop, F. Opluštil, J. DeFrank, J. Damborský, Enzymes fight chemical weapons, *Biotechnol. J.* 1 (12) (2006) 1370–1380.
- [31] A.N. Bigley, F.M. Raushel, Catalytic mechanisms for phosphotriesterases, *Biochim. Biophys. Acta Proteins Proteomics* 1834 (1) (2013) 443–453.
- [32] A.N. Bigley, D.F. Xiang, Z. Ren, H. Xue, K.G. Hull, D. Romo, et al., Chemical mechanism of the phosphotriesterase from *Sphingobium* sp. strain TCM1, an enzyme capable of hydrolyzing organophosphate flame retardants, *J. Am. Chem. Soc.* 138 (9) (2016) 2921–2924.
- [33] C. van Hooidonk, J.C.A.E. Breebaart-Hansen, Stereospecific reaction of isopropyl methylphosphonofluoridate (sarin) with α -cyclodextrin: a model for enzyme inhibition, *Recl. Trav. Chim. Pays-Bas* 89 (3) (1970) 289–299.
- [34] B. Desire, S. Saint-Andre, Interaction of soman with β -cyclodextrin, *Fundam. Appl. Toxicol.* 7 (4) (1986) 646–657.
- [35] F.C.G. Hoskin, D.M. Steeves, J.E. Walker, Substituted cyclodextrin as a model for a squid enzyme that hydrolyzes the nerve gas soman, *Biol. Bull.* 197 (2) (1999) 284–285.
- [36] P.K. Zarzycki, B. e Fenert, B.K. Glód, 17 – Cyclodextrins-based nanocomplexes for encapsulation of bioactive compounds in food, cosmetics, and pharmaceutical products: principles of supramolecular complexes formation, their influence on the antioxidative properties of target chemicals, and recent advances in selected industrial applications A2 - Grumezescu, Alexandru Mihai, *Encapsulations*, Academic Press, 2016, pp. 717–767.
- [37] D.R. Edwards, C.T. Liu, G.E. Garrett, A.A. Neverov, R.S. Brown, Leaving group assistance in the La^{3+} -catalyzed cleavage of dimethyl (o-methoxycarbonyl)aryl phosphate triesters in methanol, *J. Am. Chem. Soc.* 131 (38) (2009) 13738–13748.
- [38] C.T. Liu, A.A. Neverov, C.I. Maxwell, R.S. Brown, Demonstration of prominent Cu (II)-promoted leaving group stabilization of the cleavage of a homologous set of phosphate mono-, di-, and triesters in methanol, *J. Am. Chem. Soc.* 132 (10) (2010) 3561–3573.
- [39] C.T. Liu, A.A. Neverov, R.S. Brown, Biomimetic cleavage of RNA models promoted by a dinuclear Zn(II) complex in ethanol. Greater than 30 kcal/mol stabilization of the transition state for cleavage of a phosphate diester, *J. Am. Chem. Soc.* 130 (49) (2008) 16711–16720.
- [40] D. Williams, A.A. Neverov, R.S. Brown, Development of metal ion promoted alcoholysis as a rapid methodology for the destruction of organophosphorus CW agents, their simulants and pesticides, *Main Group Chem.* 9 (3/4) (2010) 265–281.
- [41] B. Kang, J.W. Kurutz, K.-T. Youm, R.K. Totten, J.T. Hupp, S.T. Nguyen, Catalytically active supramolecular porphyrin boxes: acceleration of the methanolysis of phosphate triesters via a combination of increased local nucleophilicity and reactant encapsulation, *Chem. Sci.* 3 (6) (2012) 1938–1944.
- [42] R.K. Totten, P. Ryan, B. Kang, S.J. Lee, L.J. Broadbelt, R.Q. Snurr, et al., Enhanced catalytic decomposition of a phosphate triester by modularly accessible bimetallic porphyrin dyads and dimers, *Chem. Commun.* 48 (35) (2012) 4178–4180.
- [43] R.K. Totten, Y.-S. Kim, M.H. Weston, O.K. Farha, J.T. Hupp, S.T. Nguyen, Enhanced catalytic activity through the tuning of micropore environment and supercritical CO_2

- processing: Al(porphyrin)-based porous organic polymers for the degradation of a nerve agent simulant, *J. Am. Chem. Soc.* 135 (32) (2013) 11720–11723.
- [44] J.L. Bolliger, A.M. Belenguer, J.R. Nitschke, Enantiopure water-soluble [Fe₄L₆] cages: host–guest chemistry and catalytic activity, *Angew. Chem. Int. Ed.* 52 (31) (2013) 7958–7962.
- [45] C. Schneider, A. Bierwisch, M. Koller, F. Worek, S. Kubik, Detoxification of VX and other V-type nerve agents in water at 37 °C and pH 7.4 by substituted sulfonatocalix[4]arenes, *Angew. Chem. (Int. Ed. English)* 55 (41) (2016) 12668–12672.
- [46] D. Dang, Y. Bai, C. He, J. Wang, C. Duan, J. Niu, Structural and catalytic performance of a polyoxometalate-based metal–organic framework having a lanthanide nanocage as a secondary building block, *Inorg. Chem.* 49 (4) (2010) 1280–1282.
- [47] F.-J. Ma, S.-X. Liu, C.-Y. Sun, D.-D. Liang, G.-J. Ren, F. Wei, et al., A sodalite-type porous metal–organic framework with polyoxometalate templates: adsorption and decomposition of dimethyl methylphosphonate, *J. Am. Chem. Soc.* 133 (12) (2011) 4178–4181.
- [48] A. Roy, A.K. Srivastava, B. Singh, D. Shah, T.H. Mahato, P.K. Gutch, et al., Degradation of sarin, DECIP and DECNP over Cu-BTC metal organic framework, *J. Porous Mater.* 20 (5) (2013) 1103–1109.
- [49] G.W. Peterson, G.W. Wagner, Detoxification of chemical warfare agents by CuBTC, *J. Porous Mater.* 21 (2) (2014) 121–126.
- [50] C. Montoro, F. Linares, E. Quartapelle Procopio, I. Senkovska, S. Kaskel, S. Galli, et al., Capture of nerve agents and mustard gas analogues by hydrophobic robust MOF-5 type metal–organic frameworks, *J. Am. Chem. Soc.* 133 (31) (2011) 11888–11891.
- [51] R. Zou, R. Zhong, S. Han, H. Xu, A.K. Burrell, N. Henson, et al., A porous metal–organic replica of α -PbO₂ for capture of nerve agent surrogate, *J. Am. Chem. Soc.* 132 (51) (2010) 17996–17999.
- [52] S. Wang, L. Bromberg, H. Schreuder-Gibson, T.A. Hatton, Organophosphorous ester degradation by chromium(III) terephthalate metal–organic framework (MIL-101) chelated to *N,N*-dimethylaminopyridine and related aminopyridines, *ACS Appl. Mater. Interfaces* 5 (4) (2013) 1269–1278.
- [53] T.J. Bandosz, M. Laskoski, J. Mahle, G. Mogilevsky, G.W. Peterson, J.A. Rossin, et al., Reactions of VX, GD, and HD with Zr(OH)₄: near instantaneous decontamination of VX, *J. Phys. Chem. C* 116 (21) (2012) 11606–11614.
- [54] B.M. Smith, Catalytic methods for the destruction of chemical warfare agents under ambient conditions, *Chem. Soc. Rev.* 37 (3) (2008) 470–478.
- [55] J.H. Cavka, S. Jakobsen, U. Olsbye, N. Guillou, C. Lamberti, S. Bordiga, et al., A new zirconium inorganic building brick forming metal organic frameworks with exceptional stability, *J. Am. Chem. Soc.* 130 (42) (2008) 13850–13851.
- [56] M.J. Katz, S.-Y. Moon, J.E. Mondloch, M.H. Beyzavi, C.J. Stephenson, J.T. Hupp, et al., Exploiting parameter space in MOFs: a 20-fold enhancement of phosphate-ester hydrolysis with UiO-66-NH₂, *Chem. Sci.* 6 (4) (2015) 2286–2291.
- [57] G.C. Shearer, S. Chavan, S. Bordiga, S. Svelle, U. Olsbye, K.P. Lillerud, Defect engineering: tuning the porosity and composition of the metal–organic framework UiO-66 via modulated synthesis, *Chem. Mater.* 28 (11) (2016) 3749–3761.
- [58] F. Vermoortele, B. Bueken, G. Le Bars, B. Van de Vooorde, M. Vandichel, K. Houthoofd, et al., Synthesis modulation as a tool to increase the catalytic activity of metal–organic frameworks: the unique case of UiO-66(Zr), *J. Am. Chem. Soc.* 135 (31) (2013) 11465–11468.

- [59] M.J. Katz, R.C. Klet, S.-Y. Moon, J.E. Mondloch, J.T. Hupp, O.K. Farha, One step backward is two steps forward: enhancing the hydrolysis rate of UiO-66 by decreasing [OH⁻], *ACS Catal.* 5 (8) (2015) 4637–4642.
- [60] P. Nunes, A.C. Gomes, M. Pillinger, I.S. Gonçalves, M. Abrantes, Promotion of phosphoester hydrolysis by the Zr^{IV}-based metal-organic framework UiO-67, *Microporous Mesoporous Mater.* 208 (2015) 21–29.
- [61] K. Uzarevic, T.C. Wang, S.-Y. Moon, A.M. Fidelli, J.T. Hupp, O.K. Farha, et al., Mechanochemical and solvent-free assembly of zirconium-based metal-organic frameworks, *Chem. Commun.* 52 (10) (2016) 2133–2136.
- [62] T. Islamoglu, M.A. Ortuño, E. Proussaloglou, A.J. Howarth, N.A. Vermeulen, A. Atilgan, et al., Presence versus proximity: the role of pendant amines in the catalytic hydrolysis of a nerve agent simulant, *Angew. Chem. Int. Ed.* 57 (7) (2018) 1949–1953.
- [63] S.-Y. Moon, G.W. Wagner, J.E. Mondloch, G.W. Peterson, J.B. DeCoste, J.T. Hupp, et al., Effective, facile, and selective hydrolysis of the chemical warfare agent VX using Zr⁶-based metal-organic frameworks, *Inorg. Chem.* 54 (22) (2015) 10829–10833.
- [64] G.W. Peterson, S.-Y. Moon, G.W. Wagner, M.G. Hall, J.B. DeCoste, J.T. Hupp, et al., Tailoring the pore size and functionality of UiO-type metal-organic frameworks for optimal nerve agent destruction, *Inorg. Chem.* 54 (20) (2015) 9684–9686.
- [65] J.E. Mondloch, W. Bury, D. Fairen-Jimenez, S. Kwon, E.J. DeMarco, M.H. Weston, et al., Vapor-phase metalation by atomic layer deposition in a metal-organic framework, *J. Am. Chem. Soc.* 135 (28) (2013) 10294–10297.
- [66] J.E. Mondloch, M.J. Katz, W.C. Isley Iii, P. Ghosh, P. Liao, W. Bury, et al., Destruction of chemical warfare agents using metal-organic frameworks, *Nat. Mater.* 14 (2015) 512.
- [67] D. Troya, Reaction mechanism of nerve-agent decomposition with Zr-based metal organic frameworks, *J. Phys. Chem. C* 120 (51) (2016) 29312–29323.
- [68] A.M. Plonka, Q. Wang, W.O. Gordon, A. Balboa, D. Troya, W. Guo, et al., In situ probes of capture and decomposition of chemical warfare agent simulants by Zr-based metal organic frameworks, *J. Am. Chem. Soc.* 139 (2) (2017) 599–602.
- [69] S.-Y. Moon, Y. Liu, J.T. Hupp, O.K. Farha, Instantaneous hydrolysis of nerve-agent simulants with a six-connected zirconium-based metal-organic framework, *Angew. Chem. Int. Ed.* 54 (23) (2015) 6795–6799.
- [70] S.-Y. Moon, E. Proussaloglou, G.W. Peterson, J.B. DeCoste, M.G. Hall, A.J. Howarth, et al., Detoxification of chemical warfare agents using a Zr⁶-based metal-organic framework/polymer mixture, *Chem. Eur. J* 22 (42) (2016) 14864–14868.
- [71] T. Islamoglu, A. Atilgan, S.-Y. Moon, G.W. Peterson, J.B. DeCoste, M. Hall, et al., Cerium(IV) vs zirconium(IV) based metal-organic frameworks for detoxification of a nerve agent, *Chem. Mater.* 29 (7) (2017) 2672–2675.
- [72] L. Bromberg, Y. Klichko, E.P. Chang, S. Speakman, C.M. Straut, E. Wilusz, et al., Alkylaminopyridine-modified aluminum aminoterephthalate metal-organic frameworks as components of reactive self-detoxifying materials, *ACS Appl. Mater. Interfaces* 4 (9) (2012) 4595–4602.
- [73] E. López-Maya, C. Montoro, L.M. Rodríguez-Albelo, S.D. Aznar Cervantes, A.A. Lozano-Pérez, J.L. Cenís, et al., Textile/metal-organic-framework composites as self-detoxifying filters for chemical-warfare agents, *Angew. Chem. Int. Ed.* 54 (23) (2015) 6790–6794.
- [74] S.-Y. Moon, A.J. Howarth, T. Wang, N.A. Vermeulen, J.T. Hupp, O.K. Farha, A visually detectable pH responsive zirconium metal-organic framework, *Chem. Commun.* 52 (16) (2016) 3438–3441.

- [75] J. Zhao, D.T. Lee, R.W. Yaga, M.G. Hall, H.F. Barton, I.R. Woodward, et al., Ultrafast degradation of chemical warfare agents using MOF–nanofiber kebabs, *Angew. Chem. Int. Ed.* 55 (42) (2016) 13224–13228.
- [76] D.T. Lee, J. Zhao, G.W. Peterson, G.N. Parsons, Catalytic “MOF-cloth” formed via directed supramolecular assembly of UiO-66-NH₂ crystals on atomic layer deposition-coated textiles for rapid degradation of chemical warfare agent simulants, *Chem. Mater.* 29 (11) (2017) 4894–4903.
- [77] D.T. Lee, J. Zhao, C.J. Oldham, G.W. Peterson, G.N. Parsons, UiO-66-NH₂ metal–organic framework (MOF) nucleation on TiO₂, ZnO, and Al₂O₃ atomic layer deposition-treated polymer fibers: role of metal oxide on mof growth and catalytic hydrolysis of chemical warfare agent simulants, *ACS Appl. Mater. Interfaces* 9 (51) (2017) 44847–44855.
- [78] D.L. McCarthy, J. Liu, D.B. Dwyer, J.L. Troiano, S.M. Boyer, J.B. DeCoste, et al., Electrospun metal-organic framework polymer composites for the catalytic degradation of methyl paraoxon, *New J. Chem.* 41 (17) (2017) 8748–8753.
- [79] D.A. Giannakoudakis, Y. Hu, M. Florent, T.J. Bandoz, Smart textiles of MOF/g-C₃N₄ nanospheres for the rapid detection/detoxification of chemical warfare agents, *Nanoscale Horizons* 2 (6) (2017) 356–364.
- [80] D.A. Giannakoudakis, N.A. Travlou, J. Secor, T.J. Bandoz, Oxidized g-C₃N₄ nanospheres as catalytically photoactive linkers in MOF/g-C₃N₄ composite of hierarchical pore structure, *Small* 13 (1) (2017). 1601758.
- [81] P. Li, S.-Y. Moon, M.A. Guelta, S.P. Harvey, J.T. Hupp, O.K. Farha, Encapsulation of a nerve agent detoxifying enzyme by a mesoporous zirconium metal–organic framework engenders thermal and long-term stability, *J. Am. Chem. Soc.* 138 (26) (2016) 8052–8055.
- [82] P. Li, S.-Y. Moon, M.A. Guelta, L. Lin, D.A. Gómez-Gualdrón, R.Q. Snurr, et al., Nanosizing a metal–organic framework enzyme carrier for accelerating nerve agent hydrolysis, *ACS Nano* 10 (10) (2016) 9174–9182.
- [83] M.B. Majewski, H. Noh, T. Islamoglu, O.K. Farha, NanoMOFs: little crystallites for substantial applications, *J. Mater. Chem. A* 6 (17) (2018) 7338–7350.
- [84] P. Li, R.C. Klet, S.-Y. Moon, T.C. Wang, P. Deria, A.W. Peters, et al., Synthesis of nanocrystals of Zr-based metal-organic frameworks with csq-net: significant enhancement in the degradation of a nerve agent simulant, *Chem. Commun.* 51 (54) (2015) 10925–10928.
- [85] E.A. Flugel, A. Ranft, F. Haase, B.V. Lotsch, Synthetic routes toward MOF nanomorphologies, *J. Mater. Chem.* 22 (20) (2012) 10119–10133.

Metal-organic frameworks for capture and degradation of organic pollutants

Peng Zhang¹, Qi Wang¹, Yu Fang¹, Wenmiao Chen¹,
Angelo A. Kirchon¹, Melih Baci¹, Mingbao Feng², Virender K. Sharma²
and Hong-Cai Zhou^{1,*}

¹Department of Chemistry, Texas A&M University, College Station, TX, United States,

²Department of Environmental and Occupational Health, School of Public Health, Texas A&M University, College Station, TX, United States

*Corresponding authors: e-mail address: zhou@chem.tamu.edu

7.1 Introduction

In the last few decades the world has seen a population and technological growth unlike any other time in history. Although this growth brings about great benefits and advantages for human kind, it has also brought about a severe impact on the earth's environment. Among the various environmental concerns produced by the major population growth, the accumulation of organic pollutants in water and soil has become one of the most prominent issues the scientific and technology communities are trying to tackle. In a recent report, the United States Environmental Protection Agency (EPA) listed organic pollutants such as antibiotics, pesticides, plasticizers, organic dyes, and other substances whose usage recently escalated on the priority pollutants list [1]. Most organic pollutants share hallmark characteristics such as being hard to metabolize, high toxicity, long-range transport, and accumulation in biological bodies.

The contamination of organic pollutants has been realized as a global challenge. One of the groundbreaking steps in circumventing pollution is the establishment of the Stockholm Convention. The Stockholm Convention is a multinational treaty that aims to eliminate and/or restrict the production and usage of persistent organic pollutants (POPs) [2]. Since its existence in 2001 (entered into force in 2004), over 180 states and parties have signed the treaty, and over 500 chemicals have been listed or considered as POPs [3].

Currently, most of the procedures to remove organic pollutants take place in sewage plants, which involves multiple steps such as anaerobic digestion, adsorption, oxidation, and disinfection using chlorine and ultraviolet light. Although relatively successful, significant attention has been given to research that could improve the current methods. For example, the existing technologies for wastewater

treatment suffer drawbacks such as high-energy requirements, incomplete pollutant removal, and generation of toxic sludge [4]. In order to apply more efficient and powerful technologies that outperform the current methods, it is widely realized that developing new materials with higher removal criteria is one of the keys.

The investigation of new materials for pollutant removal has revealed porous materials as one of the leading candidates to replace traditional platforms. Some of the porous materials, such as activated carbons and zeolites, have already been applied to pollutant removal processes. However, these currently available materials have their own set of limitations. Since it is hard to perform pore modifications within these materials, they suffer from low selectivity when acting as adsorbents. Moreover, the limited ability to make adjustments in pore sizes and shapes, make zeolites and activated carbons only practical for a specific size range of pollutants.

Metal-organic frameworks (MOFs) are one of the emerging classes of porous materials. MOFs are constructed by metal ions or metal clusters and organic linkers, and the two kinds of building blocks are connected through coordination bonds. Distinguished from common porous materials, MOFs have unique characteristics, such as extremely high surface area (up to $7000 \text{ m}^2 \text{ g}^{-1}$), designable structures, tunable porosity, and controlled functionality [5]. Because of these unique properties, MOFs have shown great potential in numerous fields including gas storage, separation, catalysis, sensing, biomedical sciences, etc. [6–9]. MOFs can play multiple roles in water treatment, and optimization of their design and synthesis will maximize their potential in treating a wide range of pollutants. In this chapter, the current research status of MOFs in organic pollutants removal will be introduced. As the fundamentals, the synthetic and postsynthetic modification methods that orient MOFs for wastewater treatment will be illustrated, followed by a discussion of their promising applications in pollutant sensing, selective adsorption, and even decomposition of organic pollutants. Furthermore, outlook and opinions on the future research of this field will be addressed.

7.2 Synthesis of metal-organic frameworks

7.2.1 Synthesis approaches

Due to the diversity of MOF structures, their synthesis processes have been an extremely attractive research topic over the last few decades. Some commonly used synthetic approaches include conventional heating (hydrothermal and solvothermal synthesis), mechanochemical synthesis, sonochemical synthesis, microwave-assisted synthesis, and electrochemical synthesis (Fig. 7.1). With continuous investigation of these synthesis procedures, scientists now have a better understanding of the mechanism of MOFs formation and growth. For example, it has been discovered that the synthetic approach used significantly affects the MOF products in many aspects, which include structure, yield, particle size, morphology, and much more [10].

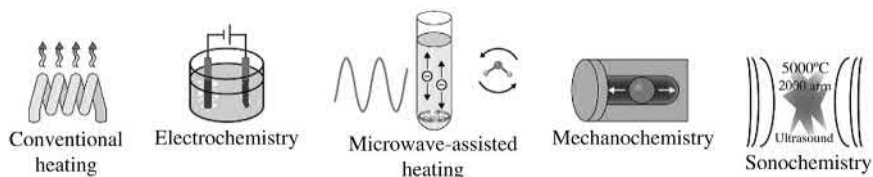


Figure 7.1 General synthetic approaches for MOFs.

Source: Reproduced from N. Stock, S. Biswas, Synthesis of metal-organic frameworks (MOFs): routes to various MOF topologies, morphologies, and composites, Chem. Rev. 112 (2012) 933–969 with permission from American Chemical Society, copyright 2012.

7.2.1.1 Hydrothermal and solvothermal synthesis

Hydrothermal and solvothermal syntheses, which are probably the most common MOF synthesis methods, generally refer to the reactions in closed containers in aqueous or nonaqueous environments under autogenous pressure at elevated temperature [11]. Energy in the form of heat is applied to overcome the activation energy barrier in the reaction between metal ions and organic ligands. There are numerous examples of solvothermal MOF synthesis, for example, MOF-5, MOF-74, HKUST-1, ZIF-8, and PCN-250 [12–16]. The synthetic conditions, such as metal/ligand ratio, solvent, modulating reagent, temperature, and more all greatly affect the growth of MOF crystals. Thus, identifying the optimized synthetic conditions for a specific MOF is extremely time-consuming and difficult. High-throughput methods have been demonstrated to be an efficient strategy to optimize the synthetic conditions [17–19].

The existence of a solvent not only provides a media to dissolve the reactants in but also functions as a template in the growth of a MOF crystal. The hydrolysis of DMF (*N,N*-dimethylformamide) and DEF (*N,N*-diethylformamide) has been shown to be able to influence the nature of the MOF product [20]. For example, in a typical solvothermal reaction between zinc nitrate and 1,4-benzenedicarboxylic acid (H_2BDC), the product could be MOF-5 ($[Zn_4(\mu_4-O)(\mu-bdc)_3]\cdot 3DEF$) or $[NH_2Et_2]_2[Zn_3(\mu-bdc)_4]\cdot 2.5DEF$ when using fresh DEF or DEF/water. $NH_2Et_2^+$ as the cation from the hydrolysis of DEF was found in the pores. The addition of NH_2Et_2Cl resulted in the same product, indicating the template effect of the $NH_2Et_2^+$ cation. A similar phenomenon was observed for DMF [20].

7.2.1.2 Mechanochemical synthesis

Mechanical force can induce chemical bond formation as well as breakage. Mechanochemistry is of great economic and environmental interest due to its several advantages such as being solvent free, having short reaction times, and even having mild reaction conditions [21,22]. The first example of solvent-free mechanochemical MOF synthesis was reported in 2006 [23]. In the study, metal salt ($Cu(OAc)_2$) and bridging organic ligand (isonicotinic acid) were ground together for only 10 minutes to achieve a MOF product. It was found that just grinding is

necessary to initiate the reaction. Furthermore, the crystallinity of the MOF continued to grow hours after the initial grinding.

7.2.1.3 Sonochemical synthesis

Sonochemical synthesis refers to a reaction that occurs in an ultrasonic environment. Under an ultrasonic environment, small bubbles and cavities are formed in the solvent due to the change of pressure. This creation of bubbles is called acoustic cavitation, which means the formation, growth, and collapse of bubbles in a liquid [24]. Cavitation empowers a unique interaction between molecules and energy. The hot spots inside the bubbles may reach 5000K and 1000 bar with heating and cooling rates of 10^{10}K s^{-1} and this energy is utilized in order to synthesize a MOF product.

The primary reason for using a sonochemical synthesis method is to achieve a rapid, environmentally friendly, and energy-efficient approach [10]. The first reported sonochemical synthesis of a MOF was $\text{Zn}_3(\text{BTC})_2 \cdot 12\text{H}_2\text{O}$ [25]. This 3D MOF nanocrystal was synthesized under room temperature and atmospheric pressure in 20% ethanol in water under ultrasound irradiation. The diameters of the obtained nanocrystals ranged from 50 to 900 nm and this was tuned by the change of reaction time.

7.2.1.4 Microwave-assisted synthesis

Microwave irradiation is a form of electromagnetic irradiation with mobile electric charges and is commonly used in organic synthesis [26,27]. Examples of microwave-assisted solid phase reactions and solvent-based reactions have recently been reported for MOF synthesis [28,29]. Generally, microwave radiation increases the rate of crystallization, therefore providing a more rapid way of synthesizing MOF crystals with smaller sizes compared to conventional heating.

The first example of microwave-assisted MOF synthesis is Cr-MIL-100 [30]. This MOF was synthesized at 220°C for 4 hours with microwave irradiation. The yield reported was 44%, which was comparable to the conventional heating approach that uses a 4-day reaction time. Since then, there have been numerous studies in this field. To understand the characteristics of microwave synthesis, ex situ powder X-ray diffraction measurements were utilized to investigate the crystallization kinetics of HKUST-1 ($\text{Cu}_3(\text{BTC})_2(\text{H}_2\text{O})_3$), a well-established MOF [31]. It was found that microwave irradiation mainly accelerates the nucleation process rather than the crystallization process. This is explained from fundamentals that the pre-exponential factor of the Arrhenius equation was significantly increased instead of the activation energy being lowered.

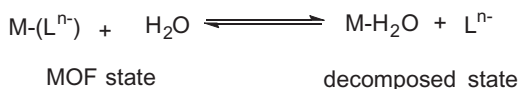
7.2.1.5 Electrochemical synthesis

In an electrochemical synthesis setup, the metal cations diffuse to the reaction medium through the anode. The organic linkers are dissolved in the electrolyte, where they react with metal cations. The primary advantage of electrochemical synthesis of MOFs is the exclusion of anions (e.g., chloride and nitrate), which has

been shown to be beneficial for large-scale production [10]. Moreover, this synthetic approach is especially suitable for the formation of MOF films and patterned coating [32].

7.2.2 Water stability of metal-organic frameworks

The stability of MOFs in water is one of the most decisive factors in determining a MOFs' potential in the application of wastewater treatment. In the presence of water, MOFs can undergo a decomposition process, as shown in Scheme 7.1 [33,34]. A lot of efforts have been made on improving water stability of MOFs, including both understanding and elucidating the origin of MOFs' stability, and especially the synthesis of water stable MOFs.



Scheme 7.1 Proposed MOF decomposition mechanism in water.

7.2.2.1 Thermodynamic stability factors and examples

Generally, with the existence of both covalent bonds and coordination bonds in MOFs, the coordination bonds between metal and ligand fundamentally determine the thermodynamic stability of MOFs. According to Pearson's hard/soft acid/base (HSAB) theory, a strong coordination bond can be formed by a hard acid and hard base, or a soft acid and soft base. HSAB theory explains two main categories of stable MOFs: high-valent metal ions (hard acid) with carboxylate ligand (hard base) and low-valent metal ions (soft acid) with azolate ligands (soft base) [35].

The stable MOFs with carboxylate ligands as hard bases usually contain high-valent metals ions, such as Zr^{4+} , Ti^{4+} , Fe^{3+} , Cr^{3+} , and Al^{3+} . Zr-based MOFs have attracted tremendous attention recently [36]. The first reported Zr-MOF is UiO-66 which consists of 12-connected Zr_6 cluster and terephthalic acid as the ligand [37]. The stability of UiO-66 is mainly due to the strong Zr–O bonds and the ability of the inner Zr_6 cluster with its ability to reversibly rearrange upon removal or addition of μ_3 -OH groups without changing the connected carboxylate ligands.

The MIL (Material Institut Lavoisier) series was developed by Férey and coworkers [38–40]. Most of the MIL series MOFs, such as MIL-53, MIL-88, MIL-100, and MIL-101, consist of trivalent metals Fe^{3+} , Al^{3+} , and Cr^{3+} . The six-connected $[\text{M}_3(\mu_3\text{-O})(\text{COO})_6]$ cluster or linear $[\text{M}(\text{OH})(\text{COO})_2]_n$ cluster are the two common trivalent metal clusters. Taking MIL-101(Cr) as an example, the MOF consists of Cr_3 clusters and terephthalic acid ligands and shows high stability with large pores and high surface area.

Stable MOFs are also formed by azolate ligands (including pyrazole, imidazole, triazole, and tetrazole) and soft acids such as Zn^{2+} , Co^{2+} , Cu^{2+} , and Mn^{2+} . The most well-established examples are zeolitic imidazolate frameworks (ZIFs) with

M^{2+} and imidazolate ligand [15]. The Yaghi group first published a series of ZIFs with exceptional chemical and thermal stability. Their stability can be explained by the strong metal–imidazole bond and the M-Im-M 145-degree angle that coincides with the Si-O-Si angle in zeolites. The topology of ZIFs can be varied by using imidazole with different R chains. Among these ZIFs, ZIF-8 ($Zn(mIM)_2$, mIM = 2-methyl imidazole), and ZIF-11 ($Zn(bIM)_2$, bIM = benzimidazole) notably display excellent chemical and thermal stability.

7.2.2.2 Kinetic stability factors and examples

Beside thermodynamics, the stability of MOFs is also affected by several kinetic factors, such as ligand length and rigidity, connectivity, and hydrophobicity of the framework [35]. The length of the ligand can affect the rate of its replacement by attacking species, and MOFs with shorter ligands show better robustness than the ones with elongated linkers. As demonstrated in Fig. 7.2, in order to leave the coordination sites, short and rigid ligands would bend to a larger angle compared to a longer and less rigid ligand. This would raise the activation energy of decomposition, therefore improving the robustness of the MOF [41]. Higher ligand-cluster connectivity also improves the stability of the framework by increasing the rate of defect repair. Besides, inclusion of hydrophobic groups into MOFs can also help repel water in the pores and avoid the coordination bond from being attacked by water. ZIF-8 with the methyl group on the imidazole ligand is a typical example of this [15]. The water attack to the ZnN_4 unit is blocked by the methyl group. And the existence of methyl group also narrows the pores, therefore facilitating desorption of the adsorbed moisture. This is proved by the narrowing of the hysteresis loop on the water adsorption–desorption isotherm [42].

7.2.3 Modifications of metal-organic frameworks

In addition to the wide library of MOF platforms, MOFs can be modified by various chemical treatments, while the porous nature and crystallinities are still maintained. This is a powerful tool that is able to induce functionalities, change the polarity, or even modify pore environments of the MOF structure. Modifications

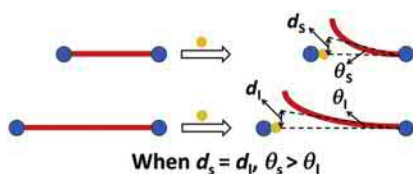


Figure 7.2 Kinetic stability of MOFs with ligands of different lengths.

Source: Reproduced from K. Wang, X.-L. Lv, D. Feng, J. Li, S. Chen, J. Sun, et al., Pyrazolate-based porphyrinic metal-organic framework with extraordinary base-resistance, *J. Am. Chem. Soc.* 138 (2016) 914–919 with permission from American Chemical Society, copyright 2016.

that are applied after the crystal is formed are known with the term of postsynthetic modifications, but they can also be applied during the formation of crystals in a way that alters the structures of the parent MOF, which usually results in the formation of composite structures [43].

7.2.3.1 Exchange of building blocks

Both metal nodes and organic linkers can be changed using postsynthetic modification (PSM) processes [44]. The resulting structures will mostly have a similar topology, with the only difference of bearing a different metal unit or linker. PSM is especially a great tool if the direct synthesis of a MOF is not feasible. Both metal and linker exchanges are done by soaking the MOF crystals into solution of desired building blocks to be exchanged considering the dynamic nature of MOFs. The optimal conditions are determined based on metal type and charge, as well as linker type and connectivity.

Exchanging the linker usually focuses on importing a functionality into the MOF pores, however, it can also be applied to gradually change the pore size [45]. To date, many functional groups have been imported to MOFs using linker exchange, including $-\text{OH}$, $-\text{NH}_2$, $-\text{N}_3^-$, and halogens. Besides, further chemistry can be performed, such as a click reaction on an azide group [46]. A linker that has the desired functional group with similar size and connectivity can be synthesized and then exchanged by soaking the MOF crystals into solution of the synthesized replacement linker. In most cases, the exchange is done with another linker of same type of connector of functional group (e.g., carboxylate). This makes the energy change of the exchange negligible, so the process follows Le Chatelier's principle. Kinetics, however, depends on the strength of the metal-linker bond and can be tuned by variables like temperature and solvent type [47].

It is possible to import functionality to a MOF by introducing different metal species by exchange, which in turn is a feasible way to produce MOFs that are not possible by straight solvothermal synthesis [48]. The exchange rate is highly dependent on the types of metal and linkers, which follows Irving–Williams series of coordination complex stability prediction. When the environment of the metal is kept identical, metals with greater crystal field stabilization energy are expected to have a more stable complex, with the order $\text{Mn(II)} < \text{Fe(II)} < \text{Co(II)} < \text{Ni(II)} < \text{Cu(II)} > \text{Zn(II)}$ [49]. The series are generated for high-spin octahedral complexes, while a different order may be obtained if different geometry or low-spin complexes are present. Because of these restrictions, it is possible to obtain partially exchanged metal clusters, which could produce interesting results for applications in catalysis [50].

7.2.3.2 Pore expansion

The majority of MOFs are in the microporous region (< 2 nm). Developing MOFs with larger pore sizes will open new opportunities for a wider range of applications. Through methods like isorecticular expansion and topologic design, pore sizes could

be increased to moderately sized mesopores. Isoreticular expansion is synthesizing new MOF structures with longer chain ligands while the metal nodes and the topology stay the same [51]. Combined with isoreticular expansion, synthesizing MOFs with certain topologies could yield pore sizes reaching 6 nm [52]. On the other hand, it is possible to form even larger pores with different shapes, though usually less ordered, by creating so-called “defects” in the MOF crystals. Defects can be considered as the absence of building blocks while other parts of the crystal will still be intact. Unlike previously mentioned modifications, careful control and manipulations are needed to manage the defects. They can be generated during synthesis by the addition of other reagents such as partial linkers or surfactants, or even by postsynthetically removing the building blocks with etching agents [53]. Thermal treatment has also proven to be an efficient approach for creating defect-rich MOFs. For example, pores of controlled sizes can be generated by a linker thermolysis process of multivariate MOFs. The selections of ligands and temperature of thermolysis are utilized to form different sizes and amounts of mesopores which could be helpful to store or remove large organic pollutants [54].

7.2.4 Metal-organic frameworks-based composites

MOFs can be combined with other functional materials, forming composites. A variety of materials such as metal nanoparticles, metal oxides, silica, carbon, polymers, or even enzymes can be incorporated with MOFs, with an aim of improving the properties and developing novel functionalities [55]. This area of research provides endless possibilities and current examples have already prove successful. Here only a few examples are discussed to demonstrate how each composite could improve different properties.

7.2.4.1 Metal-organic framework–polymer composites

It is possible to grow MOFs within the matrix of polymers, while polymers can also be synthesized within the pores of MOFs. Each of the combinations has its own advantages. For polymers grown in MOFs, much narrower weight distribution as well as more ordered polymerization can be obtained in such confined spaces [56]. On the other hand, specific nanostructures can be obtained when synthesizing MOFs on the surface of polymers [57]. Each part of the composite can be utilized to have a better control over the other one’s properties. Besides, it is possible to incorporate MOF crystals and polymers into a single chemically bound composite by employing vinyl functionalized linkers in the MOF and then polymerizing with additional monomers. Such a structure would benefit from the properties of the polymer, for example, elasticity, and the functionality of MOF [58].

7.2.4.2 Thermal annealing of metal-organic frameworks

By annealing MOFs in presence of oxygen, metal oxide nanoparticles can be produced in MOF crystals. The metal sources could be introduced into the framework

by gas or solution phase, or directly synthesized from the metal node itself. For example, catalytically active metal oxides such as Co_3O_4 [59] and Cu/ZnO [60] can be produced with controlled sizes while encapsulated in MOFs. These structures fully utilize the catalytic activity of the nanoparticles with the help of porosity provided by MOF, maximizing the active surface area in the smallest volume. Thermal annealing of MOFs in inert atmosphere derives metal oxide–carbon composites. These kinds of carbon materials have high surface area and a hydrophobic structure, and are considered as promising adsorbents of organic pollutants. In a typical example, annealing of Fe-MOFs formed porous carbon– Fe_3O_4 nanocomposites. These materials not only displayed high-performance in organic pollutant adsorption, but also allowed magnetic separation and recovery, making them one of the best materials for organic pollutant separation [61].

7.3 Applications of metal-organic frameworks in organic pollutants removal

7.3.1 Interactions between metal-organic frameworks and organic molecules

Since MOFs are inorganic–organic hybrid materials, there are a variety of interaction modes that can occur between MOFs and organic molecules. As shown in Fig. 7.3, some of these possible interactions are hydrophobic, electrostatic, acid–base, π – π effect, and hydrogen bonding [62]. The controllable functionality of MOFs allows scientists to engineer the interactions between MOFs and organic pollutants, making MOFs potential candidates for the detection, adsorption, and decomposition of organic molecules.

7.3.2 Luminescent metal-organic frameworks for organic pollutants detection

Luminescent metal-organic frameworks (LMOFs) possess the ability to have different luminescent mechanisms enabled by multivariate luminophore resources such as metal centers, aromatic organic linkers and encapsulated guest molecules, which all can be used in order to create sensors for gases, ions, organic explosives, and so on. Recently, chemists have expanded LMOF sensors into environmental applications, and their portable and real-time sensing properties greatly exceed traditional environment monitoring methods. Moreover, MOFs can not only be used as sensors, but they can also be used as traps and degradation catalysts for organic pollutants like dyes, herbicides, pesticides, and antibiotics [63].

7.3.2.1 Sensing mechanism

Generally, based on the resources of luminescence, the LMOF sensors are functionalized through organic ligands or metal cations. Guest molecules, which can either

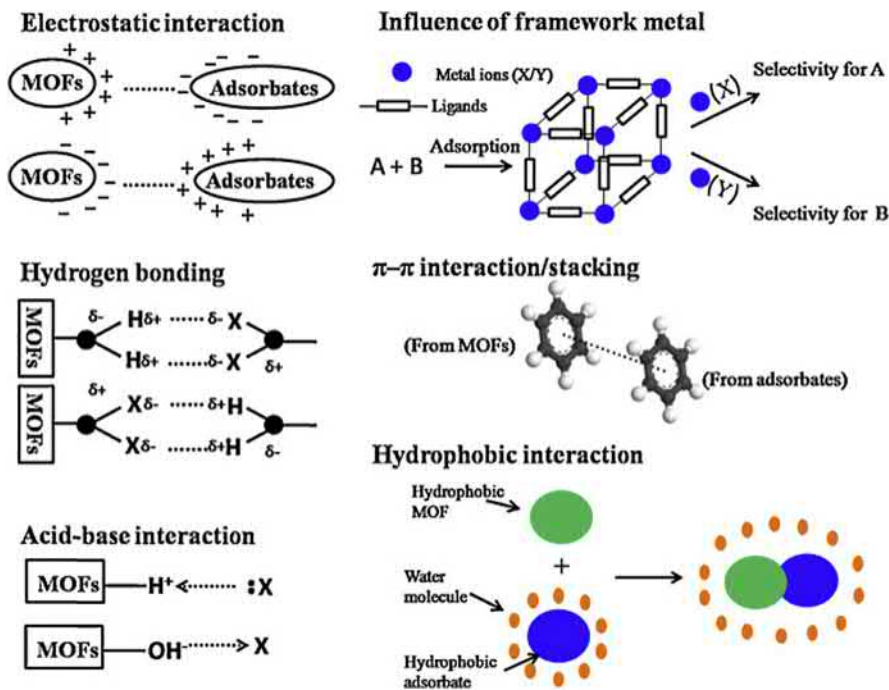


Figure 7.3 Scheme of different adsorption mechanisms for water pollutant adsorption by MOFs.

Source: Adapted from Z. Hasan, S.H. Jung, Removal of hazardous organics from water using metal-organic frameworks (MOFs): plausible mechanisms for selective adsorptions, J. Hazard. Mater. 283 (2015) 329–339 with permission of Elsevier, Inc.

be organic molecules or inorganic species, are encapsulated within the porous cavities and contribute to the emission of the framework in various ways. Thus, decoding the luminescent output within MOFs, turn-on, turn-off, or quenching, necessitates all the possible photophysical interactions integrated into account.

Purely ligand-based emission has been the most researched because of the simplified luminescent center which exists only from conjugated organic groups and can only be influenced by binding and/or coordination of guest analytes. The binding of guest molecules through covalent interactions changes the electronic character of the ligands, leading to alteration of PL properties. In contrast with organic linkers, metal ions, especially lanthanide metals, possess intense, long-lived, and sharp emissions in the visible region. They usually participate in ligand-to-metal charge transfer (LMCT) or metal-to-ligand charge transfer (MLCT) with both processes displaying significant emissions on a large scale. Recently, more complicated cases take the ligands, metals, and guests molecules into account, where the diversified interactions between them due to specific orientations greatly manipulated the photoluminescence (Fig. 7.4) [64].

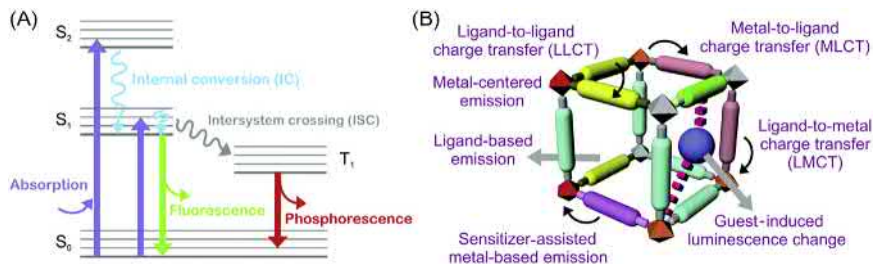


Figure 7.4 (A) Scheme of origin of photoluminescence. (B) Scheme of possible interactions within MOFs influential in photoluminescence.

Source: Adopted from W.P. Lustig, S. Mukherjee, N.D. Rudd, A.V. Desai, J. Li, S.K. Ghosh, Metal-organic frameworks: functional luminescent and photonic materials for sensing applications, *Chem. Soc. Rev.* 46 (2017) 3242–3285.

7.3.2.2 Luminescent sensors

Functionalized MOFs can work as sensors for cyanides and phosphates, which can be generated from the decomposition of organics such as dyes and pesticides. By using a postsynthetically modified phase of the M-ZIF-90 (M for modified), Ghosh and coworkers have proposed the first LMOF-based cyanide sensing (Fig. 7.5) [65]. The dicyanovinyl (DCV) group generated from the addition of malonitrile to aldehyde is highly sensitive toward nucleophilic cyanide ions through addition reaction, weakening the conjugated systems and quenching fluorescence in turn. This highly tunable aldehyde groups in ZIF-90 is a practical platform for further chemical modification and this result has opened a path for creating reaction-based sensors for organic pollutants.

Phosphorus is essential to human life and is found in many fields of life. However, it is also known to be the basis of many water pollutants such as phosphates and organophosphorous pesticides (OPPs). Qian and coworkers created a highly selective PL-quenching based sensor of PO_4^{3-} ions in a water medium by using a 2D-bilayer open framework Tb(III)-compound, TbNTA1 (NTA = nitrilotriacetate, Fig. 7.6) [66]. The specific sensitivity of this system may be explained by the tetrahedral geometry of the phosphate anions, which matches the C_{3v} symmetric cavity very well. After TbNTA1 was incorporated with PO_4^{3-} anions, the Tb-O bond may dilute the energy that is transferred to Tb^{3+} via nonradioactive relaxation.

Furthermore, Yang et al. used $\text{Fe}_3\text{O}_4@\text{SiO}_2@\text{UiO}-67$ nanocomposite as a “smart absorbent” to realize simultaneous detection and removal of OPPs [67]. FTIR, XPS, and emission spectrum were applied to investigate the adsorption/detection mechanism. After absorption, a new peak of P–O stretching emerged, indicating the forming of Zr–O–P bonds. Also, the fluorescence intensity is enhanced with the addition of glyphosate which reveals that the combination of glyphosate and Zr-OH groups promotes the electron transfer, which in turn enhances fluorescence intensity. This smart magnetic absorbent is assembled with great selectivity and sensitivity. The magnetic property of Fe_3O_4 and photoelectronic stability of SiO_2 , help shed light in exploring smart composite materials.

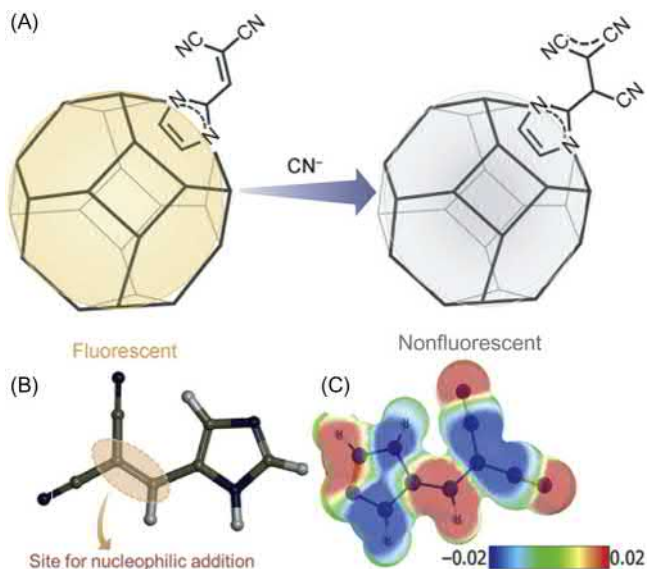


Figure 7.5 (A) Fluorescence quenching of M-ZIF-90 upon addition of CN^- ions. (B) Schematic illustration of site for nucleophilic addition within ligand. (C) Electronic potential map of the LUMO energy state of the ligand showing electron deficiency over the double bond of the DCV group.

Source: Adopted from A. Karmakar, N. Kumar, P. Samanta, A.V. Desai, S.K. Ghosh, A. Post-Synthetically Modified MOF for selective and sensitive aqueous-phase detection of highly toxic cyanide ions, *Chem. Eur. J.* 22 (2016) 864–868.

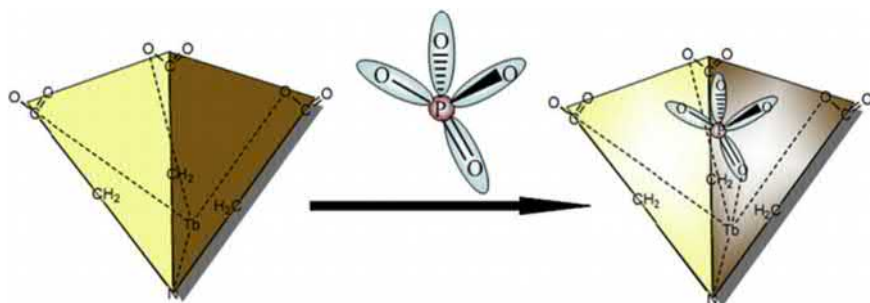


Figure 7.6 Schematic illustration of geometrical selectivity upon PO_4^{3-} .

Source: Adopted from H. Xu, Y. Xiao, X. Rao, Z. Dou, W. Li, Y. Cui, et al., A metal-organic framework for selectively sensing of PO_4^{3-} anion in aqueous solution, *J. Alloys Compd.* 509 (2011) 2552–2554.

Developing MOF sensors with ultralow limits of detection (LOD) is of great importance. Through topology analysis of D_{4h} eight-connected Zr_6 clusters and D_{3h} three-connected linkers, Zhou and coworkers reported two water stable Zr-based MOFs that can detect antibiotics and remove the pollutants from water at the same

time [68]. These MOFs can be quenched by trace nitrofurazone (NZF) and nitrofurantoin (NFT) antibiotics as low as parts per billion (ppb) levels. It is proposed that the hydrophobic nature, suitable pore size, as well as the large surface areas, play cooperative roles in improving the sensing and adsorption of the MOFs.

Li and coworkers reported LMOF-241 [$Zn_2(\text{bpdc})_2(\text{tppe})$], $\text{bpdc} = [1,1'$ -biphenyl]-4,4'-dicarboxylic acid, $\text{tppe} = 1,1,2,2$ -tetrakis(4-(pyridin-4-yl)phenyl) ethene] which selectively detects the mycotoxin aflatoxin B_1 , a highly carcinogenic toxin produced by common food-contaminating fungi in the genus *Aspergillus* [69]. The sensing takes place in dichloromethane, with the presence of the toxin inducing quenching in the LMOF emission, and has a limit of detection of 46 ppb. The selectivity of the quenching for aflatoxin B_1 of the average of the summed absolute orbital overlap between aflatoxin B_1 and LMOF-241 is 0.57, much stronger than that of aflatoxin B_2 (0.17), which facilitates a more efficient electron transfer and a higher extent of fluorescence quenching.

7.3.3 Metal-organic frameworks for organic pollutants adsorption

MOFs are considered to be a favorable platform for both gaseous phase and liquid phase adsorption [70,71], since the extremely high surface area and porosity could contribute to the accessibility of adsorption sites and diffusion through the framework. By choosing the linkers as well as adjusting the connectivity of the metal ions, the porosity of MOFs can be accurately modulated to fit different targeting adsorbates. Table 7.1 lists some of the recent studies of organic compound adsorption by MOFs. Besides high surface area and porosity, hydrophobic, electrostatic, acid–base, π – π interactions, and hydrogen bonding between MOF absorbent and pollutant frequently contribute to the adsorption. In this section, we will focus on using MOFs for the adsorption of organic residues in water, such as dyes from industry, herbicides and pesticides from agriculture, and other newly emerged organic contaminants [72]. The organic residues in water are normally at very low concentrations, and it is hard to remove them using other approaches.

7.3.3.1 Organic dyes adsorption by metal-organic frameworks

Most of the organic dyes are chemically stable and not considered biodegradable in water. Even though normal water treatment can remove a large portion of these chemicals, the extremely low concentration of organic dyes is still potentially hazardous to the environment. Typically, the organic dye molecules consist of conjugated π -bond chromophores, auxochromes ($-\text{COOH}$, $-\text{OH}$, $-\text{NH}_2$, $-\text{NHR}$, $-\text{NR}_2$, etc.), and other functional groups (such as $-\text{SO}_3^-$ group to improve water solubility). Therefore, electrostatic interactions between MOFs and adsorbed dyes is one of the important factors to achieve high adsorption performance. Haque et al. reported that NH_2 -MIL-101(Al) has a remarkable capacity for MB adsorption (up to 762 mg g^{-1}) [73]. The electrostatic interaction between the cationic MB and the electron lone pairs on the amino groups in the MOF contributes to the high

Table 7.1 Pollutant, MOFs, and their dominant interactions.

Pollutant	MOF	Q_m (mg g ⁻¹)	b (L mg ⁻¹)	$C_{\text{Pollutant}}$ (mg L ⁻¹)	C_{MOF} (mg L ⁻¹)	Interactions	Ref.
Methyl orange	NH ₂ -MIL-101(Al)	188	0.019	20–200	50	Reactive adsorption	[73]
Methylene blue	[Cd ₆ (L) ₂ (bib) ₂ (DMA) ₄]	102	–	10	100–600	Pore size	[74]
Rhodamine B	[bbpy][Bi ₄ I ₁₆]	n.a.	n.a.	4.8	3000	Hydrogen bond	[75]
Congo Red	Zn(bdc)(tib) · 3H ₂ O	60	–	35	1000	Open metal site	[76]
Methyl blue	MIL-100(Fe)	8.47	1.11	20–60	2500	Electrostatic	[77]
Isantin	MIL-100(Fe)					Electrostatic	[77]
Fluorescein dye	[Cu(INA) ₂]	67	1.364	3–18	400	Electrostatic	[78]
Methylchlorophenoxypropionic acid	UiO-66(Zr)	370	n.a.	20–170	100	Electrostatic / $\pi - \pi$	[79]
2,4-Dichlorophenoxyacetic acid	MIL-53(Cr)	556	0.168	10–150	100	Electrostatic / $\pi - \pi$	[80]
Glyphosate	UiO-67(Zr)	540	0.074	5.4–72	30	Reactive adsorption	[81]
Glufosinate	UiO-67(Zr)	538	0.465	5.1–68	30	Reactive adsorption	[81]
Dimethyl phthalate	MIL-53(Al)	206	–	25	75	$\pi - \pi$	[82]
Phthalic acid	ZIF-8	654	n.a.	n.a.	100	Acid–base	[83]
Phthalic acid	UiO-66(Zr)	187	n.a.	n.a.	100	$\pi - \pi$	[83]

Q_m is Langmuir parameter for the maximum adsorption capacity and b is Langmuir constant.

capacity. Also, the electrostatic interaction will lead to preferential adsorption when multiple dyes exist. Jia et al. reported an example of MB (cationic), methyl blue (MyB, anionic), and isatin (neutral) adsorption by MIL-100(Fe) [77]. The MOF only showed adsorption toward MB and MyB due to the electrostatic interactions between the host and the dye. Zhang et al. investigated the adsorption of MB, MO, RhB, and Congo Red (CR) by using a MOF: $[\text{Zn}(\text{bdc})(\text{tib})] \cdot 3\text{H}_2\text{O}$ (tib = 1,3,5-tri(1*H*-imidazol-1-yl)benzene and bdc = 1,4-dicarboxybenzene) [76]. It showed exclusive affinity to CR over three other dyes. The selectivity was expected to be due to the pore size and interactions between the open metal site and the CR.

7.3.3.2 *Herbicides and pesticides removal by metal-organic frameworks*

Compared to conventional adsorbents like zeolite and activated carbon, the inorganic–organic hybrid nature of MOFs is especially favorable to the adsorption of herbicides and pesticides. Seo et al. investigated the adsorption of methylchlorophenoxypropionic acid (MCP) by using UiO-66(Zr) [79]. UiO-66(Zr) showed faster and higher MCP adsorption than activated carbon. The interactions between UiO-66(Zr) and MCP were ascribed to strong electrostatic interactions as well as π – π interactions. Jung et al. applied MIL-53(Cr) for aqueous adsorption of 2,4-dichlorophenoxyacetic acid (2,4-D) [80]. They found that pH value could affect the 2,4-D adsorption. When pH is lower than the isoelectric point of the MOF, the positively charged MOF adsorbent showed strong binding to 2,4-D. In contrast, at higher pH value, only π – π interactions contributed to the adsorption. From the study by Zhu et al., UiO-67(Zr) was found to show adsorption toward glyphosate (GP) and glufosinate (GF) [81]. The Zr-OH moieties in UiO-67(Zr) adsorbent could react with the organophosphorus pesticides (GP and GF), thus forming complexes. Therefore, chemisorption rather than electrostatic adsorption is the main adsorption mechanism.

7.3.3.3 *Emerging organic contaminants*

Emerging organic contaminants refer to those compounds that have been recently developed, newly discovered in the environment, or have only recently been categorized as contaminants [82]. Compared to common organic pollutants, the methods for treatment are far from established. Therefore, removing these pollutants by an adsorption method is highly needed. Li et al. tested MIL-53(Al) for removing dimethyl phthalate (DMP) from water [83]. They showed that the MOFs synthesized from different sources displayed different textural properties, which affected the adsorption performance. The MOF synthesized from aluminum oxide outperformed all the others, showing 71% more DMP adsorption comparing to the least adsorptive adsorbent. The π – π interactions played a dominant factor in adsorption. Khan et al. compared phthalic acid (PA) and diethyl phthalate (DEP) adsorption on ZIF-8, UiO-66(Zr), and NH_2 -UiO-66(Zr) [84]. They found these MOF adsorbents showed less adsorption to DEP than PA, ascribing this to the lack of electrostatic

interactions between the MOF absorbent and the neutral DEP. Besides, it was found that acid–base interactions were the main adsorption driving force for ZIF-8, while π – π interactions dominated for UiO-66(Zr).

7.3.4 *Metal-organic frameworks for organic pollutants decomposition*

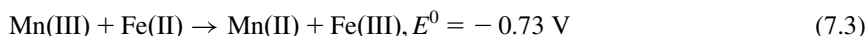
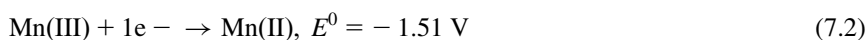
Decomposition of organic pollutants is an important method in wastewater treatment. The goal of the process is to transform the persistent or nonbiodegradable organic pollutants into less toxic fragments, and potentially even CO_2 , H_2O , and inorganic ions. One of the advantages of the decomposition method is that it can be integrated as a step in the whole process of water treatment, therefore reducing the cost of pollutant transportation and the subsequent risks of leaking, second time contamination, etc. The main reaction in the decomposition process is oxidation. Traditionally, oxidation and subsequent decomposition of organic pollutants has relied on chlorine-based strong oxidants. However, the generated products are mutagenic and carcinogenic to human health [85–88]. As an alternative and environmentally benign approach, advanced oxidation processes (AOPs) have drawn great attention in recent years. In AOPs, highly reactive and nonselective species (such as $\cdot\text{OH}$, $\cdot\text{O}_2^-$, and $\text{SO}_4^{\cdot-}$) are generated in situ via catalytic reactions such as Fenton-type reactions or photocatalysis.

Compared to conventional materials, MOFs are reported to have better performances in AOPs. The advantages of MOFs in AOPs can be summarized as follows. Since MOFs have already been proved as good sorbents, there is a great potential to combine adsorption and decomposition processes in a single material. Second, as a porous material with extremely high pore volumes and surface areas, MOFs provide adequate room for chemical reactions to occur. Finally, yet just as important, MOFs are composed of discrete metal ions or metal-oxo cluster/chains and organic linkers. Both the metal ions/clusters/chains and the organic linkers can work as catalysts. Therefore, the localized ratios between catalyst and substrate are greatly enhanced and the efficiency for the oxidation reactions will soar. The application of MOFs in AOPs, especially photocatalysis, has been reviewed by several researchers. In this section, we will focus on the type of highly active species generated by MOFs, which might inspire more great ideas in the future.

7.3.4.1 *Generation of hydroxyl radicals*

Hydroxyl radicals ($\cdot\text{OH}$) are powerful oxidants toward a wide spectrum of organic contaminants. Generally, $\cdot\text{OH}$ are formed by decomposition of H_2O_2 using Fenton or Fenton-like reactions. Among various metal species that display catalytic activities, iron is still proved to be the best candidate with good performance. A variety of catalytic iron species, including metal salts (Fe^{2+} or Fe^{3+}), metal oxides (e.g., Fe_2O_3 , Fe_3O_4), and zero-valent metal ($\text{Fe}(0)$) have been applied in $\cdot\text{OH}$ production. Iron-carboxylate MOFs have been widely studied for Fenton-type reactions. These MOFs contain trinuclear iron-oxo clusters (e.g., MIL-88 series and MIL-100) or

iron-oxo chains (e.g., MIL-53) as secondary building units (SBUs). These SBUs have similar structures as iron oxides. Therefore, they share the same mechanism in Fenton-type reactions. For example, a series of work by Guo and coworkers investigated degradation of phenol at mild conditions (neutral pH, 35°C) by MIL-53(Fe), MIL-53-NH₂(Fe), and mixed-metal MIL-53(Fe-Mn) [89–91]. Their works illustrated the important role of Fe(II) in the framework during the Fenton reaction. Moreover, performance enhancement was found when using Fe-Mn mixed-metal MOFs (Fig. 7.7), which could be due to the synergetic induction of ·OH and ·HO₂ by Fe(II)/Fe(III) and Mn(II)/Mn(III) redox repairs (Eqs. 7.1–7.3).



It is also noteworthy that ultraviolet or visible-light irradiation will promote the production of ·OH and elevate the performance of water depollution, which is known as the photo-Fenton reaction. The trinuclear Fe-oxo clusters or one-dimensional Fe-oxo chains in MOFs can be considered as downsized iron oxides. They enable the charge carriers to effectively reach the reactants adsorbed at the surface and minimize the electron-hole recombination, which is a major problem that their bulky counterparts suffer [92]. Many categories of organic pollutants have been tested in MOFs-catalyzed photo-Fenton reactions including small molecules (benzene and phenol), organic dyes, medicinal chemicals, and plasticizers.

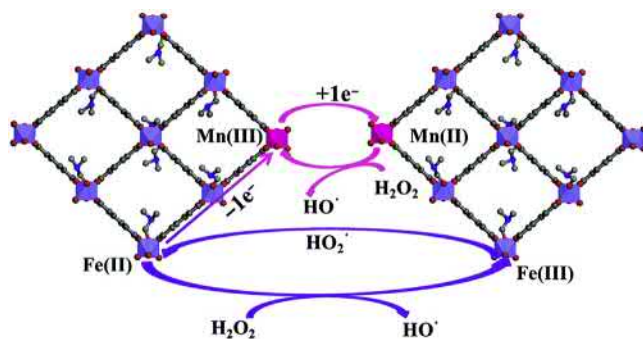


Figure 7.7 The synergistic effect between the Fe and Mn in Fe-Mn-MIL-53 on radical generation.

Source: Adopted from Q. Sun, M. Liu, K. Li, Y. Han, Y. Zuo, F. Chai, et al., Synthesis of Fe/M (M = Mn, Co, Ni) bimetallic metal organic frameworks and their catalytic activity for phenol degradation under mild conditions, *Inorg. Chem. Front.* 4 (2017) 144–153.

7.3.4.2 Generation of singlet oxygen

Singlet oxygen ($^1\text{O}_2$) is the lowest excited state of an oxygen molecule. It can be simply generated by energy transfer from an excited triplet state photosensitizer to a ground state molecular oxygen ($^3\text{O}_2$). As a highly active species, $^1\text{O}_2$ has been applied in oxidation reactions in various fields ranging from organic compound transformation [93] to photodynamic therapy [94]. It also has shown great potential in water depollution [95,96]. Since most of the photosensitizers are organic molecules, it is possible to synthesize photoactive molecules that can both work as MOF linkers and photosensitizers. Typical examples are porphyrin-based MOFs. In order to synthesize water stable porphyrinic MOFs and explore their applications in aqueous solutions, one of the best potential candidates is a series of MOFs composed of Zr-oxo clusters and tetrakis (4-carboxyphenyl)-porphyrin (TCPP) linkers. Due to the high connection number of Zr_6 clusters (up to 12 connections) and tetratopic linker, there are various structures of Zr-TCPP MOFs, which correspond to different topologies and Zr_6 node connection number. For instance, by changing the synthetic conditions, 12-connected MOF-525 [97] and PCN-223 [98], 8-connected MOF-545 (PCN-222) [99], and 6-connected PCN-224 [100] can be formed. All of them show high robustness in water, which allows for great potential for their practical application in water treatment. Due to their large surface area, relatively large pore sizes (> 1 nm), and aromaticity of porphyrinic linkers, they have shown great potential in adsorption and degradation of aromatic pollutants. One of the typical examples is the decomposition of bisphenol A (BPA), a chemical that has been widely used in plastics but can cause endocrine disruption [101]. One of the typical Zr-TCPP MOFs, PCN-222, has been used in removal of BPA. The 3.7-nm permanent channel facilitates the adsorption, of which the uptake reached as high as 487.69 ± 8.37 mg g $^{-1}$ (15 molecules per unit cell). Upon visible-light irradiation, $^1\text{O}_2$ generated from porphyrin linkers can efficiently degrade the preadsorbed BPA in 10 minutes.

7.3.4.3 Generation of sulfate radical

The sulfate radical ($\text{SO}_4^{\cdot-}$) has a high oxidation potential ($E^0 = 2.60$ V vs NHE). Due to the high oxidation activity and preference in reacting with organic compounds, sulfate radical has shown great potential in eliminating harmful pollutants in wastewater and has been considered as an important constituent of AOPs. Sulfate radicals can be formed by the activation of persulfate (PS) or peroxymonosulfate (PMS) via multiple approaches, including heat, UV, sonication, alkaline pH, and transition metal ions [102–105]. Transition metal oxides such as Fe_3O_4 , Co_3O_4 , and CuFe_2O_4 can also be used as solid activators [106,107]. MOFs have been shown to be effective activators for the generation of sulfate radicals. Compared to nonporous metal oxides, MOFs are distinguished by the properties of their highly porous nature and discrete metal nodes. Therefore, the contact between metal species, persulfates, and substrates is significantly improved, which results in the enhancement of depollution performance. Among various kinds of MOFs, Fe- and

Co-based MOFs are widely studied for activation of PS and PMS, respectively. Water-soluble large organic molecules are studied as substrates. For example, typical Fe-MOFs, including MIL-101(Fe), MIL-100(Fe), MIL-53(Fe), and MIL-88B(Fe), were studied in removing acid orange 7 (AO7). The adsorption isotherms of AO7 by four MOFs fitted well with the Langmuir model, and both the adsorption and the oxidation capability followed the order as MIL-101(Fe) > MIL-100(Fe) > MIL-53(Fe) > MIL-88B(Fe) [108]. Fe-MOFs have been proved effective in the decomposition of other dye molecules such as Orange G (OG) [109] and RhB [110]. Further enhancement can be achieved by the combination with visible light. In a typical example, under white LED irradiation, MIL-53(Fe)-catalyzed degradation of AO7 was significantly accelerated even at a low stoichiometric concentration of PS [111]. It is believed that the introduction of PS effectively suppressed the recombination of charge carriers, and the formed radicals ($\text{SO}_4^{\cdot-}$, and $\cdot\text{OH}$) promoted the photocatalytic performances.

7.4 Conclusion

In the 21st century, we have witnessed great developments in the research of MOF-based materials, both in the synthesis and developing their applications. Owing to their variable chemical composition, high porosity, special pore structure, and versatile functionalities, MOFs have drawn significant attention and have already shown great potential in organic pollutants removal and wastewater treatment. In this chapter, we have shown that MOFs can work as sensors, adsorbents, and decomposition catalysts. Nevertheless, most of the studies are still at the early stage, and it can be easily seen from the literature that there is great gap between the research of MOFs chemistry and their applications in environmental related fields. Therefore, efforts should be made by both chemists and environmental engineers to bridge this gap, and together improve the practical application of MOFs in organic pollutants removal. For future research, the emphasis will be placed on the following directions:

1. Considering the scale of water treatment and the great amount of materials needed, it is highly important to develop methods that can achieve both low-cost and large-scale synthesis of MOFs. Especially, MOFs synthesized from cheap metals will be favorable. To reduce the waste production from the synthesis, green solvent (e.g., water), recoverable solvent, or solventless methods are highly needed. Also, to enhance the performances, theoretical approaches should be applied to elucidate the interactions between MOFs and contaminants and guide the design of efficient MOFs structures from molecular level.
2. As a series of coordination materials, the stability of MOFs is always the prerequisite for practical application. As addressed in this chapter, some highly stable MOFs like Zr/Hf-carboxylates and Fe/Co/Ni-azolates have already been synthesized. The mechanisms of stability are also being systematically investigated. To apply MOFs in water depollution, one of the important direction for future research should be to improve the water stability. In addition to choosing the right combination of metal and ligands, there are a wide range of approaches to improve the water stability, such as ligand modification and polymer

coating. Moreover, MOFs should be tested in the practical conditions, which means factors such as acid/base, salts, and temperature should be fully considered.

3. Nowadays, the pore size of most reported MOFs is limited to the micropore range ($d \leq 2$ nm), which hampers their application in the adsorption of large molecules. Although the pore size of a MOF material can be increased through isoreticular expansion with elongated organic linkers, this method has proved to be successful only in limited examples. Recently, several new approaches have been reported, such as removing a portion of linkers [112], solvent expansion by supercritical CO₂ [113], using soft templates (e.g., surfactants) or hard templates (e.g., polystyrene spheres) [114,115], and forming aerogels to introduce aggregation pores [116]. As adsorbents, the hierarchical porosity of MOFs will facilitate the adsorption of a wide spectrum of pollutants, including both large organic molecules and small metal ions.
4. In addition, functionalized MOFs or hybrid materials can integrate multiple tasks on a single material, which will bring new opportunities in water depollution. For example, MOFs can work as porous hosts to incorporate catalysts or highly oxidative species into their cavities. Cooperative interactions for catalytic decomposition of organic pollutants can be expected by this combination.

References

- [1] Code of Federal Regulations (CFR), 40CFR - CHAPTER I - PART 423: Appendix A to Part 423 <http://water.epa.gov/scitech/methods/cwa/pollutants.cfm>.
- [2] Stockholm Convention, 2001. Stockholm convention on persistent organic pollutants. Full text for download in English http://www.pops.int/documents/convtext/convtext_en.pdf; other language versions at <http://www.pops.int>.
- [3] M. Scheringer, S. Stempel, S. Hukari, C.A. Ng, M. Blepp, K. Hungerbuhler, How many persistent organic pollutants should we expect? *Atmos. Pollut. Res.* 3 (2012) 383–391.
- [4] N. Ferroudj, J. Nzimoto, A. Davidson, D. Talbot, E. Briot, V. Dupuis, et al., Maghemite nanoparticles and maghemite/silica nanocomposite microspheres as magnetic Fenton catalysts for the removal of water pollutants, *Appl. Catal. B: Environ.* 136–137 (2013) 9–18.
- [5] O.M. Yaghi, M. O’Keeffe, N.W. Ockwig, H.K. Chae, M. Eddaoudi, J. Kim, Reticular synthesis and the design of new materials, *Nature* 423 (2003) 705.
- [6] D.J. Collins, H.-C. Zhou, Hydrogen storage in metal-organic frameworks, *J. Mater. Chem.* 17 (2007) 3154–3160.
- [7] J.-R. Li, R.J. Kuppler, H.-C. Zhou, Selective gas adsorption and separation in metal-organic frameworks, *Chem. Soc. Rev.* 38 (2009) 1477–1504.
- [8] R.J. Kuppler, D.J. Timmons, Q.-R. Fang, J.-R. Li, T.A. Makal, M.D. Young, et al., Potential applications of metal-organic frameworks, *Coord. Chem. Rev.* 253 (2009) 3042–3066.
- [9] X. Lian, Y. Fang, E. Joseph, Q. Wang, J. Li, S. Banerjee, et al., Enzyme-MOF (metal-organic framework) composites, *Chem. Soc. Rev.* 46 (2017) 3386–3401.
- [10] N. Stock, S. Biswas, Synthesis of metal-organic frameworks (MOFs): routes to various MOF topologies, morphologies, and composites, *Chem. Rev.* 112 (2012) 933–969.
- [11] A. Rabenau, The role of hydrothermal synthesis in preparative chemistry, *Angew. Chem. Int. Ed.* 24 (1985) 1026–1040.

- [12] N.L. Rosi, J. Eckert, M. Eddaoudi, D.T. Vodak, J. Kim, M. O’Keeffe, et al., Hydrogen storage in microporous metal-organic frameworks, *Science* 300 (2003) 1127–1129.
- [13] N.L. Rosi, J. Kim, M. Eddaoudi, B. Chen, M. O’Keeffe, O.M. Yaghi, Rod packings and metal – organic frameworks constructed from rod-shaped secondary building units, *J. Am. Chem. Soc.* 127 (2005) 1504–1518.
- [14] S.S.Y. Chui, S.M.F. Lo, J.P.H. Charmant, A.G. Orpen, I.D. Williams, A chemically functionalizable nanoporous material $[\text{Cu}_3(\text{TMA})_2(\text{H}_2\text{O})_3]_n$, *Science* 283 (1999) 1148.
- [15] K.S. Park, Z. Ni, A.P. Côté, J.Y. Choi, R. Huang, F.J. Uribe-Romo, et al., Exceptional chemical and thermal stability of zeolitic imidazolate frameworks, *Proc. Natl. Acad. Sci. U.S.A.* 103 (2006) 10186–10191.
- [16] D. Feng, K. Wang, Z. Wei, Y.-P. Chen, C.M. Simon, R.K. Arvapally, et al., Kinetically tuned dimensional augmentation as a versatile synthetic route towards robust metal–organic frameworks, *Nat. Commun.* 5 (2014) 5723.
- [17] R. Banerjee, A. Phan, B. Wang, C. Knobler, H. Furukawa, M. O’Keeffe, et al., High-throughput synthesis of zeolitic imidazolate frameworks and application to CO_2 capture, *Science* 319 (2008) 939.
- [18] S. Bauer, C. Serre, T. Devic, P. Horcajada, J. Marrot, G. Férey, et al., High-throughput assisted rationalization of the formation of metal organic frameworks in the iron(III) aminoterephthalate solvothermal system, *Inorg. Chem.* 47 (2008) 7568–7576.
- [19] E. Biemmi, S. Christian, N. Stock, T. Bein, High-throughput screening of synthesis parameters in the formation of the metal-organic frameworks MOF-5 and HKUST-1, *Microporous Mesoporous Mater.* 117 (2009) 111–117.
- [20] A.D. Burrows, K. Cassar, R.M.W. Friend, M.F. Mahon, S.P. Rigby, J.E. Warren, Solvent hydrolysis and templating effects in the synthesis of metal-organic frameworks, *CrystEngComm* 7 (2005) 548–550.
- [21] A.L. Garay, A. Pichon, S.L. James, Solvent-free synthesis of metal complexes, *Chem. Soc. Rev.* 36 (2007) 846–855.
- [22] T. Friscic, New opportunities for materials synthesis using mechanochemistry, *J. Mater. Chem.* 20 (2010) 7599–7605.
- [23] A. Pichon, A. Lazuen-Garay, S.L. James, Solvent-free synthesis of a microporous metal-organic framework, *CrystEngComm* 8 (2006) 211–214.
- [24] J.H. Bang, K.S. Suslick, Applications of ultrasound to the synthesis of nanostructured materials, *Adv. Mater.* 22 (2010) 1039–1059.
- [25] L.-G. Qiu, Z.-Q. Li, Y. Wu, W. Wang, T. Xu, X. Jiang, Facile synthesis of nanocrystals of a microporous metal-organic framework by an ultrasonic method and selective sensing of organoamines, *Chem. Commun.* (2008) 3642–3644.
- [26] C.O. Kappe, Controlled microwave heating in modern organic synthesis, *Angew. Chem. Int. Ed.* 43 (2004) 6250–6284.
- [27] C.O. Kappe, D. Dallinger, S. Murphree, *Practical Microwave Synthesis for Organic Chemists: Strategies, Instruments, and Protocols*, Wiley, 2008.
- [28] P. Horcajada, T. Chalati, C. Serre, B. Gillet, C. Sebrie, T. Baati, et al., Porous metal-organic-framework nanoscale carriers as a potential platform for drug delivery and imaging, *Nat. Mater.* 9 (2010) 172–178.
- [29] S.H. Jung, J.H. Lee, J.W. Yoon, C. Serre, G. Férey, J.S. Chang, Microwave synthesis of chromium terephthalate MIL-101 and its benzene sorption ability, *Adv. Mater.* 19 (2007) 121–124.
- [30] S.H. Jung, J.H. Lee, J.S. Chang, Microwave synthesis of a nanoporous hybrid material, chromium trimesate, *Bull. Korean Chem. Soc.* 26 (2005) 880–881.

- [31] N.A. Khan, E. Haque, S.H. Jung, Rapid syntheses of a metal-organic framework material $\text{Cu}_3(\text{BTC})_2(\text{H}_2\text{O})_3$ under microwave: a quantitative analysis of accelerated syntheses, *Phys. Chem. Chem. Phys.* 12 (2010) 2625–2631.
- [32] R. Ameloot, L. Stappers, J. Fransaer, L. Alaerts, B.F. Sels, D.E. De Vos, Patterned growth of metal-organic framework coatings by electrochemical synthesis, *Chem. Mater.* 21 (2009) 2580–2582.
- [33] H. Furukawa, F. Gándara, Y.-B. Zhang, J. Jiang, W.L. Queen, M.R. Hudson, et al., Water adsorption in porous metal-organic frameworks and related materials, *J. Am. Chem. Soc.* 136 (2014) 4369–4381.
- [34] J.J. Low, A.I. Benin, P. Jakubczak, J.F. Abrahamian, S.A. Faheem, R.R. Willis, Virtual high throughput screening confirmed experimentally: porous coordination polymer hydration, *J. Am. Chem. Soc.* 131 (2009) 15834–15842.
- [35] S. Yuan, L. Feng, K. Wang, J. Pang, M. Bosch, C. Lollar, et al., Stable metal-organic frameworks: design, synthesis, and applications, *Adv. Mater.* 30 (2018). Available from: <https://doi.org/10.1002/adma.201704303>.
- [36] Y. Bai, Y. Dou, L.-H. Xie, W. Rutledge, J.-R. Li, H.-C. Zhou, Zr-based metal-organic frameworks: design, synthesis, structure, and applications, *Chem. Soc. Rev.* 45 (2016) 2327–2367.
- [37] J.H. Cavka, S. Jakobsen, U. Olsbye, N. Guillou, C. Lamberti, S. Bordiga, et al., A new zirconium inorganic building brick forming metal organic frameworks with exceptional stability, *J. Am. Chem. Soc.* 130 (2008) 13850.
- [38] G. Férey, C.M. Draznieks, C. Serre, F. Millange, J. Dutour, S. Surble, et al., A chromium terephthalate-based solid with unusually large pore volumes and surface area, *Science* 309 (2005) 2040.
- [39] C. Serre, F. Millange, C. Thouvenot, M. Noguès, G. Marsolier, D. Louër, et al., Very large breathing effect in the first nanoporous chromium(III)-based solids: MIL-53 or $\text{Cr}^{\text{III}}(\text{OH}) \cdot \{\text{O}_2\text{C} - \text{C}_6\text{H}_4 - \text{CO}_2\} \cdot \{\text{HO}_2\text{C} - \text{C}_6\text{H}_4 - \text{CO}_2\text{H}\}_x \cdot \text{H}_2\text{O}_y$, *J. Am. Chem. Soc.* 124 (2002) 13519.
- [40] G. Férey, C. Serre, C. Mellot-Draznieks, F. Millange, D.S.J. Surblé, I. Margiolaki, A hybrid solid with giant pores prepared by a combination of targeted chemistry, simulation, and powder diffraction, *Angew. Chem. Int. Ed.* 43 (2004) 6296.
- [41] K. Wang, X.-L. Lv, D. Feng, J. Li, S. Chen, J. Sun, et al., Pyrazolate-based porphyrinic metal-organic framework with extraordinary base-resistance, *J. Am. Chem. Soc.* 138 (2016) 914–919.
- [42] N.M. Padial, E. Quartapelle Procopio, C. Montoro, E. López, J.E. Oltra, V. Colombo, et al., Highly hydrophobic isorecticular porous metal-organic frameworks for the capture of harmful volatile organic compounds, *Angew. Chem.* 125 (2013) 8448–8452.
- [43] S.M. Cohen, Postsynthetic methods for the functionalization of metal-organic frameworks, *Chem. Rev.* 112 (2012) 970–1000.
- [44] P. Deria, J.E. Mondloch, O. Karagiari, W. Bury, J.T. Hupp, O.K. Farha, Beyond post-synthesis modification: evolution of metal-organic frameworks via building block replacement, *Chem. Soc. Rev.* 43 (2014) 5896–5912.
- [45] O. Karagiari, W. Bury, E. Tylianakis, A.A. Sarjeant, J.T. Hupp, O.K. Farha, Opening metal-organic frameworks vol. 2: inserting longer pillars into pillared-paddlewheel structures through solvent-assisted linker exchange, *Chem. Mater.* 25 (2013) 3499–3503.
- [46] M. Kim, J.F. Cahill, H. Fei, K.A. Prather, S.M. Cohen, Postsynthetic ligand and cation exchange in robust metal-organic frameworks, *J. Am. Chem. Soc.* 134 (2012) 18082–18088.

- [47] M. Kim, J.F. Cahill, Y. Su, K.A. Prather, S.M. Cohen, Postsynthetic ligand exchange as a route to functionalization of ‘inert’ metal-organic frameworks, *Chem. Sci.* 3 (2012) 126–130.
- [48] C.K. Brozek, M. Dincă, Ti^{3+} -, $\text{V}^{2+/3+}$ -, $\text{Cr}^{2+/3+}$ -, Mn^{2+} -, and Fe^{2+} -substituted MOF-5 and redox reactivity in Cr- and Fe-MOF-5, *J. Am. Chem. Soc.* 135 (2013) 12886–12891.
- [49] H. Irving, R.J.P. Williams, 637. The stability of transition-metal complexes, *J. Chem. Soc.* (1953) 3192–3210.
- [50] D. Denysenko, T. Werner, M. Grzywa, A. Puls, V. Hagen, G. Eickerling, et al., Reversible gas-phase redox processes catalyzed by co-exchanged MFU-4l(arge), *Chem. Commun.* 48 (2012) 1236–1238.
- [51] H. Furukawa, Y.B. Go, N. Ko, Y.K. Park, F.J. Uribe-Romo, J. Kim, et al., Isoreticular expansion of metal–organic frameworks with triangular and square building units and the lowest calculated density for porous crystals, *Inorg. Chem.* 50 (2011) 9147–9152.
- [52] X. Lian, Y.-P. Chen, T.-F. Liu, H.-C. Zhou, Coupling two enzymes into a tandem nanoreactor utilizing a hierarchically structured MOF, *Chem. Sci.* 7 (2016) 6969–6973.
- [53] Z. Fang, J.P. Dürholt, M. Kauer, W. Zhang, C. Lochenie, B. Jee, et al., Structural complexity in metal–organic frameworks: simultaneous modification of open metal sites and hierarchical porosity by systematic doping with defective linkers, *J. Am. Chem. Soc.* 136 (2014) 9627–9636.
- [54] L. Feng, S. Yuan, L.-L. Zhang, K. Tan, J.-L. Li, A. Kirchon, et al., Creating hierarchical pores by controlled linker thermolysis in multivariate metal–organic frameworks, *J. Am. Chem. Soc.* 140 (2018) 2363–2372.
- [55] Q.-L. Zhu, Q. Xu, Metal-organic framework composites, *Chem. Soc. Rev.* 43 (2014) 5468–5512.
- [56] T. Uemura, Y. Ono, K. Kitagawa, S. Kitagawa, Radical polymerization of vinyl monomers in porous coordination polymers: nanochannel size effects on reactivity, molecular weight, and stereostructure, *Macromolecules* 41 (2008) 87–94.
- [57] H.J. Lee, W. Cho, M. Oh, Advanced fabrication of metal-organic frameworks: template-directed formation of polystyrene@ZIF-8 core-shell and hollow ZIF-8 microspheres, *Chem. Commun.* 48 (2012) 221–223.
- [58] G. Distefano, H. Suzuki, M. Tsujimoto, S. Isoda, S. Bracco, A. Comotti, et al., Highly ordered alignment of a vinyl polymer by host–guest cross-polymerization, *Nat. Chem.* 5 (2013) 335.
- [59] W. Wang, Y. Li, R. Zhang, D. He, H. Liu, S. Liao, Metal-organic framework as a host for synthesis of nanoscale Co_3O_4 as an active catalyst for CO oxidation, *Catal. Commun.* 12 (2011) 875–879.
- [60] M. Müller, S. Hermes, K. Kähler, M.W.E. van den Berg, M. Muhler, R.A. Fischer, Loading of MOF-5 with Cu and ZnO nanoparticles by gas-phase infiltration with organometallic precursors: properties of Cu/ZnO@MOF-5 as catalyst for methanol synthesis, *Chem. Mater.* 20 (2008) 4576–4587.
- [61] A. Banerjee, R. Gokhale, S. Bhatnagar, J. Jog, M. Bhardwaj, B. Lefez, et al., MOF derived porous carbon- Fe_3O_4 nanocomposite as a high performance, recyclable environmental superadsorbent, *J. Mater. Chem.* 22 (2012) 19694–19699.
- [62] Z. Hasan, S.H. Jung, Removal of hazardous organics from water using metal-organic frameworks (MOFs): plausible mechanisms for selective adsorptions, *J. Hazard. Mater.* 283 (2015) 329–339.

- [63] Y. Zhang, S. Yuan, G. Day, X. Wang, X. Yang, H.-C. Zhou, Luminescent sensors based on metal-organic frameworks, *Coord. Chem. Rev.* 354 (2018) 28–45.
- [64] W.P. Lustig, S. Mukherjee, N.D. Rudd, A.V. Desai, J. Li, S.K. Ghosh, Metal-organic frameworks: functional luminescent and photonic materials for sensing applications, *Chem. Soc. Rev.* 46 (2017) 3242–3285.
- [65] A. Karmakar, N. Kumar, P. Samanta, A.V. Desai, S.K. Ghosh, A. Post-Synthetically, Modified MOF for selective and sensitive aqueous-phase detection of highly toxic cyanide ions, *Chem. Eur. J.* 22 (2016) 864–868.
- [66] H. Xu, Y. Xiao, X. Rao, Z. Dou, W. Li, Y. Cui, et al., A metal–organic framework for selectively sensing of PO_4^{3-} anion in aqueous solution, *J. Alloys Compd.* 509 (2011) 2552–2554.
- [67] Q. Yang, J. Wang, X. Chen, W. Yang, H. Pei, N. Hu, et al., The simultaneous detection and removal of organophosphorus pesticides by a novel Zr-MOF based smart adsorbent, *J. Mater. Chem. A* 6 (2018) 2184–2192.
- [68] B. Wang, X.-L. Lv, D. Feng, L.-H. Xie, J. Zhang, M. Li, et al., Highly stable Zr(IV)-based metal–organic frameworks for the detection and removal of antibiotics and organic explosives in water, *J. Am. Chem. Soc.* 138 (2016) 6204–6216.
- [69] Z. Hu, W.P. Lustig, J. Zhang, C. Zheng, H. Wang, S.J. Teat, et al., Effective detection of mycotoxins by a highly luminescent metal–organic framework, *J. Am. Chem. Soc.* 137 (2015) 16209–16215.
- [70] Z. Xie, W. Xu, X. Cui, Y. Wang, Recent progress in metal–organic frameworks and their derived nanostructures for energy and environmental applications, *ChemSusChem* 10 (2017) 1645–1663.
- [71] T.L. Easun, F. Moreau, Y. Yan, S. Yang, M. Schroder, Structural and dynamic studies of substrate binding in porous metal-organic frameworks, *Chem. Soc. Rev.* 46 (2017) 239–274.
- [72] E.M. Dias, C. Petit, Towards the use of metal-organic frameworks for water reuse: a review of the recent advances in the field of organic pollutants removal and degradation and the next steps in the field, *J. Mater. Chem. A* 3 (2015) 22484–22506.
- [73] E. Haque, V. Lo, A.I. Minett, A.T. Harris, T.L. Church, Dichotomous adsorption behaviour of dyes on an amino-functionalised metal-organic framework, amino-MIL-101(Al), *J. Mater. Chem. A* 2 (2014) 193–203.
- [74] F.Y. Yi, J.P. Li, D. Wu, Z.M. Sun, A series of multifunctional metal–organic frameworks showing excellent luminescent sensing, sensitization, and adsorbent abilities, *Chem. Eur. J.* 21 (2015) 11475–11482.
- [75] H. Du, C. Wang, Y. Li, W. Zhang, M. Xu, S. Li, et al., A supramolecular metal-organic framework derived from bismuth iodide and 4,4'-bipyridinium derivative: synthesis, structure and efficient adsorption of dyes, *Microporous Mesoporous Mater.* 214 (2015) 136–142.
- [76] X. Zhang, Y. Gao, H. Liu, Z. Liu, Fabrication of porous metal-organic frameworks via a mixed-ligand strategy for highly selective and efficient dye adsorption in aqueous solution, *CrystEngComm* 17 (2015) 6037–6043.
- [77] Y. Jia, Q. Jin, Y. Li, Y. Sun, J. Huo, X. Zhao, Investigation of the adsorption behaviour of different types of dyes on MIL-100(Fe) and their removal from natural water, *Anal. Methods* 7 (2015) 1463–1470.
- [78] A.C. Tella, S.O. Owolude, C.A. Ojekanmi, O.S. Oluwafemi, Synthesis of copper-isonicotinate metal-organic frameworks simply by mixing solid reactants and investigation of their adsorptive properties for the removal of the fluorescein dye, *New J. Chem.* 38 (2014) 4494–4500.

- [79] Y.S. Seo, N.A. Khan, S.H. Jung, Adsorptive removal of methylchlorophenoxypropionic acid from water with a metal-organic framework, *Chem. Eng. J.* 270 (2015) 22–27.
- [80] B.K. Jung, Z. Hasan, S.H. Jung, Adsorptive removal of 2,4-dichlorophenoxyacetic acid (2,4-D) from water with a metal–organic framework, *Chem. Eng. J.* 234 (2013) 99–105.
- [81] X. Zhu, B. Li, J. Yang, Y. Li, W. Zhao, J. Shi, et al., Effective adsorption and enhanced removal of organophosphorus pesticides from aqueous solution by Zr-based MOFs of UiO-67, *ACS Appl. Mater. Interfaces* 7 (2015) 223–231.
- [82] D.J. Lapworth, N. Baran, M.E. Stuart, R.S. Ward, Emerging organic contaminants in groundwater: a review of sources, fate and occurrence, *Environ. Pollut.* 163 (2012) 287–303.
- [83] Z. Li, Y.N. Wu, J. Li, Y. Zhang, X. Zou, F. Li, The metal–organic framework MIL-53 (Al) constructed from multiple metal sources: alumina, aluminum hydroxide, and boehmite, *Chem. Eur. J.* 21 (2015) 6913–6920.
- [84] N.A. Khan, B.K. Jung, Z. Hasan, S.H. Jung, Adsorption and removal of phthalic acid and diethyl phthalate from water with zeolitic imidazolate and metal–organic frameworks, *J. Hazard. Mater.* 282 (2015) 194–200.
- [85] M.N. Chong, B. Jin, C.W.K. Chow, C. Saint, Recent developments in photocatalytic water treatment technology: a review, *Water Res.* 44 (2010) 2997–3027.
- [86] H. Yang, H. Cheng, Controlling nitrite level in drinking water by chlorination and chloramination, *Sep. Purif. Technol.* 56 (2007) 392–396.
- [87] J. Lu, T. Zhang, J. Ma, Z. Chen, Evaluation of disinfection by-products formation during chlorination and chloramination of dissolved natural organic matter fractions isolated from a filtered river water, *J. Hazard. Mater.* 162 (2009) 140–145.
- [88] H.M. Coleman, C.P. Marquis, J.A. Scott, S.S. Chin, R. Amal, Bactericidal effects of titanium dioxide-based photocatalysts, *Chem. Eng. J.* 113 (2005) 55–63.
- [89] Q. Sun, M. Liu, K. Li, Y. Zuo, Y. Han, J. Wang, et al., Facile synthesis of Fe-containing metal-organic frameworks as highly efficient catalysts for degradation of phenol at neutral pH and ambient temperature, *CrystEngComm* 17 (2015) 7160–7168.
- [90] Q. Sun, M. Liu, K. Li, Y. Han, Y. Zuo, J. Wang, et al., Controlled synthesis of mixed-valent Fe-containing metal organic frameworks for the degradation of phenol under mild conditions, *Dalton Trans.* 45 (2016) 7952–7959.
- [91] Q. Sun, M. Liu, K. Li, Y. Han, Y. Zuo, F. Chai, et al., Synthesis of Fe/M (M = Mn, Co, Ni) bimetallic metal organic frameworks and their catalytic activity for phenol degradation under mild conditions, *Inorg. Chem. Front.* 4 (2017) 144–153.
- [92] K.G.M. Laurier, F. Vermoortele, R. Ameloot, D.E. De Vos, J. Hofkens, M.B.J. Roeffaers, Iron(III)-based metal–organic frameworks as visible light photocatalysts, *J. Am. Chem. Soc.* 135 (2013) 14488–14491.
- [93] Y.-Z. Chen, Z.U. Wang, H. Wang, J. Lu, S.-H. Yu, H.-L. Jiang, Singlet oxygen-engaged selective photo-oxidation over Pt nanocrystals/porphyrinic MOF: the roles of photothermal effect and Pt electronic state, *J. Am. Chem. Soc.* 139 (2017) 2035–2044.
- [94] J. Park, Q. Jiang, D. Feng, L. Mao, H.-C. Zhou, Size-controlled synthesis of porphyrinic metal–organic framework and functionalization for targeted photodynamic therapy, *J. Am. Chem. Soc.* 138 (2016) 3518–3525.
- [95] M. Styliadi, D.I. Kondarides, X.E. Verykios, Visible light-induced photocatalytic degradation of Acid Orange 7 in aqueous TiO₂ suspensions, *Appl. Catal. B: Environ.* 47 (2004) 189–201.

- [96] D. Zhang, R. Qiu, L. Song, B. Eric, Y. Mo, X. Huang, Role of oxygen active species in the photocatalytic degradation of phenol using polymer sensitized TiO₂ under visible light irradiation, *J. Hazard. Mater.* 163 (2009) 843–847.
- [97] W. Morris, B. Volosskiy, S. Demir, F. Gándara, P.L. McGrier, H. Furukawa, et al., Synthesis, structure, and metalation of two new highly porous zirconium metal–organic frameworks, *Inorg. Chem.* 51 (2012) 6443–6445.
- [98] D. Feng, Z.-Y. Gu, Y.-P. Chen, J. Park, Z. Wei, Y. Sun, et al., A highly stable porphyrinic zirconium metal–organic framework with shp-a topology, *J. Am. Chem. Soc.* 136 (2014) 17714–17717.
- [99] D. Feng, Z.Y. Gu, J.R. Li, H.L. Jiang, Z. Wei, H.-C. Zhou, Zirconium-metalloporphyrin PCN-222: mesoporous metal–organic frameworks with ultrahigh stability as biomimetic catalysts, *Angew. Chem. Int. Ed.* 51 (2012) 10307–10310.
- [100] D. Feng, W.-C. Chung, Z. Wei, Z.-Y. Gu, H.-L. Jiang, Y.-P. Chen, et al., Construction of ultrastable porphyrin Zr metal–organic frameworks through linker elimination, *J. Am. Chem. Soc.* 135 (2013) 17105–17110.
- [101] A.-N. Meng, L.-X. Chaihu, H.-H. Chen, Z.-Y. Gu, Ultrahigh adsorption and singlet-oxygen mediated degradation for efficient synergetic removal of bisphenol A by a stable zirconium-porphyrin metal-organic framework, *Sci. Rep.* 7 (2017) 6297.
- [102] L.W. Matzek, K.E. Carter, Activated persulfate for organic chemical degradation: a review, *Chemosphere* 151 (2016) 178–188.
- [103] X. He, A.A. de la Cruz, A. Hiskia, T. Kaloudis, K. O’Shea, D.D. Dionysiou, Destruction of microcystins (cyanotoxins) by UV-254 nm-based direct photolysis and advanced oxidation processes (AOPs): influence of variable amino acids on the degradation kinetics and reaction mechanisms, *Water Res.* 74 (2015) 227–238.
- [104] X. He, A.A. de la Cruz, K.E. O’Shea, D.D. Dionysiou, Kinetics and mechanisms of cylindrospermopsin destruction by sulfate radical-based advanced oxidation processes, *Water Res.* 63 (2014) 168–178.
- [105] M. Feng, L. Cizmas, Z. Wang, V.K. Sharma, Synergistic effect of aqueous removal of fluoroquinolones by a combined use of peroxymonosulfate and ferrate(VI), *Chemosphere* 177 (2017) 144–148.
- [106] L.W. Matzek, K.E. Carter, Sustained persulfate activation using solid iron: kinetics and application to ciprofloxacin degradation, *Chem. Eng. J.* 307 (2017) 650–660.
- [107] M. Feng, R. Qu, X. Zhang, P. Sun, Y. Sui, L. Wang, et al., Degradation of flumequine in aqueous solution by persulfate activated with common methods and polyhydroquinone-coated magnetite/multi-walled carbon nanotubes catalysts, *Water Res.* 85 (2015) 1–10.
- [108] X. Li, W. Guo, Z. Liu, R. Wang, H. Liu, Fe-based MOFs for efficient adsorption and degradation of acid orange 7 in aqueous solution via persulfate activation, *Appl. Surf. Sci.* 369 (2016) 130–136.
- [109] J. Wang, J. Wan, Y. Ma, Y. Wang, M. Pu, Z. Guan, Metal-organic frameworks MIL-88A with suitable synthesis conditions and optimal dosage for effective catalytic degradation of Orange G through persulfate activation, *RSC Adv.* 6 (2016) 112502–112511.
- [110] K.-Y. Andrew Lin, H.-A. Chang, C.-J. Hsu, Iron-based metal organic framework, MIL-88A, as a heterogeneous persulfate catalyst for decolorization of Rhodamine B in water, *RSC Adv.* 5 (2015) 32520–32530.
- [111] Y. Gao, S. Li, Y. Li, L. Yao, H. Zhang, Accelerated photocatalytic degradation of organic pollutant over metal-organic framework MIL-53(Fe) under visible LED light mediated by persulfate, *Appl. Catal. B: Environ.* 202 (2017) 165–174.

-
- [112] S. Yuan, L. Zou, J.-S. Qin, J. Li, L. Huang, L. Feng, et al., Construction of hierarchically porous metal–organic frameworks through linker labilization, *Nat. Commun.* 8 (2017) 15356.
- [113] L. Peng, J. Zhang, Z. Xue, B. Han, X. Sang, C. Liu, et al., Highly mesoporous metal–organic framework assembled in a switchable solvent, *Nat. Commun.* 5 (2014) 4465.
- [114] K. Li, S. Lin, Y. Li, Q. Zhuang, J. Gu, Aqueous-phase synthesis of mesoporous Zr-based MOFs templated by amphoteric surfactants, *Angew. Chem. Int. Ed.* 57 (2018) 3439–3443.
- [115] K. Shen, L. Zhang, X. Chen, L. Liu, D. Zhang, Y. Han, et al., Ordered macro-microporous metal-organic framework single crystals, *Science* 359 (2018) 206–210.
- [116] B. Bueken, N. Van Velthoven, T. Willhammar, T. Stassin, I. Stassen, D.A. Keen, et al., Gel-based morphological design of zirconium metal-organic frameworks, *Chem. Sci.* 8 (2017) 3939–3948.

Metal-organic frameworks for detection and desensitization of environmentally hazardous nitro-explosives and related high energy materials

Partha Samanta¹, Subhajit Dutta¹ and Sujit K. Ghosh^{1,2,*}

¹Department of Chemistry, Indian Institute of Science Education and Research (IISER), Pune, India, ²Centre for Energy Science, Indian Institute of Science Education and Research (IISER), Pune, India

*Corresponding authors. e-mail address: sghosh@iiserpune.ac.in

List of abbreviations

Ad	adenine
AIE	aggregation-induced emission
BPDC	4,4'-biphenyldicarboxylic acid
BPE	1,2-bis(4-pyridyl)ethane
bpee	1,2-bipyridylethene
bpy	4,4'bipyridine
bpydb	4,4'-(4,4'-bipyridine-2,6-diyl) dibenzoate
BTB	4,4',4''-benzene-1,3,5-triyl-tribenzoate
CL-20	Hexanitrohexaazaisowurtzitane
dcbpy	2,2'-bipyridine-4,4'-dicarboxylate
DMA	<i>N,N'</i> -dimethylacetamide
DMASM	4-(4-(dimethylamino)styryl)-1-methylpyridin-1-ium
DMF	<i>N,N</i> -dimethylformamide
DMNB	2,3-dimethyl-dinitrobutane
DNT	dinitrotoluene
H₂bdc	1,4-dicarboxybenzene
H₂bdc-NH₂	2-amino-1,4-dicarboxybenzene
H₂oba	4,4'-oxybis(benzoic acid)
HAT	hbhdp: 4-(2-hydroxy-3-methoxy-benzylidenehydrazino-carbonyl)- <i>N</i> -pyridin-4-yl-benzamide
HMX	octahydro-1,3,5,7-tetranitro-1,3,5,7-tetrazocine
HOMO	highest occupied molecular orbital
IPA	isophthalate
LUMO	lowest occupied molecular orbital

Na₂H₂DSOA	disodium-2,2'-disulfonate-4,4'-oxydibenzoic acid
NB	nitrobenzene
NDC	2,6-naphthalenedicarboxylate
NE	nitroethane
NM	nitromethane
NP	nitropropane and nitrophenol
NT	nitrotoluene
NTO	3-nitro-1,2,4-triazol-5-one
PCA	4-pyridinecarboxylate
PETN	pentaerythritol tetranitrate
PXRD	powder X-ray diffraction
RDX	1,3,5-trinitroperhydro-1,3,5-triazine
SBU	secondary building unit
SDBA	4,4'-sulfonyldibenzoate
^tBu	tertiary butyl
Tetryl	2,4,6-trinitrophenylmethylnitramine
TGA	thermogravimetric analysis
TIPA	tri(4-imidazolylphenyl)amine
TNB	1,3,5-trinitrobenzene
TNP	2,4,6-trinitrophenol
TNR	2,4,6-trinitrobenzene-1,3-diol
TNT	2,4,6-trinitrotoluene
TTCA	triphenylene-2,6,10-tricarboxylate

8.1 Introduction

8.1.1 Background of explosive materials

The development and applications of explosives is not new and it has been known since 220 BCE when black powder was discovered accidentally [1]. Explosives are also known as high energy materials (HEMs) as they contain very high potential energy, which on sudden release can lead to the formation of light, sound, heat, and pressure [2–4]. Further explosive materials can be categorized in terms of the velocity of detonation, namely, high explosive and low explosive (Fig. 8.1).

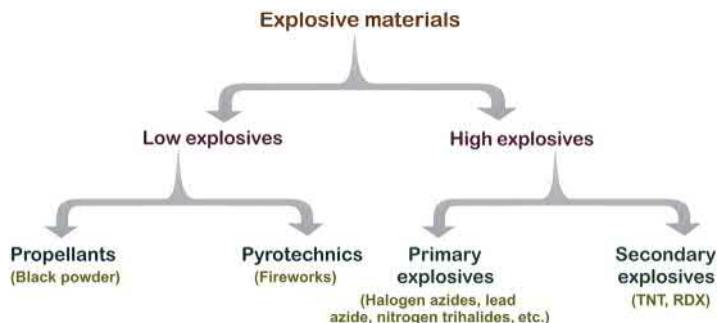
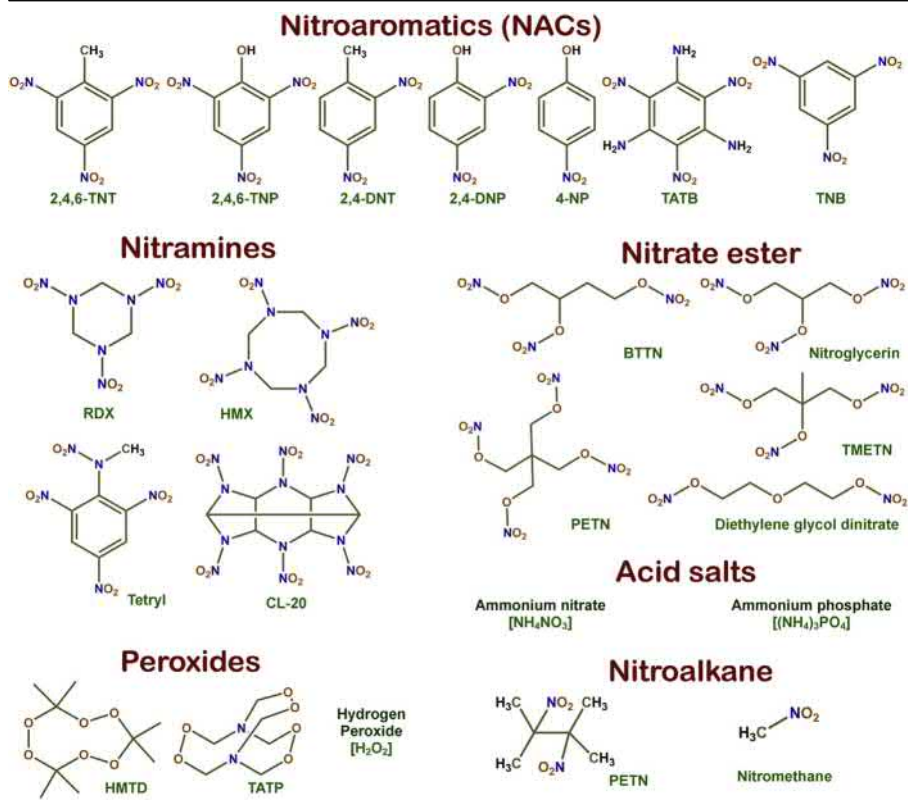


Figure 8.1 Classification of explosive materials.

Explosive materials, which decompose slowly and at a rate lesser than the speed of sound, are called low explosives. Low explosives are combustible substances which are known to deflagrate instead of detonate. In contrast, high explosives detonate rapidly and their shock waves pass through the materials with supersonic speed. Propellants (e.g., black powder) and pyrotechnics (e.g., fireworks) are the subclasses of the low explosives. High explosive materials can be categorized further in terms of sensitivity, namely, primary and secondary explosives [4–6]. Primary explosives are the materials which are very sensitive and can be detonated or exploded rapidly in the presence of various stimuli like heat, friction, and impact [5]. Among the primary explosives, a few of them are also known as contact explosives requiring very little energy for initiation. Whereas secondary explosives are comparatively less sensitive toward the aforementioned stimuli, but can release more powerful explosions as compared to the primary explosives [6]. Generally, explosive materials with greater sensitivity than PETN (pentaerythritol tetranitrate) are considered to be primary explosives, whereas materials having less sensitivity than PETN are considered to be secondary explosives [5]. Halogen azides, nitrogen trihalides, peroxy acids, oxides of xenon, acetone peroxides, alkali metal ozonides, azoclatrates, benzoyl peroxides, diazodinitrophenol, etc. are examples of primary explosives. Similarly, well-known examples of secondary explosives are TNT (2,4,6-trinitrotoluene) and RDX (research department explosive (IUPAC name: 1,3,5-trinitro-1,3,5-triazinane)). As the secondary explosive materials are less sensitive toward friction, heat, or any other impact, those materials are safe for storage and can be applied in various fields. In addition, owing to their high sensitivity, primary explosive materials are used to trigger a detonation of the main explosive part that consists of secondary explosive. Furthermore, ~250 compounds had been listed as explosive materials by November, 2010 by the Bureau of Alcohol, Tobacco, and Firearms [7]. Based on the chemical structures of such materials, those compounds have been classified into six major classes (nitroalkanes, nitroaromatics, nitramines, nitrate ester, acid salts, and peroxides) (Table 8.1). Among these materials, nitrated materials are accounted as priority explosive materials because of their high sensitivity and ability to produce powerful explosions [8].

It is noteworthy to mention that HEMs have found a wide range of applications in different areas including metallurgy industries, weapon technologies, engineering blasting, and rocket and space technologies [4]. In the metallurgy industries, to produce high quality alloys explosive materials are used to generate high pressure for welding purposes. Furthermore, explosive materials have been hugely employed in engineering blasting which includes mining, tunneling, and demolition of big structures like buildings. Mining is the largest commercial use of the explosive compounds, where a mixture of ammonium nitrate (AN) and fuel oil (FO) (denoted as, ANFO) are the mostly employed material. In addition, HEMs are also useful in the space technology where they are used as propellants to generate the kinetic energy. Furthermore, another major use of such HEMs are in the weapon technologies. Explosive materials are used in such technologies to develop modern warfare, for example, various explosive devices and nuclear warhead fuses. In general, nitroaromatic-based compounds (NACs), like TNT and 2,4,6-trinitrophenol (TNP), are

Table 8.1 Representative list of different types of explosive compounds.

considered primary military explosive materials and are found to be major components in unexploded ordnance (UXO). UXO are the materials which didn't detonate during the employment, but can pose a threat of detonation later and UXO includes land mines, bombs, grenades, and shells [9]. UXO poses threats due to not only the unusual explosion in later days, but also can lead to hazardous environmental pollution because of their NACs-based components. On the other hand, plastic explosives (which are known to be hand-moldable and soft forms of explosives) like Semtex and C-4 are made of nitrate ester (PETN is the main component of Semtex) and nitramines (RDX is the major component of C-4), respectively [8]. Another nitramine compound, namely tetryl (2,4,6-Trinitrophenylmethyl nitramine), was used extensively during the World War I and II as an explosive in the munitions. In addition, HEMs based on ammonium salts are known to be used in large amounts in various industrial applications; whereas peroxide based HEMs are known to be inexpensive and used in homemade explosives. Such explosive materials have found a wide range of applications in different industries, but on the other hand the misuse of such materials also poses a huge threat to civilian life. The rise in worldwide terrorism has become one pressing concern in recent years and the extensive

use of explosive bombs has caused the deaths of a huge number of civilians. In addition to homeland security, a few of the nitro-aromatic compounds (NACs) have also been identified as toxic water pollutants. US EPA (Environmental Protection Agency) has listed a few of the NACs as environmental pollutants and among them TNT and TNP are accounted as hazardous and toxic contaminants [10]. Worldwide, the huge usage of such explosive materials in different industries have increased the concern regarding environmental pollution as well. Due to the increasing concern across the globe, the sensing of such NACs has become one of the challenging tasks in recent years. Consequently, the sensing of NACs and HEMs has gained much attention worldwide and this chapter will cover the metal-organic frameworks (MOFs)-based detection of NACs and other HEMs. As discussed earlier, there are several types of explosive materials available, and among them nitro ($-\text{NO}_2$) group-based materials are often found to be very sensitive to stimuli like shock and friction [8]. To date, in the domain of MOFs, sensing of nitrated compounds has been very attractive in comparison to the other types of HEMs [8,10–15]. Further, the desensitization of HEMs based on MOFs has emerged in recent days [4,16]. Here, in this chapter we have discussed the MOFs-based sensing of nitro-aromatic explosive materials along with the desensitization of related HEMs.

8.1.2 Current methods/materials and mechanism for detection of nitro-aromatic compounds

The urgency to develop techniques and materials to detect NACs has become one of the priority issues in the scientific community to address the threats raised for homeland security and environmental pollution. It has been understood that methods to detect such explosive materials can be subdivided into the following classes [7]:

1. detection in vapor phase;
2. solid materials detection;
3. recognition in solution or dispersed phase.

Detection of hidden and illicit explosive materials in various common places, warzones, transportation hubs, etc. has become one of the pressing challenges in recent years. Vapor phase sensing of explosive materials is considered to be one of the effective techniques for personnel monitoring [8]. But the low vapor pressure of most of the nitro-analytes has made vapor phase detection of those analytes one of the most challenging tasks. Further, Kolla's group has reported that wrapping the analytes in plastic packaging has been found to reduce the vapor concentration of respective analytes by ~ 1000 times [17]. In addition, the detection of explosive materials in water medium has also attracted great interest in recent years. Due to increase in terrorist activities from both land and marine, recognition of those analytes in water medium has gained much interest in recent years. Again, the low solubility in water and poor saturation in concentration of those analytes because of continuous movement underwater in various water bodies have led to the detection of those explosive analytes at the ppb level. As a consequence of this, detection of those analytes both in vapor phase and in water medium is very challenging as well

as highly needed to reduce terrorist activities and environmental pollution. Current methods for the detection of such explosive materials include different techniques like trained animals, metal detectors, high-performance liquid chromatography, surface-enhanced Raman spectroscopy, ion mobility spectrometry, gas chromatography with mass spectrometry, optoacoustic spectroscopy, plasma desorption mass spectrometry, and energy dispersive X-ray diffraction [8,18–23]. Although all of these aforementioned methods have shown their advantages in recognition and quantification of explosive materials, they are also associated with drawbacks like high cost, lack of portability, and false response because of various environmental pollutants [7,8,19,20]. A fluorescence-based optical technique for sensing applications has attracted much attention in recent years due to its simplicity, low cost, portability, high sensitivity, etc. [8,13,19,20]. Further, most of the explosive materials including nitro-analytes are nonluminescent in nature which has facilitated a luminescence-based technique to recognize those analytes. In most of the cases, it has been observed that NACs can readily quench the fluorescence intensity of the luminescent probe employed for the detections due to the interaction between probe and analytes. The quenching efficiency of the fluorophore in the presence of analytes in a liquid medium can be obtained in terms of the Stern–Volmer constant (K_{sv}) and can be calculated by the following equation [10]:

$$\frac{I_0}{I_f} = 1 + K_{sv}[Q]$$

where I_0 and I_f are the initial and final (after addition of analyte) fluorescence intensities of the fluorophore, $[Q]$ is the concentration of the respective analyte.

Different types of mechanisms (such as photoinduced electron transfer (PET), Förster resonance energy transfer (FRET), intramolecular charge transfer (ICT), and electron exchange) have been proposed for such luminescence quenching behavior of probes in the presence of nitro-analytes (Fig. 8.2) [8,12]. FRET is known as a

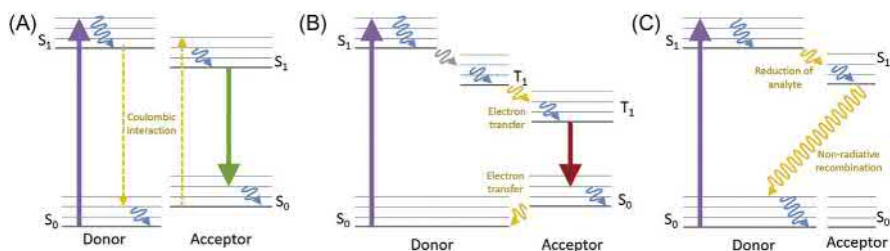


Figure 8.2 Schematic representation of mechanism for (A) Förster resonance energy transfer, (B) electron exchange, and (C) photoinduced electron transfer.

Source: Reproduced with permission from W.P. Lustig, S. Mukherjee, N.D. Rudd, A.V.

Desai, J. Li, S.K. Ghosh, Metal-organic frameworks: functional luminescent and photonic materials for sensing applications. *Chem. Soc. Rev.* 46 (2017) 3242–3285. Copyright (2017) Royal Society of Chemistry.

short range energy transfer (1–10 nm) in a nonradiative way, where a previously excited donor molecule returns back to the ground state and consequently energy is transferred to the acceptor molecule to promote an electron to an excited state [24]. In FRET, the rate of energy transfer relies on the distance and orientation of the donor and acceptor molecules, as well as on the degree of overlap between the excitation of the analytes (acceptor) and emission of the fluorescent probe (donor). The efficiency of FRET can be measured by following various techniques, like photobleaching FRET, lifetime measurement, and sensitized emission. Further, the efficiency of FRET, that is, energy transfer, can be calculated by the following equation [8]:

$$E = 1 - \frac{F}{F_0} = \frac{R_0^6}{R_0^6 + r_0^6}$$

where E is the efficiency of FRET, F_0 and F are relative fluorescence intensities of the probe before and after of addition of the analytes respectively, R_0 is critical distance for the 50% energy transfer, and r_0 is the distance between donor and acceptor.

Detection of nitro-explosives have been performed extensively with luminescent probe via the FRET mechanism. By following strategies like the formation of a Meisenheimer complex between donor and acceptor, or strong overlap between excitation of the analytes and emission of fluorophores, various luminescent probes have been designed for explosive detection [25–27]. Apart from FRET-based probes, PET is another mechanism which has also been employed extensively. PET process involves the transfer of an electron from a donor to an acceptor molecule and consequently the formation of a charge separated state with a radical cation of the donor and a radical anion of the acceptor [28]. Because of this type of electron transfer, PET is also known as a redox process [12]. As a consequence of electron transfer in PET, the luminescence quantum yield of the fluorophore as well as the lifetime have been found to be decreased. In the PET process, complex formation between donor and acceptor molecules has been observed, these are found to be returned back to the ground state without photon emission and later the extra electron is finally transferred back to the donor molecules from the acceptor [8]. Apart from quenching, in a few cases turn-on responses toward nitro-analytes have also been observed due to the PET process. In a report by Ravikanth and coworkers, a BODIPY-based luminescent probe was employed for the detection of TNP in a turn-on fashion [29]. In this report PET has played a crucial role in the luminescence enhancement upon addition of TNP. Again, time-resolved spectroscopy-based techniques are required to prove the existence of a radical formed due to PET and also to calculate its rate.

Since most of the explosive analytes are derived from nitrated compounds, FRET and PET-based probes have attracted much attention for their detection purposes. In addition, two more mechanisms, viz., ICT and electron exchange phenomenon, have been observed for the recognition of such analytes with luminescent

probes. The electron exchange process is also known as Dexter electron exchange, which is also a short range electron transfer phenomenon similar to the FRET process [12]. In this process, electron transfer occurs from the LUMO of the excited state donor to the acceptor. Further, another electron is also transferred from the HOMO of the acceptor (analytes) to the donor (fluorophore probe) molecules and this electron transfer has been observed to quench the luminescence emission of the probe. In contrast to the spectral overlap in FRET, there should be orbital overlap in case of electron exchange. Because of the requirement of orbital overlap, with the increase in distance between donor and acceptor there will be a drastic decrease in effect of electron exchange. Further, one of the less explored phenomena in NACs sensing with a fluorescent probe is the ICT. In a report by Xu et al., sensing of TNP was reported with a zwitterionic squaraine dye with a dansylamide ring appended to the molecule, DNSA-SQ. ICT has led to the desirable fluorescence change due to protonation in the Dansyl moiety [30]. Furthermore, various types of luminescent probes have been reported for the recognition of nitro-analytes. Among them, organic conjugated polymers, organic small molecules, inorganic polymers, quantum dots, dendrimers, organic macrocycle, and single-walled carbon nanotubes have seen considerable progress in this domain [8,18–20,31,32]. In last few years, MOFs-based sensing of nitro-analytes has attracted great attention. This chapter is devoted to the advancement in the domain of sensing and desensitization of different types of explosive and HEMs with MOFs.

8.2 Luminescent metal-organic frameworks

MOFs are a unique class of crystalline solid materials and have emerged with huge potential in the last two decades [33–36]. Such extended crystalline frameworks can be designed and synthesized by suitable choices of metal nodes and organic building units. In recent years, MOFs have become one of the frontrunners in the domain of porous materials because of the plethora of applications in diverse fields. The large surface area, tunable architecture, and intriguing functionalities have made MOFs suitable for various targeted applications. MOFs have already been applied for gas storage, separation of gas/solvents, sensing, drug delivery, catalysis, fuel cell applications, photonics, etc. [37–42]. Luminescent metal-organic frameworks (LMOFs) are a subclass of MOFs having huge potential in the area of sensing, optoelectronics properties, etc. [12–14,43,44]. Luminescence is the phenomena of emitting light after absorption of energy and this can be classified into two major types, that is, fluorescence and phosphorescence. Furthermore, fluorescence is the process whereupon excitation radiative transition occurs from the lowest excited singlet state (S_1) to the singlet ground state (S_0). This radiative transition is spin-allowed as it involves both the singlet states. This fluorescence process has been found to have a lifetime in the scale of not more than 10 ns. On the other hand, phosphorescence is the spin-forbidden radiative transition as it involves different spin states in this process, one singlet and one triplet state. Phosphorescence is

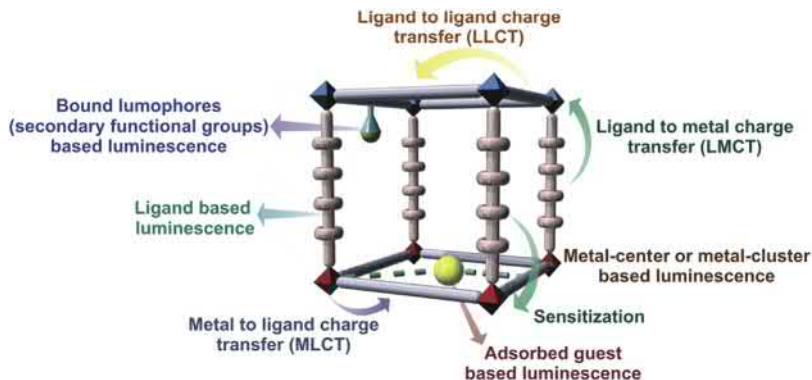


Figure 8.3 Schematic representation of different types of possibilities in the origin of luminescence in metal-organic frameworks.

described as the process which takes place from the lower triplet state (T_1) to the singlet ground state (S_0). In contrast to fluorescence, phosphorescence has a higher lifetime which is in the order of microseconds (μs) to seconds.

It has been observed that till date a lot of luminescent MOFs have been reported in the literature and in the area of MOF-based sensors, LMOFs are the most explored materials. The easy tunability in the MOF structures provides the scope to tune the photoluminescence property in MOFs, based on the ligands employed, the metal-centers or clusters used, or maybe the surface functionalizations. Such facile engineering in the luminescence property of MOFs has led researchers to design and synthesize LMOFs-based sensors for the detection of various toxic environmental pollutants, explosive materials, etc. In addition, the porous nature of MOFs also added an advantage for sensing application as targeted analytes can be adsorbed inside the pores of MOFs to produce prominent interaction between the targeted analyte and the recognition center to generate strong signals [12]. Along with this advantage of MOFs, such porous ordered networks can also lead to the preconcentration of the analyte inside the pore aperture of MOFs which is also known to enhance the sensing performance of the probe [45]. Allendorf et al. have described different phenomena (linkers-based, framework metal ions-based, adsorbed lumophores-based, exciplex formation, and lumophores bound to MOF) which are considered to be major contributors to the origin of luminescence in LMOFs (Fig. 8.3) [43].

8.2.1 Ligand-based luminescence in metal-organic frameworks

Aromatic conjugated organic ligands-based photoluminescence is the major contributor in the area of LMOFs to date. Generally, π -electron rich conjugated organic moieties are known to absorb light and consequently radiative transition leads to the photoluminescence behavior of the compounds. Furthermore, in the case of such π -rich organic ligands the selection rule can be governed by the symmetry of

both the singlet ground state and excited state as these organic compounds have little spin-orbit coupling. As a consequence of this, organic linker-based luminescence in LMOFs is mostly driven through the fluorescence process and the transitions are found to be similar to the individual organic molecules in solution which are either $\pi \rightarrow \pi^*$ or $n \rightarrow \pi^*$ in nature. Irrespective of such similarities in photoluminescence behavior between free organic lumophores (ligands) and LMOFs, often properties like maximum emission wavelength (λ_{\max}) or quantum yields (Φ) of the free lumophores may differ in the LMOFs. This can be attributed to a result of random interaction between those organic lumophores in solution; in contrast those lumophores are oriented in an organized and rigid manner in MOFs. Such ordered orientation of linkers leads to the minimization of the nonradiative decay which results in the efficient luminescent behaviors, higher quantum yield, etc. of LMOFs. Further, in the case of such linker-based LMOFs, the choice of the metal ions to construct the MOFs is also very crucial. These type of LMOFs are mostly constructed from metal ions where d-d transition is not possible due to either empty outer d-orbitals (such as Zr(IV) and Ce(IV)) or fully occupied d-orbitals (such as Zn(II), Ag(I), and Cd(II)). Again, after absorbing light by the linkers of LMOFs, the fluorescence can be originated via various pathways like interligand charge transfer (ILCT), metal to ligand charge transfer (MLCT), and ligand-to-metal charge transfer (LMCT). Since ILCT, LMCT, MLCT, etc. contribute to the luminescent property of the MOFs, so electron density of ligand as well as the electronic configuration of metal ions, coordination environment, arrangement of ligands inside the MOFs, interligand distances, etc. directly influence the photoluminescence behavior of LMOFs. Ghosh and coworkers reported Zr-MOF-based (UiO-66@NH₂) selective sensing of nitric oxide (NO), where LMCT in UiO-66@NH₂ has been described as the origin of the fluorescence in the MOF (Fig. 8.4B) [46]. Upon reaction with nitric oxide, NH₂BDC (BDC: 1,4-benzene dicarboxylic acid) ligand turned to BDC as a result of a deamination reaction. Due to such deamination of the ligand, electron density on the ligand was reduced which resulted in the lesser extent of LMCT and quenching of fluorescence.

On the other hand, Li and coworkers reported tunable white light emission by MLCT-based LMOF, [(CH₃)₂NH₂]₁₅[(Cd₂Cl)₃(TATPT)₄]₁₂DMF₁₈H₂O (TATPT: 2,4,6-tris(2,5-dicarboxylphenylamino)-1,3,5-triazine) (Fig. 8.4C) [47]. A large shift in fluorescence peak maxima and enhancement in the luminescence intensity of MOF compared to the free ligand is attributed to the MLCT in the compound. Moreover, fluorescence of the ligand in MOFs can also be affected by the electron or proton transfer in the excited state. Excited state electron transfer (ESET) is the process wherein ESET occurs from electron-donor moieties to the electron-acceptor moieties. Similarly, the transfer of proton (either join or depart) in the excited state is termed as the excited state proton transfer (ESPT). ESPT can occur through both intermolecular and intramolecular proton transfer; the latter is a faster process compared to the intermolecular process. Excited state intramolecular proton transfer (ESIPT) takes place when proton tautomerization leads to the relaxation of the photo-excited state. A well-known example of such ESIPT-based frameworks is the

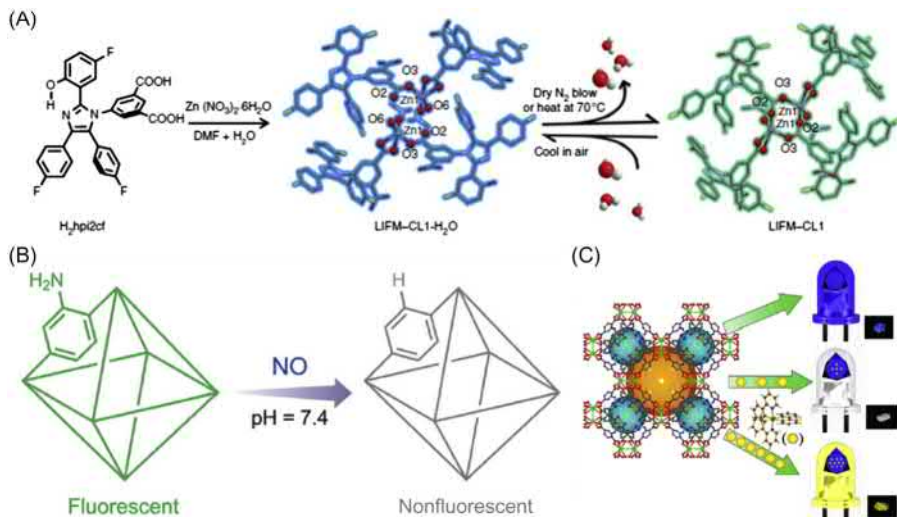


Figure 8.4 (A) Schematic representation for synthesis of LIFM-CL1-H₂O and water sensing with it. (B) Fluorescence quenching upon deamination in UiO-66@NH₂. (C) Representation of control encapsulation of [Ir(ppy)₂(bpy)]⁺ complex in 3D MOF for white light emission. *Source:* For (A) reproduced with permission from L. Chen, J.-W. Ye, H.-P. Wang, M. Pan, S.-Y. Yin, Z.-W. Wei, et al., Ultrafast water sensing and thermal imaging by a metal-organic framework with switchable luminescence, *Nat. Commun.* (2017) DOI: 10.1038/ncomms15985. Copyright (2017) Springer Nature. For (B) reported with permission from A. V. Desai, P. Samanta, B. Manna, S.K. Ghosh, Aqueous phase nitric oxide detection by an amine decorated metal-organic framework, *Chem. Commun.* 51 (2015) 6111–6114. Copyright (2015) Royal Society of Chemistry. For (C) reported with permission from C.-Y. Sun, X.-L. Wang, X. Zhang, C. Qin, P. Li, Z.-M. Su, et al., Efficient and tunable white-light emission of metal-organic frameworks by iridium-complex encapsulation, *Nat. Commun.* (2013) DOI: 10.1038/ncomms3717. Copyright (2013) Springer Nature.

2,5-dihydroxyterephthalic acid (H₂DHT) linker-based MOFs. Due to the presence of acidic hydrogen, which can participate in tautomerism at the excited state, DHT-based MOFs showed excellent ESIPT features. Maji and coworkers have demonstrated tunable luminescence property in Mg-DHT MOF on variation in the nature of corresponding solvents and this tunability has been ascribed as the consequence of the ESPT [48]. In another report, Chen et al. reported a Zn-MOF (namely, LIFM-CL1) which has been found to be ESIPT active material and further this phenomenon has been employed for the detection trace amount of water in the molecular level (Fig. 8.4A) [49]. The as-synthesized MOF was found to have coordinated water molecules and thus on dehydration and rehydration of the LIFM-CL1 gave rise to the drastic change in the photoluminescence behavior via ESIPT mechanism. This shows that ligand-based luminescence in the area of LMOFs is very essential and, furthermore, can play a huge part in the fabrication of various sensory materials.

8.2.2 Metal node or cluster-based luminescence in metal-organic frameworks

Metal node-based LMOFs are mostly constructed from the lanthanide metal ions. Last few decades has witnessed various strategies to utilize different lanthanide (Ln) metal ions to fabricate highly luminescent materials [50–52]. Due to the forbidden f-f transition by Laporte selection rule, lanthanides have inefficient excitation and low quantum yield. To overcome this problem, complexation is required for such metal ions by coupling with linkers that can efficiently absorb light and further transfer the energy. This process is known as “antenna effect” or “sensitization” and this effect can lead to the increment in the luminescence property (Fig. 8.5A) [43]. In the presence of such linkers, vibronic coupling between the linkers and lanthanides induces the charge transfer from the accessible excited state of the linker to the available energy state of the metal ion. Organic ligands-based coordination polymeric lanthanide-MOFs also have seen huge progress in the last few years in the area of optoelectronic properties and the sensing of various toxic and hazardous analytes. In the case of lanthanides (Ln), transitions occur from 4f-orbitals which are shielded by outer s-orbitals (5s) and p-orbitals (5p), in contrast to the transition metals. As a consequence of this, 4f-orbitals remain unaffected from the outer electronic environments and also similarly the 4f-4f transitions. This resulted in the characteristic sharp and narrow emission peaks for the Ln-MOFs. In the lanthanide series, the emission from UV region to the visible and the near infrared (NIR) region can be observed from all other metals except La^{3+} and Lu^{3+} . In the regime of Ln-MOFs, Eu(III) and Tb(III) metals are majorly explored to synthesize the LMOFs for different sensing and optoelectronic applications. Eu(III)-based compounds are known for their red light emission originating from ${}^5\text{D}_0 \rightarrow {}^7\text{F}_J$ (where $J = 1$ and 2 are the major contributor) transition. Whereas, on the other hand, Tb-MOFs are known to emit green luminescence owing to the transition from ${}^5\text{D}_4 \rightarrow {}^7\text{F}_J$ (where $J = 5$ is the strongest transition). Lanthanide MOFs have earned huge attention in the design of sensory materials for various toxic and hazardous analytes, temperature, etc. [53,54]. In this regard, Dong et al. reported a Tb(III)-MOF, with formula of $\{[\text{Tb}_4(\text{OH})_4(\text{DSOA})_2(\text{H}_2\text{O})_8] \cdot (\text{H}_2\text{O})_8\}_n$ (where, $\text{Na}_2\text{H}_2\text{DSOA}$: disodium-2,2'-disulfonate-4,4'-oxydibenzoic acid), based sensing of Fe(III)-ion [55]. Upon excitation at 350 nm, Tb-MOF showed emissions at 487, 542, 580, and 619 nm corresponding to the transitions of ${}^5\text{D}_4 \rightarrow {}^7\text{F}_6$, ${}^5\text{D}_4 \rightarrow {}^7\text{F}_5$, ${}^5\text{D}_4 \rightarrow {}^7\text{F}_4$, and ${}^5\text{D}_4 \rightarrow {}^7\text{F}_3$ respectively (Fig. 8.5B). A sensing study revealed that the MOF was found to be selective for Fe(III)-ion over concurrent metal ions (Fig. 8.5C). Apart from metal-based luminescence in MOFs, a few MOFs have also been reported where metal-clusters have led to the luminescent property. As an example, Huang et al. reported dodecanuclear Ag(I) chalcogenide/chalcogenolate cluster-based LMOF, viz., Ag_{12}bpy with a formula of $[\text{Ag}_{12}(\text{S}^t\text{Bu})_6(\text{CF}_3\text{COO})_6(\text{CH}_3\text{CN})_6] \cdot \text{CH}_3\text{CN}$ and quantum yield of 12.1% [56]. This MOF showed switchable luminescent property and furthermore was explored for the sensing of oxygen (O_2) and various volatile organic compounds (VOCs) via “turn-off” and “turn-on,” respectively (Fig. 8.5D). Different other LMOFs where the origin of

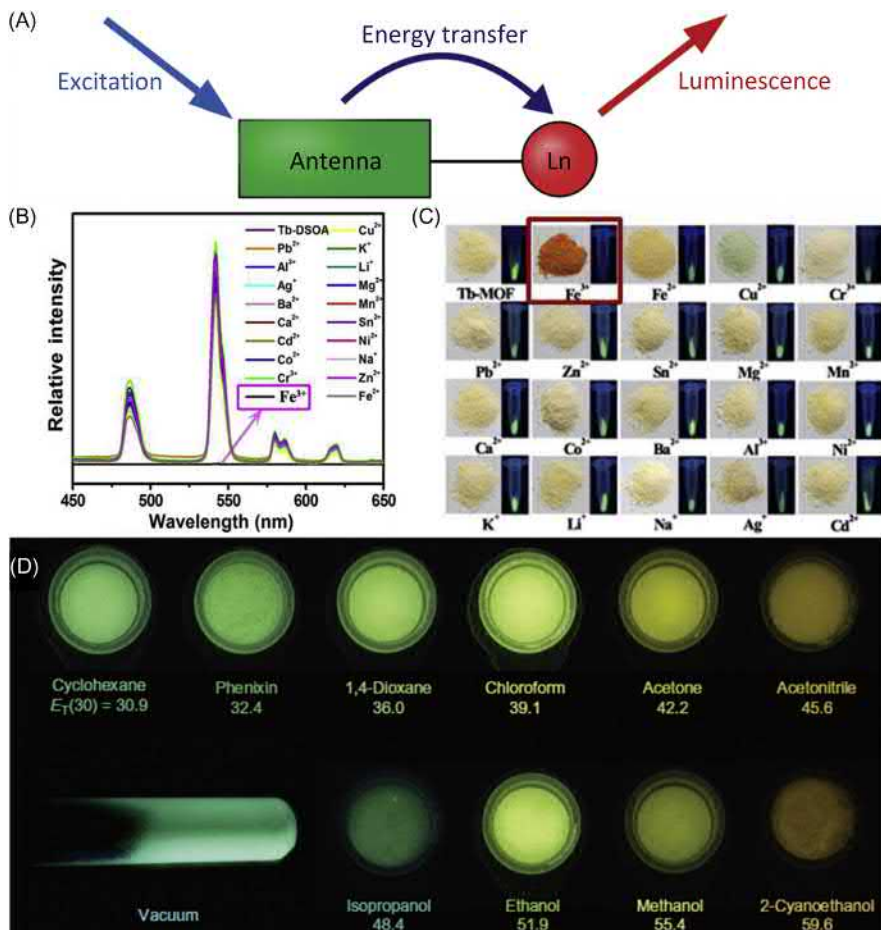


Figure 8.5 (A) Schematic representation "antenna effect." (B) Fluorescence response of Tb-MOF in presence of various metal ions. (C) Images of Tb-MOF and its luminescence in presence of Fe(III)-ion and other competing cations. (D) Images of Ag₁₂bpy MOF in presence of different volatile organic compounds under UV-lamp (365 nm).

Source: For (A) reproduced with permission from J. Heine, K. Müller-Buschbaum, Engineering metal-based luminescence in coordination polymers and metal-organic frameworks, *Chem. Soc. Rev.* 42 (2013) 9232–9242. Copyright (2013) Springer Nature. For (B) and (C) reported with permission from X.-Y. Dong, R. Wang, J.-Z. Wang, S.-Q. Zang, T. C.W. Mak, Highly selective Fe³⁺ sensing and proton conduction in a water-stable sulfonate–carboxylate Tb–organic-framework, *J. Mater. Chem. A* 3 (2015) 641–647. Copyright (2015) Royal Society of Chemistry. For (D) reported with permission from R.-W. Huang, Y.-S. Wei, X.-Y. Dong, X.-H. Wu, C.-X. Du, S.-Q. Zang, et al., Hypersensitive dual-function luminescence switching of a silver-chalcogenolate cluster-based metal-organic framework, *Nat. Chem.* 9 (2017) DOI: 10.1038/NCHEM.2718. Copyright (2017) Springer Nature.

luminescence was found to be the metal nodes or clusters have enormous potential for sensing applications.

8.2.3 Excimer or exciplex formation in metal-organic frameworks

Excimer or exciplex are the dimeric or heterodimeric short-lived species which can be generated in the excited state, but dissociate in the ground state. Generally, the homodimeric species in the excited state is termed as the excimer, whereas the heterodimeric species is known as the exciplex. In the case of MOFs, it has been understood that such species can be formed by two ways [43]:

1. if the ligands are oriented in such a way that they can form a complex in the excited state, then formation of such species is possible.
2. In the case of guest adsorbed frameworks, the excited state complex can be formed due to the interaction between the guest and the framework.

In such cases, the emission is highly dependent on the arrangement and orientation of participating units inside the frameworks. Cornil et al. demonstrated that separation of participating species in the excited state is also a very decisive factor along with the cofacial arrangement [57]. Douhal and coworkers reported excimers formation in Zr-NDC MOF (NDC: 2,6-naphthalene dicarboxylic acid) between two naphthalene moieties which led to the luminescent behavior of the compound [58]. For dilute suspension of the Zr-NDC MOF, excimers formation has been noticed between two linkers in the same MOF particle; whereas for a higher concentration suspension, excimers formation between one naphthalene moiety and neighboring MOF particle has also been observed (Fig. 8.6B). Further, solvent dependency on the excimer formation has also been explored in this study. Another report by the same group has demonstrated sensing of NACs with two Zr-MOFs where the excimer formation between two naphthalene linkers has resulted in the luminescence of the MOFs [59]. Further, pyrene-moiety-based linkers are also known to produce excimers in the excited state if they are arranged properly inside MOFs. Deria et al. reported 1,3,6,8-tetrakis(*p*-benzoic acid)pyrene linker-based MOFs (ROD-7, NU-901, NU-1000) for excited state excimer formation and their luminescent properties (Fig. 8.6A) [60].

Moreover, excimers-based luminescence profiles show broad absorption spectra along with the large full width half maxima. In many cases this feature is very much useful in the design of sensory material for various targeted analytes. Another nice example of sensing applications based on the exciplex formation between MOF and guest molecules was shown by Kitagawa and coworkers [61]. Here, porous coordination polymer with formula of $[Zn_2(\text{bdc})_2(\text{dpNDI})]_n$ has been employed for the sensing of VOCs where exciplex formation between the VOCs (benzene, toluene, anisole, cyanobenzene, iodobenzene, xylene-isomers, etc.) and linker of the MOFs has led to a drastic shift in the emission peak of MOF for corresponding VOCs (Fig. 8.6C).

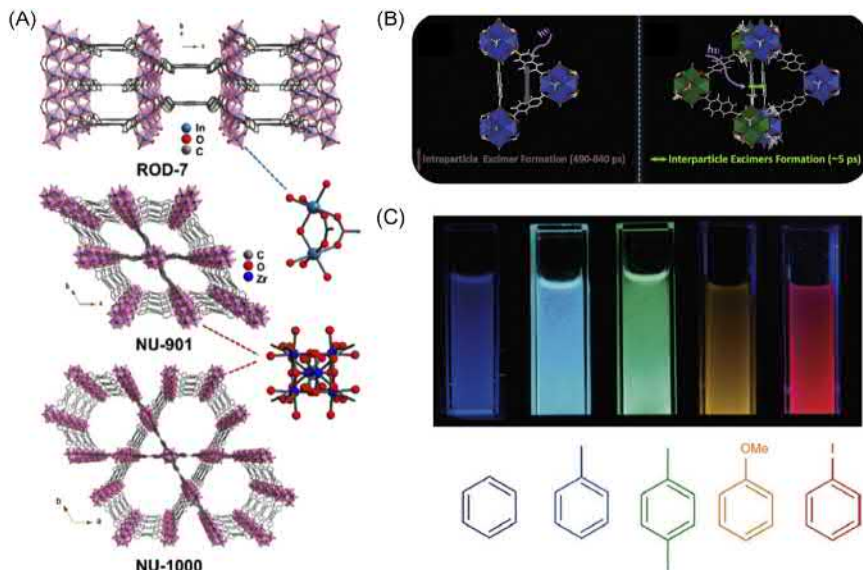


Figure 8.6 (A) Structures of pyrene-based MOFs: ROD-1, NU-901, and NU-1000 (from top to bottom, respectively). (B) Schematic representation of excimer formation in diluted suspension (left) and concentrated suspension (right) in THF of Zr-NDC MOF. (C) Images of $[\text{Zn}_2(\text{bdc})_2(\text{dpNDI})]_n$ MOF in presence of different aromatic volatile organic compounds under UV-lamp (365 nm).

Source: For (A) reproduced with permission from P. Deria, J. Yu, T. Smith, R.P. Balaraman, Ground-state versus excited-state interchromophoric interaction: topology dependent excimer contribution in metal – organic framework photophysics, *J. Am. Chem. Soc.* 139 (2017) 5973 – 5983. Copyright (2017) American Chemical Society. For (B) reported with permission from M. Gutiérrez, F. Sánchez, A. Douhal, Spectral and dynamical properties of a Zr-based MOF, *Phys. Chem. Chem. Phys.* 18 (2016) 5112–5120. Copyright (2016) Royal Society of Chemistry. For (C) reported with permission from Y. Takashima, V.M. Martínez, S. Furukawa, M. Kondo, S. Shimomura, H. Uehara, et al., Molecular decoding using luminescence from an entangled porous framework, *Nat. Commun.* (2011) DOI: 10.1038/ncomms1170. Copyright (2011) Springer Nature.

8.2.4 Adsorbed lumophores-based luminescence in metal-organic frameworks

By virtue of porosity or the ion-exchange process (in the case of i-MOFs) incorporation of lumophores inside MOFs has also emerged as a useful technique to fabricate luminescent materials. Incorporation of such lumophores can also be performed by stitching them with frameworks either with presynthetic or postsynthetic methods. Both organic (polyaromatic hydrocarbons, various luminescent dye molecules, etc.) and inorganic (different lanthanide metals mostly) compounds can serve the purpose by enhancing or tuning the luminescent properties of parent MOF materials. In this regard bio-MOF-1 $[\text{Zn}_8(\text{ad})_4(\text{BPDC})_6\text{O}\cdot 2\text{Me}_2\text{NH}_2\cdot 8\text{DMF}\cdot 11\text{H}_2\text{O}$;

(ad: Adenine, BPDC: 4,4'-biphenyldicarboxylate)] is one of the well-known examples of host framework. Rosi and coworkers have demonstrated the tunable luminescence property of MOF via exchanging the dimethylammonium cation (Me_2NH_2^+), situated inside the framework, with various lanthanide metal ions (Eu^{3+} , Tb^{3+} , Sm^{3+} , Yb^{3+}) [62]. Upon excitation of those lanthanide incorporated MOFs at 365 nm, emission spectra at 545, 614, 640, and 970 nm have been observed for Tb^{3+} @bio-MOF-1, Eu^{3+} @bio-MOF-1, Sm^{3+} @bio-MOF-1, and Yb^{3+} @bio-MOF-1, respectively. Although water is counted as a quencher, emissions for all lanthanide doped MOF materials were found to be very clear with their respective distinctive colors. This result was attributed to the sensitization role of MOF which served as an antenna to sensitize the respective lanthanide metal ions. Owing to the luminescence profile of Yb^{3+} @bio-MOF-1 at NIR region, reversible O_2 sensing has also been shown with the compound. Furthermore, bio-MOF-1 has also been employed as a host for two-photon fluorescence with an organic dye molecule [63]. In this report, Yu et al. have incorporated pyridinium hemicyanine (cationic) dye into anionic bio-MOF-1 to make the composite material for two-photon-pumped lasing. The MOF-dye composite material showed two-photon-pumped lasing at ~ 640 nm upon excitation at 1064 nm with an Nd:YAG laser (with threshold of 0.148 mJ) (Fig. 8.7B). The pore confinement effect of bio-MOF-1 and a large two-photon absorption cross-section of the dye molecules have resulted in the high luminescence efficiency of the composite material. Apart from bio-MOF-1, with another anionic MOF, namely, ZJU-28 [$(\text{Me}_2\text{NH}_2)_3[\text{In}_3(\text{BTB})_4] \cdot 12\text{DMF} \cdot 22\text{H}_2\text{O}$; BTB: 4,4',4''-benzene-1,3,5-triyl-tri-benzoate], modulation of emission properties of MOF has been demonstrated with organic compounds encapsulation via cation exchange [64]. Here, Qian and coworkers have implemented a relatively new strategy to make white light emitting materials by using a blue emissive MOF (ZJU-28) and two organic dyes 4-(*p*-dimethylaminostyryl)-1-methylpyridinium and acriflavine with red and green emission, respectively (Fig. 8.7A). Suitable composition of the respective dye molecules inside the framework has resulted in white light emission with CIE coordinates of (0.34, 0.32) and a color-rendering index value of 91 (Fig. 8.7A). These reports show also that guest molecules inside the porous architecture of MOFs can play a huge role in determining the luminescent properties of the host systems.

8.3 Recognition of nitrated high energy materials by metal-organic frameworks

MOFs have emerged as promising candidates for sensing applications in recent years owing to the suitable host–guest interaction, tunable pore surface, etc. In addition, the high luminescent properties and the possibility of facile incorporation of targeted functional groups made MOFs one of the frontrunners for the fabrication of sensory materials. MOFs have found applications in the detection of NACs and related HEMs. In the literature, the recognition of NACs has been carried out in

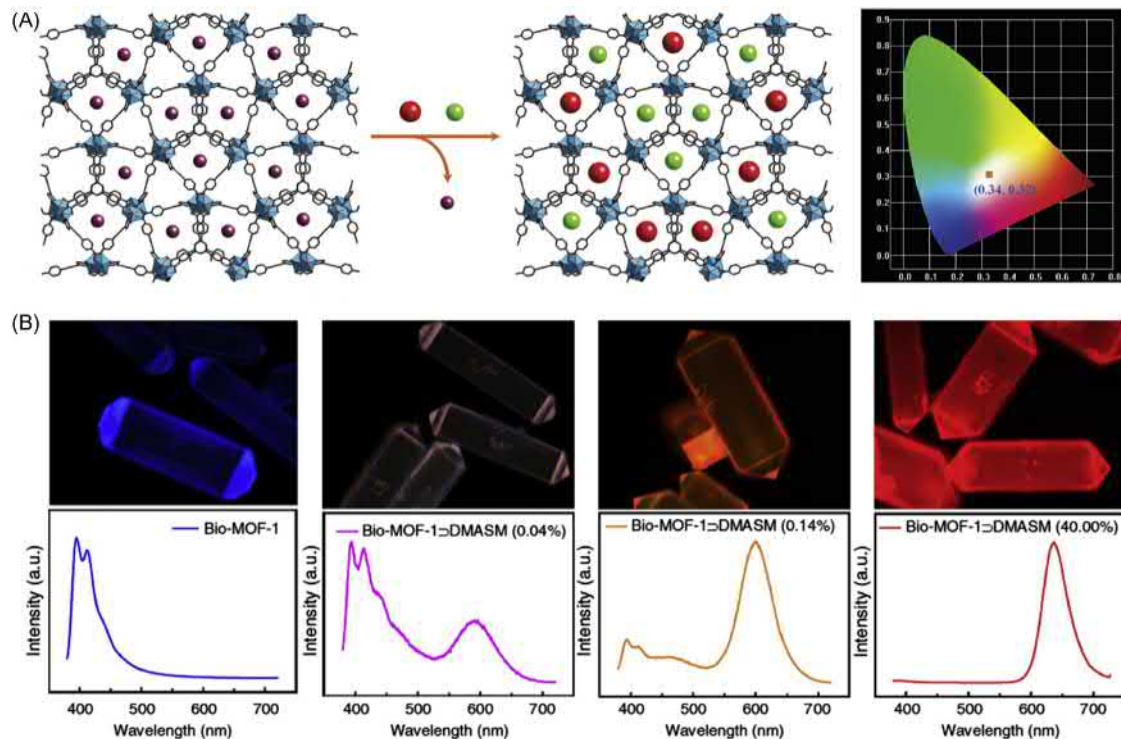


Figure 8.7 (A) Schematic representation of cationic dye encapsulation in ZJU-28 (left) and CIE 1931 chromaticity diagram of the dye encapsulated ZJU-28 \supset DSM/AF upon excitation at 365 nm (right). (B) Fluorescence microscopic images and corresponding emission spectra of different amount of DMASM dye-loaded bio-MOF-1 \supset DMASM, (from left to right 0%, 0.04%, 0.14% and 40.00%).

Source: For (A) reproduced with permission from Y. Cui, T. Song, J. Yu, Y. Yang, Z. Wang, G. Qian, Dye encapsulated metal-organic framework for warm-white LED with high color-rendering index, *Adv. Funct. Mater.* 25 (2015) 4796–4802. Copyright (2015) John Wiley & Sons. For (B) reported with permission from J. Yu, Y. Cui, H. Xu, Y. Yang, Z. Wang, B., Chen, et al., Confinement of pyridinium hemicyanine dye within an anionic metal-organic framework for two-photon-pumped lasing, *Nat. Commun.* (2013) DOI: 10.1038/ncomms3719. Copyright (2013) Springer Nature.

different media, for example, in vapor phase, in various organic solvents, and most importantly in aqueous medium.

8.3.1 Recognition of nitro-aromatic compounds in vapor phase

The tunable porous architecture of MOFs has resulted in the exploration of them in various types of host–guest chemistry. Such host–guest chemistry between the pore surface of MOFs and vapor of various toxic compounds (VOCs, explosive-related compounds, etc.) or harmful gases can lead to the generation of signals which can further result in the recognition of the targeted analytes. In this regard, LMOFs have been employed for the vapor phase sensing of explosive or explosive-related NACs-based on luminescence changes. Detection of NACs with MOF was first demonstrated by Jing Li and coworkers [65]. A luminescent Zn (II)-based MOF $[\text{Zn}_2(\text{bpdc})_2(\text{bpee})\cdot 2\text{DMF}]$; (bpdc: 4,4'-biphenyldicarboxylate; bpee: 1,2-bipyridylethene; DMF: *N,N'*-dimethylformamide) was synthesized strategically to explore sensing applications (Fig. 8.8A and B). The removal of DMF molecules from rectangular one-dimensional (1D) channels has led to guest free MOF, which was found to be highly luminescent due to the presence of π -conjugated ligands, with a pore size distribution of 7.5 Å. Moreover, the thin layer of guest free MOF was employed for the detection of one nitro-aromatic compound, namely 2,4-dinitrotoluene (DNT) and one nitro-aliphatic compound, namely 2,3-dimethyl-2,3-dinitrobutane (DMNB) by exposing the compound in equilibrated vapors of respective analytes. MOF thin layer showed fluorescence quenching within 10 seconds on exposure to nitro-compounds to the extent of 85% and 84% for DNT and DMNB, respectively. The MOF material was found to be reversible for this sensing application and regeneration of the fluorescent MOF was carried out by heating at 150°C for 1 minute.

In another report by the same research group, a fluorescent 3D Zn(II)-based MOF $[\text{Zn}_2(\text{oba})_2(\text{bpy})\cdot \text{DMA}]$; (where, H_2oba : 4,4'-oxybis(benzoic acid), bpy: 4,4'-bipyridine, DMA: *N,N'*-dimethylacetamide) was synthesized with 1D open channels [66]. The 1D channels were occupied with DMA molecules which were removed further by heating at 160°C. When a thin layer of the guest free MOF was exposed to different types of nitro-derivatives (nitrobenzene, *m*-dinitrobenzene (*m*-DNB), nitrotoluene (NT), *p*-dinitrobenzene (*p*-DNB), DNT, DMNB), it was found that the quenching efficiency followed the order: $\text{NB} > m\text{-DNB} > \text{NT} \approx p\text{-DNB} > \text{DNT}$ (Fig. 8.8B and C). Further investigation regarding differences in quenching efficiency revealed that both electron density and vapor pressure of respective analytes were directly related with the observed result. In contrast to the former example, here DMNB showed almost negligible change in the fluorescence property of the MOF. The reason behind this observation has been listed as: (1) nonplanar DMNB molecules were large enough for the pores of MOF (unlike for planar nitrobenzene); (2) weak orbital overlap between MOF and DMNB (mostly observed for nitro-aliphatic compounds); and (3) most importantly, similar reduction potential of both MOF and DMNB which prohibited the electron transfer process. This report demonstrated MOF materials can be employed for selective

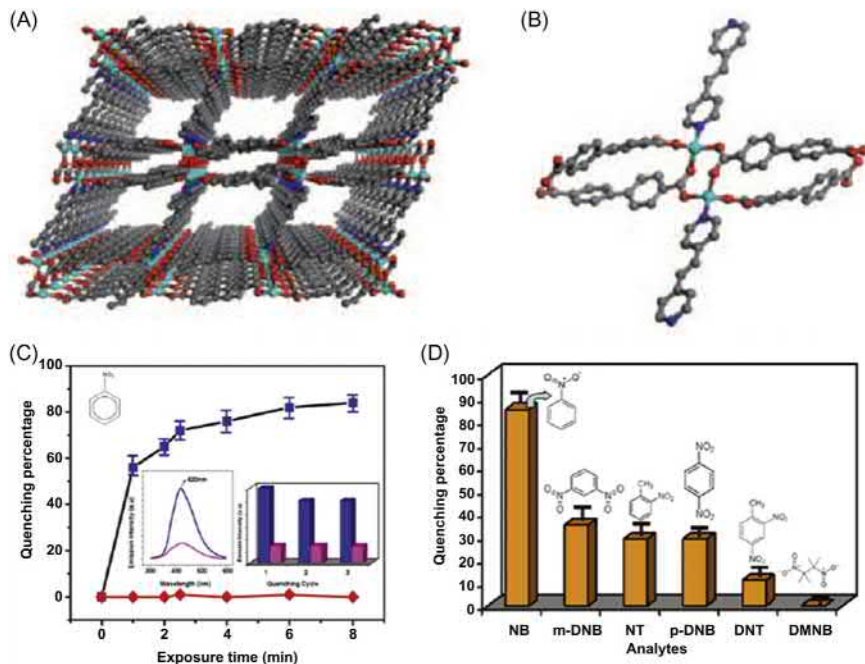


Figure 8.8 (A) Perspective view along *b* axis, and (B) SBU and coordination environment around Zn(II) in $[\text{Zn}_2(\text{bpdc})_2\text{-(bpee)}]\cdot 2\text{DMF}$. (C) Fluorescence quenching with time in presence of nitrobenzene (blue) and DMNB (red), and (D) quenching efficiency of different nitro-analytes after 15 min with $[\text{Zn}_2(\text{oba})_2(\text{bpy})]\cdot 3\text{DMA}$ MOF.

Source: For (A) reproduced with permission from A. Lan, K. Li, H. Wu, D.H. Olson, T.J. Emge, W. Ki, et al., Metal-organic framework for the fast and reversible detection of high explosives, *Angew. Chem. Int. Ed.* 48 (2009) 2334–2338. Copyright (2009) John Wiley & Sons. For (B) reported with permission from S. Pramanik, C. Zheng, X. Zhang, T.J. Emge, J. Li, New microporous metal-organic framework demonstrating unique selectivity for detection of high explosives and aromatic compounds, *J. Am. Chem. Soc.* 133 (2011) 4153–4155. Copyright (2011) American Chemical Society.

detection of explosive compounds and moreover, the emission profile of MOFs can be quenched or enhanced in the presence of electron-deficient or electron-rich analytes, respectively. In addition, Li's group further studied such differences in the extent of quenching in emission profiles of MOFs upon exposure to vapor of different analytes with the help of theoretical calculations and electrochemical measurements [67]. In this report, four MOFs have been synthesized based on Zn(II)-metal ion, 4,4'-biphenyldicarboxylic acid and different coligands [RPM1-Zn ($\text{Zn}_3(\text{bpdc})_3(\text{bpy})\cdot 4\text{DMF}\cdot \text{H}_2\text{O}$); RPM7-Zn ($\text{Zn}_3(\text{bpdc})_3(2,2'\text{-dmbpy})\cdot 4\text{DMF}\cdot \text{H}_2\text{O}$); RPM4-Zn ($\text{Zn}_2(\text{bpdc})_2(\text{bpe})\cdot 2\text{DMF}$) and RPM5-Zn ($\text{Zn}(\text{bpdc})(\text{bpe})\cdot \text{DMF}$); (bpy: 4,4'-bipyridine, 2,2'-dmbpy: 2,2'-dimethyl-4,4'-bipyridine, bpe: 1,2-bis(4-pyridyl) ethane)]. RPM1-Zn showed 85% quenching for the nitrobenzene and it was found to be selective over other nitro-analytes like *p*-DNB, DNT and nitrotoluene (NT)

(Fig. 8.9A and B). The reduction potentials (E_{red}) of MOFs were found to be smaller than the nitro-analytes and also LUMO of respective analytes are comparatively low lying as compared to the conduction-band minimum energies of the MOFs. As a consequence of this, upon excitation electrons from the conduction band of MOFs transferred to the LUMO of the nitro-analytes which resulted in the quenching phenomenon.

Furthermore, Ghosh and coworkers demonstrated a luminescent 2D π -stacked Zn(II)-MOF $[Zn_{1.5}(L)(H_2O)] \cdot 1.5\text{benzene}$; L: 4,4',4''-(benzene-1,3,5-triyltris(oxy)tribenzoic acid) based vapor phase sensing of nitro-explosive materials [68]. Guest benzene molecules were entrapped inside and found to have π - π interaction with

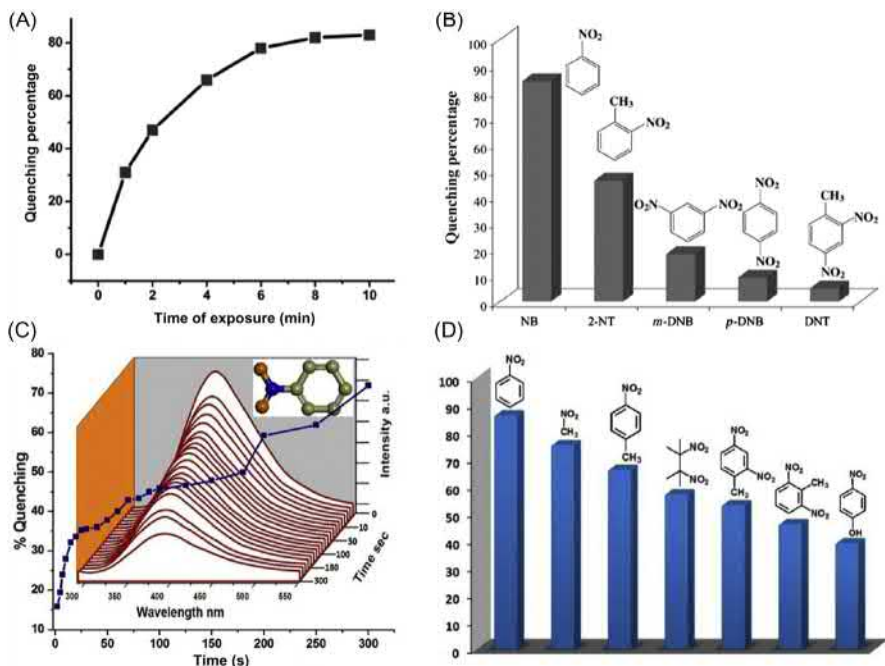


Figure 8.9 (A) Fluorescence quenching at different time intervals in presence of nitrobenzene, and (B) quenching percentage in presence of different nitro-analytes with thin film of $Zn_3(\text{bpdca})_3(\text{bpy})$ MOF. (C) Quenching profile of desolvated MOF in presence of nitrobenzene. (D) Quenching effect of different nitro-analytes with desolvated MOF in 10 min.

Source: For (A) reproduced with permission from S. Pramanik, Z. Hu, X. Zhang, C. Zheng, S. Kelly, J. Li, A systematic study of fluorescence-based detection of nitroexplosives and other aromatics in the vapor phase by microporous metal-organic frameworks, *Chem. Eur. J.* 19 (2013) 15964–15971. Copyright (2013) John Wiley & Sons. For (B) reported with permission from A.K. Chaudhari, S.S. Nagarkar, B. Joarder, S.K. Ghosh, A continuous π -stacked starfish array of two-dimensional luminescent MOF for detection of nitro explosives, *Cryst. Growth Des.* 13 (2013) 3716 – 3721. Copyright (2013) American Chemical Society.

the framework, which was further removed by gentle heating under vacuum. A thin layer of the guest free MOF was subjected to time-dependent fluorescence study after exposure to the various nitro-analytes. MOF thin layer showed significant signal change in the presence of both nitro-aromatic (NB) and nitro-aliphatic (nitromethane) compounds (Fig. 8.9D). Almost 57% quenching was observed even in the case of another aliphatic nitro-compound (which are relatively difficult to detect) DMNB (Fig. 8.9C). In another study, Liu et al. performed sensing of nitro-aromatic vapors with a blue emissive Zn(II)-MOF [Zn₂(TCPPE); where, TCPPE: tetrakis[4-(4-carboxyphenyl)phenyl]ethene] [69]. This pale-yellow colored 3D MOF consisted of 1D channels with pore dimensions of 11.4 × 9.8 Å². The emission peak at 461 nm of as-synthesized MOF was found to be red-shifted (535 nm) upon desolvation, due to the better intermolecular electronic coupling in the absence of guest solvent molecules. Effective quenching of the peak at 535 nm was observed when the activated MOF was exposed to nitrobenzene and 2,4-DNT. Hitherto, we have discussed vapor phase sensing of nitro-analytes with MOFs derived from Zn(II) metal ion. Apart from this, Zr(IV)-ion has also been explored in order to develop MOFs with high stability and in a recent report Li and coworkers showed VOCs sensing, including nitro-explosives like NB, 2-NT, 2,4-DNT, nitromethane, nitroethane, and nitropropane, with a fluorescent Zr-carboxylate MOF [Zr₆(sdba)₄(μ₃-O)₄(μ₃-OH)₄(HCOO)₂(OH)₂(H₂O)₂; sdba: 4,4'-sulfonyldibenzoate] [70]. In another report by Parkin and coworkers, the role of framework architecture of MOFs in the sensing of nitro-compounds has been demonstrated well by using a porous MOF and another MOF with much less porosity, synthesized with the same linker [71]. In this regard, two MOFs [Zn(dcbpy)(DMF)]•DMF and Dy(dcbpy)(DMF)₂(NO₃); dcbpy: 2,2'-bipyridine-4,4'-dicarboxylate with similar shape and size have been synthesized via the solvothermal procedure as well as with the microwave synthesis method. The Zn-MOF was found to have 1D channels with dimension of 10 × 8.8 Å², on the other hand minimal porosity was found for the Dy-MOF. Effective quenching in the fluorescence emission of Zn-MOF was observed for all the nitro-analytes (DMNB, NB, *p*-NT, and 2,4-DNT) used in this study. In contrast to the Zn-MOF, it was evidenced that only smaller NACs (NB and *p*-NT) were able to quench the emission of Dy-MOF selectively. Selectivity for NB and *p*-NT in the case of Dy-MOF has been raised by the minimal porosity of the framework; whereas porous Zn-MOF showed signal change for every analyte since it was porous enough to accommodate other analytes too. In addition, when Zn-MOF has been synthesized with a microwave-assisted technique, the time required for synthesis reduced from days to a few minutes. Owing to the homogeneous size and shape of the microcrystals of Zn-MOF synthesized with the microwave method, high sensitivity was observed toward the targeted analytes as compared to Zn-MOF synthesized solvothermally. Moreover, Li et al. have employed metal-organic framework nanotube (MOFNT) for the reversible detection of NACs in vapor phase [72]. The Cd(II) ion-based MOF nanotubes were prepared using the self-sacrificing strategy via ultrasound irradiation. MOFNT showed significant quenching of the emission peak at 406 nm in the presence of several NACs like NB, 2-NT, 2,4-DNT, and 4-NT. In the case of 2,4-DNT,

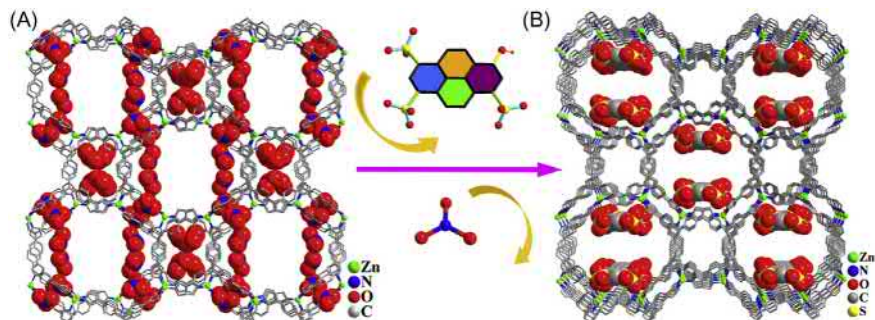


Figure 8.10 (A) Three-dimensional FIR-53 MOF, and (B) three-dimensional dye-loaded MOF, viz., SG7@FIR-53.

Source: For (A) and (B) reported with permission from H.-R. Fu, X.-X. Wu, L.-F. Ma, F. Wang, J. Zhang, Dual-emission SG7@MOF sensor via SC – SC transformation: enhancing the formation of excimer emission and the range and sensitivity of detection, *ACS Appl. Mater. Interfaces* 10 (2018) 18012 – 18020. Copyright (2018) American Chemical Society.

MOFNT was found to be reversible even after ten cycles of experiments. Such MOF nanotubes-based rapid and reversible sensing can be useful for the fabrication of various nanodevices. Furthermore, strategic incorporation of guest molecules into a MOF for detection of NACs was demonstrated by Fu et al. in a recent report [73]. 8-hydroxypyrene-1,3,6-trisulfonate (SG7) dye was incorporated in a MOF, namely FIR-53, and this composite material showed efficient sensing of nitro-aromatics in vapor phase (Fig. 8.10A and B). Apart from these aforementioned examples, vapor phase detection of nitro-explosive compounds have also been found with a few more LMOFs in the literature [8,11,13,74–76].

8.3.2 Detection of nitro-aromatic compounds by metal-organic frameworks in common organic solvents

Apart from vapor phase detection of NACs, sensing of those analytes in a solution medium has also emerged in the last few years. Various solvents like dimethyl formamide (DMF), ethanol, dimethyl acetamide (DMA), and acetonitrile (MeCN) have been utilized as media for sensing purposes. In this section, the sensing of NACs in various organic medium is discussed with suitable representative examples. An earlier report by Mukherjee and coworkers demonstrated detection of NACs with a Zn-MOF $[\{Zn_4O(L)_2 \cdot (H_2O)_3\} \cdot 3DMA \cdot 3EtOH \cdot 6H_2O]$; where H_3L : 5-(4-carboxyphenylethynyl)isophthalic acid] in ethanol medium [77]. Three-dimensional Zn-MOF was synthesized via the solvothermal method and consisted of $14.2 \times 13.5 \text{ \AA}^2$ one-dimensional pores. MOF showed blue emission at 420 nm (upon excitation at 305 nm) which was found to get quenched upon addition of nitro-aromatic analytes. Among all the NACs used in this work, TNT showed maximum quenching efficiency and furthermore the compound was recycled for up to five cycles. In another study by Qian and coworkers, nanoscale lanthanide MOF

[Eu₂(BDC)₃(H₂O)₂•(H₂O)₂; where, BDC: benzene-1,4-dicarboxylate] was synthesized with microemulsion strategy and later employed for the detection of NACs in ethanol medium [78]. In ethanol medium MOF showed three emission peaks at 590, 617, and 698 nm which correspond to the electronic transition of ⁵D₀→⁷F₁, ⁵D₀→⁷F₂, and ⁵D₀→⁷F₄, respectively. Luminescence studies revealed that NACs derived from toluene (TNT and 2,4-DNT) showed maximum quenching efficiency among other aromatic analytes. Another lanthanide MOF [{Tb(TTCA)(DMA)(H₂O)}•7DMA•9.5H₂O; where TTCA: triphenylene-2,6,10-tricarboxylate, DMA: *N,N*-dimethyl acetamide] by Lu and coworkers was reported for the detection of nitro-analytes in 2013 [79]. This 3D MOF was found to have a 1D channel along the *c*-axis with a diameter of 8 × 14 Å² and upon excitation of the MOF at 370 nm, four emission peaks were observed at 490, 546, 585, and 624 nm which were attributed to ⁵D₄→⁷F₆, ⁵D₄→⁷F₅, ⁵D₄→⁷F₄, and ⁵D₄→⁷F₃, respectively. Quenching of those emission peaks was observed for different NACs like TNT, TNP, NB, 2,4-DNT, and 2,6-DNT and was found to be selective over aromatic compounds.

Apart from sensitive detection of NACs in solution medium, selectivity is another aspect to look for in such sensing applications. Ghosh and coworkers demonstrated selective and sensitive recognition of nitrophenol derivatives (especially, TNP) over other NACs in acetonitrile medium [25]. A 3D luminescent Cd-MOF was synthesized with the formula of [{Cd(NDC)_{0.5}(PCA)}•G_x; where, NDC: 2,6-naphthalenedicarboxylate, PCA: 4-pyridinecarboxylate and G: guest molecules], and a 1D channel of 9.48 × 7.83 Å² diameter (Fig. 8.11A and B). A sensing study of NACs with Cd-MOF in MeCN medium revealed that the MOF was highly selective for TNP over other nitro-analytes like NB, TNT, DMNB, 2,4-DNT, 2,6-DNT, and RDX (Fig. 8.11C and D). The Stern–Volmer constant (*K_{sv}*) for the quenching was found to be 3.5 × 10⁴ M⁻¹ with TNP. Strong spectral overlap (excitation spectra of analytes and emission of MOF) between TNP and MOF indicated the fluorescence quenching mechanism was attributed to resonance energy transfer (RET). Along with the RET, electrostatic interaction between the TNP and pyridyl site of the PCA ligand was attributed to the selectivity of the probe. Selective sensing of TNP was also reported by Zheng and coworkers, where two luminescent Zn-MOFs, namely MOF-1 and MOF-2 with the formula of Zn₂(L)₂(dpyb) and Zn(L)(dipb)•(H₂O)₂ [where, H₂L: 3,3'-(thiophene-2,5-diyl)dibenzoic acid; dpyb: 1,4-di(pyridin-4-yl)benzene; dipb: 4,4'-di(1H-imidazol-1-yl)-1,1'-biphenyl], respectively, were synthesized for sensing purposes [80]. Upon excitation at 382 nm, dispersed phase (in DMA) of MOF-1 and MOF-2 showed emission at 533 nm and 523 nm, respectively, and the origin of the emission was speculated to be intraligand fluorescence from the aforementioned H₂L ligand. Both MOF-1 and MOF-2 showed selective detection of TNP with high sensitivity and it was found that both the MOFs could sense TNP at very low concentration of 2.5 μM. In addition, the Stern–Volmer constants (*K_{sv}*) for the quenching of fluorescence of MOF-1 and MOF-2 with TNP were found to be very high, 2.4 × 10⁴ M⁻¹ and 2.46 × 10⁴ M⁻¹, respectively. Furthermore, Ning and coworkers reported a Cd-MOF [{Cd₂(PAM)₂(dpe)₂(H₂O)₂}•0.5(dpe); where, H₂PAM: 4,4'-methylenebis(3-hydroxy-2-naphthalenecarboxylic acid), dpe: 1,2-di(4-pyridyl)ethylene] based sensing of TNP in DMSO medium

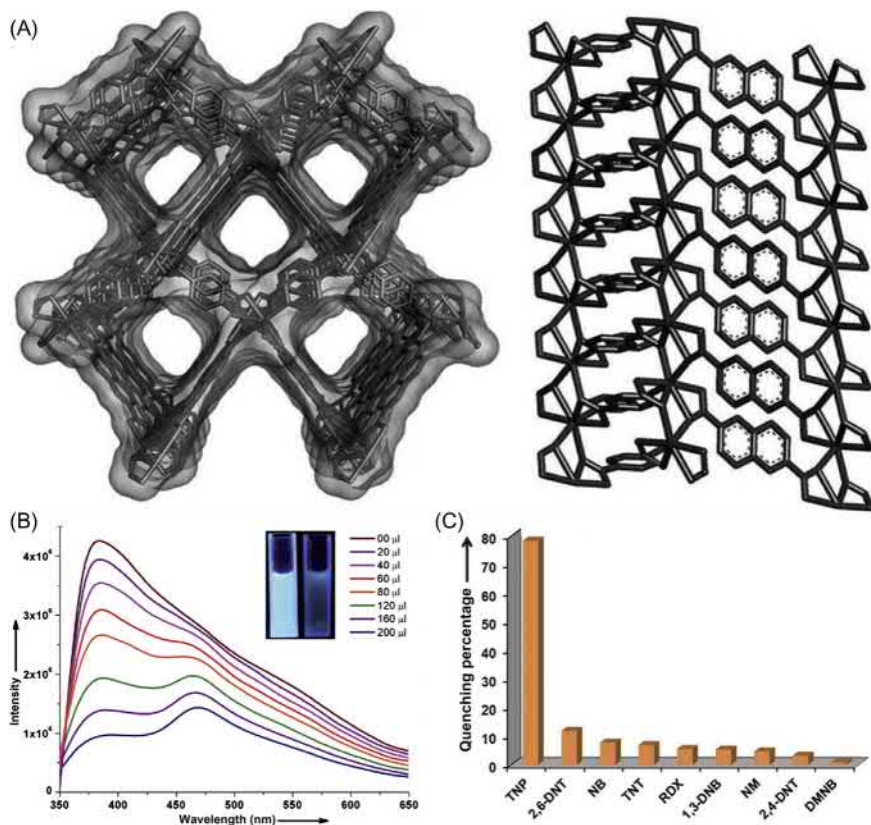


Figure 8.11 (A) Three-dimensional porous view of Cd(NDC)_{0.5}(PCA) MOF along *c*-axis (left) and one-dimensional channel with naphthalene moieties along *b* axis (guest molecules and hydrogen atoms were omitted for clarity). (B) Fluorescence quenching of the MOF dispersed in acetonitrile with incremental addition of TNP (inset photographs represents quenching of blue emission of MOF). (C) Bar diagram for quenching efficiency of different nitro-analytes with MOF.

Source: Reproduced with permission from S.S. Nagarkar, B. Joarder, A.K. Chaudhari, S. Mukherjee, S.K. Ghosh, Highly selective detection of nitro explosives by a luminescent metal-organic framework. *Angew. Chem. Int. Ed.* 52 (2013) 2881–2885. Copyright (2013) John Wiley & Sons.

[81]. This Cd-MOF showed a green emission at 502 nm (upon excitation at 371 nm) in DMSO medium and upon incremental addition of TNP the fluorescence intensity of MOF got quenched, ~98.4% of quenching was observed with 11.5 ppm TNP. This MOF was found to be selective toward TNP over the other nitro-analytes like 4-NP, 2,6-DNT, 2,4-DNT, NB, and 1,3-DNB.

Bharadwaj and coworkers reported one Tb-MOF with the formula of [Tb(L)(DMA)]•(DMA)•(0.5H₂O) (where, H₃L: 3'-hydroxybiphenyl-3,4',5-tricarboxylic acid), for the selective detection of TNP in DMF medium [82]. Additionally, it has

been observed selectivity has been achieved by researchers upon strategic incorporation of basic sites, such as different type of amines (primary, secondary, or tertiary). In this regard, the same research group demonstrated another example of selective sensing of TNP with an amine-functionalized MOF, $[\{Cd_4(L)_2(L_2)_3(H_2O)_2(8DMF)(8H_2O)\}_n]$, where, H_4L : 1,1':3',1''-Terphenyl-4,4',4'',6'-tetracarboxylic acid, L_2 : 3-amino-4,4'-bipyridine [83]. Upon excitation at 334 nm, MOF showed an emission at 457 nm and, furthermore, incremental addition of TNP to the MOF dispersed in ethanol revealed quenching of the emission peak. The MOF was found to be highly selective for TNP and the Stern–Volmer constant for this quenching was found to be $3.89 \times 10^4 M^{-1}$. In another report by Hong et al., the role of amine functionality was also demonstrated where both secondary and primary amine was employed [84]. Two Cd-MOFs with formulas of $\{[Cd_4(hbhdpy)_2(bdc)_3(DMA)_2] \cdot (H_2O)_4\}_n$ and $\{[Cd_4(hbhdpy)_2(bdc-NH_2)_3(DMA)_2] \cdot (H_2O)_4\}_n$ (where, hbhdpy: 4-(2-hydroxy-3-methoxy-benzylidenehydrazinocarbonyl)-*N*-pyridin-4-yl-benzamide, H_2bdc : 1,4-dicarboxybenzene, $H_2bdc-NH_2$: 2-amino-1,4-dicarboxybenzene and DMA: *N,N*-dimethyl acetamide) were synthesized via the solvothermal method. The former compound with secondary amine groups showed 81.7% quenching in the presence of TNP, whereas other MOFs with both primary and secondary amine groups showed 89.1% quenching in DMA. The quenching constants for both the MOFs were found to be 2.5×10^4 and $4.8 \times 10^4 M^{-1}$, respectively. Furthermore, Jiang and coworkers reported a luminescent Zn-MOF, namely USTC-7, with a formula of $Zn_2(TZBPDC)(\mu_3-OH)(H_2O)_2$ (where, $H_3TZBPDC$: 4'-(1*H*-tetrazol-5-yl)-[1,1'-biphenyl]-3,5-dicarboxylic acid) [85]. The 3D MOF was found to be stable in boiling solvents like ethyl acetate, ethanol, toluene, and hexane, along with pH 2–12 range in aqueous medium. Again, the MOF showed two strong emission peaks at 408 and 432 nm in $CHCl_3$ medium upon excitation at 370 nm. With incremental concentration of TNP, both the emission peaks of USTC-7 were found to be quenched, while only 20 μ L of the analyte showed 16.6% quenching. USTC-7 was found to be selective for TNP over other nitro-analytes such as 2,4-dinitrotoluene, 2,6-dinitrotoluene, 2,4,6-trinitrotoluene, nitrobenzene, and *m*-dinitrobenzene, which was accounted for as the interaction between nitrogen atoms in the ligand and TNP molecules. Quenching constants (K_{sv}) for the USTC-7 and TNP detection limit for this study were found to be $4.9 \times 10^4 M^{-1}$ and 2.78×10^{-4} mM, respectively. In another report by Qi et al., naked eye sensing of nitro-analyte along with luminescence change was demonstrated with a blue light emissive MOF with a formula of $[Li]_4[Cd_3Li_2(BDC)_6]$ (where, BDC: terephthalic acid) (Fig. 8.12A) [86]. In this report, with the 3D MOF, dual sensing of trinitrobenzene (TNB) and fluorescence-based selective sensing of TNP were performed. In the presence of TNB molecules MOF showed a drastic color change from colorless to pink as well as an enhancement in emissions at 557 and 598 nm which might be attributed to the charge transfer between TNB and MOF. Further, in the presence of TNP, MOF showed quenching of the emission peak at 438 nm selectively with a quenching constant of $7 \times 10^4 M^{-1}$.

Furthermore, not only linkers of the MOF materials, but also guest molecules inside the frameworks have found their suitable role in sensing applications. In a

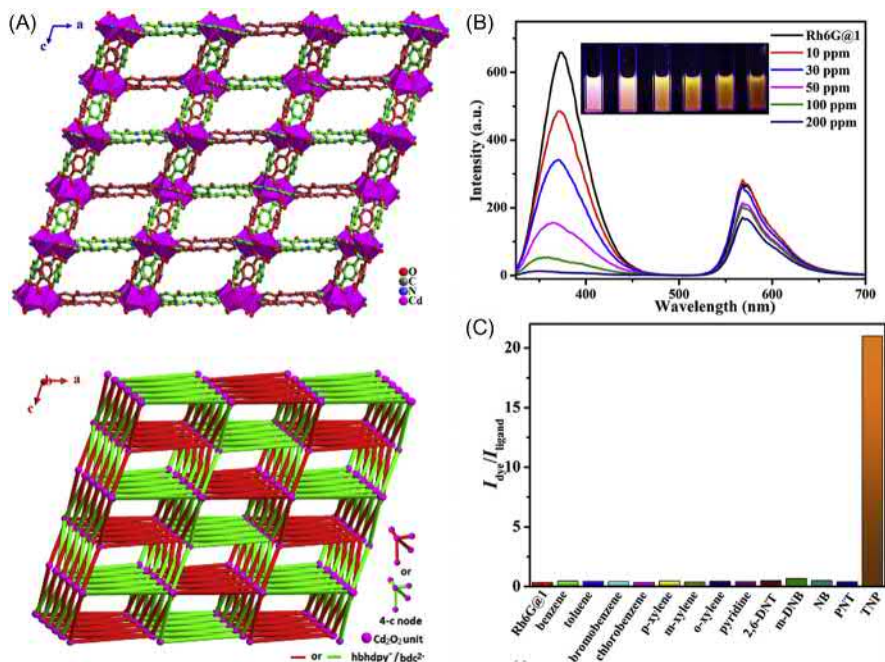


Figure 8.12 (A) Ball-and-stick model (top) and topological configuration with two same 6^6 frameworks (bottom) of the three-dimensional twofold interpenetrated framework along b axis. (B) Fluorescence quenching for dye encapsulated MOF at different concentrations of TNP (inset: color changes for dye@MOF at different TNP concentration). (C) Peak-height ratio of dye to ligand upon addition of 200 ppm of different analytes.

Source: For (A) reported with permission from X.-J. Hong, Q. Wei, Y.-P. Cai, S.-R. Zheng, Y. Yu, Y.-Z. Fan, et al., 2-Fold interpenetrating bifunctional Cd-metal – organic frameworks: highly selective adsorption for CO₂ and sensitive luminescent sensing of nitro aromatic 2,4,6-trinitrophenol, *ACS Appl. Mater. Interfaces* 9 (2017) 4701–4708. Copyright (2017) American Chemical Society. For (B) and (C) reported with permission from D.-M. Chen, N.-N. Zhang, C.-S. Liu, M. Du, Dual-emitting dye@MOF composite as a self-calibrating sensor for 2,4,6-trinitrophenol, *ACS Appl. Mater. Interfaces* 9 (2017) 24671 – 24677. Copyright (2017) American Chemical Society.

report by Bagheri et al., selective detection of TNP was demonstrated with Rhodamine B loaded TMU-5 MOF (TMU: Tarbiat Modares University) with a formula of $[Zn(oba)(4-bpdh)_{0.5}]_n \cdot 1.5DMF$ (where, H₂oba: 4,4-oxybisbenzoic acid; 4-bpdh: 2,5-bis(4-pyridyl)-3,4-diaza-2,4-hexadiene) (Fig. 8.13) [88]. It was observed that dye-loaded MOF showed more efficient selective sensing behavior for TNP as compared to the parent MOF. The quenching constant for the MOF was found to be $1.3 \times 10^5 M^{-1}$, which was one of the highest values among MOF-based TNP sensors in an organic medium. In another report by Liu, Du, and coworkers, rhodamine 6G was incorporated via the “bottle around ship” method in an anionic MOF $[\{ (NH_2Me_2)[Zn_3(\mu_3-OH)(tpt)(TZB)_3](DMF)_{12} \}_n]$; tpt: 2,4,6-tri(4-pyridyl)-1,3,5-triazine, H₂TZB: 4-(1H-tetrazol-5-yl)benzoic acid] to fabricate a luminescent probe

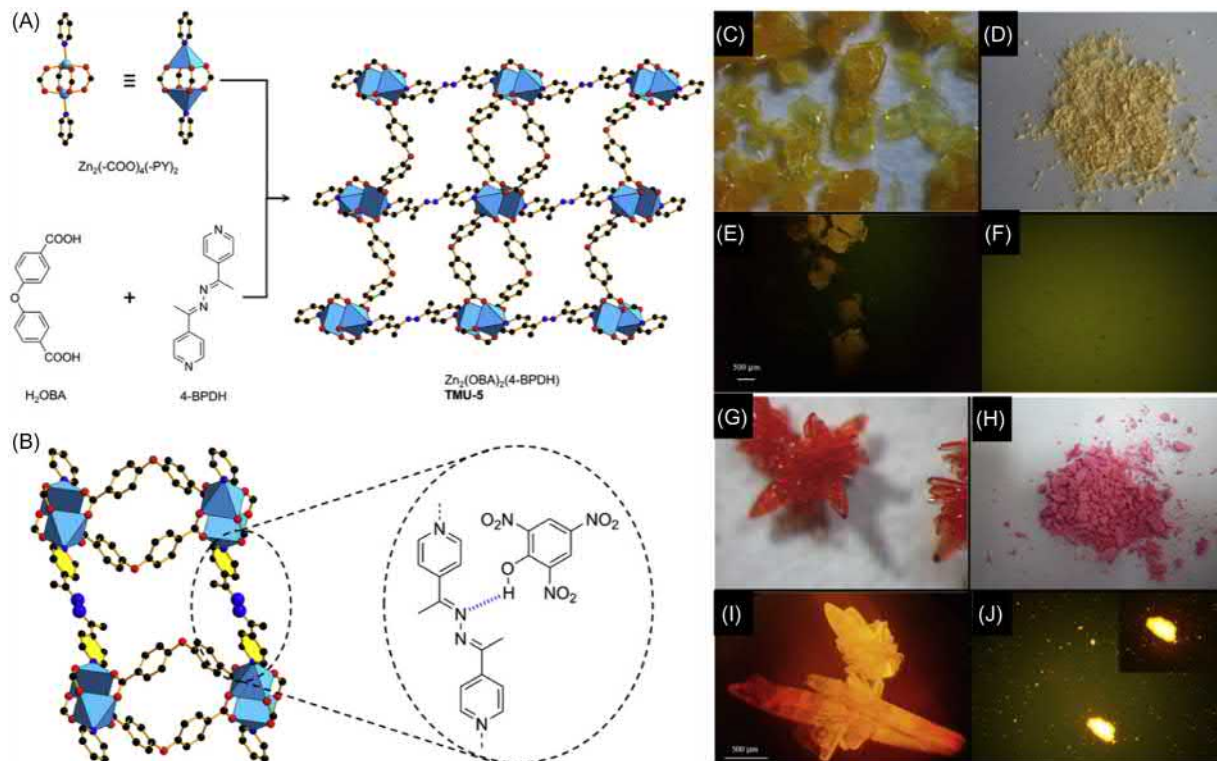


Figure 8.13 (A) Single crystal structure of TMU-5 with azine-functionalized pores. (B) Interaction between TNP molecule and azine-functionality; (C) single crystal of TMU-5; (D) powder of TMU-5; (G) single crystal of TMU-5S (RhB@TMU-5) and (H) powder of TMU-5S (RhB@TMU-5) under ambient light; (E) single crystal of TMU-5; (F) powder sample of TMU-5; (I) single crystal of TMU-5S; and (J) powder sample of TMU-5S under UV-irradiation.

Source: Reproduced with permission from X.-X. Jia, R.-X. Yao, F.-Q. Zhang, X.-M. Zhang, A fluorescent anionic MOF with Zn₄(trz)₂ chain for highly selective visual sensing of contaminants: Cr(III) ion and TNP, *Inorg. Chem.* 56 (2017) 2690 – 2696. Copyright (2016) American Chemical Society.

for selective and sensitive detection of TNP [87]. MOF showed dual emissions at 373 nm (weak) and 570 nm (strong) in DMF upon excitation at 320 nm, which originated from the respective linker and incorporated dye molecule, respectively. Upon addition of 200 ppm of TNP, composite material showed 42-fold increase in the relative ratio of those two emission intensities (Fig. 8.13B and C). Thus sensing in this work based on emission peak intensities ratios represented a self-calibrating sensory probe. Apart from these reports, many other reports based on MOF for sensing of NACs in an organic medium have been demonstrated in the literature [8,10–15,89–91].

8.3.3 Sensing of nitro-aromatic compounds with metal-organic frameworks in water medium

Sensing of nitro-analytes in water medium has become of paramount interest because of increasing terrorism activities from marines and lands which has led to contamination in soil, groundwater, etc. But poor hydrolytic stability of most of the MOFs and low solubility of organic nitro-analytes have made this job very challenging. In addition, picric acid (TNP) is found to be highly soluble in water in the picrate form which is accounted for as one of the major water pollutants along with TNT among the nitro-compounds. So, detection of such nitro-analytes in water medium is highly desirable for real-time applications.

Since the detection of nitro-analytes in aqueous phase is in demand for the real-time applications, Qin et al. have reported ionic liquid directed synthesis of [Tb(L)(OH)] \cdot x(solv) MOF (H₂L: 5-(4-carboxyphenyl)pyridine-2-carboxylate; solv: H₂O and DMF) for detection of NACs in aqueous medium [76]. When MOF was dispersed in an aqueous solution of respective nitro-analytes (NB, TNT, 2-NT, TNP, 2,4-DNT, 2,6-DNT, 1,4-DNB, 1,3-DNB), >70% quenching was observed in each cases. Especially, >99% quenching was obtained in the case of NB, TNP, TNT, and 2-NT. Further, selectivity is another important aspect in the case of sensing experiments for better applicability of the probe. In another study by the same group two lanthanide-based MOFs [Eu(BTB)H₂O and Tb(BTB)H₂O; H₃BTB: 1,3,5-benzenetrisbenzoic acid] have been synthesized via the ionic liquid directed method and further employed for the detection of NB, TNP, and 2-NT over other nitro-analytes [92]. All NB, TNP, and 2-NT showed 99% of luminescence quenching while other nitro-analytes showed <50% quenching. In both cases the mechanism for such quenching behavior has been attributed to PET from MOF particles to the electron-deficient nitro-analytes. Furthermore, detection of NB and 2,4-DNP in water have been studied with Zn₄(Hbvpv)₂(BTC)₃(HCOO)(H₂O)₂•4H₂O MOF (bvpv: 3,5-bis-(2-(pyridin-4-yl)vinyl)pyridine), by Lang and coworkers, upon excitation at 285 nm [93]. The limit of detection (LOD) of the MOF for 2,4-DNP was found to be 1.0×10^{-6} mol L⁻¹. The same group has reported another MOF [Cd(ppvppa)(1,4-NDC); ppvppa: N-(pyridin-2-yl)-N-(4-(2-(pyridin-4-yl)vinyl)phenyl)pyridin-2-amine, 1,4-H₂NDC = 1,4-naphthalenedicarboxylic acid] for detection of nitro-analytes in water medium and it was found to follow the trend: 2,4-DNP > 4-

NP > 4-nitroaniline > NB [94]. The MOF was found to be reversible even up to six cycle of experiments for 2,4-DNP.

The huge usage of TNP in various industries and its high water solubility, has made TNP one of the most hazardous water contaminants. Because of this TNP sensing in water medium has earned much attention in recent years. Ghosh and coworkers reported the first sensing of TNP in water medium with a stable MOF, namely, UiO-67@N ($Zr_6O_4(OH)_4(L)_6$; UiO: University of Oslo; H_2L : 2-phenylpyridine-5,4'-dicarboxylic acid) [95]. Guest free MOF was dispersed in water and then the emission profile at 438 nm was monitored upon excitation at 320 nm for all nitro-analytes. MOF was found to respond selectively for TNP over other analytes like TNT, 2,4-DNT, 2,6-DNT, 1,3-DNB, NB, RDX, DMNB, and NM (Fig. 8.14). This selectivity toward TNP has been attributed to the interaction between acidic TNP and the linker with a Lewis basic site (pyridyl moiety); as well as facile energy transfer between UiO-67@N and TNP molecules. It has been observed that quenching in the fluorescence of UiO-67@N can be obtained with TNP concentration as low as 2.6 μM . To check the quenching efficiency of the probe Stern–Volmer constant (K_{sv}) has been calculated and it was found to be $2.9 \times 10^4 M^{-1}$. Such selective and high quenching efficiency of UiO-67@N with TNP has been accounted for both electron and energy transfer between probe and analyte. Apart from pyridyl site, primary amine also can serve as a basic site for the selectivity toward TNP. In this regard, Ghosh and coworkers demonstrated the sensing of TNP in the water medium with stable and porous bio-MOF-1 ($[Zn_8(ad)_4(BPDC)_6O \cdot 2 Me_2NH_2] \cdot G$; G: DMF and water) (Fig. 8.15A) [96]. Due to the presence of pendant free $-NH_2$ groups, bio-MOF-1 showed a selective response for TNP over the other nitro-analytes (Fig. 8.15B and D). Higher quenching efficiency of the probe has been affirmed from the high K_{sv} value ($4.6 \times 10^4 M^{-1}$) in this study (Fig. 8.15C). Further, cocrystal of adenine and TNP has revealed the role of $-NH_2$ functionality in selectivity where H-bonding interaction has been found between the two molecules. In another report, the same research group demonstrated UiO-68@NH₂ ($Zr_6O_4(OH)_4(L)_6$; where, L: 2'-amino-[1,1':4',1''-terphenyl]-4,4''-dicarboxylate) based selective detection of TNP with a quenching constant of $5.8 \times 10^4 M^{-1}$ [97]. This UiO-68@NH₂ MOF is able to detect TNP in water with LOD of 0.4 ppm within a few seconds. Apart from aromatic amine moieties, aliphatic amine-functionality was also employed by Ghosh and coworkers to serve the purpose. In a recent report, urotropine-based Ur-MOF ($Zn_4(DMF)(Ur)_2(NDC)_4$; Ur: urotropine) was strategically designed to detect TNP selectively in water through aliphatic amine–TNP interactions [98]. Ur-MOF showed selective recognition of TNP with high quenching efficiency of $10.83 \times 10^4 M^{-1}$ and LOD of 1.63 ppm.

Furthermore, selective TNP sensing has been executed with a Tb-MOF with a formula of $Tb(L_1)1.5(H_2O) \cdot 3H_2O$ (L_1 : 2-(2-Acetoxy-propionylamino)-terephthalate) by Cao et al. [99]. The quenching of the emission peak at 541 nm has been observed upon incremental amounts of TNP. The quenching constant for this study was found to be $7.47 \times 10^4 M^{-1}$ and the mechanism has been attributed to energy transfer from linker to TNP which affected the “antenna effect” in Tb-MOF.

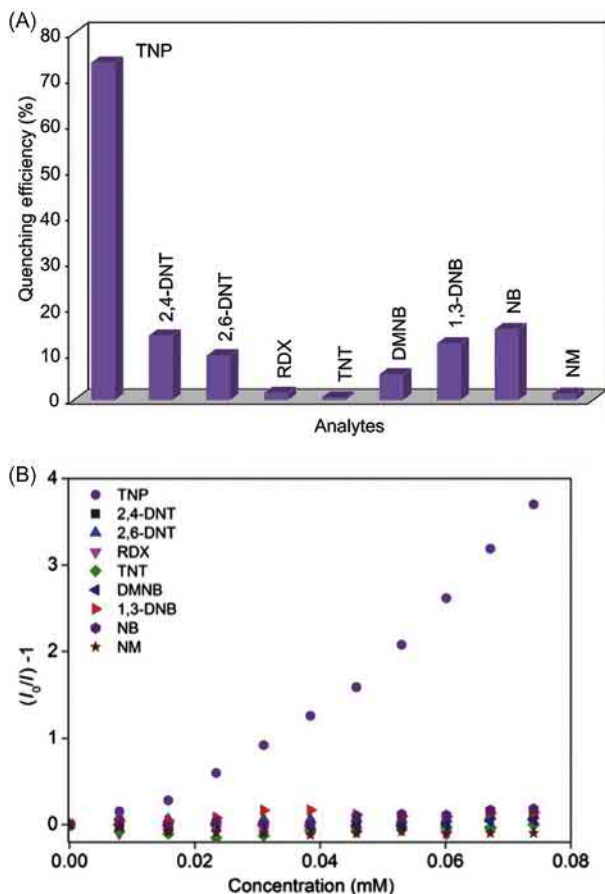


Figure 8.14 (A) Fluorescence quenching efficiency and (B) Stern–Volmer plot for different nitro-analytes with UiO-67@N.

Source: Reproduced with permission from S.S. Nagarkar, A.V. Desai, S.K. Ghosh, A fluorescent metal-organic framework for highly selective detection of nitro explosives in the aqueous phase, *Chem. Commun.* 50 (2014) 8915–8918. Copyright (2014) Royal Society of Chemistry.

Another lanthanide MOF ($[\text{Eu}_3(\text{bpydb})_3(\text{HCOO})(\mu\text{-3-OH})_2(\text{DMF})] \cdot (\text{DMF})_3(\text{H}_2\text{O})_2$; bpydb: 4,4'-(4,4'-bipyridine-2,6-diyl) dibenzoate) has been found to show rapid quenching in the presence of TNP in water and the quenching efficiency for nitro-analytes with the MOF followed the order: $\text{TNP}(\text{H}_2\text{O}) > \text{TNP}(\text{DMF}) > 4\text{-NP} > 3\text{-NP} > o\text{-NT} > m\text{-NT} \approx \text{NB} \approx \text{NM}$ [100]. In addition, Suresh and coworkers carried out detection of TNP in aqueous phase with two isostructural MOFs based on Zn (II) and Cd(II) metal ions $[\text{M}(\text{IPA})(\text{L})]$; $\text{M} = \text{Zn}$ and Cd , IPA: isophthalate; L: 3-pyridylcarboxaldehyde nicotinoylhydrazone [101]. Selective quenching of TNP has been observed with each MOF with K_{sv} of 2.16×10^4 and $1.52 \times 10^4 \text{ M}^{-1}$ for

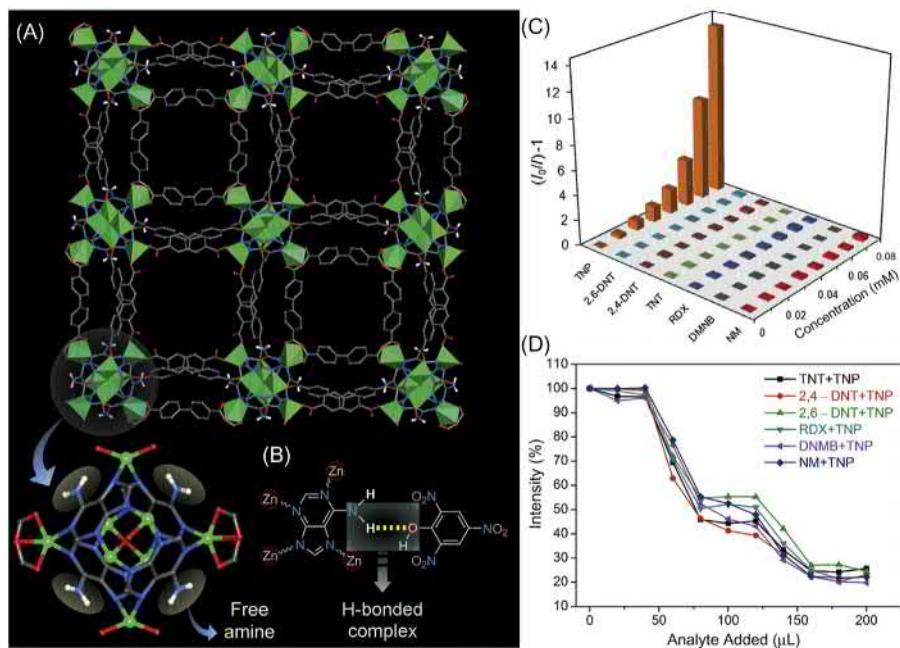


Figure 8.15 (A) Crystal structure of bio-MOF-1 along *c*-axis. (B) Representation of H-bonding interaction between TNP and adenine. (C) Quenching efficiency of bio-MOF-1 in presence of different nitro-analytes. (D) Fluorescence quenching of bio-MOF-1 with TNP in presence of other nitro-analytes.

Source: Reproduced with permission from B. Joarder, A.V. Desai, P. Samanta, S. Mukherjee, S.K. Ghosh, Selective and sensitive aqueous-phase detection of 2,4,6-trinitrophenol (TNP) by an amine-functionalized metal-organic framework, *Chem. Eur. J.* 21 (2015) 965–969. Copyright (2015) John Wiley & Sons.

Zn-MOF and Cd-MOF, respectively. The same group has further explored TNP sensing in water with a few other LMOFs [102,103]. In a recent report, Zn-MOF derived from a linker with Tröger's base has shown potential application for the sensing of phenolic-nitro-aromatics (TNP, 2,4-DNP and 4-NP) selectively [104]. Emission at 520 nm of Zn-MOF ($\text{ZnL} \cdot 2\text{H}_2\text{O} \cdot \text{DMF}$; L: bis-[*N*-(1,3-benzenedicarboxylic acid)]-9,18-methano-1,8-naphthalimide-[*b,f*] [1,5]diazocine) got quenched in the presence of phenolic-NACs with an excellent LOD of 26.3 ppb for TNP. Another report by Mandal and coworkers represented amine-functionalized Cd-MOF ($\text{Cd}(\text{ATAIA}) \cdot 4\text{H}_2\text{O}$; H_2ATAIA : 5-[(4,6-diamino-1,3,5-triazin-2-yl)amino-isophthalate]) where Cd-MOF has turned out to be a selective luminescent as well as a colorimetric sensor for TNP [105]. High quenching efficiency of the MOF has been affirmed by a K_{sv} value of $1.59 \times 10^7 \text{ M}^{-1}$ which has been ascribed as one of the most superior performances in the domain of MOFs. In addition, very low LOD (0.2 ppb) of the MOF can be well suited for the real-time applications. Another ppb-level detection of TNP in water with MOF has been demonstrated by Asha et al. [106]. This

MOF, $\text{Ca}(\text{NH}_2\text{BDC})(\text{DMF})$ [NH_2BDC : 2-amino-1,4-benzene dicarboxylate], has been synthesized solvothermally and further coated with polyvinylpyrrolidone to avoid aggregation. Limit of detection for TNP with the MOF has been obtained as low as 1.66 ppb with a quenching constant of $7.2 \times 10^3 \text{ M}^{-1}$. In another study, the same linker has been employed with another colinker to synthesize Zn-MOF [$\text{Zn}_2(\text{NH}_2\text{BDC})_2(\text{dpNDI})$]; dpNDI: *N,N'*-di(4-pyridyl)-1,4,5,8-naphthalenediimide] by Nagaraja and coworkers for the detection of TNP [107]. Further, postsynthetically modified UiO-66@NH_2 derived from the same NH_2BDC linker has been employed for the selective detection of TNP [108]. It has been observed that the mechanism of such quenching in the emission of MOF with TNP has been majorly attributed to both electron transfer and energy transfer along with electrostatic interaction (Lewis basic functional groups and acidic TNP molecules) between MOF and analytes molecules.

Apart from functionalized ligands, target specific guest molecules also have been incorporated in MOFs to fabricate composite materials for sensing applications. In a recent report, a cationic dye, DMASM (4-(4-(dimethylamino)styryl)-1-methylpyridin-1-ium), and bio-MOF-1-based composite has found to be sensitive toward nitro-analytes in water [109]. This dual emissive composite material has a “turn-off” response for the NACs (TNP, TNT, DNT and TNR), while a “turn-on” response has been obtained for aliphatic nitro-compounds in aqueous medium (Fig. 8.16). This result displays that sensing nitro-analytes with MOF as well as discrimination between aliphatic and aromatic nitro-analytes have been obtained via “turn-on” and “turn-off” responses, respectively. A few other LMOFs-based sensing of TNP in water have been demonstrated in the literature [8,10–15,45,110–112]. All these recent advancements in MOF-based sensors show the potential of such materials for real-time applications.

8.4 Non-nitro-aromatic high energy materials sensing with metal-organic frameworks

Other than nitro-aromatic-based explosive materials, rapid growth in the uses of nonaromatic nitro-explosives (RDX, nitromethane, DMNB, HMX, CL-20, PETN, etc.) as well as HEMs without nitro-groups (DAAT, nitrogen tetroxide, ATZ, etc.) have led researchers to the design and synthesis of sensory materials for the detection of non-nitroaromatic compounds. But sensing of such non-nitro-aromatic materials is a very difficult task due to weak electron transfer along with the difficulty in the energy transfer between sensory materials and respective analytes, which results in negligible signal generation. It has been understood that in most cases similar reduction potentials of nitro-analytes and luminescent probes have resulted in such prohibition in electron transfer. Although these types of HEMs possess a huge threat to the civilian safety, recognition of them still remains a challenge and only a very few MOFs have been reported which can recognize non-nitro-aromatic explosives.

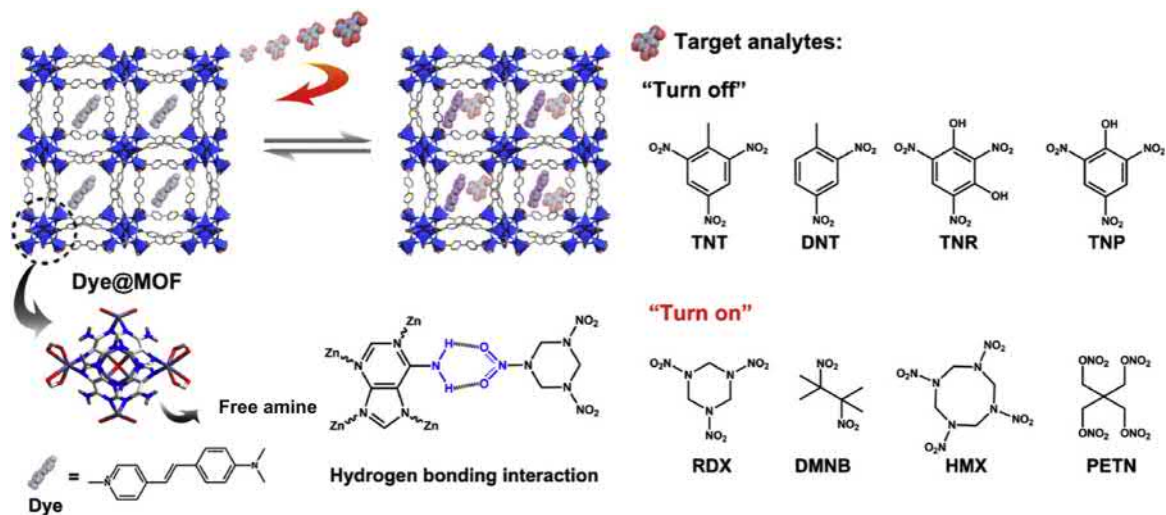


Figure 8.16 Representation of dye encapsulated bio-MOF-1 and sensing of nitro-aromatic and nitro-aliphatic compounds with the composite material.

Source: Reproduced with permission from C. Wang, L. Tian, W. Zhu, S. Wang, P. Wang, Y. Liang, et al., Dye@bio-MOF-1 composite as a dual-emitting platform for enhanced detection of a wide range of explosive molecules, *ACS Appl. Mater. Interfaces* 9 (2017) 20076 – 20085.

Copyright (2017) American Chemical Society.

RDX is known as one of the high explosive materials, but its low vapor pressure has become the major problem in vapor phase detection. Further, all nitro-compounds, having electron withdrawing moiety, are prone to show a similar quenching effect. So, it is a difficult task to distinguish a particular nitro-analyte (e.g., RDX) from all analytes having a similarity in electronic properties. In a recent report by Li and coworkers the sensing of RDX was demonstrated along with other nitro-analytes with two dynamic luminescent Zn-MOFs [113]. Both MOFs, $Zn_2(ndc)_2(bpe) \cdot 2.5DMF \cdot 0.25H_2O$ and $Zn_2(ndc)_2(bpee) \cdot 2.25DMF \cdot 0.5H_2O$ (ndc: 2,6-naphthalenedicarboxylate) showed significant quenching upon exposure to nitro-analyte vapors. Although just the changes in the fluorescence intensity cannot distinguish unambiguously the exact analyte, in conjunction with the shift in emission peak they can be useful to evaluate a particular analyte. From the emission profiles of MOFs upon exposure to analytes, a pin-point 2D map has been drawn by using emission peak shift and fluorescent intensity change as coordinates on a Cartesian system. This unique 2D map was found to be able to identify any specific nitro-analytes used in this study. Further, detection of RDX has been carried out via instant vapor sensing of cyclic ketone (cyclohexanone) which is known to be used in the recrystallization of RDX as solvent. As a consequence of this, cyclohexanone is also found to coexist in the explosive materials and thus sensing of this cyclic ketone can provide an indirect way to detect low volatile RDX. Two 3D MOFs, LMOF-201 ($Zn_2(ofdc)_2(bpy) \cdot 2.5DMF \cdot 1.25H_2O$; ofdc: 9-oxo-9H-fluorene-2,7-dicarboxylic acid) and LMOF-202 ($Zn_2(hfdc)_2(bpy) \cdot xDMA$; hfdc: 9H-fluorene-2,7-dicarboxylic acid), were employed for the vapor phase detection of cyclohexanone [114]. Selective and sensitive sensing has been demonstrated by tuning porosity as well as the electronic properties of MOF materials.

Furthermore, evolution of new generation HEMs (mostly nitrogen-rich heterocyclic compounds with/without $-NO_2$ groups) have attracted much attention due to their low friction and impact sensitivity (IS). But detection of such HEMs via a fluorescence quenching method has been found to be difficult, because those compounds have different orbital energies and are less suitable for oxidative electron transfer mechanisms. In a recent report, the sensing of HEMs based on five-member heterocyclic compounds have been demonstrated by Wang and coworkers with AIE-active MOFs.

Three MOFs, namely, TABD-MOF-1 [$Mg_2(TABD)_3(DMF)_4$], TABD-MOF-2 [$Ni(TABD)_1(DMF)_2$], and TABD-MOF-3 [$Co(TABD)_1(DMF)_2$] (TABD: 4,4'-(Z, Z)-1,4-diphenylbuta-1,3-diene-1,4-diyl)dibenzoic acid), have been synthesized via the solvothermal method (Fig. 8.17A) [115]. Among these three MOFs, only TABD-MOF-1 has been found to be highly luminescent with quantum yields (Φ_F) of 38.5% and other MOFs were barely luminescent ($\Phi_F = 1.12\%$ and 0.15% for TABD-MOF-2 and TABD-MOF-3, respectively) due to the presence of Ni^{2+} and Co^{2+} metal ions. Strong LMCT in the case of TABD-MOF-2 and TABD-MOF-3 and incompletely filled d-orbitals for Ni^{2+} and Co^{2+} ions can be the major reason for such low emissions, respectively. A sensing study of 5-nitro-2,4-dihydro-3H-1,2,4-triazole-3-one (NTO) was first carried out with TABD-MOFs. Turn-on response was observed in the case of both TABD-MOF-2 and TABD-MOF-3, with

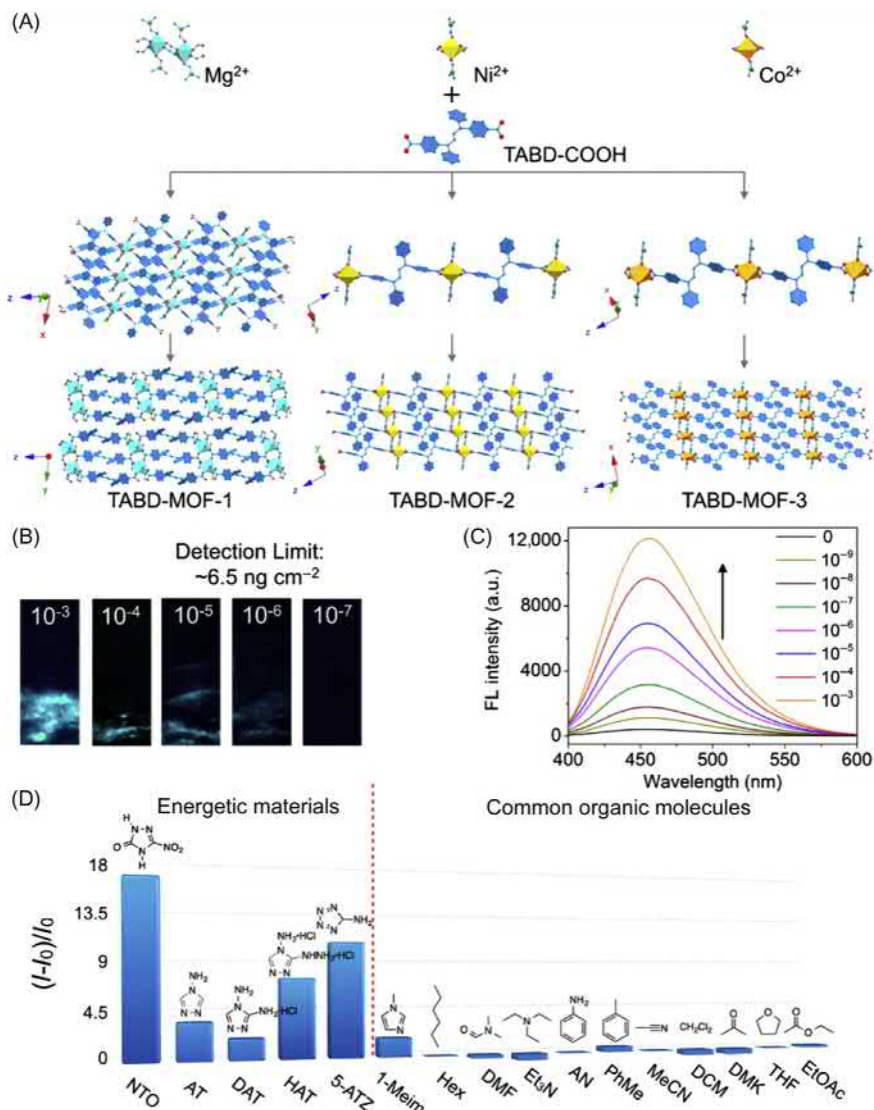


Figure 8.17 (A) Synthesis scheme of TABD-MOF-1, TABD-MOF-2 and TABD-MOF-3. (B) Images of TABD-MOF-3-deposited paper strips in the presence of different concentrations of NTO in THF under UV-light. (C) Fluorescence enhancement of TABD-MOF-3 in the presence of NTO in THF medium followed by addition of hexane. (D) Fluorescence increment efficiency of TABD-MOF-3 in the presence of various analytes. *Source:* Reproduced with permission from Y. Guo, X. Feng, T. Han, S. Wang, Z. Lin, Y. Dong, et al., Tuning the luminescence of metal – organic frameworks for detection of energetic heterocyclic compounds, *J. Am. Chem. Soc.* 136 (2014) 15485 – 15488. Copyright (2014) American Chemical Society.

a red-shift in wavelength for TABD-MOF-2 and blue emission of TABD-MOF-1 quickly shifted to a green color (Fig. 8.17C). Control experiments revealed that only THF or only TABD linker didn't show significant responses with NTO. As a reason behind this observation it has been stated that metal-carboxylate bonds of MOFs are prone to dissociate in the presence of C=N- or N=N- moieties of the heterocyclic compounds, which leads to the formation of aggregation-induced emissions of the TABD linker (Fig. 8.17D). Thus the obtained emission from linker due to aggregation has led to the generation of signal in this case. TABD-MOF-3 coated strip has been further tested for selectivity and the MOF coated strip showed turn-on emission only in the presence of five-member heterocyclic HEMs [4H-1,2,4-triazol-4-amine (AT), 5H-tetrazol-5-amine (5-ATZ), 4H-1,2,4-triazole-3,4-diamine hydrochloride (DAT), NTO and 3-hydrazinyl-4H-1,2,4-triazol-4-amine dihydrochloride (HAT)] over other NACs and various solvents (Fig. 8.17B). Hitherto, we have discussed mostly the role of the linkers in MOFs for the detection of non-nitro-aromatic HEMs, but the suitable selection of guest molecules can also play a crucial role in sensing. Recently Fu et al. have reported a dual emissive composite material of MOF and HPTS dye (8-hydroxy-1,3,6-pyrenetrisulfonic acid trisodium salt) for the detection of a broad class of nitro-explosive materials (Fig. 8.18A) [116]. Owing to the high porosity and presence of NO_3^- anions in MOF $[\text{Zn}(\text{TIPA})(\text{NO}_3^-)_2(\text{H}_2\text{O}) \cdot 5\text{H}_2\text{O}]$; TIPA: tri(4-imidazolylphenyl)amine], which has been reported earlier, guest dye molecule has been incorporated via anion exchange (Fig. 8.18A). The blue emissive MOF ($\lambda_{\text{max}} = 400 \text{ nm}$) showed yellow-green emission ($\lambda_{\text{max}} = 400$ and 525 nm) upon incorporation of HPTS dye molecules (Fig. 8.18B and C). MOF \supset HPTS composite material showed significant change in emission profile in the presence of NACs as well as aliphatic nitro-compounds RDX, HMX, and DMNB. Both RDX and HMX showed dramatic quenching of the peak at 525 nm along with the enhancement in the peak at 400 nm (Fig. 8.18D). Especially, with addition of 15 and 30 ppm RDX analyte 31% and 55% quenching was observed for peak at 525 nm while 40% and 195% enhancement was observed for peak at 400 nm , respectively. This result can be attributed to the pore filling effect with upcoming aliphatic nitro-analytes and further rigidifying the motions of the dye molecules inside the framework. This example demonstrated that host-guest chemistry in such guest-encapsulated MOFs can be well suited for the fabrication of durable sensory materials.

8.5 Desensitization of nitro-explosives and related materials by metal-organic frameworks

Recently, MOFs have emerged as suitable candidates for the capture and desensitization of nitro-explosive compounds. MOFs have become one of the superior materials over other common sensors for detection of nitro-aromatics owing to their tunable porosities and functionalized pore cavities. In addition, MOFs-based desensitization of explosives by encapsulating them inside the framework has evolved

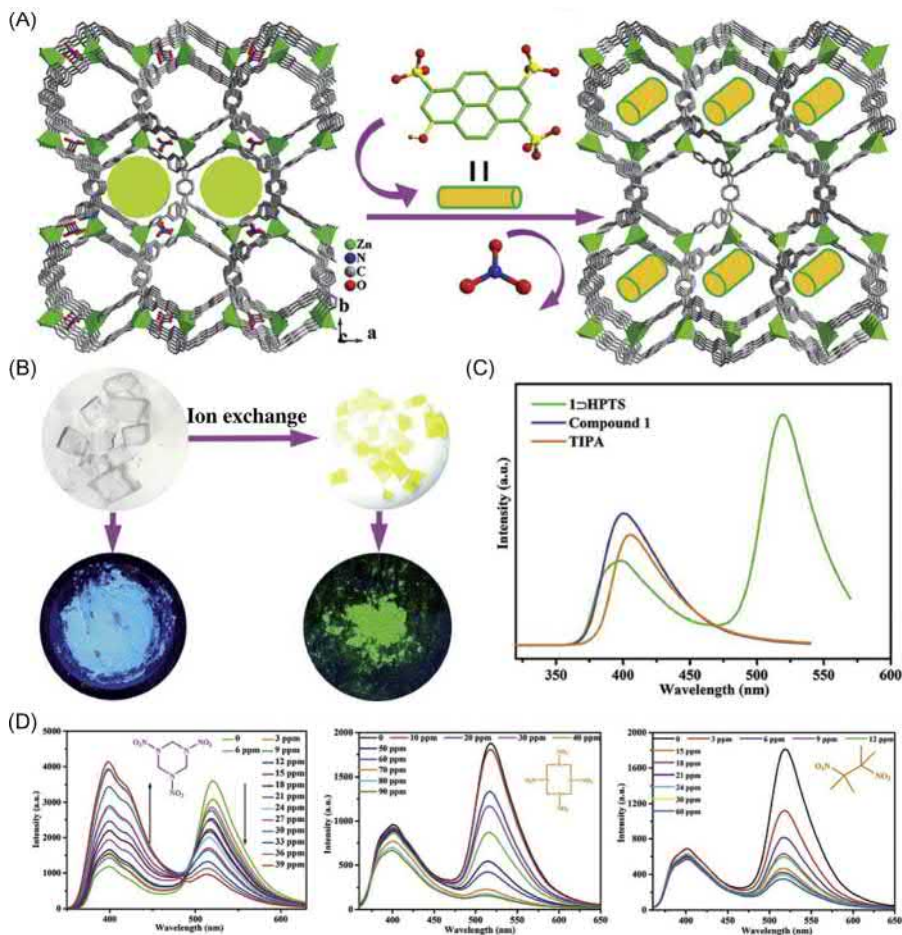


Figure 8.18 (A) Three-dimensional framework of MOF (left) and dye encapsulated MOF (right). (B) Images of single crystal (top) MOF (left) and dye encapsulated MOF composite (right) with corresponding fluorescence emission (bottom). (C) Solid-state emission of MOF (blue), ligand (orange) and dye-loaded MOF (green). (D) Turn-on responses of the composite for RDX, HMX, and DMNB (from left to right).

Source: Reproduced with permission from H.-R. Fu, L.-B. Yan, N.-T. Wu, L.-F. Ma, S.-Q. Zang, Dual-emission MOF \supset dye sensor for ratiometric fluorescence recognition of RDX and detection of a broad class of nitro-compounds, *J. Mater. Chem. A* 6 (2018) 9183–9191.

Copyright (2018) Royal Society of Chemistry.

recently showing their huge potential. High heat of detonation is the key factor for sensitivity of high energy density materials (HEDMs) and desensitization of such HEDMs are of great interest because of safe storage, transport, and other security issues [117–120]. Desensitizers are typically employed to desensitize explosive materials by absorbing the heat generated from the explosives due to impact and

friction implemented on them. Desensitizers are also used to decrease the energy density of the explosive materials, by which their initiation functioning could be affected. The development of MOFs as a new platform of next-generation HEDMs is quite fascinating owing to their inherent benefits, such as rational designing and structural diversity, which allows to introduce various energetic components inside the framework. Moreover, higher mechanical strength and favorable thermal stability and eminent density of MOFs play crucial roles for lowering their sensitivity significantly [16].

There are three important methods to desensitize explosive materials by utilizing MOFs, which are as follows:

1. construction of insensitive energetic MOFs by using N-rich linkers.
2. encapsulation of energetic components inside MOFs.
3. MOFs as scaffold in preparing insensitive energetic materials.

8.5.1 Construction of insensitive energetic metal-organic frameworks by using N-rich linkers

MOFs, designed and fabricated from N-rich ligands are expected to be promising candidates as next-generation HEDMs. Conventional energetic complexes and metal-organic salts often possess high heat densities, but comparatively low heat of detonation value for each unit mass in comparison with organic explosives, which has resulted in various environmental issues [121,122]. Recently Bushuyev et al. reported two one-dimensional energetic MOFs, composed of metal–hydrazine complexes accommodating noncoordinating anions like nitrate (NO_3^-) and perchlorate (ClO_4^-) [123]. They have synthesized nickel hydrazine perchlorate (NHP) and cobalt hydrazine perchlorate (CHP), where Ni and Co are present as the central metal node and hydrazine acts as the inner sphere binding ligand to form the linear backbone structures. Among these two MOFs, NHP was found to be highly sensitive as it resulted in three explosions during the laboratory handling. In contrast, CHP was less sensitive and could be handily initiated by spark, flame, and impact. Both compounds have comparable heats of detonation with two of the most energetic materials PETN and RDX; also both CHP and NHP were found to be very sensitive. A relatively high proportion of nitrogen content (due to hydrazine moiety) compared to metal content in both the frameworks along with weak bonds between Ni- or Co-nitrogen resulted in such high sensitivity for both CHP and NHP.

In developing desensitized HEDMs, the same research group further extended their work to prepare desensitized hydrazine functionalized MOFs by modifying them to 2D layered structures [124]. In this regard, hydrazine was employed as one of the ligands owing to its solely gaseous decomposition products, bidentate nature, and the absence of oxidizable carbon. Further, bidentate hydrazine was partially exchanged with tridentate hydrazinecarboxylate anion which resulted in two 2D polymeric sheets, viz., CHHP $\{[\text{Co}_2(\text{N}_2\text{H}_4)_4-(\text{N}_2\text{H}_3\text{CO}_2)_2][\text{ClO}_4]_2 \cdot \text{H}_2\text{O}\}$ and ZnHHP $\{[\text{Zn}_2(\text{N}_2\text{H}_4)_3-(\text{N}_2\text{H}_3\text{CO}_2)_2][\text{ClO}_4]_2 \cdot \text{H}_2\text{O}\}$. Two-dimensional CHHP and ZnHHP were found to possess a considerable amount of decrease in the sensitivity

as compared to the previously synthesized 1D CHP and NHP. In addition, DFT (density functional theory) calculation suggested that ZnHHP was endowed with higher energy content than most of the metal-based explosives. Moreover, ZnHHP was found to be insensitive to the initiation via spark ignition and also a homemade drop hammer apparatus, which revealed the remarkable lowering in the sensitivity of the material as compared to the previous case. Apart from hydrazine derivatives, heterocycles (such as triazole and tetrazole) with high nitrogen content are of great interest in the fabrication of MOFs-based HEDMs due to their high nitrogen content, adjustable coordination modes, and considerable structural stability. In another report, Chen, Wei, and coworkers demonstrated Ag-based 2D energetic CPs (coordination polymers) with triazole moieties [125]. Both compounds exhibited good insensitivity along with thermal stability up to 300°C. Moreover, both the compounds were found to be insensitive toward initiation until the impact energy is more than 40 J or the respective friction force gained to 360 N.

Three-dimensional MOFs feature more accomplished structural integrity, which could further enhance the stabilities and energetic properties in comparison with 1D linear and 2D layered structures. In this regard, in 2013, Pang and coworkers demonstrated two ecofriendly, halogen-free energetic 3D MOFs with formulas of $[\text{Cu}(\text{atrz})_3(\text{NO}_3)_2]_n$ and $[\text{Ag}(\text{atrz})_{1.5}(\text{NO}_3)]_n$ (where atrz: 4,4'-azo-1,2,4-triazole) with exceptionally high heat of detonation and comparatively low sensitivity [126]. Use of 4,4'-azo-1,2,4-triazole over hydrazine as ligand was justified with several advantages such as high nitrogen content along with a very high heat of formation. Featuring high thermal stability along with decomposition temperature of up to 313°C and with more than six N-atoms potentially coordinated, it was predicted that the use of atrz could enhance the energetic properties of the target polymers. The ISs for the Cu- and Ag-based compounds were found to be 22.5 and 30 J respectively, whereas IS values for previously reported hydrazine-based CPs were 0.5 J for CHP and 0.8 J for CHHP, which were even lower than for the free atrz ligands (14 J). In addition, both compounds were found to be insensitive not only to friction (0%), but also to electrostatic discharge (24.75 J), while highly explosive HMX has been found to possess only 0.2 J electrostatic sensitivity. Both complexes showed remarkably high heats of detonation and were found to perform relatively better than the previously reported MOF materials (such as CHP, NHP, and CHHP). Additionally, it was found that $[\text{Cu}(\text{atrz})_3(\text{NO}_3)_2]_n$ possesses a higher heat of detonation than well-known octanitrocubane, CL-20 and other powerful organic explosives.

Further, Lan, Li, Su, and coworkers in 2015, reported another 3D energetic MOF with SOD topology based on N-rich heterocycles, namely IFMC-1 with a formula of $(\text{Zn}(\text{Hdttz})) \cdot \text{DMA}$ (where Hdttz: 4,5-di(1H-tetrazol-5-yl)-2H-1,2,3-triazole) [127]. IFMC-1 showed excellent low sensitivity with a high heat of detonation ($8.26 \text{ kcal cm}^{-3}$), which was found to be five times more than that of the respective ligand, H_3dttz (1.06 kcal g^{-1}). The IS of IFMC-1 was found to be more than 40 J along with friction sensitivity more than 360 N and electrostatic sensitivity $>40 \text{ J}$. Both H_3dttz and IFMC-1 have been classified as “insensitive” materials. Heat of detonation for IFMC-1 was calculated by DFT calculations to

be three to eight times greater than TNT, CL-20, and other reported MOFs. Furthermore, Chen and coworkers reported the role of guest molecules in the contradiction between energy and safety in MOFs-based HEMs [128]. In this work, they reported a MOF-based energetic compound with a formula of $[\text{Co}_9(\text{bta})_{10}(\text{Hbta})_2(\text{H}_2\text{O})_{10}]_n \cdot [22(\text{H}_2\text{O})]_n$ which was constructed from a nitrogen-rich heterocyclic ligand (where H_2bta : (*N,N*-bis(1H-tetrazole-5-yl)-amine)). Structure of the compound revealed latticed water molecules incorporated inside the channels, which were found to be insensitive. Upon dehydration of the aforementioned compound, a new energetic compound with formula of $[\text{Co}_9(\text{bta})_{10}(\text{Hbta})_2(\text{H}_2\text{O})_{10}]_n$ was obtained. The IS value of the as-synthesized compound, $[\text{Co}_9(\text{bta})_{10}(\text{Hbta})_2(\text{H}_2\text{O})_{10}]_n \cdot [22(\text{H}_2\text{O})]$, was found to be 40 J which was much higher than the dehydrated phase (IS of 27 J). Interestingly, both compounds were found to have lower sensitivity than that of TNT and other accounted energetic coordination polymers. The sensitivity difference between these two compounds was attributed to the presence of guest water molecules in the case of the first compound where lattice water molecules played the role to decrease the sensitivity as compared to the dehydrated compound.

In 2015, another report by Chen and coworkers demonstrated the synthesis of three green energetic MOFs with formulas of $[\text{Cu}(\text{Htztr})_2(\text{H}_2\text{O})_2]_n$, $\{[\text{Cu}(\text{tztr})] \cdot \text{H}_2\text{O}\}_n$, and $[\text{Cu}(\text{Htztr})]_n$ (where Htztr: 3-(1H-tetrazol-5-yl)-1H-triazole) [129]. Among these MOFs, $[\text{Cu}(\text{Htztr})_2(\text{H}_2\text{O})_2]_n$ was found to possess a mononuclear structure, whereas $\{[\text{Cu}(\text{tztr})] \cdot \text{H}_2\text{O}\}_n$ exhibited 3D skeletons and $[\text{Cu}(\text{Htztr})]_n$ presented a layered structural feature. In spite of such differences in their structural dimensions, all three MOFs possess very low sensitivity as well as good heats of detonation. According to the authors, the presence of water molecules inside the frameworks of $[\text{Cu}(\text{Htztr})_2(\text{H}_2\text{O})_2]_n$ and $\{[\text{Cu}(\text{tztr})] \cdot \text{H}_2\text{O}\}_n$ help both MOFs to lower their sensitivity. So, these reports show the fabrication of energetic MOFs from N-rich organic linkers with low sensitivity is a very interesting but also a tricky task. There are several factors which can influence the explosive behavior of the energetic MOFs, such as nitrogen content, balance of oxygen, the type of ligands used, coordination environment, counter ions, intra- and intermolecular H-bondings, solvent molecules, and guest species remaining in the pores.

8.5.2 Encapsulation of energetic components inside metal-organic frameworks

Furthermore, MOFs could be very much useful as molecular containers to desensitize different type of high-energetic molecules as guests via encapsulation inside the frameworks. The guest molecules or the counter ions inside pores of MOFs can have strong interactions with the framework and hence the explosive nature of such compounds could be influenced (either can be increased or decreased). In 2016, Li, Pang, and coworkers came up with a new desensitizing strategy for HEDMs via entrapping explosive molecules as guests or anions within the network of MOFs and hence preventing their decomposition properties and decreasing their reactivity

[130]. It showed an adequate anion exchange process of reversible encapsulation of exclusive oxy-anion, dinitramide ion $\{N(NO_2)_2\}^-$ in a 3D cationic energetic MOF (Fig. 8.19A). The entrapping process resulted in the significant increase in the thermal stability of the respective dinitramide ion. Decomposition temperature for the dinitramide ion encapsulated compound, that is, $N(NO_2)_2^- \subset MOF(Cu)$, reached up to $221^\circ C$, and this made the compound as the most stable compound containing energetic $N(NO_2)_2^-$ ions. Moreover, $N(NO_2)_2^- \subset MOF(Cu)$ could be handled safely for real-time applications as it possesses an electrostatic sensitivity of 1.9 J, which was much higher than the static electricity that the human body can generate (0.025 J). Further, successful ion exchange of the encapsulated $N(NO_2)_2^-$ anion was carried out with contending guest anions (N_3^-) which exhibited a very fast color change (blue to deep brown), detectable by the naked eye, and hence deformation of the material from a secondary explosive to a primary explosive was obtained (Fig. 8.19B). This study provides a convenient approach for the preparation of new energetic MOFs by rapid encapsulation and release of labile energetic anions under ambient conditions and by modulation of their energetic properties.

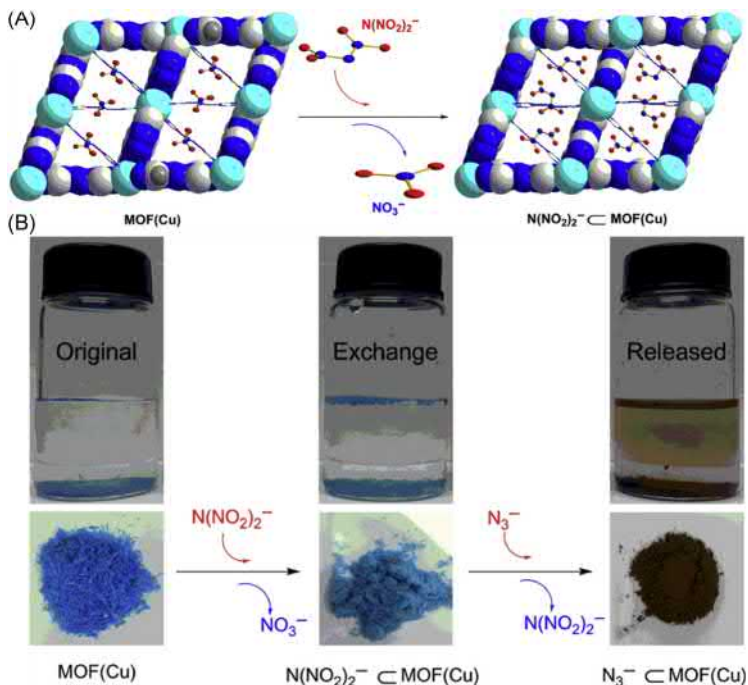


Figure 8.19 (A) Schematic representation of anion exchange in MOF. (B) Images of the color changes of crystals before and after anion exchanges.

Source: Reproduced with permission from J. Zhang, Y. Du, K. Dong, H. Su, S. Zhang, S. Li, et al., Taming dinitramide anions within an energetic metal – organic framework: a new strategy for synthesis and tunable properties of high energy materials, *Chem. Mater.* 28 (2016) 1472 – 1480. Copyright (2016) American Chemical Society.

8.5.3 Metal-organic frameworks as precursor to prepare insensitive energetic materials

The exciting evolution of the MOF-based explosive materials has shown a new avenue in the developing field of HEDMs. But a few shortcomings, such as high cost, major safety risk, and inadequate performance, have made this method more challenging. Primary explosives are considered as the most sensitive materials to friction, mechanical shock, and heat, since they will respond by detonating or burning rapidly. So, there must be a balance between resistance to flame, electrostatic sensitivity, and their initiation properties.

In 2017, B. Wang and coworkers reported a MOF-templating strategy for in situ synthesis of a primary explosive inside a carbonized MOF composite [131]. They strategically chose copper azide (CA) as the aimed primary explosive due to its high sensitivity toward flame and powerful initiation ability. Further, a Cu(II)-based MOF, viz., HKUST-1, was employed owing to the fact that carbonization of HKUST-1 can produce a carbon matrix with open mesopores with uniform distribution of copper (Fig. 8.20). High surface area resulting from carbonization of the MOF could be utilized for the in situ preparation of CA by the introduction of hydrazoic acid (HN_3) gas inside the channels. Further, the authors had calcinated

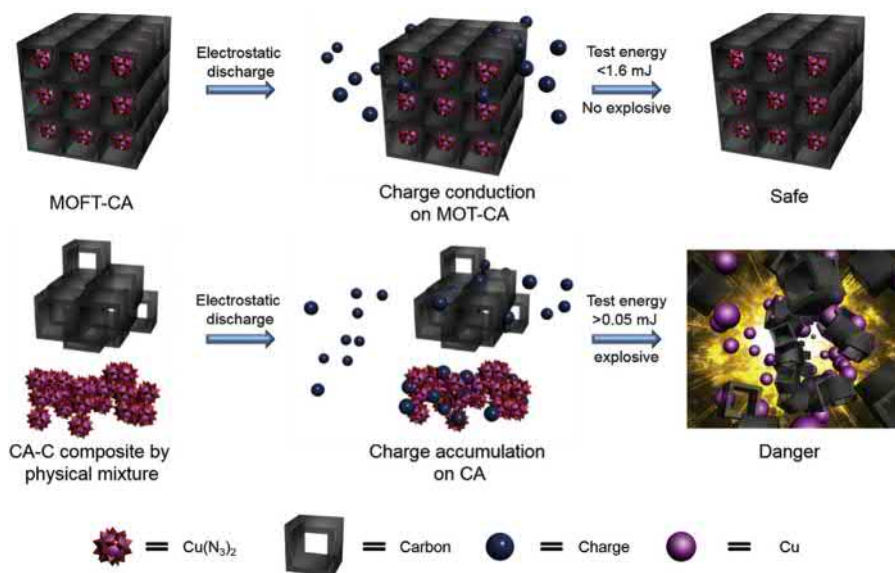


Figure 8.20 Mechanistic illustration of electrostatic sensitivity for the composites, MOFT-CA and CA-C, by physical mixture method.

Source: Reproduced with permission from X. Qu, S. Zhang, Q. Yang, Z. Su, Q. Wei, G. Xie, et al., Silver(I)-based energetic coordination polymers: synthesis, structure and energy performance, *New J. Chem.* 39 (2015) 7849–7857 respectively. Copyright (2016) John Wiley & Sons.

the HKUST-1 followed by reacting with HN_3 gas to acquire primary explosive composite, namely, MOFT-CA. The conductive nature of the carbon framework helped to prevent the charge accumulation on the primary explosive. MOFT-CA showed good flame sensitivity, excellent initiation ability, and low electrostatic sensitivity at the same time. The discharge energy at 50% (referred to as E_{50}) of the explosive MOFT-CA was found to be 1.6 mJ, which is ten times higher than LS, and much higher than the mixtures of LA and LS and other carbon composites, implying the lower electrostatic sensitivity and higher safety of the composite. Notably, only 10 mg of MOFT-CA can effectively detonate 80 mg (RDX), 30 mg mixture of LS and LA revealing an excellent initiation ability. These results support that MOFT-CA can fulfill the basic needs for practical applicability for both the civilian as well as military explosive technologies.

8.6 Conclusions and future outlooks

In conclusion, MOF has evolved as a fertile platform in the field for effective sensing and desensitization of energetic materials. The porous nature of MOFs make them advantageous for sensing of energetic materials as the aimed analyte can be adsorbed into the pores and can generate a prominent interaction between the aimed analyte and the recognition center to create strong signals. LMOFs are explored extensively in sensing and detection of various toxic environmental pollutants, explosive materials, etc. In the field of HEDMs sensing, MOFs can be utilized for turn-off detection of nitro-aromatic explosives via the charge transfer effect, and employing aggregation-induced emission phenomena, turn-on based detection of N-heterocyclic rich HEDMs via a competitive coordination strategy was acquired. These phenomena are very useful in the design of sensory materials to distinguish various targeted analytes by their small structural differences in molecules via transduction protocol. The fabrication of high-energetic ligands with metal ions via self-assembly along with the improvement of theory calculation, measurement techniques and processing ease, and the development of preparation and characterization of HEDMs has been extraordinary. For HEDMs, the choice of metal nodes along with the modification of the binding linker play important roles in producing the energetic properties of the material. Moreover, the assistance of high energy chelating linkers leads to different dimensionality of the frameworks from 1D to 3D while providing the desired properties. To desensitize energetic materials, researchers employ various energetic ligands (mostly N-rich) to fabricate insensitive energetic MOFs. Additionally, 3D HEDMs have found immense promise in this field owing to their enhanced structural reinforcement in comparison with 1D and 2D frameworks. Incorporation of inorganic anions in 3D HEDMs, such as nitrate (NO_3^-) and perchlorate (ClO_4^-) inside the pores of the HEDMs, provide stabilities and energetic properties. Encapsulation of energetic materials within the pores of the MOFs and MOF-reduced carbon materials to produce powerful but insensitive explosives are the other two strategies to prepare desensitized HEDMs by MOFs.

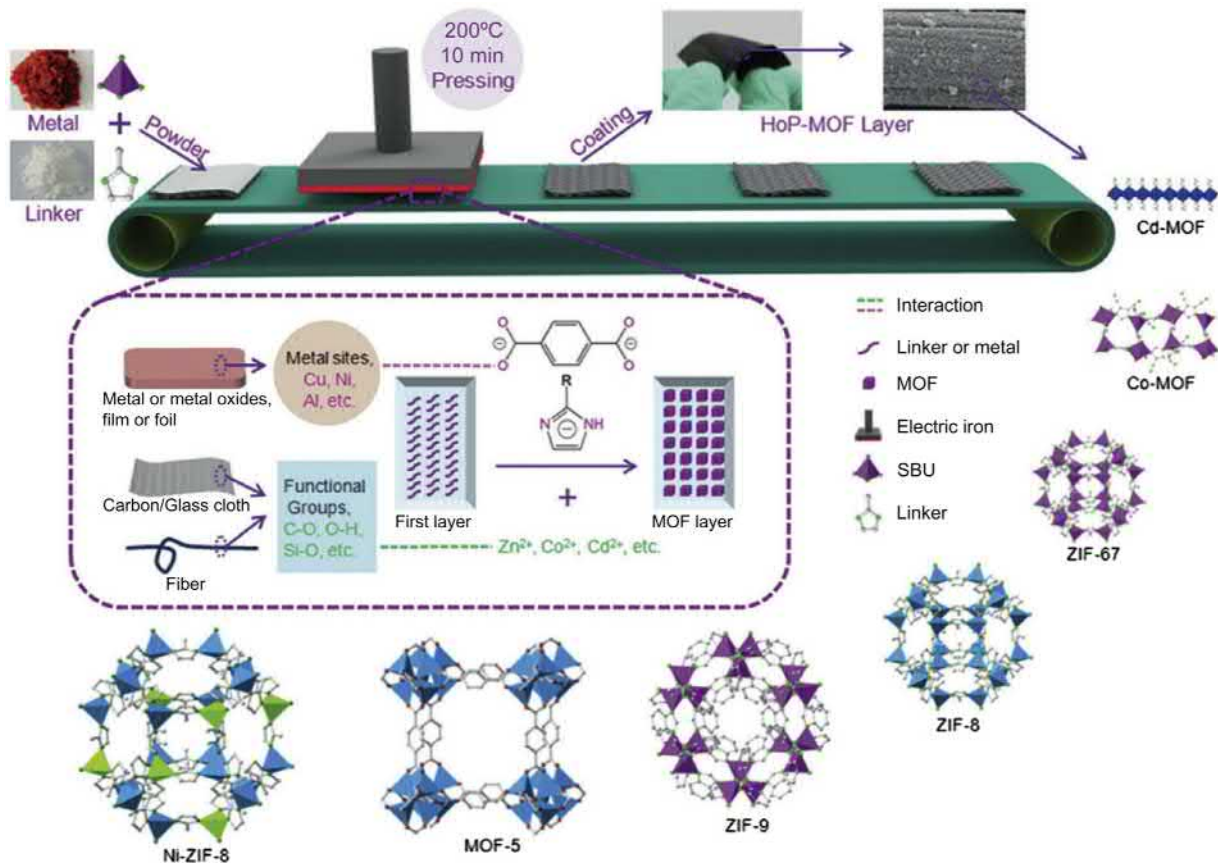


Figure 8.21 Schematic representation of the MOF coating with hot-pressing method.

Source: Reproduced with permission from Y. Chen, S. Li, X. Pei, J. Zhou, X. Feng, S. Zhang, et al., A solvent-free hot-pressing method for preparing metal-organic-framework coatings, *Angew. Chem. Int. Ed.* 55 (2016) 3419–3423 respectively. Copyright (2016) John Wiley & Sons.

The process to derive MOF-based desensitized HEDM carbon materials is simple, scalable, and economically feasible and preferred over physical mixing process and other methods because of the lesser chance of accidental explosion.

Even though momentous progress has been made in these fields, the fabrication of MOF-based membranes and devices for real-time applications rather than powders is still highly desired. Crystals of MOFs are inherently brittle in nature and arduous to process for practical applications. Mixing of MOFs with binders and additives gives an alternative way out to prevent the degradation of MOFs into fine powders or tiny particles for their applicability. In situ growth of crystals of the MOF on the device substrates is the other way to construct MOF-based devices. In this process, the device substrate is immersed in the mother liquor of the targeted MOF and stepwise growth of MOFs on the surface of the substrate occurs via electrochemical deposition, solvothermal, or microwave methods. Recently, B. Wang, and coworkers introduced a fast and facile technique called postsynthetic polymerization to attach MOF crystals to flexible polymeric chains via covalent bonding [132]. This strategy improves the interfacial interactions between polymers and MOFs by reducing the boundary defects and hence aggregation process of MOF particles gets prevented. Moreover, they employed a hot-pressing method for coating on MOFs with various binding substrates. By this method, a range of MOFs, including imidazolate-/carboxylate-assisted and mixed-metal MOFs, are found to be fruitfully fabricated on different coating substrates (Fig. 8.21) [133]. These kinds of processing methods to construct MOFs-based explosive devices or sensors will trigger the development of MOF-based devices further for explosive desensitization and explosive sensing.

Acknowledgments

PS and SD are thankful to UGC and IISER-Pune, respectively, for research fellowship. We are grateful to DST-SERB (Grant EMR/2016/000410) for financial support.

References

- [1] A.A. Dippold, T.M. Klapötke, A study of dinitro-bis-1,2,4-triazole-1,1'-diol and derivatives: design of high-performance insensitive energetic materials by the introduction of N-oxides, *J. Am. Chem. Soc.* 135 (2013) 9931–9938.
- [2] J. Zhang, J.M. Shreeve, 3,3'-Dinitroamino-4,4'-azoxyfurazan and its derivatives: an assembly of diverse N – O building blocks for high-performance energetic materials, *J. Am. Chem. Soc.* 136 (2014) 4437–4445.
- [3] D.M. Badgajar, M.B. Talawar, S.N. Asthana, P.P. Mahulikar, Advances in science and technology of modern energetic materials: an overview, *J. Hazard. Mater.* 151 (2008) 289–305.
- [4] S. Wang, Q. Wang, X. Feng, B. Wang, L. Yang, Explosives in the cage: metal–organic frameworks for high-energy materials sensing and desensitization, *Adv. Mater.* (2017). Available from: <https://doi.org/10.1002/adma.201701898>.

- [5] R. Matyáš, J. Šelešovský, T. Musil, Sensitivity to friction for primary explosives, *J. Hazard. Mater.* 213–214 (2012) 236–241.
- [6] A.L. Ramaswamy, J.E. Field, Laser-induced ignition of single crystals of the secondary explosive cyclotrimethylene trinitramine, *J. Appl. Phys.* 79 (1996) 3842–3847.
- [7] D.S. Moore, Instrumentation for trace detection of high explosives, *Rev. Sci. Instrum.* 75 (2004) 2499–2512.
- [8] X. Sun, Y. Wang, Y. Lei, Fluorescence based explosive detection: from mechanisms to sensory materials, *Chem. Soc. Rev.* 44 (2015) 8019–8061.
- [9] R. McGrath, *Landmines and Unexploded Ordnance: A Resource Book*, Pluto Press, 2000. Available from: <http://dx.doi.org/10.2307/j.ctt18fsb7f>.
- [10] S.S. Nagarkar, A.V. Desai, S.K. Ghosh, Engineering metal–organic frameworks for aqueous phase 2,4,6-trinitrophenol (TNP) sensing, *CrystEngComm* 18 (2016) 2994–3007.
- [11] L. Zhang, Z. Kang, X. Xin, D. Sun, Metal–organic frameworks based luminescent materials for nitroaromatics sensing, *CrystEngComm* 18 (2016) 193–206.
- [12] W.P. Lustig, S. Mukherjee, N.D. Rudd, A.V. Desai, J. Li, S.K. Ghosh, Metal–organic frameworks: functional luminescent and photonic materials for sensing applications, *Chem. Soc. Rev.* 46 (2017) 3242–3285.
- [13] Z. Hu, B.J. Deibert, J. Li, Luminescent metal–organic frameworks for chemical sensing and explosive detection, *Chem. Soc. Rev.* 43 (2014) 5815–5840.
- [14] Y. Cui, Y. Yue, G. Qian, B. Chen, Luminescent functional metalorganic frameworks, *Chem. Rev.* 112 (2012) 1126–1162.
- [15] Y. Zhang, S. Yuan, G. Day, X. Wang, X. Yang, H.-C. Zhou, Luminescent sensors based on metal-organic frameworks, *Coord. Chem. Rev.* 354 (2018) 28–45.
- [16] Q.H. Zhang, J.M. Shreeve, Metal–organic frameworks as high explosives: a new concept for energetic materials, *Angew. Chem., Int. Ed.* 53 (2014) 2540–2542.
- [17] P. Kolla, Detecting hidden explosives, *Anal. Chem.* 67 (1995) A184–A189.
- [18] S.J. Toal, W.C. Trogler, Polymer sensors for nitroaromatic explosives detection, *J. Mater. Chem.* 16 (2006) 2871–2883.
- [19] M.E. Germain, M.J. Knapp, Optical explosives detection: from color changes to fluorescence turn-on, *Chem. Soc. Rev.* 38 (2009) 2543–2555.
- [20] Y. Salinas, R. Martínez-Máñez, M.D. Marcos, F. Sancenón, A.M. Costero, M. Parra, et al., Optical chemosensors and reagents to detect explosives, *Chem. Soc. Rev.* 41 (2012) 1261–1296.
- [21] K.G. Furton, L.J. Myers, The scientific foundation and efficacy of the use of canines as chemical detectors for explosives, *Talanta* 54 (2001) 487–500.
- [22] K. Hakansson, R.V. Coorey, R.A. Zubarev, V.L. Talrose, P. Hakansson, Low-mass ions observed in plasma desorption mass spectrometry of high explosives, *J. Mass Spectrom.* 35 (2000) 337–346.
- [23] J.M. Sylvia, J.A. Janni, J.D. Klein, K.M. Spencer, Surface-enhanced raman detection of 2,4-dinitrotoluene impurity vapor as a marker to locate landmines, *Anal. Chem.* 72 (2000) 5834–5840.
- [24] P.C. Ray, Z. Fan, R.A. Crouch, S.S. Sinha, A. Pramanik, Nanoscopic optical rulers beyond the FRET distance limit: fundamentals and applications, *Chem. Soc. Rev.* 43 (2014) 6370–6404.
- [25] S.S. Nagarkar, B. Joarder, A.K. Chaudhari, S. Mukherjee, S.K. Ghosh, Highly selective detection of nitro explosives by a luminescent metal–organic framework, *Angew. Chem. Int. Ed.* 52 (2013) 2881–2885.

- [26] Y. Wang, A. La, C. Brückner, Y. Lei, FRET- and PET-based sensing in a single material: expanding the dynamic range of an ultra-sensitive nitroaromatic explosives assay, *Chem. Commun.* 48 (2012) 9903–9905.
- [27] D. Dinda, A. Gupta, B.K. Shaw, S. Sadhu, S.K. Saha, Highly selective detection of trinitrophenol by luminescent functionalized reduced graphene oxide through FRET mechanism, *ACS Appl. Mater. Interfaces* 6 (2014) 10722–10728.
- [28] D. Escudero, Revising intramolecular photoinduced electron transfer (PET) from first-principles, *Acc. Chem. Res.* 49 (2016) 1816–1824.
- [29] S. Madhu, A. Bandela, M. Ravikanth, BODIPY based fluorescent chemodosimeter for explosive picric acid in aqueous media and rapid detection in the solid state, *RSC Adv.* 4 (2014) 7120–7123.
- [30] Y. Xu, B. Li, W. Li, J. Zhao, S. Sun, Y. Pang, “ICT-not-quenching” near infrared ratio-metric fluorescent detection of picric acid in aqueous media, *Chem. Commun.* 49 (2013) 4764–4766.
- [31] R. Paolesse, S. Nardis, D. Monti, M. Stefanelli, C. Di Natale, Porphyrinoids for chemical sensor applications, *Chem. Rev.* 117 (2017) 2517–2583.
- [32] J.M. Schnorr, D. van der Zwaag, J.J. Walsh, Y. Weizmann, T.M. Swager, Sensory arrays of covalently functionalized single-walled carbon nanotubes for explosive detection, *Adv. Funct. Mater.* 23 (2013) 5285–5291.
- [33] M. O’Keeffe, O.M. Yaghi, Deconstructing the crystal structures of metalorganic frameworks and related materials into their underlying nets, *Chem. Rev.* 112 (2012) 675–702.
- [34] S. Furukawa, J. Reboul, S. Diring, K. Sumida, S. Kitagawa, Structuring of metal–organic frameworks at the mesoscopic/macrosopic scale, *Chem. Soc. Rev.* 43 (2014) 5700–5734.
- [35] A. Schneemann, V. Bon, I. Schwedler, I. Senkovska, S. Kaskel, R.A. Fischer, Flexible metal–organic frameworks, *Chem. Soc. Rev.* 43 (2014) 6062–6096.
- [36] C.R. Kim, T. Uemura, S. Kitagawa, Inorganic nanoparticles in porous coordination polymers, *Chem. Soc. Rev.* 45 (2016) 3828–3845.
- [37] C. He, D. Liu, W. Lin, Nanomedicine applications of hybrid nanomaterials built from metal – ligand coordination bonds: nanoscale metal – organic frameworks and nanoscale coordination polymers, *Chem. Rev.* 115 (2015) 11079–11108.
- [38] P. Horcajada, R. Gref, T. Baati, P.K. Allan, G. Maurin, P. Couvreur, et al., Metal-organic frameworks in biomedicine, *Chem. Rev.* 112 (2012) 1232–1268.
- [39] J. Aguilera-Sigalat, D. Bradshaw, Synthesis and applications of metal-organic framework–quantum dot (QD@MOF) composites, *Coord. Chem. Rev.* 307 (2016) 267–291.
- [40] Q.-L. Zhu, Q. Xu, Metal–organic framework composites, *Chem. Soc. Rev.* 43 (2014) 5468–5512.
- [41] L.E. Kreno, K. Leong, O.K. Farha, M. Allendorf, R.P. Van Duyne, J.T. Hupp, Metal-organic framework materials as chemical sensors, *Chem. Rev.* 112 (2012) 1105–1125.
- [42] Y. Bai, Y. Dou, L.-H. Xie, W. Rutledge, J.-R. Li, H.-C. Zhou, Zr-based metal–organic frameworks: design, synthesis, structure, and applications, *Chem. Soc. Rev.* 45 (2016) 2327–2367.
- [43] M.D. Allendorf, C.A. Bauer, R.K. Bhakta, R.J.T. Houk, Luminescent metal–organic frameworks, *Chem. Soc. Rev.* 38 (2009) 1330–1352.
- [44] L.V. Meyer, F. Schönfeld, K. Müller-Buschbaum, Lanthanide based tuning of luminescence in MOFs and dense frameworks – from mono- and multimetal systems to sensors and films, *Chem. Commun.* 50 (2014) 8093–8108.

- [45] B. Wang, X.-L. Lv, D. Feng, L.-H. Xie, J. Zhang, M. Li, et al., Highly stable Zr(IV)-based metal – organic frameworks for the detection and removal of antibiotics and organic explosives in water, *J. Am. Chem. Soc.* 138 (2016) 6204–6216.
- [46] A.V. Desai, P. Samanta, B. Manna, S.K. Ghosh, Aqueous phase nitric oxide detection by an amine decorated metal-organic framework, *Chem. Commun.* 51 (2015) 6111–6114.
- [47] C.-Y. Sun, X.-L. Wang, X. Zhang, C. Qin, P. Li, Z.-M. Su, et al., Efficient and tunable white-light emission of metal–organic frameworks by iridium-complex encapsulation, *Nat. Commun.* (2013). Available from: <https://doi.org/10.1038/ncomms3717>.
- [48] K. Jayaramulu, P. Kanoo, S.J. George, T.K. Maji, Tunable emission from a porous metal–organic framework by employing an excited-state intramolecular proton transfer responsive ligand, *Chem. Commun.* 46 (2010) 7906–7908.
- [49] L. Chen, J.-W. Ye, H.-P. Wang, M. Pan, S.-Y. Yin, Z.-W. Wei, et al., Ultrafast water sensing and thermal imaging by a metal-organic framework with switchable luminescence, *Nat. Commun.* (2017). Available from: <https://doi.org/10.1038/ncomms15985>.
- [50] S.V. Eliseeva, J.-C.G. Bünzli, Lanthanide luminescence for functional materials and bio-sciences, *Chem. Soc. Rev.* 39 (2010) 189–227.
- [51] M.L. Cable, J.P. Kirby, H.B. Gray, A. Ponce, Enhancement of anion binding in lanthanide optical sensors, *Acc. Chem. Res.* 46 (2013) 2576–2584.
- [52] L. Prodi, E. Rampazzo, F. Rastrelli, A. Speghinic, N. Zaccheroni, Imaging agents based on lanthanide doped nanoparticles, *Chem. Soc. Rev.* 44 (2015) 4922–4952.
- [53] J. Heine, K. Müller-Buschbaum, Engineering metal-based luminescence in coordination polymers and metal–organic frameworks, *Chem. Soc. Rev.* 42 (2013) 9232–9242.
- [54] B. Yan, Lanthanide-functionalized metal – organic framework hybrid systems to create multiple luminescent centers for chemical sensing, *Acc. Chem. Res.* 50 (2017) 2789–2798.
- [55] X.-Y. Dong, R. Wang, J.-Z. Wang, S.-Q. Zang, T.C.W. Mak, Highly selective Fe³⁺ sensing and proton conduction in a water-stable sulfonate–carboxylate Tb–organic-framework, *J. Mater. Chem. A* 3 (2015) 641–647.
- [56] R.-W. Huang, Y.-S. Wei, X.-Y. Dong, X.-H. Wu, C.-X. Du, S.-Q. Zang, et al., Hypersensitive dual-function luminescence switching of a silver-chalcogenolate cluster-based metal–organic framework, *Nat. Chem.* 9 (2017). Available from: <https://doi.org/10.1038/NCHEM.2718>.
- [57] J. Cornil, D.A. dos Santos, X. Crispin, R. Silbey, J.L. Brédas, Influence of interchain interactions on the absorption and luminescence of conjugated oligomers and polymers: a quantum-chemical characterization, *J. Am. Chem. Soc.* 120 (1998) 1289–1299.
- [58] M. Gutiérrez, F. Sánchez, A. Douhal, Spectral and dynamical properties of a Zr-based MOF, *Phys. Chem. Chem. Phys.* 18 (2016) 5112–5120.
- [59] M. Gutiérrez, R. Navarro, F. Sánchez, A. Douhal, Photodynamics of Zr-based MOFs: effect of explosive nitroaromatics, *Phys. Chem. Chem. Phys.* 19 (2017) 16337–16347.
- [60] P. Deria, J. Yu, T. Smith, R.P. Balaraman, Ground-state versus excited-state interchromophoric interaction: topology dependent excimer contribution in metal – organic framework photophysics, *J. Am. Chem. Soc.* 139 (2017) 5973–5983.
- [61] Y. Takashima, V.M. Martínez, S. Furukawa, M. Kondo, S. Shimomura, H. Uehara, et al., Molecular decoding using luminescence from an entangled porous framework, *Nat. Commun.* (2011). Available from: <https://doi.org/10.1038/ncomms1170>.
- [62] J. An, C.M. Shade, D.A. Chengelis-Czegan, S. Petoud, N.L. Rosi, Zinc-adeninate metal-organic framework for aqueous encapsulation and sensitization of near-infrared and visible emitting lanthanide cations, *J. Am. Chem. Soc.* 133 (2011) 1220–1223.

- [63] J. Yu, Y. Cui, H. Xu, Y. Yang, Z. Wang, B. Chen, et al., Confinement of pyridinium hemicyanine dye within an anionic metal-organic framework for two-photon-pumped lasing, *Nat. Commun.* (2013). Available from: <https://doi.org/10.1038/ncomms3719>.
- [64] Y. Cui, T. Song, J. Yu, Y. Yang, Z. Wang, G. Qian, Dye encapsulated metal-organic framework for warm-white LED with high color-rendering index, *Adv. Funct. Mater.* 25 (2015) 4796–4802.
- [65] A. Lan, K. Li, H. Wu, D.H. Olson, T.J. Emge, W. Ki, et al., Metal-organic framework for the fast and reversible detection of high explosives, *Angew. Chem. Int. Ed.* 48 (2009) 2334–2338.
- [66] S. Pramanik, C. Zheng, X. Zhang, T.J. Emge, J. Li, New microporous metal-organic framework demonstrating unique selectivity for detection of high explosives and aromatic compounds, *J. Am. Chem. Soc.* 133 (2011) 4153–4155.
- [67] S. Pramanik, Z. Hu, X. Zhang, C. Zheng, S. Kelly, J. Li, A systematic study of fluorescence-based detection of nitroexplosives and other aromatics in the vapor phase by microporous metal-organic frameworks, *Chem. Eur. J.* 19 (2013) 15964–15971.
- [68] A.K. Chaudhari, S.S. Nagarkar, B. Joarder, S.K. Ghosh, A continuous π -stacked starfish array of two-dimensional luminescent MOF for detection of nitro explosives, *Cryst. Growth Des.* 13 (2013) 3716–3721.
- [69] X.-G. Liu, H. Wang, B. Chen, Y. Zou, Z.-G. Gu, Z. Zhao, et al., A luminescent metal-organic framework constructed using a tetraphenylethene-based ligand for sensing volatile organic compounds, *Chem. Commun.* 51 (2015) 1677–1680.
- [70] P.-Y. Du, W.P. Lustig, S.J. Teat, W. Gu, X. Liu, J. Li, A robust two-dimensional zirconium-based luminescent coordination polymer built on a V-shaped dicarboxylate ligand for vapor phase sensing of volatile organic compounds, *Chem. Commun.* 54 (2018) 8088–8091.
- [71] M. Jurcic, W.J. Peveler, C.N. Savory, D.O. Scanlon, A.J. Kenyone, I.P. Parkin, The vapour phase detection of explosive markers and derivatives using two fluorescent metal-organic frameworks, *J. Mater. Chem. A* 3 (2015) 6351–6359.
- [72] R. Li, Y.-P. Yuan, L.-G. Qiu, W. Zhang, J.-F. Zhu, A rational self-sacrificing template route to metal-organic framework nanotubes and reversible vapor-phase detection of nitroaromatic explosives, *Small* 8 (2012) 225–230.
- [73] H.-R. Fu, X.-X. Wu, L.-F. Ma, F. Wang, J. Zhang, Dual-emission SG7@MOF sensor via SC – SC transformation: enhancing the formation of excimer emission and the range and sensitivity of detection, *ACS Appl. Mater. Interfaces* 10 (2018) 18012–18020.
- [74] C. Zhang, Y. Che, Z. Zhang, X. Yang, L. Zang, Fluorescent nanoscale zinc(II)-carboxylate coordination polymers for explosive sensing, *Chem. Commun.* 47 (2011) 2336–2338.
- [75] D. Banerjee, Z. Hu, S. Pramanik, X. Zhang, H. Wang, J. Li, Vapor phase detection of nitroaromatic and nitroaliphatic explosives by fluorescence active metal-organic frameworks, *CrystEngComm* 15 (2013) 9745–9750.
- [76] J. Qin, B. Ma, X.-F. Liu, H.-L. Lu, X.-Y. Dong, S.-Q. Zang, et al., Aqueous- and vapor-phase detection of nitroaromatic explosives by a water-stable fluorescent microporous MOF directed by an ionic liquid, *J. Mater. Chem. A* 3 (2015) 12690–12697.
- [77] B. Gole, A.K. Bar, P.S. Mukherjee, Fluorescent metal-organic framework for selective sensing of nitroaromatic explosives, *Chem. Commun.* 47 (2011) 12137–12139.
- [78] H. Xu, F. Liu, Y. Cui, B. Chen, G. Qian, A luminescent nanoscale metal-organic framework for sensing of nitroaromatic explosives, *Chem. Commun.* 47 (2011) 3153–3155.

- [79] Y.-N. Gong, L. Jiang, T.-B. Lu, A highly stable dynamic fluorescent metal–organic framework for selective sensing of nitroaromatic explosives, *Chem. Commun.* 49 (2013) 11113–11115.
- [80] Z.-Q. Shi, Z.-J. Guo, H.-G. Zheng, Two luminescent Zn(II) metal–organic frameworks for exceptionally selective detection of picric acid explosives, *Chem. Commun.* 51 (2015) 8300–8303.
- [81] J. Ye, L. Zhao, R.F. Bogale, Y. Gao, X. Wang, X. Qian, et al., Highly selective detection of 2,4,6-trinitrophenol and Cu^{2+} ions based on a fluorescent cadmium–pamoate metal–organic framework, *Chem. Eur. J* 21 (2015) 2029–2037.
- [82] S. Pal, P.K. Bharadwaj, A luminescent terbium MOF containing hydroxyl groups exhibits selective sensing of nitroaromatic compounds and Fe(III) ions, *Cryst. Growth Des.* 16 (2016) 5852–5858.
- [83] T.K. Pal, N. Chatterjee, P.K. Bharadwaj, Linker-induced structural diversity and photophysical property of MOFs for selective and sensitive detection of nitroaromatics, *Inorg. Chem.* 55 (2016) 1741–1747.
- [84] X.-J. Hong, Q. Wei, Y.-P. Cai, S.-R. Zheng, Y. Yu, Y.-Z. Fan, et al., 2-Fold interpenetrating bifunctional Cd-metal – organic frameworks: highly selective adsorption for CO_2 and sensitive luminescent sensing of nitro aromatic 2,4,6-trinitrophenol, *ACS Appl. Mater. Interfaces* 9 (2017) 4701–4708.
- [85] Y. Hu, M. Ding, X.-Q. Liu, L.-B. Sunb, H.-L. Jiang, Rational synthesis of an exceptionally stable Zn(II) metal–organic framework for the highly selective and sensitive detection of picric acid, *Chem. Commun.* 52 (2016) 5734–5737.
- [86] X. Qi, Y. Jin, N. Li, Z. Wang, K. Wang, Q. Zhang, A luminescent heterometallic metal–organic framework for the naked-eye discrimination of nitroaromatic explosives, *Chem. Commun.* 53 (2017) 10318–10321.
- [87] D.-M. Chen, N.-N. Zhang, C.-S. Liu, M. Du, Dual-emitting dye@MOF composite as a self-calibrating sensor for 2,4,6-trinitrophenol, *ACS Appl. Mater. Interfaces* 9 (2017) 24671–24677.
- [88] M. Bagheri, M.Y. Masoomi, A. Morsali, A. Schoedel, Two dimensional host – guest metal – organic framework sensor with high selectivity and sensitivity to picric acid, *ACS Appl. Mater. Interfaces* 8 (2016) 21472–21479.
- [89] X.-X. Jia, R.-X. Yao, F.-Q. Zhang, X.-M. Zhang, A fluorescent anionic MOF with $\text{Zn}_4(\text{tr})_2$ chain for highly selective visual sensing of contaminants: Cr(III) ion and TNP, *Inorg. Chem.* 56 (2017) 2690–2696.
- [90] S. Khatua, S. Goswami, S. Biswas, K. Tomar, H.S. Jena, S. Konar, Stable multiresponsive luminescent MOF for colorimetric detection of small molecules in selective and reversible manner, *Chem. Mater.* 27 (2015) 5349–5360.
- [91] S. Sanda, S. Parshamoni, S. Biswas, S. Konar, Highly selective detection of palladium and picric acid by a luminescent MOF: a dual functional fluorescent sensor, *Chem. Commun.* 51 (2015) 6576–6579.
- [92] J.-H. Qin, B. Ma, X.-F. Liu, H.-L. Lu, X.-Y. Dong, S.-Q. Zang, et al., Ionic liquid directed syntheses of water-stable Eu– and Tb–organic-frameworks for aqueous-phase detection of nitroaromatic explosives, *Dalton Trans.* 44 (2015) 14594–14603.
- [93] Y.-X. Shi, F.-L. Hu, W.-H. Zhang, J.-P. Lang, A unique Zn(II)-based MOF fluorescent probe for the dual detection of nitroaromatics and ketones in water, *CrystEngComm* 17 (2015) 9404–9412.
- [94] M.-M. Chen, X. Zhou, H.-X. Li, X.-X. Yang, J.-P. Lang, Luminescent two-dimensional coordination polymer for selective and recyclable sensing of nitroaromatic compounds with high sensitivity in water, *Cryst. Growth Des.* 15 (2015) 2753–2760.

- [95] S.S. Nagarkar, A.V. Desai, S.K. Ghosh, A fluorescent metal–organic framework for highly selective detection of nitro explosives in the aqueous phase, *Chem. Commun.* 50 (2014) 8915–8918.
- [96] B. Joarder, A.V. Desai, P. Samanta, S. Mukherjee, S.K. Ghosh, Selective and sensitive aqueous-phase detection of 2,4,6-trinitrophenol (TNP) by an amine-functionalized metal–organic framework, *Chem. Eur. J.* 21 (2015) 965–969.
- [97] S.S. Nagarkar, A.V. Desai, P. Samanta, S.K. Ghosh, Aqueous phase selective detection of 2,4,6-trinitrophenol using a fluorescent metal–organic framework with a pendant recognition site, *Dalton Trans.* 44 (2015) 15175–15180.
- [98] S. Mukherjee, A.V. Desai, B. Manna, A.I. Inamdar, S.K. Ghosh, Exploitation of guest accessible aliphatic amine functionality of a metal – organic framework for selective detection of 2,4,6-trinitrophenol (TNP) in water, *Cryst. Growth Des.* 15 (2015) 4627–4634.
- [99] L.-H. Cao, F. Shi, W.-M. Zhang, S.-Q. Zang, T.C.W. Mak, Selective sensing of Fe^{3+} and Al^{3+} ions and detection of 2,4,6-trinitrophenol by a water-stable terbium-based metal–organic framework, *Chem. Eur. J.* 21 (2015) 15705–15712.
- [100] X.-Z. Song, S.-Y. Song, S.-N. Zhao, Z.-M. Hao, M. Zhu, X. Meng, et al., Single-crystal-to-single-crystal transformation of a europium(III) metal–organic framework producing a multi-responsive luminescent sensor, *Adv. Funct. Mater.* 24 (2014) 4034–4041.
- [101] B. Parmar, Y. Rachuri, K.K. Bisht, R. Laiya, E. Suresh, Mechanochemical and conventional synthesis of Zn(II)/Cd(II) luminescent coordination polymers: dual sensing probe for selective detection of chromate anions and tnp in aqueous phase, *Inorg. Chem.* 56 (2017) 2627–2638.
- [102] Y. Rachuri, B. Parmar, K.K. Bisht, E. Suresh, Multiresponsive adenine-based luminescent Zn(II) coordination polymer for detection of Hg^{2+} and trinitrophenol in aqueous media, *Cryst. Growth Des.* 17 (2017) 1363–1372.
- [103] Y. Rachuri, B. Parmar, K.K. Bishta, E. Suresh, Mixed ligand two dimensional Cd(II)/Ni(II) metal organic frameworks containing dicarboxylate and tripodal N-donor ligands: Cd(II) MOF is an efficient luminescent sensor for detection of picric acid in aqueous media, *Dalton Trans.* 45 (2016) 7881–7892.
- [104] S. Shanmugaraju, C. Dabadie, K. Byrne, A.J. Savyasachi, D. Umadevi, W. Schmitt, et al., A supramolecular Tröger’s base derived coordination zinc polymer for fluorescent sensing of phenolic-nitroaromatic explosives in water, *Chem. Sci.* 8 (2017) 1535–1546.
- [105] P. Das, S.K. Mandal, Strategic design and functionalization of an amine-decorated luminescent metal organic framework for selective gas/vapor sorption and nanomolar sensing of 2,4,6-trinitrophenol in water, *ACS Appl. Mater. Interfaces* 10 (2018) 25360–25371.
- [106] K.S. Asha, G.S. Vaisakhan, S. Mandal, Picogram sensing of trinitrophenol in aqueous medium through a water stable nanoscale coordination polymer, *Nanoscale* 8 (2016) 11782–11786.
- [107] S.S. Dhankhar, N. Sharma, S. Kumar, T.J.D. Kumar, C.M. Nagaraja, Rational design of a bifunctional, two-fold interpenetrated ZnII-metal–organic framework for selective adsorption of CO_2 and efficient aqueous phase sensing of 2,4,6-trinitrophenol, *Chem. Eur. J.* 23 (2017) 16204–16212.
- [108] R. Dalapati, S. Biswas, Post-synthetic modification of a metal-organic framework with fluorescent-tag for dual naked-eye sensing in aqueous medium, *Sensors Actuators B* 239 (2017) 759–767.

- [109] C. Wang, L. Tian, W. Zhu, S. Wang, P. Wang, Y. Liang, et al., Dye@bio-MOF-1 composite as a dual-emitting platform for enhanced detection of a wide range of explosive molecules, *ACS Appl. Mater. Interfaces* 9 (2017) 20076–20085.
- [110] S. Senthilkumar, R. Goswami, N.L. Obasi, S. Neogi, Construction of pillar-layer metal – organic frameworks for CO₂ adsorption under humid climate: high selectivity and sensitive detection of picric acid in water, *ACS Sustainable Chem. Eng.* 5 (2017) 11307–11315.
- [111] J. Yang, Z. Wang, K. Hu, Y. Li, J. Feng, J. Shi, et al., Rapid and specific aqueous-phase detection of nitroaromatic explosives with inherent porphyrin recognition sites in metal – organic frameworks, *ACS Appl. Mater. Interfaces* 7 (2015) 11956–11964.
- [112] Y. Deng, N. Chen, Q. Li, X. Wu, X. Huang, Z. Lin, et al., Highly fluorescent metal – organic frameworks based on a benzene-cored tetraphenylethene derivative with the ability to detect 2,4,6-trinitrophenol in water, *Cryst. Growth Des.* 17 (2017) 3170–3177.
- [113] Z. Hu, S. Pramanik, K. Tan, C. Zheng, W. Liu, X. Zhang, et al., Selective, sensitive, and reversible detection of vapor-phase high explosives via two-dimensional mapping: a new strategy for MOF-based sensors, *Cryst. Growth Des.* 13 (2013) 4204–4207.
- [114] Z. Hu, K. Tan, W.P. Lustig, H. Wang, Y. Zhao, C. Zheng, et al., Effective sensing of RDX via instant and selective detection of ketone vapors, *Chem. Sci.* 5 (2014) 4873–4877.
- [115] Y. Guo, X. Feng, T. Han, S. Wang, Z. Lin, Y. Dong, et al., Tuning the luminescence of metal – organic frameworks for detection of energetic heterocyclic compounds, *J. Am. Chem. Soc.* 136 (2014) 15485–15488.
- [116] H.-R. Fu, L.-B. Yan, N.-T. Wu, L.-F. Ma, S.-Q. Zang, Dual-emission MOF ⊃ dye sensor for ratiometric fluorescence recognition of RDX and detection of a broad class of nitro-compounds, *J. Mater. Chem. A* 6 (2018) 9183–9191.
- [117] M.-H.V. Huynh, M.A. Hiskey, E.L. Hartline, D.P. Montoya, R. Gilardi, Polyazido high-nitrogen compounds: hydrazo and azo-1,3,5-triazine, *Angew. Chem. Int. Ed.* 43 (2004) 4924–4928.
- [118] D.E. Chavez, M.A. Hiskey, R.D. Gilardi, Polyazido high-nitrogen compounds: hydrazo and azo-1,3,5-triazine,3,3'-azobis(6-amino-1,2,4,5-tetrazine): a novel high-nitrogen energetic material, *Angew. Chem., Int. Ed.* 112 (2000) 1861–1863.
- [119] R. Wang, H. Xu, Y. Guo, R. Sa, J.M. Shreeve, Bis[3-(5-nitroimino-1,2,4-triazolate)]-based energetic salts: synthesis and promising properties of a new family of high-density insensitive materials, *J. Am. Chem. Soc.* 132 (2010) 11904–11905.
- [120] M.B. Talawar, R. Sivabalan, T. Mukundan, H. Muthurajan, A.K. Sikder, B.R. Gandhe, et al., Environmentally compatible next generation green energetic materials (GEMs), *J. Hazard. Mater.* 161 (2009) 589–607.
- [121] Y. Li, W.-Y. Zhao, Z.-H. Mi, L. Yang, Z.-N. Zhou, T.-L. Zhang, Graphene-modified explosive lead styphnate composites, *J. Therm. Anal. Calorim.* 124 (2016) 683–691.
- [122] W. Beck, J. Evers, M. Gobel, G. Oehlinger, T.M. Klapotke, The crystal and molecular structure of mercury fulminate (Knallquecksilber), *Z. Anorg. Allg. Chem.* 633 (2007) 1417–1422.
- [123] O.S. Bushuyev, P. Brown, A. Maiti, R.H. Gee, G.R. Peterson, B.L. Weeks, et al., Ionic polymers as a new structural motif for high-energy-density materials, *J. Am. Chem. Soc.* 134 (2012) 1422–1425.
- [124] O.S. Bushuyev, G.R. Peterson, P. Brown, A. Maiti, R.H. Gee, B.L. Weeks, et al., Metal–organic frameworks (MOFs) as safer, structurally reinforced energetics, *Chem. Eur. J.* 19 (2013) 1706–1711.

- [125] X. Qu, S. Zhang, Q. Yang, Z. Su, Q. Wei, G. Xie, et al., Silver(I)-based energetic coordination polymers: synthesis, structure and energy performance, *New J. Chem.* 39 (2015) 7849–7857.
- [126] S. Li, Y. Wang, C. Qi, X. Zhao, J. Zhang, S. Zhang, et al., 3D energetic metal–organic frameworks: synthesis and properties of high energy materials, *Angew. Chem. Int. Ed.* 52 (2013) 14031–14035.
- [127] J.-S. Qin, J.-C. Zhang, M. Zhang, D.-Y. Du, J. Li, Z.-M. Su, et al., A highly energetic N-rich zeolite-like metal-organic framework with excellent air stability and insensitivity, *Adv. Sci.* 2 (2015) 1500150.
- [128] S. Zhang, X. Liu, Q. Yang, Z. Su, W. Gao, Q. Wei, et al., A new strategy for storage and transportation of sensitive high-energy materials: guest-dependent energy and sensitivity of 3D metal–organic-framework-based energetic compounds, *Chem. Eur. J.* 20 (2014) 7906–7910.
- [129] X. Liu, W. Gao, P. Sun, Z. Su, S. Chen, Q. Wei, et al., Environmentally friendly high-energy MOFs: crystal structures, thermostability, insensitivity and remarkable detonation performances, *Green Chem.* 17 (2015) 831–836.
- [130] J. Zhang, Y. Du, K. Dong, H. Su, S. Zhang, S. Li, et al., Taming dinitramide anions within an energetic metal – organic framework: a new strategy for synthesis and tunable properties of high energy materials, *Chem. Mater.* 28 (2016) 1472–1480.
- [131] Q. Wang, X. Feng, S. Wang, N. Song, Y. Chen, W. Tong, et al., Metal-organic framework templated synthesis of copper azide as the primary explosive with low electrostatic sensitivity and excellent initiation ability, *Adv. Mater.* 28 (2016) 5837–5843.
- [132] Y. Zhang, X. Feng, H. Li, Y. Chen, J. Zhao, S. Wang, et al., Photoinduced postsynthetic polymerization of a metal–organic framework toward a flexible stand-alone membrane, *Angew Chem. Int. Ed.* 127 (2015) 4333–4337.
- [133] Y. Chen, S. Li, X. Pei, J. Zhou, X. Feng, S. Zhang, et al., A solvent-free hot-pressing method for preparing metal–organic-framework coatings, *Angew. Chem. Int. Ed.* 55 (2016) 3419–3423.

Green deoxygenation of fatty acids to transport fuels over metal-organic frameworks as catalysts and catalytic supports

Liqiu Yang and Moises A. Carreon*

Department of Chemical and Biological Engineering, Colorado School of Mines, Golden, CO, United States

*Corresponding author. e-mail address: mcarreon@mines.edu

9.1 Introduction

Fossil fuels, such as coal, oil, and natural gas, are still the prime energy sources in the world (approximately 80% of the total use) up to now [1]. However, it is anticipated that these nonrenewable energy sources will be depleted within the next 40–50 years [2]. Meanwhile, the demand of energy will continuously increase because of the rapid growth in human population. Moreover, the expected environmental issues due to the emissions of burning fossil fuels, such as global warming and acid rain, have forced the world to try to shift toward utilizing a variety of renewable and less environmentally harmful energy sources.

As expected, renewable energy sources will play an important role in the future. Renewable energy sources can produce energy repeatedly, for example, solar energy, wind energy, biomass energy, geothermal energy, and so on. As compared to other types of renewable energy resources, such as wind and solar, a biomass energy source has the following advantages, such as easily stored, and at low cost, and can be treated as a more promising energy source. Actually, biomass supplied about 75% of all renewable energy consumed in the world in 2010, and will supply 52% in 2040 [3].

Biomass can be broken into three basic categories, carbohydrates, lignin, and fat/oils [4]. Vegetable oil-based feedstock have gained significant interest because of their high energy density and structural similarity to petroleum-based fuels [5]. Vegetables oils, for example, can be obtained widely from nonedible oil crops, such like algae and jatropha. Waste fats and oils can also be an alternative as an inexpensive nonedible feedstock [6].

However, the direct use of vegetable oils (or fatty acids) as diesels is not desired because of the engine compatibility problems. Therefore several alternative techniques are developed to produce diesel-like hydrocarbons using fatty acids as starting

materials. These processes can be divided into three categories: cracking [7,8], transesterification [9,10], and deoxygenation [11,12]. Catalytic cracking technology can break down a high-molecular mass into fragments with lower molecular mass. The advantages of catalytic cracking include that no H_2 is required and atmospheric processing, leading to reduced operational cost. Although catalytic cracking is considered as a cheaper route, it is highly unselective as lots of hydrocarbons and oxygenates are formed. Therefore catalytic cracking is not a suitable upgrading process of vegetable oils (or fatty acids) to produce diesel-like hydrocarbons. Transesterification is now widely applied to produce biodiesel from fatty acid esters deriving from vegetable oils. However, this biodiesel cannot totally substitute the petroleum-based fuels due to the high oxygen content. While catalytic deoxygenation is a process that involves removal of the carboxyl group in fatty acids as carbon dioxide and/or carbon monoxide using supported metal catalyst, producing alkane and alkene as diesel-like hydrocarbons, it does not necessarily need hydrogen and can produce hydrocarbons in the diesel range with high selectivity. Therefore this chapter will focus on the research into the production of diesel-like hydrocarbons by catalytic deoxygenation of fatty acids over metal-organic frameworks (MOFs) used as catalysts and catalytic supports.

9.2 Why metal-organic frameworks can be catalysts for the deoxygenation of fatty acids to transport fuels?

Various heterogeneous catalysts, such as metals (Pd, Ni, Ru, Pt, Ir, Os, Mo, Co, Cu, and Rh) supported on carbon and numerous metal oxides (CaO-MgO, MgO- Al_2O_3 , ZrO_2 - CeO_2 , Al_2O_3 , ZrO_2 , CeO_2 , SiO_2 , and zeolites), have been employed for deoxygenation of fatty acids and their esters [13–17]. In most of this research, the support employed is either catalytically inert material like carbon or a relatively nonacidic component, like silica or nonacidic alumina. It limits the activity of catalysts to some degree. Recently, our group has reported the catalytic decarboxylation process of oleic acid to branched and aromatic hydrocarbons in a single process step over acidic and basic supports including Pt/SAPO-11 and Pt/chloride Al_2O_3 [18] and Pt/SAPO-34, Pt/DNL-6, Pt/RHO, and Pt/hydrotalcite [19].

MOFs [20,21] are an important class of novel inorganic-organic crystalline materials. One of the most attractive features of MOFs are their uniform micropores, ultrahigh surface areas, and exceptional thermal and chemical stability, making them ideal candidates for catalytic applications. MOFs consist of metal cations or metal-based clusters linked by organic molecules forming a crystalline network, which after removal of guest species may result in three-dimensional structures with permanent porosity [20,22,23]. MOF-based catalysis depends on the active sites; both metal centers and organic linkers contribute to catalytic activities [24]. Specially, the organic bridging linkers may be used as scaffolds for distinct catalytic complexes and biomolecules, and homogeneous catalysts can be immobilized

or encapsulated. The synthetic flexibility of MOF enables considerable control over the size and environment of the pores, allowing selectivity to be tuned more effectively.

Hybrid structure MOF supported on porous beads can also be adopted as a catalyst instead of powder MOF crystals. The benefits of bead catalysts are 100% recyclable, and only a thin MOF layer is required as an active part. This hybrid catalyst configuration is also amenable for scale-up and can work under continuous reaction conditions. In the following paragraphs, we summarize the relevant work on the deoxygenation of fatty acids over MOFs catalysts employed as supports and catalysts.

9.3 MOF powder catalysts for the conversion of fatty acids into transport liquid fuel hydrocarbons

Herein the catalytic decarboxylation process of oleic acid to hydrocarbons over bare and Pt-doped Cu-, Al-, and Ga-based MOF catalysts is described. To our best knowledge, this research work represents one of the first examples demonstrating the catalytic ability of a MOF used as both catalyst and support for the decarboxylation of a model fatty acid molecule.

Cu-, Al-, and Ga-based MOFs were prepared via a solvothermal approach [25]. These three isostructural MOF compositions were chosen based on the different degree of acidities of the metal species (gallium is a hard acid metal and the most acidic, and copper is a borderline acid metal and less acidic). Later these three MOFs were impregnated with platinum at 5 wt%. Oleic acid was employed as the model unsaturated fatty acid molecule. More specific details about the reaction procedure and product analysis are provided in our recent study [26].

The SEM images of Cu-, Al-, and Ga-MOFs are shown in Fig. 9.1. Cu-MOF displays well-faceted hexagonal morphology with relatively narrow size distribution in the range of $\sim 0.8\text{--}1\ \mu\text{m}$. Ga-MOF is larger ($\sim 10\ \mu\text{m}$) in dodecahedral crystalline morphology. And Al-MOF is an hexagonal morphology with a broad size



Figure 9.1 Representative SEM images of (A) Cu-MOF, (B) Ga-MOF, and (C) Al-MOF.

Source: Taken from L.Q. Yang, G.L. Ruess, M.A. Carreon, Cu, Al and Ga based metal-organic framework catalysts for the decarboxylation of oleic acid, Catal. Sci. Technol. 5 (5) (2015) 2777–2782.

distribution and average particle size in the range 0.2–0.8 μm . The X-ray diffraction (XRD) pattern of Cu-MOF (Fig. 9.2C) corresponds to the typical known structure of $\text{Cu}_3(\text{BTC})_2$ [27,28]. The metal-organic framework, $\text{Cu}_3(\text{BTC})_2$ (BTC = benzene-1,3,5-tricarboxylate) is an appealing material to employ as a catalyst for the decarboxylation of fatty acid molecules due to the presence of Lewis acid coordination sites (Cu) in its framework. Fig. 9.2A and B show the XRD patterns of Ga-MOF and Al-MOF, respectively. A shift to lower two-theta angle in the XRD patterns for these two structures was evident compared to Cu-MOF. This shift suggested a higher degree of local structural disorder that was expected due to the incorporation of larger atoms in the porous framework (Cu atomic radius = 0.127 nm; Ga atomic radius = 0.136 nm; Al atomic radius = 0.143 nm) [29].

The degree of decarboxylation of oleic acid over Cu-MOF, Al-MOF, and Ga-MOF crystals at 320°C increased in the following order: Ga-MOF > Al-MOF > Cu-MOF. More specifically, ~66%, ~45%, and ~42% degree of decarboxylation were observed for Ga-MOF, Al-MOF, and Cu-MOF powder catalyst, respectively. Interestingly the catalytic performance of these isostructural MOFs correlated with the degree of metal acidity. Gallium as a hard acid metal is the most acidic, and Cu as a borderline acid metal is the least acidic. The observed catalytic activity of these particular MOF compositions (even without a noble metal) was not surprising since these MOFs had the particular property of exposing their open metal centers making them chemically reactive. In addition, it was recently demonstrated that acidic supports can help promote the decarboxylation of fatty acid molecules [19]. The presence of H_2 promoted the hydrogenation of oleic acid to stearic acid, which then underwent facile decarboxylation. As expected the degree of decarboxylation considerably increased with the addition of 5 wt% of Pt.

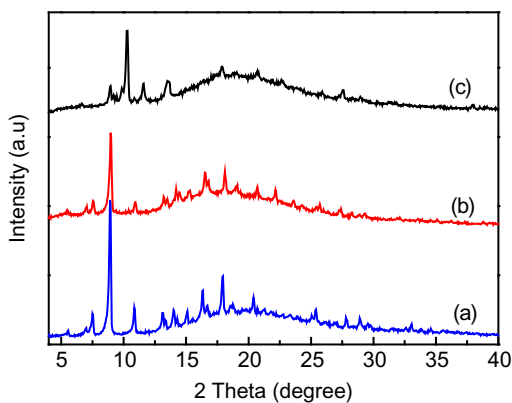


Figure 9.2 XRD patterns of (A) Ga-MOF, (B) Al-MOF, and (C) Cu-MOF.

Source: Taken from L.Q. Yang, G.L. Ruess, M.A. Carreon, Cu, Al and Ga based metal-organic framework catalysts for the decarboxylation of oleic acid, *Catal. Sci. Technol.* 5 (5) (2015) 2777–2782.

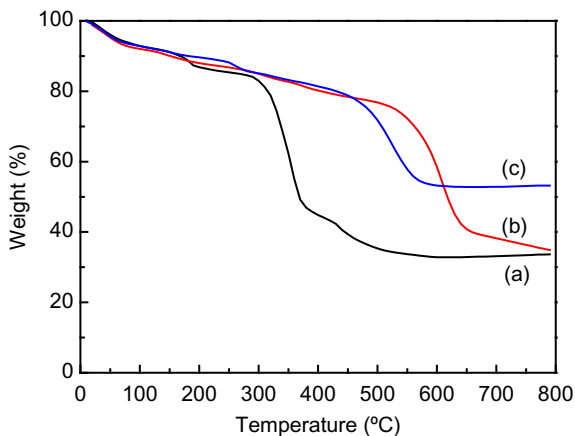


Figure 9.3 TGA profiles of (A) Cu-MOF, (B) Al-MOF, and (C) Ga-MOF.

Source: Taken from L.Q. Yang, G.L. Ruess, M.A. Carreon, Cu, Al and Ga based metal-organic framework catalysts for the decarboxylation of oleic acid, *Catal. Sci. Technol.* 5 (5) (2015) 2777–2782.

Table 9.1 Liquid product distribution for the decarboxylation of oleic acid over Pt/Ga-MOF and Ga-MOF catalysts. Reaction conditions: 10 mL oleic acid, 0.5 g catalyst, 2 h, and 20 bar at 320°C.

Catalyst	Hydrocarbons distribution (%)								
	Octadecane	Heptadecane	Dodecane	Undecane	Decane	Nonane	Octane	Heptane	Unknown
Pt/Ga-MOF	55.13	21.52	—	0.92	1.46	1.71	1.81	1.53	15.92
Ga-MOF	—	5.70	6.72	9.19	9.32	12.76	15.84	12.82	27.65

Source: Taken from L.Q. Yang, G.L. Ruess, M.A. Carreon, Cu, Al and Ga based metal-organic framework catalysts for the decarboxylation of oleic acid, *Catal. Sci. Technol.* 5 (5) (2015) 2777–2782.

Similar to the catalytic activity trend observed for the bare MOFs, the following order was observed for the Pt impregnated MOF catalysts: Pt/Ga-MOF > Pt/Al-MOF > Pt/Cu-MOF. In particular, ~92%, ~90%, and ~46% degree of decarboxylation were observed for Pt/Ga-MOF, Pt/Al-MOF, and Pt/Cu-MOF, respectively.

The influence of recycling on the catalytic performance was also investigated, and slightly lower decarboxylation percentages were observed for all recycled catalysts. This relatively low loss in catalytic activity for the recycled catalysts can be explained partly by the remarkable thermal stability of Cu-MOF, Al-MOF, and Ga-MOF crystals. As shown in Fig. 9.3, all MOFs were thermally stable at least up to ~330°C.

The detailed product distribution for the most active catalysts (Ga-MOF with and without Pt) is given in Table 9.1. The components in the liquid product included long-chain hydrocarbons (octadecane and heptadecane) and lower molecular weight hydrocarbons (mostly C7–C16 paraffins) formed by cracking. No oleic

acid was observed in the products under all reaction conditions, suggesting total conversion of oleic acid.

In summary the catalytic ability of MOFs used both as catalyst and support for the decarboxylation of a model fatty acid was demonstrated. Moderate degrees of decarboxylation were observed for bare MOF crystal catalysts. The incorporation of Pt within the porous MOF resulted in high degrees of decarboxylation. All MOF crystals displayed high thermal stability, resulting in recyclable catalysts displaying low catalytic activity loss. In particular, Ga-MOF catalysts were the most effective catalysts, displaying moderate to high degrees of decarboxylation. The better catalytic performance of Ga-MOF may be related to its higher acidity.

9.4 Supported ZIF-67 catalysts for the conversion of oleic acid into transport liquid fuel hydrocarbons

Here we summarize the most relevant results of a novel catalytic system consisting of Pt supported on zeolite 5A beads covered with ZIF-67 MOF membrane. The resultant catalytic system was evaluated for the decarboxylation of oleic acid to heptadecane [31]. To our best knowledge the catalytic performance of this catalyst system is superior to those of the state-of-the-art catalysts at mild reaction conditions.

Zeolite 5A (in typical chemical composition of $\text{Na}_x\text{Ca}_y[(\text{AlO}_2)_{12}(\text{SiO}_2)_{12}] \cdot x\text{H}_2\text{O}$) beads were chosen because of their high chemical and thermal stability, acidic sites, and commercial availability. It displays LTA topology and has uniform pores of ~ 0.5 nm with surface area of $549 \text{ m}^2/\text{g}$ [30]. ZIF-67 and ZIF-8 MOF were grown on these zeolite 5A beads hydrothermally [31]. After two rounds of hydrothermal treatments, zeolite 5A beads covered with MOFs were obtained. 1 wt % Pt was doped by a conventional wet impregnation method on MOF/zeolite 5A beads and bare zeolite 5A beads, respectively.

The catalytic performance of 1 wt% Pt/zeolite 5A bead catalyst was evaluated for the decarboxylation of oleic acid at 320°C and 20 bar, and decarboxylation as high as $\sim 98.7\%$ was observed. Heptadecane selectivity of $\sim 75\%$ was achieved for fresh catalyst. In principle the fact that only 1 wt% Pt was required to gain such high heptadecane selectivity, suggested that Pt was well dispersed on the surface of the beads, resulting in a fast surface reaction, and therefore high heptadecane selectivity. Heptadecane selectivity decreased to 52% for the first recycled catalyst, and 46% for the second recycled catalyst. This decrease in heptadecane selectivity may be partly explained by the considerable decrease in surface area of the catalyst (from 530 to $230 \text{ m}^2/\text{g}$). Pore volume also decreased from fresh to recycled catalysts, suggesting that micropores were partially blocked. Raman spectroscopy indicated the presence of surface carbonaceous species (at frequency $\sim 1500\text{--}1750 \text{ cm}^{-1}$) in the external surface for a second recycled 1 wt% Pt/zeolite 5A catalyst (Fig. 9.4).

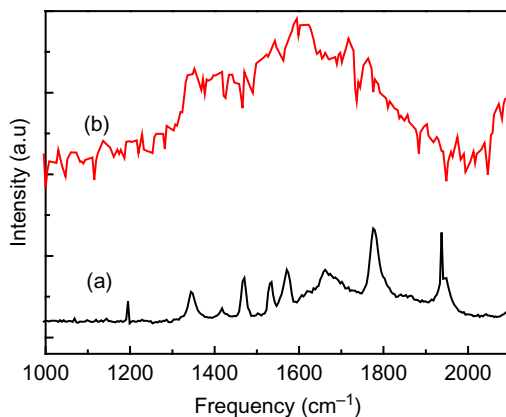


Figure 9.4 Raman spectra for (A) fresh 1 wt% Pt/zeolite 5A catalyst and (B) second recycled 1 wt% Pt/zeolite 5A catalyst.

Source: Taken from L.Q. Yang, K.L. Tate, J.B. Jasinski, M.A. Carreon, Decarboxylation of oleic acid to heptadecane over Pt supported on zeolite 5A beads, *ACS Catal.* 5 (11) (2015) 6497–6502.

Previously, our group found that microporous crystalline phases with pore sizes between ~ 0.35 and 0.38 nm can be beneficial for improving heptadecane selectivity [19]. We postulated that potentially a “molecular sieving effect” was in part responsible for this improving catalytic behavior. Based on this premise, and on the fact that transition metals such as Co have been demonstrated to be an alternative and viable replacement of Pt to improve catalyst stability [32], we incorporated a cobalt-based MOF (known as ZIF-67) membrane on the surface of zeolite 5A beads. ZIF-67 is a cobalt-based zeolitic imidazolate framework displaying SOD topology with large pores of diameter 1.16 nm that are accessible through small pore windows of diameter 0.34 nm, which has recently received considerable attention due to its desirable properties as catalyst, adsorbent, sensor, and membrane [33]. Then, zeolite 5A beads growing with ZIF-67 membrane were impregnated with 1 wt% Pt and evaluated in the decarboxylation process of oleic acid.

A representative SEM image of 1 wt% Pt/ZIF-67 membrane/zeolite 5A bead catalyst shows a continuous ZIF-67 membrane of ~ 300 μm thickness (Fig. 9.5). Decarboxylation as high as $\sim 99\%$ was reached for this catalyst (similar to the catalyst without ZIF-67 membrane) with heptadecane selectivity of 82% for the fresh catalyst. The use of a microporous ZIF-67 crystalline layer improved the heptadecane selectivity obviously, but most importantly improved the stability of the resultant catalyst. It was found that the recycled 1 wt% Pt/ZIF-67 membrane/zeolite 5A bead catalysts decreased its performance to 64% and 60% for the first recycled and second recycled catalysts, respectively. The surface area of the second recycled catalyst decreased only to 402 m^2/g as compared to 560 m^2/g of the fresh catalyst, indicating a much lower decrease in surface area as compared to the catalyst prepared in the absence of ZIF-67 membrane. XRD patterns for all



Figure 9.5 Representative SEM image of a 1 wt% Pt/ZIF-67 membrane/zeolite 5A bead catalyst.

Source: Taken from L.Q. Yang, K.L. Tate, J.B. Jasinski, M.A. Carreon, Decarboxylation of oleic acid to heptadecane over Pt supported on zeolite 5A beads, *ACS Catal.* 5 (11) (2015) 6497–6502.

studied catalysts showed the typical known structure of zeolite 5A which crystallizes in the LTA topology. This confirmed that the crystalline structure of zeolite 5A was preserved after Pt deposition, after the incorporation of ZIF-67 membrane, and after two rounds of recycling, suggesting high structural stability for all catalysts.

The detailed liquid product distribution of all studied catalysts (fresh and recycled) was given in [Table 9.2](#). The components in the liquid product included long-chain hydrocarbons (octadecane and heptadecane), and short-chain hydrocarbons (mostly C7–C16 paraffins) formed by cracking. No detectable oleic acid was observed in the products under the prevailing reaction conditions, suggesting total conversion of oleic acid (and supported by the observed high decarboxylation percentages).

To have a better understanding of the role of ZIF-67 on the surface of zeolite 5A beads, we performed TEM and EDX analysis. [Fig. 9.6A and B](#) shows representative STEM images of fresh 1 wt% Pt catalysts without and with ZIF-67 membrane. In both cases a high density of well-dispersed platinum nanoparticles was observed. However, for the catalyst without ZIF-67 membrane incorporated, some clustering of Pt was formed, indicating that Pt nanoparticles dispersed better when ZIF-67 layer was present. The Pt particle histograms shown in [Fig. 9.6C and D](#) confirmed that a relatively narrow particle size distribution centered at ~ 1 nm was observed for the catalyst containing the ZIF-67 layer ([Fig. 9.6D](#)). However, for the catalyst without the ZIF-67 layer ([Fig. 9.6C](#)), the size distribution was relatively broad, ranging from ~ 0.5 to ~ 2.5 nm. STEM shown in [Fig. 9.6](#) suggest a much better dispersion of Pt was obtained for the catalyst with the ZIF-67 membrane. The ordered porous structure of ZIF-67 served as a more uniform region in which Pt

Table 9.2 Liquid product distribution for the studied catalysts. Reaction conditions: $P = 20$ bar, $t = 2$ h, $T = 320^\circ\text{C}$, mass ratio of catalyst to oleic acid = 1:1.

Catalysts	Hydrocarbons distribution (%)				
	Octadecane	Heptadecane	Dodecane	Undecane	Decane
Zeolite 5A	11.36	59.32	3.37	5.65	5.65
Fresh Pt/zeolite 5A	22.12	74.99	0.39	0.46	0.51
First recycled Pt/zeolite 5A	46.98	51.67	0.16	0.19	0.23
Second recycled Pt/zeolite 5A	52.05	46.00	0.30	0.34	0.34
Fresh Pt/ZIF-67 membrane/zeolite 5A	17.03	79.89	0.32	0.37	0.45
First recycled Pt/ZIF-67 membrane/zeolite 5A	34.72	63.64	0.20	0.28	0.29
Second recycled Pt/ZIF-67 membrane/zeolite 5A	38.91	60.12	0.08	0.10	0.15

Catalysts	Hydrocarbons distribution (%)			
	Nonane	Octane	Heptane	Unknown
Zeolite 5A	5.17	6.72	—	2.77
Fresh Pt/zeolite 5A	0.52	0.40	0.27	0.33
First recycled Pt/zeolite 5A	0.26	0.21	0.17	0.13
Second recycled Pt/zeolite 5A	0.28	0.18	0.05	0.46
Fresh Pt/ZIF-67 membrane/zeolite 5A	0.50	0.45	0.36	0.62
First recycled Pt/ZIF-67 membrane/zeolite 5A	0.33	0.25	0.18	0.11
Second recycled Pt/ZIF-67 membrane/zeolite 5A	0.19	0.17	0.17	0.11

Source: Taken from L.Q. Yang, K.L. Tate, J.B. Jasinski, M.A. Carreon, Decarboxylation of oleic acid to heptadecane over Pt supported on zeolite 5A beads, ACS Catal. 5 (11) (2015) 6497–6502.

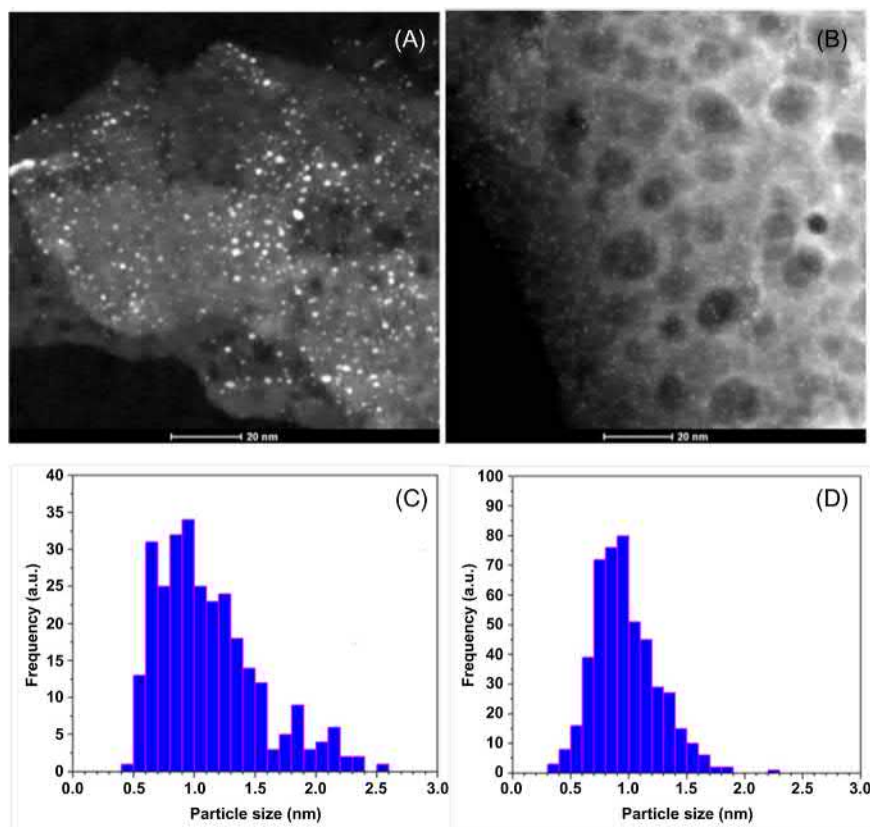


Figure 9.6 Representative STEMs of fresh (A) 1 wt% Pt/zeolite 5A, (B) 1 wt% Pt/ZIF-67 membrane/zeolite 5A bead catalysts, and Pt particle size distribution of (C) 1 wt% Pt/zeolite 5A, and (D) 1 wt% Pt/ZIF-67 membrane/zeolite 5A bead catalysts.

Source: Taken from L.Q. Yang, K.L. Tate, J.B. Jasinski, M.A. Carreon, Decarboxylation of oleic acid to heptadecane over Pt supported on zeolite 5A beads, *ACS Catal.* 5 (11) (2015) 6497–6502.

particles can be distributed. EDX analysis provided useful information on the degree of Pt leaching for the recycled catalysts. A lower Pt loss was observed when ZIF-67 was incorporated in the catalyst ($\sim 15\%$ Pt loss when ZIF-67 was used vs $\sim 26\%$ loss in the absence of ZIF-67 after second recycle). This behavior may be related to a better “grafting” of Pt particles within the ZIF-67 porous structure. Our results suggested that the addition of ZIF-67 layer, in general: (1) promoted Pt particle dispersion on the beads; (2) reduced Pt leaching after reactions, resulting in improved catalytic performance; and (3) the presence of Co as coordinating metal, resulted in a more active and stable catalysts (lower catalytic activity reduction after reactions).

It was observed that even in the absence of the ZIF-67 membrane, the catalysts were still active. Therefore the main role of cobalt was believed to be to act as cocatalyst or promoter. There are numerous examples in the literature in which Co has been used as a cocatalyst (or promoter) for hydrodeoxygenation and decarboxylation reactions. For example, Wang et al. reported a positive synergistic effect when Co was incorporated into Mo-based catalysts for an enhanced catalytic activity for hydrodeoxygenation of bio-oils [34]. Furthermore, cobalt-based catalysts enhance the C(sp²)-O cleavage via direct deoxygenation pathway [35].

To prove the benefits of having Co in the porous structure, we prepared an isostructural layer of ZIF-8 (in which instead of using Co, Zn is employed as coordinating metal) [33]. When ZIF-8 layer was employed, the yield to heptadecane for the fresh catalyst was only 57%, suggesting that indeed Co helped to promote the formation of a higher yield of heptadecane, as well as to improve catalyst stability. Besides, Pt leaching was ~24% for the second recycled catalyst with the ZIF-8 layer compared to ~15% when ZIF-67 was employed. This observation together with the poor Pt dispersion (Pt particle size distribution was in the range of 1–20 nm) on ZIF-8 coated zeolite 5A beads shown in Fig. 9.7 may explain the lower heptadecane yield observed for 1 wt% Pt/ZIF-8 membrane/zeolite 5A catalyst.

Table 9.3 compares the state-of-the-art catalysts which have been employed specifically for the catalytic conversion of oleic acid to heptadecane. Among all these catalysts, 1 wt % Pt/ZIF-67 membrane/zeolite 5A catalyst and the recently reported activated carbon [38] show the highest yields to heptadecane. Although both types of catalysts show very similar heptadecane yields (~80%), the Pt/ZIF-67 membrane/zeolite 5A catalyst developed in our group effectively catalyzes the decarboxylation reaction at mild pressure and temperature (20 bar, 320°C) as compared to 240 bar and at least 370°C required for the activated carbon.

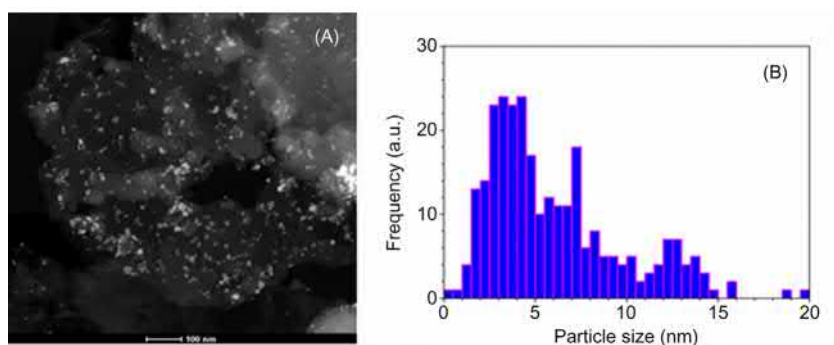


Figure 9.7 (A) Representative STEM and (B) Pt particle size distribution of fresh 1 wt% Pt/ZIF-8 membrane/zeolite 5A bead catalyst.

Source: Taken from L.Q. Yang, K.L. Tate, J.B. Jasinski, M.A. Carreon, Decarboxylation of oleic acid to heptadecane over Pt supported on zeolite 5A beads, ACS Catal. 5 (11) (2015) 6497–6502.

Table 9.3 Comparison of the catalytic conversion of oleic acid to heptadecane through different catalysts. Only the best catalytic performance of each reference is provided.

Entry	Catalyst	Reaction conditions	Mass ratio of metal to oleic acid	Conversion (%)	Heptadecane selectivity (%)	References
1	5 wt% Pd/C	$P = 15 \text{ bar}, T = 300^\circ\text{C}, t = 3 \text{ h}$	1:92	11	12	[36]
2	5 wt% Pd/C	$P = 27 \text{ bar}, T = 360^\circ\text{C}, t = 6 \text{ h}$	1:115	99	26	[37]
3	Activated carbon	$T = 370^\circ\text{C}, t = 3 \text{ h}$	–	80 ± 4	7 ± 1	[38]
4	SnAlMg-2	$T = 300^\circ\text{C}, t = 6 \text{ h}$	1:75	71.1	3.7	[39]
5	5 wt% Pt/C	$T = 623 \text{ K}, t = 3 \text{ h}$	1:409	99	71	[40]
6	Ce _{0.6} Zr _{0.4} O ₂	$T = 300^\circ\text{C}, t = 6 \text{ h}$	1:40	94.6	11	[41]
7	Fe-MSN	$P = 30 \text{ bar}, T = 290^\circ\text{C}, t = 6 \text{ h}$	1:4.7	100	12	[16]
8	Pt-Re/C	$P = 0.35 \text{ MPa}, T = 300^\circ\text{C}, t = 9 \text{ h}$	1:769	92	40	[42]
9	Pd/Si-C-4	$P = 1.5 \text{ MPa}, T = 300^\circ\text{C}, t = 1 \text{ h}$	1:89	90	31	[43]
10	Co _{0.5} Mo _{0.5}	$T = 300^\circ\text{C}, t = 3 \text{ h}$	1:40	88.1	6.1	[44]
11	Pt/SAPO-34	$P = 20 \text{ bar}, T = 325^\circ\text{C}, t = 2 \text{ h}$	1:400	98	66.9	[45]
12	MgO-Al ₂ O ₃	$T = 673 \text{ K}, t = 3 \text{ h}$	1:42	98	6.93	[46]
13	1 wt% Pd/C	$T = 300^\circ\text{C}, t = 5.5 \text{ h}$	–	12	39	[47]
14	5 wt% Pt/ γ -Al ₂ O ₃	$P = 20 \text{ bar}, T = 325^\circ\text{C}, t = 5 \text{ h}$	–	100	–	[48]
15	NiWC/Al-SBA-15	4 h in super-critical water	1:44	30.7	0.72	[49]
16	Activated carbon	$P = 24.1 \text{ MPa}, T = 370 \pm 2^\circ\text{C}$	–	99.4 ± 0.5	80.6 ± 4	[50]
17	Pd/carbon bead	$P = 20 \text{ atm}, T = 573 \text{ K}, t = 9 \text{ h}$	1:66	100	70.5	[50]
18	Pt ₃ Sn/C	$T = 350^\circ\text{C}, t = 2 \text{ h}$	1:113	100	60	[51]
19	5 wt% Pd/ γ -Al ₂ O ₃	$P = 5 \text{ MPa}, T = 330^\circ\text{C},$ LHSV = 2 h^{-1}	–	94.6	72	[15]
20	5 wt% Pt/Ga-MOF	$P = 20 \text{ bar}, T = 320^\circ\text{C}, t = 2 \text{ h}$	1:360	91	21.5	[26]
21	5 % Pt/C	$T = 330^\circ\text{C}, t = 2 \text{ h}$	1:199	–	18	[52]
22	Pt/ZIF-67/zeolite 5 A	$P = 20 \text{ bar}, T = 320^\circ\text{C}, t = 2 \text{ h}$	1:100	98.7	81.5 ± 3	[31]

Note: in entry 2, 6, 7, 11, 13, 14, 17, 19, 20 and 22, hydrogen was used.

Source: Taken from L.Q. Yang, K.L. Tate, J.B. Jasinski, M.A. Carreon, Decarboxylation of oleic acid to heptadecane over Pt supported on zeolite 5A beads, ACS Catal. 5 (11) (2015) 6497–6502.

In conclusion, the catalytic deoxygenation of oleic acid to heptadecane over Pt supported on ZIF-67/zeolite 5A beads was demonstrated. The use of a microporous ZIF-67 crystalline layer improved the heptadecane selectivity, but most importantly improved the stability of the resultant catalyst. Heptadecane yields as high as ~81% were observed for fresh catalyst. The Pt/ZIF-67 membrane/zeolite 5A bead catalyst displayed a low loss of catalytic activity after two rounds of recycling. To our best knowledge, the catalytic performance of 1 wt % Pt/ZIF-67 membrane/zeolite 5A bead catalyst was superior to those of state-of-the-art catalysts at mild reaction conditions.

9.5 Supported ZIF-67 catalysts for the conversion of saturated acids into transport liquid fuel hydrocarbons

Besides unsaturated fatty acids, saturated fatty acids have been also used as starting materials for producing liquid fuels. Therefore the deoxygenation of two representative saturated fatty acids over 0.5 wt% Pt/ZIF-67 membrane/zeolite 5A bead catalysts will be discussed in this section. In our reaction system two distinctive reaction pathways were observed depending on the reaction gas atmosphere: decarboxylation and hydrodeoxygenation. In particular, we found that the decarboxylation reaction pathway was more favorable in the presence of helium and CO₂, while the hydrodeoxygenation pathway strongly competed against the decarboxylation pathway when hydrogen was applied during the deoxygenation processes. Esters were identified as the key reaction intermediates, which converted to final products through decarboxylation and the hydrodeoxygenation pathway.

It is learnt that palmitic acid and lauric acid are present in vegetable oils in considerable amounts. For example, the composition of palmitic acid in several vegetable oils can be as high as 20% [53]. Lauric acid comprises ~50% of the fatty acid content in coconut milk, coconut oil, laurel oil, and palm kernel oil [54]. Therefore palmitic acid and lauric acid were chosen as the model saturated fatty acid molecules.

It was found that almost complete conversion (deoxygenation percentage was no less than 95%) of the two fatty acids was observed over both fresh and recycled catalyst after 2 hours reaction time. Similar catalytic performance was displayed by the recycled catalysts in comparison with the fresh ones, indicating chemical stability of the catalysts. By XRD technique we confirmed that our catalysts preserved the crystalline structure of zeolite 5A after Pt deposition, after the incorporation of ZIF-67 membrane and after one recycling, suggesting the high structural stability of these catalysts. Continuous ZIF-67 membranes of ~230–270 μm thickness were observed from SEM images of fresh and recycled 0.5 wt% Pt/ZIF-67 membrane/zeolite 5A bead catalyst. The regular and consistent ZIF-67 thickness observed for the fresh and recycled catalysts indicated good mechanical stability of the catalyst. The N₂ BET surface areas of the recycled catalysts slightly declined to

450–464 m²/g as compared to the fresh ones (470 m²/g), suggesting that the catalyst can be regenerated completely after reactions.

The deoxygenation of palmitic acid in the presence of H₂ atmosphere was carried out at 280 and 320°C, and clear liquid products were obtained at both reaction temperatures. The resultant products were long-chain hydrocarbons: hexadecane and pentadecane; and short-chain hydrocarbons: C7–C14. With decreasing temperature, long-chain hydrocarbons slightly increased in the selectivity. On the other hand, the fact that the selectivity to short-chain hydrocarbons increased at higher reaction temperature suggested cracking of hydrocarbon products happened. When lauric acid was used as a reactant under the same reaction conditions, the observed products were long-chain hydrocarbons: dodecane and undecane; and short-chain hydrocarbons: C7–C10. Similar to the case of palmitic acid, the selectivity to long-chain hydrocarbons was slightly higher at low reaction temperature, and more short-chain hydrocarbons were formed at a high reaction temperature.

We studied the effects of three distinctive reaction gas atmospheres: hydrogen (reducing); helium (inert); and CO₂ (oxidant) for deoxygenation of palmitic and lauric acid. By analyzing the product distribution, as shown in Tables 9.4 and 9.5, when He and CO₂ were supplied during reaction, we found decarboxylation was the main reaction pathway, and high selectivity to pentadecane and undecane was obtained as a result. On the other hand, major decarboxylation products (pentadecane and undecane) and minor hydrodeoxygenation products (hexadecane and dodecane) were observed when H₂ was introduced to the reaction system. Specifically, pentadecane and undecane were the main products for the deoxygenation of palmitic and lauric acids over Pt/ZIF-67 membrane/zeolite 5A catalysts under all gas atmospheres, respectively. The selectivity of pentadecane as high as ~88% and 92% was observed in the presence of He and CO₂, respectively, indicating that decarboxylation was the dominant reaction pathway. On the other hand, when H₂ was used as reaction gas, the selectivity of pentadecane decreased to ~62%. Correspondingly, the selectivity of hexadecane under this condition was much higher (~24%). These results indicated a competition between decarboxylation (pentadecane preferred) and hydrodeoxygenation (hexadecane preferred) pathway. A similar reaction pathway trend was observed for the case of lauric acid. Specifically, in the presence of He and CO₂, decarboxylation was the dominant reaction pathway, and high selectivities of undecane of ~88% and 93% were obtained, respectively. When H₂ was used as reaction gas, the undecane selectivity decreased to ~60%, and dodecane selectivity was ~36%. These results also verified that decarboxylation product (undecane) and hydrodeoxygenation product (dodecane) competed with each other.

The effect of the gas environment on the selectivity of product for the deoxygenation of several fatty acids is well documented in previous studies [55–59]. It has been learnt that direct decarboxylation and decarbonylation of fatty acids are more favorable over supported noble metal catalysts, such as Pt/C and Pd/C, leading to the production of hydrocarbons with one carbon number less than the starting materials, even under inert atmospheres [55,56]. The reaction pathway becomes more complicated with hydrogen input because hydrodeoxygenation takes place [50].

Table 9.4 Hydrocarbon product distribution for the deoxygenation of palmitic acid over 0.5 wt% Pt/ZIF-67 membrane/zeolite 5A bead catalysts.

Temperature(°C)	Gas atmosphere	Hydrocarbon distribution (%)					
		Hexadecane	Pentadecane	Tetradecane	Tridecane	Dodecane	
280	H ₂	34.89 (40.51)	62.64 (55.86)	0.16 (0.18)	0.15 (0.14)	0.61 (1.06)	
320	H ₂	23.55 (31.70)	62.84 (58.53)	0.73 (0.38)	0.74 (0.35)	1.28 (0.84)	
320	He	1.13 (1.67)	89.51 (83.93)	1.50 (2.36)	1.46 (1.71)	1.38 (1.67)	
320	CO ₂	0.69 (1.33)	91.67 (88.02)	1.18 (1.78)	1.27 (1.44)	0.69 (0.88)	
Temperature (°C)	Gas atmosphere	Hydrocarbon distribution (%)					
		Undecane	Decane	Nonane	Octane	Heptane	Unknown
280	H ₂	0.97 (1.51)	0.12 (0.10)	0.12 (0.09)	0.11 (0.08)	0.07 (0.06)	0.16 (0.41)
320	H ₂	1.78 (1.19)	1.13 (0.50)	1.14 (0.49)	1.02 (0.46)	0.74 (0.32)	5.05 (5.24)
320	He	1.61 (3.91)	0.93 (0.75)	0.75 (0.64)	0.63 (0.49)	0.29 (0.35)	0.81 (2.52)
320	CO ₂	2.25 (3.35)	0.78 (0.79)	0.51 (0.44)	0.52 (0.40)	0.20 (0.10)	0.24 (1.47)

Source: Taken from L.Q. Yang, M.A. Carreon, Deoxygenation of palmitic and lauric acids over Pt/ZIF-67 membrane/zeolite 5A bead catalyst, ACS Appl. Mater. Interfaces 9 (37) (2017) 31993–32000.

Table 9.5 Hydrocarbon product distribution for the deoxygenation of lauric acid over 0.5 wt% Pt/ZIF-67 membrane/zeolite 5A bead catalysts.

Temperature (°C)	Gas atmosphere	Hydrocarbon distribution (%)						
		Dodecane	Undecane	Decane	Nonane	Octane	Heptane	Unknown
280	H ₂	40.60 (43.83)	58.18 (54.90)	0.38 (0.38)	0.19 (0.21)	0.12 (0.13)	0.08 (0.10)	0.45 (0.45)
320	H ₂	34.74 (36.88)	59.79 (56.62)	0.67 (0.46)	0.49 (0.30)	0.40 (0.21)	0.33 (0.13)	3.58 (5.4)
320	He	3.83 (3.92)	88.69 (84.39)	0.89 (1.96)	0.82 (1.64)	0.42 (1.10)	0.27 (1.19)	5.08 (5.8)
320	CO ₂	1.76 (2.17)	93.52 (90.06)	0.84 (0.88)	0.78 (0.85)	0.62 (0.69)	0.66 (0.50)	1.82 (4.85)

Source: Taken from L.Q. Yang, M.A. Carreon, Deoxygenation of palmitic and lauric acids over Pt/ZIF-67 membrane/zeolite 5A bead catalyst, ACS Appl. Mater. Interfaces 9 (37) (2017) 31993–32000.

The hydrogenation of carboxylic acids (R-COOH) takes place rapidly in a hydrogen-rich atmosphere and they are transformed into their corresponding aldehydes (R-CHO) at the initial stage of the reaction, which is then followed by two reaction pathways: decarbonylation to produce hydrocarbons with one carbon number less and CO, or further hydrogenation to alcohol resulting in hydrocarbons with the same carbon number as the starting fatty acid [50]. Therefore the ratio of $C_nH_{2n+2}/C_{n-1}H_{2n}$ products is an indication of the hydrogenation ability of the catalyst [56]. In our case, the fact that the production of hexadecane from palmitic acid and dodecane from lauric acid increased obviously when hydrogen was introduced to the reaction system indicates that hydrodeoxygenation of these fatty acids took place.

To learn better about the deoxygenation process of the studied fatty acids over our Pt/ZIF-67 membrane/zeolite 5A bead catalyst, we collected FTIR spectra of some reaction products obtained from deoxygenation of lauric acid (H_2 and CO_2 atmosphere) as a function of temperature (seen in Fig. 9.8). The stretching bonds in the esters group (at $\sim 1750\text{ cm}^{-1}$ in FTIR spectra) were present at temperatures between 150°C and 280°C in the presence of hydrogen (Fig. 9.8A) [60] and disappeared at 300°C , suggesting that the esters formed as intermediates at low reaction temperatures and converted to the observed hydrocarbons at high reaction temperature. Interestingly, under CO_2 atmosphere the peak associated to the esters did not disappear even at 320°C . This observation of the presence (or absence) of the ester intermediates indicated that the gas atmosphere did have an influence on the reaction pathway (decarboxylation vs hydrodeoxygenation).

Based on our observations we brought up two reaction pathways for the deoxygenation of palmitic and lauric acid over Pt/ZIF-67 membrane/zeolite 5A catalysts under different gas atmospheres, as shown in Fig. 9.9. In the presence of He and CO_2 , the fatty acids converted to relative stable ester intermediates. As the reaction proceeded, these esters transformed directly via decarboxylation into hydrocarbons with one carbon number less. On the other hand, intermediate esters were also observed with H_2 input and disappeared in the $280\text{--}300^\circ\text{C}$ temperature range. We hypothesized that these esters rapidly transformed into alcohols based on the fact that aromatic and aliphatic esters can be converted rapidly into the corresponding alcohols in the presence of reducing (hydrogen) agents [61]. In this proposed pathway, the alcohol was hydrogenated completely, resulting in a hydrocarbon with the same carbon number (hydrodeoxygenation pathway). Shimizu and coworkers reported a similar reaction pathway [62]. In their work they found that the ester formed from lauric acid underwent hydrogenolysis to form alcohol, which was then hydrogenated to the corresponding alkane.

The catalytic performance of the state-of-the-art catalysts that have been employed for the deoxygenation of palmitic acid and lauric acid is summarized in Table 9.6. Two supported noble catalysts, Pt supported on carbon and Pd supported on ZrO_2 catalysts gave the best catalytic performance for the conversion of palmitic acid to pentadecane (entries 1 and 3), for example, as high as 98%–100% selectivity of pentadecane. However, high noble metal loadings (5 wt%) were required for both catalysts. Furthermore, severe reaction conditions, such as long reaction time

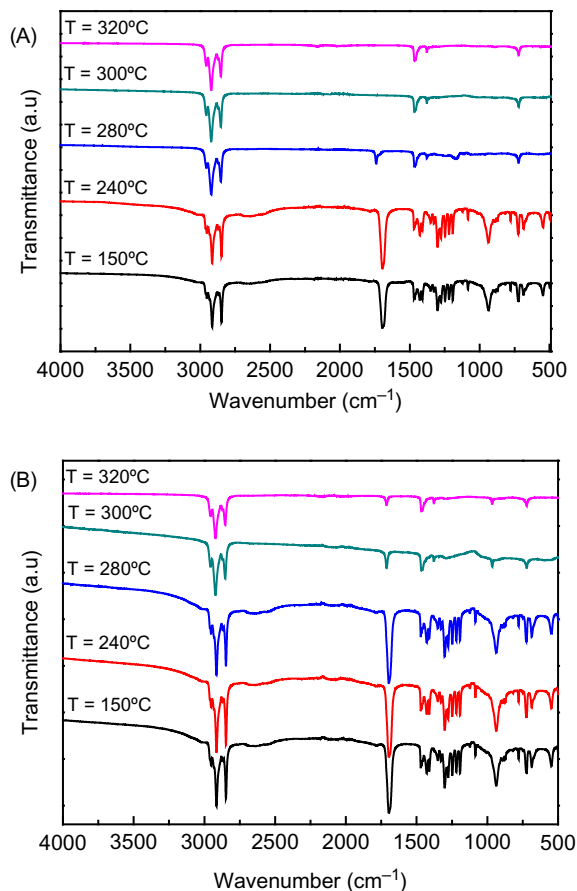


Figure 9.8 FTIR profiles for product samples obtained from deoxygenation of lauric acid at different reaction temperature under (A) H_2 atmosphere and (B) CO_2 atmosphere. Reaction conditions: mass ratio of catalyst and lauric acid = 1:1, $P = 20$ bar, $t = 0$ h.

Source: Taken from L.Q. Yang, M.A. Carreon, Deoxygenation of palmitic and lauric acids over Pt/ZIF-67 membrane/zeolite 5A bead catalyst, ACS Appl. Mater. Interfaces 9 (37) (2017) 31993–32000.

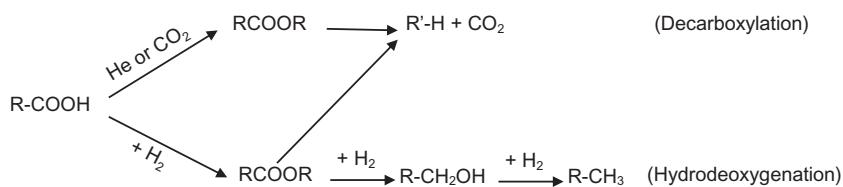


Figure 9.9 Suggested reaction pathway for the deoxygenation of fatty acids over 0.5 wt% Pt/ZIF-67 membrane/zeolite 5A bead catalysts under different reaction gas atmospheres.

Source: Taken from L.Q. Yang, M.A. Carreon, Deoxygenation of palmitic and lauric acids over Pt/ZIF-67 membrane/zeolite 5A bead catalyst, ACS Appl. Mater. Interfaces 9 (37) (2017) 31993–32000.

Table 9.6 Comparison of the catalytic conversion of palmitic acid and lauric acid through different catalysts.^a

Entry	Catalyst	Reaction conditions	Mass ratio of metal to palmitic acid	Conversion (%)	Pentadecane selectivity (%)	References
1	5 wt% Pt/C	$T = 290^{\circ}\text{C}$, $t = 6$ h	1:200	100	100	[63]
2	Activated carbon	$T = 370^{\circ}\text{C}$, $t = 3$ h	–	33 ± 13	58 ± 4	[38]
3	5 wt% Pd/ZrO ₂	$T = 260^{\circ}\text{C}$, $P = 12$ bar, $t = 2$ h	1:40	98	98	[57]
4	10% Ni/10% NbO ₂ /SiO ₂	$T = 220^{\circ}\text{C}$, $P = 25$ bar, $t = 24$ h	1:10	100	13.9	[64]
5	Ni _{1.0} P/AC	$T = 350^{\circ}\text{C}$, $t = 2.5$ h	–	99.4	74.9	[65]
6	Ni(OAc) ₂	$T = 350^{\circ}\text{C}$, $t = 4.5$ h	–	53.1	35.4	[66]
7	20 wt% Mo/HZ-C	$T = 260^{\circ}\text{C}$, $P = 40$ bar, $t = 4$ h	1:25	100	35.1	[67]
8	4 wt% Ni/HZ-3	$T = 220^{\circ}\text{C}$, $P = 40$ bar	1:125	100	44.0	[68]
9	NiMCF(9.2T-3D)	$T = 300^{\circ}\text{C}$, $t = 6$ h	–	86.4	31.8	[69]
10	5 wt% Pd/CNTs	$T = 260^{\circ}\text{C}$, $P = 40$ bar, $t = 4$ h	1:40	93.3	85.4	[70]
11	10 wt% Ni/ZrO ₂	$T = 290^{\circ}\text{C}$, $P = 55.2$ bar, $t = 6$ h	1:10	97.2	35.6	[71]
12	0.5 wt%Pt/ZIF-67/5A	$T = 320^{\circ}\text{C}$, $P = 20$ bar, $t = 2$ h	1:200	95	91.7	[72]
Entry	Catalyst	Reaction conditions	Mass ratio of metal to lauric acid	Conversion (%)	Pentadecane selectivity (%)	References
13	5 wt% Pd/C	$T = 300^{\circ}\text{C}$, $P = 13$ bar	–	80	98	[73]
14	Ni(OAc) ₂	$T = 350^{\circ}\text{C}$, $t = 4.5$ h	–	15.3	24.2	[66]
15	5 wt% Pd/SiO ₂	$T = 300^{\circ}\text{C}$, $P = 15$ bar, $t = 4$ h	1:67	100	96	[57]
16	15 wt% Ni ₂ P/SiO ₂	$T = 300^{\circ}\text{C}$, $P = 20$ bar, WHSV = 6 h^{-1}	–	98.8	87.9	[74]
17	5 wt% Pd/C	$T = 300^{\circ}\text{C}$, $P = 20$ bar, $t = 5$ h	1:200	65	86.2	[75]
18	0.5 wt%Pt/ZIF-67/5A	$T = 320^{\circ}\text{C}$, $P = 20$ bar, $t = 2$ h	1:200	95	93.5	[72]

^aOnly the best catalytic performance of each reference was shown in Table 9.6. Note: in entries 3, 4, 5, 7, 8, 10, 11, 15, 16, and 17 hydrogen is used.

Source: Taken from L.Q. Yang, M.A. Carreon, Deoxygenation of palmitic and lauric acids over Pt/ZIF-67 membrane/zeolite 5A bead catalyst, ACS Appl. Mater. Interfaces 9 (37) (2017) 31993–32000.

(6 hours) or extra hydrogen input, must be satisfied to achieve such catalytic performance for both cases. Although a slightly lower pentadecane selectivity ($\sim 92\%$, entry 12) was obtained, our catalyst composition required very low noble metal loading (0.5 wt%) and did not need hydrogen to be present. In addition, the best catalytic performance of our catalysts was observed when CO_2 , a cheap renewable feedstock, was supplied during reaction. It is found that Pd supported on SiO_2 catalyst displayed selectivity to undecane as high as $\sim 96\%$ for the conversion of lauric acid to undecane (entry 15). Similarly, high Pd loading and the presence of hydrogen was also required for this catalyst. On the other hand, our catalyst displayed selectivity to undecane of $\sim 94\%$ with very low noble metal loading (0.5 wt%) and in the presence of CO_2 (entry 18).

To conclude, the deoxygenation processes of two saturated fatty acids over 0.5 wt% Pt/ZIF-67 membrane/zeolite 5A bead catalysts under different reaction gas atmospheres were studied. Almost complete conversion of fatty acids was achieved over both fresh and recycled catalyst after 2 hours reaction time. Under all reaction conditions pentadecane and undecane were the main products with high selectivity. A lower reaction temperature was favorable to obtain high selectivity for long-chain hydrocarbons. Shorter-chain hydrocarbons generated by cracking of long-chain hydrocarbons and/or fatty acids were observed as secondary products at a high reaction temperature. The recycled catalysts displayed similar catalytic performance as the fresh ones. Two distinctive reaction pathways were observed: decarboxylation and hydrodeoxygenation, depending on the reaction gas atmosphere. Esters were identified as the key reaction intermediates, which converted to the final products through decarboxylation and hydrodeoxygenation.

9.6 Supported Ni-MOFs catalysts for the conversion of oleic acid into transport liquid fuel hydrocarbons

In this section the preparation of nickel-based metal-organic frameworks (Ni-MOFs) supported on zeolite 5A bead catalyst and their improved catalytic performance for the decarboxylation of oleic acid will be demonstrated. The synthesized materials include previously nonsynthesized MOF structures, which employ novel carboxylic acid linkers.

Most of the catalysts for decarboxylation of carboxylic acids employ noble metals (Pd, Pt, Rh, Ru, Ir, Os) as the active species to attain good catalytic performance in published studies. However, this hinders their industrial application due to limitations in cost and scale-up [13,76,77]. Few reports exist on nonnoble metal catalysts such as nickel bimetallic sulfide catalysts and other metal oxides [41,47,78]. Although nonnoble metal catalysts have the advantage of significantly lower cost, they have so far displayed limited catalytic performance compared to the noble metal catalysts. Another drawback of nonnoble bimetallic sulfide catalysts is the sulfide contamination of the resulting products. Therefore it is important to design effective nonnoble metal catalysts that display enhanced catalytic performance for

the conversion of lipid-based biomass into clean alternative hydrocarbon fuel. This could be potentially achieved by employing MOFs catalysts, which have emerged as a type of highly tunable (chemically and topologically) crystalline microporous material [79]. MOFs have such desirable properties, like uniform micropore, high surface area [80], and high thermal and chemical stability [81,82], making them ideal candidates for catalytic applications [83]. In principle the metal cations or metal-based clusters can act as the catalytic active species, and the ordered microporous structure can provide the pathway for guest and product molecules to diffuse with enhanced mass transfer [20,22,23].

Nickel is chosen as the inorganic coordinating metal because it is one of the most widely used elements in metal-based catalysts. And it is also found to play an active role in several processes, such as oxidation [84], cross-coupling [85], methanation [86], in particular in hydrogenation and reforming processes [87]. Particularly, supported nickel catalysts can afford a reasonable yield of hydrocarbons in the deoxygenation process of fatty acids even without hydrogen input [76,88]. Therefore nickel is selected as the inorganic metal cation to coordinate with our conjugated carboxylic acid linkers resulting in new MOF structures to be prepared. Novel carboxylic linkers (BM 65 and BM 73) were prepared through a Heck coupling reaction, and then directly used to coordinate with nickel nitrate salts to form Ni-MOFs. More details are provided in our study [89]. The conventional BTC linker (benzene-1,3,5-tricarboxylic acid) was also employed for comparison. After that Ni-MOF membrane/zeolite 5A bead phases were prepared through growing these Ni-based MOFs on the surface of zeolite 5A beads, which were directly used as catalysts for conversion of oleic acid into liquid hydrocarbon fuel.

It was found that Ni-BTC crystals (Fig. 9.10A) showed irregular plate-like morphology whereas Ni-BM 65 and Ni-BM 73 crystals (Fig. 9.10B and C) showed porous sphere-like structures with a “raspberry” morphology. Ni-BTC crystals had average widths of $\sim 10\ \mu\text{m}$ and lengths of varying size over $100\ \mu\text{m}$, and Ni-BM 65 crystals were a uniform size of $9.0\ \mu\text{m}$. However, two different particle sizes were observed for Ni-BM 73 crystals: 3.1 and $8.3\ \mu\text{m}$. XRD patterns (Fig. 9.11) showed that these Ni-MOFs were in a crystalline structure with varied “sharpness,” which means they have varied degrees of crystallinity. In particular, the relative larger molecule structure of BM 65 and BM 73 linkers led to overall lower crystallinity as compared to BTC. Ni-BM 65 and Ni-BM 73 presented distinctive peaks at 2θ around 33 and 36 degrees, suggested that these peaks were indicative of short range features, such as Ni-Ni distances. This was concluded after the inspection of simulated XRD patterns for more than 200 Ni-MOFs obtained from the computation-ready, experimental (CoRE) MOF database [90]. Furthermore, it was clear to note that Ni-BM 65 and Ni-BM 73 had not been previously synthesized [91]. The closest match with Ni-BTC MOF synthesized here was found from the work of Prior and Rosseinsky [92]. The surface areas of these Ni-MOFs were collected and in the range of $12\text{--}314\ \text{m}^2/\text{g}$, while Ni-BTC MOF presented the lowest BET area. The BET area correlates well with pore volume as expected, as small pore size for these Ni-MOFs was presumed [93]. The thermal stability of Ni-MOFs was determined

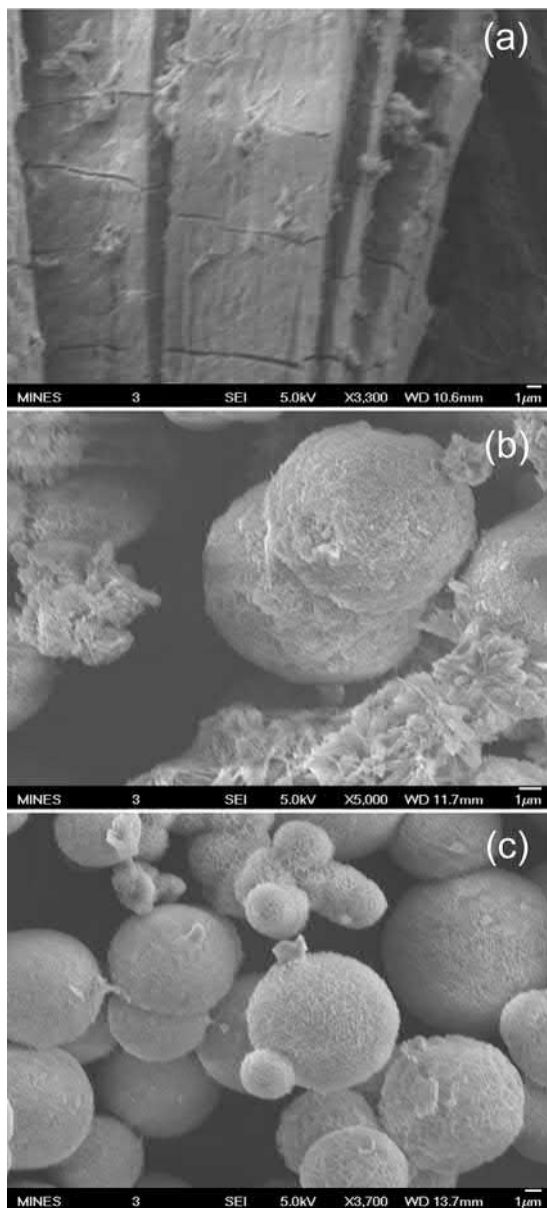


Figure 9.10 SEM images for Ni-MOF crystals (A) Ni-BTC MOF; (B) Ni-BM 65 MOF; and (C) Ni-BM 73 MOF.

Source: Taken from L.Q. Yang, B.W. McNichols, M. Davidson, B. Schweitzer, D.A. Gómez-Gualdrón, B.G. Trewyn, et al., Noble metal-free catalytic decarboxylation of oleic acid to n-heptadecane on nickel-based metal-organic frameworks (MOFs), *Catal. Sci. Technol.* 7 (14) (2017) 3027–3035.

via TGA, and it was found they can be thermally stable at least to 360°C, as shown in Fig. 9.12.

The resultant Ni-MOFs grown on the surface of zeolite 5A beads were prepared and evaluated for their catalytic ability to convert oleic acid into liquid hydrocarbons. Continuous layers of 375, 538, and 415 μm thickness were formed

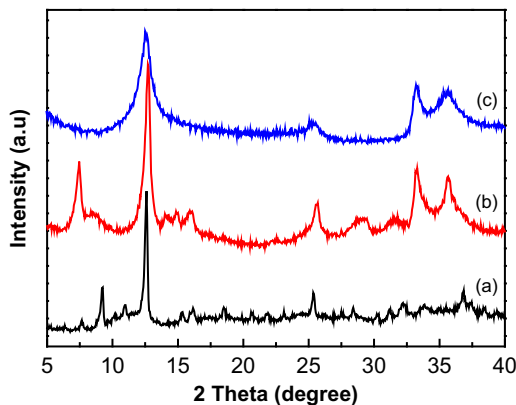


Figure 9.11 XRD patterns for Ni-MOF crystals (A) Ni-BTC MOF; (B) Ni-BM 65 MOF; and (C) Ni-BM 73 MOF.

Source: Taken from L.Q. Yang, B.W. McNichols, M. Davidson, B. Schweitzer, D.A. Gómez-Gualdrón, B.G. Trewyn, et al., Noble metal-free catalytic decarboxylation of oleic acid to n-heptadecane on nickel-based metal-organic frameworks (MOFs), *Catal. Sci. Technol.* 7 (14) (2017) 3027–3035.

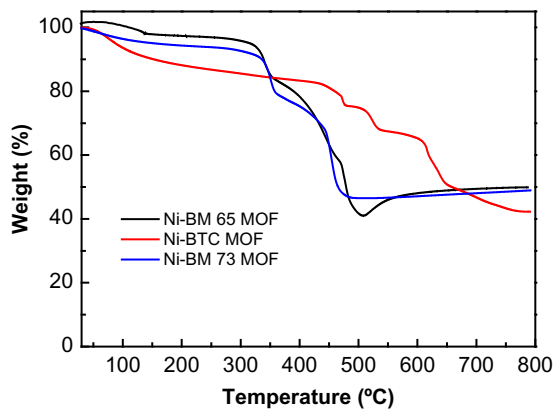


Figure 9.12 TGA profiles for the studied Ni-MOF crystals.

Source: Taken from L.Q. Yang, B.W. McNichols, M. Davidson, B. Schweitzer, D.A. Gómez-Gualdrón, B.G. Trewyn, et al., Noble metal-free catalytic decarboxylation of oleic acid to n-heptadecane on nickel-based metal-organic frameworks (MOFs), *Catal. Sci. Technol.* 7 (14) (2017) 3027–3035.

for Ni-BTC MOF, Ni-BM 65 MOF, and Ni-BM 73 MOF, respectively. All catalysts showed the crystalline structure of zeolite 5A, which was preserved after Ni-MOF deposition and recycling, indicating structural stability of these Ni-MOF membrane/zeolite 5A bead catalysts.

As high as 90% for decarboxylation percentage was obtained for all catalysts employed (fresh and recycled) under the reaction conditions. Table 9.7 summarized the distribution of liquid products for all the studied catalysts. It is important to note that pure zeolite 5A beads can only produce heptadecane with a selectivity of ~14%, and many short-chain hydrocarbons (C7–C12) were observed as the main product, which were generated through cracking of oleic acid and/or long-chain hydrocarbons [94,95]. As expected, the selectivity to heptadecane increased when the Ni-MOFs were grown on the surface of zeolite 5A beads, and the highest selectivity to heptadecane was obtained with Ni-BM 65/zeolite 5A bead catalyst. The observed hydrocarbons in liquid products were: octadecane, heptadecane, dodecane, undecane, decane, nonane, octane, and heptane. A decline of selectivity for heptadecane was detected for all recycled catalysts (seen in Table 9.7). The possible reason for decreasing catalytic activity of recycled catalysts is that the surface carbon generated during the reaction deposited on the catalysts, which may prevent access of oleic acid into the active sites. This assumption was consistent with decreases in surface area and pore volume for all recycled catalysts. Furthermore, there was negligible Ni leaching for all recycled catalysts after decarboxylation reactions from the obtained EDX result.

The acid sites on the fresh and recycled Ni-MOF membrane/zeolite 5A catalysts were also estimated and summarized in Table 9.8. Fresh catalyst exhibited significantly higher acidity than the corresponding recycled one. The recycled catalysts lost about half of their concentration of acid sites, except for Ni-BM 73 MOF/zeolite 5A bead catalyst, which also showed an increase in the temperature of the peak desorption. This observation for Ni-BM 73 MOF/zeolite 5A catalyst may be associated to its free carboxylic linker in MOF structure due to BM 73 linker's asymmetry [96].

However, the selectivity for heptadecane for decarboxylation of oleic acid over these supported Ni-MOFs catalysts did not correlate with the density of acid sites because zeolite 5A beads presented comparable acidity with Ni-BTC MOF/zeolite 5A and Ni-BM 65/zeolite 5A catalyst but with minimal heptadecane selectivity. Therefore Ni must play a key role in the catalytic decarboxylation of oleic acid. To verify this a reaction was run employing a homogeneous catalyst consisting of nickel nitrate hexahydrate and BM 65 MOF linker for comparison at the same reaction conditions as before. The high conversion (~94%) and much lower selectivity to heptadecane (47.7%) suggested that a MOF structure (and porosity) was required to achieve higher heptadecane selectivity. In addition, the catalytic activity of Ni-BM 65 MOF powders were also evaluated. Ni-BM 65 MOF powders did display good catalytic ability (~90% conversion and ~73% heptadecane selectivity), which is slightly lower than Ni-BM 65 MOF/zeolite 5A bead catalyst. Therefore Ni-BM 65 MOF and zeolite 5A both acted as reaction active sites for the conversion of oleic acid to heptadecane, but further studies were needed to

Table 9.7 Liquid product distribution for all studied catalysts.

Catalysts	Hydrocarbon distribution (%)						
	Octadecane	Heptadecane	Hexadecane	Pentadecane	Tetradecane	Tridecane	
Zeolite 5A	8.18	13.91	2.12	3.56	2.75	3.84	
Fresh Ni-BTC MOF/zeolite 5A	1.64	70.11	2.21	3.17	0.95	1.39	
Spent Ni-BTC MOF/zeolite 5A	3.18	49.37	2.16	3.68	2.06	3.05	
Fresh Ni-BM 65 MOF/zeolite 5A	2.57	76.74	1.48	2.80	0.89	1.21	
Spent Ni-BM 65 MOF/zeolite 5A	1.79	56.19	1.43	3.03	1.20	1.50	
Fresh Ni-BM 73 MOF/zeolite 5A	2.22	71.97	1.58	2.65	1.06	1.58	
Spent Ni-BM 73 MOF/zeolite 5A	2.64	52.92	1.53	3.16	1.44	2.09	
Catalysts	Hydrocarbon distribution (%)						
	Dodecane	Undecane	Decane	Nonane	Octane	Heptane	Unknown
Zeolite 5A	7.43	9.16	9.90	11.36	12.91	11.79	3.06
Fresh Ni-BTC MOF/zeolite 5A	2.25	2.81	2.30	4.24	4.67	3.04	1.22
Spent Ni-BTC MOF/zeolite 5A	4.19	5.27	5.65	7.03	7.84	5.31	1.21
Fresh Ni-BM 65 MOF/zeolite 5A	1.67	2.30	2.06	2.48	2.85	1.92	1.03
Spent Ni-BM 65 MOF/zeolite 5A	2.50	3.54	4.06	7.51	9.20	6.83	1.21
Fresh Ni-BM 73 MOF/zeolite 5A	2.28	3.03	2.40	3.39	4.07	2.65	1.12
Spent Ni-BM 73 MOF/zeolite 5A	3.45	4.42	4.99	7.08	8.13	6.41	1.74

Source: Taken from L.Q. Yang, B.W. McNichols, M. Davidson, B. Schweitzer, D.A. Gómez-Gualdrón, B.G. Trewyn, et al., Noble metal-free catalytic decarboxylation of oleic acid to n-heptadecane on nickel-based metal-organic frameworks (MOFs), Catal. Sci. Technol. 7 (14) (2017) 3027–3035.

Table 9.8 Summary of acid site density data from TPD of NH₃ postcatalysis.

Catalysts	T_{\max} (°C)	Acid site density ($\mu\text{mol g}^{-1}$)
Zeolite 5A	255	1451
Fresh Ni-BTC MOF/zeolite 5A	213	952
Spent Ni-BTC MOF/zeolite 5A	206	494
Fresh Ni-BM 65 MOF/zeolite 5A	205	1382
Spent Ni-BM 65 MOF/zeolite 5A	196	423
Fresh Ni-BM 73 MOF/zeolite 5A	300	456
Spent Ni-BM 73 MOF/zeolite 5A	196	441

Source: Taken from L.Q. Yang, B.W. McNichols, M. Davidson, B. Schweitzer, D.A. Gómez-Gualdrón, B.G. Trewn, et al., Noble metal-free catalytic decarboxylation of oleic acid to n-heptadecane on nickel-based metal-organic frameworks (MOFs), *Catal. Sci. Technol.* 7 (14) (2017) 3027–3035.

elucidate the specific role of each of them for this particular reaction. It is important to mention that only half the amount of the Ni-BM 65 powder can be recovered after reactions, while Ni-BM 65 MOF membrane/zeolite 5A bead catalyst was completely recovered.

To summarize, Ni-MOFs employing novel carboxylic acid linkers were successfully synthesized. Furthermore, the deposition of these MOFs on zeolite 5A beads was illustrated and the resulting Ni-MOF/zeolite 5A bead catalysts were tested for catalytic activity of conversion of oleic acid into liquid hydrocarbons. The resultant Ni-MOF/zeolite 5A bead catalysts displayed complete conversion of oleic acid, high heptadecane selectivity ($\sim 77\%$), and a loss in catalytic activity after recycling due to surface carbon deposition. We also demonstrated that the application of CO₂ during the decarboxylation process can lead to a more viable and cost-effective route to transform fatty acids into liquid fuels. It can be envisioned that this work will encourage the study of MOFs based on earth-abundant metals for diverse catalytic applications.

9.7 Promising metal-organic framework compositions

Nickel, which is earth-abundant and ~ 3000 times cheaper than noble metals, has been shown to be active for deoxygenation of several lipids [13,97]. Thus nickel is as a potential replacement for the expensive noble metals (Pt, Pd, and Ru) until now needed for effective catalytic decarboxylation, especially if nickel is placed in the highly tunable environment of the MOF. Therefore, synthesizing Ni-MOFs with known crystalline structure used as catalysts will allow one to have a better understanding of the structure–catalytic relationship for the deoxygenation reaction. Examples of these Ni-MOFs are DUT-9, NiSIFSIX, and Ni-MOF 74 [98–100].

DTU-9 (DTU = Dresden University of Technology) is composed of btb linker (btb = benzene-1,3,5-tribenzoate) and nickel nitrate hydrothermally. This structure has a high concentration of open metal sites per cluster and a very high porosity.

Two different types of pores are present in this structure: a smaller pore approximately 13 Å and a larger pore with a diameter of ~ 25 Å. NiSIFSIX can be prepared by using a solvent-free route [99]. This facile methodology is based firstly on mechanically mixing both the organic and inorganic solid precursors (pyrazine and NiSiF6) with a molar ratio of 4:1, followed by a wetting procedure with a few drops of water and then a careful heating procedure. This structure has a relatively sharp pore size distribution centered at 3.8 Å. Ni-MOF 74 has been synthesized using nickel nitrate as metal centers coordinated with 2, 5-dihydroxyterephthalic acid hydrothermally. Its average pore diameter is around 10 Å.

The challenge here would be how to form MOFs of these compositions in membrane form. Microwave treatment is a useful approach to synthesize porous crystals with smaller and narrow size distribution as compared to conventional solvothermal approach. Microwave treatment has the following advantages compared to conventional heating [101]: (1) the microwave heating has much higher heating rates than that of conventional heating; (2) the microwave treats chemical reactors remotely without direct contact between energy source and the reacting chemicals; (3) there is no wall or heating diffusion effect; (4) it can selectively heat because the chemicals and the contaminants do not interact equally with microwaves; and (5) there are no “hot spots.” Therefore microwave heating leads typically to more uniform crystals with narrow size distribution, which can potentially form thinner coatings on porous beads impacting the catalytic performance of the resultant hybrid catalysts. Microwave heating has been successfully employed to synthesize diverse porous crystals, including oxides [102], zeolites [103,104], and MOFs [105,106]. Future work should focus on employing the microwave approach to form thinner MOF layers leading to a positive impact on the catalytic performance of the proposed catalysts in the decarboxylation of fatty acid molecules and/or biomass to liquid fuels. Also modeling may be useful to have a better understanding at a fundamental level on how the deoxygenation reactions occur when employing these catalysts.

9.8 Outlook and conclusion

Recent research progress has been undertaken in the development of MOFs as catalysts and catalytic supports for the conversion of fatty acids into liquid transport fuels. In particular, some of these MOFs as catalytic supports display enhanced performance for the decarboxylation and deoxygenation of fatty acids to liquid fuels as compared to benchmark catalyst-support systems. Important aspects that require attention from the scientific community to envision these porous crystals as effective catalysts to convert liquid biomass into valuable liquid fuels are as follows:

1. Exploring different MOF compositions. Most of the reported MOFs for the conversion of fatty acids into liquid fuels require the presence of a noble metal (Pt) to display high catalytic activity. However, it would be highly desirable to have a MOF that could display high activity without the presence of a costly noble metal. In this respect, besides

Ni-MOFs (previous sections) other MOFs with suitable catalytic features for decarboxylation and deoxygenation reactions should be explored. These MOFs should be thermally stable at least up to 300–350°C (typical temperature at which these reactions take place, and for regeneration), chemically stable in the presence of fatty acids, and have metal active sites to catalyze the deoxygenation/decarboxylation reactions. In this respect, modeling studies may be helpful to accelerate the development and optimization of these novel catalytic systems.

2. Deoxygenation of real biomass. Future work should focus on real lipid biomass compositions as feeds instead of only model biomass molecules. The composition of lipids is far complicated than only one molecule model reactant. For example, typical animal fats, such as beef tallow and butter, have saturated and unsaturated fatty acids with carbon chains ranging from 12 to 18. This should lead to different and more complex reaction mechanisms as compared to one molecule model reactant. For instance, there would be more hydrocarbons produced in the liquid product. In addition, the more unsaturated reactant may require more hydrogen to transfer the carbon double bonds into saturated ones.
3. Integrated experimental and computational efforts. Simulation-experiment integration should help to establish fundamental structure–performance relationships to design fatty acid decarboxylation catalysts, and to better understand reaction mechanisms of fatty acid conversion to liquid fuels.

Acknowledgment

M.A. Carreon thanks National Science Foundation NSF-CBET Award # 1705675.

References

- [1] Institute for Energy Research, Encyclopedia entry fossil fuels. <<http://instituteforenergyresearch.org/topics/encyclopedia/fossil-fuels/>>
- [2] Business Standard, How long will fossil fuels last? <http://www.business-standard.com/article/punditry/how-long-will-fossil-fuels-last115092201397_1.html>, 2015.
- [3] N.L. Panwar, S.C. Kaushik, S. Kothari, Role of renewable energy sources in environmental protection: a review, *Renew. Sustain. Energy Rev.* 15 (3) (2011) 1513–1524.
- [4] T.V. Choudhary, C.B. Phillips, Renewable fuels via catalytic hydrodeoxygenation, *Appl. Catal., A* 397 (1-2) (2011) 1–12.
- [5] R.W. Gosselink, S.A.W. Hollak, S.W. Chang, J. van Haveren, K.P. de Jong, J.H. Bitter, et al., Reaction pathways for the deoxygenation of vegetable oils and related model compounds, *ChemSusChem* 6 (2013) 1576–1594.
- [6] A.B. Chhetri, K.C. Watts, M.R. Islam, Waste cooking oil as an alternate feedstock for biodiesel production, *Energies* 1 (1) (2008) 3–18.
- [7] P.M. Mortensen, J.D. Grunwaldt, O.A. Jensen, K.G. Knudsen, A.D. Jensen, A review of catalytic upgrading of bio-oil to engine fuels, *Appl. Catal., A* 407 (1-2) (2011) 1–19.
- [8] N. Taufiqurahmi, S. Bhatia, Catalytic cracking of edible and non-edible oils for the production of biofuels, *Energy Environ. Sci.* 4 (4) (2011) 1087–1112.

- [9] A.F. Lee, J.A. Bennett, J.C. Manayil, K. Wilson, Heterogeneous catalysis for sustainable biodiesel production via esterification and transesterification, *Chem. Soc. Rev.* 43 (22) (2014) 7887–7916.
- [10] V.B. Borugadda, V.V. Goud, Biodiesel production from renewable feedstocks: status and opportunities, *Renew. Sustain. Energy Rev.* 16 (7) (2012) 4763–4784.
- [11] E.S. Jimenez, M. Crocker, Catalytic deoxygenation of fatty acids and their derivatives to hydrocarbon fuels via decarboxylation/decarbonylation, *J. Chem. Technol. Biotechnol.* 87 (8) (2012) 1041–1050.
- [12] C. Zhao, T. Brück, J.A. Lercher, Catalytic deoxygenation of microalgae oil to green hydrocarbons, *Green Chem.* 15 (7) (2013) 1720–1739.
- [13] M. Snåre, I. Kubičková, P. Mäki-Arvela, K. Eränen, D.Y. Murzin, Heterogeneous catalytic deoxygenation of stearic acid for production of biodiesel, *Ind. Eng. Chem. Res.* 45 (16) (2006) 5708–5715.
- [14] A.S. Berenblyum, R.S. Shamsiev, T.A. Podoplelova, V.Y. Danyushevsky, The influence of metal and carrier natures on the effectiveness of catalysts of the deoxygenation of fatty acids into hydrocarbons, *Russian J. Phys. Chem. A* 86 (8) (2012) 1199–1203.
- [15] A. Srifa, K. Faungnawakij, V. Itthibenchapong, S. Assabumrungrat, Roles of monometallic catalysts in hydrodeoxygenation of palm oil to green diesel, *Chem. Eng. J.* 278 (15) (2015) 249–258.
- [16] K. Kandel, J.W. Anderegg, N.C. Nelson, U. Chaudhary, I.I. Slowing, Supported iron nanoparticles for the hydrodeoxygenation of microalgal oil to green diesel, *J. Catal.* 314 (2014) 142–148.
- [17] S.K. Kim, D. Yoon, S.C. Lee, J. Kim, Mo₂C/Graphene nanocomposite as a hydrodeoxygenation catalyst for the production of diesel range hydrocarbons, *ACS Catal.* 5 (6) (2015) 3292–3303.
- [18] M. Ahmadi, E.E. Macias, J.B. Jasnski, P. Ratnasamy, M.A. Carreon, Decarboxylation and further transformation of oleic acid over bifunctional, Pt/SAPO-11 catalyst and Pt/chloride Al₂O₃ catalysts, *J. Mol. Catal. A: Chem.* 386 (2014) 14–19.
- [19] M. Ahmadi, A. Nambo, J.B. Jasnski, P. Ratnasamy, M.A. Carreon, Decarboxylation of oleic acid over Pt catalysts supported on small-pore zeolites and hydrotalcite, *Catal. Sci. Technol.* 5 (1) (2015) 380–388.
- [20] K.S. Park, Z. Ni, A.P. Côté, J.Y. Choi, R.D. Huang, F.J. Uribe-Romo, et al., Exceptional chemical and thermal stability of zeolitic imidazolate frameworks, *PNAS* 103 (27) (2006) 10186–10191.
- [21] O.M. Yaghi, M. O’Keeffe, N.W. Ockwig, H.K. Chae, M. Eddaoudi, J. Kim, Reticular synthesis and the design of new materials, *Nature* 423 (6941) (2003) 705–714.
- [22] G. Férey, Hybrid porous solids: past, present, future, *Chem. Soc. Rev.* 37 (1) (2008) 191–214.
- [23] L. MacGillivray, *Metal-Organic Framework: Design and Application*, John Wiley & Sons, 2010.
- [24] A.H. Chughtai, N. Zhmad, H.A. Younus, A. Laypkov, F. Verpoort, Metal-organic frameworks: versatile heterogeneous catalysts for efficient catalytic organic transformations, *Chem. Soc. Rev.* 44 (19) (2015) 6804–6849.
- [25] K.S. Lin, A.K. Adhikari, C.N. Ku, C.L. Chiang, H. Kuo, Synthesis and characterization of porous HKUST-1 metal organic frameworks for hydrogen storage, *Int. J. Hydrogen Energy* 37 (18) (2012) 13865–13871.
- [26] L.Q. Yang, G.L. Ruess, M.A. Carreon, Cu, Al and Ga based metal-organic framework catalysts for the decarboxylation of oleic acid, *Catal. Sci. Technol.* 5 (5) (2015) 2777–2782.

- [27] K. Schlichte, T. Kratzke, S. Kaskel, Improved synthesis, thermal stability and catalytic properties of metal-organic framework compound $\text{Cu}_3(\text{BTC})_2$, *Microporous Mesoporous Mater.* 73 (1-2) (2004) 81–88.
- [28] L. Alaerts, E. Séguin, H. Poelman, F. Thibault-Starzyk, P.A. Jacobs, D.E. De Vos, Probing the Lewis acidity and catalytic activity of the metal-organic framework $[\text{Cu}_3(\text{btc})_2]$ (BTC = Benzene-1,3,5-tricarboxylate), *Chem. Eur. J.* 12 (29) (2006) 7353–7363.
- [29] W.D. Callister, D.G. Rethwisch, *Fundamentals of Materials Science and Engineering: An Integrated Approach*, John Wiley & Sons, 2012.
- [30] D. Peralta, G. Chaplais, A. Simon-Masseron, K. Barthelet, G.D. Pirngruber, Separation of C6 paraffins using zeolitic imidazolate frameworks: comparison with zeolite 5A, *Ind. Eng. Chem. Res.* 51 (12) (2012) 4692–4702.
- [31] L.Q. Yang, K.L. Tate, J.B. Jasinski, M.A. Carreon, Decarboxylation of oleic acid to heptadecane over Pt supported on zeolite 5A beads, *ACS Catal.* 5 (11) (2015) 6497–6502.
- [32] S.J. Guo, S. Zhang, L.H. Wu, S.H. Sun, Co/CoO nanoparticles assembled on graphene for electrochemical reduction of oxygenation, *Angew. Chem. Int. Ed.* 51 (47) (2012) 11770–11773.
- [33] R. Banerjee, A. Phan, B. Wang, C. Knobler, H. Furukawa, M. O’Keeffe, et al., High-throughput synthesis of zeolitic imidazolate frameworks and application to CO_2 capture, *Science* 319 (5865) (2008) 939–943.
- [34] W.Y. Wang, Y.Q. Yang, H.A. Luo, T. Hu, W.Y. Liu, Amorphous, Co-Mo-B catalyst with high activity for the hydrodeoxygenation of bio-oil, *Catal. Commun.* 12 (6) (2011) 436–440.
- [35] V.N. Bui, D. Lautenti, P. Delichère, C. Geantet, Hydrodeoxygenation of guaiacol part II: support effect for CoMoS catalysts on HDO activity and selectivity, *Appl. Catal., B* 101 (3-4) (2011) 246–255.
- [36] J.G. Immer, M.J. Kelly, H.H. Lamb, Catalytic reaction pathways in liquid-phase deoxygenation of C18 free fatty acids, *Appl. Catal., A* 375 (1) (2010) 134–139.
- [37] M. Snåre, I. Kubičková, P. Mäki-Arvela, D. Chichova, K. Eränen, D. Yu, Murzin, Catalytic deoxygenation of unsaturated renewable feedstocks for production of diesel fuel hydrocarbons, *Fuel* 87 (6) (2008) 933–945.
- [38] J. Fu, F. Shi, L.T. Thompson Jr., X.Y. Lu, P.E. Savage, Activated carbons for hydrothermal decarboxylation of fatty acids, *ACS Catal.* 1 (3) (2011) 227–231.
- [39] D.S. Tong, C.H. Zhou, M.Y. Li, W.H. Yu, J. Beltrami, C.X. Lin, et al., Structure and catalytic properties of Sn-containing layered double hydroxides synthesized in the presence of dodecylsulfate and dodecylamine, *Appl. Clay Sci.* 48 (4) (2010) 569–574.
- [40] J.G. Na, B.E. Yi, J.K. Han, Y.K. Oh, J.H. Park, T.S. Jung, et al., Deoxygenation of microalgal oil into hydrocarbon with precious metal catalysts: optimization of reaction conditions and supports, *Energy* 47 (1) (2012) 25–30.
- [41] J.O. Shim, D.W. Jeong, W.J. Jang, K.W. Jeon, B.H. Jeon, S.Y. Cho, et al., Deoxygenation of oleic acid over $\text{Ce}_{(1-x)}\text{Zr}_{(x)}\text{O}_2$ catalysts in hydrogen environment, *Renew. Energy* 65 (2014) 36–40.
- [42] D.R. Vardon, B.K. Sharma, H. Jaramillo, D.W. Kim, J.K. Choe, P.N. Ciesielski, et al., Hydrothermal catalytic processing of saturated and unsaturated fatty acids to hydrocarbons with glycerol for in situ hydrogen production, *Green Chem.* 16 (3) (2014) 1507–1520.

- [43] E. Sari, M. Kim, S.O. Salley, K.Y. Simon Ng, A highly active nanocomposite silica-carbon supported palladium catalyst for decarboxylation of free fatty acids for green diesel production: correlation of activity and catalyst properties, *Appl. Catal., A* 467 (2) (2013) 261–269.
- [44] J.O. Shim, D.W. Jeong, W.J. Jang, K.W. Jeon, S.H. Kim, B.H. Jeon, et al., Optimization of unsupported CoMo catalysts for decarboxylation of oleic acid, *Catal. Commun.* 67 (5) (2015) 16–20.
- [45] K. Hengst, M. Arend, R. Pfützenreuter, W.F. Hoelderich, Deoxygenation and cracking of free fatty acids over acidic catalysts by single step conversion for the production of diesel fuel and fuel blends, *Appl. Catal., B* 174-175 (2015) 383–394.
- [46] J.G. Na, B.E. Yi, J.N. Kim, K.B. Yi, S.Y. Park, J.H. Park, et al., Hydrocarbon production from decarboxylation of fatty acid without hydrogen, *Catal. Today* 156 (1-2) (2010) 44–48.
- [47] I. Simakova, B. Rozmysłowicz, O. Simakova, P. Mäki-Arvela, A. Simakov, D. Yu, Murzin, Catalytic deoxygenation of C18 fatty acids over mesoporous Pd/C catalyst for synthesis of biofuels, *Top. Catal.* 54 (8–9) (2011) 460–466.
- [48] A.T. Madsen, E.H. Ahmed, C.H. Christensen, R. Fehrmann, A. Riisager, Hydrodeoxygenation of waste fat for diesel production: study on model feed with Pt/alumina catalyst, *Fuel* 90 (11) (2011) 3433–3438.
- [49] A.S. Dragu, S. Kinayyigit, E.J. García-Suárez, M. Florea, E. Stepan, S. Velra, et al., Deoxygenation of oleic acid: influence of the synthesis route of Pd/mesoporous carbon nanocatalysts onto their activity and selectivity, *Appl. Catal., A* 504 (5) (2015) 81–91.
- [50] S. Popov, S. Kumar, Rapid hydrothermal deoxygenation of oleic acid over activated carbon in a continuous flow process, *Energy Fuels* 29 (5) (2015) 3377–3384.
- [51] T.M. Yeh, R.L. Hockstad, S. Linic, P.E. Savage, Hydrothermal decarboxylation of unsaturated fatty acids over PtSn_x/C catalysts, *Fuel* 156 (15) (2015) 219–224.
- [52] J. Fu, X.Y. Lu, P.E. Savage, Hydrothermal decarboxylation and hydrogenation of fatty acids over Pt/C, *ChemSusChem* 4 (4) (2011) 481–486.
- [53] J. Orsavova, L. Misurcova, J.V. Ambrozova, R. Vicha, J. Mlcek, Fatty acids composition of vegetable oils and its contribution to dietary energy intake and dependence of cardiovascular mortality on dietary intake of fatty acids, *Int. J. Mol. Sci.* 16 (6) (2015) 12871–12890.
- [54] D.J. Anneken, S. Both, R. Christoph, G. Fieg, U. Steinberner, A. Westfechtel, *Ullmann's Encyclopedia of Industrial Chemistry*, Wiley-VCH, Weinheim, 2002.
- [55] B.X. Peng, C. Zhao, S. Kasakov, S. Foraita, J.A. Lercher, Manipulating catalytic pathways: deoxygenation of palmitic acid on multifunctional catalysts, *Chem. Eur. J.* 19 (15) (2013) 4732–4741.
- [56] S.K. Kim, S. Brand, H.S. Lee, Y.J. Kim, J. Kim, Production of renewable diesel by hydrotreatment of soybean oil: effect of reaction parameters, *Chem. Eng. J.* 228 (15) (2013) 114–123.
- [57] J.P. Ford, J.G. Immer, H.H. Lamb, Palladium catalysts for fatty acid deoxygenation: influence of the support and fatty acid chain length on decarboxylation kinetics, *Top. Catal.* 55 (3-4) (2012) 175–184.
- [58] H.P. Zhang, H.F. Lin, W.Z. Wang, Y. Zheng, P.J. Hu, Hydroprocessing of waste cooking oil over a dispersed nano catalyst: kinetics study and temperature effect, *Appl. Catal., B* 150-151 (5) (2014) 238–248.
- [59] P. Mäki-Arvela, I. Kubickova, M. Snåre, K. Eränen, D.Y. Murzin, Catalytic deoxygenation of fatty acids and their derivatives, *Energy Fuels* 21 (1) (2007) 30–41.

- [60] G.C. Li, F. Zhang, L. Chen, C.H. Zhang, H. Huang, X.B. Li, Highly selective hydrodecarbonylation of oleic acid into n-heptadecane over a supported nickel/zinc oxide-alumina catalyst, *ChemCatChem* 7 (17) (2015) 2646–2653.
- [61] J. Zhang, G. Leitus, Y. Ben-David, D. Milstein, Efficient homogeneous catalytic hydrogenation of esters to alcohols, *Angew. Chem. Int. Ed.* 118 (7) (2006) 1131–1133.
- [62] K. Kon, W. Onodera, S. Takakusagi, K. Shimizu, Hydrodeoxygenation of fatty acids and triglycerides by Pt-loaded Nb₂O₅ catalysts, *Catal. Sci. Technol.* 4 (10) (2014) 3705–3712.
- [63] J. Fu, X.Y. Lu, P.E. Savage, Catalytic hydrothermal deoxygenation of palmitic acid, *Energy Environ. Sci.* 3 (3) (2010) 311–317.
- [64] Y. Shao, Q.N. Xia, X.H. Liu, G.Z. Lu, Y.Q. Wang, Pd/Nb₂O₅/SiO₂ catalyst for the direct hydrodeoxygenation of biomass-related compounds to liquid alkanes under mild conditions, *ChemSusChem* 8 (10) (2015) 1761–1767.
- [65] H. Xin, K. Guo, D. Li, H.Q. Yang, C.W. Hu, Production of high-grade diesel from palmitic acid over activated carbon-supported nickel phosphide catalysts, *Appl. Catal., B* 187 (15) (2016) 375–385.
- [66] W.J. Li, Y.J. Gao, S.Y. Yao, D. Ma, N. Yan, Effective deoxygenation of fatty acids over Ni(OAc)₂ in the absence of H₂ and solvent, *Green Chem.* 17 (8) (2015) 4198–4205.
- [67] Y.C. Shi, Y.Y. Cao, Y.N. Duan, H. Chen, Y. Chen, M.D. Yang, et al., Upgrading of palmitic acid to iso-alkanes over bi-functional Mo/ZSM-22 catalysts, *Green Chem.* 18 (17) (2016) 4633–4648.
- [68] Y.Y. Cao, Y.C. Shi, J.M. Liang, Y.L. Wu, S.B. Huang, J.L. Wang, et al., High iso-alkanes production from palmitic acid over bi-functional Ni/HZSM-22 catalysts, *Chem. Eng. Sci.* 158 (2) (2017) 188–195.
- [69] A. Méndez-Vilas, Materials and processes for energy: communicating current research and technological developments, *Formatex Res. Center* (2013).
- [70] R.R. Ding, Y.L. Wu, Y. Chen, J.M. Liang, J. Liu, M.D. Yang, Effective hydrodeoxygenation of palmitic acid to diesel-like hydrocarbons over MoO₂/CNTs catalyst, *Chem. Eng. Sci.* 135 (2) (2015) 517–525.
- [71] C. Miao, O. Marin-Flores, S.D. Davidson, T.T. Li, T. Dong, D.F. Gao, et al., Hydrothermal catalytic deoxygenation of palmitic acid over nickel catalyst, *Fuel* 166 (15) (2016) 302–308.
- [72] L.Q. Yang, M.A. Carreon, Deoxygenation of palmitic and lauric acids over Pt/ZIF-67 membrane/zeolite 5A bead catalyst, *ACS Appl. Mater. Interfaces* 9 (37) (2017) 31993–32000.
- [73] P. Mäki-Arvela, M. Snåre, K. Eränen, J. Myllyoja, D.Y. Murzin, Continuous decarboxylation of lauric acid over Pd/C catalyst, *Fuel* 87 (17–18) (2008) 3543–3549.
- [74] J.X. Chen, H. Shi, K.L. Li, Deoxygenation of methyl laurate as a model compound to hydrocarbons on transition metal phosphide catalysts, *Appl. Catal., B* 144 (2014) 870–884.
- [75] B. Rozmysłowicz, P. Mäki-Arvela, A. Tokarev, A.R. Leino, K. Eränen, D.Y. Murzin, Influence of hydrogen in catalytic deoxygenation of fatty acids and their derivatives over Pd/C, *Ind. Eng. Chem. Res.* 51 (26) (2012) 8922–8927.
- [76] J. Huang, Y.J. Jiang, V.R.R. Marthala, A. Bressel, J. Frey, M. Hunger, Effect of pore size and acidity on the coke formation during ethylbenzene conversion on zeolite catalysts, *J. Catal.* 263 (2) (2009) 277–283.

- [77] M. Busto, C.R. Vera, J.M. Grau, Optimal process conditions for the isomerization-cracking of long-chain n-paraffins to high octane isomerizate gasoline over Pt/SO₄²⁻-ZrO₂ catalysts, *Fuel Process. Technol.* 92 (9) (2012) 1675–1684.
- [78] T. Szarvas, Z. Eller, T. Kasza, T. Ollar, P. Teteni, J. Hancsok, Radioisotopic investigation of the oleic acid-1-C-14 HDO reaction pathways on sulfided Mo/P/Al₂O₃ and NiW/Al₂O₃ catalysts, *Appl. Catal., B* 165 (2015) 245–252.
- [79] D.A. Gómez-Gualdrón, Y.J. Colon, X. Zhang, T.C. Wang, Y.S. Chen, J.T. Hupp, et al., Evaluating topologically diverse metal-organic frameworks for cryo-adsorbed hydrogen storage, *Energy Environ. Sci.* 9 (10) (2016) 3279–3289.
- [80] O.K. Farha, I. Eryazici, N.C. Jeong, B.G. Hauser, C.E. Wilmer, A.A. Sarjeant, et al., Metal-organic framework materials with ultrahigh surface areas: is the sky the limit, *J. Am. Chem. Soc.* 134 (36) (2012) 15016–15021.
- [81] J.H. Cavka, S. Jakobsen, U. Olsbye, N. Guillou, C. Lamberti, S. Bordiga, et al., A new zirconium inorganic building brick forming metal-organic frameworks with exceptional stability, *J. Am. Chem. Soc.* 130 (42) (2008) 13850–13851.
- [82] J.E. Mondloch, W. Bury, D. Fairen-Jimenez, S. Kwon, E.J. DeMarco, M.H. Weston, et al., Vapor-phase metalation by atomic layer deposition in a metal-organic framework, *J. Am. Chem. Soc.* 135 (28) (2013) 10294–10297.
- [83] J. Gascon, A. Corma, F. Kapteijn, F.X. Llabres i Xamena, Metal-organic framework catalysis: quo vadis, *ACS Catal.* 4 (2) (2014) 361–378.
- [84] M.A. Carreon, V.V. Gulians, L. Yuan, A.R. Hughett, A. Dozier, G.A. Seisenbaeva, et al., Mesoporous nanocrystalline mixed metal oxides from heterometallic alkoxide precursors: cobalt-nickel oxide spinels for propane oxidation, *Eur. J. Inorg. Chem.* 24 (2006) 4983–4988.
- [85] S.Z. Tasker, E.A. Standley, T.F. Jamison, Recent advances in nickel catalysis, *Nature* 509 (7500) (2014) 299–309.
- [86] W.A.W. Abu Bakar, R. Ali, S. Toemen, Catalytic methanation reaction over supported nickel-ruthenium oxide base for purification of simulated natural gas, *Scientia Iranica C* 19 (3) (2012) 525–534.
- [87] S. De, J.G. Zhang, R. Luque, N. Yan, Ni-based bimetallic heterogeneous catalysts for energy and environmental applications, *Energy Environ. Sci.* 9 (11) (2016) 3314–3347.
- [88] R.E. Murray, E.L. Walter, K.M. Doll, Tandem isomerization-decarboxylation for converting alkenoic fatty acids into alkenes, *ACS Catal.* 4 (10) (2014) 3517–3520.
- [89] L.Q. Yang, B.W. McNichols, M. Davidson, B. Schweitzer, D.A. Gómez-Gualdrón, B. G. Trewyn, et al., Noble metal-free catalytic decarboxylation of oleic acid to n-heptadecane on nickel-based metal-organic frameworks (MOFs), *Catal. Sci. Technol.* 7 (14) (2017) 3027–3035.
- [90] Y.G. Chung, J. Camp, M. Haranczyk, B.J. Sikora, W. Bury, V. Krungleviciute, et al., Computation-ready, experimental metal-organic frameworks: a tool to enable high-throughput screening of nanoporous crystals, *Chem. Mater.* 26 (21) (2014) 6185–6192.
- [91] The Cambridge Structural Database (CSD). <<https://www.ccdc.cam.ac.uk/>>
- [92] T.J. Prior, M.J. Rosseinsky, Chiral direction and interconnection of helical three-connected networks in metal-organic frameworks, *Inorg. Chem.* 42 (5) (2003) 1564–1575.
- [93] D.A. Gómez-Gualdrón, P.Z. Moghadam, J.T. Hupp, O.K. Farha, R.Q. Snurr, Application of consistency criteria to calculate BET areas of micro- and mesoporous metal-organic frameworks, *J. Am. Chem. Soc.* 138 (1) (2016) 215–224.

- [94] R. Černý, M. Kubů, D. Kubička, The effect of oxygenates structure on their deoxygenation over USY zeolite, *Catal. Today* 204 (15) (2013) 46–53.
- [95] N. Mo, W. Tandar, P.E. Savage, Aromatics from saturated and unsaturated fatty acids via zeolite catalysis in supercritical water, *J. Supercrit. Fluids* 102 (2015) 73–79.
- [96] W. Xia, Y.M. Wang, R. Bergsträßer, S. Kundu, M. Muhler, Surface characterization of oxygen-functionalized multi-walled carbon nanotubes by high-resolution X-ray photoelectron spectroscopy and temperature-programmed desorption, *Appl. Surf. Sci.* 254 (1) (2007) 247–250.
- [97] I. Batonneau-Gener, S. Degorce, P. Ayrault, O. Ducreux, P. Magnoux, S. Mignard, Determination of the 5A zeolite acidity: an infrared study, *Stud. Surf. Sci. Catal.* 174 (part B) (2008) 857–860.
- [98] K. Gedrich, I. Senkowska, N. Klein, U. Stoeck, A. Henschel, M.R. Lohe, et al., A highly porous metal-organic framework with open nickel sites, *Angew. Chem. Int. Ed.* 49 (45) (2010) 8489–8492.
- [99] O. Shekhah, Y. Belmabkhout, K. Adil, P.M. Bhatt, A.J. Cairns, M. Eddaoudi, A facile solvent-free synthesis route for the assembly of a highly CO₂ selective and H₂S tolerant NiSIFSIX metal-organic framework, *Chem. Commun.* 51 (71) (2015) 13595–13598.
- [100] T.G. Glover, G.W. Peterson, B.J. Schindler, D. Britt, O.M. Yaghi, MOF-74 building unit has a direct impact on toxic gas adsorption, *Chem. Eng. Sci.* 66 (2) (2011) 163–170.
- [101] Y.S. Li, W.S. Yang, Microwave synthesis of zeolite membranes: a review, *J. Membr. Sci.* 316 (1-2) (2008) 3–17.
- [102] C.A. Deshmane, J.B. Jasinski, M.A. Carreon, Microwave-assisted synthesis of nanocrystalline gallium oxide, *Microporous Mesoporous Mater.* 130 (1-3) (2010) 97–102.
- [103] A. Arafat, J.C. Jansen, A.R. Ebaid, H. van Bekkum, Microwave preparation of zeolite Y and ZSM-5, *Zeolites* 13 (3) (1993) 162–165.
- [104] S.R. Venna, M.A. Carreon, Microwave assisted phase transformation of silicoaluminophosphate zeolite crystals, *J. Mater. Chem.* 19 (20) (2009) 3138–3140.
- [105] Z. Ni, R.I. Masel, Rapid production of metal-organic frameworks via microwave-assisted solvothermal synthesis, *J. Am. Chem. Soc.* 128 (38) (2006) 12394–12395.
- [106] J. Klinowski, F.A.A. Paz, P. Silva, J. Rocha, Microwave-assisted synthesis of metal-organic frameworks, *Dalton Trans.* 40 (2) (2011) 321–330.

Potential of hydrophobic metal-organic framework-based materials for environmental applications

10

*Syamantak Roy, Subhajit Laha and Tapas Kumar Maji**

Molecular Materials Laboratory, Chemistry and Physics of Materials Unit, School of Advanced Materials, Jawaharlal Nehru Centre for Advanced Scientific Research, Bangalore, India

*Corresponding author. e-mail address: tmaji@jncasr.ac.in

10.1 Introduction

Metal-organic frameworks (MOFs) are crystalline extended porous framework structures formed by the combination of a vast choice of organic linkers and metal ions [1]. Based on their molecular structures, they can be used for tailored applications ranging from gas storage and separation, catalysis to electronic devices [2]. MOFs can also be fabricated at the nanoscale (NMOFs) to magnify these properties and also induce solution processability [3]. This has led to practical applications of MOFs as optoelectronic devices, sensors, and drug delivery vehicles etc. [4]. Another approach to enhance the already existing properties of MOFs is to fabricate MOF-based nanocomposite materials. This not only retains the MOF properties, but also adds new properties in gas adsorption, biological applications, as well as potential in electrocatalyst materials for battery and fuel cell applications [5,6]. Another method to tune the existing properties of MOFs and generate newer applications is via postsynthetic modification of the MOF structures. It involves a variety of techniques, such as guest inclusion, metalation, linker modifications, metal or ligand exchange, or pyrolysis of MOF structures to induce newer properties [7]. So we see that MOF chemistry offers a large playground to search for new applications that better the existing ones. From henceforth, we will be discussing about mainly environmental applications of MOFs, focusing on oil–water separation and also greenhouse gas, mainly CO₂, capture [8].

A lot of research has been dedicated over the past two decades to the potential of MOFs in solving environmental issues like toxic and pollutant gas capture, storage, and separation [9–13]. Focus has mainly been on sequestration of pollutant gases such as CO₂, CO, and SO₂ [14,15]. H₂ storage has also garnered interest due to its environmentally friendly combustion by-product: water [16,17]. The literature on MOFs has therefore been rich with examples of design strategies and

applications of these systems in gas capture. However, there remain obstacles in generating state-of-the-art MOF materials which have the potential to meet the global industrial demands for reducing the atmospheric CO₂ to permissible levels. One of the problems is selectively capturing CO₂ from a mixture of other gases and water vapor at ambient conditions. Newer MOF materials are being discovered frequently that show exceptional selectivity toward CO₂ capture. A detailed discussion is out of the scope of this chapter and the readers are encouraged to check references given here for further study on this specific topic [18–20]. The major drawback that will be discussed in this book chapter is the competitive processes that inhibit CO₂ uptake in MOFs. Generation of unsaturated metal centers in MOFs have been found to be an useful strategy in increasing the uptake of CO₂ in MOFs [21–23]. However, this also encourages the coordination of water molecules from atmospheric moisture leading to an undesired lower uptake of CO₂ by the so-called “competitive inhibition” mechanism. As a result, MOFs which show both water repellent capability and also high CO₂ uptake are taking up the forefront of MOF research. Interestingly, fabricating such MOF structures requires a careful design strategy and to date no MOF has been found that simultaneously shows extreme water repellence as well as exceptional CO₂ uptake at ambient conditions. In this book chapter, we will discuss how to overcome this problem, by putting forward design strategies and examples of superhydrophobic MOF structures and also separately discuss the properties of materials that show appreciable CO₂ uptake. This would put forward a clearer understanding of future material design for CO₂ capture via the examples and discussions involved here (Scheme 10.1).

Oil spills are an environmental catastrophe generated from oil through land runoff, vessel and pipeline leakage, seaward petroleum production and operation, shipping activities, and most importantly accidental tanker and illegal bilge discharge in the catastrophic area [26–28]. In last 40 years, more than 5 million tons of oils was spilled due to tanker incidents [26]. The deadly impact of marine oil spills disturbs the human lifestyle either by inviting long-term health issues or by diminishing the economic status of a coastal region [27]. As well as human beings, fish, mammals, and wildlife including birds suffer from several complications due to oil spill pollution [29]. Therefore, it is very important to find out the ways to remove or separate oil from ocean water. With rising industrial oily waste as well as frequent spill accidents, scientists are looking for some materials which can separate oil from water without causing any harm to the environment. Technologies like separation, filtration, centrifugation, floatation, and electrochemical methods are predominantly used for oil spill cleanup [30]. Among the several methods reported so far, adsorptive-based separation attracts the predominant attention due to its simplicity, energy consumption, and low cost [31]. Materials with mixed features like hydrophobicity with an oleophilic nature can be the right choice as a separator. It has been also reported previously that materials which contain both the character of *superhydrophobic* (with more than 150 degrees water contact angle) and *superoleophilic* (with less than 10 degrees oil contact angle) are ideal for oil/water separation in humid conditions [32]. Traditional nature-inspired materials with low surface energy and self-cleaning surface include polymer sponges, porous graphitic carbon



Scheme 10.1 Schematic showing the bulk MOFs, nanoscale MOFs, and MOF nanocomposites for water repellent applications in oil–water separation and increased toxic gas uptake.

Reproduced with permission from T.-H. Chen, I. Popov, O. Zenasni, O. Daugulis, O.S. Miljanic, Superhydrophobic perfluorinated metal-organic frameworks, *Chem. Commun.* 49 (2013) 6846–6848; S. Roy, V.M. Suresh, A. Hazra, A. Bandyopadhyay, S. Laha, S.K. Pati, et al., Solvent modulated emission properties in a superhydrophobic oligo-(*p*-phenyleneethynylene) based 3D porous supramolecular framework, *Inorg. Chem.* 57 (2018) 8693–8696.

and its composites, polymethylsilsequioxane, aerogels, membranes with nanowires, and steel meshes and fabric [33]. However, all these materials are difficult to apply practically due to the multistep preparation procedures and highly expensive components. The environmental and economic demand emphasizes the need for a material with properties such as facile and cheap synthesis, high surface area with hierarchical pore structure, minimum water uptake, and outstanding reusability.

MOF with high water contact angles can be a potential material for this particular purpose. This approach allowed us to introduce hydrophobic–oleophilic MOFs which will admit oils (paraffin, isoparaffins, aromatics solvents, cycloalkanes, and unsaturated alkanes) by preventing water filling into the pore. A large number of superhydrophobic MOFs with long chain alkyl substituents and/or fluorinated linkers are reported in the literature [34–37]. Recently a new class of fluorinated metal-organic frameworks (FMOFs) with perfluorinated inner surface has offered an excellent oil adsorption in the presence of water or moist air. Silver(I)-3,5-bis(trifluoromethyl)-1,2,4-triazolate (AgTz) was the first example of FMOF to show high efficiency for the adsorption of conventional aromatic and aliphatic oil components [36]. Apart from using the concept of tailoring functional properties of MOF, a new concept has developed of making MOF composites with other suitable components. Zeolite imidazole frameworks (ZIFs) are very robust porous coordination polymers

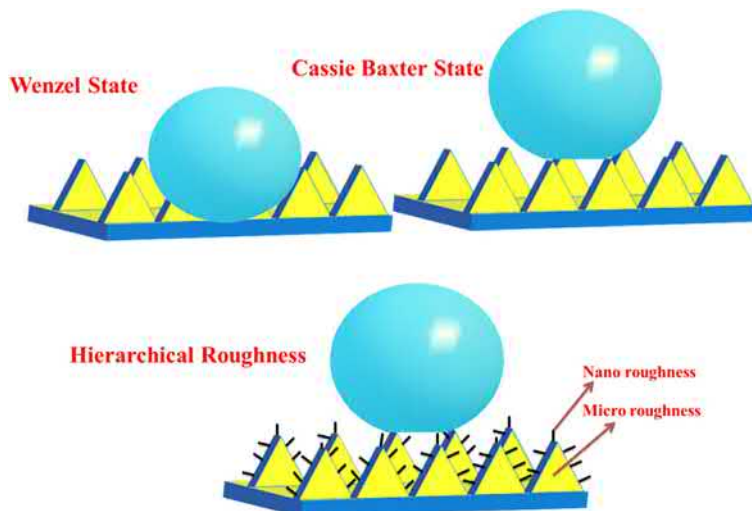
exhibiting exceptional chemical flexibility and showed a promising stability toward water as well. The hybridization of ZIF-8 with graphene and its derivatives [38–40] and carbon nitride [41] showed outstanding oil spill capture due to its dual superhydrophobic and oleophilic nature.

10.2 The lotus effect

When scientists set out to invent a new property artificially, nature provides the best design principles from which inspirations are taken. Superhydrophobicity, in the same way is strewn across the natural world and whose understanding can lead to the fabrication of water repellent artificial materials. Prime examples of natural superhydrophobic systems are the lotus leaf and the leg of the insect water-strider [42,43]. Specifically, the surface of the lotus leaf has been extensively investigated to reveal clues for the origin of its extreme water repellence [44–46]. It has been observed under SEM, that the surface contains numerous protrusions separated by a micrometer distance. This traps air pockets in between, thereby not allowing water droplets to touch the external surface. Interestingly, it was also noticed that these micro-sized protrusions had a waxy coating. This waxy coating was analyzed to have undulations at the nanoscale. Later it was realized that the combination of the micro- and nanospacings assisted in the easy rolling of water droplets on the lotus surface which was also termed as the self-cleaning effect. Therefore, the lotus leaf gives a clear idea that increased surface roughness, both at the micro- and nanoscale leads to water repellence even without the slightest external perturbation.

10.3 Models of superhydrophobicity

Young's equation ($\cos \theta = (\gamma_{sv} - \gamma_{sl}) / \gamma_{lv}$ (where θ is the contact angle between the solid–liquid interface, $\gamma_{sv,sl}$ and γ_{lv} are the corresponding surface tensions between the solid, liquid, and air interfaces) is used to describe the wettability of a smooth surface. On a rough surface, the same is explained by two models: Wenzel and Cassie–Baxter (Scheme 10.1) [47,48]. According to the Wenzel model, the water droplet on a rough surface is spherical in shape and wets the surface. As a consequence it will not roll off the surface under the slightest disturbance. A transition from the Wenzel to the Cassie–Baxter model occurs when we consider that rough textures on a surface trap air pockets in between. Therefore the water droplet cannot assume a spherical shape and rests on the rough texture with air pockets trapped in between. This results in a low adhesion of the droplet to the surface and hence on the smallest perturbation, water rolls off the surface. It is theorized and verified experimentally that low surface energy along with a hierarchical surface roughness is essential to generate such superhydrophobic structures. A hierarchical structure implies the presence of roughness at two regimes: micro and nano (Scheme 10.2). This leads to water contact angles >150 degrees giving rise to superhydrophobicity



Scheme 10.2 Schematic depicting two different theoretical models to explain water repellency of a liquid on a rough surface (Wenzel model and Cassie–Baxter model) and also the requirement of a hierarchical surface structure for the generation of superhydrophobicity and self-cleaning.

and self-cleaning applications. Along with surface roughness, surface shape, size, height, and periodic patterning could also lead to surface water contact angles in excess of 150 degrees.

For any material to be called self-cleaning, in addition to water contact angles higher than 150 degrees, tilt angle and contact angle hysteresis are important terms that must also be discussed [49,50]. Materials must have a tilt angle from the surface lower than 10 degrees, for it to qualify as self-cleaning. Additionally, one must measure the contact angle hysteresis, that is, the difference between the advancing and receding contact angles. This must be as low as possible. The value for the lotus leaf was found to be approximately 2 degrees. Advancing contact angle is the angle of contact when the water droplet is dropped on the surface whereas the receding contact angle is the angle of contact at the moment of the water droplet leaving the surface. This dynamic measurement is therefore an important criteria for characterization of a water repellent self-cleaning material [51,52].

10.4 Bulk metal-organic framework structures for superhydrophobic applications

The first foray into building superhydrophobic MOFs was initiated by the group of Seth Cohen [53]. The idea conceived by them utilized the previously discussed principle of decorating structures with water repellent functional groups to induce

water repellency. MOF structures can be easily tuned by a choice of metal nodes and organic linkers. The group first studied hydrophobic MOFs and delineated the reasons behind the hydrophobicity. Isoreticular metal-organic frameworks (IRMOFs) are cubic frameworks comprised of Zn_4O clusters and dicarboxylate ligands. The series of long alkyl chain incorporated, that is, postsynthetically modified IRMOFs that were studied, showed water repellent properties due to branched alkyl chains attached to amide groups (Fig. 10.1). The water contact angles and structural integrity remained intact over a period of 4 days. However, superhydrophobicity was not realized in these systems. The authors then ventured into more chemically robust MIL- NH_2 systems (Material Institut Lavoisier (MIL)) which were modified with long alkyl anhydrides with higher contact angles, which pushed the water contact angles into the superhydrophobic region of ≥ 150 degrees. The authors proposed that a combination of micro-crystallite sizes in combination with hydrophobic alkyl groups led to extreme water repellence or superhydrophobicity in the MIL-derived systems. This work showed that introducing hydrophobic groups into the organic component of MOFs could lead to superhydrophobic properties. However, the authors were not able to induce this property without postsynthetically modifying the MOF structure.

In another study into inducing moisture stability in NbO-type MOFs, the Zhou group utilized several tetracarboxylate-based linkers with varying lengths of alkyl side chains on the central phenyl rings to construct a series of MOFs of the formula $Cu_2(TPTC-OR)$ ($TPTC-OR = 2',5'$ -di{alkyl}oxy-[1,1':4',1''-terphenyl]-3,3'',5,5''-tetracarboxylate, $R = Me, Et, nPr, nHex$) [54]. The structures of $Cu_2TPTC-OR$ were formed by 4-connected square planar Cu_2 -paddlewheel SBUs and 4-connected rectangular planar $TPTCOR^{4-}$ organic linker. The Cu_2 -paddlewheels were held by four carboxylates from four separate $TPTCOR^{4-}$ linkers which were further bridging between two Cu^{II} ions. When two such paddlewheels are joined, NbO-type networks of $6^4 \cdot 8^2$ topology were formed. The NbO network may be described as being composed of two types of cages or channels. It was seen that upon changing the side chains from ethyl to hexyl, the water repellency increased in the resulting

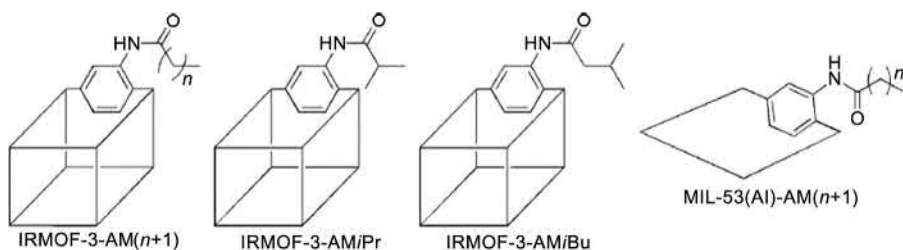


Figure 10.1 Schematic representations of the MOFs examined in this study. One modified organic ligand substituent is shown in each structure.

Source: Reproduced with permission from J.G. Nguyen, S. Cohen, Moisture-resistant and superhydrophobic metal – organic frameworks obtained via postsynthetic modification. *J. Am. Chem. Soc.* 132 (2010) 4560–4561.

MOF structure. The MOF constructed from the tetracarboxylate linker having hexyl chains portrayed superhydrophobic properties but at the same time decreased in thermal stability when compared to other MOFs in the same series. This observation was attributed to the decrease in surface free energy due to the presence of long alkyl chains that led to the water repellent behavior.

It is also well-known that fluorinated long alkyl chains with $-F$ or $-CF_3$ groups decrease the surface free energy or increase the surface roughness [55]. Seminal work by Omary et al., showed that fluorinated MOFs, or FMOFs as they are termed, have great potential for environmental applications such as oil–water separation. FMOFs were constructed from silver(I) and 3,5-bis(trifluoromethyl)-1,2,4-triazolate ($AgTz$) [36,56,57]. This imparts a fluorinated and hydrophobic inner core to the pore structure which is ideal for water repellence and uptake of nonpolar components. Therefore, these also have the potential for capturing oils and other hydrocarbons within the polar surface. In this work, the authors synthesized two such MOFs, FMOF-1 ($Ag_2[Ag_4Tz_6]$) and FMOF-2 ($[Ag(Ag_3Tz_4)]_{3/2}$) (Fig. 10.2A and B). The water adsorption profile showed no uptake of water vapor. To further prove the water repellency of FMOF-1, the degassed FMOF-1 crystals were immersed in water for several days before single crystal data were collected. The structure still remained identical to the crystal structure that was not soaked in water. This indicated that the structure did not allow any water molecules to penetrate its pore and also did not allow distortion on exposure to water. After further investigations, it was inferred that, based on the superhydrophobicity models of understanding, water molecules tend to form thin films with the outer hydrophobic surface via strong hydrogen bonding interactions [58,59]. The authors further reported the excellent uptake capacity of C6–C8 (benzene, toluene, *p*-xylene, cyclohexane, and *n*-hexane) hydrocarbons by these FMOFs, which are essential components of oil mixtures (Fig. 10.2C). Therefore, this work showed that FMOFs can selectively absorb oil components over water and prove to be excellent candidates for cleanup of oil–water mixtures. It is worth mentioning that surface water repellent investigations, such as water contact angle measurements, were not carried out and hence the extent of superhydrophobicity of the FMOF surfaces was not quantified.

Chen et al. further utilized this principle to fabricate superhydrophobic MOFs. In their design principle, they used linkers where the benzene rings were substituted with $-F$ groups (Fig. 10.3A) [24]. Two organic linkers which were synthesized had end capping carboxylic acid and tetrazolate groups, respectively. Three novel MOF structures were synthesized (Fig. 10.3B(a–c)) out of which two were hydrophobic and one superhydrophobic with an average water contact angle of 151 degrees (Fig. 10.3C). Along with the surface, the pores were also found to be water repellent. This was concluded as there was minimal uptake of water vapor when adsorption studies were carried out. Interestingly, this was the first such report of generating inherent surface superhydrophobicity in bulk MOF structures without any postsynthetic modification.

Another interesting approach to generate superhydrophobic MOF was put forward by Kitagawa and coworkers where they proposed that anisotropic crystal

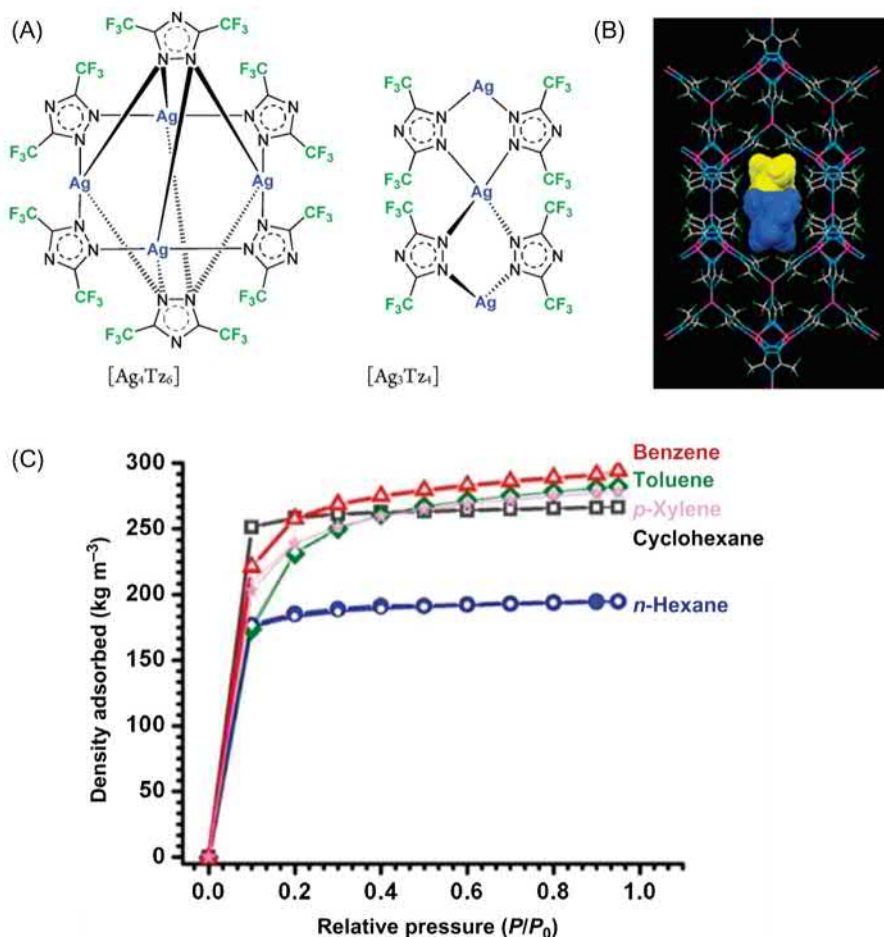


Figure 10.2 (A) Building Blocks of FMOF-1 (left) and FMOF-2 (right). (B) Crystal structure of FMOF-1.2Toluene showing toluene molecules in one large channel repeat unit and (C) Oil components adsorption in FMOF-1 using vapors of cyclohexane, *n*-hexane, benzene, toluene, and *p*-xylene. Open symbols indicate desorption.

Source: Reproduced with permission from C. Yang, U. Kaipa, Q.Z. Mather, X. Wang, V. Nesterov, A.F. Venero, et al., Fluorous metal-organic frameworks with superior adsorption and hydrophobic properties toward oil spill cleanup and hydrocarbon storage, *J. Am. Chem. Soc.* 133 (2011) 18094–18097.

morphology generated via surface corrugation through aromatic hydrocarbon moieties induces water repellence [34]. This negates the use of postsynthetic modification techniques. 1,3,5-tris(3-carboxyphenyl)benzene (H₃BTMB) ligand was used along with Zn^{II} to synthesize a 2D layered MOF [Zn₄(μ₃-OH)₂(BTMB)₂(DMF)₃(MeOH)] · (DMF)₂ · (MeOH) (PESD-1) which contained the surface projected aromatic groups decreasing surface free energy. Both the

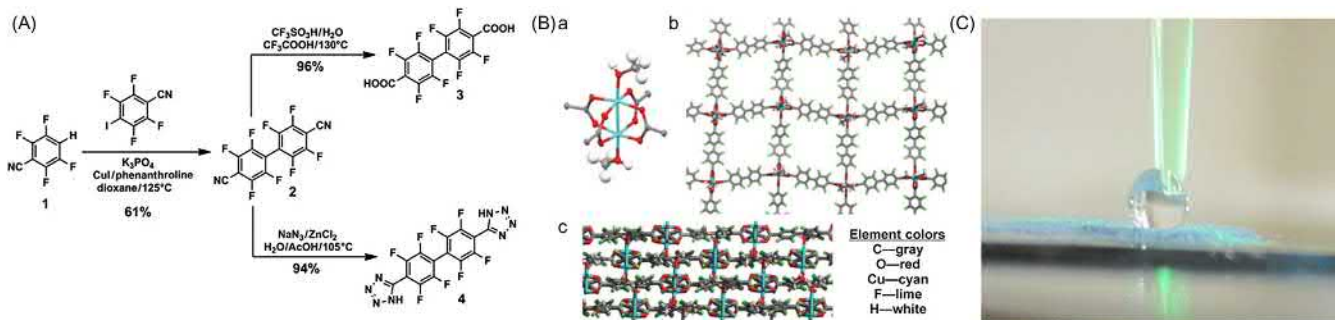


Figure 10.3 (A) Synthesis of ligands 3 and 4. (B) X-ray crystal structure of MOFF-3, $Cu^{2+}(4-2H^+)(H_2O)$. (a) Secondary building unit. (b) View along the one-dimensional channels in the structure. (c) View of the structure perpendicular to the orientation of the channels. (C) Picture of an oven-dried MOFF-3 sample, after a drop of water was placed onto it.

Source: Reproduced with permission from T.-H. Chen, I. Popov, O. Zenasni, O. Daugulis, O.S. Miljanic, Superhydrophobic perfluorinated metal-organic frameworks, Chem. Commun. 49 (2013) 6846–6848.

as-synthesized and degassed samples in single crystal, powder, and pelletized form showed water contact angles ≥ 150 degrees. A pellet of PESD-1 when placed within a mixture consisting of an organic solvent and water, floated on the water surface without breakage, and further selectively removed the organic solvent from the water.

MOF systems in the bulk showing water repellent properties have also been synthesized by us. Recently, we used an alkoxy-octyl *oligo*-(*p*-phenyleneethynylene) (OPE) linker to fabricate a Cd^{II}-based MOF $\{\text{Cd}(\text{OPE-C}_8)(\text{DMF})_2(\text{H}_2\text{O})\}$ having a permanently porous 3D supramolecular framework structure [25]. Self-assembly of OPE-C₈ with Cd(NO₃)₂·4H₂O in a DMF/ethanol mixture led to the formation of single crystals. Structural determination showed that the 1D chains of the MOF were extended in a zigzag fashion via coordination of terminal carboxylates of OPE to the Cd^{II} center (Fig. 10.4A). Supramolecular interactions between π cores and alkyl chains led to the 2D packing. Further interweaving of the 2D planes led to the 3D porous structures where coordinated DMF and water molecules occupy the pore surface (Fig. 10.4B). Surface projected alkyl chains were also found in the MOF structure (Fig. 10.4C) and gave direct proof that long surface projected alkyl chains led to the superhydrophobicity in the structure. This leads to the decrease in surface free energy and therefore higher water contact angles of 157 degrees (Fig. 10.4D and E). The contact angle also remained intact in the degassed state. The pore was also found to be superhydrophobic as it showed appreciable uptake of nonpolar solvent vapors such as benzene. The MOF also showed permanent porosity with an appreciable CO₂ uptake. Additionally, the MOF showed a guest solvent modulated emission property owing to the twisting and straightening of the OPE backbone

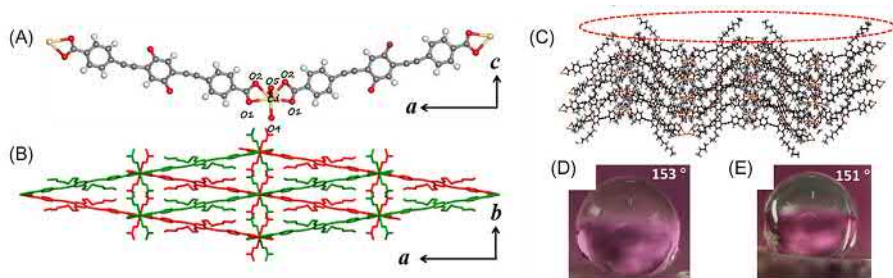


Figure 10.4 (A) Structural representations of $\{\text{Cd}(\text{OPE-C}_8)(\text{DMF})_2(\text{H}_2\text{O})\}$: (A) view of the asymmetric unit and 1D coordination chain; (B) view of the 3D structure formed via interweaving of the 2D sheets. (C) Packing diagram of $\{\text{Cd}(\text{OPE-C}_8)(\text{DMF})_2(\text{H}_2\text{O})\}$, viewed along the b axis showing surface projected alkyl chains and water contact angle of (D) $\{\text{Cd}(\text{OPE-C}_8)(\text{DMF})_2(\text{H}_2\text{O})\}$ and (E) degassed $\{\text{Cd}(\text{OPE-C}_8)(\text{DMF})_2(\text{H}_2\text{O})\}$ coated glass substrate.

Source: Reproduced with permission from S. Roy, V.M. Suresh, A. Hazra, A. Bandyopadhyay, S. Laha, S.K. Pati, et al., Solvent modulated emission properties in a superhydrophobic oligo-(*p*-phenyleneethynylene) based 3D porous supramolecular framework, *Inorg. Chem.* 57 (2018) 8693–8696.

constructing the MOF structure. When DMF molecules were removed and reintroduced into the structure, the emission shifted bathochromically back to the original color. This is an example of a superhydrophobic MOF structure that could have potential water repellent optical applications, such as sensing under moist conditions.

10.5 Nanoscale superhydrophobic/self-cleaning metal-organic frameworks based on *oligo-(p-phenyleneethynylenes)* linkers

There have been numerous reports on different synthetic procedures of NMOFs [60–62]. Some of them, like the coordination modulation method or poor solvent precipitation, have received wide acclaim and paved the way toward the synthesis of a wide variety of NMOFs showing multifunctional properties. However, in our work, we have demonstrated a novel and slightly different approach in the synthesis of NMOFs which deviates from common norms in that it uses a ligand design approach for such syntheses. Bola-amphiphilic molecules have long been known to self-assemble into interesting nanostructures in solvents of different polarity. Recently, we have reported that *oligo-(p-phenyleneethynylenes)* (OPE) dicarboxylates with octyl side chains appended to the conjugated backbone (OPE-C₈) can self-assemble with Zn(OAc)₂ · 2H₂O to form size- and shape-tunable nanostructures. The use of acetate counter anions to the Zn^{II} center acts as a coordination modulator to restrict growth, forming the nanostructure of MOFs [60]. Additionally, the flexibility of long alkyl chains in solvents of different polarity can control shape transformation of MOF nanostructures. In this work, we showed how reaction solvent and time can form MOF nanovesicles and nanotoroids. The porous nature of the MOF was further utilized to incorporate DSMP dye and the Forster Resonance Energy Transfer (FRET) process was realized in the system. Our next approach was to induce water repellent properties in similar MOF nanostructures. We therefore used predesigned OPE bola-amphiphiles [63,64] and self-assembled them with Zn^{II} ions to form MOFs structured at the nanoscale. The interesting part of the design principle was that we varied the alkyl chain lengths in different MOFs and saw that from $n = 8$ up to $n = 18$ generates superhydrophobic properties in the MOF structure. Out of these, up to $n = 12$, self-cleaning property was also induced which was unprecedented in MOF chemistry.

In one such work, we utilized the above discussed design approach to construct a NMOF, hierarchically surface structured to mimic the lotus leaf in its self-cleaning property. The rational construction of this NMOF allowed high water contact angles, corrosion resistance, and was the first reported of any MOF structure to show the self-cleaning effect [65]. Additionally, we were also able to control the formation of nanobelts and nanoscrolls of the NMOF by varying the reaction time and solvent polarity. Coordination directed self-assembly of an alkoxy-octadecyl OPE system (OPE-C₁₈) with Zn(OAc)₂ gave rise to a framework structure with

long alkyl chains projected both outwards and also within the pores to generate a superhydrophobic NMOF structure having the formula $\{Zn(OPE-C_{18}) \cdot 2H_2O\}$ (NMOF-1) (Fig. 10.5A). As was realized in our previous OPE work, we were able to reversibly transform nanobelts of NMOF to nanoscrolls keeping the superhydrophobicity intact (Fig. 10.5B). The periodic alignment of the long alkyl chains in both the nanostructures not only generated the superhydrophobicity but also protected the structure from degradation under harsh conditions. The contact angle was found to be an all-time high of 162 degrees with contact angle hysteresis of 2 degrees, the same value as that of the surface of the lotus leaf (Fig. 10.6A(a–d)). Self-cleaning effect was attained due to hierarchical surface roughness both at the micro- and nanoscale due to the periodic repetition of the rigid OPE backbone and the associated long alkyl chains (Fig. 10.7A(e–g)). 3D-AFM images showed that the MOF had the “hills and valley” type surface morphology at the microscale (Fig. 10.6B(a and b)). Upon further probing, at the nanoregime, we observed that the same “hills and valley type” morphology was present (Fig. 10.6B(c–e)). This assisted the easy rolling of water droplets from the surface of the MOF without any external perturbation. We further observed that due to inward projected alkyl chains the pore was also water repellent but adsorbed good amounts of nonpolar solvent like benzene (Fig. 10.6B(a)). Therefore, this MOF could also capture nonpolar solvents with potential applications in oil–water separations.

Buoyed by the results of the above work, we looked to expand the applicative areas of related NMOF structures to water repellent optoelectronic devices. The synthetic strategy was kept the same, the only difference here being that an alkoxydodecyl OPE linker was used to self-assemble with Zn^{II} in THF solution [66]. This resulted in the formation of nanosheets of MOF with surface projected alkyl chains (Fig. 10.7A and B). This led to high water contact angles of 157 degrees (Fig. 10.7C). As expected, the self-cleaning effect was also realized due to similar structural ordering as in the previous work. 3D-AFM images also showed an expected “hills and valley morphology.” However, the contact angle hysteresis was found to be slightly higher (5 degrees) as compared to the previous work. As expected, the pore was also hydrophobic. The MOF showed high uptakes of benzene whereas it had minimal uptake of water. Therefore, this MOF also showed potential for oil/water separation. Due to the presence of OPE within the structure, we further studied its optoelectronic property. The nanoscale architecture allowed great dispersability and smooth coating on glass substrates (Fig. 10.7D). The MOF showed excellent cyan luminescence with high quantum yields and conductivity profiles in the $10^{-5} \text{ S cm}^{-1}$ range. Interestingly, the conductivity increased upon exposing it to AM 1.5 radiation (Fig. 10.7E). This further motivated us to fabricate device structures from this MOF (Fig. 10.7F). The device showed photoresponsive Schottky barrier diode-like behavior (Fig. 10.7G). This was unprecedented in permanently porous framework structures. The rectification ratio increased from 47 to 83 upon irradiation with AM 1.5 light. This is the highest rectification value reported for MOF materials to date. Coupled with the extreme water repellence, this material could find applications in MOF devices working even under water, providing a new energy application in MOF chemistry.

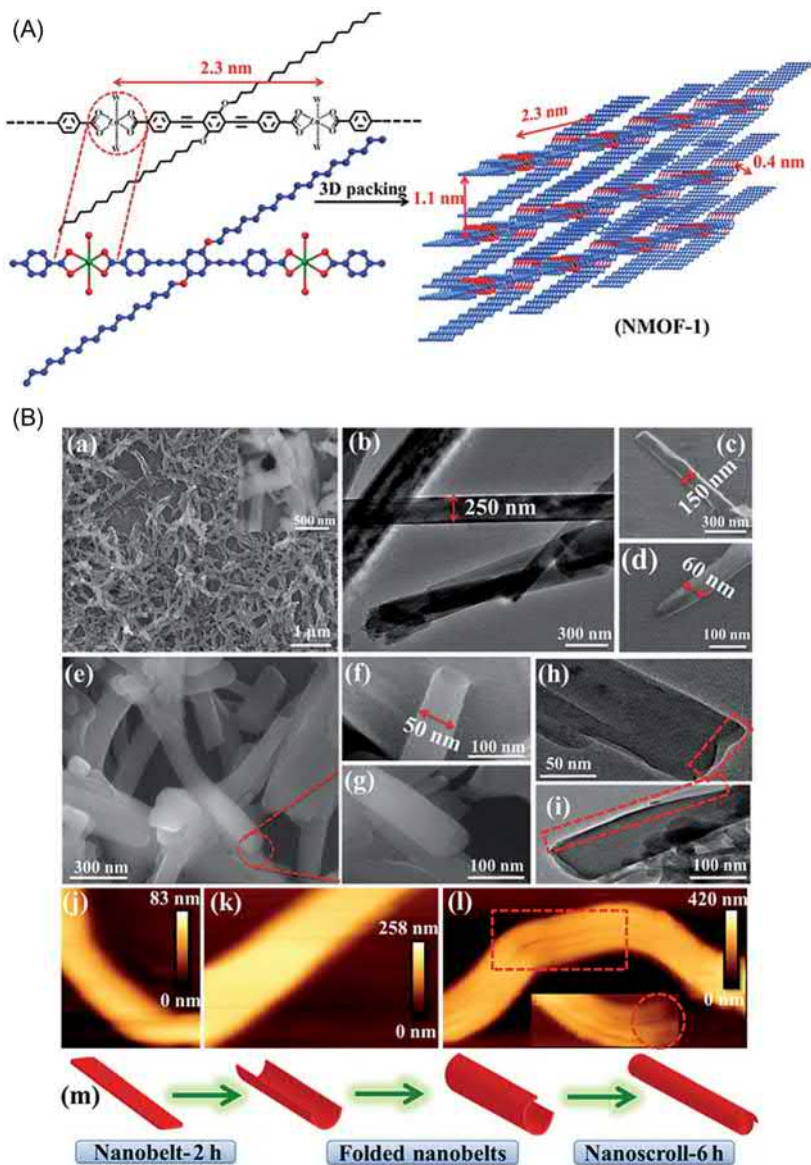


Figure 10.5 (A) Bottom-up approach for the fabrication of a self-cleaning MOF nanostructure by coordination driven self-assembly between Zn^{II} and OPE- C_{18} . (B) (a) FESEM image (inset: nanobelts at higher magnification) and (b) TEM image of NMOF-1 nanobelts. (c and d) FESEM images of semiscrolled nanobelts. (e–g) FESEM and (h and i) TEM images of nanoscrolls at different magnifications showing the changes in cross-section upon scrolling. AFM image of (j and k) nanobelt and (l) nanoscroll (inset: single nanoscroll showing opening at the mouth). (m) Schematic showing the possible morphological transformation of nanobelts to nanoscrolls in NMOF-1.

Source: Reproduced with permission from S. Roy, V.M. Suresh, T.K. Maji, Self-cleaning MOF: realization of extreme water repellence in coordination driven self-assembled nanostructures, *Chem. Sci.* 7 (2016) 2251–2256.

10.6 Metal-organic framework nanocomposites for oil/water separation

In continuation of the previous discussion of using fluorinated organic linkers for the construction of water repellent bulk MOFs for treating oil–water spillage, Ghosh and coworkers provided an in-depth study of how ultrahydrophobicity can be introduced into MOFs $[\{Cu_4L_4(DMF)_4\}(DMF)_3]_n$ (UHMOF-100) [67]. They also extensively studied and quantified surface water repellence and also experimented on the practicability of these materials to separate actual mixtures of oil and water. Single-crystal structural analysis revealed that bis(trifluoromethyl) groups from fluorinated linkers were present in the ultramicroporous channels. Expectedly, there was minimal water vapor uptake for this MOF. However, the framework showed step-wise uptake of C6–C8 hydrocarbons: benzene, ethyl benzene, toluene, and *p*-xylene. Study of the exterior surface revealed the MOF to be ultrahydrophobic with an unprecedented water contact angle of close to 177 degrees and low contact angle hysteresis of 2–4 degrees. The importance of framework formation was further illustrated when the fluorinated organic linker showed a much lesser contact angle of 136 degrees. Interestingly, when water droplets were cast on the MOF surface, they bounced away proving its extreme water repellence. The authors then spray-coated this MOF mixed with PDMS on a polypropylene polymeric support to form a reusable coated membrane. The water contact angle was found to be 135 degrees. The membrane showed volumetric oil/water (1:1) separation. The entire water portion colored with methyl orange was retained at the top of the filtering UHMOF-100/PDMS/PP membrane as the membrane was inherently water repellent. The whole oil fraction from a 1:1 oil/water mixture passed through within 1.5 hours, even in the absence of any externally applied vacuum. Other water-in-oil emulsions showed the same permeation limits for oil for UHMOF-100-based membranes. This work was an important milestone in showing real-time oil–water separation using superhydrophobic MOF-based membranes.

One such attempt to make solution processable hydrophobic/oleophilic materials was made by Fischer and coworkers via the synthesis of porous nanoscale metal-organic composites [68]. In their unique approach, the metal-organic gel (MOG) nanoparticles were initially synthesized by the self-assembly of MOF nanoparticles. The procedure is described as follows: linkage of Al^{3+} with 1,3,5-benzene tricarboxylate (BTC) linker forms MOF structures. Then, self-assembly of MOF into MOF nanoparticles occurs followed by the formation of hierarchical porous MOGs. This is through a disordered, coordination perturbed self-aggregation of the MOFNPs. Here the MOF structure had a Zeolite MTN (MTN = zeolite socony mobil thirty-nine) topology with two types of cavities of small cage 2.5 nm and large cage as 2.9 nm. The final composite, that is, fluorinated graphene oxide-MOG composite (FGO@MOG) was synthesized via the intercalation of MOG between fluorinated graphene oxide layers. As the oxide functionalities of the FGO are utilized in stabilizing the MOF nanoparticles simultaneously, it leaves pendent C-F groups toward the exterior surface in the composite structure. Therefore, the

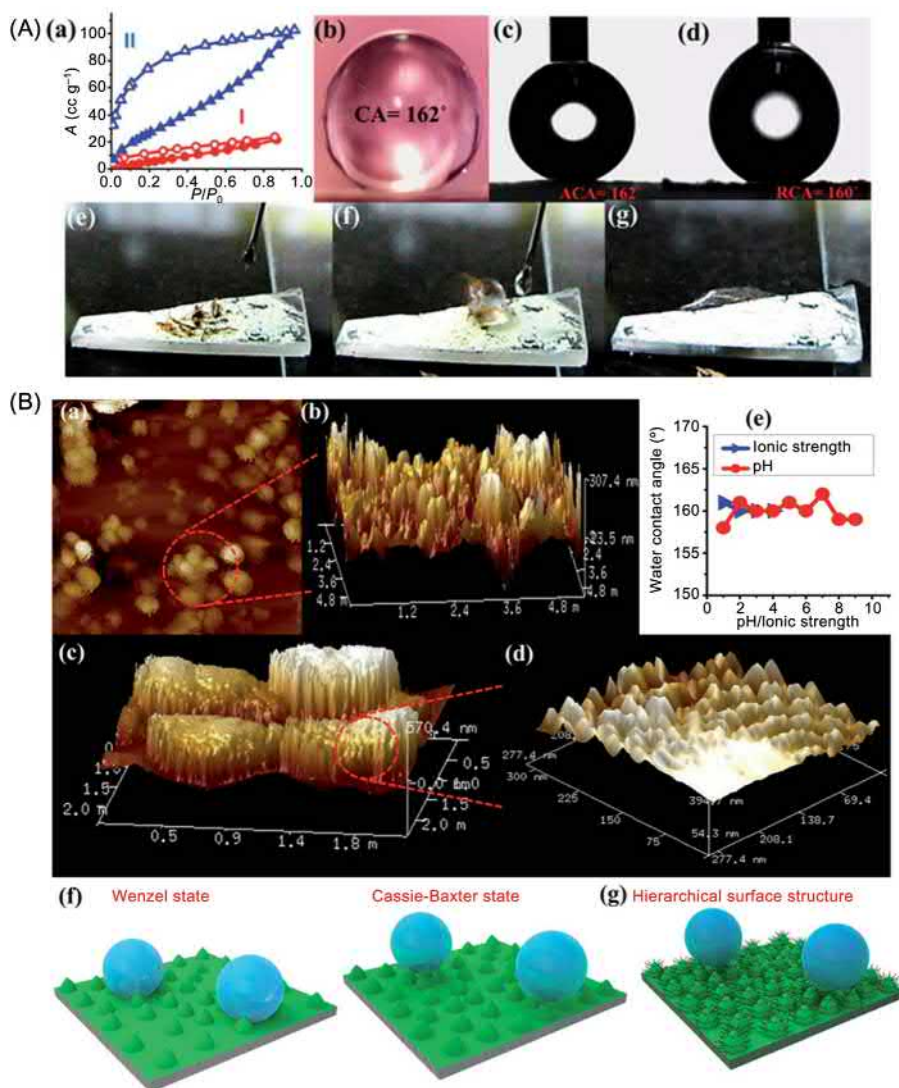


Figure 10.6 (A) (a) Solvent vapor adsorption isotherms of NMOF-1 at 298K: (I) water (red) and (II) benzene (blue), P_0 is the saturated vapor pressure; 3.17 kPa (water) and 12.60 kPa (benzene) at 298K. Water contact angles of NMOF-1 coated substrate: (b) static contact angle, (c) advancing contact angle and (d) receding contact angle (e–g). Video snapshots of self-cleaning experiment showing the removal of dirt from surface. (B) (a) 2D-AFM image of NMOF-1 microparticles on a coated glass surface and (b) corresponding 3D-AFM image. (c) 3D-AFM image of four adjacent microspheres of NMOF-1 and (d) corresponding high magnification image showing continuous nanoroughness present on each microparticle. (e) Plots showing changes in CA with pH/ionic strength. (f) Schematic diagrams showing the different states used to explain surface water repellence: left: Wenzel state or the wetting state. Right: Cassie–Baxter state or the superhydrophobic state (a transition from the Wenzel to the Cassie–Baxter model occurs when we consider that rough textures on a surface trap air pockets in between) and (g) incorporation of hierarchical surface for the generation of the self-cleaning effect in NMOF-1.

Source: Reproduced with permission from S. Roy, V.M. Suresh, T.K. Maji, Self-cleaning MOF: realization of extreme water repellence in coordination driven self-assembled nanostructures, *Chem. Sci.* 7 (2016) 2251–2256.

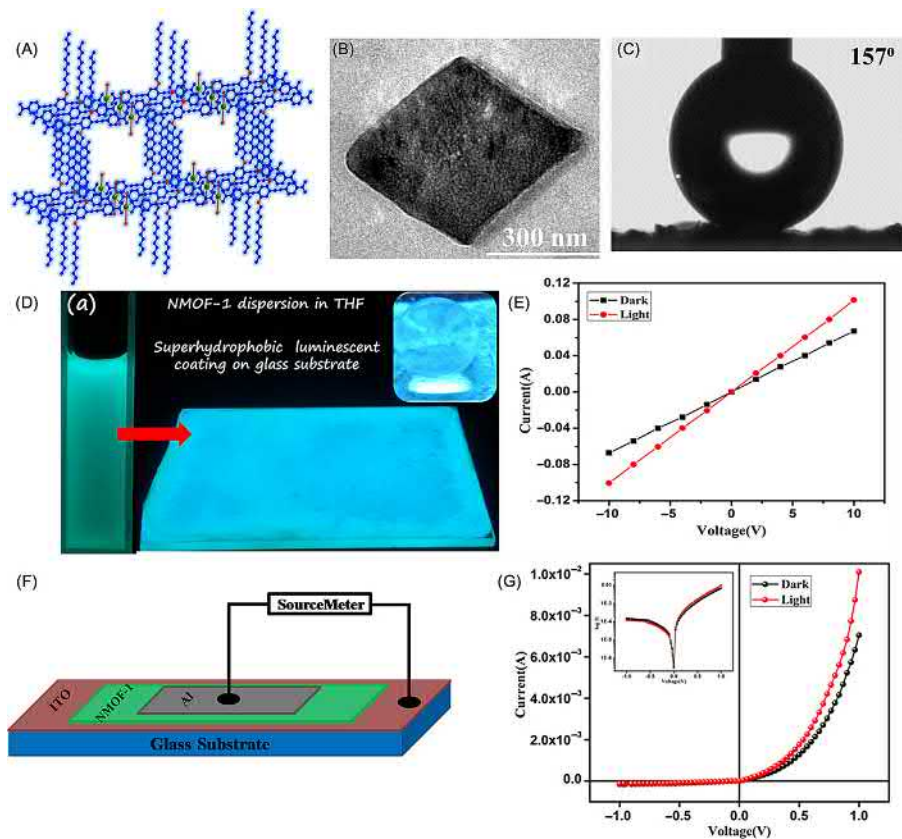


Figure 10.7 NMOF-1: (A) Structural image. (B) FESEM images of nanosheets. (C) Water contact angle coated on a glass substrate. (D) Images of bright emission under UV light of NMOF-1 in THF and on a glass substrate. Inset: Image of a water droplet on the NMOF-1 coated glass substrate under UV light. (E) Current versus voltage graph for conductivity measurement of NMOF-1 with ohmic contact in planar electrode structure. (F) Schematic showing the device structure of NMOF-1 and (G) Current – voltage ($I - V$) characteristics of the ITO/NMOF-1/Al Schottky diode.

Source: Reproduced with permission from S. Roy, M. Das, A. Bandyopadhyay, S.K. Pati, P. P. Ray, T.K. Maji, Colossal increase in electric current and high rectification ratio in a photoconducting, self-cleaning, and luminescent schottky barrier NMOF diode, *J. Phys. Chem. C*. 121 (2017) 23803–23810.

composite was envisioned to have a low surface free energy. This allowed ultrarepellence of water and also absorption of a variety of oil mixtures such as toluene, hexane, heptane, decane, octadecane, petroleum ether, crude oil, veg oil, carbon tetrachloride, and pentane. The authors reported that the adsorption capacity of FGO@MOG varied between 200% and 500% for selected oil and organic solvents. Here, CCl_4 showed the maximum capacity of 500%, whereas octane showed the

lowest but still appreciable value of 200%. This work paved the way to the design of more such MOF-based composites for environmental applications.

The same group devised another unique method to fabricate MOF composites for oil–water separation [33]. For this purpose they utilized highly fluorinated graphene oxide (HFGO) and ZIF-8 to generate a hierarchically porous superhydrophobic/superoleophilic micro–mesostructure (HFGO@ZIF-8). The structure-directing and coordination-modulating properties of surface oxygen functionalities of HFGO allowed the ZIF-8 nanocrystals to grow on the graphene oxide support where it was intercalated between the graphene oxide sheets. This also left surface fluorine groups in the composite. The authors conjectured that the micropores arose due to the presence of ZIF-8 nanoparticles, whereas the mesopores were the result of randomly organized HFGO layers separated by the ZIF-8. HFGO@ZIF-8 showed high water contact angles of 162 degrees and oil contact angles of 0 degree. The composite also showed high sorption selectivity, fast kinetics, and good absorbance for a host of nonpolar/polar organic solvents and oils from water. Buoyed by this observation, a sponge@HFGO@ZIF-8 was also fabricated by immersing a commercial sponge overnight into the reaction mixture of exfoliated HFGO and a methanolic solution of ZIF-8. Sponge@HFGO@ZIF-8 showed an adsorption capacity of 150–600 wt.% of oils, polar and nonpolar organic solvents. Interestingly, the sponge floated on water and hence the extraction of oil in an oil–water mixture was easily achieved.

In another interesting nanoscale MOF composite related wetting work, reported by Tan et al., they bypassed complicated lithographic techniques to epitaxially grow MOF mushroom shaped nanostructures at the tips of needle crystals [69]. This imparted a reentrant texture to the nanostructures which is the primary requirement for omniphobicity, that is, simultaneous oil and water repulsion property. MIL MOF structures were used for the study as they are known to be moisture stable. The authors used an aluminum oxide (AAO) membrane to grow NH_2 -MIL-53(Al) MOF on it (Fig. 10.8A). At this stage of composite formation, the substrate showed microflower-like morphology which was not water repellent and would sink when it was put in a water solution. However, upon further postsynthetic modification of the already grown surface with perfluorooctanoyl chloride, superhydrophobicity was induced and the substrate floated on the water solution. The morphology found upon SEM analysis was that of mushroom-like nanostructures (Fig. 10.8B). The nanomushrooms could support solvent molecules and the proximity of these nanostructures created very little space for solvent to seep through resulting in the omniphobic behavior. Therefore, the important outcome of this work was that a reentrant texture on the surface is a must for the omniphobic property. MOF composite materials possessing this property could ultimately have applications in antiwetting coatings on ships, car windshields, and even in paints.

Sun et al. [70], demonstrated a process of surface coating with bulky fluorinated compounds. As a representative example, they have chosen two vinyl-functionalized MOFs, ZIF-8 and MOF-5, coated with perfluoroalkyl group and the resultant MOF showed amphiphobic (superhydrophobicity with oleophobicity) property. To introduce amphiphobicity in MOF, they have incorporated

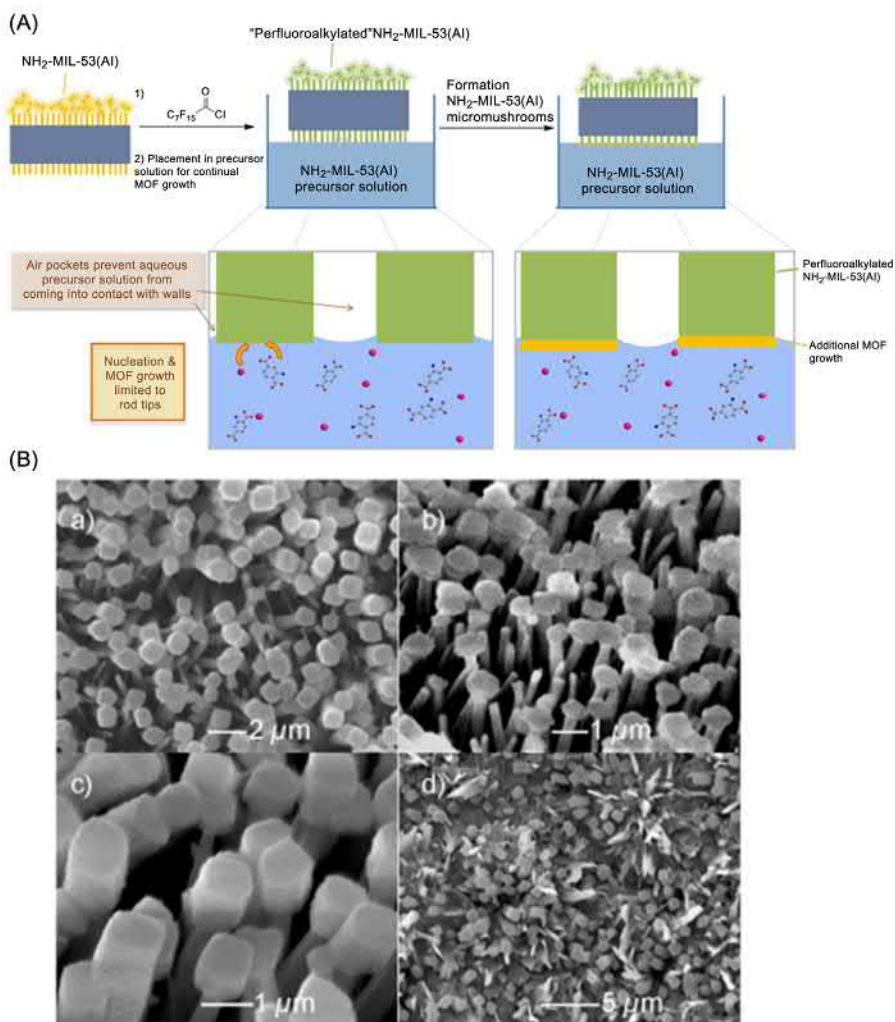


Figure 10.8 (A) Graphical representation of $\text{NH}_2\text{-MIL-53(Al)}$ micromushroom synthesis through interfacial continual growth and (B) SEM images of (a) $\text{NH}_2\text{-MIL-53(Al)}$ micromushrooms; (b) $\text{NH}_2\text{-MIL-53(Al)}$ micromushrooms at 45 degrees tilt angle; (c) $\text{NH}_2\text{-MIL-53(Al)}$ “popsicles” made from stacks of mushroom caps; (d) $\text{NH}_2\text{-MIL-53(Al)}$ film formed from fused mushroom caps.

Source: Reproduced with permission from T.T.Y. Tan, M.R. Reithofer, E.Y. Chen, A.G. Menon, T.S.A. Hor, J. Xu, et al., Tuning omniphobicity via morphological control of metal-organic framework functionalized surfaces, *J. Am. Chem. Soc.* 135 (2013) 16272–16275.

vinyl-functionalized linkers for the targeted framework. These vinyl groups are sufficiently reactive for chemical modification and remain intact during the MOF crystallization. After controllable functionalization by vinyl group, the crystals' surfaces were coated with perfluoroalkyl groups through thiol-ene reaction, and exhibited both superhydrophobicity and oleophobicity. The surface wettability of vinyl-functionalized ZIF-8 (ZIF-8-V) and perfluoroalkyl-coated ZIF-8 (ZIF-8-VF) were characterized by contact angle measurement. Interestingly, the water contact angle of the ZIF-8-VF sample was 173 degrees and exhibited an extraordinarily high superhydrophobic feature, whereas ZIF-8-V showed the water contact angle at 89 degrees. In contrast, a series of organic compounds including glycerol, 2-hydroxybenzaldehyde, benzonitrile, chlorobenzene, and dodecane were repelled by ZIF-8-VF surface with contact angles at 150, 143, 130, 129, and 92 degrees, respectively (Fig. 10.9A). The toluene adsorption isotherm exhibited 7 mg capacity for one gram of ZIF-8-VF whereas for ZIF-8-V it was 143 mg g⁻¹ (Fig. 10.9B and C). These results confirmed that the surface shielding by perfluoroalkyl groups significantly enhanced the hydrophobicity as well as oleophilicity of the material. Similarly, a typically water unstable MOF-5, which renders an extraordinary tolerance to humid CO₂, was successfully surface coated by perfluoroalkyl groups on vinyl-functionalized MOF-5. Amphiphobicity of MOF-5-VF was tested in both acidic and basic solution which revealed an extraordinary stability toward oil and water with respect to the pristine MOF. Such types of materials with amphiphobic behavior may show promising CO₂ adsorption in the presence of aqueous or other organic solvents but won't be effective for oil-water cleanup. Solid surfaces possessing both high water contact angle (hydrophobic) and low contact angle hysteresis (oleophilic) have attracted interest in fundamental research as well as practical applications in the fields of self-cleaning and industrial oily waste water treatment [71,72]. Cao and coworkers [73] recently demonstrated an example in which the wettability of MOF coatings fabricated from HKUST-1 (Cu₃(BTC)₂·3H₂O) was investigated. A facile dip coating method was adopted to prepare superhydrophobic surfaces. Typically, as-synthesized HKUST-1 was dispersed in ethanol and a thin film was formed on the glass surface by evaporating ethanol at ambient temperatures. The thin film was treated with stearic acid and PFOTS (perfluorodecyltriethoxysilane) separately in order to reduce the surface energy of HKUST-1 thin film. FESEM images showed the HKUST-1 coated surface modified by stearic acid and PFOTS presented highly porous and rough structures due to the presence of granules of size 1–2 μm (Fig. 10.10A–C). The individual MOF coating on the glass surface obtained a water contact angle of ~141.7 degrees. In contrast, MOF coated with stearic acid and PFOTS showed 158.3 and 157.6 degrees water contact angle, respectively. Surface wettability of corrosive liquids on the superhydrophobic surface was also investigated. It was also observed that maximum superhydrophobicity can be achieved by tuning the pH from a low to high value (Fig. 10.10G). The contact angle of PFOTS-modified surface varied from 152.8 to 157.6 degrees when the pH was varied from 3 to 13 (Fig. 10.10E–G). The authors additionally investigated the oleophilicity of the surface by adding 5 μL of *n*-octane. The surface modified with stearic acid and PFOTS adsorbed *n*-octane droplet in 4 and 7 seconds,

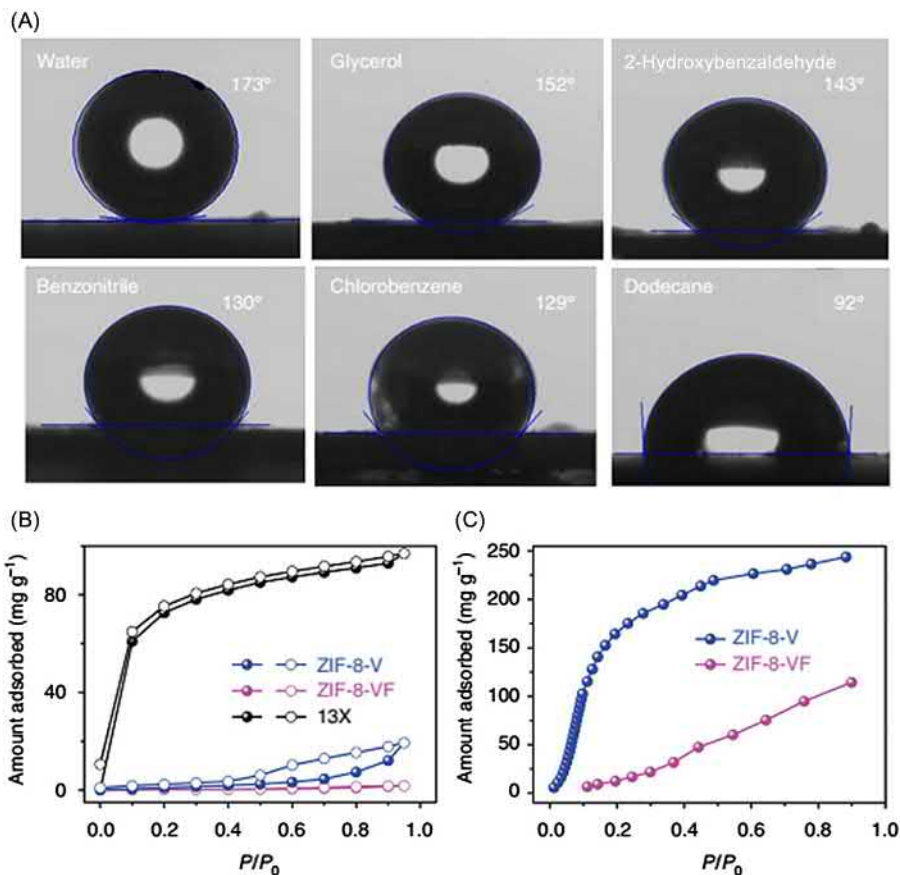


Figure 10.9 (A) Contact angles of various liquid on the pressed pellet made using ZIF-8-VF sample, (B) water adsorption (solid symbols) and desorption (open symbols) isotherms collected at 298K, and (C) toluene adsorption isotherms collected at 298K.

Source: Reproduced with permission from Q. Sun, H. He, W.-Y. Gao, B. Aguila, L. Wojtas, Z. Dai, et al., Imparting amphiphobicity on single-crystalline porous materials, *Nat. Commun.* 7 (2016) 13300.

respectively, manifesting significant superoleophilicity. All these surface modifications of MOF by using alkyl, fluorinated, or hydrophobic polymers face some disadvantages, such as tedious synthetic procedures and reduced surface area of the material. It sometimes results in MOFs that fail to tolerate different environmental conditions where the effect of acid or base is crucial and high ionic strength solvents are available. The authors explained that the presence of carboxylate-based ligands is responsible for the oleophilic nature of MOFs, whereas the exterior chemical composition and geometrical architecture induces excellent wettability toward water and oil. Sun et al. [74] recently developed a molecular-level modification strategy that imparts hydrophobic character to Zr-based MOFs (UiO-66 [$Zr_6O_4(OH)_4(OOC-C_6H_4-COO)_6$],

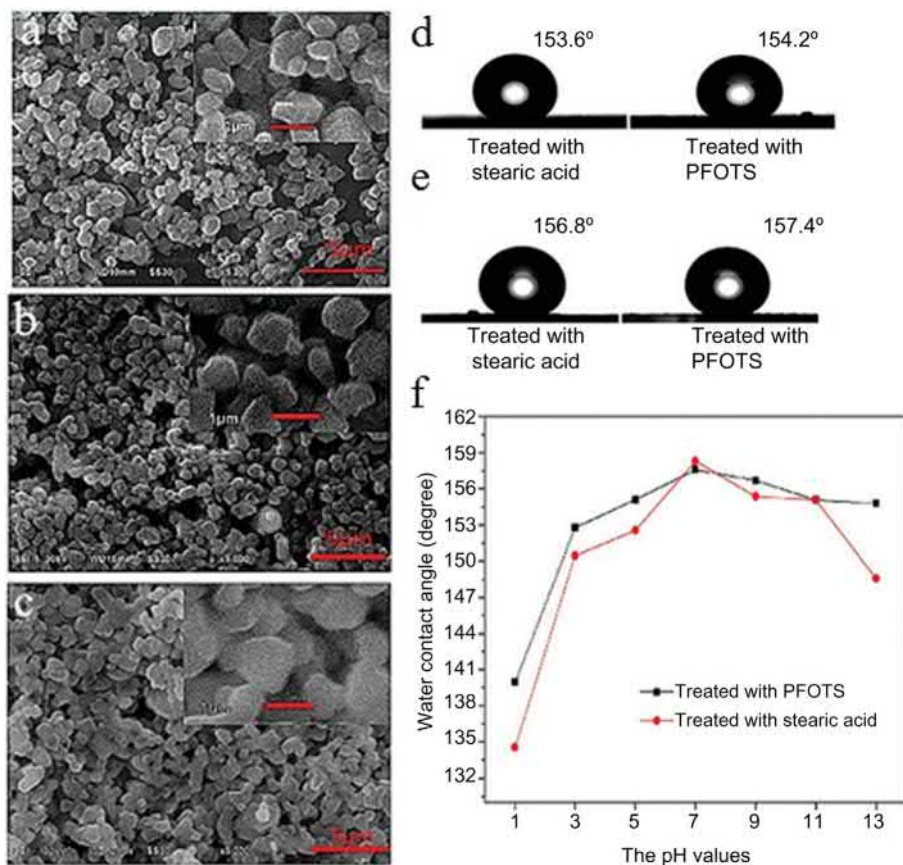


Figure 10.10 SEM images of the as-prepared $\text{Cu}_3(\text{BTC})_2 \cdot 3\text{H}_2\text{O}$ coatings: (A) without treatment; (B) treated with stearic acid; (C) treated with PFOTS. The corresponding high magnification SEM images are shown on the right upper part. (D) Profiles of the contact angles of a 5 wt.% NaCl aqueous solution on the obtained superhydrophobic surfaces; (E) profiles of the water contact angles on the superhydrophobic surface after standing for 4 months; (F) the relationship between the pH values of water droplets and the contact angles on the modified superhydrophobic surfaces.

Source: Reproduced with permission from W. Meng, Z. Feng, F. Li, T. Li, W. Cao, Porous coordination polymer coatings fabricated from $\text{Cu}_3(\text{BTC})_2 \cdot 3\text{H}_2\text{O}$ with excellent superhydrophobic and superoleophilic properties, *New J. Chem.* 40 (2016) 10554–10559.

$\text{UiO-66-SO}_3\text{H}$ [$\text{Zr}_6\text{O}_4(\text{OH})_4(\text{HSO}_3\text{BDC})_{6x}(\text{BDC})_{6-6x}$, ($x = 0.18$)], and PCN-222 [$\text{Zr}_6(\mu_3\text{-OH})_8(\text{OH})_8(\text{TCPP})_2$]; tetrakis(4-carboxyphenyl)porphyrin). In this particular approach, octadecylphosphonic acid (OPA) is coordinated to metal via M–O–P bond which provides a low surface energy with enhanced hydrophobicity. The long alkyl chains of OPA positioned on the MOF's surface generally offer a

high moisture resistance with inherent porosity (Fig. 10.11A–D). Furthermore, these OPA-MOFs exhibit fast removal of organic pollutants with a water contact angle of 150 degrees (magnitude of water contact angle for OPA-UiO-66, OPA-UiO-66-SO₃H, and OPA-PCN-222 are 160, 162, 157 degrees, respectively) They also exhibit an efficient organic/water separation which would offer a considerable platform for separating oil from industrial waste water (Fig. 10.11E). The presence of long alkyl chains on the surface with their low density helps aggregation on the water surface. In addition, the authors studied the water stability of OPA-MOF and found that it can float on water for more than a month and sink immediately in an oil phase. A comparative adsorption capacity was also studied for the composite toward various organic solvents like toluene, acetone, DMF, chloroform, and methanol (Fig. 10.11F). The high uptake values were attributed to a high surface area and hydrophobic interior of the OPA-modified MOF. A real-life oil/water separation was also performed to find out the industrial application of the material. When a mixture of water and chloroform was passed into the OPA-MOF contained in a syringe tube, chloroform freely passed through the sample and water was not able to penetrate, whereas the unmodified MOF represented no selectivity under similar treatment.

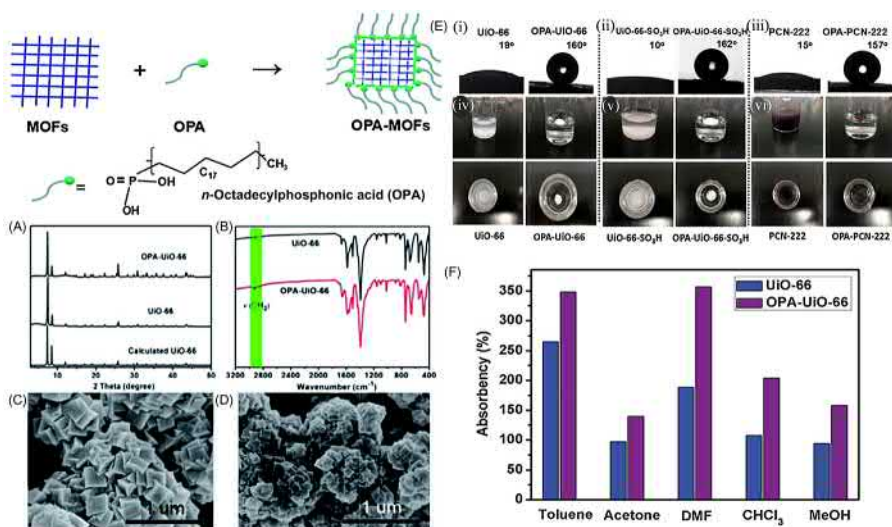


Figure 10.11 Molecular-level external modification of superhydrophobic (A) PXRD patterns and (B) FT-IR spectra of the UiO-66 sample before and after modification with OPA molecules. SEM images of (C) UiO-66 and (D) OPA-UiO-66 samples. (E) Contact angle images of (i) UiO-66, (ii) UiO-66-SO₃H, and (iii) PCN-222 samples before and after OPA modification, and digital photographs of (iv) UiO-66, (v) UiO-66-SO₃H, and (vi) PCN-222 samples dispersed in water before and after OPA modification. (F) Absorption of organic solvents with UiO-66 before and after OPA modification.

Source: Reproduced with permission from Y. Sun, Q. Sun, H. Huang, B. Aguila, Z. Niu, J.A. Perman, et al., A molecular-level superhydrophobic external surface to improve the stability of metal-organic frameworks, *J. Mater. Chem. A* 5 (2017) 18770–18776.

In summary, this molecular-level modification strategy can be extended for other prototype MOFs which are composed of metals such as Ti, Zn, and Al by forming strong coordination bonding between these metals and OPA.

To achieve superhydrophobicity, most of the materials used so far require post-treatment with low surface energy coatings. Fluorinated materials are widely used for this purpose. But these fluorinated materials are not safe with respect to an economic as well as an environmental point of view [75]. To overcome this problem, the application of environmentally friendly, fluorine-free stable superhydrophobic material has become a great challenge. Recently Zhang et al. [76] were successful in demonstrating fluorine-free, water stable material by designing a flower-shaped hierarchical micro/nanoarchitecture (Fig. 10.12A). The ultrathin hierarchical ZIF-7 ($\text{Zn}(\text{bIm})_2$, $\text{bIm} = 2\text{-benzimidazolate}$) crystals with wrinkled nanoprotusions were synthesized over Cu substrate, which provides a relatively rough surface (Fig. 10.12B–E). This in situ ligand solvothermal method showed a high water contact angle of 151.3 degrees, whereas the directly grown ZIF-7 on the mesh showed a comparatively reduced water contact angle of 130.7 degrees. To further

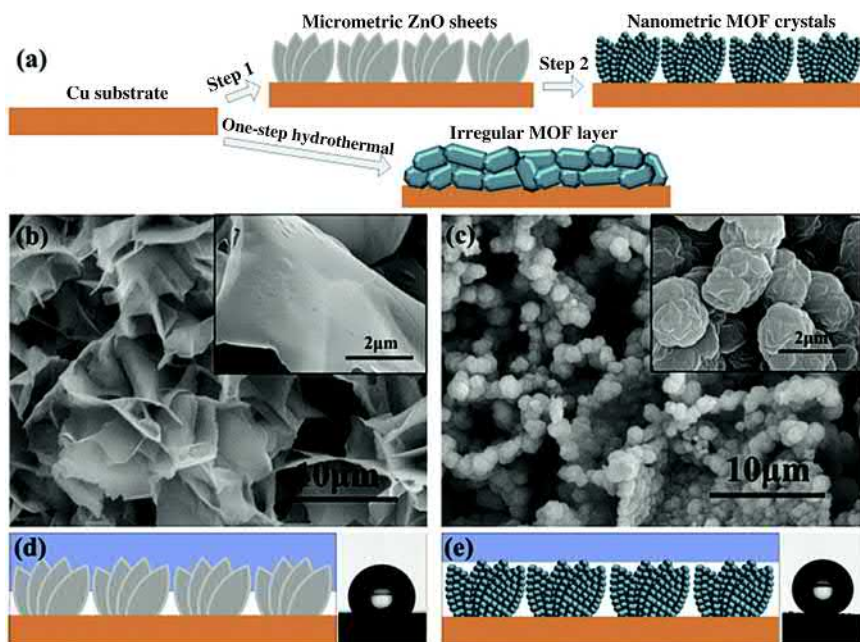


Figure 10.12 (A) Scheme of the preparation process. Typical SEM images of the (B) ZnO array coatings and (C) micro/nano-MOF array coatings; the insets are the corresponding magnified images. Schematic diagram of the contact state corresponding to the (D) ZnO array state and (E) MOF array state.

Source: Reproduced with permission from G. Zhang, J. Zhang, P. Su, Z. Xu, W. Li, C. Shen, et al., Non-activation MOF arrays as a coating layer to fabricate a stable superhydrophobic micro/nano flower-like architecture, *Chem. Commun.* 53 (2017) 8340–8343.

understand the separation efficiency of ZIF-7 array coating architecture, they treated the material with oil–water mixtures. A mixture of water and *n*-hexane (50%, v/v) was passed through ZIF-7 array coatings, and it showed excellent separation efficiency by permeating only *n*-hexane. The complete experiment was carried out in the absence of any external force and it was further tested for other organic solvents as well. The separation performance of MOF array coating for toluene, *n*-hexane, petroleum ether, and soybean oil were beyond 99.5%. The prepared MOF array coating also exhibited an excellent chemical stability even at high temperature. Furthermore, the ZIF-7 array coating architecture revealed a striking permeate flux for *n*-hexane $8.3 \times 10^4 \text{ L m}^{-2} \text{ h}^{-1}$ with a high temperature stability up to 300°C. In situ growth of MOF is a significant and simple approach where the MOF particles can grow over a certain substance by solvothermal, microwave, and ultrasound methods. This kind of technique exhibited better performance than binder/additive-based methods, hampering the composite performance by blocking pore channels.

A recent approach represents an unique way of synthesizing MOFs under solvent- and binder-free conditions by using a hot-pressing method (HoP). The HoP method is broadly applied to different kinds of MOFs to form uniform coatings, in which hot pressing under high temperature for a short time can turn a powder of the starting materials into a highly stable MOF film on various substrates, including metal foils, cloths, and fibers [77,78]. Similarly, a zeolitic imidazolate framework when fabricated on carbon cloth by the layer-by-layer HoP process might greatly improve the robustness, diversity, and multifunctionality of MOF coatings [79]. Notably, a ZIF-8 coating on carbon cloth by using hot-pressing method under solvent- and binder-free conditions exhibited a superhydrophobic film with 151 degrees water contact angle. Additionally, they studied the toxic As(V) adsorption with this highly water stable composite. A filtration device was fabricated by using MOF@Carbon cloth composite and it showed maximum 24.94 mg L^{-1} As(V) uptake for ZIF-9@Carbon cloth. Moreover, the authors believed that their efficient approach of superhydrophobic and “Janus” MOF films through layer-by-layer HoP can be scaled up and explored further by using hydrophobic COFs, CMPs, and other porous crystalline solids.

10.7 CO₂ capture and its necessity

Fossil fuels have been supplying approximately 85% of global energy demand over the past 200 years due to their abundance and innate energy density [80]. The rapid growth of industrialization has led to the extensive use of fossil fuels on a daily basis. The combustion of fossil fuels generates CO₂ as a by-product. CO₂, being a greenhouse gas, promotes global warming profoundly. A recent survey reveals that the CO₂ concentration has increased in the atmosphere from 310 to 380 ppm in last half century [81]. Aqueous alkanolamine solutions have been broadly implemented in power plants for CO₂ capture but their regeneration from carbamates inevitably leads to a huge energy penalty. MOFs are one of the most potentially promising

materials for CO₂ capture and storage. One of the efficient approaches of maximizing CO₂ uptake can be achieved by increasing the pore size and surface area of MOFs. The other way of selective and efficient CO₂ capture is decorating the pore surface by using functional groups with high polarity (such as pyridine, –OH, –NO₂, –CN, and –SH). Therefore, MOF and MOF-based materials bring forward a new horizon as a promising candidate to address the challenge of CO₂ capture, storage, and reutilization over the next 25 years.

Most of the MOF materials are 3D in structure and provide a uniform pore as well as a network channel for the capture and storage of different gas molecules. Apart from pore volume and surface area, MOFs with an unsaturated metal center offer extra and strong binding sites to enhance CO₂ activity [23,82–85].

From an industrial aspect, selective gas uptake or gas separation by MOF is one of the most attractive fields. Selective adsorption of CO₂ from other gas mixtures is primarily based on two applications; one is separating CO₂ from sour natural wells and the second is from power plant flue gas [21]. Nevertheless, a typical postcombustion flue gas contains ~75% N₂ and ~15% CO₂, and most importantly it also contains 5%–7% water, which must be thoroughly taken into consideration for realistic applications [86]. Selective adsorption of CO₂ over N₂ and CH₄ is most extensively studied, primarily based on the differences in kinetic diameter (CO₂, 3.3; N₂, 3.64, CH₄, 3.76). However, it is hard to separate CO₂ only based on a size-based principle and that is why electronic properties like quadrupolar moment, polarization, and judicious choice of building blocks also plays a significant role to fulfill this purpose [87].

Flue gas contains water vapor (5%–7%) and these polar H₂O molecules have higher affinity toward the pore surface compared to CO₂. In particular, unsaturated metal sites of MOFs will be easily blocked by an H₂O molecule as it has higher coordination affinity than CO₂. Thus the presence of only a small amount of water vapor in flue gas will competitively inhibit the CO₂ uptake of an MOF by blocking the pore volume [86]. Liu et al. [87] and Kizzie et al. [88] reported that the DOBDC series of MOFs lose their high CO₂ affinity after complete hydration. This is why affinity toward water vapor is another concern for MOFs that are to be used in CO₂ adsorption. Well-known MOFs for high CO₂ uptake, like HKUST-1 [87], DUT-4 [89], MOF-177 [90], are affected by H₂O molecules. In summary, water vapor can damage the MOF structure while capturing CO₂ in the pore. This is an important problem which requires an urgent solution to advance the application of MOFs in CO₂ capture. One possible way out could be the design of hydrophobic MOFs materials or to adopt postsynthetic modification to convert moisture sensitive MOFs to hydrophobic material which can maintain structure upon contact with moisture.

10.8 Bulk superhydrophobic metal-organic frameworks used for CO₂ storage

Adsorption of CO₂ molecules by porous materials involves either physisorption (through van der Waals interaction) or chemisorption (via covalent bonding).

Physisorption on solids is considered as an energetically favorable process in comparison to chemisorption [91]. MOFs are considered as one of the most promising materials for CO₂ capture and separation due to high porosities, structural diversity, tunable pore environments, and atomically well-defined skeletons. Although all these materials are effective at 298K, they do require the incoming gas stream to be completely dehydrated, because the presence of moisture can cause a dramatic reduction in CO₂ uptake or may result in their decomposition as well. Only a limited number of MOFs can therefore meet this particular requirement. Furthermore, most of the flue gases are hydrated and hot, with temperatures ranging from 373K to 403K [92]. Finally, it is significantly important to fabricate a material which can show the characteristic properties of high chemical stability as well as the high surface area under humid conditions. Nguyen et al. [93] reported a detailed synthesis and characterization of an isoreticular series of ZIFs (zeolitic imidazolate frameworks), in which 5(6)-bromobenzimidazolate (bbIm), 5(6)-chlorobenzimidazolate (cbIm), or 5(6)-methylbenzimidazolate (mbIm) was used with Zn^{II} atoms and 2-methylimidazolate (2-mIm) to construct CHA-type ZIFs, termed as ZIF-300, ZIF-301, and ZIF-302, respectively. The underlying motivation of incorporating these bulky hydrophobic ligands was to construct ZIFs that are water stable and can capture CO₂ even in the presence of a humid atmosphere. Taking into consideration the water stable and hydrophobic ZIF-300, ZIF-301, and ZIF-302, they are able to show a dynamic CO₂/N₂ separation under both dry and hydrated conditions. All three ZIFs were equally effective for selective separation up to three cycles and could be regenerated merely by using an N₂ flow at ambient temperature. CO₂ saturated ZIF-300, ZIF-301, ZIF-302 was simply exposed to pure N₂ flow and these were regenerated within 15, 10, and 10 minutes, respectively. Therefore, due to their tremendous performance in the presence of water, coupled with their low energy regeneration demands, these CHA-type ZIFs have beaten the key challenges associated with other porous materials and can be effective for industrial application.

It has already been discussed that most of the MOFs suffer the problem of reduced CO₂ uptake in humid conditions because of the incorporation of H₂O molecules inside the pore, which resists the CO₂ uptake. Yoon and coworkers [92] reported a microporous copper silicate which is comprised of H₂O-specific and CO₂-specific adsorption sites but does not have H₂O/CO₂-sharing sites. Therefore, it is accommodating both CO₂ and H₂O by not affecting CO₂ uptake. The crystals (SGU-29), with chemical formula Na₂CuSi₅O₁₂ are stable in air up to 550°C and can be used as a material for capturing CO₂ from humid flue gases without involving the costly prior dehydration step even at high temperature.

10.9 Effect of NMOF/MOFNPs-composite for CO₂ uptake under humid condition

Combining MOFs with a variety of functional materials has been shown to have enhanced surface area with high CO₂ uptake. In situ growth of MOF on 2D

sheet-like scaffolds, such as aminoclay [94–96], graphene oxide [38,39,97,98], and BN [99], not only helps to stabilize MOF nanoparticles but also provides an enhanced mechanical and chemical stability with high surface area, high pore volume, and high gas separation efficiency. PolyMOFs [100], a new class of composite metallopolymer, have received increasing attention due to their promising stimulus-responsive, self-healing, photo- and electroluminescence properties. Polymer–metal-organic frameworks (polyMOFs) have been an attractive field of research because they integrate the features of both organic polymers and crystalline MOFs. These polyMOFs have revealed exceptional stability in a hydrated atmosphere. Some related polymer MOF composites have been achieved by chemical cross-linking of the MOFs through the organic linkers to form polymeric monoliths. Zhang et al. [101] demonstrated a polyMOF for highly selective CO₂ adsorption from a CO₂/N₂ mixture in the presence of water. Inspired by in situ polymerization of vinyl monomers within the MOF channel [102–104], Wang and coworkers [86] recently reported a strategy that can separate the open MOF channels into confined and hydrophobic compartments by in situ polymerization of aromatic acetylenes inside the MOF pores. They chose MOF-5 as a prototype host material. Initially monomeric DEB (1,2-Diethynylbenzene) was adsorbed by MOF-5 and it was further heated to an elevated temperature to afford hydrophobic polynaphthylene (PN) inside the channels via Bergman cyclization and subsequent radical polymerization (Fig. 10.13). In contrast to water sensitive MOF-5, the resulting composite PN@MOF-5 exhibited a remarkable improvement in CO₂ adsorption capacity from 38 to 78 cm³ g⁻¹ and in CO₂/N₂ selectivity from 9 to 212 at 273K and 1 bar. As a consequence of its hydrophobic nature, the composite showed a competitive adsorption of water against CO₂. The efficient combinations of porous materials (i.e., MOFs, covalent organic frameworks, and porous polymers) with polymers will therefore provide a versatile material platform for multifunctionality and practical applications.

Jiang and coworkers [105] put forward a technology for making superhydrophobic MOF composite by fabricating the MOF surface with polydimethylsiloxane (PDMS). Via this technique, they were able to produce PDMS-coated MOFs with highly hydrophobic behavior as well as excellent moisture tolerance by keeping the inherent porosity intact. To generalize their approach for wide acceptability, three representative MOFs were chosen: MOF-5 with Zn₄O(COO)₆ clusters, HKUST-1 with paddle wheel Cu₂(COO)₄ centers, and [Zn(bdc)(ted)_{0.5}]·2DMF·2H₂O (denoted as ZnBT) with pillared square-grid Zn₂(COO)₄N₂ clusters modified by a thin hydrophobic PDMS layer via a thermal vapor deposition technique (Fig. 10.14A). Most importantly all PDMS-coated MOF showed its retained porosity and surface area similar to pristine MOF with extremely enhanced stability to the water molecule (Fig. 10.14B and C). All the pristine MOFs showed a rapid structural collapse and thus lost permanent porosity, whereas the PDMS-coated MOF showed almost similar surface area and structural integrity upon exposure to 55% relative humidity. In addition, CO₂ uptake after moisture exposure was also investigated and interestingly, the capacity of coated MOF-5, HKUST-1, and ZnBT showed almost similar uptakes at 273K and 298K (Fig. 10.14D). Finally, all coated

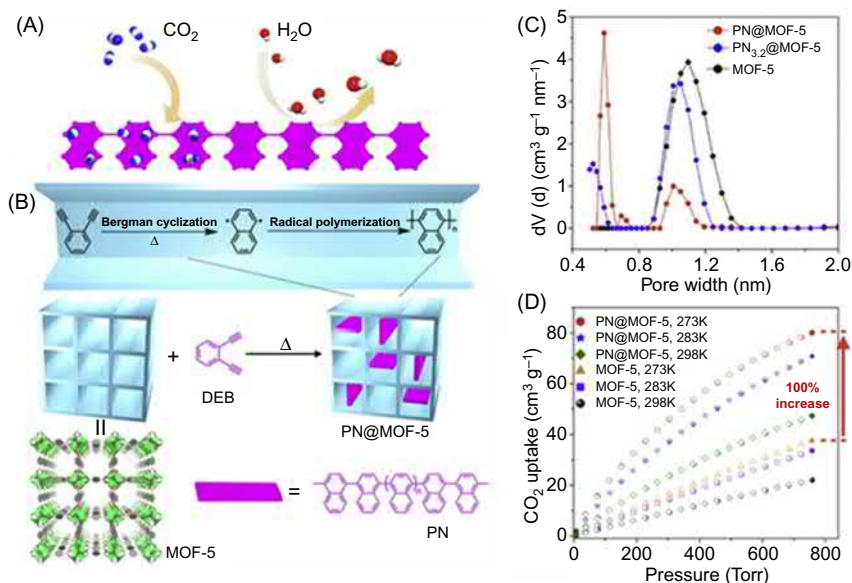


Figure 10.13 (A) Illustration of competitive adsorption of CO₂ against H₂O at the surface and edge of PN; (B) Polymerization of DEB in MOFs (C) Pore size distributions of PN@MOF-5, PN_{3.2}@MOF-5, and MOF-5 based on quenched solid-state density functional theory. (D) CO₂ sorption isotherms of PN@MOF-5 and MOF-5 at 273K, 283K, and 298K. *Source:* Reproduced with permission from N. Ding, H. Li, X. Feng, Q. Wang, S. Wang, L. Ma, et al., Partitioning MOF-5 into confined and hydrophobic compartments for carbon capture under humid conditions, *J. Am. Chem. Soc.* 138 (2016) 10100–10103.

MOFs showed an extraordinary thermal stability up to 235°C with an improved water contact angle of 130 degrees. Such a facile strategy might open up a new platform of synthesizing water stable MOFs or MOF composites for selective CO₂ capture under humid conditions.

Kim et al. [41] reported a facile synthesis approach for preparing hydrophobic MOF composites by stabilizing ZIF-8 nanocrystals on hydrophilic carbon nitride. In order to achieve fast graphitization, melanin foam was annealed at 800°C under Ar atmosphere to prepare hydrophilic CN (25.6 wt.% of N). This CN contained micrometer sized pores along with high nitrogen content and acted as a shield against water degradation of MOF nanocrystals. The composite showed a combination of type I and IV adsorption isotherm with a wide hysteresis loop which confirmed the hierarchical structure with a water contact angle of 135 degrees. The authors believed that a combination of hydrophobic and hierarchical properties enhanced an efficient CO₂ transportation to the catalytic site for converting epichlorohydrin into chloropropylene carbonate. The composite also showed excellent oil uptake. Additionally, they also performed oil encapsulation and further oil/water separation by dipping it in various organic solvents and a benzene/water mixture, respectively.

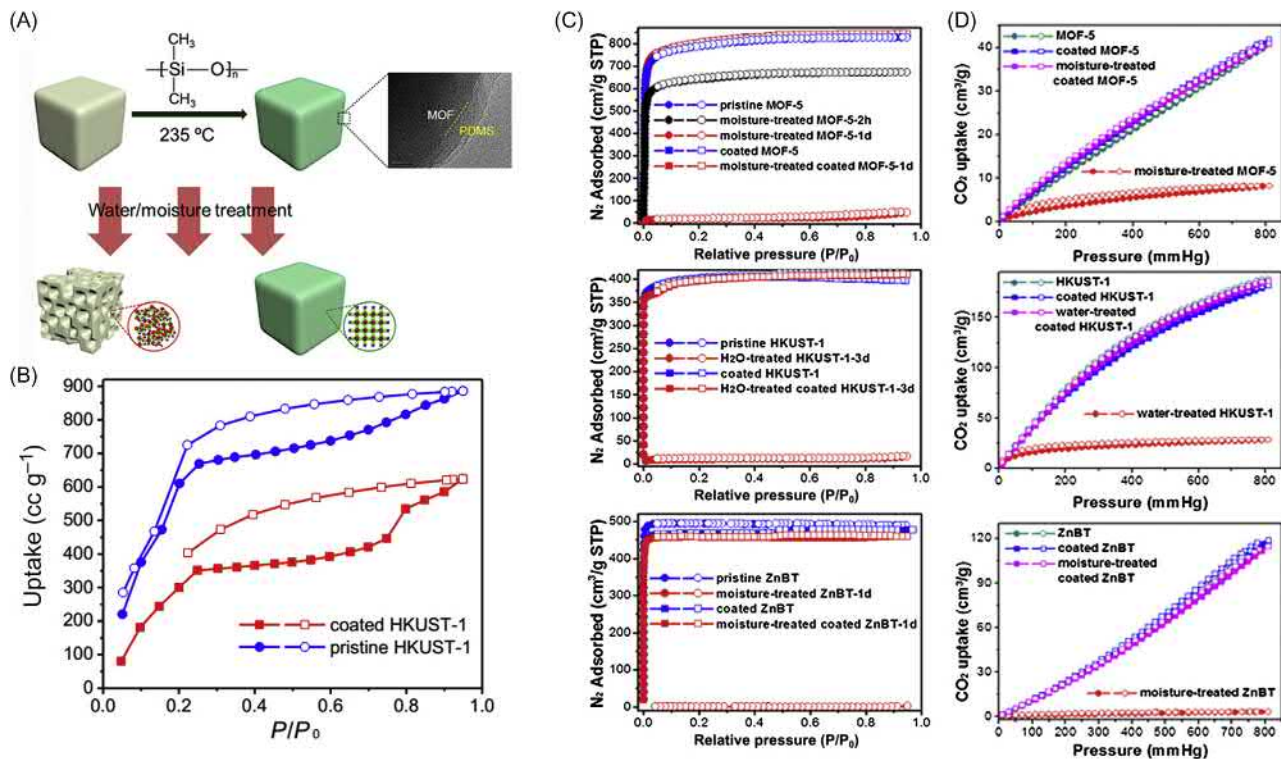


Figure 10.14 (A) Illustration of PDMS-coating on the surface of MOFs. (B) Water sorption isotherms for pristine and PDMS-coated HKUST-1 at 298 K . (C) N_2 adsorption isotherm for pristine and PDMS-coated MOF before and after moisture atmosphere. (D) CO_2 sorption isotherms for pristine and coated MOFs before and after moisture or water treatment (treated in air at 55% relative humidity).

Source: Reproduced with permission from W. Zhang, Y. Hu, J. Ge, H.-L. Jiang, S.-H. Yu, A facile and general coating approach to moisture/water-resistant metal-organic frameworks with intact porosity, *J. Am. Chem. Soc.* 136 (2014) 16978–16981.

10.10 Future outlook

MOFs and derived materials, both at the bulk and nanoscale have shown great potential for selective water repellence and oil capture. Additionally there have been reports of higher CO₂ capture in superhydrophobic MOFs. MOF research in this area definitely merits more attention because of the potential impact in environmental cleanup. Research to date has developed in the following ways: first, design principles for organic linkers that decrease surface free energy have been put forward followed by analysis of structural patterns that lead to superhydrophobicity in MOFs. Numerous applicative examples showing potential for higher CO₂ capture and oil–water separations have also been reported. A few systems have also been cast into membranes to show real-life oil–water separation with excellent separation efficiency. However, there have only been few examples where a system can simultaneously show oil–water separation as well as capture copious amounts of atmospheric CO₂. This could lead to atmospheric as well as marine cleanup to reduce pollution.

The main goal now remains to make this research area more exhaustive and find new structures that provide better gas capture and separations. The design principles already established could be a guiding light in this respect. Further, for practical viability all the reported structures should be cast into devices and membranes and the potential of these systems should be studied. This book chapter should therefore be used as an encompassing literature for researchers willing to take up the challenge of showing that MOFs can indeed be viably used in increased CO₂ capture and oil–water separations.

Acknowledgments

S.R. acknowledges UGC, Govt. of India for research fellowship. S.L. acknowledges the INSPIRE fellowship for financial support. TKM gratefully acknowledges DST, Govt. of India for the financial support (Project No. MR-2015/001019).

References

- [1] S.L. James, Metal-organic frameworks, *Chem. Soc. Rev.* 32 (2003) 276–288.
- [2] H. Furukawa, K.E. Cordova, M. O’Keeffe, O.M. Yaghi, The chemistry and applications of metal-organic frameworks, *Science* 341 (2013) 1230444–1230455.
- [3] W.J. Rieter, K.M.L. Taylor, H. An, W. Lin, W. Lin, Nanoscale metal – organic frameworks as potential multimodal contrast enhancing agents, *J. Am. Chem. Soc.* 128 (2006) 9024–9025.
- [4] A. Carné, C. Carbonell, I. Imaz, Daniel maspoch, nanoscale metal–organic materials, *Chem. Soc. Rev.* 40 (2011) 291–305.
- [5] M. Zhao, X. Zhang, C. Deng, Rational synthesis of novel recyclable Fe₃O₄@MOF nanocomposites for enzymatic digestion, *Chem. Comm.* 51 (2015) 8116–8119.

- [6] N. Sikdar, B. Konkena, J. Masa, W. Schuhmann, T.K. Maji, $\text{Co}_3\text{O}_4@ \text{Co}/\text{NCNT}$ nanostructure derived from a dicyanamide based metal-organic framework as efficient bifunctional electrocatalyst for oxygen reduction and evolution reactions, *Chem. Eur. J.* 23 (2017) 18049–18056.
- [7] Z. Yin, S. Wan, J. Yang, M. Kurmoo, M.-H. Zeng, Recent advances in post-synthetic modification of metal-organic frameworks: new types and tandem reactions, *Coord. Chem. Rev.* 378 (2019) 500–512.
- [8] E. Barea, C. Montoro, J.A.R. Navarro, Toxic gas removal – metal-organic frameworks for the capture and degradation of toxic gases and vapours, *Chem. Soc. Rev.* 43 (2014) 5419–5430.
- [9] J.-R. Li, R.J. Kuppler, H.-C. Zhou, Selective gas adsorption and separation in metal-organic framework, *Chem. Soc. Rev.* 38 (2009) 1477–1504.
- [10] J.-R. Li, Y. Ma, M. Colin McCarthy, J. Sculley, J. Yu, H.-K. Jeong, et al., Carbon dioxide capture-related gas adsorption and separation in metal-organic frameworks, *Coord. Chem. Rev.* 255 (2011) 1791–1823.
- [11] A.U. Czaja, N. Trukhan, U. Müller, Industrial applications of metal-organic frameworks, *Chem. Soc. Rev.* 38 (2009) 1284–1293.
- [12] R.B. Getman, Y.-S. Bae, C.E. Wilmer, R.Q. Snurr, Review and analysis of molecular simulations of methane, hydrogen, and acetylene storage in metal-organic frameworks, *Chem. Rev.* 112 (2012) 703–723.
- [13] S. Roy, A. Chakraborty, T.K. Maji, Lanthanide-organic frameworks for gas storage and as magneto-luminescent materials, *Coord. Chem. Rev.* 273–274 (2014) 139–164.
- [14] K. Sumida, D.L. Rogow, J.A. Mason, T.M. McDonald, E.D. Bloch, Z.R. Herm, et al., Carbon dioxide capture in metal-organic frameworks, *Chem. Rev.* 112 (2012) 724–781.
- [15] T.A. Makal, J.-R. Li, W. Lu, H.-C. Zhou, Methane storage in advanced porous materials, *Chem. Soc. Rev.* 41 (2012) 7761–7779.
- [16] L.J. Murray, M. Dinca, J.R. Long, Hydrogen storage in metal-organic frameworks, *Chem. Soc. Rev.* 38 (2009) 1294–1314.
- [17] S.S. Han, J.L. Mendoza-Cortés, W.A. Goddard III, Recent advances on simulation and theory of hydrogen storage in metal-organic frameworks and covalent organic frameworks, *Chem. Soc. Rev.* 38 (2009) 1460–1476.
- [18] H.-S. Choi, M.P. Suh, Highly selective CO_2 capture in flexible 3D coordination polymer networks, *Angew. Chem. Int. Ed.* 48 (2009) 6865–6869.
- [19] J. Yu, L.-H. Xie, J.-R. Li, Y. Ma, J.M. Seminario, P.B. Balbuena, CO_2 capture and separations using MOFs: computational and experimental studies, *Chem. Rev.* 117 (2017) 9674–9754.
- [20] S. Bhattacharyya, A. Chakraborty, A. Hazra, T.K. Maji, Tetracarboxylate linker based flexible Cu^{II} frameworks: efficient separation of CO_2 from CO_2/N_2 and C_2H_2 from $\text{C}_2\text{H}_2/\text{C}_2\text{H}_4$ mixtures, *ACS Omega* 3 (2018) 2018.
- [21] J. Liu, P.K. Thallapally, B.P. McGrail, D.R. Brown, J. Liu, Progress in adsorption-based CO_2 capture by metal-organic frameworks, *Chem. Soc. Rev.* 41 (2012) 2308–2322.
- [22] J. Park, H. Kim, S. Soo Han, Y. Jung, Tuning metal-organic frameworks with open-metal sites and its origin for enhancing CO_2 affinity by metal substitution, *J. Phys. Chem. Lett.* 3 (2012) 826–829.
- [23] S.R. Caskey, A.G. Wong-Foy, A.J. Matzger, Dramatic tuning of carbon dioxide uptake via metal substitution in a coordination polymer with cylindrical pores, *J. Am. Chem. Soc.* 130 (2008) 10870–10871.

- [24] T.-H. Chen, I. Popov, O. Zenasni, O. Daugulis, O.S. Miljanic, Superhydrophobic per-fluorinated metal–organic frameworks, *Chem. Commun.* 49 (2013) 6846–6848.
- [25] S. Roy, V.M. Suresh, A. Hazra, A. Bandyopadhyay, S. Laha, S.K. Pati, et al., Solvent modulated emission properties in a superhydrophobic oligo-(*p*-phenyleneethynylene) based 3D porous supramolecular framework, *Inorg. Chem.* 57 (2018) 8693–8696.
- [26] Dave, Remediation technologies for marine oil spills: a critical review and comparative analysis, *Am. J. Environ. Sci.* 7 (2011) 423–440.
- [27] M.A. Shannon, P.W. Bohn, M. Elimelech, J.G. Georgiadis, B.J. Mariñas, A.M. Mayes, Science and technology for water purification in the coming decades, *Nature* 452 (2008) 301–310.
- [28] A.B. Nordvik, J.L. Simmons, K.R. Bitting, A. Lewis, T. StromKristiansen, *Spill Sci. Technol. B.* 107 (1996) 3.
- [29] Z. Xue, S. Wang, L. Lin, L. Chen, M. Liu, L. Feng, et al., A novel superhydrophilic and underwater superoleophobic hydrogel-coated mesh for oil/water separation, *Adv. Mater.* 23 (2011) 4270–4273.
- [30] K. Gaaseidnes, J. Turbeville, Separation of oil and water in oil spill recovery operations, *Pure Appl. Chem.* 71 (1999) 95–101.
- [31] T. Darmanin, F. Guittard, Recent advances in the potential applications of bioinspired superhydrophobic materials, *J. Mater. Chem. A.* 2 (2014) 16319–16359.
- [32] N. García, E. Benito, J. Guzmán, P. Tiemblo, Use of *p*-toluenesulfonic acid for the controlled grafting of alkoxy-silanes onto silanol containing surfaces: preparation of tunable hydrophilic, hydrophobic, and super-hydrophobic silica, *J. Am. Chem. Soc.* 129 (2007) 5052–5060.
- [33] K. Jayaramulu, K.K.R. Datta, C. Rösler, M. Petr, M. Otyepka, R. Zboril, et al., Biomimetic superhydrophobic/superoleophilic highly fluorinated graphene oxide and ZIF-8 composites for oil-water separation, *Angew. Chem. Int. Ed.* 55 (2015) 1178–1182.
- [34] K.P. Rao, M. Higuchi, K. Sumida, S. Furukawa, J. Duan, S. Kitagawa, Design of superhydrophobic porous coordination polymers through the introduction of external surface corrugation by the use of an aromatic hydrocarbon building unit, *Angew. Chem. Int. Ed.* 53 (2014) 8225–8230.
- [35] H.J. Jeon, R. Matsuda, P. Kanoo, H. Kajiro, L. Li, H. Sato, et al., The densely fluorinated nanospace of a porous coordination polymer composed of perfluorobutyl-functionalized ligands, *Chem. Commun.* 50 (2014) 10861.
- [36] C. Yang, U. Kaipa, Q.Z. Mather, X. Wang, V. Nesterov, A.F. Venero, et al., Fluorous metal–organic frameworks with superior adsorption and hydrophobic properties toward oil spill cleanup and hydrocarbon storage, *J. Am. Chem. Soc.* 133 (2011) 18094–18097.
- [37] C.A. Fernandez, S.K. Nune, H.V. Annareddy, L.X. Dang, B.P. McGrail, F. Zheng, et al., Hydrophobic and moisture-stable metal–organic frameworks, *Dalton Trans.* 44 (2015) 13490–13497.
- [38] C. Petit, T.J. Bandoz, MOF-graphite oxide composites: combining the uniqueness of graphene layers and metal-organic frameworks, *Adv. Mater.* 21 (2009) 4753–4757.
- [39] R. Kumar, K. Jayaramulu, T.K. Maji, C.N.R. Rao, Hybrid nanocomposites of ZIF-8 with graphene oxide exhibiting tunable morphology, significant CO₂ uptake and other novel properties, *Chem. Commun.* 49 (2013) 4947–4949.
- [40] M. Jahan, Q. Bao, J.-X. Yang, K.P. Loh, Structure-directing role of graphene in the synthesis of metal – organic framework nanowire, *J. Am. Chem. Soc.* 132 (2010) 14487–14495.

- [41] D. Kim, D.W. Kim, O. Buyukcakir, M.-K. Kim, K. Polychronopoulou, A. Coskun, Highly hydrophobic ZIF-8/carbon nitride foam with hierarchical porosity for oil capture and chemical fixation of CO₂, *Adv. Funct. Mater.* 27 (2017) 1700706.
- [42] H.J. Ensikat, P. D-Kuru, C. Neinhuis, W. Barthlott, Superhydrophobicity in perfection: the outstanding properties of the lotus leaf, *Beilstein. J. Nanotechnol.* 2 (2011) 152–161.
- [43] X. Gao, L. Jiang, Biophysics: water-repellent legs of water striders, *Nature* 432 (2004) 36.
- [44] X.-M. Li, D. Reinhoudt, M. Crego-Calama, What do we need for a superhydrophobic surface? A review on the recent progress in the preparation of superhydrophobic surfaces, *Chem. Soc. Rev.* 36 (2007) 1350–1368.
- [45] K. Liu, X. Yao, L. Jiang, Recent developments in bio-inspired special wettability, *Chem. Soc. Rev.* 39 (2010) 3240–3255.
- [46] C. Neinhuis, W. Barthlott, Characterization and distribution of water-repellent, self-cleaning plant surfaces, *Ann. Bot.* 79 (1997) 667–677.
- [47] A.B.D. Cassie, S. Baxter, Wettability of porous surfaces, *Trans. Faraday Soc.* 40 (1944) 546–551.
- [48] R.N. Wenzel, Resistance of solid surfaces to wetting by water, *Ind. Eng. Chem.* 28 (1936) 988–994.
- [49] P. Roach, N.J. Shirtcliffe, M.I. Newton, Progress in superhydrophobic surface development, *Soft Matter* 4 (2008) 224–240.
- [50] T. Sun, L. Feng, X. Gao, L. Jiang, Bioinspired surfaces with special wettability, *Acc. Chem. Res.* 38 (2005) 644–652.
- [51] A. Tuteja, W. Choi, M. Ma, J.M. Mabry, S.A. Mazzella, G.C. Rutledge, et al., Designing superoleophobic surfaces, *Science*. 318 (2007) 1618–1622.
- [52] K.M. Wisdom, J.A. Watson, X. Qua, F. Liua, G.S. Watson, C.-H. Chen, Self-cleaning of superhydrophobic surfaces by self-propelled jumping condensate, *Proc. Nat. Acad. Sci. U.S.A.* 110 (2013) 7992–7997.
- [53] J.G. Nguyen, S. Cohen, Moisture-resistant and superhydrophobic metal – organic frameworks obtained via postsynthetic modification, *J. Am. Chem. Soc.* 132 (2010) 4560–4561.
- [54] T.A. Makal, X. Wang, H.-C. Zhou, Tuning the moisture and thermal stability of metal–organic frameworks through incorporation of pendant hydrophobic groups, *Cryst. Growth Des.* 13 (2013) 4760–4768.
- [55] C. Serre, Superhydrophobicity in highly fluorinated porous metal–organic frameworks, *Angew. Chem. Int. Ed.* 51 (2012) 6048–6050.
- [56] C. Yang, X. Wang, M.A. Omary, Fluorous metal – organic frameworks for high-density gas adsorption, *J. Am. Chem. Soc.* 129 (2007) 15454.
- [57] M.A. Omary, C. Yang, International Patent Application PCT/US 08/10664.
- [58] D.L. Hu, J.W.M. Bush, Meniscus-climbing insects, *Nature* 437 (2005) 733–736.
- [59] I.A. Larmour, S.E.J. Bell, G.C. Saunders, Remarkably simple fabrication of superhydrophobic surfaces using electroless galvanic deposition, *Angew. Chem., Int. Ed.* 46 (2007) 1710–1712.
- [60] V.M. Suresh, S.J. George, T.K. Maji, MOF nano-vesicles and toroids: self-assembled porous soft-hybrids for light harvesting, *Adv. Funct. Mater.* 23 (2013) 5585–5590.
- [61] A. Carne-Sanchez, I. Imaz, M. Cano-Sarabia, D. Maspoch, A spray-drying strategy for synthesis of nanoscale metal-organic frameworks and their assembly into hollow superstructures, *Nat. Chem.* 5 (2013) 203–211.
- [62] J. Della Rocca, D. Liu, W. Lin, Nanoscale metal–organic frameworks for biomedical imaging and drug delivery, *Acc. Chem. Res.* 44 (2011) 957–968.

- [63] U.H.F. Bunz, Poly(aryleneethynylene)s: syntheses, properties, structures, and applications, *Chem. Rev.* 100 (2000) 1605–1644.
- [64] S. Roy, A. Hazra, A. Bandyopadhyay, D. Raut, P.L. Madhuri, D.S. Shankar Rao, et al., Reversible polymorphism, liquid crystallinity, and stimuli-responsive luminescence in a bola-amphiphilic π -system: structure–property correlations through nanoindentation and DFT calculations, *J. Phys. Chem. Lett.* 7 (2016) 4086–4092.
- [65] S. Roy, V.M. Suresh, T.K. Maji, Self-cleaning MOF: realization of extreme water repellence in coordination driven self-assembled nanostructures, *Chem. Sci.* 7 (2016) 2251–2256.
- [66] S. Roy, M. Das, A. Bandyopadhyay, S.K. Pati, P.P. Ray, T.K. Maji, Colossal increase in electric current and high rectification ratio in a photoconducting, self-cleaning, and luminescent schottky barrier NMOF diode, *J. Phys. Chem. C* 121 (2017) 23803–23810.
- [67] S. Mukherjee, A.M. Kansara, D. Saha, R. Gonnade, D. Mullangi, B. Manna, et al., An ultrahydrophobic fluorous metal–organic framework derived recyclable composite as a promising platform to tackle marine oil spills, *Chem. Eur. J.* 22 (2016) 10937–10943.
- [68] K. Jayaramulu, F. Geyer, M. Petr, R. Zboril, D. Vollmer, R.A. Fischer, Shape controlled hierarchical porous hydrophobic/oleophilic metal-organic nanofibrous gel composites for oil adsorption, *Adv. Mater.* 29 (2017) 1605307–1605312.
- [69] T.T.Y. Tan, M.R. Reithofer, E.Y. Chen, A.G. Menon, T.S.A. Hor, J. Xu, et al., Tuning omniphobicity via morphological control of metal–organic framework functionalized surfaces, *J. Am. Chem. Soc.* 135 (2013) 16272–16275.
- [70] Q. Sun, H. He, W.-Y. Gao, B. Aguila, L. Wojtas, Z. Dai, et al., Imparting amphiphobicity on single-crystalline porous materials, *Nat. Commun.* 7 (2016) 13300.
- [71] L. Wu, J. Zhang, B. Li, A. Wang, Mechanical- and oil-durable superhydrophobic polyester materials for selective oil absorption and oil/water separation, *J. Colloid Interface Sci.* 413 (2014) 112–117.
- [72] M. Zhang, C. Wang, S. Wang, J. Li, Fabrication of superhydrophobic cotton textiles for water–oil separation based on drop-coating route, *Carbohydr. Polym.* 97 (2013) 59–64.
- [73] W. Meng, Z. Feng, F. Li, T. Li, W. Cao, Porous coordination polymer coatings fabricated from $\text{Cu}_3(\text{BTC})_2 \cdot 3\text{H}_2\text{O}$ with excellent superhydrophobic and superoleophilic properties, *New J. Chem.* 40 (2016) 10554–10559.
- [74] Y. Sun, Q. Sun, H. Huang, B. Aguila, Z. Niu, J.A. Permana, et al., A molecular-level superhydrophobic external surface to improve the stability of metal–organic frameworks, *J. Mater. Chem. A* 5 (2017) 18770–18776.
- [75] A.B. Lindstrom, M.J. Strynar, E.L. Libelo, Polyfluorinated compounds: past, present, and future, *Environ. Sci. Technol.* 45 (2011) 7954–7961.
- [76] G. Zhang, J. Zhang, P. Su, Z. Xu, W. Li, C. Shen, et al., Non-activation MOF arrays as a coating layer to fabricate a stable superhydrophobic micro/nano flower-like architecture, *Chem. Commun.* 53 (2017) 8340–8343.
- [77] H. Furukawa, N. Ko, Y.B. Go, N. Aratani, S.B. Choi, E. Choi, et al., Ultrahigh porosity in metal-organic frameworks, *Science* 329 (2010) 424–428.
- [78] R. Li, X. Ren, H. Ma, X. Feng, Z. Lin, X. Li, et al., Nickel-substituted zeolitic imidazolate frameworks for time-resolved alcohol sensing and photocatalysis under visible light, *J. Mater. Chem. A* 2 (2014) 5724–5729.
- [79] Y. Chen, S. Li, X. Pei, J. Zhou, X. Feng, S. Zhang, et al., A solvent-free hot-pressing method for preparing metal-organic-framework coatings, *Angew. Chem. Int. Ed.* 55 (2016) 3419–3423.

- [80] R.G. Watts, *Global Warming and the Future of the Earth*, Morgan & Claypool Publishers, Denver, 2007.
- [81] R. Babarao, J.W. Jiang, Molecular screening of metal – organic frameworks for CO₂ storage, *Langmuir* 24 (2008) 6270–6278.
- [82] H.L. Li, C.E. Davis, T.L. Groy, D.G. Kelley, O.M. Yaghi, *J. Am. Chem. Soc.* 120 (1998) 2186–2187.
- [83] D. Britt, H. Furukawa, B. Wang, T.G. Glover, O.M. Yaghi, Highly efficient separation of carbon dioxide by a metal-organic framework replete with open metal sites, *Proc. Natl. Acad. Sci.* 106 (2009) 20637–20640.
- [84] T. Grant Glover, G.W. Peterson, B.J. Schindler, D. Britt, O. Yaghi, MOF-74 building unit has a direct impact on toxic gas adsorption, *Chem. Eng. Sci.* 66 (2011) 163–170.
- [85] R. Zou, A.I. Abdel-Fattah, H. Xu, Y. Zhao, D.D. Hickmott, Storage and separation applications of nanoporous metal–organic frameworks, *CrystEngComm* 12 (2010) 1337–1353.
- [86] N. Ding, H. Li, X. Feng, Q. Wang, S. Wang, L. Ma, et al., Partitioning MOF-5 into confined and hydrophobic compartments for carbon capture under humid conditions, *J. Am. Chem. Soc.* 138 (2016) 10100–10103.
- [87] J. Liu, Y. Wang, A.I. Benin, P. Jakubczak, R.R. Willis, M.D. LeVan, CO₂/H₂O adsorption equilibrium and rates on metal – organic frameworks: HKUST-1 and Ni/DOBDC, *Langmuir* 26 (2010) 14301–14307.
- [88] A.C. Kizzie, A.G. Wong-Foy, A.J. Matzger, Effect of humidity on the performance of microporous coordination polymers as adsorbents for CO₂ capture, *Langmuir* 27 (2011) 6368–6373.
- [89] P. Kusgens, M. Rose, I. Senkovska, H. Froede, A. Henschel, S. Siegle, et al., Characterization of metal-organic frameworks by water adsorption, *Microporous Mesoporous Mater.* 120 (2009) 325.
- [90] Y. Li, R.T. Yang, Gas adsorption and storage in metal – organic framework MOF-177, *Langmuir* 23 (2007) 12937–12944.
- [91] S. Chaemchuen, N.A. Kabir, K. Zhou, F. Verpoort, Metal–organic frameworks for upgrading biogas via CO₂ adsorption to biogas green energy, *Chem. Soc. Rev.* 42 (2013) 9304.
- [92] S.J. Datta, C. Khumnoon, Z.H. Lee, W.K. Moon, S. Docao, T.H. Nguyen, et al., CO₂ capture from humid flue gases and humid atmosphere using a microporous copper silicate, *Science* 350 (2015) 302–306.
- [93] N.T.T. Nguyen, H. Furukawa, F. Gándara, H.T. Nguyen, K.E. Cordova, O.M. Yaghi, Selective capture of carbon dioxide under humid conditions by hydrophobic chabazite-type zeolitic imidazolate frameworks, *Angew. Chem. Int. Ed.* 53 (2014) 10645–10648.
- [94] A. Chakraborty, A. Achari, M. Eswaramoorthy, T.K. Maji, MOF–aminoclay composites for superior CO₂ capture, separation and enhanced catalytic activity in chemical fixation of CO₂, *Chem. Commun.* 52 (2016) 11378–11381.
- [95] A. Chakraborty, S. Roy, M. Eswaramoorthy, T.K. Maji, Flexible MOF–aminoclay nanocomposites showing tunable stepwise/gated sorption for C₂H₂, CO₂ and separation for CO₂/N₂ and CO₂/CH₄, *J. Mater. Chem. A* 5 (2017) 8423–8430.
- [96] A. Chakraborty, S. Laha, K. Kamali, C. Narayana, M. Eswaramoorthy, T.K. Maji, In situ growth of self-assembled ZIF-8–aminoclay nanocomposites with enhanced surface area and CO₂ uptake, *Inorg. Chem.* 56 (2017) 9426–9435.
- [97] S. Liu, L. Sun, F. Xu, J. Zhang, C. Jiao, F. Li, et al., Nanosized Cu-MOFs induced by graphene oxide and enhanced gas storage capacity, *Energy Environ. Sci.* 6 (2013) 818–823.

- [98] R. Kumar, D. Raut, U. Ramamurty, C.N.R. Rao, Remarkable improvement in the mechanical properties and CO₂ uptake of MOFs brought about by covalent linking to graphene, *Angew. Chem. Int. Ed.* 55 (2016) 7857–7861.
- [99] R. Kumar, D. Raut, I. Ahmad, U. Ramamurty, T.K. Maji, C.N.R. Rao, Functionality preservation with enhanced mechanical integrity in the nanocomposites of the metal–organic framework, ZIF-8, with BN nanosheets, *Mater. Horiz.* 1 (2014) 513–517.
- [100] Z. Zhang, H.T.H. Nguyen, S.A. Miller, S.M. Cohen, polyMOFs: a class of interconvertible polymer-metal-organic-framework hybrid materials, *Angew. Chem. Int. Ed.* 54 (2015) 6152–6157.
- [101] Z. Zhang, H.T.H. Nguyen, S.A. Miller, A.M. Ploskonka, J.B. DeCoste, S.M. Cohen, Polymer–metal–organic frameworks (polyMOFs) as water tolerant materials for selective carbon dioxide separations, *J. Am. Chem. Soc.* 138 (2016) 920–925.
- [102] T. Uemura, N. Yanai, S. Kitagawa, Polymerization reactions in porous coordination polymers, *Chem. Soc. Rev.* 38 (2009) 1228.
- [103] T. Uemura, D. Hiramatsu, Y. Kubota, M. Takata, S. Kitagawa, Topotactic linear radical polymerization of divinylbenzenes in porous coordination polymers, *Angew. Chem. Int. Ed.* 46 (2007) 4987–4990.
- [104] T. Uemura, R. Kitaura, Y. Ohta, M. Nagaoka, S. Kitagawa, Nanochannel-promoted polymerization of substituted acetylenes in porous coordination polymers, *Angew. Chem. Int. Ed.* 45 (2006) 4112–4116.
- [105] W. Zhang, Y. Hu, J. Ge, H.-L. Jiang, S.-H. Yu, A facile and general coating approach to moisture/water-resistant metal–organic frameworks with intact porosity, *J. Am. Chem. Soc.* 136 (2014) 16978–16981.

Radionuclide sequestration by metal-organic frameworks

11

Chengliang Xiao and Shuaowang*

State Key Laboratory of Radiation Medicine and Protection, School for Radiological and Interdisciplinary Sciences (RAD-X), Collaborative Innovation Center of Radiation Medicine of Jiangsu Higher Education Institutions, Soochow University, Suzhou, P.R. China

*Corresponding author. e-mail address: shuaowang@suda.edu.cn

11.1 Introduction

Nuclear energy is a major source for the generation of electricity without the emission of greenhouse gases. Recently, nuclear power production has gradually recovered after the Fukushima accident in 2011. However, one major barrier for the rapid development of civil nuclear energy utilization is the scientific and technological challenges in properly dealing with the highly radioactive waste. One origin for these challenges is the extreme complexity of the used nuclear fuel, which consists of more than 400 radionuclides (representing >40 elements) with differing physical and chemical properties. At present, the concept of a closed nuclear fuel cycle is widely accepted by most countries to reduce the volume of radiotoxic wastes and maximize the use of the fissile materials. For this purpose, the actinides and some fission products (Fig. 11.1) with long-term radiotoxicity in the used nuclear fuel are proposed to be recycled or eliminated. Generally, uranium and plutonium are recycled by a Plutonium and Uranium Reduction Extraction (PUREX) process. The minor actinides (Am and Cm) can also be separated using the soft ligands containing sulfur or nitrogen atoms based on the solvent extraction technique [1–3]. These actinides can be then sent to Accelerator Driven System–based reactors for transmuting to short-lived or stable isotopes [4]. Other hazardous radionuclides, such as ^{137}Cs and ^{90}Sr , can be removed by macrocyclic supramolecular-based extracting agents or by inorganic ion exchange materials [5,6]. For several anionic radionuclides, mostly represented by $^{99}\text{TcO}_4^-$, the anion exchange resin is proved to be an effective scavenger [7,8]. The volatile gaseous radionuclides ($^{129}\text{I}_2$, ^{133}Xe , and ^{85}Kr) should also be cautiously captured and sequestered, as these are apt to escape to the atmosphere [9–11]. On the other hand, the radionuclides leaking into the environment through mining activities or by accidents are of great concern for the sake of public safety and human health. Though many seemingly feasible methods have been developed toward radionuclide separation that are relevant to the nuclear fuel cycle, there is still considerable room for improvement. For example, the solvent

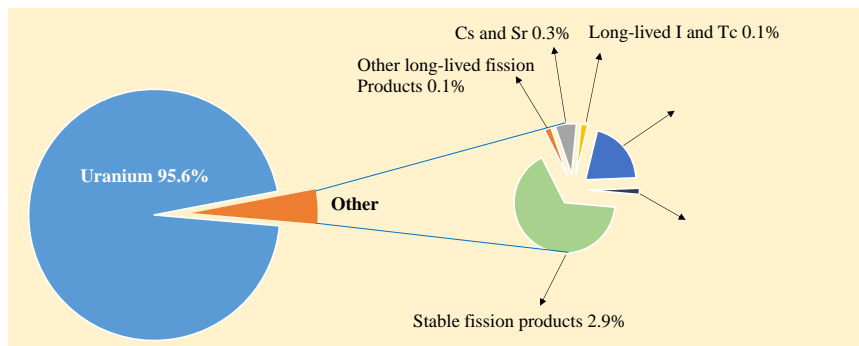


Figure 11.1 The chemical composition of the used nuclear fuel.

extraction technique has some obvious drawbacks: third phase formation, use of volatile and toxic solvents, and generation of massive amounts of radioactive wastes, etc.; the traditional ion exchange resins exhibit slow sorption rate and poor stability under a strong radiation field; the purely inorganic ion exchange materials often have a low uptake capacity when the acidity is high and poor selectivity under high salinity conditions.

Metal-organic frameworks (MOFs) represent a recently emerging type of nanoporous materials, which are assembled with functional organic linkers and metal ions or clusters nodes [12]. The high specific surface areas, tunable pore diameter, and easy postmodification endow them with unique performances in catalysis, gas separation, adsorption, optical, electrical, and biomedical applications [13–16]. Recently, the utilization of such materials for radionuclide separations has been undergoing rapid development [17–20]. We highlight here the current progress of these materials in sequestering radionuclides from radioactive wastes, including ^{137}Cs , ^{90}Sr , ^{238}U , ^{232}Th , ^{99}Tc , ^{79}Se , ^{129}I , ^{133}Xe , and ^{85}Kr , etc. The design principle of MOF materials for sequestering radionuclides, the separation properties, as well as the uptake mechanisms are briefly discussed.

11.2 Design principles of metal-organic frameworks for sequestering radionuclides

The radioactive substances in the nuclear fuel cycle can be divided into three groups: (1) cationic radionuclides, such as $^{137}\text{Cs}^+$, $^{90}\text{Sr}^{2+}$, $^{232}\text{Th}^{4+}$, and $^{238}\text{UO}_2^{2+}$; (2) anionic radionuclides, such as $^{99}\text{TcO}_4^-$, $^{129}\text{I}^-$, $^{79}\text{SeO}_3^{2-}$, and $^{79}\text{SeO}_4^{2-}$; and (3) gaseous radionuclides, such as ^{133}Xe , ^{85}Kr , and $^{129}\text{I}_2$. To achieve a decent uptake of certain radionuclides, strong and specific interactions between the host framework and radionuclide are highly desirable. These interactions include electrostatic interaction, coordination, hydrogen bond interaction, hydrophobic interaction, etc. For a specific host/guest interaction, multiple driving forces are often present. Based on

11.3 Radioactive waste sequestration by metal-organic frameworks

11.3.1 Cesium and strontium

Radioactive cesium (^{137}Cs) and strontium (^{90}Sr) are so highly radiotoxic that they can even be physically hot. These two radionuclides decay by emitting high energy β particles. As a result, they are problematic during the verification of the high-level liquid waste. To decrease the long-term hazard, diminish the radiotoxicity, and minimize the volume of radioactive waste, it is desirable to remove ^{137}Cs and ^{90}Sr from the radioactive waste. However, ^{137}Cs and ^{90}Sr hold strong solvation energy and selective removal of them based on coordination after desolvation is difficult. Therefore ^{137}Cs and ^{90}Sr are often separated using ion exchange materials [21,22]. However, very few MOF materials are reported to separate ^{137}Cs and ^{90}Sr , which might be due to the great challenges to synthesize the anionic MOFs containing non/weak-coordinated charge-balancing cationic species in the pores.

One strategy to design anionic MOFs is to take advantage of the in situ chemical decomposition of the solvents, such as *N,N*-dimethylformamide and *N,N*-diethylformamide, during the solvothermal reaction, to form $[\text{NH}_2(\text{CH}_3)_2]^+$ or $[\text{NH}_2(\text{CH}_2\text{CH}_3)_2]^+$ species, acting as the charge-balancing template in anionic MOFs. Recently, we used 3,5-di(4'-carboxylphenyl) benzoic acid and $\text{UO}_2(\text{NO}_3)_2 \cdot 6\text{H}_2\text{O}$ as raw materials to assemble a three-dimensional anionic uranyl organic framework material (Fig. 11.3) [23]. In this structure, three sets of graphene-like layers were polycatenated to construct a unique anionic framework with disordered $[\text{NH}_2(\text{CH}_3)_2]^+$ in

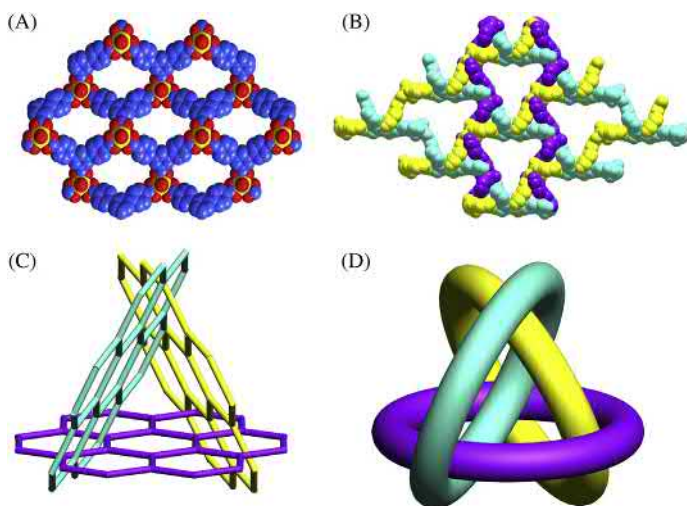


Figure 11.3 Structures of a rare case of polycatenated anionic uranyl organic framework material. (A) 2D layered structure, (B) overview of the crystal structure, (C) topological representation, and (D) simplified polycatenation.

the pores that could be used as a Cs^+ scavenger. This material exhibited fast sorption kinetics and it took only 20 minutes to reach the uptake equilibrium. In addition, the sorption capacity was 145 mg g^{-1} and such a high value was among the most efficient reported cesium-sorbents. Even with large amounts of competing metal ions, this MOF material could still remove more than 70% of cesium from aqueous solution. Additionally, this MOF material exhibited excellent radiation resistance and could retain its crystal structure after large dosages of γ and β irradiation. Aguila et al. [24] grafted sulfonic acid groups onto the hydrolytically stable MOF MIL-101 to prepare an efficient cation exchange material for the remediation of Cs^+ and Sr^{2+} . Batch experiments indicated that this MOF material possessed excellent sorption properties of Cs^+ and Sr^{2+} in a wide pH range. The removal percentage of Cs^+ and Sr^{2+} could reach 99.99% and 98.92%, respectively, corresponding to extremely high distribution coefficients (K_d). However, this material exhibited slow ion exchange rate toward Cs^+ and Sr^{2+} , which required at least 24 hours to reach the uptake equilibrium. In addition, MOF materials have extensive pores and high specific surface area, making them excellent supports for accommodating other functional groups or materials. Naeimi et al. [25] prepared a new efficient Cs^+ sorbent by impregnating potassium nickel hexacyanoferrate into the HKUST-1 MOF material. The resulting material showed very fast sorption kinetics (sorption equilibrium was reached in 30 minutes), relatively large distribution coefficient, high uptake capacity, and good selectivity.

11.3.2 Uranium

Uranium mostly exists in the form of UO_2^{2+} in radioactive waste, which should be sequestered from natural water systems owing to its combined chemotoxicity and radiotoxicity. The uranium extraction from seawater also contributes to the rapid progress of uranium sorbents [26,27]. Up until now, there have been more than 20 MOF materials reported for their UO_2^{2+} uptake capabilities. Lin et al. [28] reported the first case of the use of MOFs in the extraction of UO_2^{2+} from aqueous solution. UiO-68 was covalently modified with phosphorylurea groups and the resulting materials showed high sorption capacity of 217 mg g^{-1} toward UO_2^{2+} . Theoretical calculations disclosed the sorption mechanisms by which UO_2^{2+} was coordinated with two phosphorylurea ligands. In the same manner, MIL-101 was postmodified using carboxyl (carboxyl-derived MIL-101) and CMPO (CMPO-MIL-101) groups for selectively extracting UO_2^{2+} [29,30]. Recently, we reported the first case of amidoxime-modified UiO-66 (UiO-66-AO, Fig. 11.4) using a postsynthetic strategy for fast and effective uranium enrichment from natural seawater [31]. In 120 minutes, UiO-66-AO showed a 94.8% extraction of UO_2^{2+} from Bohai seawater and the capacity of UO_2^{2+} reached as high as 2.68 mg g^{-1} when tested in the real seawater solution, which was comparable to the most efficient uranium sorbent materials from seawater. Such an excellent sorption capability was attributed to the binding of multiple amidoxime motifs to UO_2^{2+} , as revealed by the extended X-ray adsorption fine structure (EXAFS) spectra of the uranium incorporated material.

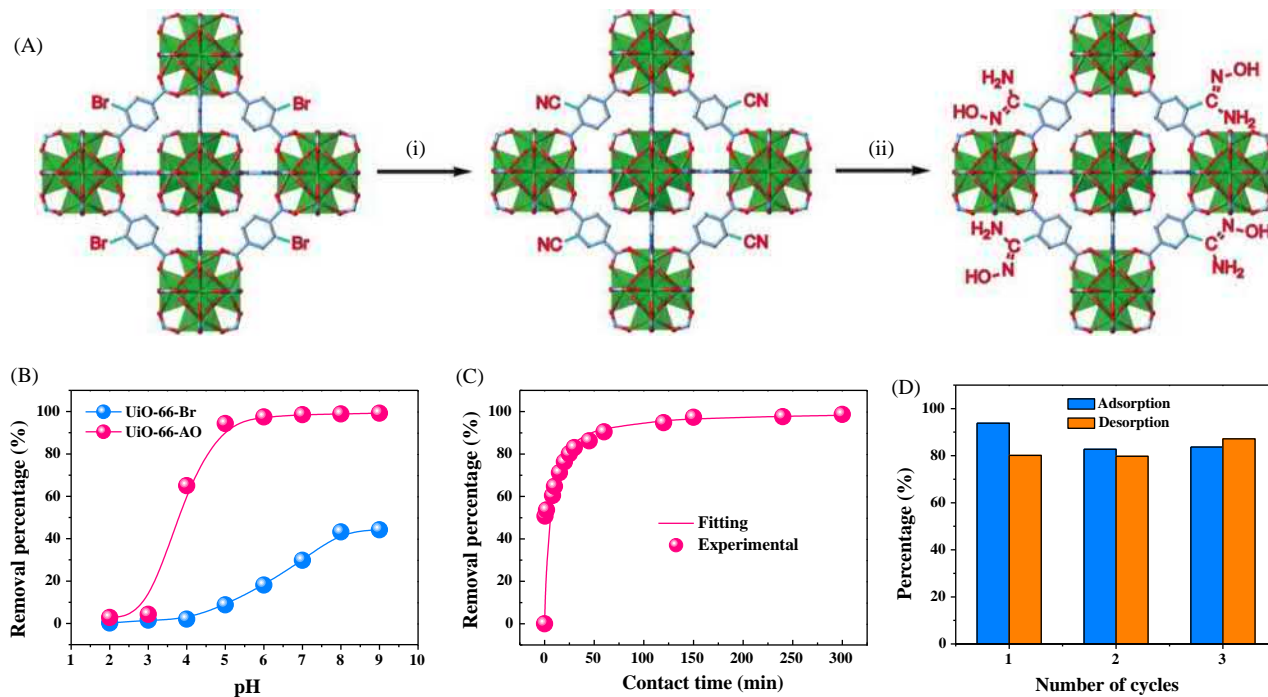


Figure 11.4 (A) Postsynthetic route for UiO-66-AO. (B) Sorption of uranyl by UiO-66-Br and UiO-66-AO as a function of pH value. (C) Effect of contact time on the sorption of uranyl from Bohai seawater by UiO-66-AO. (D) Reusability of UiO-66-AO for Bohai seawater containing extra 500 ppb uranium.

Another postmodification strategy is making use of open metal sites to attach organic functional groups for selectively capturing UO_2^{2+} . Taking advantage of open Cr sites, organic amine groups could be facily grafted onto MIL-101. Compared with the original MIL-101, the modified materials had a significant increase in the uranium sorption capacity [32,33]. The sorption capacities of MIL-101-NH₂, MIL-101-ED (ED = ethanediamine), and MIL-101-DETA (DETA = diethylenetriamine) were 90, 200, and 350 mg g⁻¹, respectively, which were superior to that of the original MIL-101 (20 mg g⁻¹) [34]. In addition, Zhang et al. [35] reported the modification of Zn-MOF-74 with coumarin groups with the help of the open Zn sites, achieving a sorption capacity of 360 mg g⁻¹ for UO_2^{2+} . However, the attachment of an -NH₂ group onto UiO-66 did not improve the sorption properties [36]. A one-pot synthesis strategy could also be used to incorporate UO_2^{2+} -selective ligands into the body of MOF materials. Zn(HBTC)(L)·(H₂O)₂ and Zn(ADC)(4,4'-BPE)_{0.5} belonged to this type and were shown to be efficient for extracting UO_2^{2+} [37].

Interestingly, the bare MOFs with no functionalization still exhibit decent sorption capability toward UO_2^{2+} . That might largely originate from the defects of MOF materials, exposing noncomplexing -COOH groups for potential complexation with UO_2^{2+} . MOF-76 [38] and HKUST-1 [39] could both efficiently remove UO_2^{2+} with remarkable uptake capacities of 298 and 787.4 mg g⁻¹, respectively. The rational utilization of defect engineering to create rich active sorption sites for UO_2^{2+} in MOF materials was originally developed by Shi et al. [40]. They controlled the defects in UiO-66 materials by adjusting the added amounts of benzoic acid. Benzoic acid was then removed after treatment with HCl, which was beneficial for expanding the narrow aperture and the pore volume, and boosting the active Zr-OH or carboxylic functional groups in UiO-66. As shown in Fig. 11.5, after employing the defects, the sorption properties of UO_2^{2+} were substantially improved. The sorption capacities of defects-modified materials were much higher than that of the original UiO-66, reaching 350 mg g⁻¹. Moreover, these modified MOFs still retained their structures even under highly acidic solutions.

The fatal weakness of MOFs is their limited stability in water. In some cases, the radioactive waste containing uranium is highly acidic. Therefore it is extremely challenging to develop MOF sorbents to sequester UO_2^{2+} from highly acidic solutions. To overcome this challenge, we synthesized several extremely hydrolytically stable zirconium phosphonate MOFs (Fig. 11.6) in ionic liquids using tetrakis[4-(dihydroxyphosphoryl)phenyl]methane or 1,3,5,7-tetrakis(4-phosphonophenyl)adamantine and ZrCl₄ as raw materials [41], which represented the first single crystals of such a type of MOFs. Zirconium(IV) phosphonate MOFs showed ultrastability in acidic solutions, even in fuming acids and aqua regia. SZ-2 and SZ-3 were tested to eliminate UO_2^{2+} from aqueous solution with different pH values. Generally, most adsorbents showed a weak uptake ability toward UO_2^{2+} at low pH due to the protonation and structure collapse. On the contrary, SZ-2 could remove nearly 62.4% of UO_2^{2+} at pH 1.0. The sorption mechanism was disclosed by the combined EXAFS spectra and molecular dynamics (MD) simulations. The strong electrostatic forces pulled UO_2^{2+} into the pores of SZ-2 and then UO_2^{2+} was tightly trapped by a dense hydrogen bonding network.

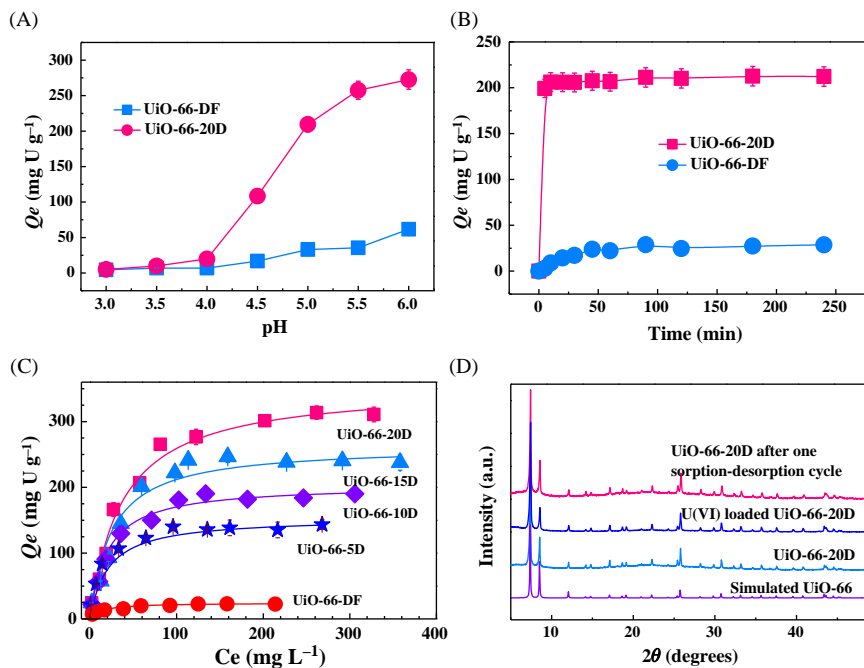


Figure 11.5 (A) UO_2^{2+} sorption onto UiO-66-DF and UiO-66-20D as a function of pH value. (B) Sorption kinetics of UO_2^{2+} onto UiO-66-DF and UiO-66-20D. (C) Sorption isotherms of UO_2^{2+} . (D) Stability assessment by PXRD.

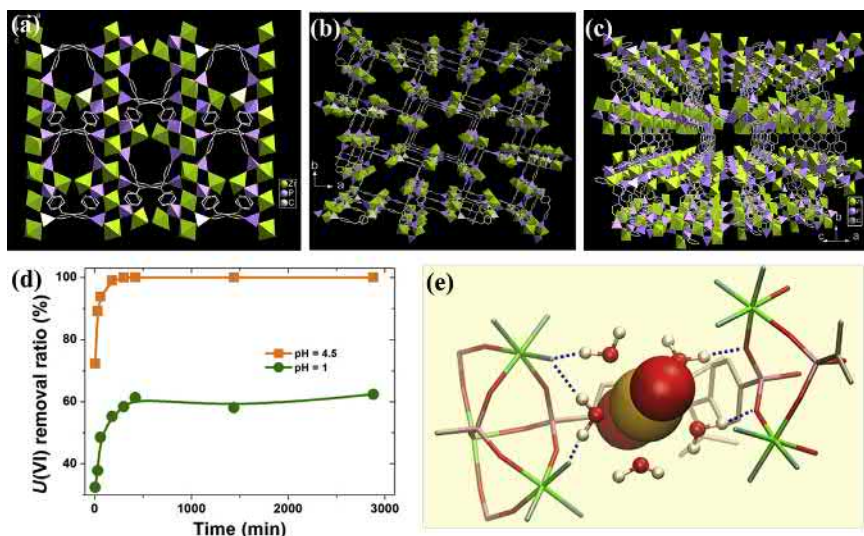


Figure 11.6 Crystal structures of (A) SZ-1; (B) SZ-2; and (C) SZ-3 (SZ = Suzhou). (D) Sorption of UO_2^{2+} as a function of contact time by SZ-2. (E) Sorption mechanism between UO_2^{2+} and SZ-2 proposed by molecular dynamics simulations.

Owing to the high sorption capability and fluorescent property, lanthanide-based MOFs are an excellent type of sensor for uranium. MOF-76 represented the first example for both removing and detecting uranium, but the detection limit was relatively high. Recently, a fluorescent Tb-based MOF with a mesoporous nature was used to detect UO_2^{2+} (Fig. 11.7A). Due to the existence of abundant open nitrogen sites in the pores, the UO_2^{2+} ions could be selectively adsorbed, then resulting in the quench of the luminescence of this MOF (Fig. 11.7B and C). The detection limit in pure water was calculated to be $0.9 \mu\text{g L}^{-1}$, which was much lower than the maximum contamination standard of $30 \mu\text{g L}^{-1}$ in drinking water (EPA) [42]. Another anionic Tb-based MOF, $[\text{Tb}(\text{BPDC})_2] \cdot (\text{CH}_3)_2\text{NH}_2$ (DUT-101, BPDC = biphenyl-4,4'-dicarboxylate) was synthesized by Ye et al. [43] for UO_2^{2+} detection. The

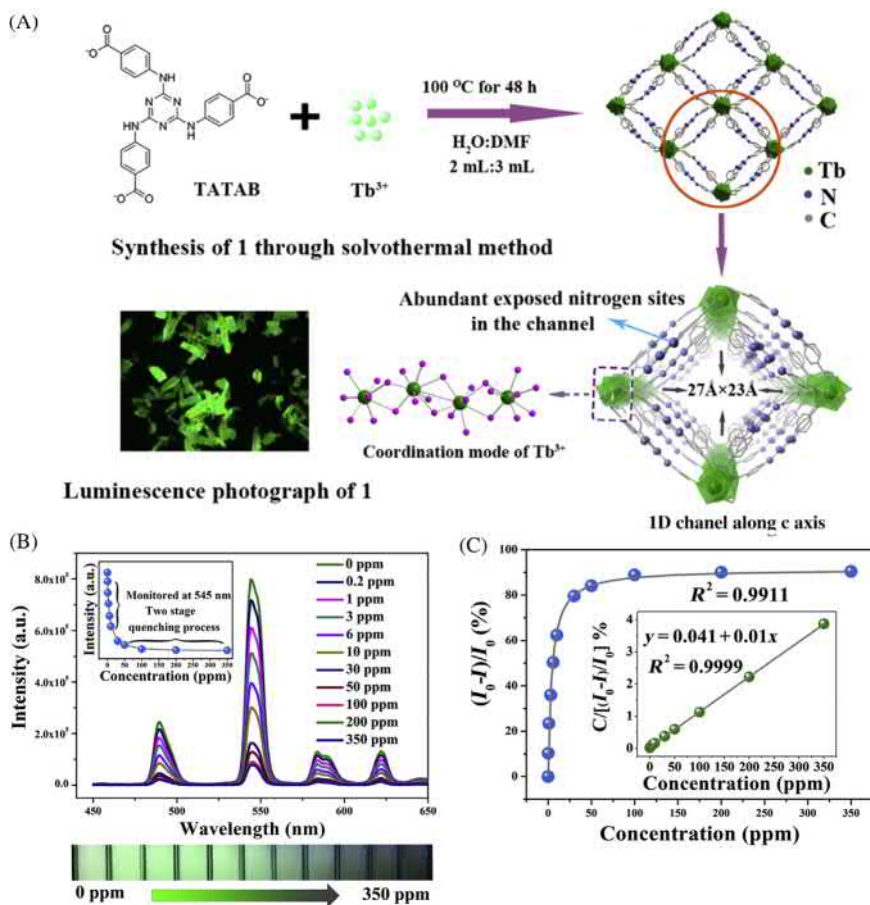


Figure 11.7 (A) Schematic of the synthesis route and the structure of mesoporous Tb-based MOF. (B) Emission spectra of Tb-based MOF in UO_2^{2+} solution. (C) Correlation between $(I_0 - I)/I_0$ and UO_2^{2+} concentration.

detection limit of uranium for DUT-101 was measured to be $8.34 \mu\text{g L}^{-1}$. In addition, Sun et al. [44] designed a robust fluorescent cobalt MOF based on 4,6-di(2-methyl-imidazol-1-yl)-pyrimidine and 1,4-naphthalenedicarboxylic acid. The structure held a *pcu* network with pyrimidyl Lewis base sites for selective complexation with metal ions. Upon addition of 1 mM UO_2^{2+} solution, the luminescence intensity of this MOF material at 400 nm was gradually quenched. Even by adding 20 μL of 1 mM UO_2^{2+} solution, the decrease of luminescence intensity could be still detected and the calculated lowest response value was $13.2 \mu\text{M UO}_2^{2+}$.

11.3.3 Thorium

Compared to uranium, the investigation into the separation of thorium (^{232}Th) by solid sorbent materials receives less attention. One reason for this is that the fissile material in most current nuclear reactors is uranium rather than thorium. However, thorium has a larger natural abundance than uranium and emerges as a core part of molten salt reactors. On the other hand, the dominating oxidation state of thorium is Th(IV) and therefore it can serve as a useful surrogate for transuranic cations Np (IV) and Pu(IV), yielding valuable knowledge on properly treating these highly radiotoxic radionuclides. Shi et al. [45] reported the first case of Th(IV) sequestration from an acidic solution by MOF materials. They found the attachment of carboxyl groups onto the UiO-66 MOF would decrease the pore volumes and specific surface areas, but the sorption properties toward Th(IV) was significantly improved. The uptake capacity of UiO-66-(COOH)₂ toward Th(IV) was 350 mg g^{-1} , which was much larger than those of UiO-66 and UiO-66-COOH (Fig. 11.8A). Furthermore, these MOFs exhibited rapid sorption rate and good selectivity toward Th(IV) even under the condition of multiple competing metal ions (Fig. 11.8B and C). The sorption mechanism between Th(IV) and UiO-66-COOH/UiO-66-(COOH)₂ was attributed to the strong coordination of functional carboxyl groups to Th(IV). Kaykhaili et al. [46] chose a hydroxyl-functionalized UiO-66 for thorium enrichment from aqueous solution. Though it could enrich thorium 250 times compared to the original concentration and the resulting detection limit was $0.35 \mu\text{g L}^{-1}$, the maximum sorption capacity was relatively low at 47.5 mg g^{-1} .

In addition, thorium usually exists as intergrowths with rare earth elements in the ores. To avoid the radioactive pollution during rare earth mining, thorium is generally removed from rare earth waste residues. Sun et al. [47] synthesized a MnSO-MOF analog material using 1,4-dibromo-2,3,5,6-tetrakis(4-carboxyphenyl) benzene and Mn(III) salen (Fig. 11.8D). After treatment with H_2O_2 , Mn(III) was selectively demelated to create open uncoordinated sites for thorium. It was found that the sorption capacity of this material toward thorium was 46.3 mg g^{-1} and the separation factors of $\text{Th}^{4+}/\text{La}^{3+}$, $\text{Th}^{4+}/\text{Eu}^{3+}$, and $\text{Th}^{4+}/\text{Lu}^{3+}$ were 10.7, 16.4, and 10.3, respectively. A combined characterization of energy dispersive spectrometer (EDS) and electrospray ionization mass spectrometry (ESI-MS) showed that Th^{4+} was coordinated to the nitrogen and oxygen atoms of salen molecules. This is the first case of thorium separation from rare earth by a MOF material.

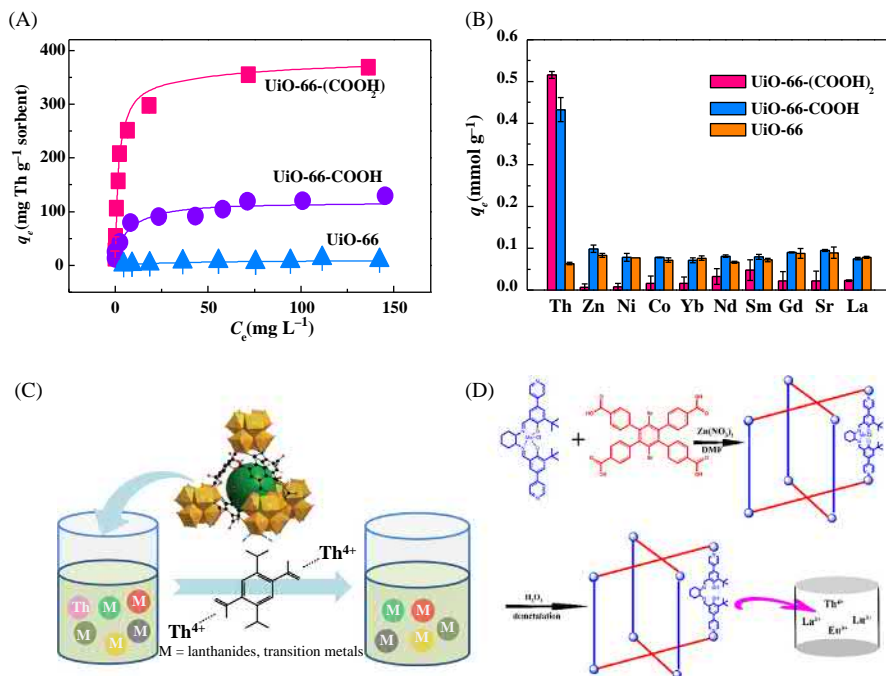


Figure 11.8 Sorption properties of UiO-66, UiO-66-COOH, and UiO-66-(COOH)₂: (A) sorption isotherms, (B) selectivity, (C) schematic, and (D) synthesis of Salen-functionalized MOF material.

Though the sequestrations of UO_2^{2+} and Th^{4+} have been extensively studied, few investigations on the separation of transuranic cations (e.g., NpO_2^+ , Pu^{4+} , Am^{3+} , and Cm^{3+}) by MOFs have been conducted.

11.3.4 Selenium and technetium

The main anion radionuclides in radioactive wastewaters are $^{129}\text{I}^-$, $^{79}\text{SeO}_3^{2-}$, $^{79}\text{SeO}_4^{2-}$, and $^{99}\text{TcO}_4^-$. All of them have long-term radioactivity. These anions have large solubility in aqueous solution and most of the natural mineral cannot efficiently block them, resulting in high mobility in the environment. Among them, anionic ^{79}Se and ^{99}Tc species were most problematic and it is still a challenge to separate them from radioactive wastes. Inorganic materials consisting of cationic frameworks are found to effectively capture anionic contaminants, but such a type of materials is little reported and the sorption capacity is very limited [48]. Ion exchange resins are commercial products exhibiting high sorption capacity and excellent distribution coefficients for radioactive anions, but they show slow sorption kinetics and unstable characteristics toward high basicity and radiation.

Until now, very few MOFs have been reported to remove ^{79}Se from aqueous solution [49]. Farha et al. [50] firstly studied the sorption properties of

SeO_3^{2-} and SeO_4^{2-} by several stable Zr-based MOFs (UiO-66, UiO-66-NH₂, UiO-66-(NH₂)₂, UiO-66-(OH)₂, UiO-67, NU-1000, and NU-1000BA). The batch experimental results showed that NU-1000 represented the best material among all the MOFs studied with high sorption capacity and fast sorption kinetics for these two anionic selenium species. The saturated sorption capacities of SeO_3^{2-} and SeO_4^{2-} by NU-1000 were 95 and 85 mg g⁻¹, respectively. Impressively, the sorption mechanism was unraveled by the pair distribution function spectra, which showed that one SeO_3^{2-} or SeO_4^{2-} anion was coordinated to two Zr metal centers in a $\eta_2\mu_2$ fashion (Fig. 11.9). Following this idea, Wang et al. [51] and Sun et al. [52] also investigated the selenite/selenate uptake onto zirconium-based MOFs using a combined theoretical and experimental method.

A large number of cationic MOFs have been reported in the capture of anionic pollutants, but few were used in the removal of radioactive $^{99}\text{TcO}_4^-$ [48]. Previous investigations show ReO_4^- is an excellent surrogate for TcO_4^- during sorption or ion exchange process unless redox reaction is involved. Oliver et al. [53] reported an extremely high sorption capacity of 602 mg g⁻¹ for ReO_4^- using a cationic two-dimensional layered MOF material, SLUG-21. However, this MOF was not quite stable under a hydrolytical condition and the exchanged out anions, ethane disulfonate, might be adverse to the vitrification of radioactive wastes. Banerjee et al. [54] reported an amine-functionalized Zr-based MOF for removing ReO_4^- from aqueous solution. The sorption selectivity was not satisfied, as the higher-charged anions such as SO_4^{2-} outcompeted with ReO_4^- during the anion exchange process.

Recently, a hydrolytically-stable three-dimensional cationic MOF material, SCU-100 (SCU = Soochow University), was assembled through a tetrakis[4-(1-imidazol-yl)-phenyl]methane ligand and two-coordinate Ag^+ cations with open metal sites [55]. SCU-100 contained large amounts of one-dimensional channels with a size of 6.9×6.9 Å, which were filled with disordered NO_3^- . This MOF material was quite stable in a wide pH range and high ionizing radiation. SCU-100 was the first MOF material that was directly tested for its sorption properties with radioactive $^{99}\text{TcO}_4^-$. The batch experimental results showed it could rapidly remove all the

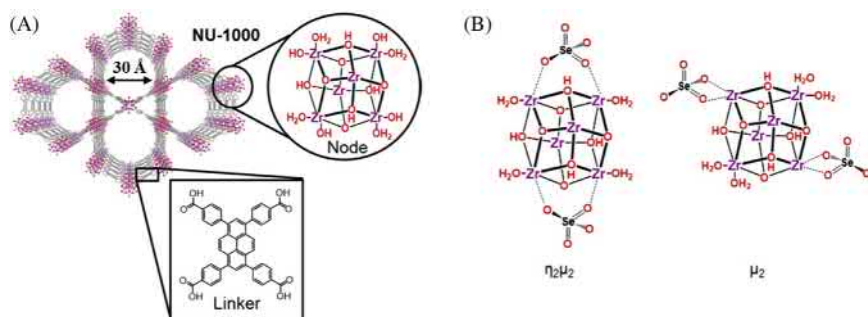


Figure 11.9 (A) Crystal structures of NU-1000 and (B) probable sorption mechanisms between NU-1000 and SeO_3^{2-} / SeO_4^{2-} .

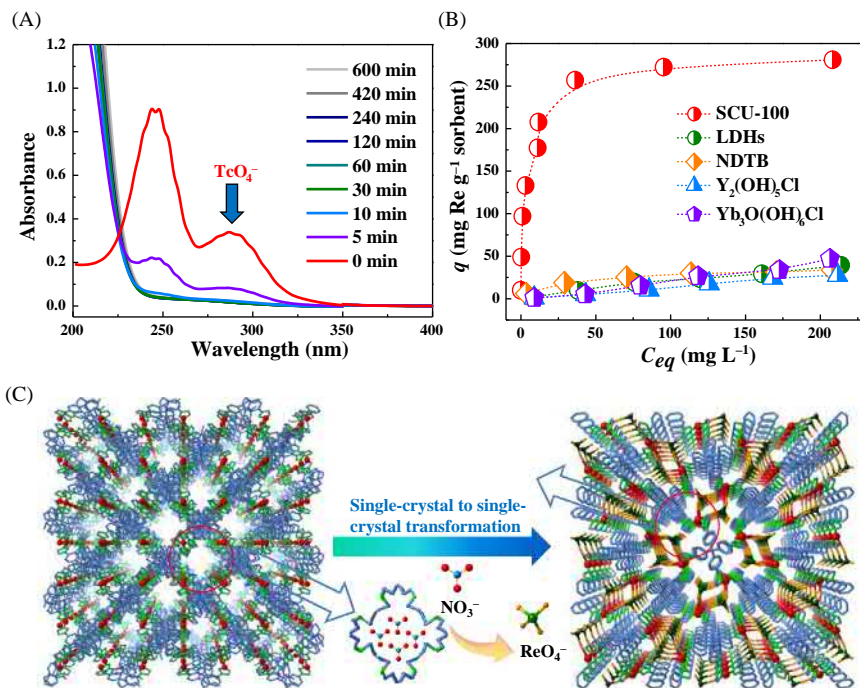


Figure 11.10 (A) Sorption properties of SCU-100 toward TcO_4^- as a function of contact time. (B) Comparison of the sorption capacity of ReO_4^- by SCU-100 and other inorganic cationic sorbents. (C) Schematic of sorption mechanism between ReO_4^- and SCU-100.

TcO_4^- from water within 30 minutes (Fig. 11.10A). The saturated uptake capacity of SCU-100 toward ReO_4^- was 553 mg g^{-1} (Fig. 11.10B). Impressively, the removal efficiency of TcO_4^- in the presence of a large excess of competitive anions (NO_3^- , SO_4^{2-} , CO_3^{2-} , and PO_4^{3-}) was little affected. Even in the complicated simulated Hanford low-level waste, SCU-100 was still able to capture nearly 87% of TcO_4^- . With the help of the single-crystal X-ray diffraction technique, the sorption mechanism was demonstrated to be a single-crystal-to-single-crystal transformation process (Fig. 11.10C). It was found that the eightfold interpenetrated framework in original SCU-100 was transformed to a fourfold interpenetrated framework and the disordered NO_3^- anions were totally exchanged by ReO_4^- anions. The open Ag^+ sites played an important role in the capture of ReO_4^- through forming strong $\text{Ag}-\text{O}-\text{Re}$ bonds. Furthermore, the ReO_4^- anions were surrounded by an extremely dense hydrogen bonding, which was another important factor to determine such excellent sorption properties toward $\text{ReO}_4^-/\text{TcO}_4^-$.

However, due to the single-crystal-to-single-crystal transformation mechanism, large single crystals of SCU-100 would transform into small crystallines after an ion-exchange process, making it unsuitable for industrial column chromatographic separation. We then designed another robust 3D nickel-based MOF, SCU-101 [56],

using the same ligand. This material was able to have anion exchange without framework structure transformation, therefore overcoming the former issue. The overall structure of SCU-101 was a typical porous cationic extended framework, where each nickel ion was coordinated by four neutral tipm ligands and one oxalate, affording a high positive charge density on the framework (Fig. 11.11A and B). Disordered nitrate anions filled in the pores to keep charge balance and could be facily exchangeable. The sequestration equilibrium was reached within 10 minutes, obviously faster than the commercial ion exchange resins and other scavengers. The distribution coefficient and the maximum uptake capacity for ReO_4^- were $7.5 \times 10^5 \text{ mL g}^{-1}$ and 217 mg g^{-1} , respectively. Impressively, SCU-101 could selectively sequester TcO_4^- from aqueous solution containing large amounts of NO_3^- and SO_4^{2-} and even in the presence of 6000 times of SO_4^{2-} compared to TcO_4^- would not considerably affect the removal of TcO_4^- . The sorption mechanism was unraveled by the single-crystal X-ray diffraction technique. In the TcO_4^- -sorbed SCU-101, TcO_4^- anions preferred to occupy the channel of A rather than B and C (Fig. 11.11C). A deeper examination on the single-crystal structure of TcO_4^- -sorbed SCU-101 disclosed that TcO_4^- anions were trapped in a dense hydrogen bonding network constructed with H atoms from phenyl and imidazolyl groups (Fig. 11.11D). Furthermore, the DFT calculation showed that the binding energy was $-20.42 \text{ kcal mol}^{-1}$, which was thermodynamically favorable. This is the first case of a single-crystal structure containing TcO_4^- trapped in a porous sorbent material.

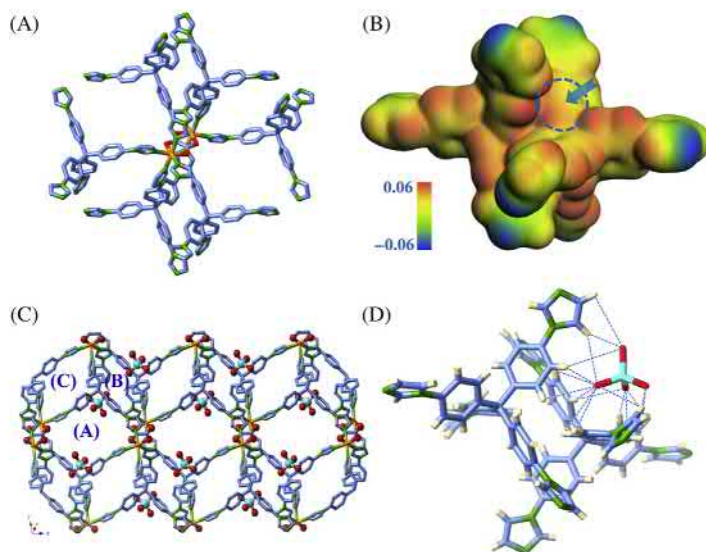


Figure 11.11 (A) Coordination environment of nickel ion with four tipm molecules and one oxalate. (B) Electrostatic potential (ESP) distribution of partial frameworks. (C) TcO_4^- trapped in A type of channels in SCU-101. (D) TcO_4^- surrounded by a dense hydrogen bonding network.

In addition, we have also reported a one-dimensional cationic MOF material, $\text{Ag}(4,4'\text{-bipyridine})\text{NO}_3$ (SBN), which shows remarkably efficient removal of ReO_4^- . The uptake capacity reached as high as 786 mg g^{-1} [57], which was the largest value among all the reported cationic MOF materials. Furthermore, once captured, ReO_4^- was immobilized in an extremely insoluble solid (Fig. 11.12) and no ReO_4^- would be exchanged out even in the presence of 1000 times of nitrate anions compared to ReO_4^- . From this perspective, SBN could be considered as a potential waste form for directly immobilizing TcO_4^- . Both single-crystal structure and DFT calculations clearly revealed that the $\text{ReO}_4^-/\text{TcO}_4^-$ anions in the resulting compound were strongly trapped in the crystal lattice with multiple hydrogen bonding and $\text{Ag}-\text{O}-\text{Re}$ bonds. The open Ag^+ sites played an important role in determining the selectivity of SBN toward $\text{ReO}_4^-/\text{TcO}_4^-$, which shed light on designing such similar highly efficient cationic MOFs for capturing TcO_4^- .

Additionally, our endeavors in the design of cationic frameworks for TcO_4^- sequestration have been extended to actinide-based MOF materials, such as SCU-6, SCU-7, and SCU-8 series [58,59]. Very recently, Farha et al. [60] investigated the capture of by TcO_4^- NU-1000. Though the NU-1000 was not a cationic framework, it still showed a high uptake capacity of 210 mg g^{-1} for ReO_4^- and the sorption equilibrium required only 5 minutes to occur. Structure refinement indicated that the zirconium cluster in the structure of MOF played a very important role in the sequestration of $\text{ReO}_4^-/\text{TcO}_4^-$. There were two respective binding modes in the pores of NU-1000, including chelating and nonchelating perchrenate (Fig. 11.13). The hydroxyl ($-\text{OH}$) and water ($-\text{OH}_2$) of the Zr nodes were replaced by ReO_4^- through the ligand exchange mechanism. More specifically, an $-\text{OH}$ group and an $-\text{OH}_2$ group were replaced by ReO_4^- via a chelating mode; another single $-\text{OH}$ group was exchanged by ReO_4^- in a nonchelating manner.

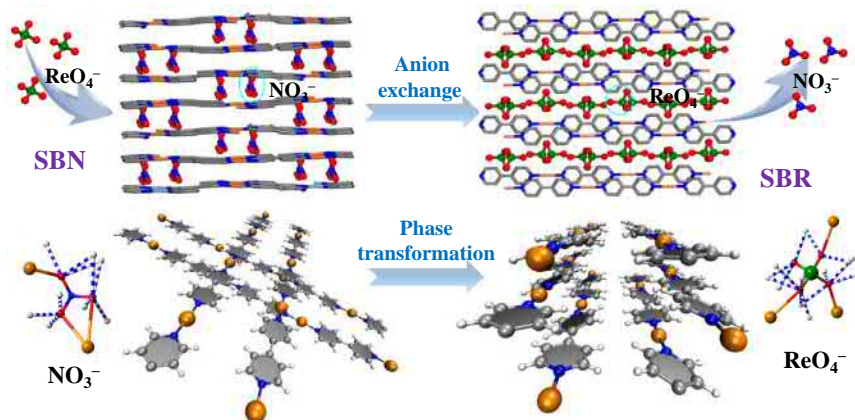


Figure 11.12 Sequestration mechanism between ReO_4^- and SBN.

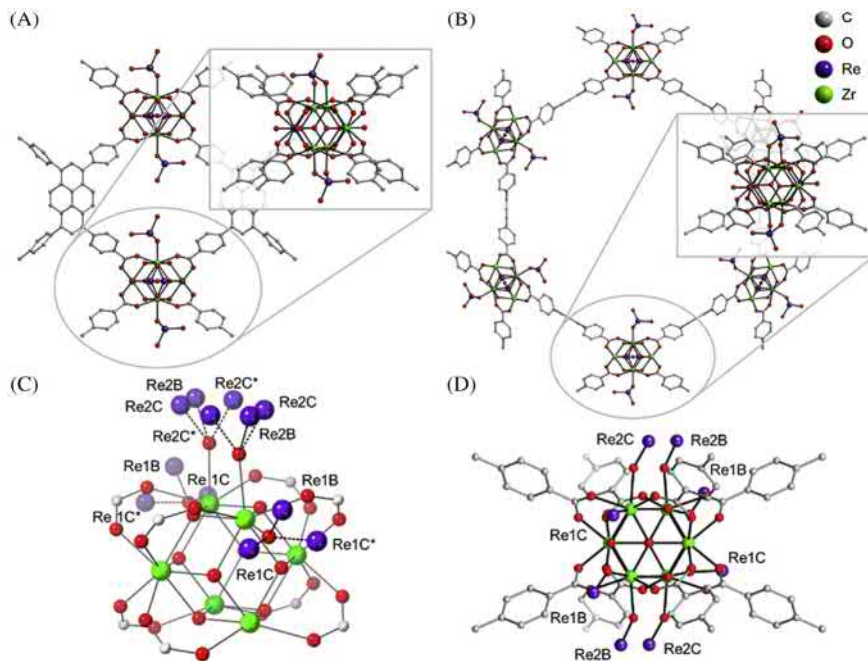


Figure 11.13 Crystal structure of NU-1000 after sorbed ReO_4^- . (A) Chelating ReO_4^- in the small pores, (B) Chelating ReO_4^- in the large pores, (C) Nonchelating ReO_4^- binding to the -OH groups, and (D) Nonchelating ReO_4^- in the small and large pores.

11.3.5 Iodine

Iodine (I_2) should be captured in nuclear fuel reprocessing or nuclear accidents mainly due to its long-lived ^{129}I isotope ($t_{1/2} = 1.57 \times 10^7$ years) [10,61]. Though MOF materials showed superior sorption properties toward I_2 over silver-based sorbents and activated carbon [62], most of the experiments were performed in organic solvent (i.e., cyclohexane) rather than gaseous state, which is not ideal for real applications [63–68]. A 3D zinc saccharate MOF was firstly tested for gaseous I_2 removal, but the uptake was only 16.6 wt% I_2 [69]. Sava et al. [70] systematically investigated the uptake of gaseous I_2 by MOF materials, which indicated that the judiciously selected ZIF-8 could trap as high as 125 wt% I_2 . With the help of high resolution synchrotron powder X-ray diffraction, PDF spectra, and theoretical calculations, the sorption mechanism was revealed. Two individual molecular I_2 sorption sites were refined inside the β -cage entitled “ I_a ” and “ I_b ” (Fig. 11.14). Furthermore, the sorption process was clearly identified by aqueous solution calorimetry [71]. The energetics of I_2 capture within the cage of ZIF-8 were larger than that of the sorption on the surface. In the cages, two charge transfer complexes were formed between I_2 and the opposing 2-methylimidazolate linkers to maximize the retention amounts. In addition, HKUST-1 broke the record of the highest I_2 sorption capacity to 175 wt% I_2 , which could selectively capture I_2 from water

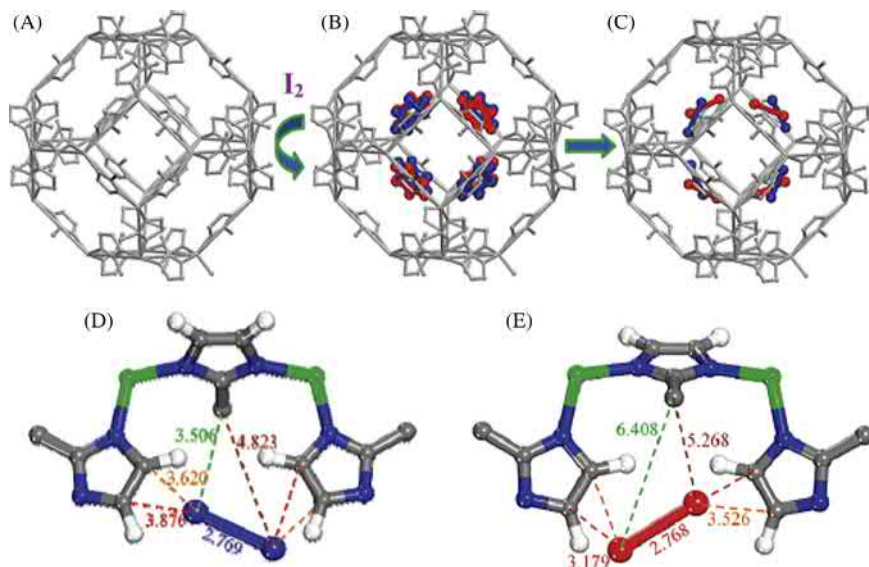


Figure 11.14 (A) Structure of ZIF-8 cage. (B, C) Two different molecular I₂ sorption sites refined inside the β -cage, (D) the I_a site, and (E) the I_b site.

vapor. I₂ preferred to adsorb in the smallest cages near the copper paddle wheel cluster and the main pores with benzene tricarboxylate organic linker of the HKUST-1 framework [72]. After being trapped in the pores, I₂ would form a hydrophobic barrier to inhibit the uptake of water vapor, which was quite beneficial for selective I₂ sequestration from mixed gas streams in scenarios of nuclear fuel reprocessing and accident remediation. Although further attempts have been made to improve the sorption properties of I₂ by MOF materials, such as Ni^{II}(pz)₄ [Ni^{II}(CN)₄] [73] and Ni(II)-MOF [74], the properties were all inferior to ZIF-8 and HKUST-1.

Except for I₂ molecules, radioactive organic iodides (methyl iodide and ethyl iodide) are also generated during the used fuel reprocessing and should be selectively captured in a safe manner. There is very little research work in this area. Recently, Li et al. [75] reported a new type of highly efficient MOF-based scavenger for organic iodides. Taking advantage of the strong interaction between open metal sites on the Cr trinuclear secondary building unit and nitrogen atoms, they grafted triethylenediamine (TED) and hexamethylenetetramine (HMTA) onto MIL-101 to prepare such functionalized sorbents (Fig. 11.15A). Impressively, 120 and 136 wt% CH₃I could be rapidly sorbed onto the MIL-101-Cr-TED and MIL-101-Cr-HMTA materials in the initial 10 minutes at 30°C. When the sorption reached the equilibrium at 120 minutes, the uptake amounts of CH₃I were 160 and 174 wt% for MIL-101-Cr-TED and MIL-101-Cr-HMTA, respectively. Such high capacity showed a clear advance over traditional activated carbon-based adsorbents and silver-functionalized porous materials. Even at elevated working temperature

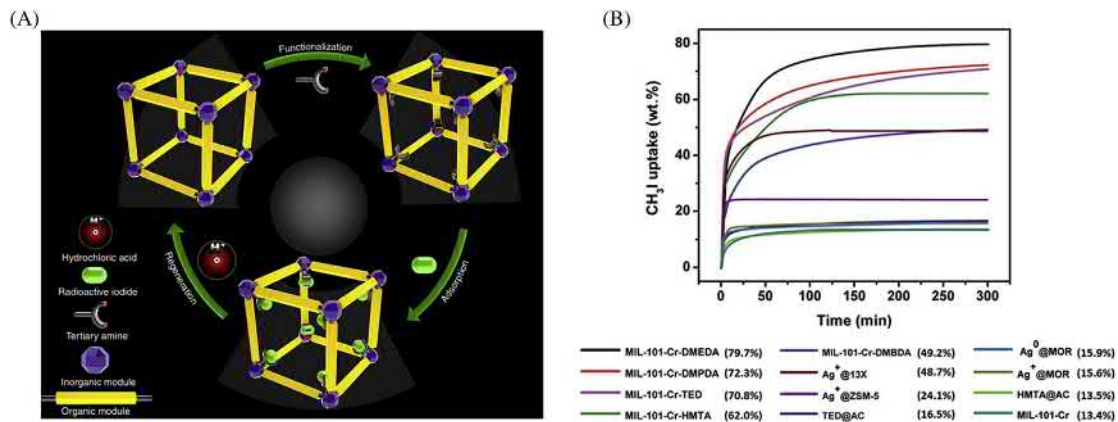


Figure 11.15 (A) Design strategy of amine-functionalized MIL-101-Cr materials for efficiently capturing radioactive organic iodides from nuclear waste. (B) Comparison of the sorption isotherms of CH_3I in amine-functionalized MIL-101-Cr materials with other traditional sorbents.

(150°C), the MIL-101-Cr-TED material still held extremely large sorption amounts of 71 wt% for CH₃I. This material also exhibited very high decontamination factors in the range of 4.8×10^3 to 6.3×10^3 under a simulated real-world off-gas reprocessing condition with low concentration of CH₃I, corresponding to around 99.98% removal, which considerably surpassed the reprocessing facility regulatory requirements. In addition, such a type of material could be easily recovered using 3M HCl and ethanol solution. The strong sorption of MIL-101-Cr-TED and MIL-101-Cr-HMTA toward radioactive organic iodides was attributed to the formation of ionic species (R₃N-CH₃)⁺I⁻ between amines groups and CH₃I at high temperatures. Then, the same group screened the effect chain length of diamine on the sorption of organic iodides. The diamine with longer chain length would block the pores of MIL-101-Cr, resulting in a decrease of CH₃I uptake amount [76]. The MIL-101-Cr-DMEDA (DMEDA = *N,N*-dimethylethylenediamine) material exhibited the highest sorption capacity of 80% at 150°C, which was much higher than that of the industrial material, Ag⁰@MOR (15 wt%) (Fig. 11.15B).

11.3.6 Krypton and xenon

⁸⁵Kr ($t_{1/2} = 10.76$ years) and ¹³³Xe ($t_{1/2} = 5.25$ days) are the volatile fission products of ²³⁵U and ²³⁹Pu. After the used nuclear fuel is stored for several years, ¹³³Xe will decay to nonradioactive Xe. However, when the fuel is reprocessed, ⁸⁵Kr is still a radioactive element that should be sequestered and stored in a specific facility. Because of the presence of the large volume of Xe, to minimize the storage scale, Xe should be selectively separated from ⁸⁵Kr. Therefore the Xe/Kr separation selectivity and capacity are equally important for sorbent materials [77]. Compared with zeolites and activated carbon, the MOF materials have tunable pore diameter, large specific surface areas, and easy postmodification, showing a promising application in Xe/Kr separation [11,78–90].

In 2015 Thallapally et al. [9] reported an account of xenon and krypton separation by MOFs, which sheds light on how to design an ideal material for Xe/Kr separation. It was found that it was highly beneficial to have polar or accessible unsaturated metal centers, narrow uniform pores with diameters slightly larger than the size of Xe or Kr, additional polarized alien species, or temperature-dependent separation of the gas mixture. Some selected MOFs for Xe sorption and separation are shown in Fig. 11.16. After systematic comparison under the same conditions, Co₃(HCOO)₆ exhibits the best Xe/Kr selectivity (~11) and Ag@Ni-DOBDC shows the highest Xe uptake capacity (1.5–2.0 mol kg⁻¹).

To pursue better properties, several MOFs were deliberately designed and tested for Xe/Kr separation. Xiong et al. [91] synthesized a zinc tetrazolate framework ([Zn(mtz)₂]) (Hmtz = methyl-1*H*-tetrazole) that exhibited high sorption capacity of Xe (2.7 mol kg⁻¹) and excellent Xe/Kr selectivity. In addition, two hybrid ultramicroporous MOF materials, CROFOUR-1-Ni and CROFOUR-2-Ni [92], constructed by saturated metal centers with CrO₄²⁻ anions and functionalized organic linkers, were reported to show higher Xe/Kr separation factors of 22 and 15.5. Recently, after screening of ~125,000 MOF structures using high-throughput computational

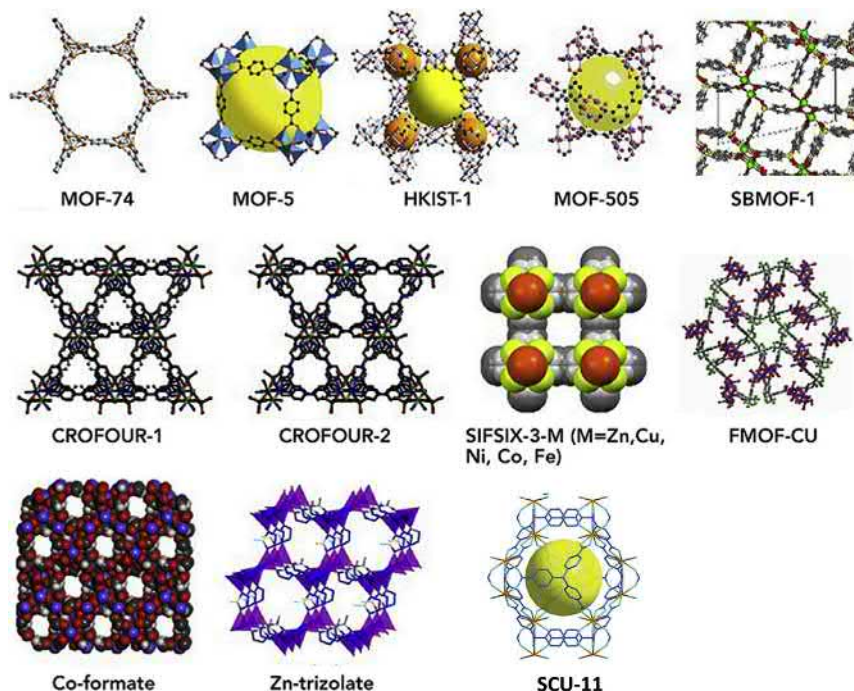


Figure 11.16 Structures of selected MOFs for Xe sorption and separation.

simulations, Thallapally et al. [93] successfully obtained an SBMOF-1 (CaSDB, SDB = 4,4-sulfonyldibenzoate) MOF that exhibited the highest xenon capture capacity and a strong affinity toward xenon when tested in a similar condition to nuclear fuel reprocessing (Fig. 11.17A and B). Furthermore, with the help of the single-crystal X-ray diffraction technique and molecular models, the structures after uptake of Xe and Kr in SBMOF-1 were disclosed. As shown in Fig. 11.17C, Xe occupied the sites close to the midpoint of the channel of SBMOF-1, strongly interacting with the aromatic rings in the channel wall through van der Waals forces. The exactly matching size of SBMOF-1 (4.2 Å) with Xe (4.1 Å) was responsible for the excellent selectivity toward Xe.

11.4 Summary and outlook

In summary, MOFs hold ultrahigh specific surface area, tunable porosity, and flexible postmodification, endowing them with outstanding properties in the sequestration of radioactive wastes.

As for radioactive cations, the sequestration is mostly achieved by selective grafting of organic groups onto MOF via one-pot or postmodification methods. The

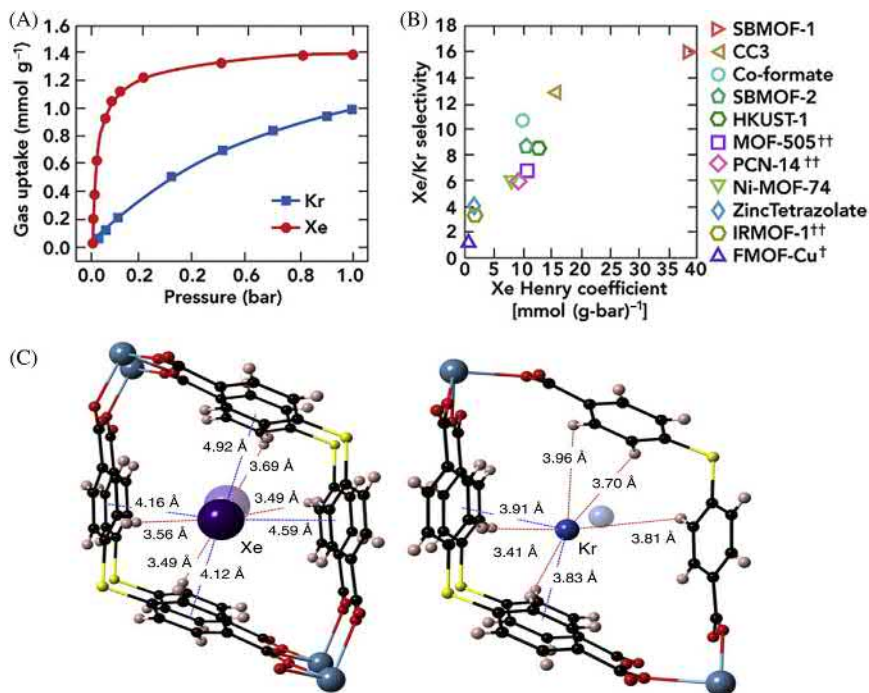


Figure 11.17 (A) Xe and Kr sorption isotherms by SBMOF-1. (B) Comparison of the promising porous materials for Xe/Kr separation. (C) Xe and Kr positions in SBMOF-1 determined by single-crystal X-ray diffraction.

type of anionic MOFs containing facily exchangeable cations is limited, dependent only on the decomposition of organic solvent during the synthesis of MOF or sulfonation of the pristine MOFs. Other effective strategies to design new types of anionic MOFs are in great request. Assembly of the metal ions with the functionalized organic linkers with negative charge may be one good route for the preparation of anionic MOFs. Additionally, to utilize the host–guest supramolecular chemistry is also an efficient strategy to design MOFs with tunable pores or cavities that exactly match the size of cations (i.e., Sr²⁺, Cs⁺). Moreover, because of the unstable nature of most MOFs, the extraction of actinide from the aqueous solution with low pH values is still a great challenge. In batch experiments should be cautiously conducted at pH > 5. The measured capacity may be inaccurate due to the potential precipitations/hydrolysis of actinides under this condition. Furthermore, simply chasing the extremely high capacity is impractical. The design of experimental parameters should be close to the real conditions, such as used fuel reprocessing solutions, rare earth tailings, and seawater. The investigation of the separation of transuranic cations (e.g., NpO₂⁺, Pu⁴⁺, Am³⁺, and Cm³⁺) by MOFs remains to be explored.

Recently, the study of the cationic MOFs for remediating environmental pollutants has grown exponentially. A large number of cationic MOFs reported for nonradioactive anions (i.e., AsO_4^{3-} , CrO_4^{2-} , ClO_4^-) removal are good references for the design of similar materials for the sequestration the anionic radionuclides. Self-assembly of neutral molecules containing multiple nitrogen atoms with transition metals is still the most efficient strategy to prepare the cationic MOFs for anionic radionuclides separation. Three design rules may be beneficial: (1) the non/weak-coordinated anion is highly recommended to add during the preparation of cationic MOFs, which can act a template to form desired pores and, meanwhile, a facilely exchangeable anion; (2) abundant open metal sites in the cationic MOFs are beneficial for the selectivity; (3) the hydrophobicity of MOFs is another important factor for separating TcO_4^- from SO_4^{2-} and NO_3^- .

Up to now, the applications of MOFs in sequestering I_2 have been mostly performed in organic solvent (i.e., cyclohexane) rather than in a gaseous state, so it is difficult to summarize some common rules for the design of MOFs for selectively trapping gaseous I_2 . However, the MOFs with abundant microspores, large specific surface areas, and open metal sites may be excellent candidates. With respect to Xe/Kr separation, the pore size of synthesized MOFs should be mildly larger than the size of Xe. More polarizable groups, open metal sites, and nanoparticles in the MOFs are also helpful.

With an increase of computational power and optimized simulation algorithms, the structure–property relationship of MOFs could be initially established by using the high-throughput computational simulations [94–97]. Therefore the application of such large-scale computation in screening good MOF candidates for radionuclides sequestration will be a growing tendency. In addition, multiple advanced characterization techniques (such as XANES, EXAFS, SC-XRD, and PDF) can provide insights into the interaction mechanism between the radionuclides and MOFs on an atomic scale level.

Finally, the preparation of MOF materials with large crystal sizes (hundred micrometers) is highly desirable for use in the industrial column chromatographic separation. Except for growing big crystals, cellulose, chitosan, and ion exchange resins are all excellent supports that could be used to blend with powdered MOFs to make the packing materials. MOF/magnet mixture [98] and MOF-based membrane materials [99] will also emerge in practical applications in the remediation of radionuclides in the near future.

Acknowledgments

This work was supported by the National Natural Science Foundation of China (21790370, 21790374, U1532259, 11605118, U1732112, 21876124), the Natural Science Foundation of Jiangsu Province (BK20150313), the Priority Academic Program Development of Jiangsu Higher Education Institutions (PAPD), and the “Young Thousand Talented Program” in China.

References

- [1] A. Leoncini, J. Huskens, W. Verboom, Ligands for f-element extraction used in the nuclear fuel cycle, *Chem. Soc. Rev.* 46 (2017) 7229–7273.
- [2] C.L. Xiao, Q.Y. Wu, C.Z. Wang, Y.L. Zhao, Z.F. Chai, W.Q. Shi, Quantum chemistry study of uranium(VI), neptunium(V), and plutonium(IV, VI) complexes with preorganized tetradentate phenanthrolineamide ligands, *Inorg. Chem.* 53 (2014) 10846–10853.
- [3] M.J. Hudson, L.M. Harwood, D.M. Laventine, F.W. Lewis, Use of soft heterocyclic N-donor ligands To separate actinides and lanthanides, *Inorg. Chem.* 52 (2013) 3414–3428.
- [4] J.O. Blomeke, A.G. Croff, Nuclear waste partitioning and transmutation, *Nucl. Technol.* 56 (1982) 361–371.
- [5] C. Xiao, A. Zhang, Z. Chai, Synthesis and characterization of novel macroporous silica-polymer-calixcrown hybrid supramolecular recognition materials for effective separation of cesium, *J. Hazard Mater.* 267 (2014) 109–118.
- [6] C.L. Xiao, A.Y. Zhang, Z.F. Chai, Synthesis and characterization of a novel organic-inorganic hybrid supramolecular recognition material and its selective adsorption for cesium, *J. Radioanal. Nucl. Chem.* 299 (2014) 699–708.
- [7] B.H. Gu, G.M. Brown, P.V. Bonnesen, L.Y. Liang, B.A. Moyer, R. Ober, et al., Development of novel bifunctional anion exchange resins with improved selectivity for pertechnetate sorption from contaminated groundwater, *Environ. Sci. Technol.* 34 (2000) 1075–1080.
- [8] P.V. Bonnesen, G.M. Brown, S.D. Alexandratos, L.B. Bavoux, D.J. Presley, V. Patel, et al., Development of bifunctional anion-exchange resins with improved selectivity and sorptive kinetics for pertechnetate: batch-equilibrium experiments, *Environ. Sci. Technol.* 34 (2000) 3761–3766.
- [9] D. Banerjee, A.J. Cairns, J. Liu, R.K. Motkuri, S.K. Nune, C.A. Fernandez, et al., Potential of metal-organic frameworks for separation of xenon and krypton, *Acc Chem. Res.* 48 (2015) 211–219.
- [10] B.J. Riley, J.D. Vienna, D.M. Strachan, J.S. McCloy, J.L. Jerden, Materials and processes for the effective capture and immobilization of radioiodine: a review, *J. Nucl. Mater.* 470 (2016) 307–326.
- [11] D. Banerjee, C.M. Simon, S.K. Elsaidi, M. Haranczyk, P.K. Thallapally, Xenon gas separation and storage using metal-organic frameworks, *Chem* 4 (2018) 466–494.
- [12] J.L.C. Rowsell, O.M. Yaghi, Metal-organic frameworks: a new class of porous materials, *Micropor. Mesopor. Mater.* 73 (2004) 3–14.
- [13] H. Furukawa, K.E. Cordova, M. O’Keeffe, O.M. Yaghi, The chemistry and applications of metal-organic frameworks, *Science* 341 (2013) 1230444.
- [14] H. Wang, W.P. Lustig, J. Li, Sensing and capture of toxic and hazardous gases and vapors by metal-organic frameworks, *Chem. Soc. Rev.* 47 (2018) 4729–4756.
- [15] J.R. Li, J. Sculley, H.C. Zhou, Metal-organic frameworks for separations, *Chem. Rev.* 112 (2012) 869–932.
- [16] S.T. Meeck, J.A. Greathouse, M.D. Allendorf, Metal-organic frameworks: a rapidly growing class of versatile nanoporous materials, *Adv. Mater.* 23 (2011) 249–267.
- [17] P. Kumar, A. Pournara, K.-H. Kim, V. Bansal, S. Rapti, M.J. Manos, Metal-organic frameworks: challenges and opportunities for ion-exchange/sorption applications, *Prog. Mater. Sci.* 86 (2017) 25–74.
- [18] E.A. Dolgoplova, A.M. Rice, N.B. Shustova, Actinide-based MOFs: a middle ground in solution and solid-state structural motifs, *Chem. Commun.* 54 (2018) 6472–6483.

- [19] J. Li, X. Wang, G. Zhao, C. Chen, Z. Chai, A. Alsaedi, et al., Metal-organic framework-based materials: superior adsorbents for the capture of toxic and radioactive metal ions, *Chem. Soc. Rev.* 47 (2018) 2322–2356.
- [20] M. Mon, R. Bruno, J. Ferrando-Soria, D. Armentano, E. Pardo, Metal-organic framework technologies for water remediation: towards a sustainable ecosystem, *J. Mater. Chem. A* 6 (2018) 4912–4947.
- [21] X. Liu, G.R. Chen, D.J. Lee, T. Kawamoto, H. Tanaka, M.L. Chen, et al., Adsorption removal of cesium from drinking waters: a mini review on use of biosorbents and other adsorbents, *Bioresour. Technol.* 160 (2014) 142–149.
- [22] M.A. Olatunji, M.U. Khandaker, H.N.M.E. Mahmud, Y.M. Amin, Influence of adsorption parameters on cesium uptake from aqueous solutions- a brief review, *RSC Adv.* 5 (2015) 71658–71683.
- [23] Y.L. Wang, Z.Y. Liu, Y.X. Li, Z.L. Bai, W. Liu, Y.X. Wang, et al., Umbellate distortions of the uranyl coordination environment result in a stable and porous polycatenated framework that can effectively remove cesium from aqueous solutions, *J. Am. Chem. Soc.* 137 (2015) 6144–6147.
- [24] B. Aguila, D. Banerjee, Z. Nie, Y. Shin, S. Ma, P.K. Thallapally, Selective removal of cesium and strontium using porous frameworks from high level nuclear waste, *Chem. Commun.* 52 (2016) 5940–5942.
- [25] S. Naeimi, H. Faghihian, Performance of novel adsorbent prepared by magnetic metal-organic framework (MOF) modified by potassium nickel hexacyanoferrate for removal of Cs^+ from aqueous solution, *Sep. Purif. Technol.* 175 (2017) 255–265.
- [26] Y. Yue, R.T. Mayes, J. Kim, P.F. Fulvio, X.G. Sun, C. Tsouris, et al., Seawater uranium sorbents: preparation from a mesoporous copolymer initiator by atom-transfer radical polymerization, *Angew. Chem.* 52 (2013) 13458–13462.
- [27] L. Zhou, M. Bosscher, C. Zhang, S. Ozcubukcu, L. Zhang, W. Zhang, et al., A protein engineered to bind uranyl selectively and with femtomolar affinity, *Nat. Chem.* 6 (2014) 236–241.
- [28] M. Carboni, C.W. Abney, S. Liu, W. Lin, Highly porous and stable metal-organic frameworks for uranium extraction, *Chem. Sci.* 4 (2013) 2396.
- [29] J. De Decker, K. Folens, J. De Clercq, M. Meledina, G. Van Tendeloo, G. Du Laing, et al., Ship-in-a-bottle CMPO in MIL-101(Cr) for selective uranium recovery from aqueous streams through adsorption, *J. Hazard Mater.* 335 (2017) 1–9.
- [30] J. De Decker, J. Rochette, J. De Clercq, J. Florek, P. Van Der Voort, Carbamoylmethylphosphine oxide-functionalized MIL-101(Cr) as highly selective uranium adsorbent, *Anal. Chem.* 89 (2017) 5678–5682.
- [31] L. Chen, Z. Bai, L. Zhu, L. Zhang, Y. Cai, Y. Li, et al., Ultrafast and efficient extraction of uranium from seawater using an amidoxime appended metal-organic framework, *ACS Appl. Mater. Interf.* 9 (2017) 32446–32451.
- [32] J.Y. Zhang, N. Zhang, L. Zhang, Y. Fang, W. Deng, M. Yu, et al., Adsorption of uranyl ions on amine-functionalization of MIL-101(Cr) nanoparticles by a facile coordination-based post-synthetic strategy and X-ray absorption spectroscopy studies, *Sci. Rep.* 5 (2015) 13514.
- [33] L. Li, W. Ma, S. Shen, H. Huang, Y. Bai, H. Liu, A combined experimental and theoretical study on the extraction of uranium by amino-derived metal-organic frameworks through post-synthetic strategy, *ACS Appl. Mater. Interf.* 8 (2016) 31032–31041.
- [34] Z.-Q. Bai, L.-Y. Yuan, L. Zhu, Z.-R. Liu, S.-Q. Chu, L.-R. Zheng, et al., Introduction of amino groups into acid-resistant MOFs for enhanced U(VI) sorption, *J. Mater. Chem. A* 3 (2015) 525–534.

- [35] L. Zhang, L.L. Wang, L. Gong, X.F. Feng, M.B. Luo, F. Luo, Coumarin-modified microporous-mesoporous Zn-MOF-74 showing ultra-high uptake capacity and photo-switched storage/release of U(VI) ions, *J. Hazard Mater.* 311 (2016) 30–36.
- [36] B.-C. Luo, L.-Y. Yuan, Z.-F. Chai, W.-Q. Shi, Q. Tang, U(VI) capture from aqueous solution by highly porous and stable MOFs: UiO-66 and its amine derivative, *J. Radioanal. Nucl. Chem.* 307 (2015) 269–276.
- [37] L.L. Wang, F. Luo, L.L. Dang, J.Q. Li, X.L. Wu, S.J. Liu, et al., Ultrafast high-performance extraction of uranium from seawater without pretreatment using an acylamide- and carboxyl-functionalized metal-organic framework, *J. Mater. Chem. A* 3 (2015) 13724–13730.
- [38] W. Yang, Z.Q. Bai, W.Q. Shi, L.Y. Yuan, T. Tian, Z.F. Chai, et al., MOF-76: from a luminescent probe to highly efficient U(VI) sorption material, *Chem. Commun.* 49 (2013) 10415–10417.
- [39] Y. Feng, H. Jiang, S. Li, J. Wang, X. Jing, Y. Wang, et al., Metal-organic frameworks HKUST-1 for liquid-phase adsorption of uranium, *Colloids Surfaces A* 431 (2013) 87–92.
- [40] L. Yuan, M. Tian, J. Lan, X. Cao, X. Wang, Z. Chai, et al., Defect engineering in metal-organic frameworks: a new strategy to develop applicable actinide sorbents, *Chem. Commun.* 54 (2018) 370–373.
- [41] T. Zheng, Z. Yang, D. Gui, Z. Liu, X. Wang, X. Dai, et al., Overcoming the crystallization and designability issues in the ultrastable zirconium phosphonate framework system, *Nat. Commun.* 8 (2017) 15369.
- [42] W. Liu, X. Dai, Z. Bai, Y. Wang, Z. Yang, L. Zhang, et al., Highly sensitive and selective uranium detection in natural water systems using a luminescent mesoporous metal-organic framework equipped with abundant Lewis basic sites: a combined batch, X-ray absorption spectroscopy, and first principles simulation investigation, *Environ. Sci. Technol.* 51 (2017) 3911–3921.
- [43] J. Ye, R.F. Bogale, Y. Shi, Y. Chen, X. Liu, S. Zhang, et al., A water-stable dual-channel luminescence sensor for UO_2^{2+} ions based on an anionic terbium(III) metal-organic framework, *Chem. Eur. J.* 23 (2017) 7657–7662.
- [44] W.-M. Chen, X.-L. Meng, G.-L. Zhuang, Z. Wang, M. Kurmoo, Q.-Q. Zhao, et al., A superior fluorescent sensor for Al^{3+} and UO_2^{2+} based on a Co(II) metal-organic framework with exposed pyrimidyl Lewis base sites, *J. Mater. Chem. A* 5 (2017) 13079–13085.
- [45] N. Zhang, L.Y. Yuan, W.L. Guo, S.Z. Luo, Z.F. Chai, W.Q. Shi, Extending the use of highly porous and functionalized MOFs to Th(IV) capture, *ACS Appl. Mater. Interf.* 9 (2017) 25216–25224.
- [46] Z.S. Moghaddam, M. Kaykhaii, M. Khajeh, A.R. Oveisi, Synthesis of UiO-66-OH zirconium metal-organic framework and its application for selective extraction and trace determination of thorium in water samples by spectrophotometry, *Spectrochim. Acta A Mol. Biomol. Spectrosc.* 194 (2018) 76–82.
- [47] X.G. Guo, S. Qiu, X. Chen, Y. Gong, X. Sun, Postsynthesis modification of a metallosalen-containing metal-organic framework for selective Th(IV)/Ln(III) separation, *Inorg. Chem.* 56 (2017) 12357–12361.
- [48] D. Banerjee, D. Kim, M.J. Schweiger, A.A. Kruger, P.K. Thallapally, Removal of TeO_4^- ions from solution: materials and future outlook, *Chem. Soc. Rev.* 45 (2016) 2724–2739.
- [49] A.J. Howarth, Y. Liu, J.T. Hupp, O.K. Farha, Metal-organic frameworks for applications in remediation of oxyanion/cation-contaminated water, *CrystEngComm* 17 (2015) 7245–7253.

- [50] A.J. Howarth, M.J. Katz, T.C. Wang, A.E. Platero-Prats, K.W. Chapman, J.T. Hupp, et al., High efficiency adsorption and removal of selenate and selenite from water using metal-organic frameworks, *J. Am. Chem. Soc.* 137 (2015) 7488–7494.
- [51] J. Li, Y. Liu, X. Wang, G. Zhao, Y. Ai, B. Han, et al., Experimental and theoretical study on selenate uptake to zirconium metal-organic frameworks: effect of defects and ligands, *Chem. Eng. J.* 330 (2017) 1012–1021.
- [52] J. Wei, W. Zhang, W. Pan, C. Li, W. Sun, Experimental and theoretical investigations on Se(IV) and Se(VI) adsorption to UiO-66-based metal-organic frameworks, *Environ. Sci. Nano* 5 (2018) 1441–1453.
- [53] H. Fei, M.R. Bresler, S.R. Oliver, A new paradigm for anion trapping in high capacity and selectivity: crystal-to-crystal transformation of cationic materials, *J. Am. Chem. Soc.* 133 (2011) 11110–11113.
- [54] D. Banerjee, W. Xu, Z. Nie, L.E. Johnson, C. Coglan, M.L. Sushko, et al., Zirconium-based metal-organic framework for removal of perchlorate from water, *Inorg. Chem.* 55 (2016) 8241–8243.
- [55] D. Sheng, L. Zhu, C. Xu, C. Xiao, Y. Wang, Y. Wang, et al., Efficient and selective uptake of TcO_4^- by a cationic metal-organic framework material with open Ag^+ sites, *Environ. Sci. Technol.* 51 (2017) 3471–3479.
- [56] L. Zhu, D. Sheng, C. Xu, X. Dai, M.A. Silver, J. Li, et al., Identifying the recognition site for selective trapping of $^{99}\text{TcO}_4^-$ in a hydrolytically stable and radiation resistant cationic metal-organic framework, *J. Am. Chem. Soc.* 139 (2017) 14873–14876.
- [57] L. Zhu, C. Xiao, X. Dai, J. Li, D. Gui, D. Sheng, et al., Exceptional perchlorate/pertechnetate uptake and subsequent immobilization by a low-dimensional cationic coordination polymer: overcoming the Hofmeister bias selectivity, *Environ. Sci. Technol. Lett.* 4 (2017) 316–322.
- [58] Z. Bai, Y. Wang, Y. Li, W. Liu, L. Chen, D. Sheng, et al., First cationic uranyl-organic framework with anion-exchange capabilities, *Inorg. Chem.* 55 (2016) 6358–6360.
- [59] Y. Li, Z. Yang, Y. Wang, Z. Bai, T. Zheng, X. Dai, et al., A mesoporous cationic thorium-organic framework that rapidly traps anionic persistent organic pollutants, *Nat. Commun.* 8 (2017) 1354.
- [60] R.J. Drout, K. Otake, A.J. Howarth, T. Islamoglu, L. Zhu, C. Xiao, et al., Efficient capture of perchlorate and pertechnetate by a mesoporous Zr metal-organic framework and examination of anion binding motifs, *Chem. Mater.* 30 (2018) 1277–1284.
- [61] S.U. Nandanwar, K. Coldsnow, V. Utgikar, P. Sabharwall, D. Eric Aston, Capture of harmful radioactive contaminants from off-gas stream using porous solid sorbents for clean environment—a review, *Chem. Eng. J.* 306 (2016) 369–381.
- [62] H. Sun, P. La, Z. Zhu, W. Liang, B. Yang, A. Li, Capture and reversible storage of volatile iodine by porous carbon with high capacity, *J. Mater. Sci.* 50 (2015) 7326–7332.
- [63] P. Cui, L. Ren, Z. Chen, H. Hu, B. Zhao, W. Shi, et al., Temperature-controlled chiral and achiral copper tetrazolate metal-organic frameworks: syntheses, structures, and I_2 adsorption, *Inorg. Chem.* 51 (2012) 2303–2310.
- [64] C. Falaise, C. Volkringer, J. Facqueur, T. Bousquet, L. Gasnot, T. Loiseau, Capture of iodine in highly stable metal-organic frameworks: a systematic study, *Chem. Commun.* 49 (2013) 10320–10322.
- [65] X.-L. Hu, F.-H. Liu, H.-N. Wang, C. Qin, C.-Y. Sun, Z.-M. Su, et al., Controllable synthesis of isoreticular pillared-layer MOFs: gas adsorption, iodine sorption and sensing small molecules, *J. Mater. Chem. A* 2 (2014) 14827–14834.

- [66] T. Kojima, W. Choi, M. Kawano, Single-crystal growth of coordination networks via the gas phase and dependence of iodine encapsulation on the crystal size, *Chem. Commun.* 50 (2014) 13793–13796.
- [67] J. Wang, J. Luo, X. Luo, J. Zhao, D.-S. Li, G. Li, et al., Assembly of a three-dimensional metal-organic framework with copper(I) iodide and 4-(pyrimidin-5-yl) benzoic acid: controlled uptake and release of iodine, *Cryst. Growth Des.* 15 (2015) 915–920.
- [68] Z.Q. Jiang, F. Wang, J. Zhang, Adsorption of iodine based on a tetrazolate framework with microporous cages and mesoporous cages, *Inorg. Chem.* 55 (2016) 13035–13038.
- [69] M.H. Zeng, Q.X. Wang, Y.X. Tan, S. Hu, H.X. Zhao, L.S. Long, et al., Rigid pillars and double walls in a porous metal-organic framework: single-crystal to single-crystal, controlled uptake and release of iodine and electrical conductivity, *J. Am. Chem. Soc.* 132 (2010) 2561–2563.
- [70] D.F. Sava, M.A. Rodriguez, K.W. Chapman, P.J. Chupas, J.A. Greathouse, P.S. Crozier, et al., Capture of volatile iodine, a gaseous fission product, by zeolitic imidazolate framework-8, *J. Am. Chem. Soc.* 133 (2011) 12398–12401.
- [71] J.T. Hughes, D.F. Sava, T.M. Nenoff, A. Navrotsky, Thermochemical evidence for strong iodine chemisorption by ZIF-8, *J. Am. Chem. Soc.* 135 (2013) 16256–16259.
- [72] D.F. Sava, K.W. Chapman, M.A. Rodriguez, J.A. Greathouse, P.S. Crozier, H. Zhao, et al., Competitive I₂ sorption by Cu-BTC from humid gas streams, *Chem. Mater.* 25 (2013) 2591–2596.
- [73] G. Massasso, J. Long, J. Haines, S. Devautour-Vinot, G. Maurin, A. Grandjean, et al., Iodine capture by Hofmann-type clathrate Ni(II)(pz)[Ni(II)(CN)₄], *Inorg. Chem.* 53 (2014) 4269–4271.
- [74] X.M. Zhang, C.W. Zhao, J.P. Ma, Y. Yu, Q.K. Liu, Y.B. Dong, A Ni(II)-MOF: reversible guest adsorption and heterogeneous catalytic properties for silylcyanation of aromatic aldehydes, *Chem. Commun.* 51 (2015) 839–842.
- [75] B. Li, X. Dong, H. Wang, D. Ma, K. Tan, S. Jensen, et al., Capture of organic iodides from nuclear waste by metal-organic framework-based molecular traps, *Nat. Commun.* 8 (2017) 485.
- [76] B. Li, X. Dong, H. Wang, D. Ma, K. Tan, Z. Shi, et al., Functionalized metal organic frameworks for effective capture of radioactive organic iodides, *Faraday Discuss* 201 (2017) 47–61.
- [77] L. Chen, P.S. Reiss, S.Y. Chong, D. Holden, K.E. Jelfs, T. Hasell, et al., Separation of rare gases and chiral molecules by selective binding in porous organic cages, *Nat. Mater.* 13 (2014) 954–960.
- [78] P.K. Thallapally, J.W. Grate, R.K. Motkuri, Facile xenon capture and release at room temperature using a metal-organic framework: a comparison with activated charcoal, *Chem. Commun.* 48 (2012) 347–349.
- [79] Y.-S. Bae, B.G. Hauser, Y.J. Colón, J.T. Hupp, O.K. Farha, R.Q. Snurr, High xenon/krypton selectivity in a metal-organic framework with small pores and strong adsorption sites, *Micropor. Mesopor. Mater.* 169 (2013) 176–179.
- [80] J. Liu, C.A. Fernandez, P.F. Martin, P.K. Thallapally, D.M. Strachan, A Two-column method for the separation of Kr and Xe from process off-gases, *Ind. Eng. Chem. Res.* 53 (2014) 12893–12899.
- [81] J. Liu, D.M. Strachan, P.K. Thallapally, Enhanced noble gas adsorption in Ag@MOF-74Ni, *Chem. Commun.* 50 (2014) 466–468.
- [82] J.J. Perry, S.L. Teich-McGoldrick, S.T. Meek, J.A. Greathouse, M. Haranczyk, M.D. Allendorf, Noble Gas Adsorption in metal-organic frameworks containing open metal sites, *J. Phys. Chem. C* 118 (2014) 11685–11698.

- [83] H. Wang, K. Yao, Z. Zhang, J. Jagiello, Q. Gong, Y. Han, et al., The first example of commensurate adsorption of atomic gas in a MOF and effective separation of xenon from other noble gases, *Chem. Sci.* 5 (2014) 620–624.
- [84] X. Chen, A.M. Plonka, D. Banerjee, R. Krishna, H.T. Schaef, S. Ghose, et al., Direct observation of Xe and Kr adsorption in a Xe-selective microporous metal-organic framework, *J. Am. Chem. Soc.* 137 (2015) 7007–7010.
- [85] O.V. Magdysyuk, D. Denysenko, I. Weinrauch, D. Volkmer, M. Hirscher, R.E. Dinnebier, Formation of a quasi-solid structure by intercalated noble gas atoms in pores of Cu(I)-MFU-4l metal-organic framework, *Chem. Commun.* 51 (2015) 714–717.
- [86] D. Banerjee, S.K. Elsaidi, P.K. Thallapally, Xe adsorption and separation properties of a series of microporous metal–organic frameworks (MOFs) with V-shaped linkers, *J. Mater. Chem. A* 5 (2017) 16611–16615.
- [87] S.K. Elsaidi, M.H. Mohamed, C.M. Simon, E. Braun, T. Pham, K.A. Forrest, et al., Effect of ring rotation upon gas adsorption in SIFSIX-3-M (M = Fe, Ni) pillared square grid networks, *Chem. Sci.* 8 (2017) 2373–2380.
- [88] S.K. Elsaidi, D. Ongari, W. Xu, M.H. Mohamed, M. Haranczyk, P.K. Thallapally, Xenon recovery at room temperature using metal-organic frameworks, *Chem. Eur. J.* 23 (2017) 10758–10762.
- [89] H. Wang, J. Li, General strategies for effective capture and separation of noble gases by metal-organic frameworks, *Dalton Trans.* 47 (2018) 4027–4031.
- [90] Y. Wang, W. Liu, Z. Bai, T. Zheng, M.A. Silver, Y. Li, et al., Employing an unsaturated Th⁴⁺ site in a porous thorium-organic framework for Kr/Xe uptake and separation, *Angew. Chem.* 57 (2018) 5783–5787.
- [91] S. Xiong, Q. Liu, Q. Wang, W. Li, Y. Tang, X. Wang, et al., A flexible zinc tetrazolate framework exhibiting breathing behaviour on xenon adsorption and selective adsorption of xenon over other noble gases, *J. Mater. Chem. A* 3 (2015) 10747–10752.
- [92] M.H. Mohamed, S.K. Elsaidi, T. Pham, K.A. Forrest, H.T. Schaef, A. Hogan, et al., Hybrid ultra-microporous materials for selective xenon adsorption and separation, *Angew. Chem.* 55 (2016) 8285–8289.
- [93] D. Banerjee, C.M. Simon, A.M. Plonka, R.K. Motkuri, J. Liu, X. Chen, et al., Metal-organic framework with optimally selective xenon adsorption and separation, *Nat. Commun.* 7 (2016) (ncomms11831).
- [94] B.J. Sikora, C.E. Wilmer, M.L. Greenfield, R.Q. Snurr, Thermodynamic analysis of Xe/Kr selectivity in over 137 000 hypothetical metal–organic frameworks, *Chem. Sci.* 3 (2012) 2217.
- [95] Y. Gurdal, S. Keskin, Predicting noble gas separation performance of metal organic frameworks using theoretical correlations, *J. Phy. Chem. C* 117 (2013) 5229–5241.
- [96] B. Assfour, T. Assaad, A. Odeh, In silico screening of metal organic framework for iodine capture and storage, *Chem. Phys. Lett.* 610–611 (2014) 45–49.
- [97] C.M. Simon, R. Mercado, S.K. Schnell, B. Smit, M. Haranczyk, What are the best materials to separate a xenon/krypton mixture? *Chem. Mater.* 27 (2015) 4459–4475.
- [98] X. Min, W. Yang, Y.F. Hui, C.Y. Gao, S. Dang, Z.M. Sun, Fe₃O₄@ZIF-8: a magnetic nanocomposite for highly efficient UO₂²⁺ adsorption and selective UO₂²⁺/Ln³⁺ separation, *Chem. Commun.* 53 (2017) 4199–4202.
- [99] T. Wu, X. Feng, S.K. Elsaidi, P.K. Thallapally, M.A. Carreon, Zeolitic imidazolate framework-8 (ZIF-8) membranes for Kr/Xe separation, *Ind. Eng. Chem. Res.* 56 (2017) 1682–1686.

MOF-based devices for detection and removal of environmental pollutants

12

Raffaele Ricco^{1,*}, Mark J. Styles² and Paolo Falcaro¹

¹Institute of Physical and Theoretical Chemistry, Graz University of Technology, Graz, Austria, ²CSIRO Manufacturing, Clayton South, VIC, Australia

*Corresponding author. e-mail address: raffaele.ricco@tugraz.at

12.1 Introduction

Metal-organic frameworks (MOFs) are emerging materials with great potential for environmental remediation. There is an ongoing development focused on the development and fabrication of practical devices exploiting the unique properties of MOFs for the detection and control of environmental pollution. To highlight the importance of this field of research, an analysis of the publication trends related to MOF-based devices for environmental applications over the past decade (2008—18) is reported in Fig. 12.1. Over this period, the number of MOF related studies has increased from about 500 in 2007 up to about 4000 in 2017 (dark gray bars); in the same timeframe, the number of studies on MOF-based devices followed a similar trend (blue bars). As a subset, MOF-based devices for environmental applications (red bars) are increasing as the number of protocols suitable for device fabrication continues to grow [1]. Furthermore, pollution is a global challenge that seems to be intensifying over time [2]; this adds impetus to the technological progress in decontamination and potentially provides commercial opportunities for MOFs to help mitigate anthropogenic environmental changes.

This chapter is organized into three parts: the classification of MOF-based devices designed for pollution remediation and control (Section 12.2); the description of sensors in which MOFs, as the active material, are devoted to the sensing of different types of noxious substances such as gases, volatile organic compounds (VOCs), and species present in the aqueous environment (Section 12.3); and the identification of different devices suitable for the removal of pollutants from a wide variety of solid, liquid, and gaseous sources (Section 12.4). As the properties of MOF-based devices can depend on different variables, such as the type of MOF, the synthetic conditions, and the positioning protocols [1], in this chapter we specify the fabrication methodology and related preparation conditions when considered relevant for the preparation of the MOF-based devices for environmental remediation.

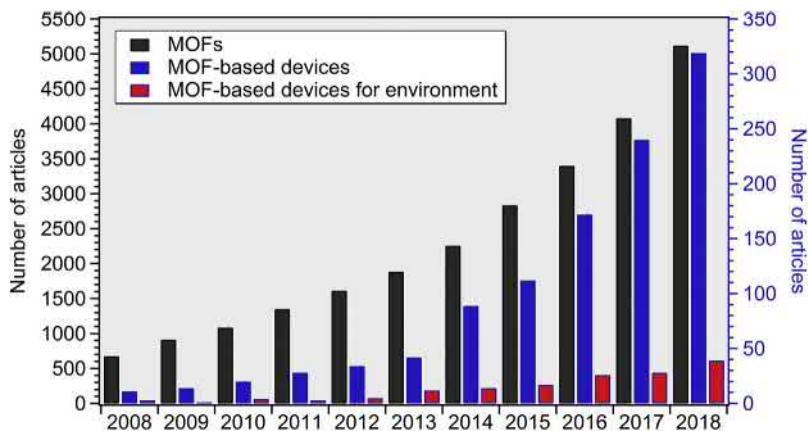


Figure 12.1 Evolution of the number of papers related to metal-organic frameworks (MOFs, black columns and left Y-axis), MOF-based devices (blue columns and right Y-axis), and MOF-based devices for environmental applications (red columns and right Y-axis).

Source: Scopus. Analysis conducted in March 2019, using the following keywords: “*metal AND organic AND framework**” (dark gray), “*metal AND organic AND framework* AND device**” (blue), “*metal AND organic AND framework* AND device* AND (pollut* OR environment*)*” (red).

Different criteria can be used for the classification of MOF-based devices; these can include the chemical composition of the MOF (e.g., type of cations, ligand), the MOF structure (e.g., topology or porosity) or the application of the final device (sensor or removal devices). As shown in Fig. 12.2, one section is dedicated to *sensing devices* (Section 12.3), and another section is focused on *removal devices* (Section 12.4).

12.2 Classification of metal-organic framework–based devices for sensing

For the classification of MOF-based sensing devices, we have identified three major principles used to detect and/or measure the presence of specific environmental pollutants: (1) variations in mechanical response; (2) variations in optical properties; and (3) variations in electrochemical properties [3]. Within the first category, quartz crystal microbalance (QCM) and systems based on surface acoustic wave (SAW) technology can be considered the main methodologies used to measure the variation of a mechanical stress. Within the second category of MOF-based devices, variations in optical properties refer to spectroscopic measurements of features such as electronic transitions, fluorescence, phosphorescence, and refractive index. Finally, electrochemical-based devices mostly focus on changes in the conductive properties; examples are amperometric or impedance variations.

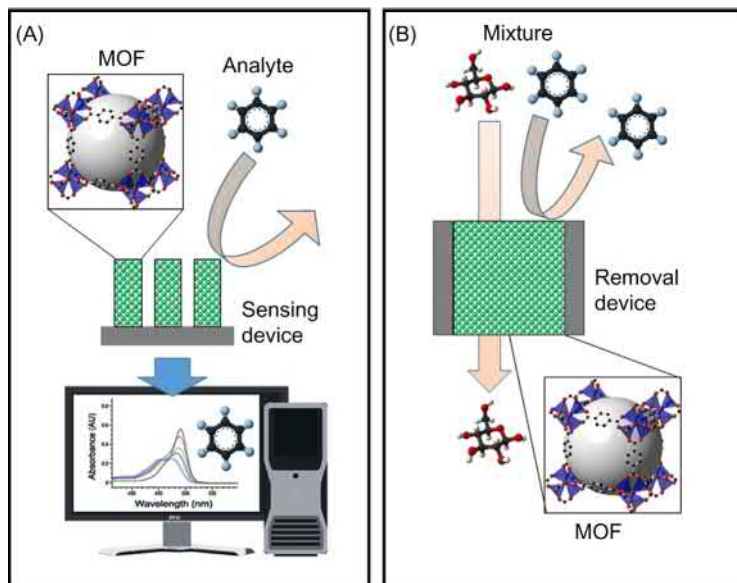


Figure 12.2 (A) The concept of using MOFs for sensors: the device uses the MOF as an active material to retain the analyte, due to the interaction with the cavity. The device then detects the presence of the analyte via different responses (mechanochemical, electrical, optical) and the generated signal is then read. (B) The concept of using MOFs as a removal device: the device uses the MOF as an active material to separate different compounds from a mixture thanks to the size exclusion mechanism and the interaction with the pores.

12.2.1 Mechanochemical response

The selective absorption of analytes results in a change of mass and this variation can be promptly detected. Promising sensors falling into this category are based on SAW [4–7] or QCM [8–11] systems. Although SAW sensors have been developed using a variety of materials, such as metal oxides [12,13], carbon-based nanostructures [14,15], and polymers [16,17], only a few works have been published using MOFs for environmental control. In 2012, a pioneering computational work by Allendorf's group [18] revealed the potential of PCN-14 [19] for methane sensing. An experimental evidence that MOFs could be used in SAW devices was reported during the same year; $\text{Cu}_3(\text{BTC})_2$ MOF (a.k.a. HKUST-1) was exploited for the ultrasensitive detection of humidity [20]. This proof-of-concept was then adopted for the detection of other analytes. For example, in 2017 Paschke et al. [21] selected MOFs constructed from benzobistriazole ligands, named MFU-4 [22] and MFU-4L [23], were used as active sensing materials. The MOF thin films were directly grown on LiNbO_3 SAW chips via a solvothermal method; a miniaturized plasma desorption mass spectrometry reaction chamber was fabricated to limit the MOF growth in the desired area, producing a uniform 200-nm-thick coverage. Phase shifts were induced by the mass change, with the largest positive shift for

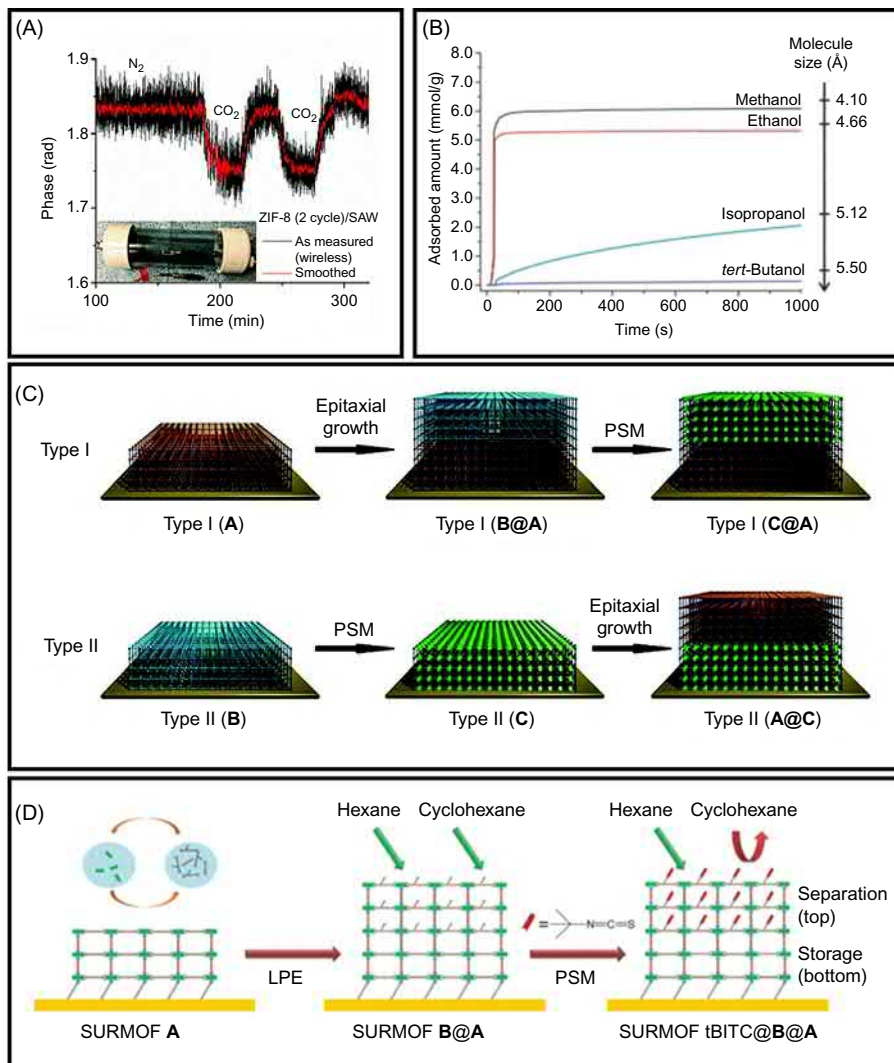


Figure 12.3 (A) Real-time wireless phase measurement of a two-cycle film-coated surface acoustic wave (SAW) sensor for pure carbon dioxide (flow of 70 L min⁻¹), performed using a commercial whip antenna (inset). (B) The graph shows a time-dependent mass uptake of size-increasing alcohols by a film of [Zn₄O(dmcapz)₃]_n MOF. The analysis was conducted at 20°C and a relative humidity (RH) of 85%. (C) This scheme reports three different types of heterostructured-MOFs films, with **A**: [Cu₂(ndc)₂(dabco)], **B**: [Cu₂(NH₂-bdc)₂(dabco)], and **C**: [Cu₂(HOOC(CH₂)₂OCNH-bdc)₂(dabco)]. PSM refers to the postsynthetic modification of the amino groups in MOF **B** with succinic anhydride. (D) The illustration schematizes the programmed functionalization of SURMOFs via liquid phase heteroepitaxial (LPE) growth and postsynthetic modification (PSM): initially [Cu₂(bdc)₂(dabco)] (**A**) was deposited on pyridyl-terminated self-assembled monolayers on Au covered QCM. [Cu₂(NH₂-bdc)₂(dabco)] (**B@A**) was then deposited on top of **A** via LPE. Finally, PSM was performed on **B@A** to yield SURMOF **1B1TC@B@A**, where the top layer is separated and the bottom layer is stored.

carbon dioxide, a little positive shift for argon, a little negative shift for helium and hydrogen, and the largest negative shift for methane. For helium and hydrogen, the sensitivity was limited. However, these results indicated the possibility to discriminate between gases. Importantly, the device was still operative 2 years after fabrication; this demonstration of high stability suggests that MOFs combined with SAW technology can be used for practical applications. In a recent work (2018), Devkota et al. [24] used MOF-based SAW systems for the detection of carbon dioxide and methane. The authors employed the Zeolitic Imidazolate Framework 8, also known as ZIF-8, made of zinc(II) nodes and 2-methylimidazolate ligands. It is worth mentioning that this porous framework has a good stability to atmospheric conditions and several protocols are available for its deposition [1,25,26]. Y-LiNbO₃ piezoelectric crystals were coated by one to three dipping cycles of ZIF-8 layers, obtaining films with thickness between 100 and 300 nm (Fig. 12.3A). QCM systems were also investigated. This sensor demonstrated selectivity toward carbon dioxide and methane over carbon monoxide and hydrogen, and higher sensitivity for carbon dioxide than methane (about two orders of magnitude difference). These MOFs (i.e., MFU-4 and ZIF-8) were selected because of their structural and chemical robustness, along with thermal resistance (up to 500°C in inert atmospheres), small pore aperture (e.g., 2.5 Å for MFU-4), and high surface area (above 1000 m² g⁻¹).

In the case of QCM-based sensors, the groups of Allendorf and Fischer have made substantial progress in the fabrication and application of MOFs for the detection of gaseous and VOCs pollutants. In 2008 Allendorf and coworkers demonstrated the possibility of chemical detection by measuring the stress in HKUST-1 [30]. An array of 10 gold-coated microcantilevers, each incorporating a built-in piezometric sensor, was used as a sensing platform. The cantilevers produced a signal in response to a change in stress. For the deposition of HKUST-1 coatings, the cantilevers were consecutively immersed in separate solutions of copper(II) acetate and trimesic acid, for 20 cycles using the so-called layer-by-layer (LbL) approach [1]. After synthesis, the coordination sites of HKUST-1 were occupied by water; by heating the device with a warm (50°C) flow of nitrogen the authors measured the response of the cantilever in hydrated and dehydrated states; the change in hydration was also accompanied by a change in the MOF color from blue to purple. The

◀ (B) was deposited on A using the LPE procedure giving rise to SURMOF B@A. The final PSM of SURMOF B@A was conducted with *tert*-butyl isothiocyanate (tBITC).

Source: (A) Adapted from J. Devkota, et al., Zeolitic imidazolate framework-coated acoustic sensors for room temperature detection of carbon dioxide and methane. *Nanoscale* 10 (2018) 8075–8087; (B) A. Bétard, S. Wannapaiboon, R.A. Fischer, Assessing the adsorption selectivity of linker functionalized, moisture-stable metal-organic framework thin films by means of an environment-controlled quartz crystal microbalance. *Chem. Commun.* 48 (2012) 10493; (C) M. Tu, S. Wannapaiboon, R.A. Fischer, Liquid phase stepwise growth of surface mounted metal-organic frameworks for exploratory research and development of applications. *Inorg. Chem. Front.* 1 (2014) 442; (D) M. Tu, S. Wannapaiboon, R.A. Fischer, Programmed functionalization of SURMOFs via liquid phase heteroepitaxial growth and post-synthetic modification. *Dalton Trans.* 42 (2013) 16029 with permission from The Royal Society of Chemistry.

sensor was found to respond rapidly (e.g., within 1 minute), even in the presence of low amounts of water vapor (0.18% mol.); the sensitivity was found to be higher for methane and ethanol vapors than to nitrogen and oxygen. Interestingly, when the MOF was in the dehydrated state, a high selectivity toward carbon dioxide was measured. This selectivity was explained by a weaker stress response when the axial copper sites coordinate carbon dioxide instead of water.

In other studies conducted between 2010 and 2012, guidelines were provided for the further design of MOF-coated microcantilever systems for chemical recognition of gases [31–33]. The authors optimized the sensor fabrication procedures and, through a detailed computational analysis, demonstrated that the sensing response improves with the increase in Young's modulus and Poisson's ratio of the MOF [33], although the former has the greatest effect. Interestingly, the homogeneity of the MOF layer had a negligible effect on the response. In 2013 two other studies from Allendorf's team were dedicated to VOC sensing using piezoresistive microcantilevers. HKUST-1 was used to sense methanol, isopropanol, and acetone vapors [34]. Based on response time, it was possible to discriminate the different analytes. Subsequently, the sensing properties for chloroform and toluene detection were investigated [35]. The molecular sieve properties of HKUST-1 were used to discriminate molecules based on their size. The stable sensing performance was measured up to 18 months.

In 2012 Fisher's group used a film of $\text{Zn}_4\text{O}(\text{dmcapz})_3$ (dmcapz = 3,5-dimethyl-4-carboxypyrazolate ligand) on QCM for the detection of different VOCs [27]. A set of simple alcohols with increased molecular sizes was tested (i.e., methanol, ethanol, isopropanol, and *tert*-butanol). From the uptake curves, the molecular size selectivity of the MOF was demonstrated: $\text{Zn}_4\text{O}(\text{dmcapz})_3$ was able to uptake both methanol and ethanol within seconds; the curve collected for isopropanol showed a slower uptake, while *tert*-butanol was too bulky to be adsorbed (Fig. 12.3B). Subsequently, molecules with similar size to the MOF pore cavities (toluene and aniline) were tested, and the highest affinity was measured for the nonpolar toluene over the polar aniline as the MOF used was hydrophobic. Finally, another significant difference was observed in the size distinction between *para*- and *ortho*-xylene due to the different steric hindrance. In 2013 the SURMOF (surface mounted MOF, Fig. 12.3C) [28,36] technique was applied on a QCM using $\text{Cu}_2(\text{NH}_2\text{BDC})_2\text{dabco}$ as the LbL deposited MOF (Fig. 12.3D) [29]. In this case, the self-assembled monolayer (SAM) used as a promoting layer [37] to grow the MOF on Cu was pyridyl terminated; this allowed for an improved affinity between the substrate and the MOF grown during 20 LbL cycles. The SURMOF was postfunctionalized with *tert*-butyl isothiocyanate, to increase the size selectivity. Indeed, the presence of this bulky moiety prevented the sorption of cyclohexane vapors and permitted the absorption of *n*-hexane. In the absence of *tert*-butyl isothiocyanate functionalization both VOCs could be indiscriminately harvested. In 2014 a similar study used a dual layer of MOF (i.e., HKUST-1 on $\text{Cu}_2(\text{ndc})_2\text{dabco}$) as an active porous material for QCM mass measurements [38]. A total of 40 LbL cycles were performed, 20 for each type of MOF. The uptake of 1,3,5-trimethylbenzene and 1,3,5-triisopropylbenzene (TIPB) was evaluated; the first VOC was appreciably collected by films made

with HKUST-1 on $\text{Cu}_2(\text{ndc})_2\text{dabco}$ or a combination of both. TIPB could interact only with $\text{Cu}_2(\text{ndc})_2\text{dabco}$, because the other two systems had pores too small for its efficient detection. In 2015 further research on VOC detection via QCM by the same group was dedicated to ZIFs [39]. In this case the LbL thin-film fabrication of MOF was performed on silica-coated (50 nm) silicon wafers and commercial silica-coated QCM substrates. Depositions of metal and linkers, as well as the methanol sensing, were performed using an automatic programmable dosing system. 30 LbL cycles were used to produce the MOF coating. The detection of the alcohol series from methanol to hexanol was evaluated with six ZIFs having sodalite-type (*sod*) topology:¹ ZIF-8 and ZIF-67 (with cobalt and 2-methylimidazole), ZIF-7 and ZIF-9 (with zinc or cobalt and benzimidazole), ZIF-65 and ZIF-90 (with 2-nitroimidazole or 2-imidazolecarboxaldehyde and zinc). The ZIFs on QCM hybrid devices exhibited different selective sensing performances due to the properties of the different MOFs (i.e., difference in surface hydrophobicity and flexibility) and the different physical properties of the analytes. The selective sorption properties toward hydrocarbons such as benzene, toluene, ethylbenzene, xylene isomers, and hexane isomers revealed that different ZIFs on QCM devices could be used for real applications in biofuel recovery and separation of isomers.

In 2011 Kitagawa's group identified a different strategy for QCM-based detection [40]. Two approaches were used to deposit HKUST-1 crystals on Au-coated QCM substrates. A stable mother liquor of copper acetate and trimesic acid with dodecanoic acid in butanol as a modulator was used to grow MOFs via a "slow nucleation" process. Upon ethanol addition (dilution factor = 1), in 12 hours large HKUST-1 crystals (c. 600 nm) were grown on the substrate. Higher amounts of ethanol (dilution factor = 8) produced smaller crystals (c. 130 nm) within 1 hour. Prolonged growth time (up to 6 hours) enlarged the crystal size. The films were tested for the detection of methanol and hexane as VOCs; smaller crystals resulted in a faster sensor response for low concentrations of analyte.

12.2.2 Optical response

In 2010 Kreno and coworkers developed a MOF thin film for sensing gases using surface plasmon resonance (SPR) [41]. The authors prepared an array of silver nanoparticles (40 nm) by thermal evaporation on a monolayer of polystyrene spheres (PS), with diameters ranging between 290 and 390 nm. Subsequently, the PS@Ag nanoparticles were soaked in mercaptoundecanoic acid to develop a SAM. Then, HKUST-1 was grown in an LbL fashion using copper acetate and trimesic acid precursors; 20 cycles were enough to obtain a homogeneous MOF film (Fig. 12.4A). The porous sensing system was tested using carbon dioxide and sulfur hexafluoride as model gases, with nitrogen as a carrier gas. The direct sensing of

¹ See Fig. 12.9A for a graphical representation of this type of geometrical feature.

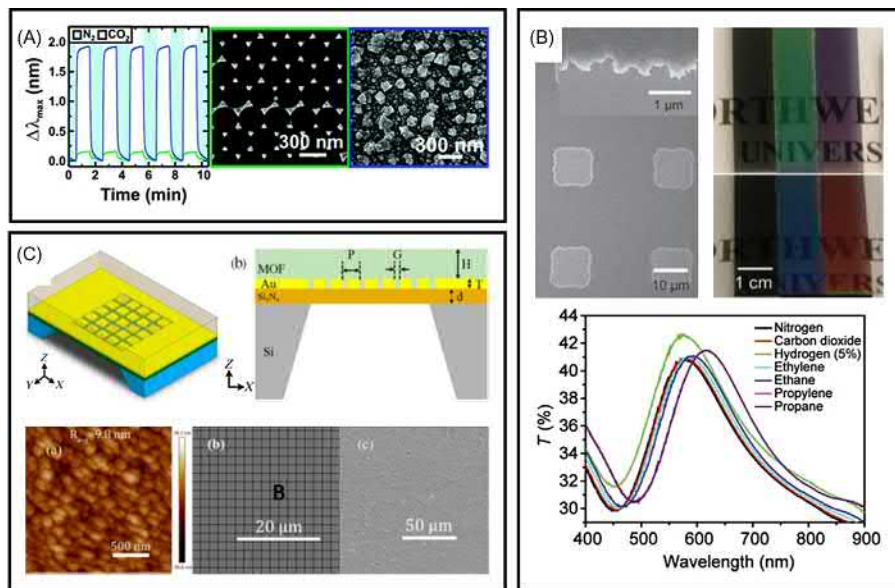


Figure 12.4 (A) Left: comparison of the response of an Ag nanoparticle sensor array (green) and the HKUST-1-coated analog (blue) toward CO₂ (with N₂ purging). Center: SEM images of an Ag nanoparticle array fabricated by lithography on a glass substrate. Right: SEM images of an analogous array coated with 20 cycles of polycrystalline HKUST-1 film. (B) Photolithography and photographs of the glass-supported hybrid films containing bilayers of Pd/ZIF-8 with different thickness (100–300 nm) observed from different viewing angles. Below a transmission spectra of a glass-supported hybrid film on exposure to various gases is reported. (C) Schematic view of the top (left) and cross section (right) of the device supporting the Au/MOF thin film, with the corresponding AFM image (lower left) of ZIF-8 thin film and SEM image before (lower center) and after (lower right) coating with the MOF thin film.

Source: (A) Adapted with permission from L.E. Kreno, J.T. Hupp, R.P. Van Duyne, Metal – organic framework thin film for enhanced localized surface plasmon resonance gas sensing. *Anal. Chem.* 82 (2010) 8042–8046; (B) G. Lu, O.K. Farha, W. Zhang, F. Huo, J.T. Hupp, Engineering ZIF-8 thin films for hybrid MOF-based devices. *Adv. Mater.* 24, (2012) 3970–3974; (C) X. Chong, et al., Surface-enhanced infrared absorption: pushing the frontier for on-chip gas sensing. *ACS Sens.* 3 (2018) 230–238. Copyright (2010–2018) American Chemical Society.

pure CO₂ and SF₆ was demonstrated by measuring the change in refractive index without the need for signal enhancement.

In 2012 Hupp's team grew a patterned thin film of ZIF-8 via a multistep process [42]. Alternate immersions in an alcoholic solution of the zinc nitrate precursor, and the 2-methylimidazole ligand at room temperature, produced a 200-nm-thick ZIF-8 film. After spin-coating a positive photoresist on top of the MOF film, a chromium mask was used for the UV light irradiation of selected regions. The exposed areas resulted in a localized softening of the resist, which was selectively

etched with a basic solution. A further immersion into an acid solution dissolved the exposed ZIF-8. Finally, an organic solvent was used to wash away the remaining protective photoresist, fabricating a MOF pattern array of $11\ \mu\text{m}$ squares (Fig. 12.4B). The authors produced ZIF-8/Pt/ZIF-8 sandwich layers, and variable numbers of Pd/ZIF-8 alternated layers. These MOF coatings were used to sense the presence of different vapors and gases (ethane, ethylene, propane, propylene, carbon dioxide, nitrogen, and hydrogen) via an optical detection method. In particular, exposing the hybrid film to hydrogen elicited an increase in transmittance, a property useful in the evaluation of threshold concentrations for air–hydrogen explosive mixtures (p_{H_2} about 0.04 bar).

In 2013 Song's group synthesized a luminescent europium(III)-based MOF using the ligand 2',5'-bis(methoxymethyl)-[1,1':4',1''-terphenyl]-4,4''-dicarboxylic acid for VOC sensing [44]. The synthesis was performed in a *N,N*-dimethylformamide (DMF)/water mixture at 80°C for 3 days, obtaining needle-shaped MOF crystals. The authors found that, in the presence of water, the framework displays a much weaker luminescence under UV irradiation. Instead, DMF triggered an eightfold enhancement of luminescence, superior to all the other tested polar, apolar, and protic analytes. The luminescent property was regenerated by soaking the crystalline powders in water, and the MOF was reused without noticeable loss of selectivity. The emission intensity change was explained by considering the interactions of Eu with the O–H bonds of coordinating water molecules (luminescence quenching) [45]. When water molecules start to be replaced by solvent molecules, O–H bonds around the Eu centers diminish, and the Eu emission enhancement can be measured.

In 2018 Chong et al. developed a device consisting of a gold nanopatch array (Au-NPA) deposited on a Si_3N_4 layer, covered by a thin layer of ZIF-8 film (Fig. 12.4C). This system was used to detect CO_2 by the surface-enhanced infrared absorption method [43]. This spectroscopic technique can identify molecular fingerprints by resonant detection of infrared vibrational modes coupled with plasmonic modes produced by metallic nanostructures [46,47]. The thickness of the MOF layer was revealed to be a critical parameter: the thicker the MOF, the more molecules were adsorbed and the larger the interaction with the infrared radiation. It is also true that larger volumes of sorbent and analyte provided additional higher order modes, and longer time is needed to reach the equilibrium state of gas adsorption. Considering both performance and engineering feasibility, the suggested optimized MOF thickness was $2.7\ \mu\text{m}$ and the maximum enhancement factor for CO_2 quantitative detection by the membrane exceeded 1800.

12.2.3 Electrochemical response

In 2013 Zhan et al. produced ZnO@ZIF-8 nanorods via sacrificial templating of prefabricated zinc oxide nanorods on fluorine-doped tin oxide glass slides, using a DMF and water mixture [48]. The obtained sensor was investigated for the photo electrochemical sensing of hydrogen peroxide. As stated by the authors, H_2O_2 diffused through the pore windows of ZIF-8, thus oxygen gas was obtained as a result

of photogenerated holes on the surface of ZnO nanorods. Conversely, bulkier ascorbic acid could not diffuse through the MOF and by-products were not detected. This demonstrated the potential use of ZIF-8 for size-selective photo electrochemical sensing (Fig. 12.5A). The nanorod array could be used to detect concentrations of H_2O_2 down to 0.1 mM in serous buffer solutions, providing an efficient device to monitor H_2O_2 . As the production of H_2O_2 can be an indication of dangerous oxidative stress in humans [51,52], it is envisaged that bioindicators could provide information about environmental changes.

In a recent study by Okada et al. using an established conversion mechanism [53,54], HKUST-1 was grown on gold electrodes through the conversion of Cu(OH)₂ nanobelts [55]. In the first step, the nanobelts, previously synthesized from copper sulfate, ammonia, and NaOH solutions, were spin-coated on gold electrodes. Subsequently, they were converted into HKUST-1 by immersing the electrodes in an ethanol/water solvent mixture containing trimesic acid. To investigate the size selectivity, three electroactive species were analyzed: ferrocene, iron(III) acetylacetonate, and iron(II) phthalocyanine, demonstrating that the latter was not able to penetrate the MOF layer and interact with the electrode (Fig. 12.5B). The system was then used for the electrochemical sensing of glucose via cyclic voltammetry and chronoamperometric analysis, with a sensitivity of $273 \mu\text{A mM}^{-1} \text{cm}^2$.

MOFs have also been investigated as active materials in chemoresistive or capacitive sensors [56]. As MOFs are mostly insulating materials, their use is limited by the low availability of porous frameworks with suitable electrical conductivity [57]. Multiple fabrication techniques have been tested, from solvated paste [58–60] to solvent-free mechanical methods [61], from drop-casting [61,62] to in situ film growth (Fig. 12.5C) [49]. In 2009 Achmann et al. investigated MIL-53, Fe-BTC (also commercially available as Basolite F300) along with the Li-doped and Fe(II)-doped analogous materials, and HKUST-1 [63]. Interdigitated electrodes coated with MOF thick films and pressed pellets were measured, varying the concentrations of oxygen, carbon dioxide, propane, nitrogen monoxide, hydrogen, ethanol, and methanol, over a range of temperature and humidity levels. The authors found that only Fe-BTC displayed a good response to ethanol, methanol, and water, this last species provided the most intense response of all. In 2014 Chen et al. prepared a cobalt imidazolate framework with *zni* topology for the detection of trimethylamine ((CH_3)₃N) in the vapor phase [64]. The device displayed promising long-term stability; however, issues such as slow response and recovery times arose because of the poor conductivity at room temperature of this porous material. Operating temperatures up to 75°C were used to improve the conductivity, although the material needed a longer response time. Hosseini et al. reported in 2016 the fabrication of a capacitive sensor using HKUST-1 directly grown on a copper substrate via electrochemical synthesis [59]. The substrate acted as a back electrode, while on top of the MOF film an electrode was prepared by connecting spots of conductive Ag paste. This device displayed a reversible turn-on capacitance response time to ethanol and methanol vapors on the order of several minutes. A weak response was observed for hexane. In the same year, Yassine et al. reported a sensor made by growing thin films of an yttrium fumarate-based MOF. This porous coating was

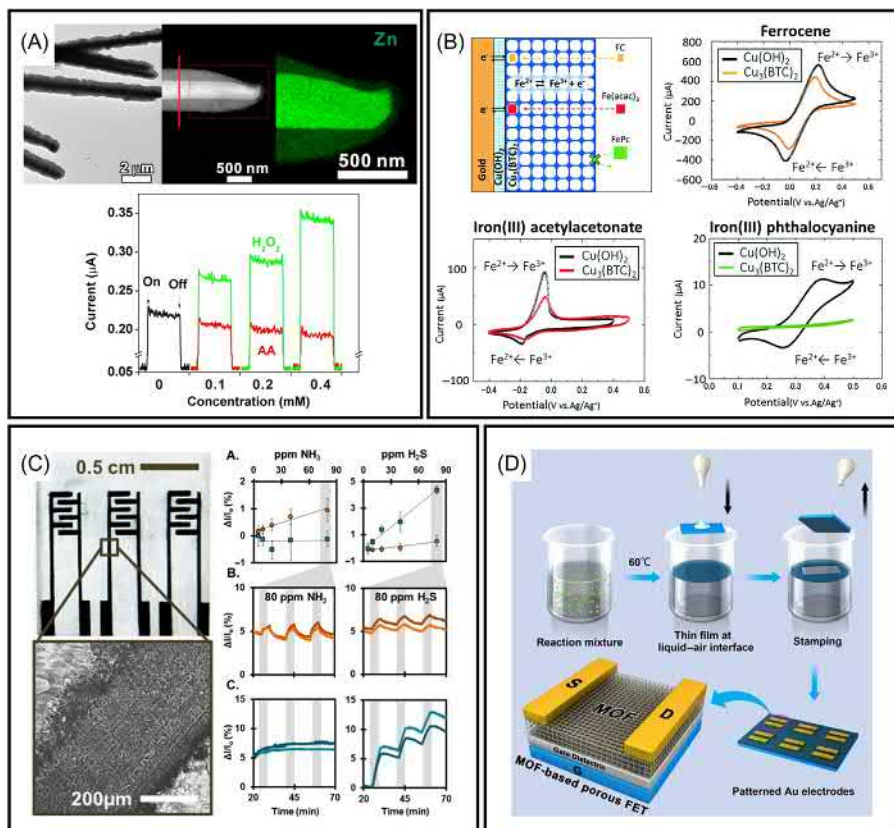


Figure 12.5 (A) TEM image, HAADF-STEM image, and cross-sectional composition profile of ZnO/ZIF-8 nanorod. The graph shows the photocurrent responses of a ZnO@ZIF-8 nanorod array in the presence of hydrogen peroxide (H_2O_2) and ascorbic acid (AA) at different concentrations. (B) Schematic representation of the size-selective sensing device using a HKUST-1-coated gold electrode, with cyclic voltammetry graphs for the copper(II) hydroxide nanobelts and the HKUST-1 coatings using ferrocene, iron(III) acetylacetonate, and iron(III) phthalocyanine (all species at 1 M concentration). (C) Photograph of a typical chemoresistor and the SEM image of the graphitic wire. The graphs show (a) the concentration dependent sensing response for ammonia and hydrogen sulfide using Cu_3HHTP_2 (orange) and Ni_3HHTP_2 (blue); (b) the sensing traces for Cu_3HHTP_2 ; and (c) the sensing traces for Ni_3HHTP_2 . (D) Schematic representation of the preparation of MOF-based porous FETs.

Source: (A) Adapted with permission from W. Zhan, et al., Semiconductor@metal-organic framework core-shell heterostructures: a case of ZnO@ZIF-8 nanorods with selective photoelectrochemical response. *J. Am. Chem. Soc.* 135 (2013) 1926–1933; (B) M.K. Smith, K.E. Jensen, P.A. Pivak, K.A. Mirica, Direct self-assembly of conductive nanorods of metal-organic frameworks into chemiresistive devices on shrinkable polymer films. *Chem. Mater.* 28 (2016) 5264–5268; (C) G. Wu, J. Huang, Y. Zang, J. He, G. Xu, Porous field-effect transistors based on a semiconductive metal-organic framework. *J. Am. Chem. Soc.* 139 (2017) 1360–1363. Copyright (2013–2017) American Chemical Society. (D) Adapted from Okada, K. et al., Electrochemical sensing and catalysis using Cu_3 (BTC) $_2$ coating electrodes from $\text{Cu}(\text{OH})_2$ films. *CrystEngComm* 19 (2017) 4194–4200 with permission from The Royal Society of Chemistry.

grown on 11-mercaptoundecanol SAM-functionalized interdigitated Au electrodes [65]. The obtained capacitive sensor displayed excellent sensitivity and selectivity toward H₂S vapors at room temperature (below 100 ppb) over NO₂, methane, hydrogen, and toluene. A linear response was demonstrated over a wide range of H₂S concentrations (i.e., from 100 ppb to 100 ppm), while the performance was maintained for over 3 months.

In 2015 Campbell et al. fabricated chemoresistive sensors based on Cu₃(HITP)₂ (HITP = 2,3,6,7,10,11-hexaiminotriphenylene) [62]. These highly π -conjugated layered 2D-MOFs, based on the triphenylene building block, are among the first examples of electrically conductive MOF-based sensors operating at room temperature [66–68]. Campbell et al. showed that by applying a voltage of 100 mV, ammonia vapors could be detected in the ppm range. The device was successfully tested in the presence of dry air and air with 60% of relative humidity (RH). Interestingly, the isostructural MOF Ni₃(HITP)₂ did not have the same properties when exposed to identical conditions; this highlights the importance of using the proper chemical structure to achieve the desired sensor response. Subsequently, the same research team reported the use of an array of sensors based on Ni₃(HITP)₂, Cu₃(HITP)₂, and Cu₃(HHTP)₂ (HHTP = 2,3,6,7,10,11-hexahydroxytriphenylene) 2D-MOFs, for the detection of several VOCs, at 200 ppm concentration levels [61]. The individual MOFs within the sensor had different chemoresistive responses to various chemicals, suitable for distinguishing VOCs with excellent accuracy (above 90%). In 2016 Smith et al. reported the direct growth of M₃(HHTP)₂ films (M = Cu, Ni) on graphite electrodes pattern-deposited onto polymer films [49]. In agreement with previous studies, these devices displayed a response toward ammonia vapor when Cu was used for the MOF nodes, whereas no response was observed with Ni-based MOFs. The authors further investigated the potential use of M₃(HHTP)₂ active materials in sensor arrays for the selective detection of other analytes such as water, ammonia, NO, and H₂S.

Along with chemoresistors, field effect transistors (FETs) are suitable sensing devices. They have interesting features such as robustness, sensitivity, and compatibility with scalable fabrication processes [69,70]; however, FETs have been rarely prepared using MOFs (Fig. 12.5D) [50,71]. For the analysis of vapors, MOFs without appreciable electrical conductivity can be employed and changes in the work function through the Kelvin probe technique can be measured [56]. The first example of this approach was reported by Pohle et al. in 2011 with HKUST-1 [72]. The authors analyzed several VOCs and gases (hexanal, pentanal, toluene, dimethyl ether, ethanol, acetone, ammonia, and hydrogen sulfide), in the 25–200°C temperature range. It was observed that the higher the temperature the stronger the response. Due to the narrow pore distribution of MOFs, molecular sieving abilities were observed, for example in the cases regarding the pentanal/hexanal couple, and when discriminating ammonia and hydrogen sulfide from dimethyl ether. Also, the metal used for the back electrode (Au or Pt) influenced the response, suggesting an interaction with the MOF coating. In 2014 Davydovskaya et al. used the series M-BTC (M = Co, Ni, Cd, Al) to assess the performance upon exposure to linear alkanes and aliphatic alcohols [73]. Nonpolar alkanes had a negligible effect on the

work function, whereas the polar alcohols produced detectable variations. The authors observed that the longer the alcohol molecule, the stronger the responses. Notably, all the investigated MOFs showed similar sensing behavior, independent of the type of metal used for the MOF nodes. Conversely, in a study by Pentylala et al. in 2016 for the alcohol sensor based on Zn-BTC MOF [74], it was found that the metal ions used (in this case Zn^{2+}) in the crystal structure acted as specific adsorption sites for molecules with strong donor functions, like oxygen from a hydroxyl functional group. Along with the previously mentioned work by Campbell et al. [62] and Smith et al. [49], these contrasting results suggest that further studies are needed to understand the influence of different metal centers on the sensing behavior of MOFs.

12.3 Metal-organic framework–based sensors for gaseous and aqueous environments

This section describes some of the most important MOF-based devices recently investigated for the detection of toxic gases (Section 12.3.1), VOCs (Section 12.3.2), and organic or inorganic noxious species in aqueous solutions (Section 12.3.3).

12.3.1 Detection of toxic gases

In the last few years, MOFs have been used to detect various different gases, such as:

- carbon dioxide (CO_2), due to its potent greenhouse effect and its toxic effect when present at a concentration above 5000 ppm [75,76];
- nitric oxides (NO_x , such as NO and NO_2), as pollutants present in car emissions and coreponsible for acid rains;
- hydrogen sulfide (H_2S), a poisonous and flammable gas produced in industrial processes; and
- nerve agents, as relevant gases used in terrorist actions.

In 2008 Yeom et al. fabricated a detector of toxic gases based on a microelectro-mechanical system (MEMS) [77]. In their device, the authors designed micro-preconcentrators (μ PCs) starting from an Au-coated Si chip; Then an array of micro spots (depth of c. 40 μ m) was obtained by deep reactive ion etching. Subsequently, the array was coated with IRMOF-1 (a.k.a. MOF-5). The μ PC was housed in a durable Vespel case equipped with inlets and outlets for gas flow and electrical contacts. The MOF concentrated the model toxic gas (isopropylsulfonylchloride) from its mixture with air; then the μ PC was pulsed with current, causing a short burst of localized heat that liberated the enriched fraction of gas; this reacted with an oxime [78], producing cyanide ions which were subsequently measured with a selective electrode placed downstream of the device. The μ PC reached 250°C within 100 ms,

consuming only 1.2 J. To test the effectiveness of the device, the μ PC was exposed to 200 ppb of toxic gas; then a 3-second pulse was used to release the analyte from the MOF. The downstream detector was able to measure down to 10 ppb of gas (signal-to-noise ratio = 20).

In 2015 Yue et al. produced a flexible MOF based on the 1,2,3-benzotriazole-5-carboxylic acid (H_2btca) ligand with a MIL-53 structure using zinc as the metal node. The compound of interest showed a unique dynamic gas adsorption and high selectivity to carbon dioxide versus nitrogen, argon, and helium, strongly dependent on the interaction between gas molecules and the framework, as measured by Fourier transform infrared analysis [79].

In 2016 Ameloot's group developed a sensor based on NH_2 -UiO-66(Zr) to detect nerve agents [80]. The chosen framework constituted the active part of a Kelvin probe setup, in which the shift in contact potential difference was correlated to the amount of analyte (dimethoxymethylphosphate, a simulant of the most dangerous sarin gas). The detector worked both in dry and in 50% RH air, and was able to detect the analyte down to 3 ppb. The authors suggested a real-world implementation of this probe with a so-called suspended gate chemical FET (ChemFET) [70].

During the same year, Chong et al. prepared an ultrasensitive near infrared sensor for carbon dioxide based on the coating of HKUST-1 on single-mode optical fiber (SMF) [81]. Due to the hydrophilicity of the copper-based MOF, water vapor was observed to be a major interference. Nevertheless, the system was able to detect carbon dioxide down to 100 ppm for each cm of SMF. In a follow-up study (2017), the same group produced a nanophotonic device consisting of plasmonic 40-nm-thick Au nanopatch arrays on sapphire (2000-nm-wide square patches separated by 250 nm gaps); this chip was covered with a ZIF-8 coating in the 500–2700 nm range [82]. This integration permitted the construction of a sensor for carbon dioxide detection, demonstrating a 1100-fold enhancement factor, defined as the ratio between the equivalent optical path length, provided by the plasmonic device, and the MOF layer. This device was considered suitable for lab-on-a-chip applications as an alternative to conventional gas cells.

In 2017 Mirica's group described a straightforward method to incorporate moderately conductive MOFs into chemoresistive sensors via mechanical abrasion [83]. Various metal nodes were selected among Fe, Ni, Co, or Cu, using 2,3,6,7,10,11-hexahydroxytriphenylene (HHTP) ligand that can produce 2D frameworks with very large pores. Subsequently, this MOF was blended with high purity graphite via ball milling for 5 minutes, compressed into pellets and abraded onto commercial electrodes made either of 220 nm interdigitated gold patterns on ceramics, or 1 mm gold pattern electrodes on paper. The assembled chemoresistive devices, loaded into Teflon enclosures, were then exposed to gaseous streams of analytes diluted in dry N_2 (0.5–8.0 ppm range; Fig. 12.6A). The sensing measurements showed a remarkable capacity for detecting and differentiating toxic gases. Cu_3HHTP_2 was the best performing active material toward all toxic gases considered (ammonia, nitric oxide, and hydrogen sulfide), and was able to distinguish between 80 ppm of the gases in the presence of 7000 ppm of water. The limit of detection (LOD) was between 17 ppm (for NO) and 35 ppm (for H_2S), in line with the limits established

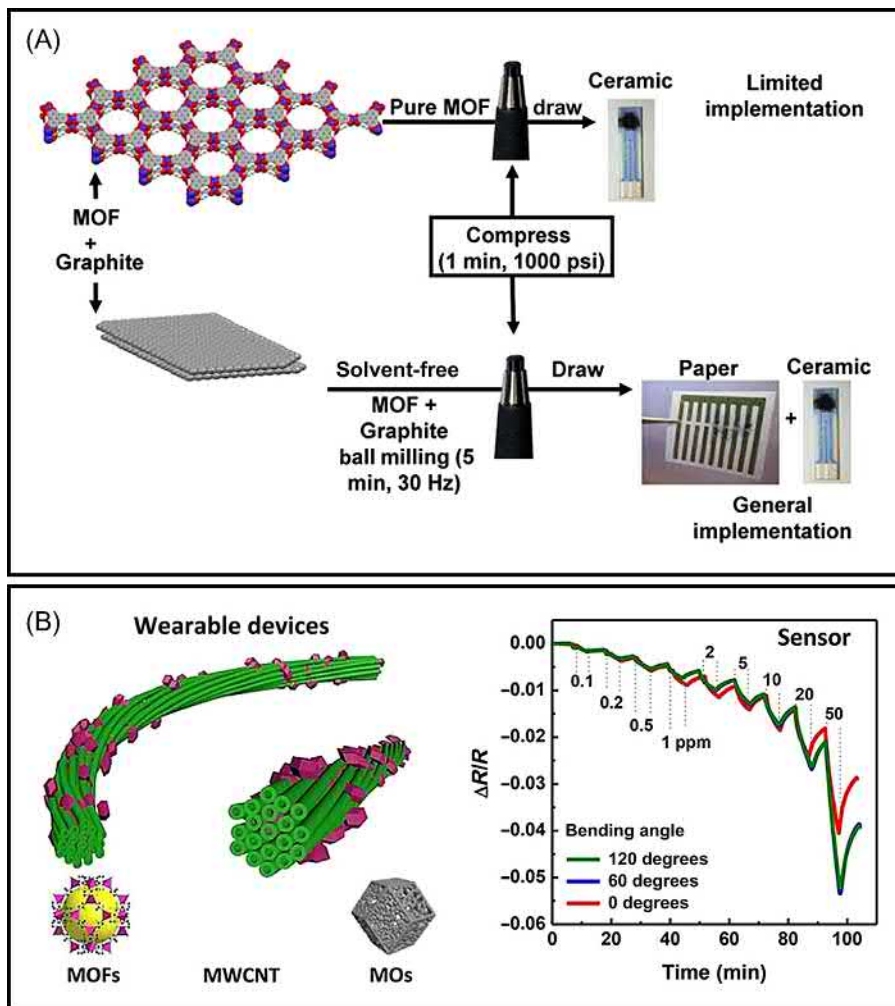


Figure 12.6 (A) The stepwise process for the integration of M_3HHTP_2 MOF-based materials into a chemoresistive device. The blend obtained by ball milling of MOF and graphite was compressed into a pellet which is loaded into a pencil-style holder, followed by mechanical abrasion directly on paper or ceramic devices equipped with gold electrodes, producing chemoresistors with different architectures. (B) Schematic illustration of the wearable MOF/MWCNT fibers and graph showing a comparison of the responsive resistance of ZIF-67-Co/MWCNT hybrid fibers toward nitrogen dioxide gas at fixed bending angles (0, 60, and 120 degrees) in a concentration range of 0.1–50 ppm (MOs = metal oxides).

Source: (A) Adapted with permission from M. Ko, A. Aykanat, M. Smith, K. Mirica, Drawing sensors with ball-milled blends of metal-organic frameworks and graphite. *Sensors* 17 (2017) 2192. Copyright (2017) American Chemical Society. (B) Reproduced with permission from K. Rui, et al., Dual-function metal-organic framework-based wearable fibers for gas probing and energy storage. *ACS Appl. Mater. Interfaces* 10 (2018) 2837–2842 with Creative Commons License CC BY 4.0.

by the US Occupational Safety and Health Administration (OSHA) agency. Another system developed in the same year by this group integrated MOFs with textiles, introducing these MOFs into the field of wearable electronics [84]. Their self-organized frameworks on textile devices exploited fabrics as they are chemically modifiable, physically tunable, low cost, renewable, and compatible with the integration into garments, personal protective equipment, and other goods. For the preparation of these devices, both natural woven cotton fabrics and synthetic non-woven polymer battings were employed, demonstrating that the devices could work regardless of the fabric nature. Two MOFs, Ni_3HHTP_2 and Ni_3HITP_2 (HITP = 2,3,6,7,10,11-hexaiminotriphenylene), were chosen for their relatively high bulk conductivity in the $0.01\text{--}2.0\text{ S cm}^{-1}$ range. The assembly was obtained by immersing the fabrics into the precursor solution with overnight stirring at 80°C . Ammonia was added to the reaction vessel when using the HITP ligand. To assess the sensing performance, the detection of NO and H_2S was conducted in the 0.1–80 ppm range. In a dry nitrogen stream, the calculated limits of detection were found to be 0.16 ppm for NO (using Ni_3HITP_2) and 0.23 ppm for H_2S (using Ni_3HHTP_2). Importantly, the devices retained their performance in 18% RH and were fully recoverable and washable.

In 2017 Yao et al. synthesized thin films of $\text{Cu}_3(\text{HHTP})_2$ (HHTP = 2,3,6,7,10,11-hexahydroxytriphenylene) on gold films, interdigitated electrodes, silicon, Si/SiO₂, quartz, and sapphire, by liquid LbL spray deposition [85]. Due to its appreciable conductivity of 20 mS cm^{-1} at room temperature, the authors produced a chemoresistive sensor toward ammonia gas, not only extensively used in industry, but also a biomarker for kidney and liver diseases [86]. With a MOF thickness of 20 nm, the sensor was able to selectively detect NH_3 in the 1–100 ppm range with one of the highest resistance changes detected for similar devices at room temperature (c. 130% of average resistance change), within 2 minutes and a response retention above 88% after 3 months.

Nonconductive MOFs were also integrated into wearables; in this case, carbon nanotubes were used as a conductive material. In 2018 Rui et al. developed a procedure to produce hybrid ZIF-67(Co) or MIL-88(Fe) and multiwalled carbon nanotube (MWCNT) fibers (Fig. 12.6B) [87]. These MOFs were annealed and converted into Co_3O_4 and Fe_3O_4 fibers and woven into cotton to produce a chemoresistive flexible device for the detection of nitrogen dioxide (NO_2) gas down to 0.1 ppm. However concerns about the toxicity of carbon nanotubes, as reported in literature [88,89], could potentially limit this type of application.

12.3.2 Detection of volatile organic compounds

VOCs are organic compounds with high vapor pressure at room temperature [90]. The term is typically used for noxious chemicals, although many molecules that act as scents and messengers in plant and plant/animal communications fall under this nomenclature. Anthropogenic VOCs are usually harmful for humans, especially polycyclic aromatic hydrocarbons (PAHs), which often possess carcinogenic properties [91]; thus their indoor maximum concentration is generally regulated by law.

In this context MOFs, due to their tunable porosity, high accessible surface area and tunable chemical affinity, are considered to be outstanding sorbent materials for the efficient capture of VOCs.

One of the first techniques for the preparation of films of $Zn_3(\text{BTC})_2$ from zinc metal was developed by Zou et al. in 2009; the method involved the reaction in an autoclave of zinc slices (previously activated with hot H_2O_2) with a solution of trimelic acid. The MOF film was used to sense dimethylamine in water, ethanol, and acetonitrile solutions by means of fluorescence spectroscopy, exciting at 327 nm [92]. The authors were able to detect methanol, acetone, propylamine, butylamine, and aniline in ethanol. The highly sensitive and selective fluorescence intensity to dimethylamine was considered relevant for possible applications in VOCs sensing.

In 2010 Bein's team developed a method for the orientation of the MOF CAU-1 on different SAMs on gold [93]. This MOF was prepared in bulk using aluminum chloride and 2-aminoterephthalic acid under solvothermal conditions. To grow the porous crystals on surfaces exposing either $-\text{OH}$ or $-\text{COOH}$ groups, SAM-functionalized gold slides were placed into MOF precursor solutions for different times (i.e., from 16 hours to 14 days). The authors found a preferential orientation of the CAU-1 crystals either in the [011] or [002] directions when using the OH-terminated SAMs, whereas highly oriented crystal growth occurred only in the [002] direction when the carboxylic acid functionalized SAMs were used. This protocol was used to grow MOFs on QCM supports; then the MOF-based device was exposed to ethanol, as model adsorbate. The observed Type I isotherm indicated the microporous character of CAU-1, with approximately 5 mmol g^{-1} of ethanol adsorbed before reaching condensation.

Lu and Hupp prepared in 2010 a Fabry–Perot interferometer based on ZIF-8 thin films for selective gas sensing [94]. Using zinc nitrate and 2-methylimidazole as precursors with the LbL technique, the MOF was grown on silicon or glass substrates (Fig. 12.7A). QCM measurements were performed to estimate the amount of deposited MOF, and a relationship between thickness and number of cycles was identified. Different thicknesses provided different colors due to the optical interference in the visible region. Thanks to the dual function provided by the ZIF-8 absorption properties and the resonating properties of the interferometer, the authors found that the collected transmission spectra were influenced by the various vapors. The peak shift was correlated to the concentration of gaseous analytes. A quasi-linear relationship was found in the case of propane, and it was also possible to differentiate between linear hexane and cyclohexane. Additionally, ethanol was detected in water as low as 100 ppm.

In 2011 Huang et al. presented a synthesis of MIL-101(Cr) on QCMs for the detection of six types of VOCs: hexane, toluene, butanone, dichloromethane, methanol, and butylamine [95], without the need for hydrofluoric acid (HF). Using the Dubinin–Astakhov equation to describe the physical adsorption of gases on microporous solids [96], the authors were able to identify the limiting adsorption capacities for each volatile compound; the highest affinity was found for butylamine (13 mmol g^{-1}). The researchers observed that Cr(III) metal sites influenced the

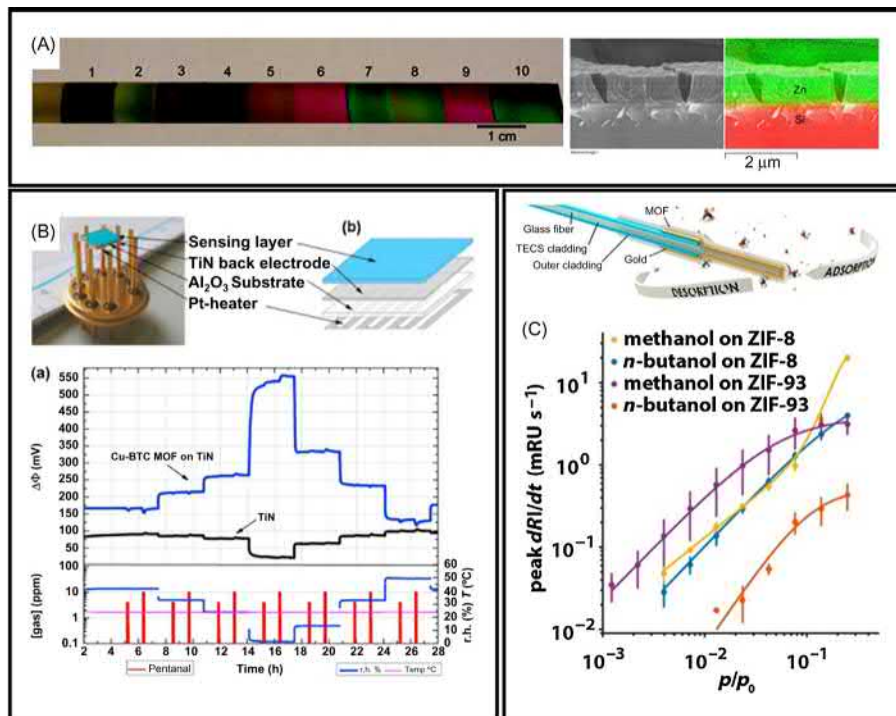


Figure 12.7 (A) Photograph of a series of ZIF-8 films of various thicknesses grown on silicon, and the EDX map of a ZIF-8 film grown with 10 cycles. Copyright © 2010 by John Wiley & Sons, Inc. (B) Photo and schematic view of a Kelvin Probe sample, showing the alumina substrate with platinum heating element, titanium nitride back electrode and the blue sensing layer of HKUST-1 MOF. The measurement shows the work function response $\Delta\Phi$ of the MOF layer (blue line) and the blank titanium nitride back electrode (black line) upon exposure to pentanal (valeraldehyde), performed in synthetic air (20% oxygen, 80% nitrogen, flow 1 L min⁻¹), at 25°C and in relative humidity ranging from 0% to 50%. (C) Scheme of a surface plasmon resonance probe (not in scale) consisting of an optical fiber (diameter: 400 μm), a 39-nm-thick gold layer necessary for the SPR phenomenon, and a final coating with the MOF recognition layer. The graph shows calibration curves for the ZIF-8 and ZIF-93 SPR sensors with methanol and *n*-butanol vapors. Copyright (2017) American Chemical Society.

Source: (A) Reprinted with permission from G. Lu, J.T. Hupp, Metal – organic frameworks as sensors: a ZIF-8 based Fabry – Pérot device as a selective sensor for chemical vapors and gases. *J. Am. Chem. Soc.* 132 (2010) 7832–7833. (B) Adapted with permission from P. Davydovskaya, R. Pohle, A. Tawil, M. Fleischer, Work function based gas sensing with Cu-BTC metal-organic framework for selective aldehyde detection. *Sens. Actuators B Chem.* 187 (2013) 142–146. (C) Reprinted with permission from W. Vandezande et al., Parts per million detection of alcohol vapors via metal organic framework functionalized surface plasmon resonance sensors. *Anal. Chem.* 89 (2017) 4480–4487.

sorption process, and the modification of unsaturated metal sites was suggested as an alternative methodology for the regulation the sorption ability of MIL-101.

Davydovskaya et al. produced in 2013 a Kelvin Probe detector by coating an alumina substrate (area: 5 mm × 5 mm) with 2 μm of titanium nitride, then drop-casting on top few μL of a dispersion of HKUST-1 (Fig. 12.7B). A Pt heating element was screen-printed on the bottom side of the substrate. Then the device was tested against the C₂–C₆ family of linear aldehydes, finding that pentanal (a.k.a. valeraldehyde) was the most sensitive analyte at the optimal conditions of 24°C, and 40% RH, in a synthetic air mixture of O₂/N₂ 1:4 [97]. A similar sensitivity to the same substrate was observed in absence of oxygen. A deeper investigation revealed that the work function was influenced by humidity and by other aldehydes.

In 2013 Fisher's group prepared the so-called surface mounted MOFs (SURMOFs) using a LbL approach with thiolated SAMs on commercially available gold QCM substrates [98]. 40 cycles of alternate immersions in metal and ligand solutions were performed, depositing crystalline layers Cu₂(ndc)₂(dabco) with different crystalline orientations ([100] and [001]) and exploited for the uptake of VOCs such as benzene, toluene, and *p*-xylene. SURMOF[100] performed better for benzene than SURMOF[001], with a fourfold increase in the adsorption rate, whereas for the other analytes the difference was minimal. In a subsequent study, Fisher and coworkers investigated the heteroepitaxial growth of Cu₂(X)₂dabco on QCM, where X = H₂bdc, H₂NH₂bdc, or H₂ndc ligands [99], testing several combinations. A triple layer of SURMOF was also prepared with 15 cycles of LbL deposition for each type of MOF. The gas adsorption study was tested on 4-fluorophenylisothiocyanate (FPI), because it can react with the amino groups of the intermediate film containing H₂NH₂bdc ligand. The hybrid SURMOFs exhibited distinct adsorption kinetics of FPI due to the different pore environments within the core, core–shell and core–shell–shell structures of the SURMOF crystallites. However, a detailed quantitative analysis was not performed.

A significant quality improvement in the fabrication of heterostructured MOF films was reported in 2014 by Wannapaibon et al. by using a continuous and automated liquid phase epitaxy (LPE) process monitored by QCM [100]. The study involved the preparation of pyrazolate-based MOFs of the general formula [Zn₄O(L)₃]_n, with L = disubstituted carboxypyrazolate derivatives. The adsorption properties toward methanol were estimated with the mass changes monitored thanks to the microbalance sensitivity, using dry helium gas as the VOC carrier in the full *p/p*₀ range. The robustness of the film was also tested after water adsorption, showing that only 95% of humidity can reduce the adsorption capacity by c. 50% when using dmcapz as the ligand for the MOF film. A further advancement in the LPE manufacturing of MOF layers on SAM-functionalized Au-coated QCM substrates was demonstrated in 2015 by growing [Zn₄O(MI)₃]_n on [Zn₄O(DM)₃]_n heteroepitaxial MOFs (with MI = 3-methyl-5-isopropyl-4-carboxypyrazolate and DM = 3,5-dimethyl-4-carboxypyrazolate) [101]. The adsorption properties were tested for methanol and isopropanol vapors with excellent results (up to 0.13 g g⁻¹ of methanol harvested), well above the <1 mmol g⁻¹ observed for the single component

$[\text{Zn}_4\text{O}(\text{DM})_3]_n$. Moreover, due to the hydrophobicity of the frameworks, water absorption is prevented and the selectivity toward methanol molecules promoted.

A nonlinear electrostatically actuated MEMS resonator for gas sensing was fabricated in 2016 by Eddaoudi's research team by coating a clamped–clamped micro beam with HKUST-1 via inkjet printing [102]. Under a nitrogen stream, the sensor could detect a mass variation of only 395 pg of water. This demonstration proved the high sensitivity of the MOF-based device.

Soft lithography was implemented by Faustini's group in 2016, preparing submicron ZIF-8 based 2D photonic structures for vapor sensing [103]. Two approaches were used for the MOF-based device fabrication: (1) the drop-casting of a colloidal solution of ZIF-8 nanocrystals on a hard surface, followed by a patterned PDMS stamp pressed on the cast, to obtain a nanopatterned ZIF-8 surface, and (2) the embossing of a TiO_2 sol–gel film (with the same PDMS stamp) followed by dip-coating of the ZIF-8 colloid, to obtain a ZIF-8/ TiO_2 heterostructure. In both cases, diffraction gratings with 1000 nm periodicity were fabricated. It is noteworthy that the optical response upon irradiation with white light was collected with a common CCD sensor typically used in smartphones. The MOF patterned surfaces were investigated in two different sensing experiments: in the first, the authors exposed the substrates to isopropyl alcohol vapors, ascertaining the better stability of the ZIF-8/ TiO_2 heterostructures over the nanopatterned ZIF-8; in the second, styrene was detected in the presence of water. This toxic monomer was revealed down to 57 ppm in moist air using planar ellipsometry. The measurement revealed a fast initial uptake of this VOC on the MOF particle surface, with a subsequent absorption into the microporosity. Tests were performed for other organic solvents like cyclohexane, xylene, and toluene, confirming the dual regime behavior.

In 2016 Homayoounia and Zeinali developed a capacitive sensor based on HKUST-1 for the detection of different concentrations of methanol, ethanol, isopropanol, and acetone [60]. The authors drop-cast a preformed ethanol suspension of HKUST-1 particles onto $2 \times 2 \text{ cm}^2$ Cu plates. Ag paste drops were then placed on top and interconnected to fabricate the sensor. The electrical contacts were made exclusively on the bottom electrode and the patterned Ag electrode using copper wires. The sensor was then positioned in a 2 L chamber, where the VOC vapors were produced by injecting predetermined amounts of liquid on a microheater, to create concentrations of 250, 500, 1000, and 1500 ppm of VOCs in atmospheric air. The results showed that the minimum detectable concentrations for sensing methanol, ethanol, isopropanol, and acetone was 61.99, 71.05, 77.80, and 100.18 ppm, respectively. However, different sensing behaviors were observed and related to the different dielectric constant and environmental variables. Eight months aging did not have a significant effect on the sensor, which could be regenerated by moderate reheating for 10 minutes.

Between 2016 and 2017, de Smet's group reported two examples of capacitive sensors for the detection of alcohols in the gas phase, obtained by mixing NH_2 -MIL-53(Al) into a Matrimid polymer matrix [104,105]. Using impedance spectroscopy, the authors evaluated parameters such as MOF loading, type of analyte (methanol, ethanol, isopropanol) and concentration, concurrent presence of water,

and temperature. These MOF-polyimide composite devices showed higher response toward alcohol, and lower LOD, than the polymer alone or the bare electrodes. Although the use of these kinds of hybrid materials for sensing has not been extensively explored, these composites demonstrated promising sensing properties.

In 2017 Qu et al. used ZIF-8 and mixed Ni-Zn hydroxides as sources to prepare ZnO/Ni_{0.9}Zn_{0.1}O double-shelled nanocages [106]. The chemoresistive system was used to sense ammonia, nitrogen dioxide, methanol, ethanol acetone, toluene, and xylene, and was found to be more sensitive for the latter. The response was linear up to 100 ppm, and sensitive to 1 ppm stepwise increments of the analyte.

A very recent (2018) method was developed by Zhou et al. and involved the coating of vertically aligned ZnO nanorod arrays with ZIF-8 or ZIF-71, using 4,5-dichloroimidazole as ligand. The resulting devices showed minor responsiveness (expressed as the ratio between the average electrical currents in target gas and air) toward ammonia and benzene, moderate responsiveness for hydrogen, whereas using ZIF-71 the obtained signal response was enhanced for ethanol and acetone [107].

A fiber optic-based surface plasmon resonance (FO-SPR) sensor was developed in 2017 by Vandezande et al. for the detection of alcohol vapors [108]. In this work, ZIF-8 and ZIF-93 (using 4-methyl-5-imidazolecarboxaldehyde as a ligand) were grown on a multimode TECS² optical fiber (Fig. 12.7C), previously coated with a 39 nm gold layer acting as the deposition surface for the ZIFs. The applicability of the coatings was tested for the detection of methanol, ethanol, *n*- or *iso*-propanol, and *n*-butanol, within a very narrow window of refractive indices ($\Delta n = 0.065$). Whereas ZIF-93 had better affinity to methanol due to both high hydrophilicity and smaller cavity size, ZIF-8 lacked polar groups and thus showed better affinity with *n*-butanol. Moreover, the affinity for *n*-propanol was higher than *iso*-propanol in both MOFs due to steric hindrance. The limits of detection oscillated between 2.5 ppm for methanol and 73 ppm for *n*-butanol.

12.3.3 Detection of pollutants in water

Early research into MOF-based devices for environmental applications involved organic solvents, due to the limited water stability of the first MOFs studied. For example, Falcaro's group investigated the use of repositionable sorbents based on MOF-5 or IRMOF-3 combined with magnetic particles for the uptake of different chemical species (e.g., dyes, PAHs, Ag⁺) in tetrahydrofuran (THF) or methanol [109–111]. However, the subsequent development of more water stable MOFs has enabled the sensing of different species in the presence of water. Asha et al. in 2014 used a luminescent interpenetrated zinc-based MOF with H₂ndc and bpy ligands as selective sensors for nitro-aromatic explosives [112]. The principle of

²TECS: Technology Enhanced Clad Silica, a fiber developed by 3M and now manufactured by Thorlabs Inc.

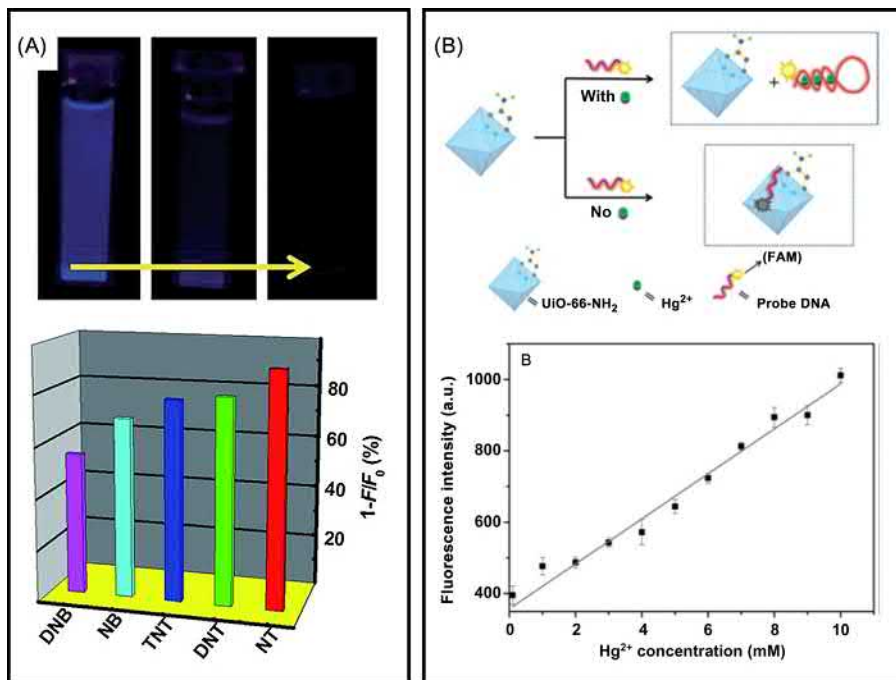


Figure 12.8 (A) The gradually reducing emission of fluorescent MOF $[\text{Zn}_2(\text{NDC})_2(\text{bpy})]$ under UV light in presence of nitrotoluene (NT). The graph reports the fluorescence quenching percentage of the MOF with different nitro-aromatic analytes at room temperature. (B) Schematic concept of the fluorescent MOF/DNA hybrid sensing system for mercury(II) and linear relationship between the emission intensity (measured at 518 nm) and the ion concentration (in the range 0.1–10.0 μM).

Source: (A) Adapted with permission from K.S. Asha, K. Bhattacharyya, S. Mandal, Discriminative detection of nitro aromatic explosives by a luminescent metal-organic framework. *J. Mater. Chem. C* 2 (2014) 10073–10081. Copyright (2014) American Chemical Society. (B) Adapted from L.-L. Wu, et al., A metal-organic framework/DNA hybrid system as a novel fluorescent biosensor for mercury(II) ion detection. *Chem. Eur. J.* 22 (2016) 477–480 with permission from The Royal Society of Chemistry.

detection is based upon quenching of the luminescent properties by an effective electron transfer from the conduction band of the MOF to the LUMO³ of the analyte (Fig. 12.8A). The effect was found to be smaller for dinitrobenzene and greater for nitrotoluene, with 2,4,6-trinitrotoluene in the middle of the trend.

Wu et al. developed in 2016 an innovative fluorescent sensor for Hg^{2+} detection in aqueous solutions using $\text{NH}_2\text{-UiO-66}(\text{Zr})$ along with a T base-rich single-strand DNA, labeled with a fluorescein-based dye called FAM [113]. Without $\text{Hg}(\text{II})$ ions, the FAM-tagged probe DNA interacted with the MOF crystals, bringing the dye

³Lowest unoccupied molecular orbital.

moiety close to the $\text{NH}_2\text{-UiO-66(Zr)}$ surface, resulting in a fluorescence quenching due to the photoinduced energy transfer. In the presence of Hg^{2+} , that is known to strongly interact with thymine–thymine mismatched base pairs [114], the DNA formed hairpin-like $\text{T-Hg}^{2+}\text{-T}$ structures, liberating the FAM dye and permitting its fluorescence emission (Fig. 12.8B). The fluorescence intensity gained a significant enhancement in the presence of Hg^{2+} , whereas other heavy metal ions showed a smaller response. The detection limit was found to be very low, around 18 nM, well below the 30 nM limit set by the World Health Organization (WHO)⁴. Moreover, the response was linear in the 0–100 μM range.

In the same year, Nazari et al. fabricated an optical fiber-based Fabry–Perot device for the detection of contaminants in water by using UiO-66(Zr) as the active MOF material [115]. The exposed end of a conventional single-mode fiber, with a core diameter of 8.2 μm , was preliminarily coated with a plasma polymer film, produced from diglyme in a custom-built RF glow discharge reactor. The fiber was then immersed in the UiO-66(Zr) precursor solution inducing MOF growth on the fiber tip end. The authors then tested this system for aqueous solutions of Rhodamine B, a model pollutant due to its usage in the textile industry, in the 0.1–15 mM concentration range. The lowest amount detectable was down to 48 ppm.

12.4 Metal-organic framework–based devices for the removal of noxious species

This section illustrates the use of MOF devices for the separation of pollutants from different substrates. The first part (Section 12.4.1) focuses on the production of solid-phase extractors for the preconcentration of various types of analytes. The second part (Section 12.4.2) discusses relevant applications using filtration devices in which MOFs act as sorbents. The third part (Section 12.4.3) describes separation devices using fluidic systems in which a constant stream is exposed to the presence of MOFs. Parameters such as limit of detection (LOD), adsorption capacity (generally expressed in mg of harvested species per g of MOF), recovery, and recyclability, will be examined.

12.4.1 Preconcentrators

Solid-phase extraction (SPE) is a typical preparative method to concentrate, isolate, and purify samples of interest from different matrices, and can be coupled with suitable analytical equipments (for example chromatographic instruments) [116].

In the 2009 report from Cui et al., HKUST-1 ($\text{Cu}_3(\text{BTC})_2$, a.k.a. MOF-199) was immobilized on stainless steel fibers for micro solid-phase extraction (μSPE) of

⁴Corresponding to 6 $\mu\text{g/L}$, as stated from the online source “Mercury in Drinking water”: https://www.who.int/water_sanitation_health/dwq/chemicals/mercuryfinal.pdf.

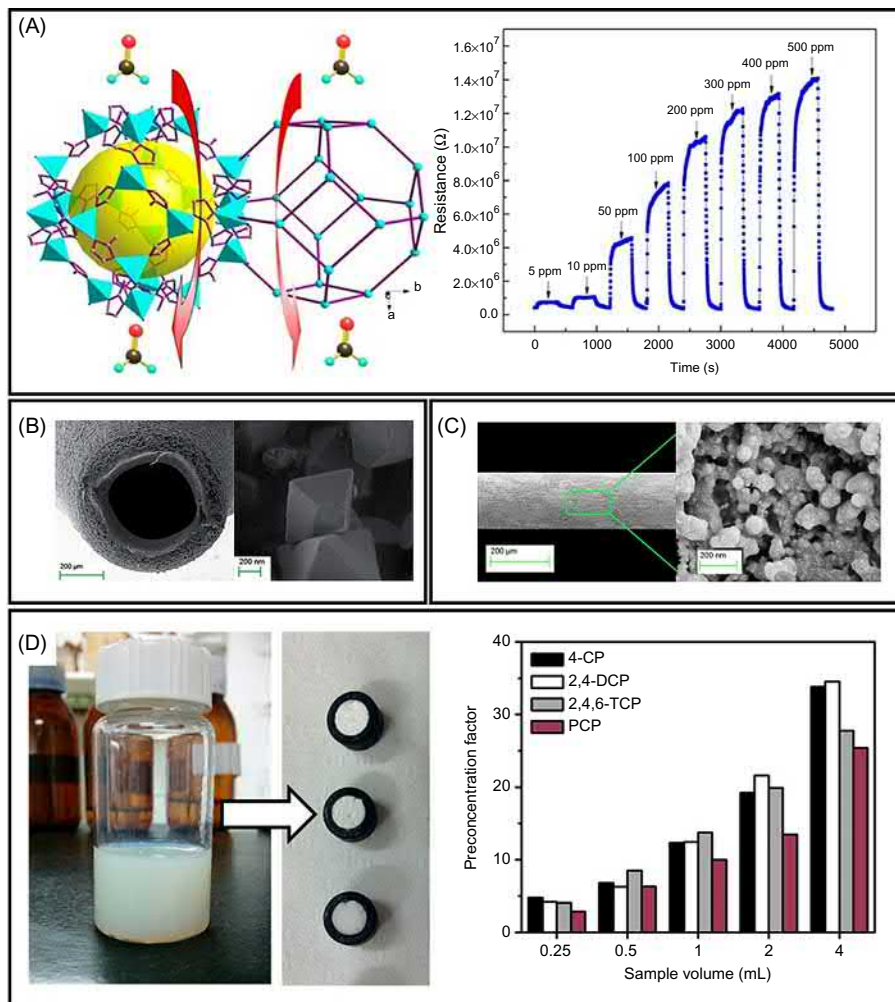


Figure 12.9 (A) The *sod* topology of ZIF-67 and the response-recovery curve of the ZIF-67 sensor to various concentrations of formaldehyde gas, measured at 150°C. (B) SEM images of the cross section of a hollow fiber used to support MIL-101 sorbent and the crystal shape of MIL-101 after 80 cycles of polychlorinated biphenyls extraction. (C) SEM images of the surface of the fiber coated with the Yb-MOF materials. (D) Photograph of a ZnO nanoparticle dispersion (10 wt.%), and the nanoparticle-containing polymer monoliths (NPMs) obtained (5 mm length \times 4.6 mm internal diameter). The graph shows the pre-concentration factors obtained using different sample volumes on the extraction of 100 $\mu\text{g L}^{-1}$ chlorophenols using the ZIF-NPM-butylamine column at room temperature. *Source:* (A) Reprinted with permission from E.-X. Chen, H. Yang, J. Zhang, Zeolitic imidazolate framework as formaldehyde gas sensor. *Inorg. Chem.* 53 (2014) 5411–5413. Copyright © 2014 by John Wiley & Sons, Inc. (B) Adapted from H. Zang, et al., Hollow fiber-protected metal-organic framework materials as micro-solid-phase extraction adsorbents for the determination of polychlorinated biphenyls in water samples by gas chromatography-

volatile benzene derivatives [117]. The fabrication involved HF etching of a 0.15 mm diameter metallic fiber, to generate a rough surface, then the fiber was exposed to an in situ hydrothermal growth of HKUST-1 in a Teflon-lined autoclave, and eventually inserted into a gas chromatography microsyringe. The obtained 40- μm -thick MOF layer corresponded to c. 2 mg of material. The authors used the SPE syringe to concentrate vaporized samples of VOCs (benzene, toluene, chlorobenzene, ethylbenzene, *p*-xylene, styrene, and trimethylbenzene) in a chamber. Tests were performed in presence and absence of water, to evaluate the effect of relative humidity (RH%). The enhancement factors for the collection of aromatic VOCs ranged from c. 20,000 (for benzene) to c. 110,000 (for *p*-xylene) ng L^{-1} ; very low LODs were found (from 8.3 ng L^{-1} for toluene to 62.1 ng L^{-1} for styrene). The authors also collected air samples from real indoor environments (a public market, a bedroom, and an office) demonstrating that benzene, toluene, *p*-xylene, and styrene can be reliably detected for an effective and practical monitoring of pollutants.

Gu et al. prepared in 2010 a sorbent system based on MOF-5 for in-field sampling and preconcentration, followed by thermal desorption, of atmospheric formaldehyde [118]. The material was packed into 9-cm-long quartz tubes and compared with other kinds of sorbents. Samples (from indoor and outdoor locations) were collected using an air sampling pump and subsequently desorbed and analyzed via gas chromatography/mass spectrometry (GC-MS). Control samples were prepared by vaporizing formaldehyde solution into sampling bags with N_2 as diluter. Water was also added in various amounts to evaluate the effect of RH%. The concentrations of formaldehyde were verified using a recognized standard method (EPA TO-11A).⁵ The MOF-5-based sorbent was more sensitive than the selected commercial molecular sieves towards the analyte, and also more sensitive than Tenax sorbent, the state-of-the-art sorbent for these applications [57]. The detection limit was as low as 0.6 $\mu\text{g m}^{-3}$, and the superior MOF performance was attributed to the ability of the zinc centers to coordinate with formaldehyde [119]. In 2014 Chen et al. used a more stable ZIF-67 coatings on interdigitated Ag-Pd electrodes to detect the same VOC in the 5–500 ppm range (Fig. 12.9A) [58]. These results hold promise for the practical utilization of MOF for the preconcentration of contaminants.

tandem mass spectrometry. Anal. Methods 5 (2013) 4875 with permission from The Royal Society of Chemistry. (C) Reproduced with permission from Q.-L. Li, X. Wang, X.-F. Chen, M.-L. Wang, R.-S. Zhao, In situ hydrothermal growth of ytterbium-based metal-organic framework on stainless steel wire for solid-phase microextraction of polycyclic aromatic hydrocarbons from environmental samples. J. Chromatogr. A 1415 (2015) 11–19. Elsevier. (D) Adapted with permission from del M. Darder, et al., Nanoparticle-directed metal-organic framework/porous organic polymer monolithic supports for flow-based applications. ACS Appl. Mater. Interfaces 9 (2017) 1728–1736. Copyright (2017) American Chemical Society.

⁵ Method available from the online source: <https://www3.epa.gov/ttnamti1/files/ambient/airtox/to-11a.pdf>.

The 2013 work of Zang et al. investigated the use of MIL-101(Cr) as an active sorbent for SPE of seven different polychlorinated biphenyls (PCBs) [122]. PCBs were used primarily as electrical insulating fluids, but due to their persistency in the environment were banned by the US Environmental Protection Agency (EPA) in the 1970s [123]. MIL-101(Cr) was dispersed in acetone and slowly injected into one open end of a polypropylene hollow fiber having an internal diameter of 600 μm and a length of 10 cm (Fig. 12.9B). After sizing down to 2-cm-long pieces, the fibers were sealed and immersed in aqueous solutions of standards or PCBs samples. Parameters like agitation speed, extraction time, temperature, ionic strength, preconditioning of the fibers with organic solvents, and desorption solvent were considered. The optimized extraction conditions for μSPE of PCBs from water sample solutions were found when using an extraction time of 40 minutes at 40°C, under 1000 rpm agitation in the presence of 5% (w/v) sodium chloride. Toluene was used as a preconditioner. Desorption was performed for 10 minutes with 5 mL of hexane in an ultrasonic bath. The results showed a very wide range of linearity in the 5–1000 ng L^{-1} range, with a LOD between 0.15 and 0.63 ng L^{-1} . Real water samples were collected from a river and a recovery of between 80% and 116% was measured.

In 2015 Pino and coworkers investigated three MOFs (HKUST-1, MIL-53, and MOF-5) as sorbents for the uptake of parabens from different sources [124]. Parabens are preservatives used in cosmetics and the pharmaceutical industry, of the general formula $\text{HO-C}_6\text{H}_4\text{-COOR}$ (i.e., esters of *p*-hydroxybenzoic acid). They have been connected with some endocrine disorders [125], and also found in tumor cells [126,127]. The authors used μSPE methods to detect the presence of parabens within the original products and in associated matrices such as human fluids and environmental water. HKUST-1 was the most effective sorbent, with an uptake of up to 0.4 mg g^{-1} in ideal conditions. The LOD determined by high-performance liquid chromatography (HPLC) was down to 0.1 $\mu\text{g L}^{-1}$, with a minimal usage of organic solvent for desorption processes (only 2 mL of methanol per sample).

Wang et al. studied two MOFs, MIL-101(Cr) and MIL-100(Fe), as active materials in μSPE devices [128]. After hydrothermal synthesis, the material was sealed into a polypropylene membrane sheet and exposed to standard aqueous solutions of six different phthalate esters, commonly used plasticizers with an almost ubiquitous presence in water, foodstuff, and soil. Desorption from the sorbent device was performed in methanol under sonication, and the obtained samples were analyzed via GC-MS. The enhancement factors of extraction were found to be between 140 and 190, with efficiencies of recovery between 74% and 94%. LODs were in the 0.004–0.02 $\mu\text{g L}^{-1}$ range. The authors modeled the interaction mode between MOFs and the phthalate esters, finding that MIL-101(Cr) exhibited a higher adsorption strength than MIL-100(Fe). The binding strength trend was also consistent with the enhancement factor obtained experimentally.

In 2015 Asiabi et al. prepared a MOF-5-based μSPE device for the extraction of two model estrogenic drugs, levonorgestrel and megestrol acetate, from human urine [129]. The device used a modified MOF-5 having a methyl-terephthalic acid as ligand with superior water stability compared to the parent MOF-5 [130].

Subsequently, the CH₃-MOF-5 was integrated into a polyacrylonitrile (PAN) nanofiber via electrospinning, using a voltage of 18 kV between the syringe tip and the aluminum foil collection screen. DMF was used as the solvent. A disc of these nanofibers (average diameter of the fiber c. 0.85 μm) was inserted into a 1 mL syringe and fixed with polyethylene frits. Centrifuged and diluted urine samples were then treated with this μSPE device and, after elution with methanol, analyzed via HPLC. The CH₃-MOF-5-enriched PAN nanofibers were remarkably superior to the sole polymer, with LODs around 0.02 μg L⁻¹, one order of magnitude smaller than previously reported methods, with validated recovery in the 82%–95% range.

In a 2015 report by Li et al., MIL-101(Cr) was exploited for μSPE of triazine and phenylurea-based herbicides from vegetable oil samples [131]. The protocol used by the authors (called “reverse extraction”) involved the dilution of an oil sample with hexane. After adding the stationary MOF phase, this mixture was then sonicated for 15 minutes. After centrifugation, the material was diluted with hexane and the analyte eluted from the MIL-101 using methanol in ultrasonic conditions. After another step of centrifugation, the supernatant was dried and dissolved in methanol, then analyzed with HPLC. The authors compared this protocol with another type of extraction method named *QuEChERS* [132]. In this procedure, the oil was mixed with water, acetonitrile, sodium chloride, and magnesium sulfate. The mixture was then placed horizontally and cooled to -20°C, so the upper organic phase containing the extracted compounds remained liquid, whereas the lower oil was frozen. The supernatant was then subsequently purified and dried, then reconstituted with methanol as above. The results for vegetable oil showed a LOD range for the μSPE between 0.585 and 1.04 μg L⁻¹, with a recovery between 93% and 102%. The *QuEChERS* method for the same substrate provided instead a LOD between 1.64 and 2.48 μg L⁻¹, and a recovery between 88% and 100%. The authors attributed the superior selectivity of their method to the way in which the analytes are adsorbed and extracted, while fat and most of the interfering substances remained in the sample solution.

Another example of MOF-immobilized fibers for SPE was provided by Li et al. in the same period, using an Yb-based MOF with 5-aminoisophthalic acid and bpy as ligands [120]. The active layer was hydrothermally grown in situ on pre-etched 2 cm stainless steel wires, which were then immobilized in a microsyringe for sample collection (Fig. 12.9C). A wide range of two- to six-membered rings PAHs was tested in water solutions and analyzed via GC-MS, using EPA Method 610 for validation.⁶ Soil samples were also tested; the analytes were extracted with a 4:1 hexane/acetone mixture and reconstituted in acetonitrile. The results showed very low LODs, ranging from 0.07 (fluoranthene) to 1.67 (naphthalene) ng L⁻¹, with enhancing factors in the 300–2500 range. The authors finally applied the extraction method to real spring water samples, with recovery above 70%.

Leidinger et al. developed in 2016 a solid state gas preconcentrator and sensor of benzene for indoor applications [133]. The authors evaluated both Basolite A100

⁶Method available from the online source: https://www.epa.gov/sites/production/files/2015-10/documents/method_610_1984.pdf.

and C300, the commercially available MIL-53(Al) and HKUST-1, respectively. Tenax was used as the standard sorbent material. The MOF powders were suspended in dibutylether and drop cast on a $3 \times 3 \text{ mm}^2$ alumina heater substrate; an approximate amount of 30 mg of active porous material was deposited. The gas streams were brought onto the heater in suitable chambers that also permitted the outflowing streams to be collected for mass spectrometry monitoring. When using HKUST-1, the system was able to detect benzene as low as 10 ppb; additionally, both MOFs outperformed Tenax by more than two orders of magnitude.

In 2016 Cerdà's team produced a composite of polystyrene (PS)-based beads coated with ZnO@ZIF-8 for the SPE adsorption of phenols. The preparation of the stationary phase involved at the beginning the coating of the beads with a ZnO layer, generated by hydrolysis of zinc acetate with ammonia [134]. After the reaction, the surface of the beads was completely covered with a uniform, crack-free, layer of ZnO about $0.7 \mu\text{m}$ thick. In a subsequent conversion step [135], the immersion of the PS@ZnO beads in a 2-methylimidazole solution in methanol at 80°C enabled the formation of a ZIF-8 layer. The overall thickness increased to $1.5 \mu\text{m}$ due to the expanded structure of the MOF compared to the dense ZnO. The material was then packed into a SPE column and different aqueous solution of phenols were passed through. The adsorption extraction towards bisphenol A for the PS@ZnO@ZIF-8 beads was 50 times higher than the PS@ZnO, with an adsorption capacity of 20 mg g^{-1} . The material was also able to simultaneously uptake two phenols, 4-*tert*-octylphenol and 4-*n*-nonylphenol, with a 100-fold preconcentration of pollutants. Recyclability was tested for c. 10 cycles. In 2017 the same group developed a two-step nanoparticle-directed route for the preparation of macroporous polymer monoliths, in which the pore surface is covered with ZIF-8 [121]. Initially, the bulk monoliths were produced by dispersing ZnO nanoparticles ($<130 \text{ nm}$) in methacrylic acid, that was later co-polymerized in presence of ethylene dimethacrylate, with 2,2'-azobis(2-methylpropionitrile) (AIBN) as radical initiator, in a 1:9 methanol/1-dodecanol mixture. To extend the versatility of this process, the ZnO-polymer composite was also prepared in fused silica capillaries and on PEEK O-rings (Fig. 12.9D). The conversion into ZIF-8 was performed either in batch (for monoliths and PEEK) or in flow (for capillaries under solvothermal conditions, using a 50% DMF solvent mixture in presence of 2-methylimidazole). The monoliths were also converted at room temperature, with the optional addition of butylamine as a promoter of MOF crystallization. The uptake and preconcentration of chlorophenols was monitored by HPLC analysis, demonstrating that ZIF-based monoliths enabled the quantification of chlorophenols at parts per billion level ($3.0\text{--}5.6 \mu\text{g L}^{-1}$).

A recent study conducted by Tokalioglu et al. in 2017 employed SPE to measure the amount of lead in cereals, beverages, and water samples. The authors used the Zr-based MOF-545, with tetrakis(4-carboxyphenyl) porphyrin as ligand and an accessible surface area of $2192 \text{ m}^2 \text{ g}^{-1}$. The measured adsorption capacity for Pb^{2+} was quantified as 73 mg g^{-1} while recyclability up to 40 cycles was successfully tested [136].

In the same period, Wang and Lei used MOF-177, a zinc-based framework with 1,3,5-tris(4-carboxyphenyl)benzene ligand, as the active phase of a head-space μ SPE device for harvesting five types of phenols from water [137]. The work expanded on a similar study conducted earlier by the same team for the uptake of polyhydroxyalkanoates (PHAs) [138]. In both cases, the MOF was attached to a previously etched stainless steel wire of a GC syringe with a silicone-based sealant, with a coating 1 cm in length and about 30 μ m in thickness. The device provided a better response for chlorinated phenols rather than methylated phenols; the measured LODs for PHAs were between 0.016 and 0.027 μ g L⁻¹. Higher values of about 0.04 μ g L⁻¹ were found for methyl phenols. The authors also tested the device with surface, river, and waste waters, obtaining recoveries between 84% and 94%.

12.4.2 Filtration devices

Barreto et al. explored in 2010 the use of a MOF made with 90% lanthanum, 10% europium, and pyridine-2,6-dicarboxylic acid as the ligand to harvest pesticides [139]. The obtained material was isostructural with previously reported La-based MOFs. Lettuce samples were treated using the matrix solid-phase dispersion method as an alternative to the conventional μ SPE technique [140]. The excellent performance of the sorbent toward different classes of pesticides (carbamates, organophosphates, dicarboximides, organochlorines) was demonstrated by the low LOD ranging from 0.02 to 0.05 ppm. Lettuce samples obtained from local markets contained 0.18 ppm of the pirimicarb insecticide, below the law limit of 1 ppm.

The removal of sulfur-based compounds can improve the quality of fuel and reduce motor vehicle pollution. In 2013 Lin et al. developed a polyimide membrane absorber with HKUST-1 for desulfurization [141]. The device was prepared by dispersing the polymer in DMF and THF in the presence of PEG-400 to control the membrane morphology. After gradual addition of HKUST-1 crystals at different loadings (up to 50% in weight), the mixture was cast on a glass plate. The absorber membrane was integrated with a fuel cell using hydrocarbons as the source of hydrogen to demonstrate the effectiveness of the MOF sorbent against thiophene and dibenzothiophene (Fig. 12.10A). The adsorption capacity increased with the HKUST-1 content up to 14.7 mg g⁻¹. Isopropanol was found to be the best viscosity modulator to permit an optimal adsorption; however, ethanol was used for higher fluxes. In the first five cycles, sulfur removal performance showed a regeneration efficiency exceeding 90%.

In 2014 Khanjani and Morsali coated silk fabrics with MOF-5 to obtain a sorbent for the mutagenic Congo Red dye [144]. To obtain the MOF composite, the fabric was preliminarily immersed in a basic activation solution to negatively charge the surface of the fibers, thanks to the abundance of aspartic and glutamic acid residues. Two deposition routes were followed: the first involved LbL deposition of MOF-5 by repeating the following procedure: (1) immersions in a DMF solution of zinc acetate; (2) washing with pure DMF to remove the zinc excess; (3) immersion in a DMF solution containing terephthalic acid and with triethylamine; and

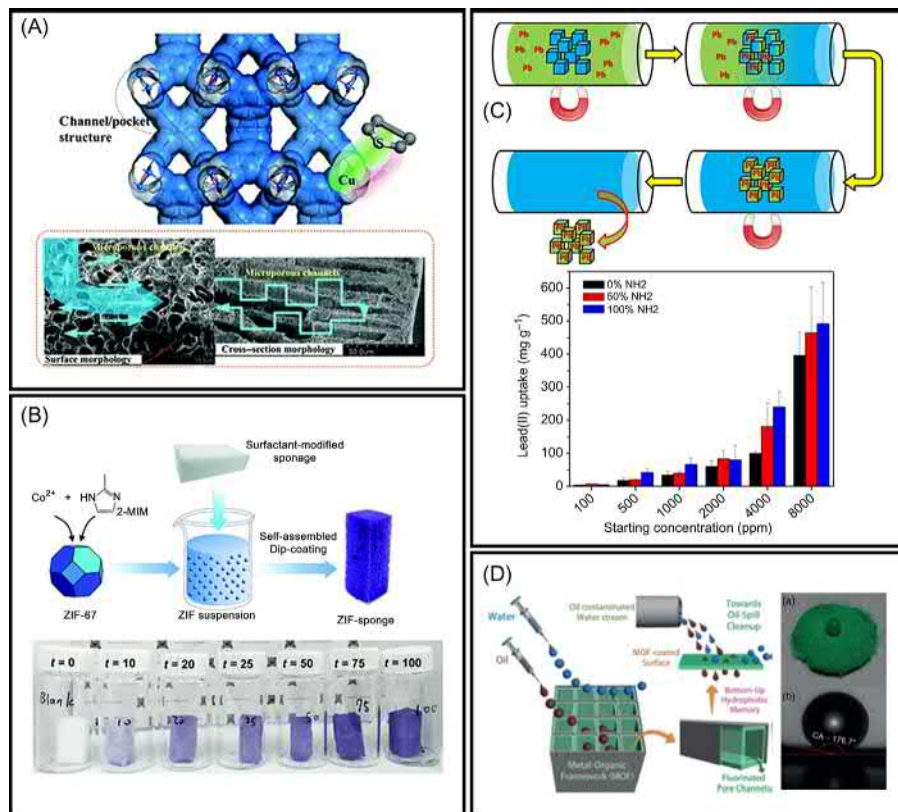


Figure 12.10 (A) The structure of HKUST-1 and its π -complex with thiophene, and the schematic diagram of the microporous channels of the polyimide/HKUST-1 membrane absorber. (B) The preparation process of the Cobalt ZIF-67 sponge requires a surfactant-assisted dip-coating into the MOF dispersion. The photograph shows ZIF sponges prepared at different dip-coating times (in minutes) using 3 g L^{-1} of SDBS as surfactant, at room temperature. (C) Representation of the heavy metal uptake process using magnetic framework composites (MFCs), and lead(II) uptake in water by variously amino-functionalized MIL-53 MFCs with different initial concentrations of Pb(II) ion (100–8000 ppm). (D) Illustration of a fluorinated linker-based porous surface as a potential method for MOF ultrahydrophobicity in MOFs. In the photographs, a water droplet is suspended on a UHMOF-100 pellet; the water-repellent surface has a contact angle of about 176 degrees.

Source: (A) Adapted from L. Lin, et al., Membrane adsorber with metal organic frameworks for sulphur removal. *RSC Adv.* 3 (2013) 9889; (B) K.-Y. Andrew Lin and H.-A. Chang, A zeolitic imidazole framework (ZIF)–sponge composite prepared via a surfactant-assisted dip-coating method. *J. Mater. Chem. A* 3 (2015), 20060–20064; (C) R. Ricco, et al., Lead(II) uptake by aluminium based magnetic framework composites (MFCs) in water. *J. Mater. Chem. A* 3 (2015) 19822–19831 with permission from The Royal Society of Chemistry. (D) Reprinted with permission from S. Mukherjee, et al., An ultrahydrophobic fluororous metal-organic framework derived recyclable composite as a promising platform to tackle marine oil spills. *Chem. Eur. J.* 22 (2016) 10937–10943. Copyright © 2016 by John Wiley & Sons, Inc.

(4) washing with pure DMF to remove the ligand excess. The second deposition route was carried out under ultrasonic conditions at ambient temperature; however, the sequential alternate dipping into the metal and ligand solutions were maintained. After the MOF activation, the fabric composites were immersed in aqueous solutions of dye with a concentration between 5 and 50 ppm. Using the highest dye concentration, a complete adsorption was obtained in 75 minutes.

In 2015 Lin and Chang prepared a composite of ZIF-67 (made with cobalt and 2-methylimidazole) grown on a commercially available melamine-formaldehyde sponge. The composite was used for the adsorption of the model pollutant Malachite Green dye [145]. The device was made by simply dip-coating the surfactant modified sponge into a MOF suspension (Fig. 12.10B). Four different surfactants were selected: SDBS (anionic), CTAB (cationic), Span-80 (nonionic and hydrophobic), and Triton X-100 (nonionic and hydrophilic). After washing with water and ethanol and drying, the maximum combined loading of surfactant and ZIF-67 was obtained with Span-80 (mass increase of 255%), followed by SDBS (155%). For the SDBS sponges, a $1710 \text{ m}^2 \text{ g}^{-1}$ was measured using the Brunauer–Emmett–Teller (BET) theory. The composite was able to take up a remarkable quantity of malachite green dye, up to 4093 mg g^{-1} , without performance loss after four cycles, along with the absence of Co leaching in solution, and no release of MOF crystals during the regeneration processes.

An example of a material tested for heavy metals capture in water was proposed in 2015 by Ricco et al., in which a series of MIL-53(Al)-based magnetic framework composites (MFCs) [146] was prepared with iron oxide nanoparticles, by tuning the 2-aminoterephthalic/terephthalic acid ratio [142]. An advantage of MFCs is the responsiveness to an external magnetic field that allows for dynamic localization [109–111], permitting an easy recovery from solutions, and improving the recyclability (Fig. 12.10C). The materials were tested for Pb^{2+} sequestration capabilities in various solvents (methanol, DMSO, and water) over a wide range of metal ion concentrations (10–8000 ppm). The Pb^{2+} sorption capacity increased when the percentage of $-\text{NH}_2$ groups in the material increased, indicating the important role of amino groups in the Pb^{2+} capture process. This observation was confirmed by density functional theory calculations, revealing a stronger interaction between Pb^{2+} and the MIL-53(Al)- NH_2 matrix. A maximum sorption capacity of nearly 500 mg g^{-1} was found, and the material was also regenerated under magnetic heating. Referring to heavy metals in water, in 2018 Queen's group employed a Fe-BTC treated with dopamine for the uptake of heavy metals and a maximum sorption capacity of nearly 400 mg g^{-1} was found for Pb^{2+} and 1600 mg g^{-1} was measured for Hg^{2+} [147].

In 2016 Mukherjee et al. developed a new Cu-based MOF with a hydrophobic ligand with potential application in marine oil spill remediation [143]. The UHMOF-100 was produced using the 4,4'-{[3,5-bis(trifluoromethyl)phenyl]azanediy}dibenzoic acid ligand, integrated with cross-linked PDMS/PMHS in toluene, and sprayed onto a nonwoven polypropylene fabric film (thickness: $110 \mu\text{m}$) to produce a membrane sorbent, with a contact angle (*vs* water) of 135 degrees (whereas the pure UHMOF-100 registered a value of 176 degrees), evidencing the high

hydrophobic nature of the resulting membrane (Fig. 12.10D). The device was tested with different organic solvents, and also with biodiesel and crude oil, with adsorption capacity between 40% and 70%, almost unaffected by the membrane recycling, using a flux⁷ of about 85 mL s⁻¹ (calculated considering an effective membrane area of around 8.5 cm²).

In the same period, Ragab and coworkers developed a hybrid PTFE/ZIF-8 membrane for water microfiltration; the composite membrane was found to be suitable for the removal of estrogen pollutants [148]. The authors mixed different weight percentages of ZIF-8 in deionized water with pieces of commercial PTFE membranes for 24 hours, followed by drying. To test the material, recirculation experiments were performed at different estrogen concentrations, showing about 85% removal efficiency after three cycles when using PEG-400 as membrane regenerator.

In 2016 Zhang et al. prepared electrospun fibers for the collection of particulate matter (PM) from air using different MOFs (ZIF-8, NH₂-UiO-66(Zr), MOF-199, and Mg-MOF-74) and polymers (PAN, Ps, PVP) [149]. The UiO/PAN filters with a thickness of 33 μm could capture the PM in a real air-polluted environment with high efficiency (PM_{2.5} and PM₁₀ above 88%), and effectively and selectively adsorb toxic gases such as SO₂, with a capacity of 0.019 g g⁻¹, with exceptionally low pressure drop of 20 Pa under a flow rate of 50 mL min⁻¹.

Selenium and arsenic are two toxic elements that are difficult to remove due to their various oxidations states and high solubility. In the 2017 work from He et al., UiO-66(Zr) was tested for the uptake of these elements from aqueous environments [150]. The authors produced thin-film nanocomposite (TFN) membranes by doctor-blading a glass plate with polyether sulfone, followed by a treatment with piperazine and 1,3,5-benzenetricarbonyltrichloride in hexane, containing the UiO-66(Zr) particles with different sizes (30, 100, and 500 nm). The results demonstrated that the particle sizes were not relevant in the rejection⁸ of the considered anions (selenite, selenate, and hydrogen arsenate) from the water solutions. The authors chose the 30 nm composite membrane for its high flux, up to 11.5 LMH bar⁻¹.⁹ Compared to the thin-film composite without MOF, the TFN membranes exhibited

⁷ Here the flux or, better, the *volumetric flux* is intended as the volume of fluid moving per unit area per time (see J.R. Mihelcic Fundamentals of Environmental Engineering, 1999, ISBN: 978-0471243137), although the authors give the information about the area separately.

⁸ The term “rejection” (sometimes found as “retention”) indicates the ability of a membrane to retain the solute in the upstream fluid (retentate) rather than in the downstream one (permeate). The definition comes from the *rejection coefficient* r (or R), using the equation $r = 1 - (C_p/C_r)$, with C_p = concentration in the permeate fluid and C_r = concentration in the retentate fluid. If $r = 1$, the membrane is fully impermeable, and rejection is 100%, if $r = 0$, the membrane is fully permeable, and rejection is 0%. For further information the reader can consult J.D. Ferry, Chem. Rev. 18 (3) (1936) 373–455; L.J. Zeman, J. Membr. Sci. 15 (3) (1983) 213–230; S Poyen et al., J. Membr. Sci. 43 (1) (1989) 47–67; and references thereafter.

⁹ LMH = L/m²/h.

higher rejections for both pollutants (above 96%) due to their smaller pore size and higher hydrophilicity.

In 2017 Karmakar and collaborators evaluated aluminum fumarate (commercially marketed as Basolite A520) in a mixed matrix membrane (MMM) system incorporating cellulose acetate phthalate (CAP) [151]. This MMM was produced by casting a solution of MOF and CAP in DMF on a nonwoven polyester fabric attached to a glass plate. The authors intended to use the MMM for fluoride removal in aqueous solutions, reaching an uptake of 179 mg g^{-1} when using a membrane with a 10% aluminum fumarate loading. The system was also able to remove other contaminants like iron and alkaline substances, reducing hardness and total dissolved solids.

12.4.3 Fluidic devices

The possibility to use MOFs as sorbent materials for continuous separation was investigated in 2013 by Van Assche and Denayer with the production of a microseparator device [152], in five steps: initially, a $100 \mu\text{m}$ PEEK layer was applied on one side of $300\text{-}\mu\text{m}$ -thick copper sheets. After precise milling of the track needed as a channel for flowing the analyte, a PEEK back cover was applied to induce formation of HKUST-1 only inside the channel. By using an electrochemical synthesis method, the MOF layer was rapidly grown inside the microchannels and, after removing the plastic covers, the copper sheets were placed inside a custom-built aluminum holder, using a fluoropolymer gasket between the final sheet and the holder bottom (Fig. 12.11A). Methanol and *n*-hexane were chosen as polar and non-polar VOCs to be adsorbed on the HKUST-1 material at 40°C . The device was found to be leak free and allowed for the separation of *n*-hexane and methanol vapors, with a 400 mg g^{-1} methanol adsorption capability. Adsorption rates for the microseparator were one order of magnitude faster when compared to a conventional packed bed.

In 2015 Ferreira et al. presented a study involving MIL-53(Al) for the purification of methane from carbon dioxide. The authors used the commercially available version of this MOF (Basolite A100) and integrated it in a Pressure Swing Adsorption (PSA) system (Fig. 12.11B). This technology enables the separation of gas mixtures according to the characteristics of the components and the affinity to the adsorbent materials [155]. A stainless steel cylindrical column ($284 \text{ cm long} \times 21.6 \text{ cm wide}$) was packed with 52.3 g of MIL-53(Al). Three thermocouples were placed in three different positions (near the two extremities and in the center) to monitor the temperature, and the gas flows were monitored with an infrared analyzer. Both lab scale and industrial scale PSA systems were evaluated, and the Langmuir model was considered to describe the adsorption isotherms thanks to its simplicity, thermodynamic consistency, and easy usability in simulations. The authors considered two case studies involving biogas and natural gas. In the first process, both carbon dioxide and methane were obtained with high purity and recovery (CO_2 : 95.4% purity and 99.6% recovery; CH_4 : 99.4% purity and 95.8% recovery), with a power consumption of $17 \text{ W h mol}^{-1} \text{ CH}_4$. In the second process, only methane was

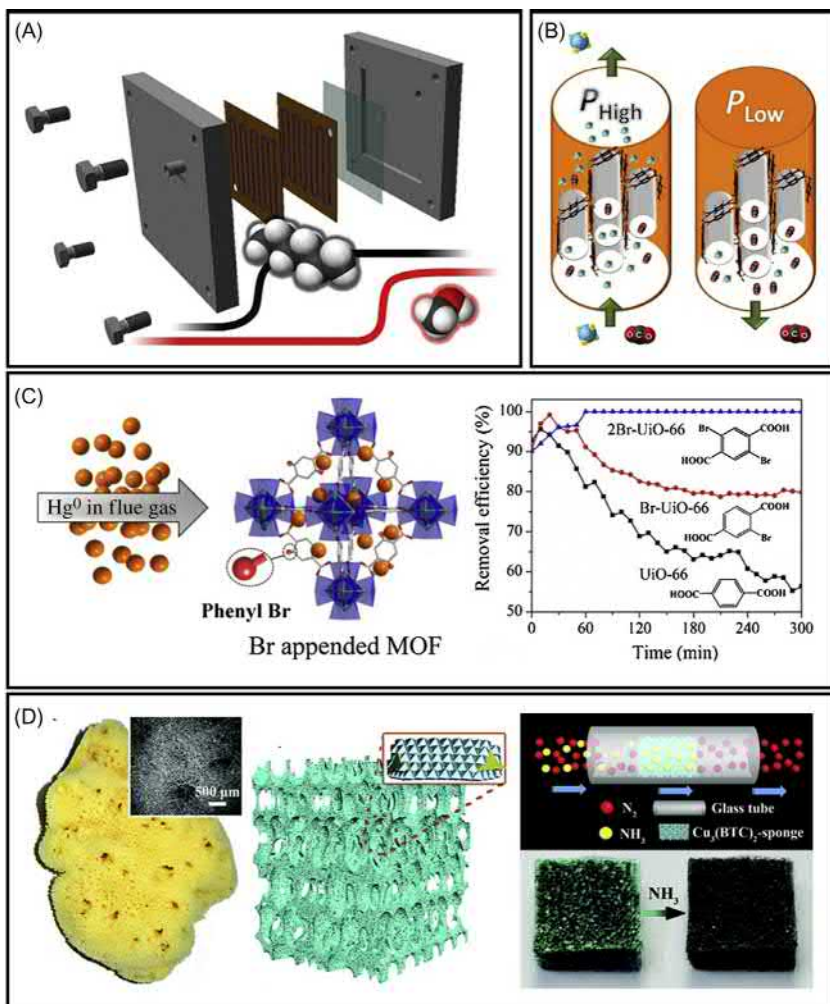


Figure 12.11 (A) A microseparator assembly, used for the partition between hexane and methanol, showing the sheets containing the HKUST-1-coated microchannels (brown). (B) A representation of a Pressure Swing Adsorption module used to separate carbon dioxide and methane with MIL-53(Al) MOF as sorbent. (C) The bromine-modified UiO-66 MOF is here illustrated as a sorbent for mercury vapor in flue gas, along with a graph of the efficiency versus time curves of the UiO-66 series. (D) Photographs of a marine sponge with an electron microscope image of its porous structure in the inset, and a schematic illustration of the sponge skeleton and the crystal-coating of the HKUST-1/sponge. On the right, the scheme shows the dynamic adsorption process of ammonia and the color change of the HKUST-1/sponge before (left) and after (right) ammonia adsorption.

Source: (A) Reproduced with permission from T.R.C. Van Assche, J.F.M. Denayer, Fabrication and separation performance evaluation of a metal-organic framework based microseparator device. *Chem. Eng. Sci.* 95 (2013) 65–72; (B) A.F.P. Ferreira, A.M. Ribeiro, A. S. Kulaç, A.E. Rodrigues, Methane purification by adsorptive processes on MIL-53(Al). *Chem. Eng. Sci.* 124 (2015) 79–95; (C) X. Zhang, B. Shen, S. Zhu, H. Xu, L. Tian, UiO-66 and its Br-modified derivatives for elemental mercury removal. *J. Hazard. Mater.* 320 (2016) 556–563. Elsevier. (D) Adapted from H. Li, et al., Three dimensional MOF–sponge for fast dynamic adsorption. *Phys. Chem. Chem. Phys.* 19 (2017) 5746–5752 with permission from the PCCP Owner Societies.

appreciably recovered (72.9%) with high purity (97.3%), with a power consumption of $5.1 \text{ W h mol}^{-1} \text{ CH}_4$.

In the same period, Zhang et al. developed brominated versions of UiO-66(Zr) MOF, using 2-bromo or 2,5-dibromo terephthalic acid as ligand, for the removal of elemental mercury from simulated flue gas [153]. Nitrogen was used as the carrier gas to introduce Hg(0) vapors into a U-shaped mixing chamber containing the MOF (Fig. 12.11C). The removal efficiency at different temperatures (80°C, 120°C, 160°C, 200°C, and 240°C) was investigated, obtaining a 49% enhancement when the temperature was increased from 80°C to 120°C for the dibromo-derivative (with an almost complete removal of mercury at 200°C). Water had a negative effect on the sorbent owing to the decomposition of the porous crystals. SO₂ led to an enhanced Hg(0) removal efficiency due to an enrichment in sulfite active sites.

In the 2017 study from Li et al., HKUST-1 modified polyurethane sponges were obtained by immersion into an ethanol solution of the precursors (copper nitrate and trimesic acid) [154]. The material was then used for the adsorption of ammonia gas by flowing it in nitrogen and collecting downstream into an aqueous solution containing the indicator methyl orange (Fig. 12.11D). By monitoring the color change via absorption spectroscopy (related to the pH in solution and thus the amount of ammonia), the authors could obtain an adsorption capacity of 101.6 mg g^{-1} of ammonia. The experiment was repeated also for the uptake of rhodamine B in aqueous solution following the color intensity change. In this case the HKUST-1/sponge system reached an adsorption capacity of 10.4 mg g^{-1} at full saturation.

12.5 Summary

In this chapter we discussed the current status of MOF-based devices for environmental remediation. The progress in the field of MOF-based devices has been dictated by several components, including the preparation of customized MOFs with a high affinity toward the adsorbate, the fabrication of MOFs with improved water stability, and the development of suitable MOF positioning methods. MOFs have demonstrated outstanding properties for the detection and the removal of different pollutants. These properties have been exploited for both pollutant detection and removal. Major developments in sensing applications focused on gas phase or vapors. Among the different platforms used for the detection of these species, the mechanical response is the most widely studied (e.g., QCM methods). A different and emerging approach is the chemoresistive response, which requires MOFs or composites with specific electrical properties (e.g., Kelvin probe). Although optical responses are still under development, a rapid expansion of this methodology can be envisaged, due to the increasing portability of different spectrometers. The research into MOF-based devices for pollutant sequestration is still at an early stage, and further development should be done to bring this class of porous materials toward practical applications. However, the suitability of MOFs as potent

preconcentrator sorbents for SPE and molecular sieves has been largely demonstrated. With the increasing availability of customized synthetic methodologies, it will be possible to push forward the preparation of fluidic devices for continuous sequestration.

References

- [1] P. Falcaro, et al., MOF positioning technology and device fabrication, *Chem. Soc. Rev.* 43 (2014) 5513–5560.
- [2] Y. Wen, G. Schoups, N. van de Giesen, Organic pollution of rivers: combined threats of urbanization, livestock farming and global climate change, *Sci. Rep.* 7 (2017) 43289.
- [3] B. Liu, Metal–organic framework-based devices: separation and sensors, *J. Mater. Chem.* 22 (2012) 10094.
- [4] T.M.A. Gronewold, Surface acoustic wave sensors in the bioanalytical field: recent trends and challenges, *Anal. Chim. Acta* 603 (2007) 119–128.
- [5] K. Länge, B.E. Rapp, M. Rapp, Surface acoustic wave biosensors: a review, *Anal. Bioanal. Chem.* 391 (2008) 1509–1519.
- [6] X. Ding, et al., Surface acoustic wave microfluidics, *Lab. Chip* 13 (2013) 3626.
- [7] L.E. Kreno, et al., Metal–organic framework materials as chemical sensors, *Chem. Rev.* 112 (2012) 1105–1125.
- [8] C.K. O’Sullivan, G.G. Guilbault, Commercial quartz crystal microbalances—theory and applications, *Biosens. Bioelectron* 14 (1999) 663–670.
- [9] A. Janshoff, H.-J. Galla, C. Steinem, Piezoelectric mass-sensing devices as biosensors—an alternative to optical biosensors? *Angew. Chem.* 39 (2000) 4004–4032.
- [10] K.A. Marx, Quartz crystal microbalance: a useful tool for studying thin polymer films and complex biomolecular systems at the solution–surface interface, *Biomacromolecules* 4 (2003) 1099–1120.
- [11] Y. Sun, Z. Hu, D. Zhao, K. Zeng, Probing nanoscale functionalities of metal–organic framework nanocrystals, *Nanoscale* 9 (2017) 12163–12169.
- [12] C. Wang, L. Yin, L. Zhang, D. Xiang, R. Gao, Metal oxide gas sensors: sensitivity and influencing factors, *Sensors* 10 (2010) 2088–2106.
- [13] D.W. Greve, et al., Surface acoustic wave devices for harsh environment wireless sensing, *Sensors* 13 (2013) 6910–6935.
- [14] S. Sivaramakrishnan, et al., Carbon nanotube-coated surface acoustic wave sensor for carbon dioxide sensing, *Sens. Actuators B Chem.* 132 (2008) 296–304.
- [15] S. Xu, et al., Carbon dioxide sensors based on a surface acoustic wave device with a graphene–nickel–L-alanine multilayer film, *J. Mater. Chem. C* 3 (2015) 3882–3890.
- [16] K. Korsah, C.L. Ma, B. Dress, Harmonic frequency analysis of SAW resonator chemical sensors: application to the detection of carbon dioxide and humidity. Research sponsored by the Laboratory Directed Research and Development Program of Oak Ridge National Laboratory, managed by Lockheed Martin Energy Research Corporation for the US Department of Energy under Contract No. DE-AC05-96OR22464.1, *Sens. Actuators B Chem.* 50 (1998) 110–116.
- [17] C. Lim, W. Wang, S. Yang, K. Lee, Development of SAW-based multi-gas sensor for simultaneous detection of CO₂ and NO₂, *Sens. Actuators B Chem.* 154 (2011) 9–16.

- [18] T.R. Zeitler, M.D. Allendorf, J.A. Greathouse, Grand canonical Monte Carlo simulation of low-pressure methane adsorption in nanoporous framework materials for sensing applications, *J. Phys. Chem. C* 116 (2012) 3492–3502.
- [19] S. Ma, et al., Metal-organic framework from an anthracene derivative containing nanoscopic cages exhibiting high methane uptake, *J. Am. Chem. Soc.* 130 (2008) 1012–1016.
- [20] A.L. Robinson, et al., Ultrasensitive humidity detection using metal–organic framework-coated microsensors, *Anal. Chem.* 84 (2012) 7043–7051.
- [21] B. Paschke, A. Wixforth, D. Denysenko, D. Volkmer, Fast surface acoustic wave-based sensors to investigate the kinetics of gas uptake in ultra-microporous frameworks, *ACS Sens.* 2 (2017) 740–747.
- [22] S. Biswas, et al., A cubic coordination framework constructed from benzobistriazolate ligands and zinc ions having selective gas sorption properties, *Dalton Trans.* 0 (2009) 6487–6495.
- [23] D. Denysenko, et al., Elucidating gating effects for hydrogen sorption in MFU-4-type triazolate-based metal-organic frameworks featuring different pore sizes, *Chem. Eur. J.* 17 (2011) 1837–1848.
- [24] J. Devkota, et al., Zeolitic imidazolate framework-coated acoustic sensors for room temperature detection of carbon dioxide and methane, *Nanoscale* 10 (2018) 8075–8087.
- [25] I. Stassen, et al., Chemical vapour deposition of zeolitic imidazolate framework thin films, *Nat. Mater.* 15 (2015) 304–310.
- [26] K. Liang, et al., Biomimetic replication of microscopic metal–organic framework patterns using printed protein patterns, *Adv. Mater.* 27 (2015) 7293–7298.
- [27] A. Bétard, S. Wannapaiboon, R.A. Fischer, Assessing the adsorption selectivity of linker functionalized, moisture-stable metal–organic framework thin films by means of an environment-controlled quartz crystal microbalance, *Chem. Commun.* 48 (2012) 10493.
- [28] M. Tu, S. Wannapaiboon, R.A. Fischer, Liquid phase stepwise growth of surface mounted metal–organic frameworks for exploratory research and development of applications, *Inorg. Chem. Front.* 1 (2014) 442.
- [29] M. Tu, S. Wannapaiboon, R.A. Fischer, Programmed functionalization of SURMOFs via liquid phase heteroepitaxial growth and post-synthetic modification, *Dalton Trans.* 42 (2013) 16029.
- [30] M.D. Allendorf, et al., Stress-induced chemical detection using flexible metal–organic frameworks, *J. Am. Chem. Soc.* 130 (2008) 14404–14405.
- [31] Lee, J.-H. et al. Investigation of microcantilever array with ordered nanoporous coatings for selective chemical detection, in: T. George, M.S. Islam, A.K. Dutta (Eds.), *Proceedings Volume 7679, Micro- and Nanotechnology Sensors, Systems, and Applications II; 767927*, Orlando, FL, 2010. doi:10.1117/12.850217.
- [32] A.L. Robinson, M. Allendorf, V. Stavila, S.M. Thornberg, MOF films for microsensor coatings, *MRS Proc* 1366 (2011).
- [33] A. Venkatasubramanian, et al., MOF @ MEMS: design optimization for high sensitivity chemical detection, *Sens. Actuators B Chem.* 168 (2012) 256–262.
- [34] I. Ellern, et al., Characterization of piezoresistive microcantilever sensors with metal organic frameworks for the detection of volatile organic compounds, *ECS Trans.* 50 (2013) 469–476.
- [35] P. Hesketh, et al., HKUST-1 coated piezoresistive microcantilever array for volatile organic compound sensing, *Micro Nano Lett.* 8 (2013) 766–769.

- [36] L. Heinke, M. Tu, S. Wannapaiboon, R.A. Fischer, C. Wöll, Surface-mounted metal-organic frameworks for applications in sensing and separation, *Microporous Mesoporous Mater.* 216 (2015) 200–215.
- [37] P. Falcaro, D. Buso, A.J. Hill, C.M. Doherty, Patterning techniques for metal organic frameworks, *Adv. Mater.* 24 (2012) 3153–3168.
- [38] M. Tu, R.A. Fischer, Heteroepitaxial growth of surface mounted metal–organic framework thin films with hybrid adsorption functionality, *J. Mater. Chem. A* 2 (2014) 2018–2022.
- [39] M. Tu, S. Wannapaiboon, K. Khaletskaia, R.A. Fischer, Engineering zeolitic-imidazolate framework (ZIF) thin film devices for selective detection of volatile organic compounds, *Adv. Funct. Mater.* 25 (2015) 4470–4479.
- [40] H. Uehara, et al., Porous coordination polymer hybrid device with quartz oscillator: effect of crystal size on sorption kinetics, *J. Am. Chem. Soc.* 133 (2011) 11932–11935.
- [41] L.E. Kreno, J.T. Hupp, R.P. Van Duyne, Metal–organic framework thin film for enhanced localized surface plasmon resonance gas sensing, *Anal. Chem.* 82 (2010) 8042–8046.
- [42] G. Lu, O.K. Farha, W. Zhang, F. Huo, J.T. Hupp, Engineering ZIF-8 thin films for hybrid MOF-based devices, *Adv. Mater.* 24 (2012) 3970–3974.
- [43] X. Chong, et al., Surface-enhanced infrared absorption: pushing the frontier for on-chip gas sensing, *ACS Sens.* 3 (2018) 230–238.
- [44] Y. Li, S. Zhang, D. Song, A luminescent metal-organic framework as a turn-on sensor for DMF vapor, *Angew. Chem. Int. Ed.* 52 (2013) 710–713.
- [45] Y. Haas, G. Stein, Pathways of radiative and radiationless transitions in europium(III) solutions. The role of high energy vibrations, *J. Phys. Chem.* 75 (1971) 3677–3681.
- [46] A. Hatta, T. Ohshima, W. Suëtaka, Observation of the enhanced infrared absorption of *p*-nitrobenzoate on Ag island films with an ATR technique, *Appl. Phys. A* 29 (1982) 71–75.
- [47] A. Hartstein, J.R. Kirtley, J.C. Tsang, Enhancement of the infrared absorption from molecular monolayers with thin metal overlayers, *Phys. Rev. Lett.* 45 (1980) 201–204.
- [48] W. Zhan, et al., Semiconductor@metal–organic framework core–shell heterostructures: a case of ZnO@ZIF-8 nanorods with selective photoelectrochemical response, *J. Am. Chem. Soc.* 135 (2013) 1926–1933.
- [49] M.K. Smith, K.E. Jensen, P.A. Pivak, K.A. Mirica, Direct self-assembly of conductive nanorods of metal–organic frameworks into chemiresistive devices on shrinkable polymer films, *Chem. Mater.* 28 (2016) 5264–5268.
- [50] G. Wu, J. Huang, Y. Zang, J. He, G. Xu, Porous field-effect transistors based on a semiconductive metal–organic framework, *J. Am. Chem. Soc.* 139 (2017) 1360–1363.
- [51] A.A. Karyakin, et al., Prussian blue based nanoelectrode arrays for H₂O₂ detection, *Anal. Chem.* 76 (2004) 474–478.
- [52] A.E. Albers, V.S. Okreglak, C.J. Chang, A FRET-based approach to ratiometric fluorescence detection of hydrogen peroxide, *J. Am. Chem. Soc.* 128 (2006) 9640–9641.
- [53] K. Okada, et al., Copper conversion into Cu(OH)₂ nanotubes for positioning Cu₃(BTC)₂ MOF crystals: controlling the growth on flat plates, 3D architectures, and as patterns, *Adv. Funct. Mater.* 24 (2014) 1969–1977.
- [54] P. Falcaro, et al., Centimetre-scale micropore alignment in oriented polycrystalline metal-organic framework films via heteroepitaxial growth, *Nat. Mater.* 16 (2017) 342–348.
- [55] K. Okada, et al., Electrochemical sensing and catalysis using Cu₃ (BTC)₂ coating electrodes from Cu(OH)₂ films, *CrystEngComm* 19 (2017) 4194–4200.

- [56] M. Campbell, M. Dincă, Metal–organic frameworks as active materials in electronic sensor devices, *Sensors* 17 (2017) 1108.
- [57] M. Fuentes-Cabrera, D.M. Nicholson, B.G. Sumpter, M. Widom, Electronic structure and properties of isorecticular metal-organic frameworks: The case of M-IRMOF1 (M = Zn, Cd, Be, Mg, and Ca), *J. Chem. Phys.* 123 (2005) 124713.
- [58] E.-X. Chen, H. Yang, J. Zhang, Zeolitic imidazolate framework as formaldehyde gas sensor, *Inorg. Chem.* 53 (2014) 5411–5413.
- [59] M.S. Hosseini, S. Zeinali, M.H. Sheikhi, Fabrication of capacitive sensor based on Cu-BTC (MOF-199) nanoporous film for detection of ethanol and methanol vapors, *Sens. Actuators B Chem.* 230 (2016) 9–16.
- [60] S. Homayoonnia, S. Zeinali, Design and fabrication of capacitive nanosensor based on MOF nanoparticles as sensing layer for VOCs detection, *Sens. Actuators B Chem.* 237 (2016) 776–786.
- [61] M.G. Campbell, S.F. Liu, T.M. Swager, M. Dincă, Chemiresistive sensor arrays from conductive 2D metal–organic frameworks, *J. Am. Chem. Soc.* 137 (2015) 13780–13783.
- [62] M.G. Campbell, D. Sheberla, S.F. Liu, T.M. Swager, M. Dincă, Cu₃ (hexaiminotriphenylene)₂: an electrically conductive 2D metal-organic framework for chemiresistive sensing, *Angew. Chem. Int. Ed.* 54 (2015) 4349–4352.
- [63] S. Achmann, et al., Metal-organic frameworks for sensing applications in the gas phase, *Sensors* 9 (2009) 1574–1589.
- [64] E.-X. Chen, H.-R. Fu, R. Lin, Y.-X. Tan, J. Zhang, Highly selective and sensitive trimethylamine gas sensor based on cobalt imidazolate framework material, *ACS Appl. Mater. Interfaces* 6 (2014) 22871–22875.
- [65] O. Yassine, et al., H₂S sensors: fumarate-based FCU-MOF thin film grown on a capacitive interdigitated electrode, *Angew. Chem. Int. Ed.* 55 (2016) 15879–15883.
- [66] M. Hmadeh, et al., New porous crystals of extended metal-catecholates, *Chem. Mater.* 24 (2012) 3511–3513.
- [67] T. Kambe, et al., π -Conjugated nickel bis(dithiolene) complex nanosheet, *J. Am. Chem. Soc.* 135 (2013) 2462–2465.
- [68] D. Sheberla, et al., High electrical conductivity in Ni₃ (2,3,6,7,10,11-hexamino-triphenylene)₂, a semiconducting metal–organic graphene analogue, *J. Am. Chem. Soc.* 136 (2014) 8859–8862.
- [69] S. Joo, R.B. Brown, Chemical sensors with integrated electronics, *Chem. Rev.* 108 (2008) 638–651.
- [70] J. Janata, Thirty years of CHEMFETs—a personal view, *Electroanalysis* 16 (2004) 1831–1835.
- [71] T. Panda, R. Banerjee, High charge carrier mobility in two dimensional indium (III) isophthalic acid based frameworks, *Proc. Natl. Acad. Sci. India Sect. Phys. Sci.* 84 (2014) 331–336.
- [72] R. Pohle, A. Tawil, P. Davydovskaya, M. Fleischer, Metal organic frameworks as promising high surface area material for work function gas sensors, *Procedia Eng.* 25 (2011) 108–111.
- [73] P. Davydovskaya, et al., Work function based sensing of alkanes and alcohols with benzene tricarboxylate linked metal organic frameworks, *Sens. Actuators B Chem.* 193 (2014) 911–917.
- [74] V. Pentyala, P. Davydovskaya, M. Ade, R. Pohle, G. Urban, Metal–organic frameworks for alcohol gas sensor, *Sens. Actuators B Chem.* 222 (2016) 904–909.

- [75] B.L. Newman, Carbon dioxide (carbonic acid gas), *Am. Ind. Hyg. Assoc. J.* 25 (1964) 519–521.
- [76] Documentation of the Threshold Limit Values and Biological Exposure Indices, ACGIH Worldwide, 7th Edition, 2001, ISBN:9781882417438.
- [77] J. Yeom et al., Enhanced toxic gas detection using a MEMS preconcentrator coated with the metal organic framework absorber, in: 21st IEEE International Conference on Micro Electro Mechanical Systems, MEMS 2008 Tucson, Tucson, AZ, IEEE, 2008, pp. 232–235. doi:10.1109/MEMSYS.2008.4443635.
- [78] I. Oh, R.I. Masel, Electrochemical organophosphate sensor based on oxime chemistry, *Electrochem. Solid-State Lett* 10 (2007) J19–J22.
- [79] Y. Yue, et al., A flexible metal–organic framework: guest molecules controlled dynamic gas adsorption, *J. Phys. Chem. C* 119 (2015) 9442–9449.
- [80] I. Stassen, et al., Towards metal–organic framework based field effect chemical sensors: UiO-66-NH₂ for nerve agent detection, *Chem. Sci.* 7 (2016) 5827–5832.
- [81] X. Chong, et al., Near-infrared absorption gas sensing with metal-organic framework on optical fibers, *Sens. Actuators B Chem.* 232 (2016) 43–51.
- [82] X. Chong, et al., Plasmonic nanopatch array with integrated metal–organic framework for enhanced infrared absorption gas sensing, *Nanotechnology* 28 (2017) 26LT01.
- [83] M. Ko, A. Aykanat, M. Smith, K. Mirica, Drawing sensors with ball-milled blends of metal-organic frameworks and graphite, *Sensors* 17 (2017) 2192.
- [84] M.K. Smith, K.A. Mirica, Self-organized frameworks on textiles (SOFT): conductive fabrics for simultaneous sensing, capture, and filtration of gases, *J. Am. Chem. Soc.* 139 (2017) 16759–16767.
- [85] M.-S. Yao, et al., Layer-by-layer assembled conductive metal-organic framework nano-films for room-temperature chemiresistive sensing, *Angew. Chem. Int. Ed.* 56 (2017) 16510–16514.
- [86] N. Nidamanuri, S. Saha, Metal-organic frameworks with tunable electrical and optical properties, in: R. Banerjee (Ed.), *Monographs in Supramolecular Chemistry*, Royal Society of Chemistry, 2017, pp. 217–246. doi:10.1039/9781788010276-00217.
- [87] K. Rui, et al., Dual-function metal–organic framework-based wearable fibers for gas probing and energy storage, *ACS Appl. Mater. Interfaces* 10 (2018) 2837–2842.
- [88] Y. Liu, Y. Zhao, B. Sun, C. Chen, Understanding the toxicity of carbon nanotubes, *Acc. Chem. Res.* 46 (2013) 702–713.
- [89] W. Qi, et al., Curing the toxicity of multi-walled carbon nanotubes through native small-molecule drugs, *Sci. Rep.* 7 (2017) 2815.
- [90] S.D. Piccot, J.J. Watson, J.W. Jones, A global inventory of volatile organic compound emissions from anthropogenic sources, *J. Geophys. Res. Atmospheres* 97 (1992) 9897–9912.
- [91] B. Armstrong, E. Hutchinson, J. Unwin, T. Fletcher, Lung cancer risk after exposure to polycyclic aromatic hydrocarbons: a review and meta-analysis, *Environ. Health Perspect.* 112 (2004) 970–978.
- [92] X. Zou, G. Zhu, I.J. Hewitt, F. Sun, S. Qiu, Synthesis of a metal–organic framework film by direct conversion technique for VOCs sensing, *Dalton Trans.* (2009) 3009–3013. Available from: <https://doi.org/10.1039/B822248G>.
- [93] F. Hinterholzinger, C. Scherb, T. Ahnfeldt, N. Stock, T. Bein, Oriented growth of the functionalized metal–organic framework CAU-1 on –OH- and –COOH-terminated self-assembled monolayers, *Phys. Chem. Chem. Phys.* 12 (2010) 4515.

- [94] G. Lu, J.T. Hupp, Metal–organic frameworks as sensors: a ZIF-8 based Fabry–Pérot device as a selective sensor for chemical vapors and gases, *J. Am. Chem. Soc.* 132 (2010) 7832–7833.
- [95] C.-Y. Huang, M. Song, Z.-Y. Gu, H.-F. Wang, X.-P. Yan, Probing the adsorption characteristic of metal–organic framework MIL-101 for volatile organic compounds by quartz crystal microbalance, *Environ. Sci. Technol.* 45 (2011) 4490–4496.
- [96] M.M. Dubinin, V.A. Astakhov, Development of the concepts of volume filling of micropores in the adsorption of gases and vapors by microporous adsorbents, *Bull. Acad. Sci. USSR Div. Chem. Sci.* 20 (1971) 3–7.
- [97] P. Davydovskaya, R. Pohle, A. Tawil, M. Fleischer, Work function based gas sensing with Cu-BTC metal-organic framework for selective aldehyde detection, *Sens. Actuators B Chem.* 187 (2013) 142–146.
- [98] B. Liu, M. Tu, R.A. Fischer, Metal-organic framework thin films: crystallite orientation dependent adsorption, *Angew. Chem. Int. Ed.* 52 (2013) 3402–3405.
- [99] B. Liu, M. Tu, D. Zacher, R.A. Fischer, Multi variant surface mounted metal-organic frameworks, *Adv. Funct. Mater.* 23 (2013) 3790–3798.
- [100] S. Wannapaiboon, M. Tu, R.A. Fischer, Liquid phase heteroepitaxial growth of moisture-tolerant MOF-5 isotype thin films and assessment of the sorption properties by quartz crystal microbalance, *Adv. Funct. Mater.* 24 (2014) 2696–2705.
- [101] S. Wannapaiboon, et al., Hierarchical structuring of metal–organic framework thin-films on quartz crystal microbalance (QCM) substrates for selective adsorption applications, *J. Mater. Chem. A* 3 (2015) 23385–23394.
- [102] A. Bouchaala, et al., Nonlinear-based MEMS sensors and active switches for gas detection, *Sensors* 16 (2016) 758.
- [103] O. Dalstein, et al., Nanoimprinted, submicrometric, MOF-based 2D photonic structures: toward easy selective vapors sensing by a smartphone camera, *Adv. Funct. Mater.* 26 (2016) 81–90.
- [104] S. Sachdeva, et al., Polymer–metal organic framework composite films as affinity layer for capacitive sensor devices, *ACS Sens.* 1 (2016) 1188–1192.
- [105] S. Sachdeva, et al., Gas phase sensing of alcohols by metal organic framework–polymer composite materials, *ACS Appl. Mater. Interfaces* 9 (2017) 24926–24935.
- [106] F. Qu, et al., Metal-organic frameworks-derived porous ZnO/Ni_{0.9}Zn_{0.1}O double-shelled nanocages as gas sensing material for selective detection of xylene, *Sens. Actuators B Chem.* 252 (2017) 649–656.
- [107] T. Zhou, et al., Pore size dependent gas-sensing selectivity based on ZnO@ZIF nanorod arrays, *Sens. Actuators B Chem.* 258 (2018) 1099–1106.
- [108] W. Vandezande, et al., Parts per million detection of alcohol vapors via metal organic framework functionalized surface plasmon resonance sensors, *Anal. Chem.* 89 (2017) 4480–4487.
- [109] P. Falcaro, et al., Dynamic control of MOF-5 crystal positioning using a magnetic field, *Adv. Mater.* 23 (2011) 3901–3906.
- [110] C.M. Doherty, et al., Magnetic framework composites for polycyclic aromatic hydrocarbon sequestration, *J. Mater. Chem.* 22 (2012) 11470.
- [111] P. Falcaro, et al., Positioning an individual metal–organic framework particle using a magnetic field, *J. Mater. Chem. C* 1 (2013) 42–45.
- [112] K.S. Asha, K. Bhattacharyya, S. Mandal, Discriminative detection of nitro aromatic explosives by a luminescent metal–organic framework, *J. Mater. Chem. C* 2 (2014) 10073–10081.

- [113] L.-L. Wu, et al., A metal-organic framework/DNA hybrid system as a novel fluorescent biosensor for mercury(II) ion detection, *Chem. Eur. J.* 22 (2016) 477–480.
- [114] N. Dave, M.Y. Chan, P.-J.J. Huang, B.D. Smith, J. Liu, Regenerable DNA-functionalized hydrogels for ultrasensitive, instrument-free mercury(II) detection and removal in water, *J. Am. Chem. Soc.* 132 (2010) 12668–12673.
- [115] M. Nazari, et al., UiO-66 MOF end-face-coated optical fiber in aqueous contaminant detection, *Opt. Lett.* 41 (2016) 1696.
- [116] M.-C. Hennion, Solid-phase extraction: method development, sorbents, and coupling with liquid chromatography, *J. Chromatogr. A* 856 (1999) 3–54.
- [117] X.-Y. Cui, et al., In situ hydrothermal growth of metal–organic framework 199 films on stainless steel fibers for solid-phase microextraction of gaseous benzene homologues, *Anal. Chem.* 81 (2009) 9771–9777.
- [118] Z.-Y. Gu, G. Wang, X.-P. Yan, MOF-5 metal–organic framework as sorbent for in-field sampling and preconcentration in combination with thermal desorption GC/MS for determination of atmospheric formaldehyde, *Anal. Chem.* 82 (2010) 1365–1370.
- [119] J.L.C. Rowsell, Gas adsorption sites in a large-pore metal-organic framework, *Science* 309 (2005) 1350–1354.
- [120] Q.-L. Li, X. Wang, X.-F. Chen, M.-L. Wang, R.-S. Zhao, In situ hydrothermal growth of ytterbium-based metal–organic framework on stainless steel wire for solid-phase microextraction of polycyclic aromatic hydrocarbons from environmental samples, *J. Chromatogr. A* 1415 (2015) 11–19.
- [121] M. Darder, M. del, et al., Nanoparticle-directed metal–organic framework/porous organic polymer monolithic supports for flow-based applications, *ACS Appl. Mater. Interfaces* 9 (2017) 1728–1736.
- [122] H. Zang, et al., Hollow fiber-protected metal–organic framework materials as micro-solid-phase extraction adsorbents for the determination of polychlorinated biphenyls in water samples by gas chromatography-tandem mass spectrometry, *Anal. Methods* 5 (2013) 4875.
- [123] M.D. Erickson, R.G. Kaley, Applications of polychlorinated biphenyls, *Environ. Sci. Pollut. Res.* 18 (2011) 135–151.
- [124] P. Rocío-Bautista, et al., The metal–organic framework HKUST-1 as efficient sorbent in a vortex-assisted dispersive micro solid-phase extraction of parabens from environmental waters, cosmetic creams, and human urine, *Talanta* 139 (2015) 13–20.
- [125] S. Oishi, Effects of propyl paraben on the male reproductive system, *Food Chem. Toxicol.* 40 (2002) 1807–1813.
- [126] G. Shanmugam, B.R. Ramaswamy, V. Radhakrishnan, H. Tao, GC–MS method for the determination of paraben preservatives in the human breast cancerous tissue, *Microchem. J.* 96 (2010) 391–396.
- [127] P.D. Darbre, P.W. Harvey., Parabens can enable hallmarks and characteristics of cancer in human breast epithelial cells: a review of the literature with reference to new exposure data and regulatory status, *J. Appl. Toxicol.* 34 (2014) 925–938.
- [128] T. Wang, et al., Metal–organic framework MIL-101(Cr) as a sorbent of porous membrane-protected micro-solid-phase extraction for the analysis of six phthalate esters from drinking water: a combination of experimental and computational study, *Analyst* 140 (2015) 5308–5316.
- [129] M. Asiabi, A. Mehdinia, A. Jabbari, Preparation of water stable methyl-modified metal–organic framework-5/polyacrylonitrile composite nanofibers via electrospinning and their application for solid-phase extraction of two estrogenic drugs in urine samples, *J. Chromatogr. A* 1426 (2015) 24–32.

- [130] J. Yang, A. Grzech, F.M. Mulder, T.J. Dingemans, Methyl modified MOF-5: a water stable hydrogen storage material, *Chem. Commun.* 47 (2011) 5244–5246.
- [131] N. Li, et al., Dispersive micro-solid-phase extraction of herbicides in vegetable oil with metal–organic framework MIL-101, *J. Agric. Food Chem.* 63 (2015) 2154–2161.
- [132] E. Sobhanzadeh, N.K.A. Bakar, M.R.B. Abas, K. Nemati, A simple and efficient multi-residue method based on QuEChERS for pesticides determination in palm oil by liquid chromatography time-of-flight mass spectrometry, *Environ. Monit. Assess.* 184 (2012) 5821–5828.
- [133] M. Leidinger, M. Rieger, T. Sauerwald, C. Alépée, A. Schütze, Integrated pre-concentrator gas sensor microsystem for ppb level benzene detection, *Sens. Actuators B Chem.* 236 (2016) 988–996.
- [134] M. del Rio, et al., Metal oxide assisted preparation of core-shell beads with dense metal-organic framework coatings for the enhanced extraction of organic pollutants, *Chem. Eur. J.* 22 (2016) 11770–11777.
- [135] K. Sumida, et al., Sol–gel processing of metal–organic frameworks, *Chem. Mater.* 29 (2017) 2626–2645.
- [136] Ş. Tokaloğlu, E. Yavuz, S. Demir, Ş. Patat, Zirconium-based highly porous metal-organic framework (MOF-545) as an efficient adsorbent for vortex assisted-solid phase extraction of lead from cereal, beverage and water samples, *Food Chem.* 237 (2017) 707–715.
- [137] G.-H. Wang, Y.-Q. Lei, Fabrication of metal–organic framework MOF-177 coatings on stainless steel fibers for head-space solid-phase microextraction of phenols, *Bull. Environ. Contam. Toxicol.* 99 (2017) 270–275.
- [138] G. Wang, Y. Lei, H. Song, Exploration of metal-organic framework MOF-177 coated fibers for headspace solid-phase microextraction of polychlorinated biphenyls and polycyclic aromatic hydrocarbons, *Talanta* 144 (2015) 369–374.
- [139] A.S. Barreto, et al., Potential of a metal-organic framework as a new material for solid-phase extraction of pesticides from lettuce (*Lactuca sativa*), with analysis by gas chromatography-mass spectrometry, *J. Sep. Sci.* 33 (2010) 3811–3816.
- [140] V. de Carvalho, et al., Two-dimensional coordination polymer matrix for solid-phase extraction of pesticide residues from plant *Cordia salicifolia*, *J. Sep. Sci.* 32 (2009) 2132–2138.
- [141] L. Lin, et al., Membrane adsorber with metal organic frameworks for sulphur removal, *RSC Adv.* 3 (2013) 9889.
- [142] R. Ricco, et al., Lead(II) uptake by aluminium based magnetic framework composites (MFCs) in water, *J. Mater. Chem. A* 3 (2015) 19822–19831.
- [143] S. Mukherjee, et al., An ultrahydrophobic fluorinated metal-organic framework derived recyclable composite as a promising platform to tackle marine oil spills, *Chem. Eur. J.* 22 (2016) 10937–10943.
- [144] S. Khanjani, A. Morsali, Ultrasound-promoted coating of MOF-5 on silk fiber and study of adsorptive removal and recovery of hazardous anionic dye “congo red”, *Ultrason. Sonochem.* 21 (2014) 1424–1429.
- [145] K.-Y. Andrew Lin, H.-A. Chang, A zeolitic imidazole framework (ZIF)–sponge composite prepared via a surfactant-assisted dip-coating method, *J. Mater. Chem. A* 3 (2015) 20060–20064.
- [146] R. Ricco, L. Malfatti, M. Takahashi, A.J. Hill, P. Falcaro, Applications of magnetic metal–organic framework composites, *J. Mater. Chem. A* 1 (2013) 13033–13045.
- [147] D.T. Sun, et al., Rapid, selective heavy metal removal from water by a metal–organic framework/polydopamine composite, *ACS Cent. Sci.* 4 (2018) 349–356.

-
- [148] D. Ragab, et al., Micropollutants removal from water using microfiltration membrane modified with ZIF-8 metal organic frameworks (MOFs), *Chem. Eng. J.* 300 (2016) 273–279.
- [149] Y. Zhang, et al., Preparation of nanofibrous metal–organic framework filters for efficient air pollution control, *J. Am. Chem. Soc.* 138 (2016) 5785–5788.
- [150] Y. He, Y.P. Tang, D. Ma, T.-S. Chung, UiO-66 incorporated thin-film nanocomposite membranes for efficient selenium and arsenic removal, *J. Membr. Sci.* 541 (2017) 262–270.
- [151] S. Karmakar, S. Bhattacharjee, S. De, Experimental and modeling of fluoride removal using aluminum fumarate (AlFu) metal organic framework incorporated cellulose acetate phthalate mixed matrix membrane, *J. Environ. Chem. Eng.* 5 (2017) 6087–6097.
- [152] T.R.C. Van Assche, J.F.M. Denayer, Fabrication and separation performance evaluation of a metal–organic framework based microseparator device, *Chem. Eng. Sci.* 95 (2013) 65–72.
- [153] X. Zhang, B. Shen, S. Zhu, H. Xu, L. Tian, UiO-66 and its Br-modified derivates for elemental mercury removal, *J. Hazard. Mater.* 320 (2016) 556–563.
- [154] H. Li, et al., Three dimensional MOF–sponge for fast dynamic adsorption, *Phys. Chem. Chem. Phys.* 19 (2017) 5746–5752.
- [155] A.F.P. Ferreira, A.M. Ribeiro, S. Kulaç, A.E. Rodrigues, Methane purification by adsorptive processes on MIL-53(Al), *Chem. Eng. Sci.* 124 (2015) 79–95.

Index

Note: Page numbers followed by “*f*” and “*t*” refer to figures and tables, respectively.

A

- Absorption processes, 161
- Acetaldehyde, 154–155
- Acetone, 154–155
- Acetone peroxides, 232–233
- Acetonitrile (MeCN), 252–253
- Acetylcholine (ACh), 181–182
- Acetylcholinesterase (AChE), 181–182, 182*f*
- Acetylene (C₂H₂), 22
 - physical parameters, 22*f*
 - purification, 22
- ACh. *See* Acetylcholine (ACh)
- AChE. *See* Acetylcholinesterase (AChE)
- Acid gas removal (AGR), 20–21
- Acid orange 7 (AO7), 220–221
- Acoustic cavitation, 206
- Acrolein, 154–155
- Actinide-based MOF materials, 369
- Activated carbons (ACs), 23, 27–28
- Adsorbed lumophores-based luminescence in MOFs, 245–246
- Adsorbent performance indicator (API), 17
- Adsorbent performance score (APS), 18
- Adsorption, 1–2
 - adsorption–desorption cycle time, 15–16
 - kinetics, 14–15
 - of metal cations, 86
 - process, 124, 151–152, 158–159, 161
 - selectivity, 11, 148
- Advanced oxidation processes (AOPs), 218
- AFSSs. *See* Amine-functionalized sites (AFSSs)
- Ag (4,4′-bipyridine)NO₃ (SBN), 369
 - sequestration mechanism between ReO₄[−] and SBN, 369*f*
- “Age of gas”, 5
- AGR. *See* Acid gas removal (AGR)
- AIBN. *See* 2,2′-Azobis(2-methylpropionitrile) (AIBN)
- Air
 - pollution, 2–3
 - quality, 142
- Al-based MOFs, 287, 287*f*
 - TGA profiles, 289*f*
- Al-porphyrin POPs (Al-PPOPs), 187–188
- Al-PPOPs. *See* Al-porphyrin POPs (Al-PPOPs)
- Alcohols, 142–143, 150–154
 - adsorption isotherms, 154*f*
 - dynamical structural transformation, 152*f*
 - LPE process for fabrication, 153*f*
 - sensor based on Zn-BTC MOF, 394–395
- Aldehydes, 154–157
- Alkali carbonate-based process, 25
- Alkali metal ozonides, 232–233
- Alkanes, 145
- Alkanolamines, 19
- Alkenes, 145
- Alkoxy-octyl OPE, 328–329
- Alkyl halide, 102
- α-cyclodextrin, 185–186, 186*f*
- Aluminum fumarate, 415
- Aluminum oxide (AO), 335
- Amidoxime-modified UiO-66 (UiO-66-AO), 359, 360*f*
- AMIMs. *See* Amine-modified inorganic materials (AMIMs)
- Amine scrubbing, 19–20
- Amine-functionalized sites (AFSSs), 28–32, 35–38
- Amine-modified ILs, 23–24
- Amine-modified inorganic materials (AMIMs), 25
- Amine-modified porous materials, 8
- Ammonia gas, 398

- Ammonium nitrate (AN), 233–235
- Anion(s), 96–98, 109–111, 110*f*
- anion-modulated luminescence behavior, 111
 - capture in metal–organic frameworks, 102
 - exchange process, 99, 120*f*
 - in Zn(II)-based cationic MOF, 112*f*
 - exchange resins, 99–100
 - recognition, 102, 103*f*
 - trapping, 102
- Anionic pollutants
- classification, 98–99
 - recognition and sequestration of anionic pollutants by MOFs, 103–131
 - capture of toxic anionic species, 111–130
 - MOFs compared with known materials, 130–131
 - sensing of anionic pollutants, 103–111
- Anionic radionuclides, 355–357
- Antenna effect, 242–244, 243*f*
- Anthropogenic VOCs, 398–399
- Anxiety, 150
- AO. *See* Aluminum oxide (AO)
- AO7. *See* Acid orange 7 (AO7)
- AOPs. *See* Advanced oxidation processes (AOPs)
- API. *See* Adsorbent performance indicator (API)
- APS. *See* Adsorbent performance score (APS)
- Aqueous alkanolamine solutions, 342–343
- Aqueous environment, MOF–based sensors for, 395–405
- Aromatic conjugated organic ligands-based photoluminescence, 239–240
- Aromatics, 145
- Arrhenius equation, 206
- Arsenate (AsO_4^{3-}), 96–98
- Arsenic (As), 414–415
- arsenic-based oxoanion pollutants, 124–125
 - arsenic-based oxoanions sorption, 131
- Artificial trees technology, 21–22
- AT. *See* 4H-1,2,4-Triazol-4-amine (AT)
- 5-ATZ. *See* 5H-Tetrazol-5-amine (5-ATZ)
- AuNPs. *See* Gold nanoparticles (AuNPs)
- Auxochromes, 215–217
- 2,2'-Azobis(2-methylpropionitrile) (AIBN), 410
- Azoclathrates, 232–233
- ## B
- Barometers, 77
- Basolite F300, 392–394
- bbIm. *See* 5(6)-Bromobenzimidazolate (bbIm)
- BDC. *See* 1,4-Benzenedicarboxylate (BDC)
- Benzene tribenzoate (BTB), 116
- Benzene-1,3,5-tricarboxylate (BTC), 67, 68*f*, 287–288
- 1,4-Benzenedicarboxylate (BDC), 16, 28
- Benzobistriazolate ligands, 385–387
- Benzoic acid, 361
- 1,2,3-Benzotriazole-5-carboxylic acid (H_2btca), 396
- Benzoyl peroxides, 232–233
- β -cyclodextrin, 185–186, 186*f*
- Bicarbonate, 20
- Bidentate hydrazine, 268–269
- Bio-MOF-1, 245–246
 - bio-MOF-1-based composite, 262
- Biomass, 285
- Biomimetic oxidase-like catalytic properties, 75–76
- 4,4'-Biphenyldisulfonic acid (BPSA), 129
- 4,4'-Bipyridine (bipy), 16, 28
- Bis(4-nitrophenyl) phosphate (BNPP), 189–190
- Bisphenol A (BPA), 220
- BNPP. *See* Bis(4-nitrophenyl) phosphate (BNPP)
- BODIPY-based luminescent probe, 237
- “Bottle around ship” method, 255–258
- BPA. *See* Bisphenol A (BPA)
- BPSA. *See* 4,4'-Biphenyldisulfonic acid (BPSA)
- Breakthrough experiments, 13
- Bromide ions, 72–73
- 5(6)-Bromobenzimidazolate (bbIm), 343–344
- BTB. *See* Benzene tribenzoate (BTB)
- BTC. *See* Benzene-1,3,5-tricarboxylate (BTC)
- Bulk MOFs, 321*f*
 - structures for superhydrophobic applications, 323–329

C

- C-4, 233–235
- C-capture. *See* Carbon capture (C-capture)
- C7–C14, 298
- CA. *See* Copper azide (CA)
- Cadmium, 65–68
- calcium-based MOF FJI-H9, 65–66
 - copper-based MOF utilizing sulfonic acid moieties, 67–68
 - health and hazards, 65
 - MOF for Cr(VI) sensing and sorption, 70–71
 - speciation, 65
- CaL technology. *See* Calcium looping technology (CaL technology)
- Calamine. *See* Zinc carbonate
- Calcium looping technology (CaL technology), 25
- Calcium-based MOF FJI-H9, 65–66
- coordination environment of FJI-H9, 66*f*
 - fluorescence emission spectra for FJI-H9, 67*f*
- Cambridge Structural Database (CSD), 16
- CAP. *See* Cellulose acetate phthalate (CAP)
- Capacitive sensor based on HKUST-1, 402
- Capture, 1–3
- of toxic anionic species
 - of inorganic pollutants, 111–127
 - of organic anionic pollutants, 127–130
- Carbon capture (C-capture), 6–9, 20–21
- in amine-modified silica, 25–26
 - comparison of strengths and weaknesses, 7*t*
- Carbon capture and sequestration (CCS), 6–9
- societal relevance, 5–9
- Carbon dioxide (CO₂), 2–3, 5–6, 142–143, 395
- bulk superhydrophobic MOFs used for storage, 343–344
 - capture and requirement, 342–343
 - capture technologies, 18–23
 - conditions, 19*t*
 - DAC, 21–22
 - industrial trace CO₂ removal, 22–23
 - point-source CO₂ capture, 18–21, 18*f*
- NMOF/MOFNPs-composite effects for CO₂ uptake, 344–347
- physical parameters, 22*f*
 - removal technologies, 21
 - selectivity, 11–14
 - trace removal of, 5–6
- Carbon monoxide (CO), 142, 163–165, 165*f*
- Carbon-based adsorbents, 27–28
- Carbon/hydrogen/nitrogen analysis (CHN analysis), 66
- Carbonyl compounds, 154–157, 156*f*
- acetic acid concentration over time inside closed chamber, 158*f*
 - Henry's constant of acetic acid adsorption, 157*t*
- Carboxylate groups, 89
- Carboxylic acids, 154–157
- 5(6)-Carboxynaphthofluorescein (CNF), 194
- Cassie–Baxter model, 322–323, 323*f*
- Catalytic cracking technology, 285–286
- Catalytic deoxygenation, 285–286
- Cationic inorganic pollutants, 63
- Cationic MOFs, 101, 127
- composites, 194–196
 - NU-1000–5, 195*f*
 - structure of PCN-128y and NU-1003, 196*f*
- Cationic radionuclides, 356–357
- cbIm. *See* 5(6)-Chlorobenzimidazole (cbIm)
- CCS. *See* Carbon capture and sequestration (CCS)
- Cd(II) ion-based MOF nanotubes, 250–252
- CDC. *See* Center of disease control and prevention (CDC)
- Cell toxicity, 108
- Cellulose acetate phthalate (CAP), 415
- Center of disease control and prevention (CDC), 163–164
- Cesium (Cs), 358–359
- CHA-type ZIFs, 343–344
- ChemFET. *See* Chemical FET (ChemFET)
- Chemical adsorbents/chemisorbents, 25–27
- Chemical detoxification, 179
- Chemical FET (ChemFET), 396
- Chemical warfare agents (CWAs), 179, 181–183
- Chemisorption, 37–38, 343–344, 403
- functions, 6–8
 - by liquid amines, 23

- Chloride, 72–73
Chlorine, 179–180
5(6)-Chlorobenzimidazolone (cbIm), 343–344
CHN analysis. *See* Carbon/hydrogen/nitrogen analysis (CHN analysis)
CHP. *See* Cobalt hydrazine perchlorate (CHP)
Chromate, 72, 72*f*
Chromium, 68–73
 cadmium MOF for Cr(VI) sensing and sorption, 70–71
 health and hazards, 69
 speciation and reactivity, 69–70
 zirconium MOF MOR-2 high Cr(VI) adsorption, 71–73
Chromium-based MOF (Cr-MOF), 86, 87*f*, 88*f*
Chronoamperometric method, 75
Civil nuclear energy utilization, 355–356
Cluster-based LMOFs. *See* Metal node LMOFs
CNF. *See* 5(6)-Carboxynaphthofluorescein (CNF)
Cobalt hydrazine perchlorate (CHP), 268
Cobalt imidazolone framework, 392–394
Cobalt-based catalysts, 295
“Competitive inhibition” mechanism, 319–320
Computation-ready, experimental MOF database (CoRE MOF database), 305–307
Congo Red (CR), 215–217
Coordinatively unsaturated sites (CUS), 146, 146*f*
Copper azide (CA), 272–273
Copper-based MOF utilizing sulfonic acid moieties, 67–68
CoRE MOF database. *See* Computation-ready, experimental MOF database (CoRE MOF database)
Corrosion-resistant transition metal chromium, 68–73
CR. *See* Congo Red (CR)
Cr-MOF. *See* Chromium-based MOF (Cr-MOF)
Cr(VI) oxoanions, 105
Cr(VI) sensing and sorption, 70–71
Cr(VI)-based oxoanion pollutants, 111–119
 encapsulation of dichromate anions, 114*f*
 presence of aligned sulfate anions, 116*f*
 SC-SC transformation
 for anion exchange process, 115*f*
 in SLUG-21, 113*f*
Cracking, 285–286
Cryogenic distillation, 161
Cryptand inspired MOF for detection and adsorption, 85–86
CSD. *See* Cambridge Structural Database (CSD)
Cu-based MOFs, 287, 287*f*
 TGA profiles, 289*f*
Cu₂TPTC-OR, 324–325
Cu₃(BTC)₂ MOF. *See* HKUST-1
Cu₃HHTP₂, 396–398
Current-voltage (CV), 75–76
CUS. *See* Coordinatively unsaturated sites (CUS)
CV. *See* Current-voltage (CV)
CWAs. *See* Chemical warfare agents (CWAs)
Cyanide (CN⁻), 96–98, 107–108, 109*f*
- D**
DAAC. *See* 3,6-Diaminoacridinium cations (DAAC)
DAAP. *See* Dialkylaminopyridine ligands (DAAP)
DAC. *See* Direct air capture (DAC)
DAT. *See* 4H-1,2,4-Triazole-3,4-diamine hydrochloride (DAT)
DCV. *See* Dicyanovinyl group (DCV)
DEA. *See* Diethanolamine (DEA)
DEB. *See* 1,2-Diethynylbenzene (DEB)
Decarbonized fuel gas, 20–21
Decarboxylation, 297, 304
DEF. *See* *N,N*-diethylformamide (DEF)
Degradation, 179
DENP. *See* Diethyl *p*-nitrophenyl phosphate (DENP)
Density functional theory (DFT), 72–73, 268–269
Deoxygenation, 285–286
DEP. *See* Diethyl phthalate (DEP)
Depression, 150

- Desensitization of nitro-explosives and related materials, 266–273
 encapsulation of energetic components inside MOFs, 270–271
 insensitive energetic MOFs by using N-rich linkers, 268–270
 MOFs as precursor to preparing insensitive energetic materials, 272–273
- Desensitizers, 266–268
- DESH. *See* 2-(Diisopropylamino)ethanethiol (DESH)
- Desorption
 kinetics, 14–15
 process, 155
- DETA. *See* Diethylenetriamine (DETA)
- Detonation, high heat of, 266–268
- Detrimental effects, 142–145
- Dexter electron exchange. *See* Electron exchange process
- DFP. *See* Diisopropyl fluorophosphate (DFP)
- DFT. *See* Density functional theory (DFT)
- 3,5-Di(4'-carboxylphenyl) benzoic acid, 358–359
- Dialkylaminopyridine ligands (DAAP), 190, 190f
- 3,6-Diaminoacridinium cations (DAAC), 108
- Dianionic anion, 98–99
- Diazoniumdiolate, 166–168
- Diazodinitrophenol, 232–233
- 2,4-Dichlorophenoxyacetic acid (2,4-D), 217
- Dichromate ($\text{Cr}_2\text{O}_7^{2-}$), 72, 72f, 96–98
- Dichromate anion, 111–112
- Dicyanovinyl group (DCV), 107–108, 213
- Dietary intake, 65
- Diethanolamine (DEA), 19
- Diethyl *p*-nitrophenyl phosphate (DENP), 190
- Diethyl phthalate (DEP), 217–218
- Diethylenetriamine (DETA), 37–38, 361
- 1,2-Diethynylbenzene (DEB), 344–345
- 2,5-Dihydroxyterephthalic acid linker-based MOFs (H_2DHT linker-based MOFs), 240–241
- Diisopropyl fluorophosphate (DFP), 194
- 2-(Diisopropylamino)ethanethiol (DESH), 189–192
- Dimethyl acetamide (DMA), 252–253
- Dimethyl chlorophosphate (DMCP), 195
- Dimethyl formamide (DMF), 252–253
- Dimethyl methylphosphate (DMMP), 189–190
- Dimethyl *p*-nitrophenyl phosphate (DMNP), 183–186, 184f
- Dimethyl phthalate (DMP), 217–218
- 2,3-Dimethyl-2,3-dinitrobutane (DMNB), 248
- Dimethylacetamide (DMA0, 147–148
- 4-(4-(Dimethylamino)styryl)-1-methylpyridin-1-ium (DMASM), 262
- 2,2-Dimethylbutane (22DMB), 148–149
- 2,3-Dimethylbutane (23DMB), 148–149
- 2,4-Dinitrotoluene (DNT), 248, 254–255
- Direct air capture (DAC), 21–22. *See also* Point-source CO_2 capture
- DMA. *See* Dimethyl acetamide (DMA)
- DMASM. *See* 4-(4-(Dimethylamino)styryl)-1-methylpyridin-1-ium (DMASM)
- 22DMB. *See* 2,2-Dimethylbutane (22DMB)
- 23DMB. *See* 2,3-Dimethylbutane (23DMB)
- DMCP. *See* Dimethyl chlorophosphate (DMCP)
- DMEDA. *See* *N,N*-dimethylethylenediamine (DMEDA)
- DMF. *See* Dimethyl formamide (DMF); *N,N*-dimethylformamide (DMF)
- DMMP. *See* Dimethyl methylphosphate (DMMP)
- DMNB. *See* 2,3-Dimethyl-2,3-dinitrobutane (DMNB)
- DMNP. *See* Dimethyl *p*-nitrophenyl phosphate (DMNP)
- DMP. *See* Dimethyl phthalate (DMP)
- DNT. *See* 2,4-Dinitrotoluene (DNT)
- Dresden University of Technology (DUT), 310–311
- Dubinín–Astakhov equation, 399–401
- E**
- ED. *See* Ethylenediamine (ED)
- EDS. *See* Energy-dispersive X-ray spectroscopy (EDS)

- Electrochemical
DNA-functionalized porphyrinic MOF,
75–77
electrochemical-based devices, 384
reduction, 75
response of MOF-based sensor device,
391–395
synthesis, 206–207
- Electron exchange process, 236–238, 236*f*
- Electroplating metal, 68–69
- Elemental analysis, 70
- Elemental and mercuric forms, 78–79
- Emission sources, 142–145
- EMPA. *See* Ethyl methylphosphonic acid (EMPA)
- Encapsulation of energetic components
inside MOFs, 270–271
- Energy-consuming processes, 161
- Energy-dispersive X-ray spectroscopy
(EDS), 71
- Enthalpy of adsorption, 14–15
- Environmental pollutants
classification of MOFs–based devices for
sensing, 384–395
evolution of papers related to
MOFs, 384*f*
MOF–based devices for noxious species
removal, 405–417
MOF–based sensors for gaseous and
aqueous environments, 395–405
detection of toxic gases, 395–398
detection of volatile organic
compounds, 398–403
pollutants detection in water, 403–405
- Environmental pollution, 2
- ESET. *See* Excited state electron transfer (ESET)
- ESIPT. *See* Excited state intramolecular
proton transfer (ESIPT)
- ESPT. *See* Excited state proton transfer
(ESPT)
- Esters, 297
- Ethane molecules, 146–147
- 1,2-Ethanedisulfonate anions, 112
- Ethanol, 142–143
- Ethyl methylphosphonic acid (EMPA),
190–192
- Ethylbromoacetate, 179–180
- Ethylenediamine (ED), 155–156
- EXAFS. *See* Extended X-ray absorption fine
structure (EXAFS)
- Excimer or exciplex formation in MOFs,
244
- Excited state electron transfer (ESET),
240–241
- Excited state intramolecular proton transfer
(ESIPT), 240–241
- Excited state proton transfer (ESPT),
240–241
- Explosive materials, 232–235, 232*f*, 234*t*
- Extended ligands (X-ligands), 42
- Extended X-ray absorption fine structure
(EXAFS), 66, 359
- F**
- Fabry–Perot interferometer, 399
- Facile regeneration, 98
- Facile synthesis approach, 346
- Fe-MOFs, 220–221
- Fe(III) based MOF (FeP-MOF), 75, 76*f*, 77*f*
- Fe₃O₄@SiO₂@UiO-67 nanocomposite, 213
- FeP-MOF. *See* Fe(III) based MOF (FeP-
MOF)
- FETs. *See* Field effect transistors (FETs)
- FGO@MOG. *See* Fluorinated graphene
oxide–MOG composite
(FGO@MOG)
- Fiber optic–based surface plasmon
resonance sensor (FO-SPR sensor),
403
- Field effect transistors (FETs), 394–395
- Filtration devices, 411–415
- Fission products, 355–356
- Five-member heterocyclic HEMs, 264–266
- Flanders Fields, 179–180
- Flue gas, 343
desulfurization, 158
- Fluidic devices, 415–417
- Fluorescent/fluorescence, 238–239
detection experiments, 88–89
optical technique for sensing applications,
235–236
sensory probe, 105
Tb-based MOF, 363–364
- Fluoride ion capture, 131
- Fluorinated graphene oxide–MOG
composite (FGO@MOG), 332–335
- Fluorinated materials, 341–342

- Fluorinated oxy anions (FOXY anions), 43
Fluorine-free stable superhydrophobic material, 341–342
Fluorophenylisothiocyanate (FPI), 401
Fluorophore, 81
Fluorous metal–organic frameworks (FMOFs), 321–322, 325
FMOFs. *See* Fluorous metal–organic frameworks (FMOFs)
FO. *See* Fuel oil (FO)
FO-SPR sensor. *See* Fiber optic–based surface plasmon resonance sensor (FO-SPR sensor)
Food/textile industries, 96–98
Formaldehyde, 154–155
Förster resonance energy transfer (FRET), 236–237, 236*f*, 329
Fossil fuels, 6–9, 285, 342–343
Fourier-transform IR (FT-IR), 64, 68*f*, 83*f*
FOXY anions. *See* Fluorinated oxy anions (FOXY anions)
FPI. *See* Fluorophenylisothiocyanate (FPI)
FRET. *See* Förster resonance energy transfer (FRET)
FT-IR. *See* Fourier-transform IR (FT-IR)
Fuel hydrocarbons, 297–304
Fuel oil (FO), 233–235
Functional chelating groups, 356–357
Functionalized MOFs, 213
- G**
Ga-based MOFs, 287, 287*f*
TGA profiles, 289*f*
Gamma radiation resistance ensures application to HLW solutions, 88, 89*f*
Gas chromatography (GC), 405–407
Gas chromatography/mass spectrometry (GC-MS), 407
Gas mask/respirator models, 179
Gaseous environment, MOF–based sensors, 395–405
Gaseous radionuclides, 356–357
GC. *See* Gas chromatography (GC)
GC-MS. *See* Gas chromatography/mass spectrometry (GC-MS)
GF. *See* Glufosinate (GF)
Gibbs energy, 99
Global-scale implementation, 98
Glufosinate (GF), 217
Glyphosate (GP), 217
Gold nanoparticles (AuNPs), 75
Gold nanopatch array (Au-NPA), 391
GP. *See* Glyphosate (GP)
Gravimetric saturation uptake capacity, 10
Green deoxygenation of fatty acids to transport fuels
MOFs
catalysts, 286–287
compositions, 310–311
powder catalysts, 287–290
supported Ni-MOFs catalysts for conversion of oleic acid, 304–310
supported ZIF-67 catalysts for conversion of oleic acid, 290–297
of saturated acids, 297–304
Guest benzene molecules, 250–252
- H**
H₂btca. *See* 1,2,3-Benzotriazole-5-carboxylic acid (H₂btca)
H₂DHT linker-based MOFs. *See* 2,5-Dihydroxyterephthalic acid linker-based MOFs (H₂DHT linker-based MOFs)
H₂PATP. *See* ((Pyridin-1-ium-2-ylmethyl) ammonio)terephthalate (H₂PATP)
H₃BTMB. *See* 1,3,5-Tris(3-carboxyphenyl) benzene (H₃BTMB)
Hairpin probe (HP), 75
Halogen azides, 232–233
Halogen-free energetic 3D MOFs, 269
Hard/soft acid/base theory (HSAB theory), 63–64, 98–99, 207
HAT. *See* 3-Hydrazinyl-4H-1,2,4-triazol-4-amine dihydrochloride (HAT)
Hazardous biological, 179
Hazardous radionuclides, 355–356
Health and hazards
cadmium, 65
chromium, 69
lead, 73
mercury, 78
radioactive wastes, 85
Heavy metal, 63
HEDMs. *See* High energy density materials (HEDMs)
HEMs. *See* High energy materials (HEMs)

- Henry's law, 12
selectivity, 11
- Herbicides removal by MOFs, 217
- Heterogeneous catalysts, 286
- Hexadecane, 298
- 2,3,6,7,10,11-Hexahydroxytriphenylene (HHTP), 394, 396–398
- 2,3,6,7,10,11-Hexaminitriphenylene (HITP), 394, 396–398
- Hexamethylenetetramine (HMTA), 371–373
- Hexane, 389
- 2,5-Hexanedione, 145
- Hexavalent oxidation states, 69
- HF free synthesis, 399–401
- HHTP. *See* 2,3,6,7,10,11-Hexahydroxytriphenylene (HHTP)
- High energy density materials (HEDMs), 266–268
- High energy materials (HEMs), 232–235
- High explosives, 232–233
- High-level Waste (HLW), 85
- High-performance liquid chromatography (HPLC), 408
- High-resolution thermogravimetric analysis, 16
- HITP. *See* 2,3,6,7,10,11-Hexaminitriphenylene (HITP)
- HKUST-1, 385–388, 392, 411, 412*f*
capacitive sensor based on, 402
modified polyurethane sponges, 417
- HLW. *See* High-level Waste (HLW)
- HMTA. *See* Hexamethylenetetramine (HMTA)
- HN₃. *See* Hydrazoic acid (HN₃)
- Hofmeister effect, 99
- Hot-pressing method (HoP), 342
- HP. *See* Hairpin probe (HP)
- HPLC. *See* High-performance liquid chromatography (HPLC)
- HPTS dye. *See* 8-Hydroxy-1,3,6-pyrenetrisulfonic acid trisodium salt (HPTS dye)
- HSAB theory. *See* Hard/soft acid/base theory (HSAB theory)
- Human activity, 160–161
- Humic acids, 69–70, 89
- HUMs. *See* Hybrid ultramicroporous materials (HUMs)
- Hybrid organic–inorganic materials, 41
- Hybrid ultramicroporous materials (HUMs), 8–9, 41–45
- Hydrazine, 268–269
energy, 99
- 3-Hydrazinyl-4H-1,2,4-triazol-4-amine dihydrochloride (HAT), 264–266
- Hydrazoic acid (HN₃), 272–273
- Hydrocarbons, 145–150, 290–297
pore structure, 149*f*
selectivity
for binary mixtures, 149*t*
for selected adsorbents, 147*t*
series of materials composed of apolar adsorbents, 146*f*
- Hydrodeoxygenation, 297, 304
- Hydrogen (H₂), 23
purification, 23
- Hydrogen sulfide (H₂S), 160–163, 162*f*, 163*f*, 395
- Hydrogenation of carboxylic acids, 298–301
- Hydrolytic stability, 16
- Hydrophilic character, 150
- Hydrophobic MOFs-based materials
bulk MOFs, nanoscale MOFs, and MOF, 321*f*
bulk MOFs structures for superhydrophobic applications, 323–329
bulk superhydrophobic MOFs used for CO₂ storage, 343–344
CO₂ capture and requirement, 342–343
lotus effect, 322
models of superhydrophobicity, 322–323
MOFs nanocomposites for oil/water separation, 332–342
nanoscale superhydrophobic/self-cleaning MOFs based on OPE linkers, 329–331
NMOF/MOFNPs-composite effects for CO₂ uptake, 344–347
- Hydrophobicity/hydrophilicity balance, 144–145
- Hydrophobic–oleophilic MOFs, 321–322
- Hydrothermal synthesis, 205
- 8-Hydroxy-1,3,6-pyrenetrisulfonic acid trisodium salt (HPTS dye), 264–266
- Hydroxyl radicals(·OH), 218–219
generation, 218–219
- Hydroxyl-functionalized UiO-66, 364

8-Hydroxypyrene-1,3,6-trisulfonate dye
(SG7 dye), 250–252

Hypochlorite (OCl^-), 96–98

I

IAST. *See* Ideal adsorbed solution theory
(IAST)

ICP. *See* Inductively coupled plasma (ICP)

ICT. *See* Intramolecular charge transfer
(ICT)

Ideal adsorbed solution theory (IAST),
12–13, 150–151

Ideal selectivity (IS), 11

IFMC-1, 269–270

ILCT. *See* Interligand charge transfer (ILCT)

ILs. *See* Ionic liquids (ILs)

ILW. *See* Intermediate-level Waste (ILW)

iMOFs. *See* Ionic metal–organic
frameworks (iMOFs)

Impact sensitivity (IS), 264

Impedance spectroscopy, 402–403

Inductively coupled plasma (ICP), 66

Industrial trace CO_2 removal, 22–23

acetylene purification, 22

hydrogen purification, 23

natural gas sweetening, 22–23

Infrared spectroscopy (IR spectroscopy), 70,
151–152

Inorganic anions, 43, 96–98

in 3D HEDMs, 273–275

trapping of, 125–127

Inorganic pollutants

arsenic-based oxoanion pollutants,
124–125

Cr(VI)-based oxoanion pollutants,
111–119

radioactive oxoanion pollutants, 119–123

selenium-based oxoanion pollutants, 123

trapping of inorganic anions, 125–127

Insensitive energetic materials, 272–273

Insensitive energetic MOFs by using N-rich
linkers, 268–270

Interligand charge transfer (ILCT), 239–240

Intermediate-level Waste (ILW), 85

Intramolecular charge transfer (ICT),
236–238

Iodine (I_2), 370–373

design strategy of amine-functionalized
MIL-101-Cr materials, 372*f*

structure of ZIF-8 cage, 371*f*

Ion exchange, 63–64

process, 102, 109–111, 120

resins, 365

studies, 121–122

Ionic liquids (ILs), 8, 23–24

Ionic metal–organic frameworks (iMOFs),
101, 101*f*

Ionizing radiation, 85

IR spectroscopy. *See* Infrared spectroscopy
(IR spectroscopy)

IRMOFs. *See* Isorecticular metal–organic
frameworks (IRMOFs)

Irreversible barium adsorption, 86–87

Irving–Williams series, 209

IS. *See* Ideal selectivity (IS); Impact
sensitivity (IS)

Isopropanol, 142–143, 411

Isopropyl methylphosphonofluoridate, 181

Isorecticular metal–organic frameworks
(IRMOFs), 323–324

Isosteric enthalpy of adsorption, 15

K

Kelvin Probe detector, 401

Ketones, 154–157

Krypton (^{85}Kr), 373–374, 375*f*

L

Langmuir model, 67–68, 415–417

Lanthanide metal ions (Ln metal ions),
242–244

Lanthanide-based MOFs, 363–364
luminescence intensities of $^5\text{D}_4$ – $^7\text{F}_5$
transitions, 74*f*

for selective detection of Pb(II), 74–75

Laporte selection rule, 242–244

Lauric acid, 297

Layer-by-layer approach (LbL approach),
387–389, 401

Layered double hydroxides (LDHs), 99–100

LbL approach. *See* Layer-by-layer approach
(LbL approach)

LBSs. *See* Lewis basic sites (LBSs)

LCA. *See* Life-cycle assessment studies
(LCA)

LDHs. *See* Layered double hydroxides
(LDHs)

Le Chatelier's principle, 209

- Lead (Pb), 73–77
 electrochemical DNA-functionalized porphyrinic MOF for Pb(II) sensing, 75–77
 health and hazards, 73
 lanthanide-based MOF for selective detection of Pb(II), 74–75
 lead-containing chromate, 68–69
 speciation, 73–74
- Lewis acids, 185
 catalyst yields dimethyl hydrogen phosphate, 183–185
 cation, 63–64
 Lewis acid–base interaction, 63–64
 metalloporphyrin boxes, 186
- Lewis basic sites (LBSs), 34–35
- Life-cycle assessment studies (LCA), 2
- Ligand-based LMOFs, 239–241
- Ligand-to-metal charge transfer (LMCT), 72, 104, 212, 239–240
- Limit of quantification (LOQ), 72
- Limits of detection (LOD), 72, 214–215, 396–398
- Liquefaction natural gas (LNG), 5–6
- Liquid amines, 6
 absorption, 19
 CCS technologies, 6–9
 liquid amine-based “wet scrubbers”, 6
- Liquid chemisorbents, 6–7
- Liquid fuel hydrocarbons, 287–290, 304–310
- Liquid phase epitaxy (LPE), 401–402
- Liquid-phase epitaxial growth technique (LPE growth technique), 152–153
- LLW. *See* Low-level Waste (LLW)
- LMCT. *See* Ligand-to-metal charge transfer (LMCT)
- LMOFs. *See* Luminescent metal–organic frameworks (LMOFs)
- Ln metal ions. *See* Lanthanide metal ions (Ln metal ions)
- LNG. *See* Liquefaction natural gas (LNG)
- LOD. *See* Limits of detection (LOD)
- Long-chain hydrocarbons, 298
- LOQ. *See* Limit of quantification (LOQ)
- Lotus effect, 322
- Low explosives, 232–233
- Low-level Waste (LLW), 85
- LPE. *See* Liquid phase epitaxy (LPE)
- LPE growth technique. *See* Liquid-phase epitaxial growth technique (LPE growth technique)
- Luminescence, 238–239
- Luminescent interpenetrated zinc-based MOF, 403–404
- Luminescent metal–organic frameworks (LMOFs), 211, 238–246, 239*f*.
 See also Metal–organic frameworks (MOFs)
 adsorbed lumophores-based luminescence, 245–246
 excimer or exciplex formation, 244
 ligand-based, 239–241
 LMOF-241 compound, 214–215
 metal node or cluster-based, 242–244
 for organic pollutants detection, 211–215
 luminescent sensors, 213–215
 sensing mechanism, 211–212
- Luminescent probes, 237–238
- Luminescent sensors, 213–215
 fluorescence quenching of M-ZIF-90, 214*f*
 geometrical selectivity upon PO_4^{3-} , 214*f*
 photoluminescence, 212, 213*f*
- Luminescent Zn(II)-based MOF, 248
- M**
- m*-dinitrobenzene (*m*-DNB), 248–250, 254–255
- M-MOF-74, 32–33
- Magnetic framework composites (MFCs), 413
- Malachite Green dye, 413
- Mass spectrometry (MS), 13
- Mass-detoxification, 182–183
- Material Institut Lavoisier (MIL), 323–324
- mbIm. *See* 5(6)-Methylbenzimidazolone (mbIm)
- MCPP. *See* Methylchlorophenoxypropionic acid (MCPP)
- MD simulations. *See* Molecular dynamics simulations (MD simulations)
- MDEA. *See* Methyl-diethanolamine (MDEA)
- MEA. *See* Monoethanolamine (MEA)
- Mechanical stability, 16
- Mechanochemical response of MOF-based sensor device, 385–389, 386*f*
- Mechanochemical synthesis, 17, 205–206
- Mechanochemistry, 205–206

- MeCN. *See* Acetonitrile (MeCN)
- MEK. *See* Methyl ethyl ketone (MEK)
- Membrane technology, 23
- MEMS. *See* Microelectromechanical system (MEMS)
- Mercury (Ag), 77–84
health and hazards, 78
nickel-based MOF for visual detection and selective remediation, 83–84
postsynthetically modified UiO-66 for selective detection, 79–80
speciation, 78–79
UiO-66-NH₂ DNA, 81–82
- Mesoporous silicas, 25
- Metal, 335–341
cations, 304–305
clusters and organic linkers, 63–64
metal-anion bond, 100
metal-based clusters, 304–305
metal–ligand bond, 125
node LMOFs, 242–244
- Metal to ligand charge transfer (MLCT), 212, 239–240
- Metal–organic framework nanotube (MOFNT), 250–252
- Metal–organic frameworks (MOFs), 1–3, 28–45, 63–64, 97*t*, 100, 144–145, 185–186, 189*f*, 204, 319, 321–322, 321*f*, 356, 383, 392–394, 408
application in organic pollutants removal, 211–221
for capture of toxic chemicals, 158–168
for capture of VOCs
alcohols, 150–154
carbonyl compounds, 154–157
hydrocarbons, 145–150
catalysts, 189–194
structure of NU-1000 and MOF-808, 192*f*
structures of homogenous buffers, 193*f*
varying connectivity of Zr₆O₄(OH)₄-based node, 192*f*
CO₂ sorption data, 29*t*
design principles for sequestering radionuclides, 356–357
modifications, 208–210
exchange of building blocks, 209
pore expansion, 209–210
MOF-177, 411
MOF-based devices, 383–384
classification for sensing, 384–395, 385*f*
MOF-based ion traps for irreversible barium adsorption, 86–87
MOF-based SAW systems, 385–387
MOF-DNA system's fluorescence intensity, 81
MOF-dye composite material, 245–246
MOF-based sensors for gaseous and aqueous environments, 395–405
MOFs-based composites, 210–211
MOFs–polymer composites, 210
thermal annealing, 210–211
MOFs-based detection, 233–235
nanocomposites for oil/water separation, 332–342
for organic pollutants adsorption, 215–218
emerging organic contaminants, 217–218
herbicides and pesticides removal by MOFs, 217
organic dyes adsorption by MOFs, 215–217
pollutant, MOFs, and dominant interactions, 216*t*
for organic pollutants decomposition, 218–221
generation of hydroxyl radicals, 218–219
generation of singlet oxygen, 220
generation of sulfate radical, 220–221
radioactive waste sequestration by, 358–374
synthesis approaches, 204–207, 205*f*
water stable, 207–208, 207*f*
- Metal–organic materials (MOMs), 28
- Metal–organic resin (MOR), 105, 106*f*, 119*f*
- Methane (CH₄), 22
physical parameters, 22*f*
- Methanol, 150, 389
- Methyl ethyl ketone (MEK), 155
- Methyl parathion hydrolase (MPH), 185
- Methyl red (MR), 127–128
- 5(6)-Methylbenzimidazolates (mbIm), 343–344
- Methylchlorophenoxypropionic acid (MCPPE), 217

- Methyldiethanolamine (MDEA), 19
2-Methylimidazolate (2-mIm), 343–344
2-Methylpentane (2MP), 148–149
MFCs. *See* Magnetic framework composites (MFCs)
Micro solid-phase extraction (μ SPE), 405–407
Microelectromechanical system (MEMS), 395–396
Micropreconcentrators (μ PCs), 395–396
Microwave
 irradiation, 206
 microwave-assisted synthesis, 40–41, 206
 treatment, 311
MIL. *See* Material Institut Lavoisier (MIL)
MIL-100(Fe), 408
MIL-101(Cr), 409
MIL-53(Al)-based MFCs, 413
2-mIm. *See* 2-Methylimidazolate (2-mIm)
Mining, 233–235
Mixed matrix membrane system (MMM system), 415
MLCT. *See* Metal to ligand charge transfer (MLCT)
MMM system. *See* Mixed matrix membrane system (MMM system)
Mnemonic DEADLY
 METHYLMERCURIALS, 78, 78f
MOFNT. *See* Metal–organic framework nanotube (MOFNT)
MOFs. *See* Metal–organic frameworks (MOFs)
Molar selectivity, 11
Molecular dynamics simulations (MD simulations), 361
Molecular sieves, 8
Molecular sieving effect, 153, 291
MOMs. *See* Metal–organic materials (MOMs)
Monoanionic anion, 98–99
Monoethanolamine (MEA), 19
MOR. *See* Metal–organic resin (MOR)
2MP. *See* 2-Methylpentane (2MP)
MPH. *See* Methyl parathion hydrolase (MPH)
MR. *See* Methyl red (MR)
MS. *See* Mass spectrometry (MS)
Multiwalled carbon nanotube (MWCNT), 398
- N**
N,N-diethylformamide (DEF), 205
N,N-dimethylethylenediamine (DMEDA), 371–373
N,N-dimethylformamide (DMF), 205, 391, 408–409
N-methyl-2-pyrrolidone (NMP), 128
N-methylmorpholine, 193–194
N-rich linkers, insensitive energetic MOFs by using, 268–270
NACs. *See* Nitro-aromatic compounds (NACs)
Nanoscale MOFs (NMOFs), 319, 321f.
 See also Luminescent metal–organic frameworks (LMOFs)
 based on OPE linkers, 329–331
 NMOF/MOFNPs-composite effects for CO₂ uptake, 344–347
2,6-Naphthalene dicarboxylic acid (NDC), 244
Natural ecosystems, 96–98
Natural gas (NG), 5–6
 sweetening, 22–23
NDC. *See* 2,6-Naphthalene dicarboxylic acid (NDC)
Near infrared region (NIR region), 242–244
Negative emissions, 21
Nerve agents, 181
 Benjamin I. Lane’s respirator patent, 180f
 catalytic MOF composites, 194–196
 chemical structures, common names, and US Army symbols, 181f
 detoxification pathways and simulants, 182–185, 184f
 early generation supramolecular catalysts, 185–189
 MOF catalysts, 189–194
Neutral MOFs, 100
NFT. *See* Nitrofurantoin (NFT)
NG. *See* Natural gas (NG)
NH₂-UiO-66(Zr), 396
NHP. *See* Nickel hydrazine perchlorate (NHP)
Ni-4PyC, 39
Ni-BTC crystals, 305–307
Nickel, 305, 310
 nickel-based MOF for visual detection and selective remediation, 83–84
Nickel hydrazine perchlorate (NHP), 268

- NIR region. *See* Near infrared region (NIR region)
- NiSIFSIX, 310–311
- Nitrate, 72–73
- Nitrated high energy material recognition, 246–262
- detection of nitro-aromatic compounds, 252–258
 - nitro-aromatic compound recognition in vapor phase, 248–252
 - sensing of nitro-aromatic compounds with MOFs in water medium, 258–262
- Nitrated materials, 232–233
- Nitric dioxide (NO₂), 398
- Nitric oxide (NO), 165–168, 395
- adsorption–desorption isotherms, 167*f*
 - average adsorption capacity and residual capacity, 166*t*
 - synthesis by postfunctionalization, 168*f*
- 5-Nitro-2,4-dihydro-3H-1,2,4-triazole-3-one (NTO), 264–266
- Nitro-aliphatic compound, 250–252
- Nitro-aromatic compounds (NACs), 233–235, 250–252
- current methods/materials and mechanism for detection, 235–238
 - detection by MOF in common organic solvents, 252–258
 - recognition in vapor phase, 248–252
- Nitro-explosives detection, 237
- Nitrobenzene, 254–255
- Nitrofurantoin (NFT), 214–215
- Nitrofurazone (NZF), 214–215
- Nitrogen, 417
- Nitrogen trihalides, 232–233
- 4-Nitrophenol (NP), 183–185
- Nitrotoluene (NT), 248–250
- NMOFs. *See* Nanoscale MOFs (NMOFs)
- NMP. *See* *N*-methyl-2-pyrrolidone (NMP)
- “Node-and-linker” concept, 28
- Non-methane hydrocarbons, 142–143
- Non-nitro-aromatic high energy materials
- sensing with MOFs, 262–266
- Nonconductive MOFs, 398
- Noncovalent interactions, 103–104
- Nonlinear electrostatically actuated MEMS resonator, 402
- Nonnoble bimetallic sulfide catalysts, 304–305
- Non-noble metal catalysts, 304–305
- Nonpolar alkanes, 394–395
- Noxious species removal, MOF–based
- devices for, 405–417
 - filtration devices, 411–415
 - fluidic devices, 415–417
 - preconcentrators, 405–411
- Noxious substances, 383
- NP. *See* 4-Nitrophenol (NP)
- NT. *See* Nitrotoluene (NT)
- NTO. *See* 5-Nitro-2,4-dihydro-3H-1,2,4-triazole-3-one (NTO)
- NU-1000, 192–193, 192*f*, 365–366, 366*f*, 370*f*
- Nuclear
- energy, 119, 355–356
 - power plants, 96–98
 - power production, 355–356
- NZF. *See* Nitrofurazone (NZF)
- O**
- O*-dianisidine chlorosulfonate (Sneezing agent), 179–180
- O*-ethyl-*S*-(2-diisopropylamino-ethyl)-methyl-phosphonothiolate, 181
- Octadecylphosphonic acid (OPA), 335–341
- OG. *See* Orange G (OG)
- Oil spills, 320–321
- Oil/water separation, MOFs nanocomposites
- for, 332–342
 - contact angles of various liquid, 338*f*
 - graphical representation of NH₂-MIL-53 (Al) micromushroom synthesis, 336*f*
 - molecular-level external modification of superhydrophobic, 340*f*
 - preparation process, 341*f*
 - SEM images of as-prepared Cu₃(BTC)₂·3H₂O coatings, 339*f*
- Oligo*-(*p*-phenyleneethynylene) (OPE), 328–329
- One-dimensional channels (1D channels), 248
- OPA. *See* Octadecylphosphonic acid (OPA)
- OPAA. *See* Organophosphorus acid anhydrolase (OPAA)
- OPCW. *See* Organisation for Prohibition of Chemical Weapons (OPCW)
- OPE. *See* *Oligo*-(*p*-phenyleneethynylene) (OPE)

- Open metal sites. *See* Unsaturated metal centers (UMCs)
- OPPs. *See* Organophosphorous pesticides (OPPs)
- Optical fiber-based Fabry–Perot device, 405
- Optical response of MOF-based sensor device, 389–391
- Orange G (OG), 220–221
- Organic anionic pollutants, capture of, 127–130, 128*f*
coordination environment
in Ag(I)-MOF, 129*f*
and packing diagram of Ni(II)-MOF, 130*f*
- Organic contaminants, 217–218
- Organic dyes adsorption by MOFs, 215–217
- Organic linker functionalization, 156–157
- Organic pollutants, 203
modifications of MOFs, 208–210
MOF application in removal
interactions between MOFs and organic molecules, 211
LMOFs for organic pollutants
detection, 211–215
MOFs for organic pollutants adsorption, 215–218
MOFs for organic pollutants
decomposition, 218–221
MOFs-based composites, 210–211
synthesis of MOFs, 204–211
water stable MOFs, 207–208, 207*f*
- Organic solvents, 335–341
- Organisation for Prohibition of Chemical Weapons (OPCW), 180–181
- Organophosphorous nerve agents, 183
- Organophosphorous pesticides (OPPs), 213
- Organophosphorous acid anhydrolase (OPAA), 195–196
- Organophosphorus compounds, 181
- Organophosphorus ester hydrolysis, 183, 183*f*
- Oxides of xenon, 232–233
- Oxoanion pollutants, 104–107, 104*f*
bar diagram showing differential response, 108*f*
change in fluorescence emission intensity, 107*f*
- Oxy-fuel combustion, 21
- Oxy-fuel process. *See* Oxy-fuel combustion
- Ozone (O₃), 142
- P**
- p*-dinitrobenzene (*p*-DNB), 248–250
- p*-nitrophenyl dibutyl phosphate (PNPDBP), 186
- p*-nitrophenyl diphenyl phosphate (PNPDPP), 186
- p*-nitrophenyl dipropyl phosphate (PNPDPrP), 186
- PA. *See* Phthalic acid (PA)
- PAHs. *See* Polycyclic aromatic hydrocarbons (PAHs)
- Palmitic acid, 297
- PAN. *See* Polyacrylonitrile (PAN)
- Paraoxonase 1 (PON1), 185
- Particulate matter (PM), 414
- PCBs. *See* Polychlorinated biphenyls (PCBs)
- PCPs. *See* Porous coordination polymers (PCPs)
- PDMS. *See* Plasma desorption mass spectrometry (PDMS);
Polydimethoxysilane (PDMS)
- PEI. *See* Polyethyleneimine (PEI)
- Pelletized activated carbon, 143
- Pentadecane, 298
- Pentaerythritol tetranitrate (PETN), 232–233
- Percent regenerability, 18
- Perfluorodecyltriethoxysilane (PFOTS), 335–341
- Peroxy acids, 232–233
- Peroxymonosulfate (PMS), 220–221
- Persistent organic pollutants (POPs), 203
- Persulfate (PS), 220–221
- Pertechnetate (TcO₄⁻), 96–98
- Pesticides removal by MOFs, 217
- PET. *See* Photoinduced electron transfer (PET)
- PETN. *See* Pentaerythritol tetranitrate (PETN)
- PFOTS. *See* Perfluorodecyltriethoxysilane (PFOTS)
- PHAs. *See* Polyhydroxyalkanoates (PHAs)
- Phosphorescence, 238–239
- Phosphorus, 213
- Photo-Fenton reaction, 220
- Photoinduced electron transfer (PET), 81, 236–237, 236*f*

- Photoluminescence, 86, 212, 213*f*
Photosynthesis, 165–166
Phthalic acid (PA), 217–218
Physical adsorbents/physisorbents, 27–28
Physisorbents, 15, 23
Physisorption, 8–9, 343–344
 π -electron rich conjugated organic moieties, 239–240
PIB. *See* Polyisobutylene (PIB)
Picric acid (TNP), 258
Pilot-scale MOF production, 17
Pinacolyl methylphosphonofluoridate, 181
Plasma desorption mass spectrometry (PDMS), 385–387
Plastic explosives, 233–235
Plutonium, 85
Plutonium and Uranium Recovery by Extraction (PUREX), 84, 355–356
PM. *See* Particulate matter (PM)
PMS. *See* Peroxymonosulfate (PMS)
PN. *See* Polynaphthylene (PN)
PNPDBP. *See* *p*-nitrophenyl dibutyl phosphate (PNPDBP)
PNPDPP. *See* *p*-nitrophenyl diphenyl phosphate (PNPDPP)
PNPDPrP. *See* *p*-nitrophenyl dipropyl phosphate (PNPDPrP)
Point-source CO₂ capture, 18–21, 18*f*
 oxy-fuel combustion, 21
 postcombustion, 19–20
 precombustion, 20–21
Polar adsorbents, 147–148
Pollutants, 63. *See also* Environmental pollutants; Organic pollutants
 cationic inorganic, 63
 Cr(VI)-based oxoanion, 111–119
 detection in water, 403–405
 oxoanion, 104–107, 104*f*
 radioactive oxoanion, 119–123
 selenium-based oxoanion, 123, 124*f*
 state-of-art for remediation of, 99–100
Pollution, 383
Polyacrylonitrile (PAN), 408–409
Polycatenated anionic uranyl organic framework, 358–359, 358*f*
Polychlorinated biphenyls (PCBs), 408
Polycyclic aromatic hydrocarbons (PAHs), 398–399
Polydimethoxysilane (PDMS), 345–346
Polyethyleneimine (PEI), 15, 37–38, 193–194
Polyhydroxyalkanoates (PHAs), 411
Polyisobutylene (PIB), 194
Polymer–metal–organic frameworks (polyMOFs), 344–345
Polynaphthylene (PN), 344–345
Polysaccharide, 72
Polystyrene (PS), 410
PON1. *See* Paraoxonase 1 (PON1)
POPs. *See* Persistent organic pollutants (POPs); Porous organic polymers (POPs)
Pore chemistry, 9, 38–41
Pore size, 9, 38–41
Porous adsorbents, 143–144
Porous carbons, 100
Porous coordination polymers (PCPs), 1, 99–100
Porous materials, 2
Porous organic polymers (POPs), 187–188
Porous physisorbents, 8
Postcombustion, 19–20
Postmodification strategy, 359
Postsynthetic modification (PSM), 35, 100, 107–108, 209, 325–328
Postsynthetically modified UiO-66 for selective detection, 79–80, 79*f*, 80*f*
Powder X-ray diffraction (PXRD), 68*f*, 70, 86
 variable-temperature, 16
Precombustion, 20–21
Preconcentrators, 405–411
Pressure swing adsorption (PSA), 14–15, 14*f*, 415–417
Pressure-temperature swing adsorption (PTSA), 16
Primary explosives, 232–233, 272
 1-Propanol, 150–151, 151*f*
 2-Propanol, 150–151
Propellants, 232–233
PS. *See* Persulfate (PS); Polystyrene (PS)
PSA. *See* Pressure swing adsorption (PSA)
PSM. *See* Postsynthetic modification (PSM)
PTSA. *See* Pressure-temperature swing adsorption (PTSA)

- PUREX. *See* Plutonium and Uranium Recovery by Extraction (PUREX)
- PXRD. *See* Powder X-ray diffraction (PXRD)
- 4PyC. *See* 4-Pyridinecarboxylate (4PyC)
- Pyrazolate-based MOFs, 401–402
- Pyrene-moiety-based linkers, 244
- ((Pyridin-1-ium-2-ylmethyl)ammonio) terephthalate (H₂PATP), 71, 71f
- 4-Pyridinecarboxylate (4PyC), 39
- Pyrotechnics, 232–233
- Q**
- Quartz crystal microbalance (QCM), 384
- QCM systems, 385–387
- QCM-based sensors, 387–388
- QuEChERS* method, 409
- Quenching
- effects, 74–75
- efficiency of fluorophore, 235–236
- process, 104–105
- R**
- Radioactive organic iodides, 371–373
- Radioactive oxoanion pollutants, 119–123, 122f
- Radioactive wastes, 84–89, 356
- cryptand inspired MOF for detection and adsorption, 85–86
- health and hazards, 85
- MOF-based ion traps for irreversible barium adsorption, 86–87
- sequestration by MOFs
- cesium and strontium, 358–359
- iodine, 370–373
- krypton and xenon, 373–374
- selenium and technetium, 365–369
- thorium, 364–365
- uranium, 359–364
- speciation, 85, 85f
- terbium-based MOF for selective uranium detection, 88–89
- Radionuclide sequestration
- chemical composition of nuclear fuel, 356f
- design principles of MOFs, 356–357, 357f
- radioactive waste sequestration by MOFs, 358–374
- RDX. *See* Research department explosive (RDX)
- Reactivity of chromium, 69–70
- Recognition of nitrated high energy materials, 246–262
- Recognized standard method, 407
- Recyclability, 16
- Redox process. *See* Photoinduced electron transfer (PET)
- Regenerability, 14–16
- enthalpy of adsorption, 15
- sorption kinetics, 15–16
- Regeneration process, 155
- Regenerative thermal oxidizers (RTOs), 143
- Rejection coefficient, 414
- Relative humidity (RH), 156–157, 394
- Remediation, visual detection, 83–84
- Renewable energy sources, 285
- Research department explosive (RDX), 232–233, 264
- Resonance energy transfer (RET), 253–254
- RET. *See* Resonance energy transfer (RET)
- Reverse extraction, 409
- RH. *See* Relative humidity (RH)
- Rhodamine B, 405
- Robust 3D nickel-based MOF, 367–368
- RTOs. *See* Regenerative thermal oxidizers (RTOs)
- S**
- Salt inclusion technique, 102
- SAM. *See* Self-assembled monolayer (SAM)
- Saturated metal centers (SMCs), 28–32, 38–45
- MOFs in organic ligands, 38–41
- ultramicroporous materials, 41–45
- Saturated to unsaturated molecules, 145–150
- SAW. *See* Surface acoustic wave (SAW)
- SBMOF-1, 373–374, 375f
- SBN. *See* Ag (4,4'-bipyridine)NO₃ (SBN)
- SBUs. *See* Secondary building units (SBUs)
- Scale-up feasibility, 17
- SCR. *See* Selective Catalytic Reduction (SCR)
- SCU-100, 366–367
- sorption properties of, 367f

- Secondary building units (SBUs), 218–219
- Secondary explosives, 232–233
- Selective Catalytic Reduction (SCR), 166
- Selective TNP sensing, 259–262
- Selectivity, 64
- Selenate (SeO_4^{2-}), 96–98, 123, 131
- Selenite (SeO_3^{2-}), 123, 131
- Selenium (Se), 365–369, 414–415
 - selenium-based oxoanion pollutants, 123, 124*f*
- Self-assembled monolayer (SAM), 388–389
- Self-cleaning, 323
 - MOFs based on OPE linkers, 329–331
 - bottom-up approach for fabrication, 331*f*
 - NMOF-1, 334*f*
 - solvent vapor adsorption isotherms, 333*f*
- Semivolatile organic compounds (SVOCs), 154–155
- Semtex, 233–235
- Sense dimethylamine, 399
- Sensing, 1–3
 - of anionic pollutants, 103–111
 - cyanide, 107–108
 - other anions, 109–111
 - oxoanion pollutants, 104–107
 - of inorganic cationic pollutants
 - cadmium, 65–68
 - cationic inorganic pollutants, 63
 - chromium, 68–73
 - design of metal clusters and organic linkers, 63–64
 - detection, 64
 - lead, 73–77
 - mercury, 77–84
 - radioactive wastes, 84–89
 - selectivity, 64
 - mechanism, 211–212
 - MOF-based devices for, 384–395, 385*f*
 - electrochemical response, 391–395
 - mechanochemical response, 385–389
 - optical response, 389–391
 - real-time wireless phase measurement, 386*f*
 - of nitro-aromatic compounds with MOFs in water medium, 258–262
- Sensitization, 242–244
- Separation, 155
 - factor for breakthrough experiment, 13–14
 - potential, 18
- Sequestration, 2–3, 98
 - cadmium, 65–68
 - cationic inorganic pollutants, 63
 - chromium, 68–73
 - design of metal clusters and organic linkers, 63–64
 - detection, 64
 - lead, 73–77
 - mercury, 77–84
 - radioactive wastes, 84–89
 - selectivity, 64
- SG7 dye. *See* 8-Hydroxypyrene-1,3,6-trisulfonate dye (SG7 dye)
- Shear viscosity, 23–24
- Short range energy transfer. *See* Förster resonance energy transfer (FRET)
- Short-chain hydrocarbons, 298
- SIFSIX-1-Cu, 42–43
- SIFSIX-3-Cu, 43
- SIFSIX-3-Ni, 43
- SIFSIX-3-Zn, 42–43
- “Silent killer”. *See* Carbon monoxide (CO)
- Silver(I)-3,5-bis(trifluoromethyl)-1,2,4-triazolate (AgTz), 321–322, 325
- Single-crystal structural analysis, 151–152
- Single-crystal X-ray, 70
- Single-crystal-to-single-crystal transformation mechanism, 367–368
- Single-mode optical fiber (SMF), 396
- Single-stranded DNA (ssDNA), 81
- Singlet oxygen ($^1\text{O}_2$), 220
 - generation, 220
- Size exclusion, 8
- SMCs. *See* Saturated metal centers (SMCs)
- SMF. *See* Single-mode optical fiber (SMF)
- Soda lime process, 6, 25
- Solid adsorbents, 24–28
 - chemical adsorbents/chemisorbents, 25–27
 - physical adsorbents/physisorbents, 27–28
- Solid chemisorbents, 6
- Solid-phase extraction (SPE), 405
- Solvation energy, 99
- Solvent extraction technique, 355–356
- Solvothermal synthesis, 205
- Sonochemical synthesis, 206

Sorbents

- for CO₂ capture, 23–28
 - ILs, 23–24
 - solid adsorbents, 24–28
- cost based upon substrates, 16
- performance evaluation, 17–18
- spectrum of performance parameters and criteria, 9–17, 10*f*
- CO₂ selectivity, 11–14
- feasibility of scale-up, 17
- recyclability, 16
- regenerability, 14–16
- working capacity, 10–11, 11*f*

Sorption, 89

- kinetics, 15–16

SPE. See Solid-phase extraction (SPE)**Speciation**

- cadmium, 65
- chromium, 69–70
- lead, 73–74
- mercury, 78–79
- radioactive wastes, 85

ssDNA. See Single-stranded DNA (ssDNA)**Stearic acid, 335–341****Step-by-step deposition. See Liquid-phase epitaxial growth technique (LPE growth technique)****Stern–Volmer constant (K_{sv}), 235–236, 253–254****Stockholm Convention, 203****Strontium (Sr), 85, 358–359****Structural integrity, 269****Sulfate radical (SO₄^{•-}), 220–221**

- generation, 220–221

Sulfate/sulfonic acid functionalization, 86**Sulfur dioxide, 158–160****Sulfur-containing compounds**

- crystal structure, 160*f*
- hydrogen sulfide, 160–163
- sulfur dioxide, 158–160

Superhydrophobic condition, 320–321**Superhydrophobic MOF, 319–320, 325–328****Superhydrophobicity, 322–323, 335–341****Superoleophilic condition, 320–321****Supported Ni-MOFs catalysts, 304–310**

- acid site density data, 310*t*
- liquid fuel hydrocarbons, 304–310
- SEM images for Ni-MOF crystals, 306*f*
- XRD patterns, 307*f*

Supported ZIF-67 catalysts

- for conversion of oleic acid into transport liquid fuel, 290–297
- hydrocarbons, 290–297
- liquid product distribution for studied catalysts, 293*t*
- for conversion of saturated acids into transport liquid, 297–304
- fuel hydrocarbons, 297–304

Supramolecular catalysts, early generation, 185–189

- aluminum porphyrin box highlighting nucleophilic Al-OMe moieties, 187*f*

Fe₄L₆ cage and terphenylene-based linker, 188*f*

- idealized representation of La-based porous organic polymers, 188*f*

Surface acoustic wave (SAW), 384**Surface coating process, 335–341****Surface mounted MOFs (SURMOFs), 388–389, 399–401****SVOCs. See Semivolatile organic compounds (SVOCs)****Synchrotron powder analysis, 151–152****Syngas, 20–21****Synthesis approaches for MOFs, 204–207, 205*f***

- electrochemical synthesis, 206–207
- hydrothermal and solvothermal synthesis, 205

- mechanochemical synthesis, 205–206

- microwave-assisted synthesis, 206

- sonochemical synthesis, 206

Synthetic methods, 17**T****TABD-MOF-1, 264–266, 265*f*****TABD-MOF-2, 264–266, 265*f*****TABD-MOF-3, 264–266, 265*f*****Task-specific ILs (TSILs). See Amine-modified ILs****Tb-MOF. See Terbium MOF (Tb-MOF)****TCPP. See Tetrakis(4-carboxyphenyl) porphyrin (TCPP)****TDI. See Toluene diisocyanate (TDI)****Technetium (Tc), 365–369****Technological readiness levels (TRLs), 17****TED. See Triethylenediamine (TED)**

- Temperature swing adsorption (TSA), 14–15, 14*f*
- Terbium MOF (Tb-MOF), 88, 90*f*
for selective uranium detection, 88–89
- Tertyl, 233–235
- Tetrakis(4-carboxyphenyl)porphyrin (TCPP), 116, 220
- Tetrakis[4-(carboxyphenyl)-oxamethyl]methane, 150–151
- 3,3',5,5'-Tetramethylbenzidine (TMB), 75
- 5H-Tetrazol-5-amine (5-ATZ), 264–266
- TFN. *See* Thin-film nanocomposite (TFN)
- TG-MS. *See* Thermogravimetry-mass spectrometry (TG-MS)
- Thermal annealing of MOFs, 210–211
- Thermal stability, 16
- Thermogravimetry-mass spectrometry (TG-MS), 66
- Thermometers, 77
- Thin-film nanocomposite (TFN), 414–415
- Thorium (²³²Th), 364–365
- Three-dimension (3D)
luminescent Cd-MOF, 253–254
MOFs, 269
zinc saccharate MOF, 370–371
- Thymine–thymine (T–T), 81
- Time-resolved spectroscopy-based techniques, 237
- TIPA. *See* Tri(4-imidazolylphenyl) amine (TIPA); Triisopropanolamine (TIPA)
- TIPB. *See* 1,3,5-Triisopropylbenzene (TIPB)
- TMB. *See* 3,3',5,5'-Tetramethylbenzidine (TMB)
- TNB. *See* Trinitrobenzene (TNB)
- TNP. *See* 2,4,6-Trinitrophenol (TNP)
- TNT. *See* 2,4,6-Trinitrotoluene (TNT)
- Toluene diisocyanate (TDI), 194
- Toxic anionic species, capture of, 111–130
- Toxic chemicals, MOFs for capture of
carbon monoxide, 163–165
nitric oxide, 165–168
sulfur-containing compounds, 158–163
- Toxic ethyl-*N,N*-dimethylphosphoramidocyanidate, 181
- Toxic gas detection, 395–398
- Transesterification, 285–286
- Transition metal oxides, 220–221
- Trapping of inorganic anions, 125–127
- TRI-PE-MCM-41, 26
- Tri(4-imidazolylphenyl) amine (TIPA), 264–266
- Trianionic anion, 98–99
- 4H-1,2,4-Triazol-4-amine (AT), 264–266
- 4H-1,2,4-Triazole-3,4-diamine hydrochloride (DAT), 264–266
- Triethylenediamine (TED), 371–373
- Triisopropanolamine (TIPA), 70, 70*f*
- 1,3,5-Triisopropylbenzene (TIPB), 388–389
- Trimethylamine, 193–194
- 1,3,5-Trimethylbenzene, 388–389
- 1,3,5-Trinitro-1,3,5-triazinane. *See* Research department explosive (RDX)
- Trinitrobenzene (TNB), 254–255
- 2,4,6-Trinitrophenol (TNP), 233–235
- 2,4,6-Trinitrophenylmethylnitramine.
See Tertyl
- 2,4,6-Trinitrotoluene (TNT), 232–233, 254–255
- 1,3,5-Tris(3-carboxyphenyl)benzene (H₃BTMB), 325–328
- Trivalent oxidation states, 69
- TRLs. *See* Technological readiness levels (TRLs)
- TSA. *See* Temperature swing adsorption (TSA)
- TSE. *See* Twin-screw extrusion (TSE)
- “Turn-off” responses, 262
- “Turn-on” responses, 262
- Twin-screw extrusion (TSE), 17
- Type I isotherm, 399
- U**
- UiO-66-AO. *See* Amidoxime-modified UiO-66 (UiO-66-AO)
- UiO-66-NH₂ DNA, 81–82, 81*f*
- UiO-66-PSM crystal structure, 80
- UiO-66(Zr), 217
- UiO-67, 190–192, 191*f*
- Ultramicroporous porous materials, 38
- Ultraviolet-visible (UV-Vis)
absorption, 75
diffuse reflectance, 64
- UMCs. *See* Unsaturated metal centers (UMCs)
- Unexploded ordnance (UXO), 233–235
- United States Environmental Protection Agency (US EPA), 96–98, 203

- Unsaturated metal centers (UMCs), 28–35.
See also Saturated metal centers (SMCs)
- Unsaturated molecules, 147–148
- $\text{UO}_2(\text{NO}_3)_2 \cdot 6\text{H}_2\text{O}$, 358–359
- Uranium (U), 85, 359–364
crystal structures of SZ-1, SZ-2 and SZ-3, 362*f*
ore, 84
postsynthetic route for UiO-66-AO, 360*f*
terbium-based MOF for selective uranium detection, 88–89
 UO_2^{2+} sorption, 362*f*
- Urotropine-based Ur-MOF, 259
- US Environmental Protection Agency (US EPA), 70–71, 233–235, 408
- US EPA. *See* United States Environmental Protection Agency (US EPA)
- USTC-7, 254–255
- UXO. *See* Unexploded ordnance (UXO)
- V**
- Vacuum swing adsorption (VSA), 14–15, 14*f*
- Valence, 145–146
- Vapor phase sensing of explosive materials, 235–236
- Variable-temperature PXRD, 16
- VCPs. *See* Volatile chemical products (VCPs)
- Vegetables oils, 285
- Visual detection and selective remediation, 83–84
- VOCs. *See* Volatile organic compounds (VOCs)
- Volatile chemical products (VCPs), 142–143
- Volatile gaseous radionuclides, 355–356
- Volatile organic compounds (VOCs), 142–143, 242–244, 383, 398–399, 405–407
detection of, 398–403
detrimental effects, emission sources, and removal, 142–145
MOFs for capture, 145–157
of toxic chemicals, 158–168
- Volumetric flux, 414
- Volumetric saturation uptake capacity, 10
- VSA. *See* Vacuum swing adsorption (VSA)
- W**
- Waste, 84
- Water pollution, 2–3, 127
- Water stable MOFs, 207–208. *See also* Luminescent metal–organic frameworks (LMOFs)
kinetic stability factors and examples, 208
thermodynamic stability factors and examples, 207–208
- Water vapor, 8
- Wellman–Lord process, 158
- Wenzel model, 322–323, 323*f*
- Working capacity (WC), 10–11, 11*f*, 17
- World Health Organization (WHO), 2, 82, 98, 158, 404–405
- X**
- X-ligands. *See* Extended ligands (X-ligands)
- X-ray diffraction (XRD), 76, 80, 287–288, 288*f*
- X-ray photoelectron spectroscopy (XPS), 64
- Xeon (^{133}Xe), 373–374, 374*f*, 375*f*
- Xylene isomers, 150
- Y**
- Y-LiNbO₃ piezoelectric crystals, 385–387
- Yellowcake (U_3O_8), 84
- Young's equation, 322–323
- Z**
- Zeolites, 8, 27, 100, 143–144, 150, 161
5A beads, 290
NaX, 27
- Zeolitic imidazolate frameworks (ZIFs), 38–39, 207–208, 321–322, 342
- ZIF-8, 385–387, 390–391
cage structure, 371*f*
coating, 342
films, 400*f*
layer, 295
for size-selective photo electrochemical sensing, 391–392
- ZIF-67
composite, 413
membrane, 291–292, 295
- Zinc carbonate, 65

- Zirconium (Zr)
MOF MOR-2 high Cr(VI) adsorption,
71–73
zirconium-loaded polymer resin, 131
Zr-bonded hydroxides, 116–117
Zr-MOF, 207
Zr-NDC MOF, 244
Zirconium-based MOF (Zr-MOF), 86, 87*f*,
88*f*
Zirconium(IV) phosphonate MOFs, 361
- Zn-MOF, 250–252
[Zn₄O(3-methyl-5-isopropyl-4-
carboxypyrazolate)₃]_n (Zn-MI),
152–153
[Zn₄O(3,5-dimethyl-4-carboxypyrazolate)₃]_n
(Zn-DM), 152–153
ZnHHP, 268–269
Zr-MOF. *See* Zirconium-based MOF (Zr-
MOF)
Zwitterionic linkers, 101

METAL-ORGANIC FRAMEWORKS (MOFs) FOR ENVIRONMENTAL APPLICATIONS

Edited by Sujit K. Ghosh

Associate Professor, Indian Institute of Science Education and Research (IISER), Pune, India

Presents the latest research in MOFs and the remediation of environmental pollutants.

Over the last decade, metal-organic frameworks (MOFs) have emerged as applicable real-time sorbent materials for the recognition, capture and destruction of environmentally toxic species. In *Metal-Organic Frameworks (MOFs) for Environmental Applications*, **Dr. Sujit K. Ghosh** brings together leading experts in the field for up-to-date coverage on this important topic. Chapters here present the latest research in potential materials and methods for the remediation of pressing pollution issues, including heavy-metal contaminants in water streams, radioactive waste disposal, marine oil-spillage, treatment of textile and dye industry effluents, clean-up of trace amounts of explosives in land and water, and many other topics. *Metal-Organic Frameworks (MOFs) for Environmental Applications* will provide an invaluable resource for researchers working in this area within inorganic chemistry and materials science, as well provide valuable information to graduate students studying MOFs and their applications.

Key Features

- Examines the applications of Metal-Organic Frameworks for the remediation of environmental pollutants.
- Features leading experts researching the applications of MOFs from around the world, including contributions from the United States, Europe, India and China.
- Explores possible solutions to some of today's most pressing environmental challenges, such as heavy-metal contamination in bodies of water, oil spills, and clean-up of explosives hidden in land and water.
- Provides an excellent reference for researchers and graduate students studying in the areas of inorganic chemistry, materials chemistry and environmental science.

Dr. Sujit K. Ghosh received his B.Sc. degree from Burdwan University (India) and completed his M.Sc. from Banaras Hindu University (India). He obtained his PhD degree from the Indian Institute of Technology (IIT), Kanpur (India) in 2006. After a post-doctoral stint at Kyoto University (Japan) with Prof. Susumu Kitagawa, subsequently joined the Indian Institute of Science Education and Research (IISER), Pune (India). Dr. Ghosh's group is mainly working on the development and functional studies of metal-organic frameworks (MOFs)/porous coordination polymers (PCPs) for chemical industry, energy and environmental applications. His group has published several papers in the domain of detection and sequestration of environmental toxins, and **Dr. Ghosh** has more than 100 publications (inclusive of book-chapters and reviews), with over 75 publications as independent researcher.

Science / Chemistry / Inorganic



ELSEVIER

elsevier.com/books-and-journals

ISBN 978-0-12-814633-0



9 780128 146330